

Paolo Mele · Kosmas Prassides
Chiara Tarantini · Anna Palau · Petre Badica
Alok K. Jha · Tamio Endo *Editors*

Superconductivity

From Materials Science to Practical
Applications



Springer

Superconductivity

Paolo Mele • Kosmas Prassides • Chiara Tarantini
Anna Palau • Petre Badica • Alok K. Jha
Tamio Endo
Editors

Superconductivity

From Materials Science to Practical
Applications

 Springer

Editors

Paolo Mele
SIT Research Laboratories
Shibaura Inst. Tech. (Omiya campus)
Tokyo, Japan

Kosmas Prassides
Osaka Prefecture University
Sakai
Osaka, Japan

Chiara Tarantini
Applied Superconductivity Center,
National High Magnetic Field Laboratory
Florida State University
Tallahassee, FL, USA

Anna Palau
Campus UAB
Institute of Material Science of Barcelona,
ICMAB-CSIC
Bellaterra, Spain

Petre Badica
Lab of Magnetism & Superconductivity
National Institute of Materials Physics
Magurele, Romania

Alok K. Jha
Department of Materials Science and
Engineering
Kyushu Institute of Technology
Kitakyushu, Japan

Tamio Endo
Japan Advanced Chemicals
Atsugi, Japan

ISBN 978-3-030-23302-0 ISBN 978-3-030-23303-7 (eBook)
<https://doi.org/10.1007/978-3-030-23303-7>

© Springer Nature Switzerland AG 2020

This work is subject to copyright. All rights are reserved by the Publisher, whether the whole or part of the material is concerned, specifically the rights of translation, reprinting, reuse of illustrations, recitation, broadcasting, reproduction on microfilms or in any other physical way, and transmission or information storage and retrieval, electronic adaptation, computer software, or by similar or dissimilar methodology now known or hereafter developed.

The use of general descriptive names, registered names, trademarks, service marks, etc. in this publication does not imply, even in the absence of a specific statement, that such names are exempt from the relevant protective laws and regulations and therefore free for general use.

The publisher, the authors, and the editors are safe to assume that the advice and information in this book are believed to be true and accurate at the date of publication. Neither the publisher nor the authors or the editors give a warranty, express or implied, with respect to the material contained herein or for any errors or omissions that may have been made. The publisher remains neutral with regard to jurisdictional claims in published maps and institutional affiliations.

This Springer imprint is published by the registered company Springer Nature Switzerland AG.
The registered company address is: Gewerbestrasse 11, 6330 Cham, Switzerland

Scope of the Book

Superconducting materials are an enabling technology for future sustainable energy production, transport and storage, as well as for medical applications, novel electronic devices and fundamental research.

Over the last 30 years, several new medium- and high-temperature superconducting materials have been discovered (cuprates, MgB_2 , Fe-based pnictides), while the materials science of traditional low-temperature superconductors, including the classical metallic superconductors Nb-Ti and Nb_3Sn , has progressed. Up to now, the majority of applications are still based on low-temperature superconductors that require cooling by liquid helium. Great efforts are still required to improve the existent or discover new high-temperature superconducting materials for practical applications, as well as to develop more effective materials processing, microfabrication and cryogenic technologies. Moreover, identifying and improving vortex pinning mechanisms in superconductors is one of the major challenges nowadays for its relevance in applications requiring manipulation of flux quanta or enhanced critical currents.

This book aims to bridge the gap between materials science and applications of superconductors while being aware of the importance of understanding the fundamental phenomena underlying these materials. The purpose is to collect the state-of-the-art techniques and methodologies involved in superconducting materials growth, characterization and processing.

This book will give a deep insight in the intriguing science of superconducting materials. It serves as a fundamental information source on the actual techniques and methodologies involved in superconducting materials growth, characterization and processing. This book involves widespread contributions on several categories of medium- and high-temperature superconducting materials: cuprate oxides, borides and iron-based chalcogenides and pnictides. Synthesis, characterization and processing of superconducting materials will be covered, as well as the nanoengineering approach to tailor the properties of the used materials at the nanoscale level. Space will be dedicated to the important topics of grain boundaries effects and interfacial superconductivity. The state of the art of films added with artificial pinning centres will also be discussed.

This book will be invaluable to the experts to consolidate their knowledge and provide insight and inspiration to beginners wishing to learn about superconducting materials.

Introduction

This book originates from the Symposium A-3 ‘Superconducting materials and applications’ organized in the framework of the conference IUMRS-ICAM 2017 (International Union of Materials Research Societies—International conference on Advanced materials) from August 27 to September 1, 2017, at Yoshida Campus of Kyoto University, in Kyoto, Japan (<http://www.iumrs-icam2017.org/>).

The Symposium A-3 (<http://www.iumrs-icam2017.org/program/forums/a-3.html>) focused on state of the art of superconductivity, from materials science to applications. Its wide scope covered a variety of topics: metals, alloys, oxides, sulphides, selenides, and Fe-based superconducting materials, in the form of thin films and bulk, single crystals; considering synthesis and characterization, devices development, theory and applications, Symposium A-3 was highly successful, extending for 4 days (Monday–Thursday), with 19 sessions/in parallel (one of the only three symposia in IUMRS-ICAM organized with parallel sessions).

Symposium A-3 counted 79 talks (10 keynotes—49 invited) and 12 posters. High level of presentations and lively discussion contributed to the quality of the symposium.

Social part was also included, with a symposium dinner on August 29 on the roof garden of a famous hotel on Kamo River, the pulsing heart of historical Kyoto City.

Symposium A-3 was one of the ‘Bilateral MRS-J/E-MRS’ symposia at IUMRS-ICAM 2017. Financial support from MRS-J and endorsement by THO (Team Harmonized Oxides, Japan) are acknowledged.

Many outstanding oral and invited presentations were given during the symposium. The symposium organizers were inspired by them to disclose such excellent papers to the widest scientific community. This is a reason why we invited our distinguished colleagues to share their results and we publish this book entitled *Superconductivity: From Materials Science to Practical Applications*.

Tokyo, Japan
Osaka, Japan
Tallahassee, FL, USA
Barcelona, Spain
Magurele, Romania
Kitakyushu, Japan
Mie, Japan
May 9, 2019

Paolo Mele
Kosmas Prassides
Chiara Tarantini
Anna Palau
Petre Badica
Alok K. Jha
Tamio Endo

Contents

1 Targeted Selection and Characterisation of Contemporary HTS Wires for Specific Applications	1
Stuart C. Wimbush	
2 Pinning Efficiency of Artificial Pinning Centers in Superconductor Nanocomposite Films	29
Judy Wu, Bibek Gautam, and Victor Ogunjimi	
3 Control of Vortex Pinning in YBCO Thin Films by Incorporating APCs Through Surface Modified Target Approach	53
Alok K. Jha and Kaname Matsumoto	
4 Progress in Thick Film 2G-HTS Development	73
Goran Majkic	
5 Superconducting $\text{YBa}_2\text{Cu}_3\text{O}_{7-\delta}$ Nanocomposite Films Using Preformed ZrO_2 Nanocrystals via Chemical Solution Deposition	133
H. Rijckaert and I. Van Driessche	
6 High Vortex Activation Energies in the AC Magnetic Response of Superconductors Close to the DC Irreversibility Line	169
Lucica Miu, Ion Ivan, Alina M. Ionescu, Adrian Crisan, Dana Miu, Traian Petrisor, and Paolo Mele	
7 An Atomic-Scale Perspective of the Challenging Microstructure of $\text{YBa}_2\text{Cu}_3\text{O}_{7-x}$ Thin Films	189
Bernat Mundet, Roger Guzmán, Elena Bartolomé, Andrew R. Lupini, Steven Hartman, Rohan Mishra, and Jaume Gázquez	
8 Growth, Properties, and Device Fabrication of Iron-Based Superconductor Thin-Films	213
Hidenori Hiramatsu and Hideo Hosono	

9	Future Potential of New High T_c Iron-Based Superconductors	243
	Shiv J. Singh and Paolo Mele	
10	Grain Boundaries in Fe-Based Superconductors	269
	Jens Hänisch and Kazumasa Iida	
11	Control of the Critical Current Density Through Microstructural Design by Ho_2O_3 and Te Co-addition into MgB_2 Processed by Ex Situ Spark Plasma Sintering	303
	P. Badica, G. Aldica, M. Burdusel, M. Grigoroscuta, A. M. Ionescu, V. Sandu, S. Popa, M. Enculescu, I. Pasuk, and A. Kuncser	
12	Superconductivity in the Two-Dimensional Electron Gas at Transition Metal Oxide Interfaces	325
	J. C. Nie	
13	Prospects of Superconducting Magnet Technology in the Medical Field: A New Paradigm on the Horizon?	353
	Santosh Miryala	
	Editorial Note	361
	Index	363

Contributors

G. Aldica National Institute of Materials Physics, Magurele, Romania

P. Badica National Institute of Materials Physics, Magurele, Romania

Elena Bartolome Escola Universitària Salesiana de Sarrià (EUSS), Barcelona, Spain

M. Burdusel National Institute of Materials Physics, Magurele, Romania

Adrian Crisan Laboratory of Magnetism and Superconductivity, National Institute of Materials Physics, Magurele, Romania

M. Enculescu National Institute of Materials Physics, Magurele, Romania

Bibek Gautam Department of Physics and Astronomy, University of Kansas, Lawrence, KS, USA

Jaume Gazquez Department of Superconductivity, Institut de Ciència de Materials de Barcelona (ICMAB-CSIC), Barcelona, Spain

M. Grigorescu National Institute of Materials Physics, Magurele, Romania

Roger Guzman Department of Superconductivity, Institut de Ciència de Materials de Barcelona (ICMAB-CSIC), Barcelona, Spain

Jens Hänisch Institute for Technical Physics, Karlsruhe Institute of Technology, Eggenstein-Leopoldshafen, Germany

Steven Hartman Institute of Materials Science and Engineering, Washington University in St. Louis, St. Louis, MO, USA

Hidenori Hiramatsu Laboratory for Materials and Structures, Institute of Innovative Research, Tokyo Institute of Technology, Yokohama, Japan
Materials Research Center for Element Strategy, Tokyo Institute of Technology, Yokohama, Japan

Hideo Hosono Laboratory for Materials and Structures, Institute of Innovative Research, Tokyo Institute of Technology, Yokohama, Japan
Materials Research Center for Element Strategy, Tokyo Institute of Technology, Yokohama, Japan

Kazumasa Iida Department of Materials Physics, Nagoya University, Chikusa, Nagoya, Japan

Alina M. Ionescu Laboratory of Magnetism and Superconductivity, National Institute of Materials Physics, Magurele, Romania

Ion Ivan Laboratory of Magnetism and Superconductivity, National Institute of Materials Physics, Magurele, Romania

Alok K. Jha Department of Materials Science and Engineering, Kyushu Institute of Technology, Kitakyushu, Japan

A. Kuncser National Institute of Materials Physics, Magurele, Romania

Andrew R. Lupini Institute for Functional Imaging of Materials Oak Ridge National Laboratory, Oak Ridge, TN, USA
Materials Sciences and Technology Division Oak Ridge National Laboratory, Oak Ridge, TN, USA

Goran Majkic Department of Mechanical Engineering, Texas Center for Superconductivity, Advanced Manufacturing Institute, University of Houston, Houston, TX, USA

Kaname Matsumoto Department of Materials Science and Engineering, Kyushu Institute of Technology, Kitakyushu, Japan

Paolo Mele SIT Research Laboratories, Shibaura Inst. Tech. (Omiya campus), Tokyo, Japan

Santosh Miryala Faculty of Arts and Science, University of Toronto, Toronto, ON, Canada

Rohan Mishra Institute of Materials Science and Engineering, Washington University in St. Louis, St. Louis, MO, USA
Department of Mechanical Engineering and Materials Science, Washington University in St. Louis, St. Louis, MO, USA

Dana Miu Laser Department, National Institute of Laser, Plasma, and Radiation Physics, Magurele, Romania

Lucica Miu Laboratory of Magnetism and Superconductivity, National Institute of Materials Physics, Magurele, Romania

Bernat Mundet Department of Superconductivity, Institut de Ciència de Materials de Barcelona (ICMAB-CSIC), Barcelona, Spain

J. C. Nie Department of Physics, Beijing Normal University, Beijing, People's Republic of China

Victor Ogunjimi Department of Physics and Astronomy, University of Kansas, Lawrence, KS, USA

I. Pasuk National Institute of Materials Physics, Magurele, Romania

Traian Petrisor Center of Superconductivity, Spintronics, and Surface Science, Technical University of Cluj-Napoca, Cluj-Napoca, Romania

S. Popa National Institute of Materials Physics, Magurele, Romania

H. Rijckaert Department of Chemistry, Ghent University, Ghent, Belgium

V. Sandu National Institute of Materials Physics, Magurele, Romania

Shiv J. Singh Clarendon Laboratory, Department of Physics, University of Oxford, Oxford, UK

I. Van Driessche Department of Chemistry, Ghent University, Ghent, Belgium

Stuart C. Wimbush The Robinson Research Institute of Victoria University of Wellington, Wellington, New Zealand

Judy Wu Department of Physics and Astronomy, University of Kansas, Lawrence, KS, USA

About the Editors

Paolo Mele is currently Professor at SIT Research Laboratories, in Omiya campus of Shibaura Institute of Technology, Tokyo, Japan. He obtained a Master's degree in Chemistry and PhD in Chemical Sciences at University of Genoa (Italy). In 2003 he moved to ISTEC-SRL in Tokyo to study melt-textured ceramic superconductors. Then he worked as Postdoc at Kyoto University (JSPS fellowship) from 2004 to 2007, at Kyushu Institute of Technology (JST fellowship) from 2007 to 2011, at Hiroshima University (as Lecturer) from 2011 to 2014 and at Muroran Institute of Technology (as Associate Professor) from 2015 to 2018 before reaching his current position. His research interests include materials for energy and sustainable development (superconductors and thermoelectrics); fabrication and characterization of thin films of oxides, ceramics and metals; study of the effect of nanostructuration on the physical properties; thermal transport; and vortex matter. He is the author of more than 100 papers in international scientific journals and 4 book chapters and has 2 patents and has contributed to hundreds of communications at international conferences. He edited three books for Springer.

Kosmas Prassides was born in Kavala, Greece, and read Chemistry at Oxford University where he also completed his doctoral research on inorganic mixed valency compounds under the supervision of Professor P. Day FRS. He was then the Drapers' Research Fellow at St. Anne's College, Oxford, working closely with Professor P.N. Schatz (University of Virginia) on the development of the PKS theoretical model for mixed valency systems. Following a spell as Assistant Professor of Chemistry at the University of Crete, Greece, he returned in 1989 to the UK at the University of Sussex where he remained until 2004 and he was successively Lecturer, Reader and Professor of Solid State Chemistry. In 2005, he took up a Chair in Materials Chemistry at the Department of Chemistry, Durham University. In October 2014, he relocated to Japan as a Professor at Tohoku University and Principal Investigator at the Advanced Institute for Materials Research (WPI-AIMR). In October 2018, he accepted a Chair in Materials Science at the Graduate School of Engineering, Osaka Prefecture University. His research interests are multidisciplinary and encompass a range of structural, magnetic and electronic

problems in modern materials, straddling the areas of condensed matter physics and chemistry. His primary focus is currently on the study of strongly correlated electron systems, which typically display remarkable electronic properties that challenge existing theory for satisfactory explanations. The delicate balance between localized and itinerant behaviour related to the strongly correlated nature of the systems and the metallic, insulating and superconducting states lies at the heart of his ongoing research. He has been using core chemical approaches to access unusual structures and electronic, conducting and magnetic ground states and probe the physics in key materials, especially metal fulleride solids. He has advanced the understanding of molecular superconductivity and magnetism and the generic problem of the metal-Mott insulator transition, unveiling the fullerides as model members of the high-Tc superconductivity family, potentially holding the key to the understanding of the prerequisites for high-Tc superconductivity when electron correlation is important.

Chiara Tarantini is a Staff Research Faculty Member of the Applied Superconductivity Center at the National High Magnetic Field Laboratory, Florida State University in Tallahassee, Florida, USA. She was trained as a Condensed Matter Physicist at the University of Genoa, Italy, and obtained her PhD in 2007. Her research activities have been focused on the investigation of numerous superconducting materials, such as MgB_2 , Nb_3Sn and other A15 phases, Fe-based superconductors and $YBa_2Cu_3O_{7-\delta}$. Her interests span from fundamental aspects, like multiband and unconventional superconductivity, to properties of interest for applications, like vortex pinning optimization, uniformity of superconducting samples, increase of the upper critical field and irreversibility field and enhancement of the critical current density. She was awarded with the 2014 Lee Osheroff Richardson Science Prize for research in physical science.

Anna Palau is currently a Tenured Scientific at the Institute of Materials Science, ICMAB-CSIC, Barcelona, Catalonia, Spain. She received a BS in Physics (1999), BS in Materials Science (2000) and PhD in Materials Science (2005) at Barcelona and performed a Postdoctoral stay (2005–2007) at the University of Cambridge (UK). Her scientific interest includes functional properties of oxides with focus on superconducting and magnetic materials. Her main current research activity is devoted to study the outstanding physical properties of functional oxides and vortex matter physics, with strong effort in the opportunities that nanotechnology can bring to high temperature superconductors. She has co-authored more than 80 peer-reviewed scientific papers and 3 book chapters and holds 3 licensed patents. She has delivered more than 30 invited talks in international workshops and conferences and participated in more than 25 national and international projects. She is actually Master Lecturer on Advanced Nanoscience and Nanotechnology at UAB (Barcelona), Member of the Editorial Board of *Scientific Reports* and Technical Editor of *IEEE Transactions on Applied Superconductivity*. Researcher ID: C-2947-2014.

Petre Badica is a Senior Scientist 1st degree (Res. Prof.) at the National Institute for Materials Physics, Magurele, Romania. He graduated MSc in 1992 from Politehnica

University of Bucharest and was awarded a PhD in Engineering Sciences from the National Technical University of Ukraine, 'Kiev Polytechnical Institute', in 1996. His interest is in technology of different materials by traditional and unconventional methods and in their applied physics. He published more than 210 articles. He is a former JSPS-STA, NIMS, NEDO, MANA and Alexander von Humboldt Fellow and Visiting Professor of Nanyang Technological University, Singapore, and Tohoku University, Japan.

Alok K. Jha is currently a tenure-track Assistant Professor at the Department of Materials Science and Engineering, Kyushu Institute of Technology, Japan. He earned his Master of Science in Physics at Tilka Manjhi (TM) Bhagalpur University, Bhagalpur, India, and PhD in Physics at IIT Delhi, New Delhi, India. After completing his PhD in the year 2012, he moved to Kyushu Institute of Technology for postdoctoral assignment in Prof. Kaname Matsumoto's research group and has been there ever since. During his postdoctoral tenure, he studied the vortex pinning properties of YBCO thin films, incorporating different kinds of artificial pinning centres. His current focus is on using hybrid artificial pinning centres to control and improve the angular variation of critical current density in YBCO thin films. He has written several articles in journals of repute and has given many talks on this issue in several international conferences.

Tamio Endo holds PhD (Kyoto University, Japan) and MsD (Gifu University, Japan) degrees. He is Emeritus Professor at Mie University (Japan), Gifu University Special Researcher (Japan), Honorary Professor of Southwest Jiaotong University (China) and Visiting Researcher at University of California, San Diego, 1995 (USA). He is currently Special Adviser at Japan Advanced Chemicals, Atsugi (Japan), after being a Gifu University Special Researcher (Japan). His research interests include oxide thin films, heterostructures, plasma effects and bonding of polymer films. He has been part of many international academic projects such as the Japan-India Cooperative Science Program. He has been Organizer and Plenary Speaker of many of international conferences and has given many foreign university guest talks and a Representative of 'Team Harmonized Oxides'.

Chapter 1

Targeted Selection and Characterisation of Contemporary HTS Wires for Specific Applications



Stuart C. Wimbush

1.1 Present Status of Large-Scale Applications of HTS

Large-scale HTS applications have now been successfully demonstrated in almost every proposed sphere [1]: e.g., motors [2], fault current limiters [3], power cables [4], maglev trains [5], magnetic [6] and flywheel [7] energy storage systems, transformers [8], wind generators [9], research (beamline [10] and high-field [11]) magnets, magnetic resonance imaging [12] and nuclear magnetic resonance [13] devices. About the only outstanding application that has yet to be demonstrated is the fusion reactor, and here too device construction and testing is already underway [14, 15]. The field of applied, technological superconductivity is now moving beyond these preliminary demonstrators to the industrial development of commercially viable machines and devices. At this stage, it is no longer proof of concept that governs conception but rather proof of viability. New drivers emerge such as cost-effectiveness, reliability, practicality and competitiveness with incumbent technologies.

At the same time, the number of commercial HTS wire manufacturers active in the industry has grown quite considerably in recent years and continues to grow. Whereas in the past, choice was limited to three or four established manufacturers, often operating at capacity, now there are a dozen advertising the ability to supply significant quantities of wire on a commercial basis, with a similar number in a pre-production ramp-up phase. It must be said, however, that total production capacity remains well below projected demand, meaning that supply issues continue to play a role.

S. C. Wimbush (✉)

The Robinson Research Institute of Victoria University of Wellington, Wellington, New Zealand
e-mail: stuart.wimbush@vuw.ac.nz

In this context, a new requirement arises, which is for the informed and targeted selection of appropriate wire for a given project in the face of a broad selection of widely varying and poorly specified material combined with uncertainty of supply. Where a significant investment decision is to be made on the open market, rather than a particular wire supplier being pre-specified under the terms of a joint research programme, the need to confirm that performance requirements will be satisfied and to secure the optimum economic outcome becomes an important task in the project. Even for a relatively small build of any practical device, wire cost at present prices constitutes a significant fraction of the total build cost so the saving to be made by not over-specifying the wire cannot be overlooked, and indeed may make the difference in viability of the project as a whole. This chapter examines the benefits of detailed project-specific wire characterisation, and the opportunities that targeted wire selection offers to improve the efficiency and economy of device designs.

1.2 Wire Characterisation Systems

The requirement outlined above for more detailed wire characterisation than is commonly provided by suppliers at this time in terms of the critical current, I_c , under different conditions of temperature, magnetic field and field angle, targeting the specific application, has begun to be recognised [16, 17]. The high performance of contemporary HTS wires presents a particular challenge due to the multiple kiloamps of current now needed to adequately characterise full wires under the conditions of interest for many applications. The majority of characterisation systems described in the literature [18–21] continue to rely on liquid helium for their operation; however, this limits both their speed of operation and their ultimate cost effectiveness, with even the best-designed systems [20] consuming upwards of 0.5 l of liquid helium per I_c data point acquired.

At the Robinson Research Institute, we have developed and refined our own in-house HTS wire critical current measurement system [22], shown in Fig. 1.1, over a period of several years. Our system relies on a cryocooled 8 T split-pair HTS magnet to provide a horizontal magnetic field within which out-of-plane sample rotation is relatively easily accomplished whilst accommodating the hefty current leads required to convey kiloamps of current to the sample without excessive heating. A circulating cryocooled helium gas sample cooling circuit likewise provides continuous liquid cryogen free operation down to a base temperature (with sample and current leads inserted) presently around 12 K. Full automation of the measurement routine allows for long but efficient characterisation runs generating upwards of 100 distinct IV curve measurements per hour, with automatic determination of I_c and n -value at each point. Sample exchange can conveniently be performed while the system remains cold and is typically completed within 30 min, opening the possibility of high-throughput characterisation of many wire segments under more highly targeted (but still application-relevant) conditions.

Fig. 1.1 The Robinson Research Institute's SuperCurrent I_c measurement system enables the automated electrical characterisation of full HTS wires at temperatures down to 15 K, magnetic fields up to 8 T, and currents up to 1 kA. Complete 360° rotation of the sample within the magnetic field allows detailed characterisation of the wire anisotropy in addition to the more common temperature and field dependences of the critical current



All of the experimental data presented here was acquired on this system, and much of it is available to download freely from our publicly accessible HTS wire database [23] located at <https://www.victoria.ac.nz/robinson/hts-wire-database>. By making this exemplary data widely available, it is our intention to encourage superconducting device designers to investigate how their designs could be modified to operate more efficiently on the basis of the availability of this information, and in the remainder of this chapter, we address some of the approaches successfully employed to achieve this, illustrated by a number of case studies highlighting specific aspects of the actual device design process.

1.3 Wire Characterisation Under Different Regimes

Understanding the behaviour of different wires under different regimes of operating parameters is central to the efficient design of superconducting devices, with the range of variation across commercially available materials being extremely large and different wires being optimised in often only partially understood ways for different nominal applications that may not tally particularly well with actual real-

world conditions. The primary operating conditions of relevance to superconducting materials are the temperature and the magnetic field. Due to the inherent anisotropy of the HTS materials, as well as the intentional introduction of microstructural defects aimed at enhancing performance through improved flux pinning, the direction of the magnetic field relative to the crystal structure of the superconductor is also an essential parameter, often equally as significant as its magnitude. Each of these parameters—temperature, magnetic field and field angle—will be addressed in turn.

1.3.1 Temperature Regime

The most basic question to be asked of any potential application is its intended temperature of operation. If a device is to operate immersed in an open bath of liquid nitrogen then this fixes this parameter at the most commonly reported temperature of 77 K. In practice, this arrangement would be rare for a practical device, however. More common is that the application must be considered to exist across a range of temperatures, for example in the transition from cryogenic to room temperature in the gas above the bath, or in the case of sub-cooled liquid nitrogen in the temperature range from the nitrogen triple point of 63 K at the coolest part of the bath to 77 K at its warmest. Even an open liquid nitrogen bath will vary in temperature by up to a few degrees depending on the ambient air pressure (and therefore altitude).

Where an electrical cryocooler is to be used, the situation may be turned on its head, with the operating temperature being dictated instead by the requirements of the application, and an appropriately powered cryocooler being specified on this basis. In this situation also, it is appropriate to speak of a range of temperatures, since in powered (rather than passive) applications, accommodations must be made for the varying load on the cryocooler, and in practical terms also for the variation in cryocooler performance between maintenance periods.

The establishment of the intended operating temperature regime is a crucial first step in the decision-making process regarding wire selection, immediately demarcating a number of broad boundaries. Common choices include 77 K liquid nitrogen, 65 K sub-cooled liquid nitrogen, 30 K cryocooled, 10 K cryocooled and 4.2 K liquid helium, but the choices are essentially limitless, to be dictated by the other design constraints imposed on the application.

It is now well established, nor is it surprising given the complexity of the flux pinning process that ultimately governs the wire I_c as well as the vast range of advanced processing techniques employed in wire manufacture, that it is impossible to predict purely on the basis of, for example, 77 K performance, what the performance of a particular 2G HTS wire will be at a distant temperature, for example 30 K, and that even extrapolations over relatively limited temperature ranges from 77 K to 65 K are fraught. The most immediate example of this has been presented in [24], where two wire samples are compared, one of which performs

better at 77 K and the other at 20 K. In light of the potential for such a reversal in relative performance, it is evident that given no knowledge of a wire other than its 77 K performance, no reliable prediction can be made of its performance at another temperature, or under a given magnetic field. It is important to recognise that where such correlations have been demonstrated to exist [25], these have been between pairs of carefully selected temperature/field combinations at a single field orientation and amongst samples of a highly similar nature, for example identically prepared materials differing only in degree of chemical doping. No such correlation is generally applicable, nor could it ever be.

The reason for this is clear: the wire performance is determined by the flux pinning effectiveness, and different pinning centres have strengths that vary in dependence upon the temperature and magnetic field in different ways. It will only ever, therefore, be possible to correlate wire performance across temperatures in samples that possess the same population of pinning defects (both controlled and uncontrolled), and this is what is seen in practice. For a reliable evaluation of the performance of an arbitrary sample, there is simply no alternative to measuring its performance within the proposed operating temperature regime (see **Case Study: Traction Transformer**).

An inadequately resolved matter confronting the research community at the present time is the identification and implementation of an effective low-temperature pinning defect. All of the most prominent pinning centres, for example BaZrO_3 nano-columns, lose their effectiveness at low temperatures [26]. Is this merely a result of the relative ease with which experimental investigations can be performed at 77 K encouraging greater empirical effort in this regime, is it that pre-existing natural sources of pinning become stronger at low temperatures as vortices stiffen, obscuring attempts to further strengthen the pinning force, or is there a fundamental lack of effective low-temperature pinning structures? The answers to these questions are presently unclear.

To date, the most promising route to low-temperature performance enhancement has been using the method of ion irradiation to create flux pinning damage track defects running through the material [26, 27]. The direct applicability of this method to industrial production is questionable, but not to be ruled out [28]. Most likely, an improved understanding of low-temperature flux pinning processes is required to be derived from such studies, before more practical processing techniques can be developed to generate the appropriate defect structures in a more facile manner.

Case Study: Traction Transformer

The development of superconducting transformers for use on trains offers the particular advantage of reduced component weight, in addition to the increased efficiency and reduced fire risk that is of benefit to all types of

(continued)

superconducting transformers. A transformer is an inherently AC device, and consequently the design of any practical superconducting transformer is centred on the management of AC loss. If the aim is to achieve an efficiency target of 99% in a transformer that may have a power rating of 6.5 MVA, for example, then it is immediately apparent upon taking into account a realistic cooling penalty (ratio of cooling power required at room temperature to extract a given amount of heat at low temperature) of ~ 15 at 65–77 K that the total losses (AC loss plus thermal load due to current leads, etc.) cannot be allowed to exceed 4 kW. Furthermore, not only the transformer unit itself, but also its associated cooling system must meet the stringent design limitations of overall size and weight. At the same time, in contrast to the high-field electromagnets that form the core of many superconducting devices, the magnetic fields experienced by the superconductor in this application lie squarely at the low end of the scale, unlikely to exceed about 0.5 T. Given the low field requirement in combination with the intrinsically mobile nature of the application, a cooling system based on liquid nitrogen or operating at the higher end of the temperature scale in order to minimise the cooling penalty and reduce the complexity of the cooling system is most practicable.

A survey of the temperature-dependent performance of commercial wires available in the quantity (~ 15 km) required to accomplish the build (Fig. 1.2)

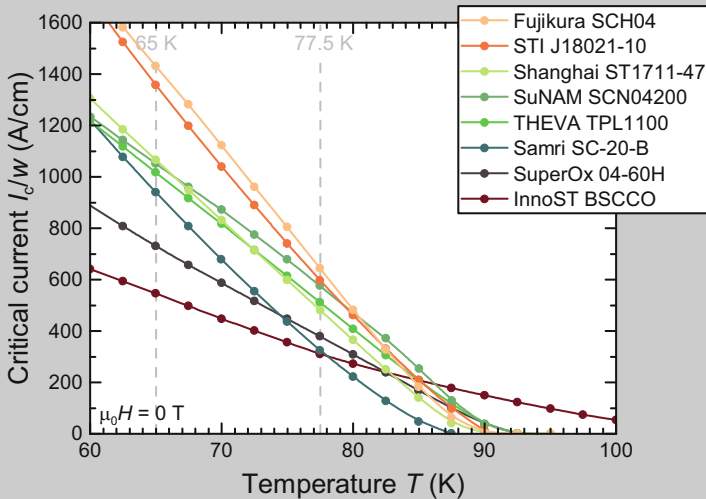


Fig. 1.2 Self-field temperature-dependent performance comparison of commercial HTS wires sourced from various manufacturers in the sub-cooled liquid nitrogen temperature range, highlighting that in general different wires may perform better at 65 K than those that perform best at 77 K

(continued)

indicated that even the best available wires provided insufficient performance to operate at 77 K, and so an operating environment of sub-cooled liquid nitrogen extending down to 65 K was adopted. It is notable that even this relatively small variation in operating temperature already introduces a different ranking to the relative performance of the wires than would be obtained at the commonly specified temperature of 77 K.

To further qualify the potential wires for this application, and to facilitate detailed and accurate modelling of the AC loss critical to successful operation of the device, the full angle dependence of the critical current of each wire under consideration was determined at fine intervals throughout the relevant field range from 0 T to 0.5 T, with a particular focus on fields below 0.2 T where in particular, the in-plane performance of the wires varies rapidly. From these full angle dependencies were extracted the minimum and maximum I_c values at each field, as shown for the intended operating temperature of 65 K in Fig. 1.3. In most cases, these minimum and maximum I_c values correspond with those obtained for fields oriented parallel and perpendicular to the wire direction, respectively, but in some cases, there were significant deviations (see Sect. 1.3.3).

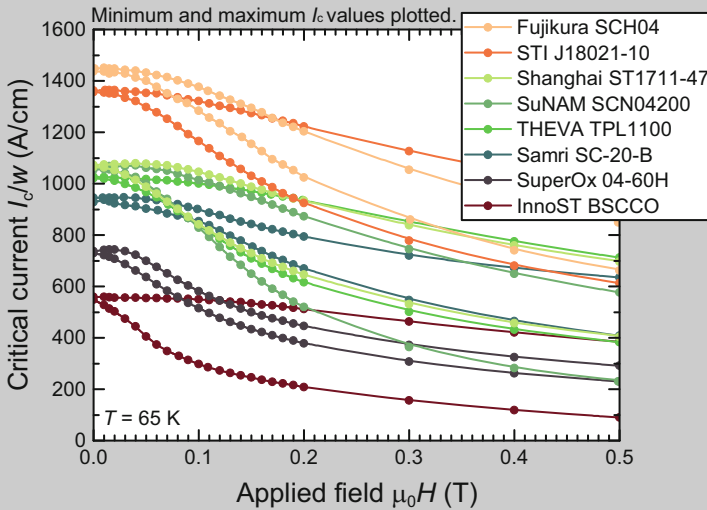


Fig. 1.3 Low-field performance comparison of available commercial HTS wires sourced from various manufacturers at the temperature of sub-cooled liquid nitrogen (65 K). Minimum and maximum I_c values extracted from full angle dependencies under each condition are plotted in order to encompass the full range of performance at each field value

(continued)

As detailed in Sect. 1.3.2, careful examination of the behaviour of widely available superconducting wires in the low-field regime reveals a large array of hitherto underexplored features and subtleties that should be taken into account in any data-based design.

On the basis of this data, we conclude that Fujikura and STI wires offer a level of performance under the conditions of relevance to this application that lies significantly ahead of other contenders. A number of other suppliers then occupy the mid-range, although here the situation is not so clear-cut since the critical region of the transformer is going to be at the end turns of the windings, where significant out-of-plane fields will impinge on the wire, and the performance of some of the wires under these conditions is seen to be poorer in spite of better performance overall.

Ultimately, a full numerical model serves to indicate whether a given wire performance is adequate to realise successful operation of the device, and from there an economic decision can guide the purchasing choice.

1.3.2 *Field Regime*

A relatively common form of wire characterisation is the field dependence of I_c measured at a particular temperature (most commonly 77 K), usually for fields applied both perpendicular and parallel to the plane of the tape (Fig. 1.4). This is the sort of product data that the more established wire manufacturers typically provide (for a good example, see [30]). The choice of the two orthogonal field orientations is based on the supposition that these provide some measure of extreme (minimum and maximum) values, but this is a hangover from the specific case of 1G (BSCCO) wire, where it can broadly be relied upon to be true [31]. In the case of 2G (REBCO) wire, this supposition, unchecked, can be highly misleading as will be evidenced in Sect. 1.3.3. In particular, the perpendicular field I_c , initially observed to represent the minimum value, has over time become a metric for performance enhancement through the introduction of artificial pinning centres, but the consequent focus on enhancements in this specific field direction has tended to overlook the fact that the minimum I_c has shifted elsewhere, and that little usable performance enhancement may actually have been achieved (see Fig. 1.5). Instead, it can be preferable in the case where a visual overview of comparative wire performance is required to plot the true minimum and maximum values (as shown, for example, on Fig. 1.3), although this does typically require the measurement of the full angular dependence of I_c under each condition to reliably determine, and it runs the risk of introducing its own overestimations of performance if it is subsequently assumed that the minimum occurs for fields applied in the perpendicular direction, and that the I_c experienced when fields are oriented in other directions will be higher.

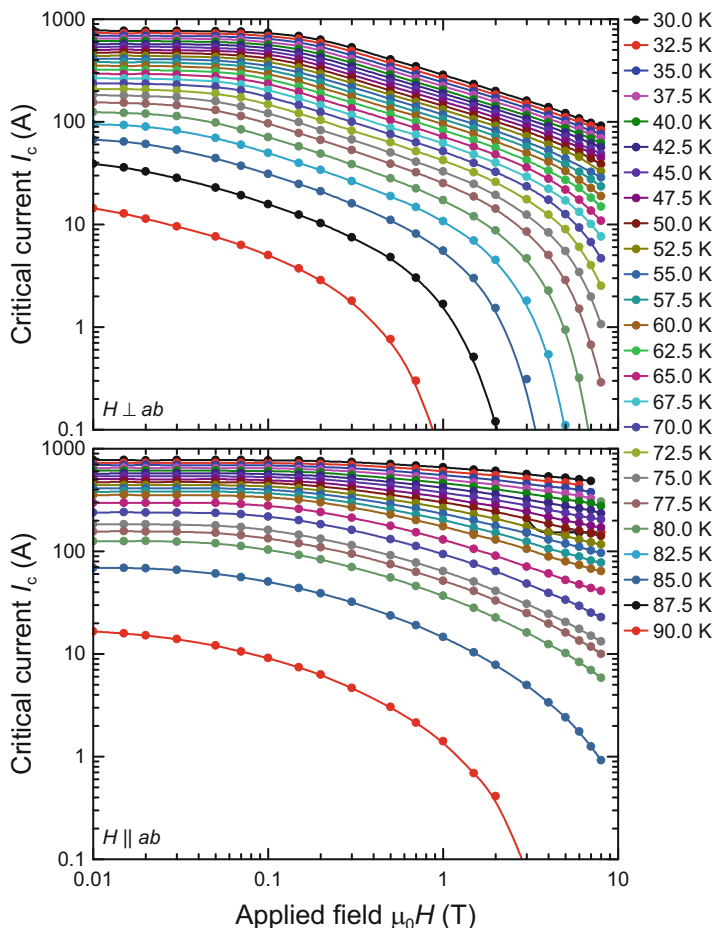


Fig. 1.4 Field dependence of the critical current of a SuperOx 2G HTS wire sample over a range of temperatures (lowest temperature corresponding to highest I_c) for fields applied perpendicular (upper panel) and parallel (lower panel) to the plane of the wire. A pronounced sensitivity to out-of-plane fields is evident on this double logarithmic scale, common to most 2G wires. Data from [29]

Out-of-Plane Field Hysteresis

The basic behaviour exhibited by the field dependences is that as the field is increased, and correspondingly the number of flux vortices present within the superconductor increases, the strongest available pinning sites become occupied and successively weaker pinning sites begin to be populated, leading to a reduction in I_c to higher fields until the irreversibility field is reached and I_c drops to zero. At the lowest fields and lower temperatures, grain boundary derived limitation of the superconducting cross-section may dominate the behaviour, resulting in a plateau region of constant I_c [33].

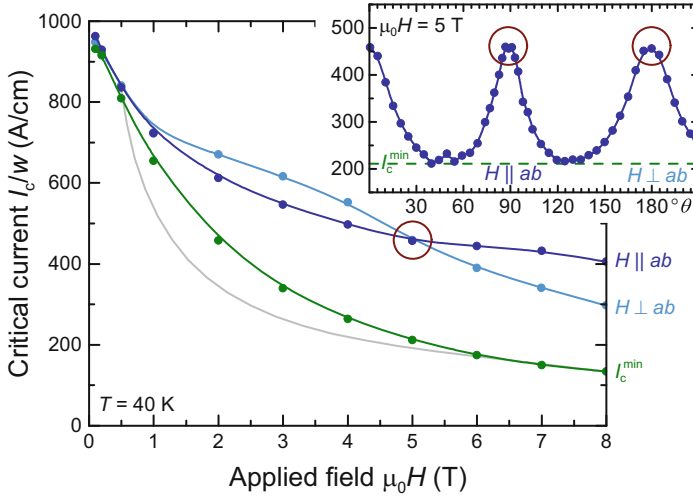
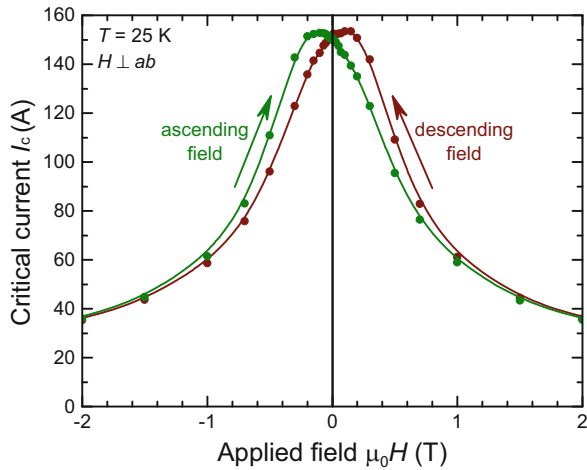


Fig. 1.5 Field dependence of the critical current of an American Superconductor 2G HTS wire insert with strongly enhanced c -axis pinning introduced via ion irradiation, highlighting how a focus on parallel and perpendicular field behaviour can obscure the true envelope of performance of the wire as accurately represented by the minimum I_c value. The grey curve indicates the original (unirradiated) minimum I_c , showing the true extent of the performance enhancement due to irradiation. The angle dependence of I_c (inset) under the highlighted condition shows how the situation of apparent isotropy can arise in the case of pinning-enhanced material. After [32]

Fig. 1.6 The field dependence of I_c at low temperatures exhibits hysteresis at low fields depending on the direction of the field sweep as flux vortices get trapped within the grains such that the field in the grain boundaries (which limits I_c) reaches zero before the applied field. Where only a single non-virgin field quadrant is swept, this can lead to an underestimation of the true zero field I_c , or a spurious peak effect



When we examine the field-dependent I_c for fields applied perpendicular to the wire in both the increasing and decreasing sense (Fig. 1.6), we observe a hysteretic behaviour at low fields (typically less than 1 T). The maximum I_c value is seen not to occur at zero applied field, but rather to occur *before* zero field is reached (in

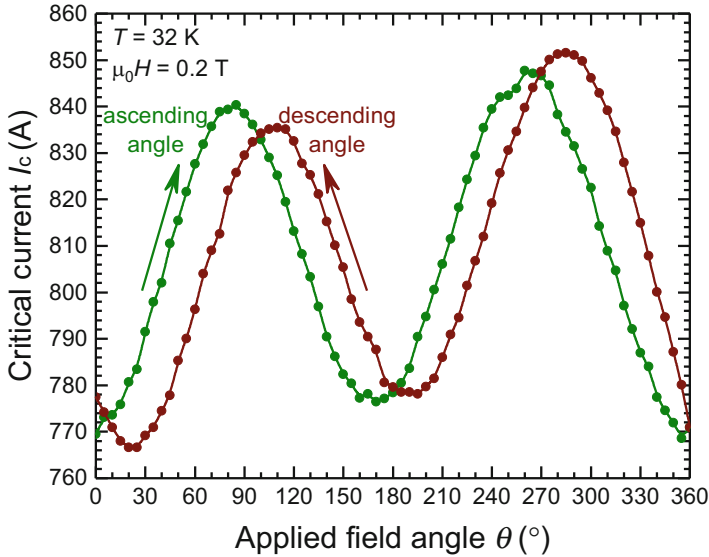


Fig. 1.7 The angle dependence of I_c at low temperatures is shifted in angle at low fields due to field trapping within the grains

whichever direction the field is being swept). This effect has been well documented in granular materials [34] and in films containing engineered large-angle grain boundaries [35], and it is found to be ubiquitous in coated conductors due to their inherent grain boundary network [36]. The proposed explanation is that the field (comprising flux vortices) becomes trapped within the grains, causing the grain boundaries to reach zero localised field before the applied field reaches zero. Since it is the grain boundaries that limit I_c in the low-field regime, this reduced grain boundary field is immediately reflected in the measured I_c .

Less commonly observed [37] is that this out-of-plane field hysteresis carries through also to the angle dependences of I_c , where the offset between the results obtained with increasing and decreasing field angle can be rather large, as much as 30° (Fig. 1.7). Again it is observed most strongly at low fields and low temperatures, and as with the field hysteresis, the angular peaks in I_c are observed to occur “too soon.” To get an accurate measure of the correct angular location of the curve, there is no option but to measure in both directions and then to shift the curves equally into alignment, or to measure each point after zero field cooling at that angle. Otherwise, the true angular position of the curve must be inferred.

In-Plane Field Asymmetry

A well-reported effect in 2G wires [38] is the asymmetry of the field dependence of the critical current to positive and negative in-plane fields, attributed to the

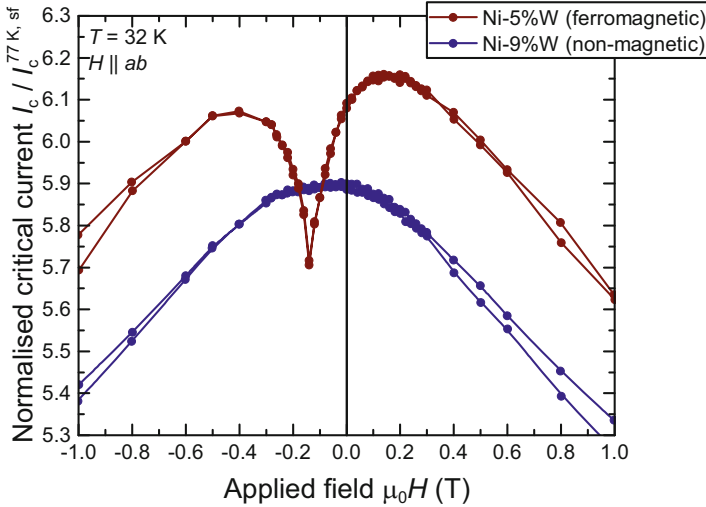


Fig. 1.8 Asymmetry about zero field in the in-plane field dependence of I_c at low fields caused by differing surface barriers to vortex motion, and additional general enhancement and localised suppression of I_c at non-zero field caused by the presence of a ferromagnetic substrate. Note that no hysteresis is observed in these in-plane measurements. I_c is plotted normalised to allow direct comparison of the two effects since the wires on different substrates have different I_c . After [39]

difference between the surface barriers to vortex motion at the interface between superconductor and dielectric buffer layers on one hand, and superconductor and metallic capping layer on the other. Since reversal of the field direction reverses the direction of the Lorentz force acting on the vortices, they encounter one or other of these surface barriers, leading to a different I_c (for small fields). Reversal of the current direction is confirmed to produce the same effect.

A recently reported extension of this observation [39] highlights the additional, superimposed effect of a sharply reduced dip in I_c over a narrow, non-zero field range in the presence of a ferromagnetic substrate (such as the Ni-5%W alloy commonly used in the RABiTS process), reproduced in Fig. 1.8. Again, the effect was confirmed to reverse in field in case of reversal of the current transport direction, or if the sample was placed face-up instead of face-down (reversing the direction of the Lorentz force relative to the wire). Furthermore, exfoliation of the sample from the magnetic substrate was demonstrated to eliminate the dip in I_c , while sandwiching the sample between two Ni-5%W foils was seen to produce a double dip to either side of zero field. Finite element modelling shows the effect to be the result of field shaping by the ferromagnetic substrate causing a significant perpendicular field component to be generated within the wire by the self-field resulting from the transport current even though the applied field lies strictly within the plane. A notable side-effect of this field shaping is a reduction in the overall field seen by the superconductor, resulting in a general enhancement of I_c [40].

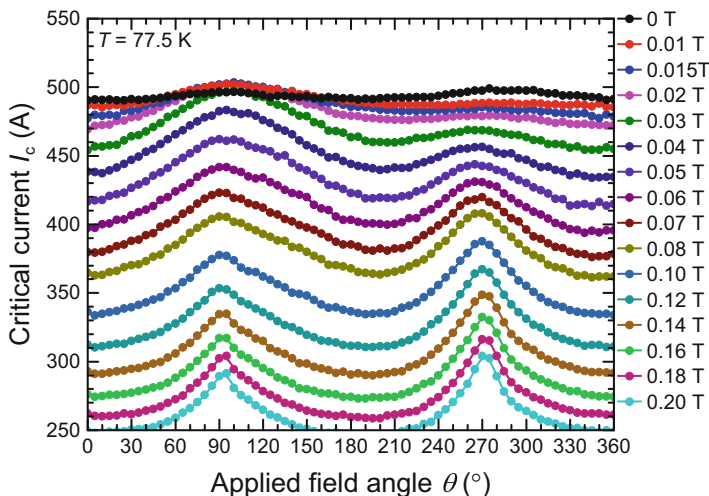


Fig. 1.9 The in-plane (90°) peak in the angle dependence of I_c of a Fujikura 2G HTS wire sample at low fields exceeds the zero-field value due to the in-plane field asymmetry highlighted in Fig. 1.8. The peak for fields applied in the opposite (270°) direction is correspondingly diminished

The consequence of these effects is an apparent irregularity and the loss of 180° periodicity in the angle dependence of I_c of these materials at low fields, and in particular at low temperatures (where the I_c is high). The effect also gives rise to a characteristic peak in the angle dependence at low fields that exceeds the zero-field I_c value (see Fig. 1.9). This particular combination of conditions is not a common one for present applications, but the effect is present to a lesser degree at higher temperatures also, as Fig. 1.9 demonstrates, so it may be important to take into account in any low-field application such as power cables, transformers or fault current limiters.

Case Study: Wind Power Generator

A prototype HTS wind power generator was designed and constructed at the 10 kW scale [41], in part to test the use of a brushless exciter to energise the HTS rotor coils in a non-contact manner through the walls of the rotating cryostat [42]. Although the design was informed by measurements of the performance of the HTS wire used in its construction, the paucity of available wire data from different suppliers meant that it was not possible to select wire specifically targeted to this application.

(continued)

Table 1.1 Comparison of the constructed design for a 10 kW HTS wind power generator with a refined design utilising data for an optimally selected alternative wire

		Original design	Refined design
Design specifications	Rated output power	10.3 kW	
	Rotational speed	300 rpm	
	Operating temperature	30 K	
HTS rotor coil design	Width of racetrack coil bobbin	25 mm	
	Total width of racetrack coil	95.5 mm	68.5 mm
	Effective length of racetrack coil	170 mm	200 mm
	Turns of HTS per coil	235	145
	Operating current	91 A	336 A
	Current margin	40% below I_c	
	Number of poles	6	
	Number of coil layers per pole	4 (QPC)	2 (DPC)
	Total length of HTS wire required	3 km	1 km
	Results	Inductance	0.15 H
Overall diameter of the generator		453.3 mm	183.5 mm
Maximum magnetic field on coil		2.2 T	5.8 T
Max. perpendicular magnetic field		1.1 T	2 T

Original design from [41]; refinement calculation courtesy of H.-J. Sung

Post-construction, it was of interest to run the design model using a range of datasets of alternative wires that could have been used had this data been available. Table 1.1 highlights the design modifications and the resulting benefits that could potentially have been realised in the best case.

By selecting the best available wire for the specific operating conditions of the target application (30 K, reduced sensitivity to perpendicular fields), it would have been possible to increase the operating current significantly whilst maintaining the safety margin to I_c , optimally balancing the field on the coils against the operating current to minimise the coil size, and ultimately reducing the amount of wire required for construction from 3 km to 1 km at the same time as halving the overall build diameter of the generator. It is likely that under an economic analysis, these benefits would outweigh any additional cost associated with the superior wire. A fully detailed wire characterisation is also likely to increase confidence in the actual wire performance, enabling a reduction in the operating current margin and consequent further design gains.

1.3.3 Angular Regime

The full power of detailed wire characterisation is realised when complete angle-dependent variations in I_c are measured and utilised in device designs. Combined with numerical models able to account for the full wire anisotropy, great improvements in the efficiency of wire utilisation can be achieved (see [Case Study: MRI Magnet](#)) as we move from designs based on the anticipated minimum I_c of the wire for a given field–temperature combination to designs able to fully utilise the performance benefit available from HTS wires in regions of partial in-plane field.

This potential performance gain is exemplified in the data shown in Fig. 1.10, where it is seen that for a relatively wide angular range around the in-plane

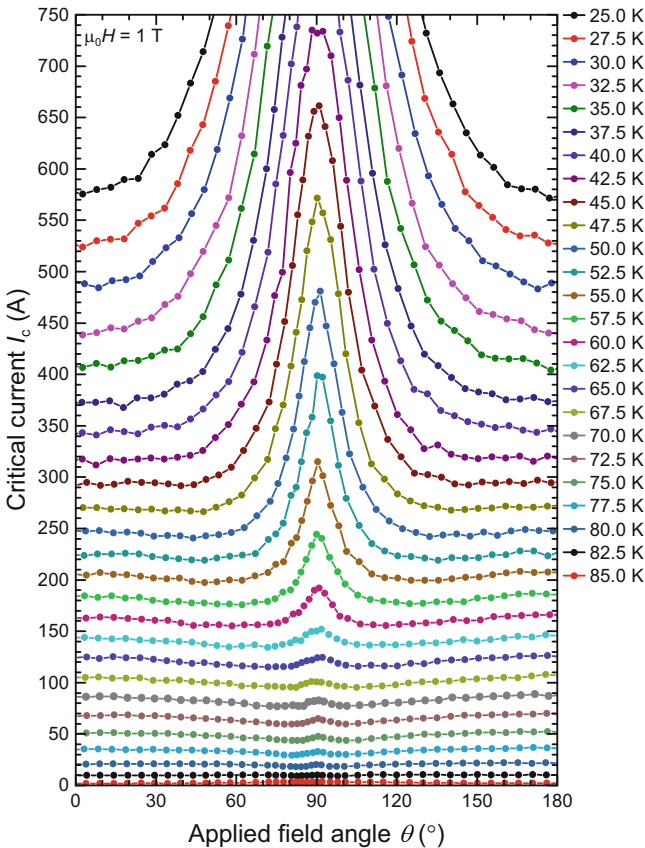


Fig. 1.10 Angle dependence of the critical current of an American Superconductor 2G HTS wire sample over a range of temperatures (lowest temperature corresponding to highest I_c) at an applied field of 1 T. The performance gain available when the field is aligned close to the in-plane (90°) direction is evident at low temperatures, as is the fact that to higher temperatures as the peak narrows the true I_c minimum is not located at 0° but closer to the base of the peak, even for this non artificially pinning-enhanced wire. Data from [43]

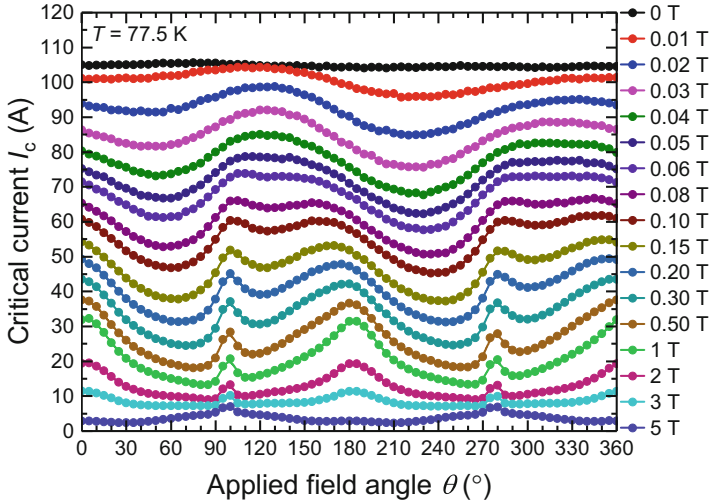


Fig. 1.11 Full 360° angle dependence of the critical current of a SuperPower AP 2G HTS wire sample over a range of applied magnetic fields (lowest field corresponding to highest I_c), showing a high degree of asymmetry about the in-plane (90°) peak at high temperature, low field, due to the addition of correlated pinning centres aligned with the perpendicular direction. Towards higher fields, this asymmetry is reduced and then eliminated concurrently with the suppression of the out-of-plane (180°) peak as these artificial pinning centres become ineffective. A further, more subtle, asymmetry between half-revolutions is also seen to evolve, with I_c values in the second half cycle being slightly lower at low fields, then rising to slightly higher values at fields around 0.1 T, before equalising at higher fields. This same effect is also seen in the earlier, non pinning-enhanced, data of Fig. 1.9

field direction, particularly at low temperatures, significantly higher I_c values are available to utilise than the minimum I_c approximated by the out-of-plane value. This dataset also serves to highlight that even in 2G wires with a relatively simple angular behaviour and an absence of intentionally added artificial pinning centres, the true I_c minimum is not necessarily obtained for fields applied perpendicular to the plane of the wire, but can be located closer to the base of the in-plane peak. A much more complex (and more common) example of the angular anisotropy of I_c in the presence of artificial pinning centres will be shown in the next section (Fig. 1.11).

Wire Asymmetry

Detailed studies of pinning-enhanced wires under conditions of high temperature and low field reveal a surprising degree of asymmetry in the angular dependence of I_c about the in-plane direction (Fig. 1.11). The I_c to one side of the in-plane pinning peak can be significantly (up to 30%) greater than to the other side. This raises the

prospect of some clever engineering being applied to utilise this potential benefit, by paying careful attention to the wire orientation when winding a coil.

Hybrid coils using 1G wire in the central windings (where the field is predominantly parallel to the plane of the wire) and 2G wire in the end windings (where the field diverges towards the perpendicular direction) have been investigated [44]. However, the present data highlights the importance of carefully controlling the orientation of the 2G end coils to ensure that the direction of divergence of the field matches the orientation of best performance. In this manner, a significant overall performance gain can be expected [45].

Also of note in the data of Fig. 1.11 is the extreme repositioning of the minimum I_c value much closer to the base of the in-plane peak than to the perpendicular direction. A relatively small deviation in field direction of $\pm 30^\circ$ from in-plane takes the wire all the way from its maximum I_c to its minimum I_c , although as highlighted above this minimum I_c may be significantly different to either side of the peak. As discussed in Sect. 1.3.2, using the perpendicular I_c as an inaccurate estimate of the minimum I_c in this case would overestimate the true value by up to a factor two.

A particularly striking example of wire asymmetry under all operational conditions arises in the case of films textured via the method of inclined substrate deposition (ISD) [46], as shown on Fig. 1.12. Here, due to the growth mode, the crystal structure of the superconductor is not aligned with the coordinate system of the wire. In contrast to the more commonly employed ion beam assisted deposition (IBAD) method of texturing, where an inclination of up to a few degrees is common (see offset of the in-plane peak to the right of 90° at high fields on Fig. 1.11), or the RABiTS textured substrate which produces film growth exactly perpendicular to the substrate, here the intentional inclination of the substrate during deposition leads to a pronounced offset of 30° to the growth direction. In this case, “parallel” and “perpendicular” field orientations are particularly meaningless unless that is the actual direction in which the field is to be aligned in application. In the case of the ISD wire shown, I_c values parallel (0°) and perpendicular (90°) to the wire may be similar since they both lie between the minimum (30°) and maximum (120°) values. However, such an offset in the orientation of the peak I_c of the wires could make them highly beneficial if employed as the end turns in a hybrid coil structure as just described.

In-Plane Field Angle Variation

It is the observation at 77 K [48], and has been assumed to be true under all conditions, that the angular variation in I_c obtained for fields applied *within the plane* of the superconductor follows a simple geometric behaviour that sees it pass from some maximum value (limited by flux-line cutting or other effects) in the Lorentz force-free configuration of field and current parallel to a minimum value (under which most characterisation measurements are typically conducted) when the applied field and transport current are perpendicular, generating the maximum Lorentz force on the vortices which causes them to overcome their pinning.

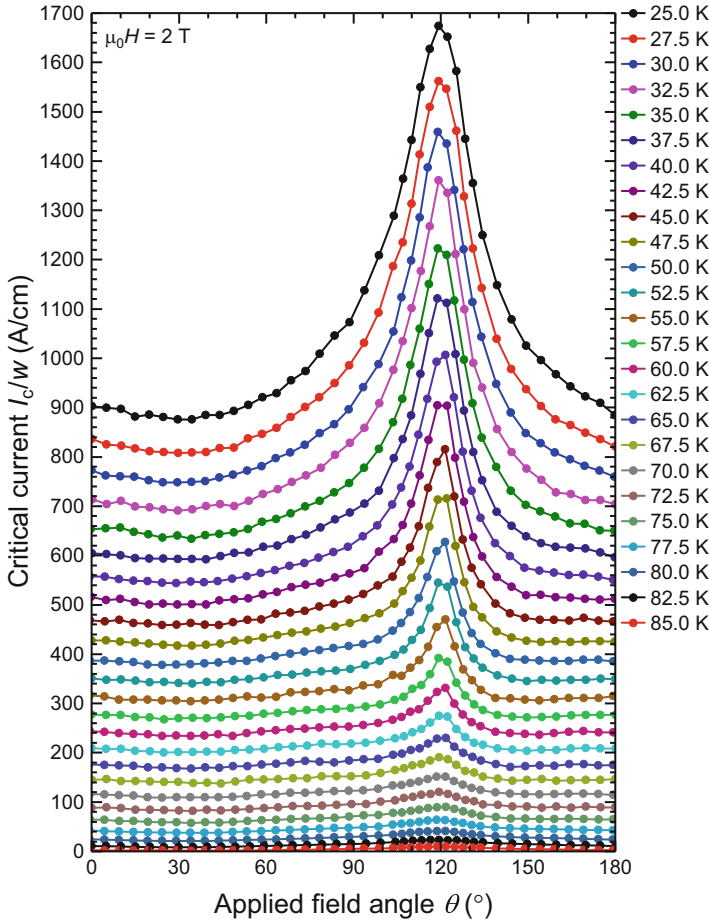


Fig. 1.12 Angle dependence of the critical current of an inclined substrate deposited 2G HTS wire sample from THEVA over a range of temperatures (lowest temperature corresponding to highest I_c) at an applied field of 2 T. The in-plane peak in I_c is shifted by 30° from 90° to 120° , reflecting the offset in the crystallographic orientation of the substrate. Data from [47]

However, it has been observed (Fig. 1.13) that this is not universally the case and that in particular at low temperatures and high fields, this typical behaviour can fully invert. I_c values as much as one third reduced have been observed in the force-free configuration compared to the usually measured maximum Lorentz force configuration, hard to explain by any reasonable degree of sample mismounting. This is a concern for any application seeking to utilise HTS wires under these

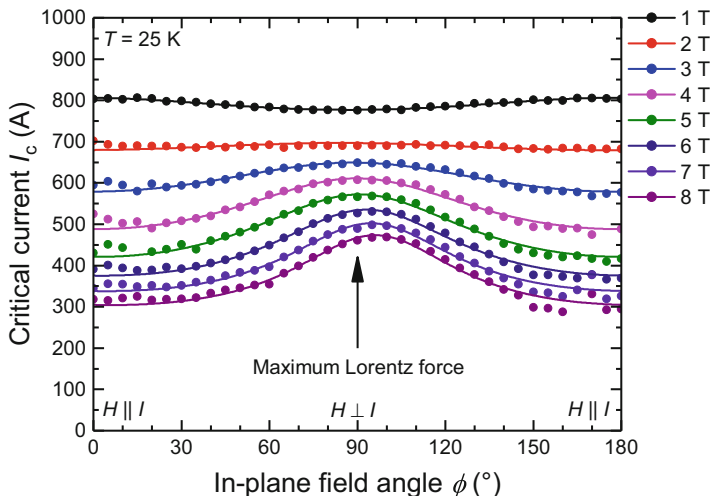


Fig. 1.13 In-plane angle dependence of the critical current of an American Superconductor 2G HTS wire sample, showing that at low temperature, high field, I_c values as much as 30% lower are obtained in the force-free configuration of field and current parallel (0°) than in the commonly measured maximum Lorentz force configuration of field perpendicular to current (180°). After [49]

sorts of extreme conditions, since this source of potential I_c variation is not commonly considered, with the maximum Lorentz force geometry usually taken as representing a worst case I_c .

Case Study: MRI Magnet

The coil design for a 3 T HTS MRI magnet is shown in Fig. 1.14. The design requirement is for the coil pack to generate a field of 3 T across a 6 cm diameter spherical volume at the centre of the bore, suitable for pre-clinical or extremity imaging. This requirement together with the proposed coil layout (optimised for field homogeneity, etc.) dictates the current required in the superconducting windings. In addition to calculating the resulting field within the bore of the magnet, the corresponding field distribution within the windings themselves can also be determined by finite element modelling, and it is this that is shown in terms of the colour map on the left panel of the figure indicating the local field strength and the field lines on the central panel indicating the local field orientation.

(continued)

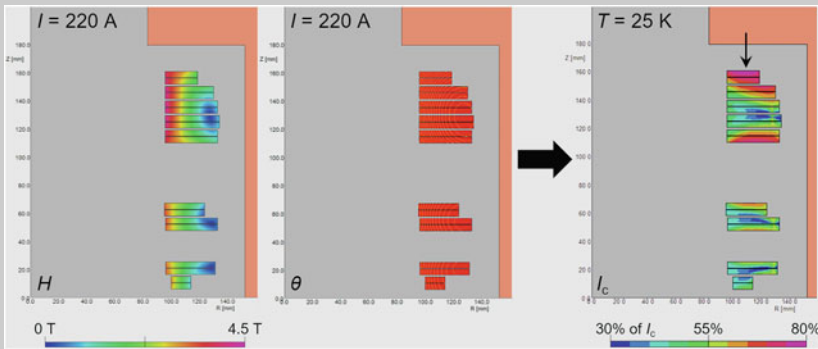


Fig. 1.14 Coil design of a 3 T HTS MRI magnet [12]. The magnet is rotationally symmetric about an axis along the left side of the image, and only the upper half of the symmetric magnet is shown, with the centre of the imaging volume at the bottom left corner of the image. The entire magnet comprises 18 double-pancake coils (9 shown) of varying internal and external radius designed to produce a homogeneous field region across a 6 cm diameter spherical volume at the centre of the bore when energised to 220 A. The left panel shows the field strength mapped across the coils, while the centre panel shows the field orientation at each point within the coils. Together with the detailed wire characterisation $I_c(T, B, \theta)$, these combine to produce the map shown on the right panel of the current at each point in the coils expressed as a fraction of the local I_c under those precise field conditions, for a given operating temperature chosen to yield the desired operating current margin. The critical region of the coil (closest to I_c) is indicated by an arrow

On the basis of this local field profile (strength and orientation) at each point in the conductor, it is possible to index these values with the local critical current under these exact field conditions and a given operating temperature, as determined by the detailed wire characterisation, and thereby to produce a plot showing the current in the coil as a fraction of the wire I_c at each point. A suitable operating temperature can then be chosen such that the coil remains below an acceptable fraction of the wire I_c , for example 80% of I_c as results here for a chosen operating temperature of 25 K. Such a plot is shown on the right panel of the figure, and a number of quite general observations can be made on the basis of this example.

First, the critical region of the coil (where the current most closely approaches I_c) is at neither the point of highest field strength (4.3 T on the innermost edge of the upper coil pack) nor the point of least favourable field orientation (field closely perpendicular to the tape) but rather it is located in the region of the coil where these two factors combine to produce the least favourable overall operating condition. This further highlights the potential advantages to be gained from a hybrid magnet design, as discussed in section “Wire Asymmetry”, using superior wire in the coils forming these

(continued)

critical regions, while utilising lower performance wire in less critical regions, many of which fall below 50% of I_c .

At this critical point in the coil, the precise field condition is a field strength of 2.8 T at an angle of 52° to the normal to the wire. Designing conservatively for a minimum I_c condition at 3 T would have resulted in a current limit of 240 A, which when derated to 80% of I_c would have limited the operating current to 190 A, requiring correspondingly more wire throughout the magnet in order to achieve the target field. Instead, utilising the full angle dependent wire characterisation allowed use of the full available wire performance, recognising its true I_c under these conditions of 280 A, 15% higher than the minimum value.

By utilising the full wire characterisation dataset at the design stage, the magnet design can be optimised to use the minimum amount of wire necessary to maintain the desired safety margin, greatly impacting on the overall cost of the magnet. Alternatively, detailed modelling on the basis of known wire performance can be used to safely raise the permissible operating temperature of a constructed magnet, allowing for longer periods of image acquisition, or greater intervals between cryocooler maintenance [23].

1.4 n -Value

An increasingly important engineering property of high-temperature superconductors is the n -value, or the exponent of the IV curve, which is typically lower (the curve is closer to linear) than its counterpart in the low-temperature superconductors (LTS). Microscopically, the n -value is determined by the form of the pinning potential, and thereby reflects the creep rate of flux within the superconductor [50], a thermally activated process of consequently greater significance in HTS than LTS [51]. It has a role to play in the operation of novel superconducting devices such as SQUIDS and flux pumps [52], magnet stability, quench behaviour, ramping rate, AC loss [53], etc. Unlike I_c , the n -value as determined from transport measurements is a poorly defined property since it relies on an assumed functional form of the IV curve, not merely the point at which it crosses a predefined value. This functional form is usually taken to be a power law although this is not an entirely accurate representation since actual experimental data deviates in both directions, below I_c where the data vanishes below the noise level and above I_c where heating effects or the transition to the flux flow regime cause a variation in the observed behaviour (in opposing senses). The power law is thus only an approximation to the functional form of the observed data in the vicinity of I_c . The I_c and n parameters of the IV curve fitting function are also highly interdependent, and Fig. 1.15 shows

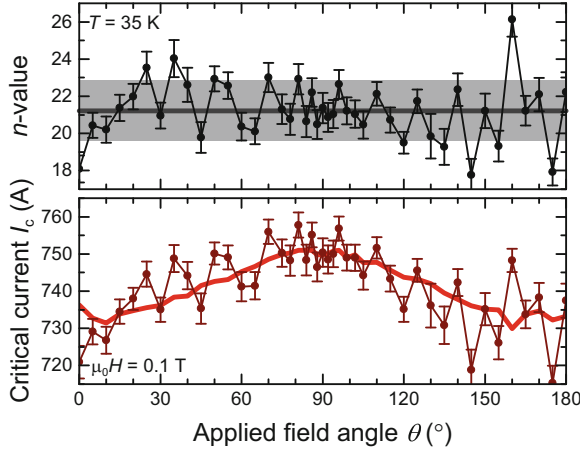


Fig. 1.15 Typical IV -curve fitting results for I_c and n (data points), highlighting the strong correlation between errors in the two fitting parameters due to their high interdependency. By smoothing the variation in n (in this case by simply fixing it at the average value across the curve), an improvement in the fidelity of the angular variation in I_c is simultaneously obtained (thick lines). The resulting fitting error in I_c in this case is indicated by the thickness of the line

how constraining (or smoothing) n can lead to a corresponding improvement in the determination of I_c . Modern measurement systems offer increased fidelity of n -value measurement in addition to I_c as exemplified in Fig. 1.16. Complex behaviours are seen to emerge and evolve across the measurement parameter space covering wide ranges of exponents from values as low as 5 at moderate fields, more commonly associated with 1G conductor materials, to values as high as 28 at zero field, approaching those of LTS [55].

At the higher fields shown, the simple variation in n -value with applied field angle featuring a cusp-like peak around 90° could easily be supposed to reflect a correlation with the typical form of the angle dependence of I_c of an anisotropic superconductor [54]. However, the I_c data of this particular pinning-enhanced wire (Fig. 1.11) bears no resemblance to this simple form, having a much narrower in-plane peak, and a broader and stronger out-of-plane peak resulting from the artificial pinning that is not at all reflected in the n -value data. Comparison with the data presented in [21] shows a similar evolution of behaviour towards lower fields, with a gradual flattening (isotropisation) of the curve towards 1 T, followed by the emergence of a broad 180° peak and steady growth of a sharp 90° peak, and then the re-emergence of a smoothly geometrical variation peaking around 90° , while the n -value steadily increases with reducing field, as is usually observed [56].

An often overlooked consequence of this systematic, uncorrelated, non-monotonic variation in n -value for pinning-enhanced samples, highlighted in [22], is that the *form* of the angular dependence of I_c can be made to vary depending on the particular arbitrary criterion chosen to define I_c , as shown in Fig. 1.17. This is incompatible with attempts to attribute this functional form directly to

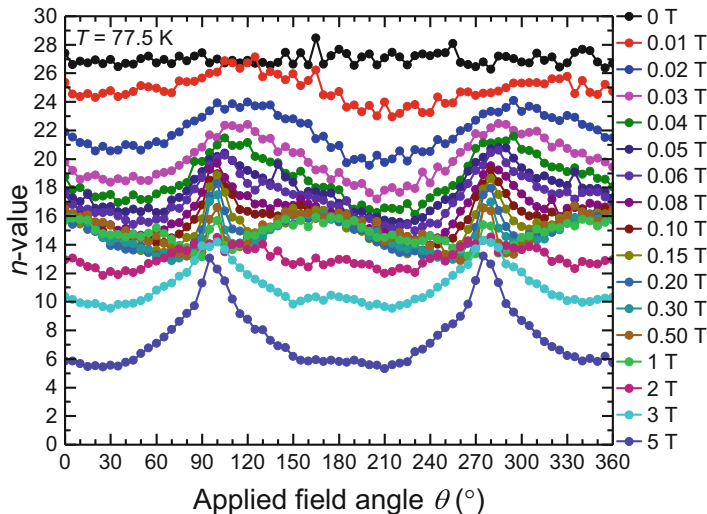


Fig. 1.16 Angle dependence of the n -value of the SuperPower AP 2G HTS wire sample for which the I_c data is shown in Fig. 1.11. A clear, systematic variation in n with both field and field angle is observed across the dataset. The curves converge between 0.1 T and 1 T, but deviate either side of this field range to values as high as 28 at 0 T and as low as 5 at 5 T

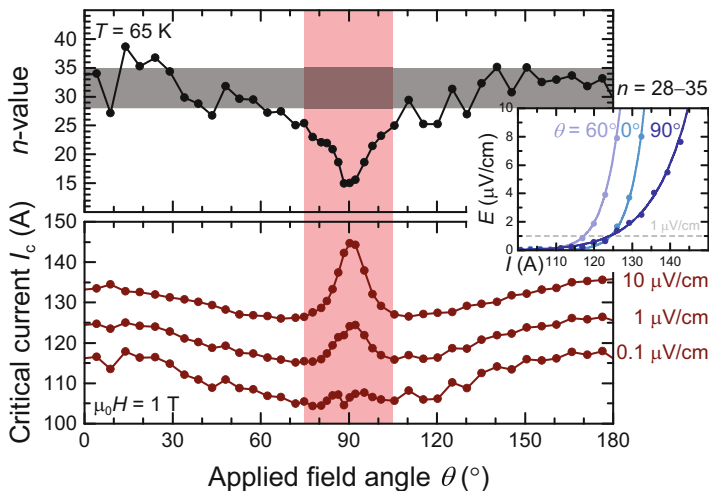


Fig. 1.17 Effect of a varying n -value (upper panel) on the perceived variation in I_c (lower panel) under different commonly employed electric field criteria used to define I_c . In this case, there is no doubt from the form of the IV curves (inset) that the variation in n -value is real making the definition of I_c in terms of a fixed arbitrary electric field criterion problematic. Data from the sample shown in Fig. 1.10. After [22]

microstructural pinning properties of the material [57] and indicates that a deeper understanding is required of the influences governing the variation in n -value with field angle in particular, and to the proper separation of the I_c and n parameters of the IV curve. Since there can be no doubt that the shape of the underlying IV curves does indeed vary, attempts to define a more fundamental measure of I_c may be required [58, 59].

1.5 Mechanical Strength

An aspect of wire characterisation that commonly takes second place to considerations of electrical performance, but which becomes critical at the point of device construction, is the mechanical strength of the wires. For 2G wires in particular, the point at which they fail due to delamination of the superconducting layer from the supporting substrate is critical, typically leading to imminent localised failure and burn-out.

A range of different methods exist for characterising this “delamination strength,” and it is important on comparing different results to be aware of what has actually been measured in each case. The mode I interfacial fracture energy (G_{IC}), as measured in a climbing drum peel test [60], is a well-defined physical property of a composite material considered to accurately reflect the parameter of importance to this application. Under a survey of high-quality production wire inserts (with only thin silver stabiliser) that have been demonstrated to be robust in use, this parameter is found to be remarkably consistent at around 5 J/m^2 , with interfacial failure eventually occurring within the buffer stack. Counterintuitively, a greater interfacial toughness is measured for those wires incorporating softer substrate materials such as stainless steel (rather than Hastelloy) or even better the Ni–W alloy used in the RABiTS process. This is explained as being due to deformation of the substrate absorbing some of the interfacial strain and thereby enabling the composite to survive intact to higher stresses.

Similarly, it is possible to positively influence the interfacial toughness by plating the HTS layer on the upper side with the usual copper electrical stabilisation layer, absorbing strain on that side of the conductor. Recent results (Mataira, private communication, 2018) starting from the same wire and applying successively thicker electroplated copper layers have indicated that it is possible to vary the resulting interfacial toughness of the wire over a wide range, extending up to at least 15 J/m^2 for plating thicknesses in excess of $100 \mu\text{m}$. Thus, it appears that any desired interfacial strength can be tailored from any given wire (of sufficient robustness), and so wire selection on the basis of electrical performance can proceed independently of strength considerations.

1.6 Targeted Wire Selection for Specific Applications

At the present time, many potentially beneficial applications of HTS technology are cost-limited. We find ourselves in the situation, common to many fledgling industries, where for the cost of the HTS wire to come down, the volume of demand must go up, but for demand to increase, the costs must come down.

By applying an improved understanding of the detailed properties of contemporary HTS wires, and thereby avoiding the excessive over-engineering of devices that results from a generalised or limited understanding of specific wire performance under conditions relevant to the target application, a significant reduction in the quantity of wire required for a particular device can be realised, with no reduction in device performance or reliability, and in many cases with a simultaneous improvement. With wire cost presently the major portion of the total device cost in many instances, this saving directly carries through to the final device cost. In this way, the arguments for the benefits of HTS-based technologies can be enhanced on an economic basis, where they often fall short.

While wire development continues apace, it is inevitable that targeted wire characterisation will be a necessary prerequisite for any large new project in order to achieve the above. In time, however, it is to be hoped that wire manufacturers will be in a position to fully specify their product, and that informed selection of the most appropriate wire for a given application will become possible on the basis of manufacturer specifications.

Acknowledgements The author gratefully acknowledges the significant contribution of his colleague Nicholas M. Strickland to the work summarised here.

References

1. P. Tixador, Development of superconducting power devices in Europe. *Phys. C* **470**, 971 (2010)
2. B. Gamble, G. Snitchler, T. MacDonald, Full power test of a 36.5 MW HTS propulsion motor. *IEEE Trans. Appl. Supercond.* **21**, 1083 (2011)
3. A. Hobl, W. Goldacker, B. Dutoit, L. Martini, A. Petermann, P. Tixador, Design and production of the ECCOFLOW resistive fault current limiter. *IEEE Trans. Appl. Supercond.* **23**, 5601804 (2013)
4. M. Stemmler, F. Merschel, M. Noe, A. Hobl, AmpaCity — advanced superconducting medium voltage system for urban area power supply, in *2014 IEEE PES T&D Conf. Expo* (2014). <https://doi.org/10.1109/TDC.2014.6863566>
5. G.G. Sotelo, R.A.H. de Oliveira, F.S. Costa, D.H.N. Dias, R. de Andrade, R.M. Stephan, A full scale superconducting magnetic levitation (MagLev) vehicle operational line. *IEEE Trans. Appl. Supercond.* **25**, 3601005 (2015)
6. R. Gupta, M. Anerella, P. Joshi, J. Higgins, S. Lalitha, W. Sampson, J. Schmalzle, P. Wanderer, Design, construction, and testing of a large-aperture high-field HTS SMES coil. *IEEE Trans. Appl. Supercond.* **26**, 5700208 (2016)

7. S. Mukoyama, K. Nakao, H. Sakamoto, T. Matsuoka, K. Nagashima, M. Ogata, T. Yamashita, Y. Miyazaki, K. Miyazaki, T. Maeda, H. Shimizu, Development of superconducting magnetic bearing for 300 kW flywheel energy storage system. *IEEE Trans. Appl. Supercond.* **27**, 3600804 (2017)
8. N. Glasson, M. Staines, N. Allpress, M. Pannu, J. Tanchon, E. Pardo, R. Badcock, R. Buckley, Test results and conclusions from a 1 MVA superconducting transformer featuring 2G HTS Roebel cable. *IEEE Trans. Appl. Supercond.* **27**, 5500205 (2017)
9. J. Kellers, Development of a superconductive wind power generator within the EcoSwing project. Presented at the 25th International Conference on Magnet Technology, Amsterdam (2017)
10. D.M. Pooke, V. Chamritski, M. Fee, S. Gibson, B.T. King, J.L. Tallon, M. Meissner, R. Feyerherm, S.R. Olsen, S.J. Kennedy, R.A. Robinson, HTS 5 tesla synchrotron and neutron beamline magnets. *IEEE Trans. Appl. Supercond.* **19**, 1372 (2009)
11. S. Yoon, J. Kim, K. Cheon, H. Lee, S. Hahn, S.-H. Moon, 26 T 35 mm all-GdBa₂Cu₃O_{7-x} multi-width no-insulation superconducting magnet. *Supercond. Sci. Technol.* **29**, 04LT04 (2016)
12. B.J. Parkinson, K. Bouloukakis, R.A. Slade, A compact 3 T all HTS cryogen-free MRI system. *Supercond. Sci. Technol.* **30**, 125009 (2017)
13. M.V. Silva Elipe, N. Donovan, R. Krull, D. Pooke, K.L. Colson, Performance of new 400-MHz HTS power-driven magnet NMR technology on typical pharmaceutical API, cinacalcet HCl. *Magn. Reson. Chem.* **56**, 817 (2018)
14. B.N. Sorbom, J. Ball, T.R. Palmer, F.J. Mangiarotti, J.M. Sierchio, P. Bonoli, C. Kasten, D.A. Sutherland, H.S. Barnard, C.B. Haakonsen, J. Goh, C. Sung, D.G. Whyte, ARC: a compact, high-field, fusion nuclear science facility and demonstration power plant with demountable magnets. *Fusion Eng. Des.* **100**, 378 (2015)
15. A. Sykes, A.E. Costley, C.G. Windsor, O. Asunta, G. Brittles, P. Buxton, V. Chuyanov, J.W. Connor, M.P. Gryaznevich, B. Huang, J. Hugill, A. Kukushkin, D. Kingham, A.V. Langtry, S. McNamara, J.G. Morgan, P. Noonan, J.S.H. Ross, V. Shevchenko, R. Slade, G. Smith, Compact fusion energy based on the spherical tokamak. *Nucl. Fusion* **58**, 016039 (2017)
16. P.M. Leys, M. Klaeser, F. Schleissinger, T. Schneider, Angle-dependent $U(I)$ measurements of HTS coated conductors. *IEEE Trans. Appl. Supercond.* **23**, 8000604 (2013)
17. K. Tsuchiya, A. Kikuchi, A. Terashima, K. Suzuki, K. Norimoto, M. Tawada, M. Masuzawa, N. Ohuchi, X. Wang, Y. Iijima, T. Takao, S. Fujita, M. Daibo, Y. Iijima, Critical current characterization of commercial REBCO coated conductors at 4.2 and 77 K. *IEEE Trans. Appl. Supercond.* **27**, 6600205 (2017)
18. P. Sunwong, J.S. Higgins, D.P. Hampshire, Probes for investigating the effect of magnetic field, field orientation, temperature and strain on the critical current density of anisotropic high-temperature superconducting tapes in a split-pair 15 T horizontal magnet. *Rev. Sci. Instrum.* **85**, 065111 (2014)
19. H. Ma, H. Liu, F. Liu, H. Zhang, L. Ci, Y. Shi, L. Lei, Critical current measurements of high-temperature superconducting short samples at a wide range of temperatures and magnetic fields. *Rev. Sci. Instrum.* **89**, 015102 (2018)
20. C. Barth, M. Bonura, C. Senatore, High current probe for $I_c(B, T)$ measurements with ± 0.01 K precision: HTS current leads and active temperature stabilization system. *IEEE Trans. Appl. Supercond.* **28**, 9500206 (2018)
21. M. Lao, J. Hänisch, S. Kauffmann-Weiss, R. Gehring, H. Fillinger, A. Drechsler, B. Holzpfafel, High current variable temperature electrical characterization system for superconducting wires and tapes with continuous sample rotation in a split coil magnet. *Rev. Sci. Instrum.* **90**, 015106 (2019)
22. N.M. Strickland, C. Hoffmann, S.C. Wimbush, A 1 kA-class cryogen-free critical current characterization system for superconducting coated conductors. *Rev. Sci. Instrum.* **85**, 113907 (2014)
23. S.C. Wimbush, N.M. Strickland, A public database of high-temperature superconductor critical current data. *IEEE Trans. Appl. Supercond.* **27**, 8000105 (2017)

24. V. Selvamanickam, Y. Yao, Y. Chen, T. Shi, Y. Liu, N.D. Khatri, J. Liu, C. Lei, E. Galstyan, G. Majkic, The low-temperature, high-magnetic-field critical current characteristics of Zr-added (Gd, Y)Ba₂Cu₃O_x superconducting tapes. *Supercond. Sci. Technol.* **25**, 125013 (2012)
25. A. Xu, L. Delgado, M. Heydari Gharahcheshmeh, N. Khatri, Y. Liu, V. Selvamanickam, Strong correlation between $J_c(T, H||c)$ and $J_c(77K, 3T||c)$ in Zr-added (Gd, Y)BaCuO coated conductors at temperatures from 77 down to 20 K and fields up to 9 T. *Supercond. Sci. Technol.* **28**, 082001 (2015)
26. S. Awaji, M. Namba, K. Watanabe, H. Kai, M. Mukaida, S. Okayasu, Flux pinning properties of correlated pinning at low temperatures in ErBCO films with inclined columnar defects. *J. Appl. Phys.* **111**, 013914 (2012)
27. N.M. Strickland, S.C. Wimbush, J.V. Kennedy, M.C. Ridgway, E.F. Talantsev, N.J. Long, Effective low-temperature flux pinning by Au ion irradiation in HTS coated conductors. *IEEE Trans. Appl. Supercond.* **25**, 6600905 (2015)
28. M.W. Rupich, S. Sathyamurthy, S. Fleshler, Q. Li, V. Solovyov, T. Ozaki, U. Welp, W.-K. Kwok, M. Leroux, A.E. Koshelev, D.J. Miller, K. Kihlstrom, L. Civale, S. Eley, A. Kayani, Engineered pinning landscapes for enhanced 2G coil wire. *IEEE Trans. Appl. Supercond.* **26**, 6601904 (2016)
29. S.C. Wimbush, N.M. Strickland, Critical current characterisation of SuperOx 2G HTS superconducting wire, figshare (2016), <https://doi.org/10.6084/m9.figshare.3759315.v1>
30. Sumitomo Electric Industries, Ltd., *Sumitomo BSCCO Wire (DI-BSCCO) Type H Specifications* (2018). Available at: https://global-sei.com/super/hts_e/type_h.html. Accessed 30 Nov 2018
31. S.C. Wimbush, N.M. Strickland, N.J. Long, Low-temperature scaling of the critical current in 1G HTS wires. *IEEE Trans. Appl. Supercond.* **25**, 6400105 (2015)
32. N.M. Strickland, S.C. Wimbush, The magnetic-field dependence of critical current: what we really need to know. *IEEE Trans. Appl. Supercond.* **27**, 8000505 (2017)
33. D.T. Verebelyi, D.K. Christen, R. Feenstra, C. Cantoni, A. Goyal, D.F. Lee, M. Paranthaman, P.N. Arendt, R.F. DePaula, J.R. Groves, C. Prouteau, Low angle grain boundary transport in YBa₂Cu₃O_{7- δ} coated conductors. *Appl. Phys. Lett.* **76**, 1755 (2000)
34. K.-H. Müller, D.N. Matthews, A model for the hysteretic critical current density in polycrystalline high-temperature superconductors. *Phys. C* **206**, 275 (1993)
35. M. Däumling, E. Sarnelli, P. Chaudhari, A. Gupta, J. Lacey, Critical current of a high T_c Josephson grain boundary junction in high magnetic field. *Appl. Phys. Lett.* **61**, 1355 (1992)
36. A.A. Gapud, D.K. Christen, R. Feenstra, F.A. List III, A. Khan, On narrowing coated conductor film: the emergence of granularity-induced field hysteresis of transport critical current. *Supercond. Sci. Technol.* **21**, 075016 (2008)
37. Y. Nakagawa, Y. Mawatari, H. Yamasaki, M. Murugesan, K. Develos-Bagarinao, Angular hysteresis in the critical current density of laser-patterned REBa₂Cu₃O_y films. *IEEE Trans. Appl. Supercond.* **17**, 3597 (2007)
38. S.A. Harrington, J.L. MacManus-Driscoll, J.H. Durrell, Practical vortex diodes from pinning enhanced YBa₂Cu₃O_{7- δ} . *Appl. Phys. Lett.* **95**, 022518 (2009)
39. N.M. Strickland, S.C. Wimbush, M.W. Rupich, N.J. Long, Asymmetries in the field and angle dependences of the critical current in HTS tapes. *IEEE Trans. Appl. Supercond.* **29**, 8001304 (2019)
40. F. Gömöry, J. Šouc, E. Seiler, M. Vojenčiak, X. Granados, Modification of critical current in HTSC tape conductors by a ferromagnetic layer. *J. Phys.: Conf. Ser.* **97**, 012096 (2008)
41. H.-J. Sung, B.-S. Go, H. Park, R.A. Badcock, M. Park, I.-K. Yu, Design, fabrication, and analysis of HTS coils for a 10-kW wind power generator employing a brushless exciter. *IEEE Trans. Appl. Supercond.* **27**, 5202305 (2017)
42. C.W. Bumby, R.A. Badcock, H.-J. Sung, K.-M. Kim, Z. Jiang, A.E. Pantoja, P. Bernardo, M. Park, R.G. Buckley, Development of a brushless HTS exciter for a 10 kW HTS synchronous generator. *Supercond. Sci. Technol.* **29**, 024008 (2016)
43. S.C. Wimbush, N.M. Strickland, Critical current characterisation of AMSC Amperium 2G HTS superconducting wire, figshare (2014), <https://doi.org/10.1063/1.4902139>

44. Z. Jiang, N.J. Long, M. Staines, R.A. Badcock, C.W. Bumby, R.G. Buckley, N. Amemiya, AC loss measurements in HTS coil assemblies with hybrid coil structures. *Supercond. Sci. Technol.* **29**, 095011 (2016)
45. Z. Jiang, N. Endo, S.C. Wimbush, J. Brooks, W. Song, D. Miyagi, M. Tsuda, Exploiting asymmetric wire critical current for the reduction of AC loss in HTS coil windings. *Supercond. Sci. Technol.* submitted (2019)
46. W. Prusseit, G. Sigl, R. Nemetschek, C. Hoffmann, J. Handke, A. Lümke, H. Kinder, Commercial coated conductor fabrication based on inclined substrate deposition. *IEEE Trans. Appl. Supercond.* **15**, 2608 (2005)
47. S.C. Wimbush, N.M. Strickland, Critical current characterisation of THEVA pre-production 2G HTS superconducting wire, figshare (2016), <https://doi.org/10.6084/m9.figshare.3759327.v1>
48. J.R. Clem, M. Weigand, J.H. Durrell, A.M. Campbell, Theory and experiment testing flux-line cutting physics. *Supercond. Sci. Technol.* **24**, 062002 (2011).
49. S.C. Wimbush, N.M. Strickland, N.J. Long, In-plane field angle dependence of the critical current of RBCO wires at low temperatures. *Phys. Proc.* **81**, 81 (2016)
50. L. Opherden, M. Sieger, P. Pahlke, R. Hühne, L. Schultz, A. Meledin, G. Van Tendeloo, R. Nast, B. Holzapfel, M. Bianchetti, J. L. MacManus-Driscoll, J. Hänisch, Large pinning forces and matching effects in $\text{YBa}_2\text{Cu}_3\text{O}_{7-\delta}$ thin films with $\text{Ba}_2\text{Y}(\text{Nb}/\text{Ta})\text{O}_6$ nano-precipitates. *Sci. Rep.* **6**, 21188 (2016)
51. M. Chudy, Z. Zhong, M. Eisterer, T. Coombs, n -values of commercial YBCO tapes before and after irradiation by fast neutrons. *Supercond. Sci. Technol.* **28**, 035008 (2015)
52. M.D. Ainslie, C.W. Bumby, Z. Jiang, R. Toyomoto, N. Amemiya, Numerical modelling of dynamic resistance in high-temperature superconducting coated-conductor wires. *Supercond. Sci. Technol.* **31**, 074003 (2018)
53. N. Amemiya, K. Miyamoto, N. Banno, O. Tsukamoto, Numerical analysis of AC losses in high T_c superconductors based on $E - j$ characteristics represented with n -value. *IEEE Trans. Appl. Supercond.* **7**, 2110 (1997)
54. S. Oh, H. Choi, C. Lee, S. Lee, J. Yoo, D. Youm, H. Yamada, H. Yamasaki, Relation between the critical current and the n value of ReBCO thin films: a scaling law for flux pinning of ReBCO thin films. *J. Appl. Phys.* **102**, 043904 (2007)
55. D.M.J. Taylor, D.P. Hampshire, Relationship between the n -value and critical current in Nb_3Sn superconducting wires exhibiting intrinsic and extrinsic behaviour. *Supercond. Sci. Technol.* **18**, S297 (2005)
56. B. Dutoit, M. Sjöström, S. Stavrev, Bi(2223) Ag sheathed tape I_c and exponent n characterization and modelling under DC applied magnetic field. *IEEE Trans. Appl. Supercond.* **9**, 809 (1999)
57. S.C. Wimbush, N.J. Long, The interpretation of the field angle dependence of the critical current in defect-engineered superconductors. *New J. Phys.* **14**, 083017 (2012)
58. E.F. Talantsev, N.M. Strickland, S.C. Wimbush, W.P. Crump, The onset of dissipation in high-temperature superconductors: self-field experiments. *AIP Adv.* **7**, 125230 (2017)
59. E.F. Talantsev, N.M. Strickland, S.C. Wimbush, J. Brooks, A.E. Pantoja, R.A. Badcock, J.G. Storey, J.L. Tallon, The onset of dissipation in high-temperature superconductors: magnetic hysteresis and field dependence. *Sci. Rep.* **8**, 14463 (2018)
60. N.J. Long, R.C. Maitra, E. Talantsev, R.A. Badcock, Mode I delamination testing of REBCO coated conductors via climbing drum peel test. *IEEE Trans. Appl. Supercond.* **28**, 6600705 (2018)

Chapter 2

Pinning Efficiency of Artificial Pinning Centers in Superconductor Nanocomposite Films



Judy Wu, Bibek Gautam, and Victor Ogunjimi

2.1 Introduction

The discovery of the high-temperature superconductivity (HTS) by Bednorz and Müller [1] in 1986 has triggered extensive research and redevelopment of HTS materials for various applications in electronics and electrical devices, and systems. A great impact on reducing energy loss and environment impact is anticipated from adopting superconducting devices and systems [2], ranging from lightweight electric propulsion and power generation in aircraft, to more efficient and reliable wind-powered generators, to high efficiency power grid, etc. [3–7]. For example, the superconductor's ability to carry high current densities would, by one design, reduce the mass of a wind turbine by approximately 35%, while increasing the maximum power output from 5 to 8 MW, as compared to its copper-based counterpart [6]. Significant market penetrations of HTS technologies, however, require performance-cost balanced HTS materials and put an urgent demand for basic material research to resolve the critical issues relevant to practical applications.

2.1.1 Critical Current Density and Fundamental Limiting Factors

The electrical current carrying capability of HTS materials is quantitatively described by critical current density J_c and critical current I_c and has been regarded as one of the most important parameters for practical applications [8, 9]. For example, HTS coated conductors (HTScc), the so-called second-generation HTS

J. Wu (✉) · B. Gautam · V. Ogunjimi
Department of Physics and Astronomy, University of Kansas, Lawrence, KS, USA
e-mail: jwu@ku.edu; gautbibe@ku.edu; victorogunjimi@ku.edu

wires that employ a strategy of epitaxy of HTS films on metal tapes of textured surface templates, are expected to carry large I_c on the order of a few hundreds to thousands Amperes per centimeter width at the liquid nitrogen temperature (77 K) on many kilometers of lengths to meet the requirement of power applications [2, 10, 11]. J_c is also a difficult parameter since it is affected by both intrinsic and extrinsic properties of the HTS materials. Among others, grain boundaries (GBs) are the decisive barriers to current flow and have posed a particularly interesting and difficult problem whose solution is vital to HTS applications. First of all, J_c is highly anisotropic in HTS materials due to their layered structures and higher J_c flows along the ab -planes. This requires HTS films to be epitaxy with not only c -axis orientation, but also in-plane grain alignment of GB angles as small as $\sim 2\text{--}3^\circ$ above which an exponential decrease of J_c with GB angle has been observed [12–16]. Reducing the large-angle GBs and hence its limiting effect on J_c has motivated exciting process in the research and development of the HTScc [11, 17, 18]. The HTScc employ epitaxy of HTS thin and thick films on flexible metal substrates. With minimization of the detrimental large-angle GB effect, high $J_c > 1 \text{ MA/cm}^2$ at self-field and at 77 K and high I_c up to thousands of Amperes per centimeter width have been demonstrated on many kilometers of lengths of HTScc [2, 10, 11, 17, 19, 20].

Depairing current density J_d is regarded as the ultimate limit of the J_c , which can be calculated using the Ginzburg-Landau equation: $J_d = \frac{c\phi_0}{12\sqrt{3}\pi^2\lambda_a^2\xi_a}$, where ϕ_0 is the magnetic flux quantum and λ_a and ξ_a are the transverse (perpendicular to the ab -plane) London penetration depth and Pippard coherence length, respectively [21]. Using the relevant parameters for REBa₂Cu₃O_{7- δ} (RE-123, RE = rare earth including Y, Gd, Sm, etc.), J_d (77 K, self-field) is around 40–50 MA/cm². However, in practical superconductors even epitaxial thin films that do not have significant detrimental GB effects, the best reported J_c is still much lower than J_d . A major hurdle in achieving J_d is in minimizing the dissipation associated with the motion of quantized magnetic vortices in HTSs. Strong nanoscale vortex pins with lateral dimension approaching $2\xi_a$ on the order of a few nanometers in HTSs must be generated to suppress the dissipation of vortex motion.

Furthermore, applications like generators and motors require HTScc to operate in magnetic fields (H) of $\sim 3\text{--}5 \text{ T}$, especially under varying H orientations [11]. When measured as function of the H orientations, defined by angle θ of H with respect to the normal (or c -axis) of the HTS in the plane perpendicular to the electric current, a strong peak of J_c at $B//ab$ -plane ($\theta = 90^\circ$) is observed. This peak is due to the intrinsic pinning of the planar structure of HTSs, in contrast to the much lower J_c values at $B//c$ -axis ($\theta = 0^\circ$) where correlated pinning is lacking. To better pin the vortices at an applied B at different B orientations, the HTS films must contain pinning centers of desired shape, dimension, and density. This has prompted extensive efforts in past decade or so and exciting results have been obtained in generating nanoscale artificial pinning centers (APCs) in HTSs [9, 11, 22–55].

2.1.2 Implementation of Artificial Pinning Centers (APCs) in HTS Nanocomposites

Strong pinning of quantized magnetic vortices by nanoscale APCs can lead to significantly enhanced J_c in HTSs. Among others, self-assembled c -axis aligned one-dimensional (1D) APCs have received most attention since they provide correlated pinning [56] to the magnetic vortices when the applied B is parallel to the 1D APCs. Specifically, significantly improved correlated pinning has been demonstrated in enhanced J_c at $B//c$ -axis if B is comparable to or less than the accommodation field $B_{max} = n_{1D} \phi_0$, where n_{1D} is the areal concentration of the 1D APCs. For large-scale applications the low-cost, self-assembly of APCs in APC/RE-123 nanocomposites via growth is certainly a preferred approach. It is particularly worth mentioning that quite a few impurity dopants including BaZrO₃ (BZO) [26, 41–44], BaSnO₃ (BSO) [45, 57], BaHfO₃ (BHO) [38, 46–50], and other rare earth tantalates, niobates, and hafnates [29, 46, 47, 51–54] have been found to self-assemble into c -axis aligned 1D APCs in APC/RE-123 nanocomposites. These 1D APCs provide strong correlated pinning [37, 56] as reflected in a prominent peak of J_c at $B//c$ -axis up to several Teslas at/near 77 K [9, 25–29]. Consequently, the J_c anisotropy between the $B//c$ and $B//ab$ directions is decreased. Many practical applications, such as superconducting magnets, transformers, and generators, require H orientation-independent J_c . This means the HTS nanocomposites should have not only c -axis aligned 1D APCs to address the issue of the weak pinning in layer-structured HTS, but also equivalent pinning in all other magnetic field directions. This requires APCs of mixed morphologies [20, 58–60].

Another benefit of the c -axis aligned 1D APCs is the constant pinning force density $F_p = J_c \times B$ through HTS film thickness. HTScc must carry I_c values on the order of hundreds to thousands Amperes per centimeter width for power applications [2, 8, 9, 61]. Given the “optimized” J_c of typically 4–5 MA/cm² at 77 K and SF on the standard RE-123 films, this requires HTS coating in HTScc to be several micrometers in thickness. Surprisingly, a monotonic decrease of J_c at 77 K and SF was observed in HTS films with film thickness t [9, 62]. This mysterious J_c - t behavior fitted well by $J_c \sim 1/\sqrt{t}$, persists despite the improvement made in achieving uniform chemical composition and crystalline structure across the film thickness [63, 64] In undoped YBCO films, the dominant pinning centers are point defects. According to the weak collective pinning (CP) model [56], the F_p exerted on a vortex of length $L < L_c$ ($L \sim t$ when H is along the film normal) scales as $L^{1/2}$ while the Lorentz force scales as L . This leads to the $J_c \sim 1/\sqrt{t}$ behavior because the vortex lines are rigid within the Larkin length L_c , which is on the order of few micrometers for a strong pinning system like YBCO [65] and cannot bend to accommodate different pinning centers nearby. Although thermally activated flux motion adds further complication on the J_c - t issue, the CP behavior has been confirmed in YBCO films in a wide range of temperature (T) and magnetic field (B) [66]. One resolution to this unfavorable thickness dependence is to chop vortices shorter [67] by making thick YBCO films into multilayers with insulating spacers.

For an n -layer sample, F_p can be increased by a factor of \sqrt{n} [68]. Alternatively, c -axis aligned 1D APCs can provide constant F_p /vortex length by overpowering the point defects and hence surpass the CP mechanism as demonstrated recently in thick YBCO films with BZO 1D APCs [69, 70] and nanotube pores (NTPs) [66].

2.1.3 Challenges and Critical Issues

Despite exciting progress made in enhancing J_c in APC/RE-123 nanocomposites, challenges remain in controllable self-assembly of APCs with precisely designed morphology, orientation, density, and APC/RE-123 interface. In particular, little is known on the controlling parameters that dictate the pinning efficiency of the APCs quantitatively. The lack of such understanding and control has prevented achievement of the APCs to function optimally based on the basic physics design rules.

First of all, the selection of APC materials has been primarily empirical and the few reported successful APCs, especially the c -axis aligned 1D APCs, are among many tested experimentally [71]. A question arises on what are the relevant parameters determining the APC morphology (shape, dimension, etc.) and can we ever predict the APC morphology before lengthy and tedious try-and-error experimental test?

In addition, little is known towards controlling the c -axis aligned 1D APC/RE-123 interface for optimal pinning efficiency. Fundamentally, a sharp superconductor/insulator interface at an atomic scale is desired for optimal pinning efficiency, which is in contrast to the strained and often defective 1D APC/RE-123 interfaces reported in nanocomposites using high-resolution transmission electron microscopy (HRTEM) [41, 72, 73]. Achieving a quantitative correlation between the pinning efficiency and the interface quality is not only imperative but also critical to engineering (or repairing) such an interface for optimal pinning efficiency.

Furthermore, higher density n_{1D} is desired for higher B_* that defines the operational magnetic field range of HTS devices. Unfortunately, a monotonically reduced superconducting transition temperature T_c with APC volume portion is common in doped YBCO and the serious T_c degradation at moderate APC doping, such as BZO 1D APCs, prevents applications at 77 K [25, 26]. This problem may be attributed to overlap of the strain field in a column of several nanometers in thickness surrounding the 1D APCs [41, 72, 74–76]. A substantial interface strain is revealed that can affect the electronic structure of the YBCO matrix through oxygen disorder induced in the strained YBCO columns [72]. This results in 1D APCs with lateral dimension $\gg 2\xi_a$, leading to reduced T_c as well as J_c due to reduced pinning efficiency and the effective cross-sectional area for electrical current flow, and B_* due to overlap of the strained YBCO columns at moderate-to-high 1D APC concentrations.

Finally, a pinning landscape with APCs of mixed morphologies of 1D, 2D (planar APCs), and 3D (nanoparticles of few nanometers in dimension) is necessary

ultimately for a B orientation-independent or θ -independent J_c [20, 58, 77]. For example, most 1D APCs have nearly perfect alignment along the c -axis. While a prominent peak of J_c appears at $B//c$ -axis ($\theta = 0^\circ$), the in-field J_c is not much improved or even reduced at H orientations deviating from the c -axis. In most cases, the J_c at $B//ab$ -plane ($\theta = 90^\circ$) is significantly reduced. This is unfortunate to many HTS applications, such as motors and generators, wherein the strong magnetic field may bend or twist causing the vortices to stray from the correlated pins. Splaying 1D APCs around the c -axis may extend the benefit of correlated pinning to a larger θ range. A theoretical work by Hwa et al. predicted that splayed 1D APCs force vortex entanglement and enhance J_c at an optimal splaying angle of $\theta_c \sim 10^\circ$ [78]. In experiment, splayed 1D defects produced by ion irradiation in HTS samples was found to carry higher J_c in magnetic fields than those with the same density of uniformly oriented linear tracks [79, 80]. The challenge is hence whether 1D APCs with desired splay, or in general, an optimally designed combination of APCs of different 1D, 2D, and 3D morphologies, could be generated in HTS nanocomposites via growth to yield a high and B orientation-independent J_c . This may be achieved by controlling the strain at microscopic scales using either one type of APC or multiple APC materials. Towards this goal, understanding a mixed APC landscape correlating quantitatively to the strain field at microscopic scale is important.

2.2 The Effect of the Strained Interfaces on APC's Microstructure and Pinning Efficiency

2.2.1 Strain-Mediated In Situ Self-Organization of APCs in APC/RE-123 Nanocomposites

In the in situ deposition processes such as pulsed laser deposition (PLD), sputtering, and metal-organic chemical vapor deposition, epitaxial APC/RE-123 nanocomposite films grow in the layer-by-layer mode. Phase segregation of the impurity APC materials from the RE-123 matrix at the initial stage of the growth results in primarily three coherent or semi-coherent (as defects appear) interfaces at APC/RE-123, APC/substrate, and RE-123/substrate interfaces as shown schematically in Fig. 2.1. Strains arise because of the lattice mismatches at these interfaces and are complicated by the different elastic properties of RE-123, APC, and substrate materials. Considering the much larger thickness of the substrates by many orders of magnitude, the contribution of the substrate elastic property can be neglected assuming only RE-123 and APCs will accommodate to the strain field generated. The resultant strain field serves as the driving force in the strain-mediated self-organization of the APCs in the APC/RE-123 nanocomposites. Considering the APC and RE-123 materials are elastic ceramics; the strain extends further from an interface into the epitaxial APC/RE-123 nanocomposite films. This means that the strain field may be highly non-uniform in the APC/RE-123 nanocomposite films.

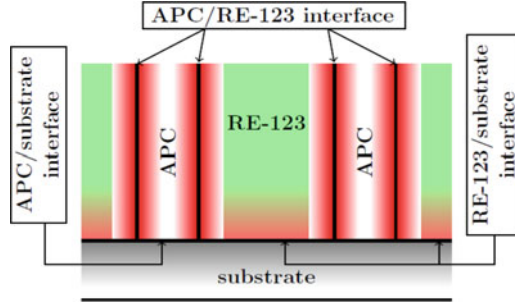


Fig. 2.1 Self-organization of 1D APCs driven by the combined strains originated from the strained interfaces. Three strained interfaces of 1D APC/RE-123 matrix, APC/substrate, and RE-123/substrate are illustrated schematically. Reproduced from [58] © IOP Publishing Ltd. All rights reserved

Modeling the strain field in APC/RE-123 nanocomposites therefore becomes a key to a thorough understanding its effect on the microstructure, such as APC morphology, dimension, orientation, concentration, and functionality especially the pinning efficiency of the APCs. Motivated by this, we have developed an elastic strain model [58, 81–83] to quantify the effect of the elastic properties of APC and RE-123 matrix (c_{ij}) and the lattice mismatch along ab -plane and c -axis (f_1 and f_3) at the APC/RE-123 interface on the APC landscape and functionality. Figure 2.2 highlights the simulation results on the material selection to form c -axis aligned 1D APCs and 3D APCs (Fig. 2.2a), the correlation of the elastic properties of APC materials on the 1D APC diameters (red symbols—experimentally confirmed [28, 41, 57, 84–92] and blue symbols—theoretically predicted) (Fig. 2.2b), and the orientation preference of the 1D APCs (c -axis), to mixed 1D + 2D APCs *at/near* the theoretically calculated phase boundary (solid line), to 2D APCs (ab -aligned) as the strain field is systematically tuned by varying the vicinal angle of the substrate (or RE-123/substrate lattice mismatch f_s) and APC doping level (Fig. 2.2c), symbols are experimental data). We have further integrated the modeling with advanced synthesis and characterization to correlate the microstructure and superconducting properties of the APC/RE-123 nanocomposites. This unique capability of integrated modeling + synthesis + characterization has enabled design of APC/RE-123 nanocomposites towards an optimal $J_c(B, T, \theta)$ and search for new functional APCs.

The insights revealed from the modeling of the strain-mediated microscopic growth mechanism of the APCs illustrate the critical effect of the strain field on the morphology, dimension, and orientation of APCs in the RE-123 nanocomposite films. These insights are certainly helpful to controllable generation of APC/RE-123 nanocomposite for enhanced pinning of vortices and hence enhanced J_c at applied magnetic field of different orientations through strain field manipulation to obtain desired APC landscape.

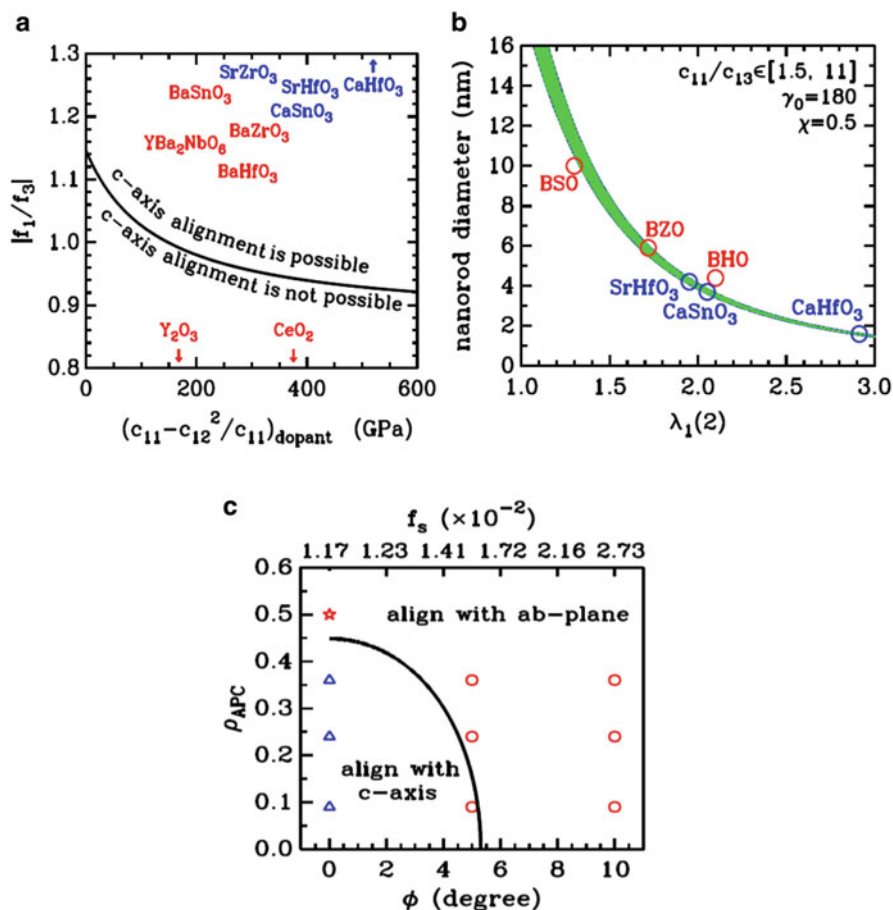


Fig. 2.2 (a) Solid line: calculated $|f_1/f_3|$ threshold as function of the elastic constants ($C_{11} - C_{13}^2/C_{33}$) above which the c-axis alignment of the 1D APCs is energetically preferred in YBCO films. Red: experimentally confirmed APCs and Blue: theoretically predicted possible APC materials to form 1D APCs in RE-123. (b) 1D APC diameter as function of the $\lambda_1(2)$ at different elastic constants c_{11}/c_{13} of APC. The green band represents the upper and lower bounds of the diameter at a given $\lambda_1(2)$ for the given c_{11}/c_{13} of APC. Several experimentally confirmed 1D APCs (red) and theoretically predicted ones (blue) are also included. (c) Orientation phase diagram of BZO 1D APCs in RE-123 matrix defined by the solid line from theoretical modeling. ρ_{APC} estimated from TEM is BZO 1D APC volume concentration and ϕ is the vicinal angle of STO substrate. The substrate/RE-123 lattice mismatch f_s at the major ticks of ϕ is marked on the top edge. The symbols are the experimentally observed cases. Reproduced from [58] © IOP Publishing Ltd. All rights reserved

2.2.2 Effect of the 1D APC/RE-123 Interface on the Pinning Efficiency of 1D APCs

Pinning efficiency is the primary functionality of an APC. Taking 1D APCs as an example, a fundamental question arises on whether 1D APCs all have a comparable pinning efficiency, if not what determines the pinning efficiency of an individual 1D APC? Theoretically, the pinning potential energy is proportional to the sharpness of the APC (insulator)/RE-123 (superconductor) interface. An optimal pinning efficiency is anticipated when such an interface is atomically sharp. The interface between the 1D APC and RE-123 matrix is generally strained and defective. Figure 2.3a depicts an HRTEM image of such a strained interface at BZO 1D APC/RE-123 reported by Cantoni et al. [72] In addition, through a comparison of the theoretically calculated strain distribution based on a coherent BZO/RE-123 interface (blue curve in Fig. 2.3b) with the experimentally measured one (red symbols in Fig. 2.3b) in the RE-123 surrounding the BZO 1D APC, two different concentric columns are revealed (separated by the dashed line in Fig. 2.3b, c). In the smaller column, a large concentration of defects, such as dislocations marked with white errors in Fig. 2.3a on the BZO/RE-123 interface, form which causes the deviation of the strain distribution in this column from the theoretical curve for a coherent BZO/RE-123 interface. This defective YBCO column of a few nanometers in thickness has been found highly oxygen deficient, leading to a much lower T_{c2} (estimated to be 60–70 K from the oxygen deficiency [72]) than the T_{c1} (5–6 K lower than $T_{c,YBCO}$) in the larger strained column [93] or measured on BZO/RE-123 nanocomposites [41, 72, 75, 76].

The detrimental impact of the defective, semi-coherent BZO 1D APC/YBCO interface may be attributed quantitatively to the large lattice mismatch along the c -axis of YBCO and BZO and rigidity of the APC (BZO in this case). In order to confirm this hypothesis, we have carried out a comparative study of the pinning efficiency of BZO 1D APCs and BHO 1D APCs of comparable diameters of 5–6 nm (see Table 2.1) in 2–6 vol.% doped BZO and BHO 1D APC/YBCO nanocomposites synthesized using PLD at the optimal condition identified for each of them [73, 94]. Figure 2.4 compares the F_p (H) curves measured at 65 K on 4 vol.% BZO 1D APC/YBCO (blue) and 4 vol. % BHO 1D APC/YBCO (red) nanocomposite films. In contrast to a peak value $F_{p,max} \sim 72.4$ GN/m³ at $B_{max} \sim 5.0$ T in the BZO/YBCO sample, which is comparable to the best so far reported on BZO/YBCO nanocomposites [44], the F_p increases monotonically with increasing B . It reaches to a record high $F_p = 182$ GN/m³ at $B = 9.0$ T (instrument limitation) in BHO/YBCO sample, which is 2.5 times of the best reported in the BZO 1D APC/YBCO counterpart [44, 73]. The insets of Fig. 2.4 (top) illustrate the HRTEM fast Fourier filtered images taken on the two samples. A major difference between the two cases is in the higher concentration of dislocations (white marks) at the BZO 1D APC/YBCO interface (top left), which may be explained by the larger BZO/YBCO lattice mismatch (7.7%) and higher rigidity of BZO [49, 81]. In contrast, a coherent BHO/YBCO interface (top right) may be attributed to

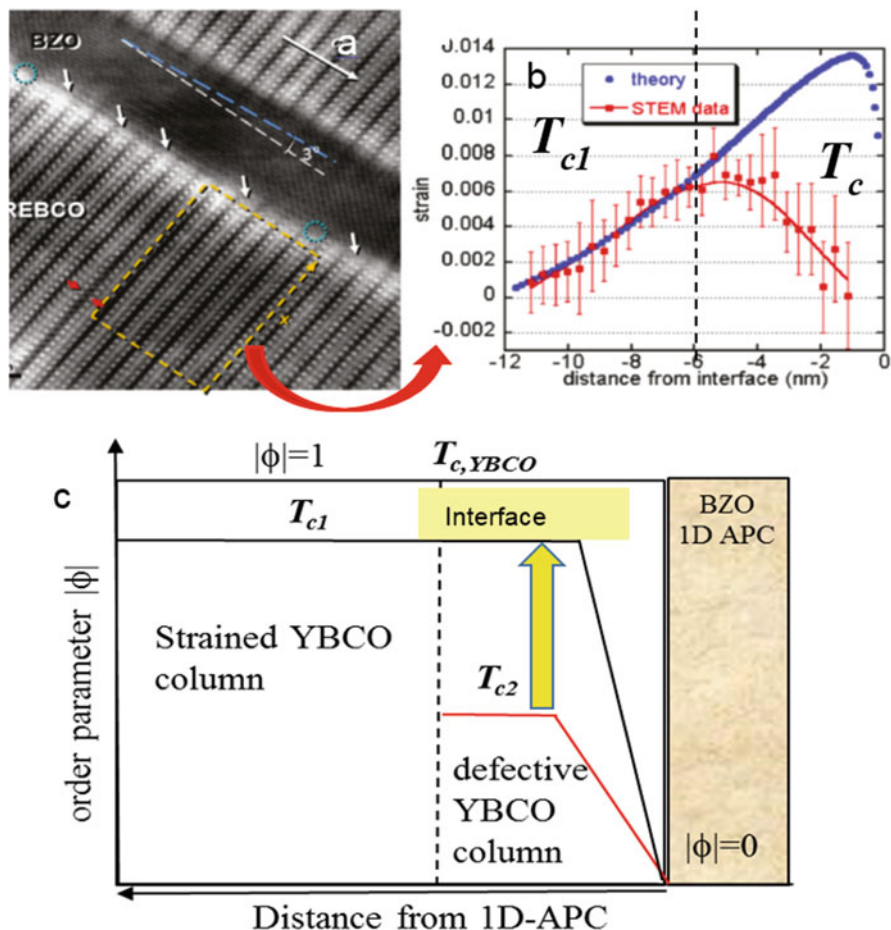


Fig. 2.3 (a) HRTEM of BZO/YBCO interface, and (b) calculated strain (blue) and HRTEM measured strain distributions in YBCO around the 1D BZO/YBCO c. Schematic of the superconducting order parameter $|\phi|$ as function of the distance from the BZO 1D APC. Two concentric YBCO columns are surrounding the BZO 1D APC with the larger one representing the strained YBCO of T_{c1} and the smaller one of lower T_{c2} due to a defective semi-coherent BZO 1D APC/YBCO interface. The yellow arrow illustrates the effect of BZO/YBCO interface repair using Ca-diffusion to reduce the oxygen disorder and hence raise the T_{c2} . Source for (a and b) C. Cantoni et al., ACS Nano 2011 [72]. Adapted with permission from ACS Publishing

the slightly smaller lattice mismatch (7.1%) and lower rigidity of the latter. The accommodation of the BHO and YBCO lattices through their strained coherent interface is illustrated in the wavy ab -planes in the HRTEM fast Fourier filtered images and elongated c -axis lattice constant in the range of 11.77 Å–11.78 Å for BHO/YBCO samples with BHO doping of 2–6 vol.% [73]. This means there is no inner YBCO column around the BHO 1D APC, or there is only one YBCO column

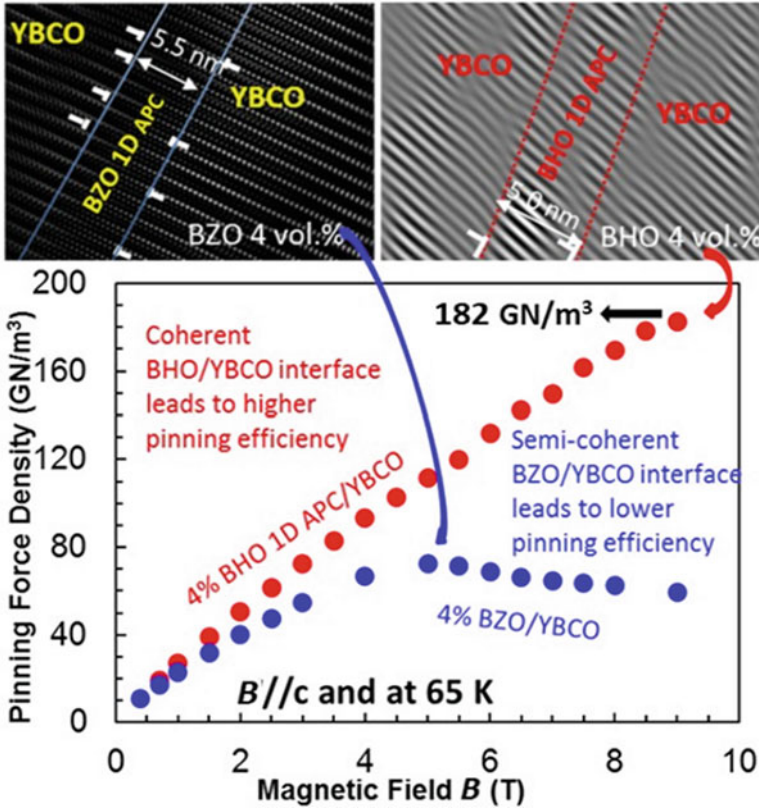


Fig. 2.4 F_p vs. B curves measured on 4% BZO 1D APC/YBCO (blue) and BHO 1D APC/YBCO (red) nanocomposite films of ~ 200 nm in thickness at $B//c$ -axis and 65 K. A record high $F_p = 182$ GNm^{-3} is demonstrated on the 4% BHO 1D APC/YBCO at $B \sim 9.0$ T. The insets show HRTEM fast Fourier filtered images of the cross-section of BZO 1D APC/YBCO (top left) with a semi-coherent interface due to a large concentration of dislocations (white marks on the APC/YBCO interface) in contrast to a coherent interface for the BHO 1D APC/YBCO sample. The SL and ML samples were made at $T_s = 810$ °C using PLD

around the BHO 1D APC with T_{c1} (Fig. 2.3c). The BZO/YBCO interface, however, is highly defective as expected due to the larger concentration of the dislocations with a further reduced $T_{c2} \sim 60\text{--}70$ K [72] that is significantly lower than that of the larger strained YBCO column shown in Fig. 2.3c typically in the range of $T_{c1} \sim 84\text{--}88$ K measured on the nanocomposites (Table 2.1).

This result reveals the important role of the 1D APC/RE-123 interface quality in the APC pinning efficiency. In particular, the BZO and BHO 1D APCs have comparable diameters of 5–6 nm, while $F_{p,max} \sim 182$ GNm^{-3} of the BHO 1D APC is 2.5 times of the best reported on BZO 1D APC [44, 73]. This is the best $F_{p,max} \sim 182$ GNm^{-3} reported so far at 65 K, and is about 1.5 times, 1.8 times, and 1.5 times higher, respectively, than the highest claimed $F_{p,max} \sim 120$ GNm^{-3}

Table 2.1 A summary of the c -axis lattice constant, FWHM of YBCO (005) peak, T_c , 1D APC diameters D , average 1D APC spacing d (center-to-center) with uncertainty of 1 nm, matching field $B_* = \Phi_0/d^2$, $F_{p,max}$ and H_{max} for the 2–4 vol.% BZO 1D APC/YBCO and BHO 1D APC/YBCO in single-doped (SD) and double-doped (DD) nanocomposite films

Sample ID	c -axis lattice constant (\AA)	FWHM of YBCO (005) peak	T_c (K)	1D APC Diameter (nm)	1D APC Spacing (d) (nm) ± 1 nm	B_* (T)	$B//c$ -axis and at 77 K		$B//c$ -axis and at 65 K	
							$F_{p,max}$ (GN/m ³)	B_{max} (T)	$F_{p,max}$ (GN/m ³)	B_{max} (T)
2 vol.% BHO SD	11.77	0.42	88.85	4.6 \pm 0.5	31.0	2.0	11.8	5.0	76.9	7.0
2 vol.% BZO SD	11.82	0.35	89.27	5.2 \pm 0.5	20.0	5.0	18.4	3.0	73.1	3.5
4 vol.% BHO SD	11.76	0.51	85.84	4.8 \pm 0.4	13.0	12.2	22.8	7.5	182.0	>9.0
4 vol.% BZO SD	11.71	0.35	87.48	5.8 \pm 0.6	15.0	9.2	13.33	4.0	72.37	5.0
4 vol.% BHO DD	11.75	0.75	86.6	4.8 \pm 0.5	13.0	12.2	7.36	4.0	67.72	7.5
4 vol.% BZO DD	11.72	0.82	87.69	5.7 \pm 0.6	15.0	9.2	3.33	5.5	49.49	8.0

Table 2.2 Comparison of 1D APC diameter (D), inter-1D APC distance, (record high) maximum pinning forces $F_{p,max}$ and matching field ($B_* = \Phi_0/d^2$), B_{max}/B_* of BM(=Zr, Sn and Hf)O on RE(=Y, Sm) BCO thin films in this work and published works

Sample information	D (nm)	Average inter 1D APC distance d (nm)	$F_{p,max}$ (GN/m ³) at 65 K	B_* (T)	B_{max}/B_* at 65 K	Ref.
2 vol.% BZO/YBCO	5.2	20 0	73.1	5.0	0.70	[71]
	5.0–6.0	approx. 20	74.0	6.0	0.83	[44]
4 vol.% BZO/YBCO	5.8	15.0	72.4	9.2	0.54	[71]
	5.0–6.0	11.0–13.0	~62.0	15	0.40	[44]
4 vol.% BHO/YBCO	5.0	13.0	182.0	12.2	0.74	[71]
3.8 vol.% BHO/SmBCO	5.0–6.0	Not provided	120.0	6.0	0.83	[97]
3.48 vol.% BSO/YBCO	8.4	21.0	103.0	4.8	0.63	[45]
5.0 mol.% BaNbOy+5.0 mol.% Y ₂ O ₃ /YBCO	10–15	Not provided	122.0	2.0	2.5	[54]

for BHO/RE-123, $F_{p,max} \sim 103$ GN/m³ for BSO/RE-123 [45], and $F_{p,max} \sim 122$ GN/m³ for double perovskites (5.0 mol.% BaNbOy plus 5.0 mol.% Y₂O₃)/RE-123 [54] nanocomposites, respectively (Table 2.2). This result reveals that the APC/RE-123 interface plays a critical role in determining the pinning efficiency of a 1D APC. Specifically, the difference in the T_c of the superconducting RE-123 column immediately surrounding a 1D APC seems to link intimately to the pinning efficiency of the 1D APC. In another word, achieving a higher T_c close to the $T_{c,YBCO}$ in the RE-123 column is a key to reach the optimal pinning efficiency of a 1D APC.

2.2.3 Effect of the 1D APC/RE-123 Interface on the Matching Field B_*

The matching field B_* is an important parameter in 1D APC/RE-123 nanocomposites and can be calculated based on the areal density of 1D APCs measured in TEM. High B_* is desired for high-field applications assuming the best pinning efficiency would be obtained when the applied field is around B_* , or all vortices are accommodated by strong 1D APCs. For many impure materials that form 1D APCs in RE-123, B_* has been found to be proportional linearly to the impurity doping concentration [44, 58]. Therefore, high B_* could be obtained by doping high concentration of impurity in the APC/RE-123 nanocomposites. BZO presents

an excellent example and the B_* indeed increases linearly with the BZO doping in the range 2–6 vol.% as shown in Table 2.1. Also included in Table 2.1 are BHO-doped YBCO nanocomposite samples with the same doping range of 2–6 vol.%. In contrast to the linear increasing trend of the B_* vs. BZO doping, a peak value of the B_* occurs at 4 vol.% of BHO doping [73, 95]. Based on the TEM analysis, the B_* increases with BHO doping from 2 to 4 vol.%, followed with a decrease of B_* at higher BHO doping. This observation raises a question on how the 1D APC/RE-123 interfacial strain affects the strain field distribution in the APC/RE-123 nanocomposites and how quantitatively the strain field, especially as the strain field of individual 1D APCs overlap at high APC doping, affects the formation of the 1D APCs at high APC doping? Furthermore, the BHO 1D APC pinning efficiency varies in the BHO/RE-123 nanocomposites synthesized at different substrate temperatures (T_s) as revealed in our preliminary study with the optimal $T_s = 810$ °C, raising a further question on how the BHO/RE-123 interface is affected by the T_s below or above this temperature?

The comparison between the BZO 1D APC/RE-123 and BHO 1D APC/RE-123 nanocomposites suggests that the 1D APC/RE-123 interface not only affects the individual 1D APC pinning efficiency but also the B_{max} (or areal density of the 1D APC). Specifically, the semi-coherent BZO 1D APC/RE-123 interface may relieve the interfacial strain through formation of the defective inner column of RE-123 of lower T_{c2} that reduces the pinning efficiency, but on the other hand enable more BZO 1D APCs to form at high BZO doping for high B_* .

2.2.4 Correlation Between B_{max} and the Matching Field B_*

Considering the best overall pinning efficiency is expected at $B \sim B_*$, the location B_{max} at which the peak value of the pinning force density $F_{p,max}$ on the $F_p(B)$ curve occurs should be associated to the B_* considering $B_{max}/B_* \sim 1$ corresponds to one vortex pinned by one 1D APC. Therefore, the ratio B_{max}/B_* can provide a quantitative evaluation of the portion of effective pins in the generated 1D APCs. However, it should be realized that the assumption that all generated 1D APCs are efficient vortex pins might not be proper depending on the APC/RE-123 interface as discussed in previous sections.

Interestingly, the $F_{p,max}$ does not occur at $B_{max}/B_* \sim 1$ in the comparative study of 2–6 vol.% BZO and BHO 1D APC/RE-123 nanocomposites [73]. Even at comparable B_* values for the two types of the nanocomposites, very different H_{max} values were observed on BZO 1D APC/YBCO and BHO 1D APC/YBCO nanocomposites shown in Table 2.1. For example, the B_{max}/B_* ratio is up to 3.5 in the BHO 1D APC in contrast to 0.7 in the latter at 65 K. If $B_{max}/B_* \sim 1$ corresponds to one vortex pinned by one 1D APC, the $B_{max}/B_* < 1$ ratio in the BZO 1D APC case suggests a substantial portion of the BZO 1D APCs may be inefficient pins at 65 K. This is due to the comparable T_{c2} in the range of 60–70 K of the inner YBCO column around the BZO 1D APCs. Remarkably, the $B_{max}/B_* > 1$ observed

on BHO 1D APC/RE-123 may be attributed to the very strong pinning efficiency of the BHO 1D APCs to allow a small size ordered lattice of vortices to be pinned by one BHO 1D APC. It should be realized that this can only occur at large magnetic fields to allow an ordered vortex lattice to form and the inter-vortex interaction becomes important. When some of the vortices on the lattice are pinned by strong 1D APCs, such as BHO 1D APCs, the entire lattice may be pinned effectively if the energy threshold to shear the lattice is reasonably high with respect to the thermal activation.

2.2.5 The Impact of Strain Field on APC's Pinning Efficiency

The theoretical study of the elastic strain field shown in Fig. 2.2c indicates APCs of mixed 1D and 2D (planar) may be obtained from a single APC material at/near the calculated phase boundary (solid line) in Fig. 2.2c by implementing the RE-123/substrate interfacial strain to the nanocomposites. This has been indeed confirmed experimentally (symbols in Fig. 2.2c) by varying the substrate vicinal angle [85] or/and by varying the APC doping level. On flat SrTiO₃ (STO) substrates (Fig. 2.5a–c), only *c*-axis aligned 1D APCs can be obtained when the BZO doping is varied in 2–6 vol.%. On 5° vicinal STO, while mixed 1D + 2D BZO can be obtained at low BZO doping up to 4 vol.% (Fig. 2.5d–e), only *ab*-aligned APCs are present at higher BZO doping (Fig. 2.5f).

A fundamental difference exists in the strain fields of YBCO matrix in the nonvicinal and vicinal BZO/YBCO nanocomposites, which is the reversal of the strain direction from the tensile strain along the *c*-axis on the YBCO lattice in the former to the compressive one in the latter at a small vicinal angle $\phi \leq 10^\circ$. This strain reversion in YBCO lattice explains the reduced T_c in the former while almost undegraded T_c in the latter [39, 96]. This has profound effects on the pinning efficiency of the BZO APCs as shown in Fig. 2.6a. Much higher J_c by 100–400% can be observed in BZO/YBCO nanocomposites on vicinal STO of $\phi \leq 10^\circ$ (1D + 2D APCs, red and blue) at all *B* orientations as compared to their counterpart (BZO 1D APC only)

on nonvicinal STO (black). A similar trend can be seen in Fig. 2.6b at different BZO doping of 2–6 vol.%. Interestingly, the BZO 1D APCs have almost identical diameter and density on 5° vicinal (red) and nonvicinal STO (black). This result illustrates an important impact of the strain field in YBCO matrix on the pinning efficiency of the APCs in the APC/RE-123 nanocomposites. Specifically, with implementation the in-plane tensile strain on YBCO using vicinal substrates and hence compensation of the detrimental tensile strain induced from the 1D APC/RE-123 interface in the *c*-axis, we show the pinning efficiency of the BZO 1D APCs can be enhanced. While a systematic investigation is necessary, we hypothesize that the *c*-axis strain direction reversal in vicinal BZO/YBCO nanocomposites may reduce the defects in the inner YBCO column around the BZO 1D APCs, indicating a possible way to repair the BZO 1D APC/YBCO interface and hence increase F_p and

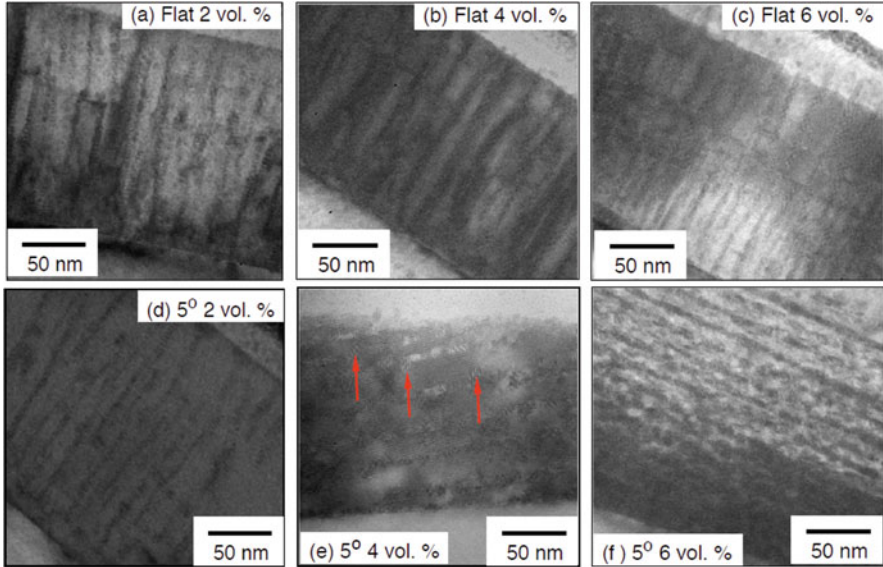


Fig. 2.5 TEM cross-sectional images of BZO/YBCO films on the flat (top row) and $\phi = 5^\circ$ vicinal (bottom row) STO substrates with (a) and (d) 2%; (b) and (e) 4%; (c) and (f) 6% BZO doping. Reproduced from [77] Fig. 2.2. © IOP Publishing Ltd. All rights reserved

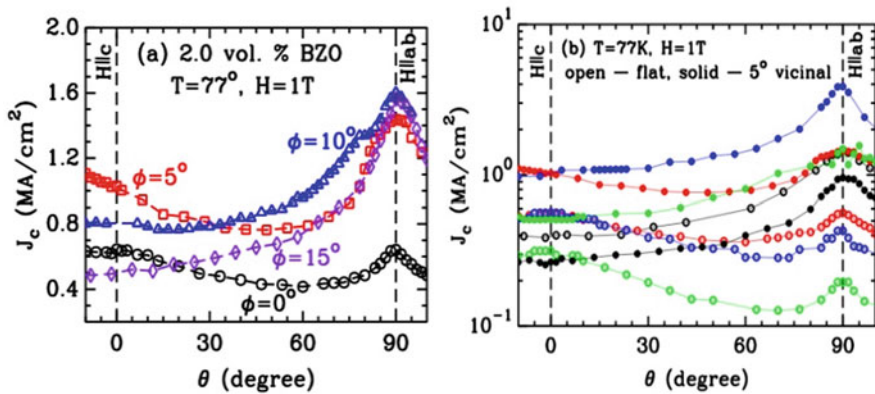


Fig. 2.6 J_c - θ curves at $B = 1$ T and 77 K of (a) BZO/YBCO films on 5° (red), 10° (blue) and 15° (purple) vicinal STO substrates, respectively. The J_c - θ curve for nonvicinal counterpart (black) is also included for comparison; and (b) J_c - θ curves at $B = 1$ T and 77 K for the BZO doping of 0 vol.% (black), 2 vol.% (red), 4 vol.% (blue), and 6 vol. % (green) BZO/YBCO nanocomposite films on flat (open) and 5° vicinal (solid) STO substrates. Reproduced from [58] © IOP Publishing Ltd. All rights reserved

J_c in BZO/RE-123 nanocomposites. In addition, the c-axis strain direction reversal also benefits pinning in almost all B orientations as shown in Fig. 2.6. This is in contrast to degraded intrinsic pinning by the ab-planes in RE-123 due to the ab-plane buckling, leading to overall higher F_p and J_c in almost all B orientations.

It is well known that the strained 1D APC/RE-123 interface plays a critical role in self-assembly of the 1D APCs in 1D APC/RE-123 nanocomposites [58, 81, 82]. However, a nonlinear B_* vs. BHO doping with B_* peaked at 4 vol.% is observed in our preliminary study, which is in contrast to the linear increase of the B_* with BZO doping in the same range of doping 2–6 vol.%. If the strain overlap is the limiting factor that prevents further increase of the B_* in BHO/YBCO with doping >4 vol.%, small angle vicinal substrates may provide a resolution and will be explored for BHO/YBCO nanocomposites. The obtained accommodation field B_* vs. APC doping trends will be correlated with the strain field distributions in these two types of APC nanocomposites. This experimental study will be combined with simulation using elastic strain model to elucidate how strain field affects the linearity of the B_* with the APC doping. In particular, this study will provide insights on how interfacial strain affects the strain field distribution in the APC/RE-123 nanocomposites and how quantitatively the strain field, especially as the strain field of individual 1D APCs overlap at high APC doping, affects the formation of the 1D APCs at high APC doping [72, 97].

Figure 2.7 depicts $J_c(\theta)$ curves taken on 4 vol.% BZO/YBCO and BHO/YBCO nanocomposite samples. It is clearly shown that the difference in the APC/YBCO interface (Fig. 2.3) has impacts beyond $B//c$ -axis. Specifically, at both 77 K and 65 K, the coherent BHO/YBCO interface leads to overall higher J_c and much

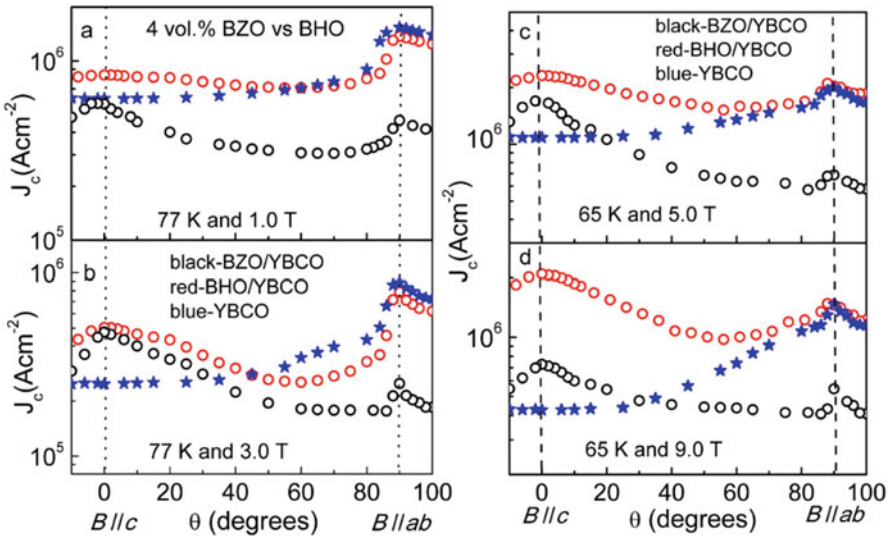


Fig. 2.7 J_c - θ curves for 4 vol.% BZO/YBCO (black) and 4 vol.% BHO/YBCO (red) at (a) 77 K and 1 T, (b) 77 K and 3 T, (c) 65 K and 5 T, and (d) 65 K and 9 T. Undoped YBCO film (blue) is also included for reference. Reproduced from [73] © AIP Publishing Ltd. All rights reserved

less B orientation-dependence of the BHO/YBCO sample (red) as compared to the BZO/YBCO and reference YBCO samples. By extending the microstructure and transport $J_c(B, T, \theta)$ study to the entire doping range of 2–8 vol.%, we seek ways to generate high concentration 1D APCs with optimal pinning efficiency.

2.2.6 Towards Magnetic Field Orientation-Independent J_c

This prompts a question on whether an alternative scheme can be developed to generate mixed APCs of 1D + 2D + 3D at high APC concentrations for strong and B orientation-independent J_c in high-applied magnetic fields above a few Tesla. Among the 1D APC materials shown in Fig. 2.2a, BHO has the lowest rigidity since it is the closest to the phase change boundary (solid line from simulation). This makes BHO more adaptive to local strain generated by 3D APCs such as Y_2O_3 nanoparticles. In an exploratory study, a mixed 1D + 2D + 3D APC landscape [38, 49] is obtained using double doping of BHO and Y_2O_3 .

At and near the calculated phase boundary, the two orientation phases of 1D and 2D APCs could coexist in the nanocomposite films. Furthermore, by selecting different ϕ or f_s values to apply different tensile strains on the YBCO matrix, the concentrations of the two orientation phases may be quantitatively controlled [92]. On the top of the Fig. 2.2c, the lattice mismatch between the film and substrate f_s is marked considering the equivalent tensile strain at a given vicinal angle ϕ . This means vicinal substrates can be replaced with a spacer layer with a desired f_s to generate tensile strain on the YBCO ab -plane (and hence compressive strain on c -axis) [82] to form 1D + 2D mixed APCs on the calculated phase boundary. In the proposed work, this ab -plane “stretching” will be explored using a spacer layer such as Sm_2O_3 (0.5%) to Nd_2O_3 (1.8%) [98–100] to form a multilayer (ML) with APC/RE-123. These strain engineered MLs will minimize the c -axis tensile strain and hence T_c degradation of RE-123 matrix due to c -axis 1D APC due to compressive strain on c -axis of RE-123 induced by the spacer layer. An additional advantage of these multilayers is extension of the strong pinning effect to a large thickness much beyond the critical thickness $<1 \mu\text{m}$ [101] from the YBCO/substrate interfacial strain. PLD will be used to fabricate the ML samples and the PLD conditions and ML design parameters will be optimized with respect to the pinning performance from the $J_c(B, T, \theta)$ measurement. For the APC materials, both single-doped (SD) BZO (BHO) 1D APCs and double-doped (DD) BZO (BHO) 1D APC (primary) and Y_2O_3 (secondary) will be considered in these strain engineered MLs. HRTEM studies of the APC microstructure and transport J_c measurement in the ML samples will be compared with that on vicinal substrates to validate the ML approach for generating mixed APC pinning landscape especially at higher APC concentration and larger nanocomposite thickness.

In a preliminary study of single-layer BZO and BHO DD samples [36, 38, 43, 49, 102], we have found BHO provides a particular interesting primary APC to form both 1D APC in c -axis and 2D APC in ab -plane, resulting in 1D + 2D + 3D

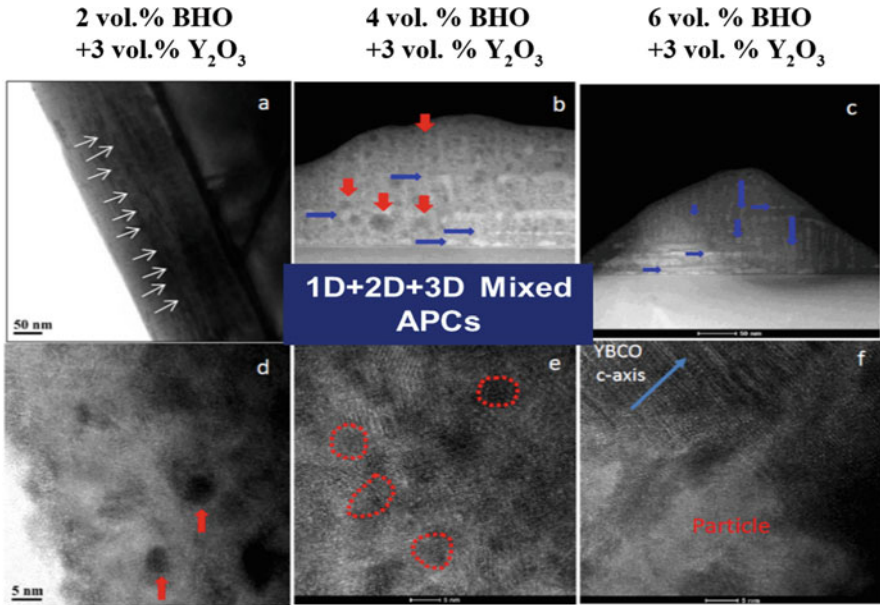


Fig. 2.8 TEM images of 2, 4, and 6% BHO DD nanocomposite films (a–c) at low magnification, respectively, (d–f) at high magnification, respectively. Scale bar 50 nm is same for (a–c) and 5 nm is same for (d–f). Reproduced from [38] © IOP Publishing Ltd. All rights reserved

mixed APCs as shown in Fig. 2.8 [49]. This is in contrast to the 1D BZO +3D Y_2O_3 APC in BZO DD samples [36, 95, 103, 104]. The difference in the APC morphology between the BHO and BZO DD samples is attributed to the smaller BHO/YBCO lattice mismatch and smaller rigidity of the BHO as compared to BZO [49, 81]. This difference in the APC morphology leads to a much smaller B orientation-dependence as shown in Fig. 2.9 that compares 2 vol.% double-doped BZO + Y_2O_3 /YBCO and BHO + Y_2O_3 /YBCO nanocomposite. For example, the J_c variation for the 2% BHO/YBCO nanocomposite is only about 18% in the entire θ range from $B//c$ -axis ($\theta = 0^\circ$) to $B//ab$ -plane ($\theta = 90^\circ$) with an overall $J_c > 1 \text{ MA/cm}^2$ at 65 K and 9.0 T. It illustrates APCs of mixed morphologies by modeling-guided double doping can indeed provide a scheme for generation of a strong and isotropic pinning landscape in HTS nanocomposites.

A much less H -dependent approach for quantifying pinning anisotropy is illustrated in Fig. 2.10. The BZO DD sample shows a more uniform $B_{\max}(\theta)$ (Fig. 2.10a) and $\alpha(\theta)$ (Fig. 2.10b) relative to the BZO SD sample. In addition, the DD film offers better pinning efficiency since its H_{\max} values (α values) are generally higher (lower) than the other two samples. At 65 K, the DD film's B_{\max} values are in the high range of 8–9 T and its α values are in the low range of 0.12–0.22. This uniformity and the higher pinning efficiency point to a more isotropic and stronger pinning landscape in the double-doped film compared to the single-doped and reference YBCO samples.

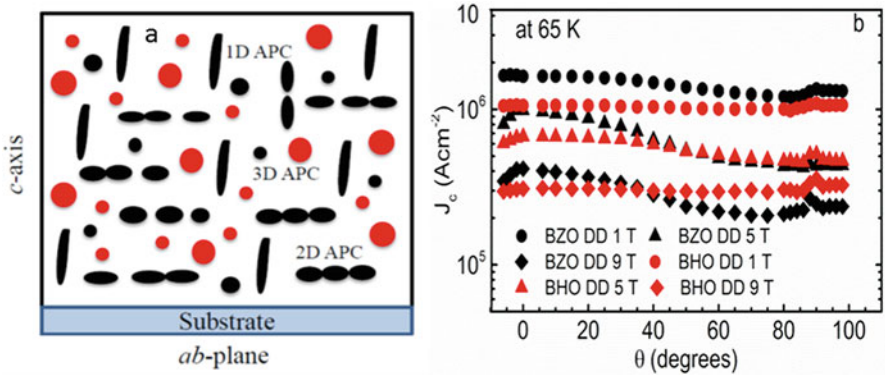


Fig. 2.9 (a) Schematic of the microstructure distribution in the BHO + Y₂O₃ double-doped (DD) YBCO nanocomposites. Color codes: BHO 1D, 2D, and 3D APCs (black), Y₂O₃ 3D APCs (red). (b) Angular dependence of J_c measured on 2 vol.% BHO DD (red) and BZO DD (black) nanocomposite films at 1 T (circle), 5 T (triangle), and 9 T (diamond) at 65 K. (a) Reproduced from [38] © IOP Publishing Ltd. (b) Reproduced from [49] © AIP Publishing Ltd. All rights reserved

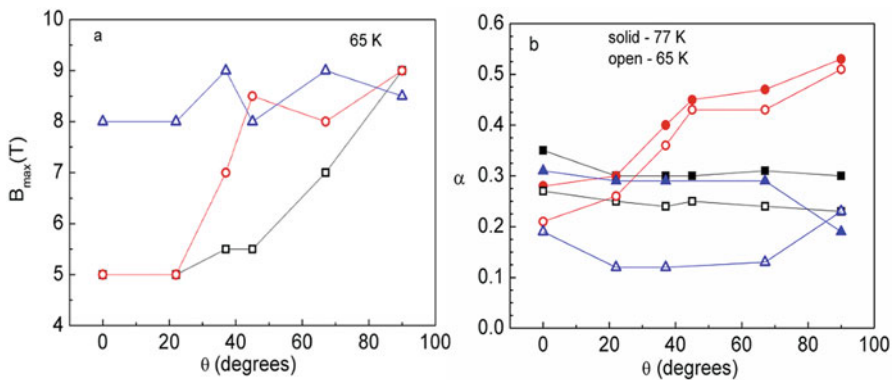


Fig. 2.10 $B_{max}(\theta)$ (a) and $\alpha(\theta)$ (b) data at 77 K (solid symbols) and 65 K (open symbols) for the samples- 4% BZO SD (red circle), 4% BZO DD (blue triangle), and undoped YBCO (black square)

The DD approaches will be investigated systematically for enhanced pinning and mechanical properties, and key to this enhanced performance is to achieve a coherent APC/HTS interface and will be further developed in the proposed research. Besides BZO and BHO, the theoretically predicted 1D APC materials of small diameters approaching $2\xi_a$ and self-repair mechanism, such as CaHfO₃, and CaSnO₃ will also be studied for mixed APC landscape for high pinning efficiency. Doping of these materials in YBCO will be conducted using sectional PLD targets for flexibility of doping level control. The PLD growth of the nanocomposite films will be combined with microstructure analysis using HRTEM and transport $J_c(T, B, \theta)$ measurements at 0–9 T, 50–77 K, and B orientations from $B//c$ -axis ($\theta = 0^\circ$)

to $B//ab$ -plane ($\theta = 90^\circ$). Two primary parameters to be investigated include growth temperature and the doping level.

2.3 Conclusion

Superconductors can carry electric currents without loss, which is one of the most exotic physical phenomena in nature and is described quantitatively by superconducting critical current density J_c . Superconductivity therefore offers opportunities in electronics and electric applications, such as restoring the reliability of the power grid and increasing its capacity and efficiency. The discovery of HTSs has not only provided possibility for superconductor applications at liquid nitrogen temperature, but also presented a fascinating research topic due to their unusual d-wave symmetry in electronic structure and anisotropy stemming from the layered crystalline structures, resulting in profound effects on their physical properties especially J_c . Raising J_c in HTSs has been the focus of worldwide efforts in the field of applied superconductivity during the past three decades. In particular, a long-standing question is whether the theoretical depairing limit J_d can be reached in practical HTS conductors, such as RE-123 through strain-mediated self-assembly of strong nanoscale APCs designed to pin the quantized magnetic vortices in APC/RE-123 nanocomposites. Answering this question demands capability in engineering the microstructure and interfaces of APC/RE-123 nanocomposites at nanoscales based on a thorough understanding of fundamental physics governing the pinning landscape and pinning efficiency of APCs in the HTS nanocomposites.

With exciting progress made so far in development of APC/RE-123 nanocomposites with enhanced pinning, development of more quantitative approaches, through integration of modeling, synthesis, and characterization, to correlate microstructures and pinning efficiency becomes imperative and urgent. The result presented in this chapter represents an exploratory effort in this regard. Through comparative studies of the two model systems of BZO and BHO 1D APCs in APC/YBCO nanocomposite films, we show the strained APC/RE-123 interfaces not only affect the 1D APC microstructure in strain-mediated self-assembly of APCs, but also impact their pinning efficiency in APC/RE-123 nanocomposites. The quantitative correlation of the APC/RE-123 quality with their B_* , B_{max} , and F_{pmax} reveals the critical importance in controlling the APC/RE-123 interface towards achieving optimal pinning landscape with high pinning efficiency including high F_{pmax} at 77 K or close, high B_{max} especially high B_{max}/B_* ratio, low magnetic field orientation-dependence, etc. Nevertheless, many more questions remain. For example, what determines the pinning efficiency quantitatively of a formed APC? Would strong APCs allow enhancement of J_c approaching J_d ? What would be the limit of the pinning force density F_p at high magnetic fields and different H orientations to meet the specification of practical applications? In order to answer these questions to achieve controllable APCs with precisely designed morphology, orientation, density, and APC/RE-123 interface approaching the optimal pinning efficiency, new

approaches transitioning from the traditionally empirical try-and-error to material-by design with a precise guidance of fundamental physics must be developed.

Acknowledgments The authors acknowledge support in part by ARO contracts No. ARO-W911NF-16-1-0029, and NSF contracts Nos. NSF-ECCS-1809293/1809284 and NSF-DMR-1508494 and DMR-1909292.

References

1. J.G. Bednorz, K.A. Muller, *Zeitschrift Fur Physik B-Condensed Matter* **64**(2), 189–193 (1986)
2. www.sc.doe.gov/bes/reports/abstracts.html#sc (2005)
3. C.A. Luongo, P.J. Masson, T. Nam, D. Mavris, H.D. Kim, G.V. Brown, M. Waters, D. Hall, *IEEE Trans. Appl. Supercond.* **19**(3), 1055–1068 (2009)
4. R.L. Holtz, R.J. Soulen, M. Osofsky, J.H. Claassen, G. Spanos, D.U. Gubser, R. Goswami, M. Patten, *Mater. Sci. Technol.*, 1–3 (2006)
5. P.N. Barnes, M.D. Sumption, G.L. Rhoads, *Cryogenics* **45**(10–11), 670–686 (2005)
6. J.N.A. Matthews, *Phys. Today* **62**(4), 25–26 (2009)
7. X. Obradors, T. Puig, Z. Li, C. Pop, B. Mundet, N. Chamorro, F. Vallés, M. Coll, S. Ricart, B. Vallejo, *Supercond. Sci. Technol.* **31**(4), 044001 (2018)
8. A.P. Malozemoff, *Nat. Mater.* **6**(9), 617–619 (2007)
9. S.R. Foltyn, L. Civale, J.L. Macmanus-Driscoll, Q.X. Jia, B. Maiorov, H. Wang, M. Maley, *Nat. Mater.* **6**(9), 631–642 (2007)
10. M.P. Paranthaman, T. Izumi, *MRS Bull.* **29**(8), 533–536 (2004)
11. D. Larbalestier, A. Gurevich, D.M. Feldmann, A. Polyanskii, *Nature* **414**(6861), 368–377 (2001)
12. D. Dimos, P. Chaudhari, J. Mannhart, *Phys. Rev. B* **41**(7), 4038–4049 (1990)
13. A. Schmehl, B. Goetz, R.R. Schulz, C.W. Schneider, H. Bielefeldt, H. Hilgenkamp, J. Mannhart, *Europhys. Lett.* **47**(1), 110–115 (1999)
14. G. Hammerl, A. Schmehl, R.R. Schulz, B. Goetz, H. Bielefeldt, C.W. Schneider, H. Hilgenkamp, J. Mannhart, *Nature* **407**(6801), 162–164 (2000)
15. X.Y. Song, G. Daniels, D.M. Feldmann, A. Gurevich, D. Larbalestier, *Nat. Mater.* **4**(6), 470–475 (2005)
16. M.H. Gharahcheshmeh, G. Majkic, E. Galstyan, A. Xu, Y. Zhang, X. Li, V. Selvamanickam, *Phys. C: Superconduct. Appl.* **553**, 26–32 (2018)
17. A. Goyal, *Second-Generation HTS Conductors* (Springer, New York, 2005)
18. T. Sueyoshi, Y. Furuki, T. Fujiyoshi, F. Mitsugi, T. Ikegami, A. Ichinose, N. Ishikawa, *Supercond. Sci. Technol.* **31**(12), 125002 (2018)
19. X. Obradors, T. Puig, *Supercond. Sci. Technol.* **27**(4), 044003 (2014)
20. K. Matsumoto, P. Mele, *Supercond. Sci. Technol.* **23**(1), 014001 (2009)
21. M. *Tinkham* (McGraw-Hill, New York, 1996)
22. T. Haugan, P.N. Barnes, R. Wheeler, F. Meisenkothen, M. Sumption, *Nature* **430**(7002), 867–870 (2004)
23. T. Aytug, M. Paranthaman, A.A. Gapud, S. Kang, H.M. Christen, K.J. Leonard, P.M. Martin, J.R. Thompson, D.K. Christen, R. Meng, I. Rusakova, C.W. Chu, T.H. Johansen, *J. Appl. Phys.* **98**(11), 5 (2005)
24. J.L. Macmanus-Driscoll, S.R. Foltyn, Q.X. Jia, H. Wang, A. Serquis, L. Civale, B. Maiorov, M.E. Hawley, M.P. Maley, D.E. Peterson, *Nat. Mater.* **3**(7), 439–443 (2004)
25. K. Matsumoto, T. Horide, K. Osamura, M. Mukaida, Y. Yoshida, A. Ichinose, S. Horii, *Phys. C Superconduct. Appl.* **412**, 1267–1271 (2004)

26. S. Kang, A. Goyal, J. Li, A.A. Gapud, P.M. Martin, L. Heatherly, J.R. Thompson, D.K. Christen, F.A. List, M. Paranthaman, D.F. Lee, *Science* **311**(5769), 1911–1914 (2006)
27. J. Gutierrez, A. Llordes, J. Gazquez, M. Gibert, N. Roma, S. Ricart, A. Pomar, F. Sandi-umenge, N. Mestres, T. Puig, X. Obradors, *Nat. Mater.* **6**(5), 367–373 (2007)
28. C.V. Varanasi, J. Burke, H. Wang, J.H. Lee, P.N. Barnes, *Appl. Phys. Lett.* **93**(9), 092501 (2008)
29. S.A. Harrington, J.H. Durrell, B. Maiorov, H. Wang, S.C. Wimbush, A. Kursumovic, J.H. Lee, J.L. MacManus-Driscoll, *Superconduct. Sci. Technol.* **22**(2), 022001 (2009)
30. T.J. Haugan, P.N. Barnes, T.A. Campbell, N.A. Pierce, F.J. Baca, I. Maartense, *IEEE Trans. Appl. Supercond.* **17**(2), 3724–3728 (2007)
31. Y. Yoshida, K. Matsumoto, Y. Ichino, M. Itoh, A. Ichinose, S. Horii, M. Mukaida, Y. Takai, *Jpn. J. Appl. Phys. Part 2 Lett. Exp. Lett.* **44**(1–7), L129–L132 (2005)
32. P.N. Barnes, J.W. Kell, B.C. Harrison, T.J. Haugan, C.V. Varanasi, M. Rane, F. Ramos, *Appl. Phys. Lett.* **89**(1), 3 (2006)
33. Y. Yoshida, K. Matsumoto, M. Miura, Y. Ichino, Y. Takai, A. Ichinose, M. Mukaida, S. Horii, *Phys. C Superconduct. Appl.* **445**, 637–642 (2006)
34. T. Matsushita, *Flux Pinning in Superconductors* (Springer, Berlin, 2007)
35. J.Z. Wu, R.L.S. Emergo, X. Wang, G. Xu, T.J. Haugan, P.N. Barnes, *Appl. Phys. Lett.* **93**(6), 3 (2008)
36. S. Chen, M.A. Sebastian, B. Gautam, J. Wilt, Y. Chen, L. Sun, Z. Xing, T. Haugan, J. Wu, *Supercond. Sci. Technol.* **30**(12), 125011 (2017)
37. V. Chepikov, N. Mineev, P. Degtyarenko, S. Lee, V. Petrykin, A. Ovcharov, A. Vasiliev, A. Kaul, V. Amelichev, A. Kamenev, *Supercond. Sci. Technol.* **30**(12), 124001 (2017)
38. B. Gautam, M.A. Sebastian, S. Chen, T.J. Haugan, W. Zhang, J. Huang, H. Wang, J.Z. Wu, *Supercond. Sci. Technol.* **31**, 025008 (2018)
39. J. Wu, J. Shi, *Supercond. Sci. Technol.* **30**(10), 103002 (2017)
40. Y. Yoshida, S. Miura, Y. Tsuchiya, Y. Ichino, S. Awaji, K. Matsumoto, A. Ichinose, *Supercond. Sci. Technol.* **30**(10), 104002 (2017)
41. A. Goyal, S. Kang, K.J. Leonard, P.M. Martin, A.A. Gapud, M. Varela, M. Paranthaman, A.O. Ijaduola, E.D. Specht, J.R. Thompson, D.K. Christen, S.J. Pennycook, F.A. List, *Superconduct. Sci. Technol.* **18**(11), 1533–1538 (2005)
42. T. Horide, K. Taguchi, K. Matsumoto, N. Matsukida, M. Ishimaru, P. Mele, R. Kita, *Appl. Phys. Lett.* **108**(8), 082601 (2016)
43. S. Chen, M.A. Sebastian, B. Gautam, J. Wilt, T. Haugan, Z. Xing, J. Wu, *IEEE Trans. Appl. Supercond.* **27**(4), 4–8 (2017)
44. S.H. Wee, Y.L. Zuev, C. Cantoni, A. Goyal, *Sci. Rep.* **3**, 2310 (2013)
45. P. Mele, K. Matsumoto, A. Ichinose, M. Mukaida, Y. Yoshida, S. Horii, R. Kita, *Phys. C: Superconduct.* **469**(15), 1380–1383 (2009)
46. H. Tobita, K. Notoh, K. Higashikawa, M. Inoue, T. Kiss, T. Kato, T. Hirayama, M. Yoshizumi, T. Izumi, Y. Shiohara, *Superconduct. Sci. Technol.* **25**(6), 062002 (2012)
47. T. Matsushita, H. Nagamizu, K. Tanabe, M. Kiuchi, E.S. Otabe, H. Tobita, M. Yoshizumi, T. Izumi, Y. Shiohara, D. Yokoe, T. Kato, T. Hirayama, *Superconduct. Sci. Technol.* **25**(12) (2012)
48. P. Pahlke, M. Lao, M. Eisterer, A. Meledin, G. Van Tendeloo, J. Hanisch, M. Sieger, A. Usoskin, J. Stromer, B. Holzapfel, L. Schultz, R. Huhne, *IEEE Trans. Appl. Supercond.* **26**(3) (2016)
49. B. Gautam, M.A. Sebastian, S. Chen, J. Shi, T. Haugan, Z. Xing, W. Zhang, J. Huang, H. Wang, M. Osofsky, *AIP Adv.* **7**(7), 075308 (2017)
50. S. Miura, Y. Yoshida, Y. Ichino, Y. Doki, A. Ibi, T. Izumi, T. Kato, *IEEE Trans. Appl. Supercond.* **26**(4), 1–5 (2016)
51. A. Goyal, S.-h. Wee, J. Shin, C. Cantoni, E. Specht and Y. Zuev, Presented at the Materials Science & Technology 2010, Houston (2010)
52. M.Z. Khan, M. Malmivirta, Y. Zhao, X. Wu, R. Jha, V.P.S. Awana, H. Huhtinen, P. Paturi, *Phys. C: Superconduct.* **555**, 15 (2018)

53. L. Opherden, M. Sieger, P. Pahlke, R. Hühne, L. Schultz, A. Meledin, G. Van Tendeloo, R. Nast, B. Holzapfel, M. Bianchetti, *Sci. Rep.* **6**, 21188 (2016)
54. D. Feldmann, T. Holesinger, B. Maiorov, S. Foltyn, J. Coulter, I. Apodaca, *Supercond. Sci. Technol.* **23**(9), 095004 (2010)
55. N.M. Hapipi, S.K. Chen, A.H. Shaari, M.M.A. Kechik, K.B. Tan, K.P. Lim, *J. Mater. Sci. Mater. Electron.* **29**(21), 18684–18692 (2018)
56. G. Blatter, M.V. Feigel'man, V.B. Geshkenbein, A.I. Larkin, V.M. Vinokur, *Rev. Mod. Phys.* **66**(4), 1125 (1994)
57. C. Varanasi, J. Burke, L. Brunke, H. Wang, J. Lee, P. Barnes, *J. Mater. Res.* **23**(12), 3363–3369 (2008)
58. J. Wu, J. Shi, *Superconduct. Sci. Technol.* **30**(10), 103002 (2017)
59. P. Mele, M.I. Adam, T. Suzuki, Y. Yoshida, S. Awaji, A. Ichinose, S. Saini, A.K. Jha, K. Matsumoto, *Sci. Adv. Mater.* **9**(6), 1042–1050 (2017)
60. P. Pahlke, M. Sieger, R. Ottolinger, M. Lao, M. Eisterer, A. Meledin, G. Van Tendeloo, J. Hänisch, B. Holzapfel, L. Schultz, *Supercond. Sci. Technol.* **31**(4), 044007 (2018)
61. M. A. Susner and T. J. Haugan, Presented at the 2018 AIAA/IEEE electric aircraft technologies symposium, (2018)
62. S.R. Foltyn, Q.X. Jia, P.N. Arendt, L. Kinder, Y. Fan, J.F. Smith, *Appl. Phys. Lett.* **75**(23), 3692–3694 (1999)
63. B.W. Kang, A. Goyal, D.R. Lee, J.E. Mathis, E.D. Specht, P.M. Martin, D.M. Kroeger, M. Paranthaman, S. Sathyamurthy, *J. Mater. Res.* **17**(7), 1750–1757 (2002)
64. K.J. Leonard, S. Kang, A. Goyal, K.A. Yarbrough, D.M. Kroeger, *J. Mater. Res.* **18**(7), 1723–1732 (2003)
65. A. Gurevich, *Superconduct. Sci. Technol.* **20**(9), S128 (2007)
66. X. Wang, J.Z. Wu, *Phys. Rev. B* **76**(18), 5 (2007)
67. X. Wang, J.Z. Wu, *Appl. Phys. Lett.* **88**(6), 3 (2006)
68. Q.X. Jia, S.R. Foltyn, P.N. Arendt, J.F. Smith, *Appl. Phys. Lett.* **80**(9), 1601–1603 (2002)
69. X. Wang, F.J. Baca, R.L.S. Emergo, J.Z. Wu, T.J. Haugan, P.N. Barnes, *J. Appl. Phys.* **108**(11), 5 (2010)
70. G. Majkic, R. Pratap, A. Xu, E. Galstyan, V. Selvamanickam, *Sci. Rep.* **8**(1), 6982 (2018)
71. T. Horide, S. Nagao, R. Izutsu, M. Ishimaru, R. Kita, K. Matsumoto, *Supercond. Sci. Technol.* **31**(6), 065012 (2018)
72. C. Cantoni, Y.F. Gao, S.H. Wee, E.D. Specht, J. Gazquez, J.Y. Meng, S.J. Pennycook, A. Goyal, *ACS Nano* **5**(6), 4783–4789 (2011)
73. B. Gautam, M.A. Sebastian, S. Chen, S. Misra, J. Huang, F. Javier Baca, R. Emergo, T. Haugan, Z. Xing, H. Wang, *Appl. Phys. Lett.* **113**(21), 212602 (2018)
74. P. Mele, K. Matsumoto, T. Horide, A. Ichinose, M. Mukaida, Y. Yoshida, S. Horii, R. Kita, *Superconduct. Sci. Technol.* **21**(3), 5 (2008)
75. M. Peurla, H. Huhtinen, M.A. Shakhov, K. Traito, Y.P. Stepanov, M. Safonchik, P. Paturi, Y.Y. Tse, R. Palai, R. Laiho, *Phys. Rev. B* **75**(18), 6 (2007)
76. M. Peurla, P. Paturi, Y.P. Stepanov, H. Huhtinen, Y.Y. Tse, A.C. Boodi, J. Raittila, R. Laiho, *Superconduct. Sci. Technol.* **19**(8), 767–771 (2006)
77. J.Z. Wu, J.J. Shi, F.J. Baca, R. Emergo, J. Wilt, T.J. Haugan, *Superconduct. Sci. Technol.* **28**(12), 125009 (2015)
78. T. Hwa, P. Ledoussal, D.R. Nelson, V.M. Vinokur, *Phys. Rev. Lett.* **71**(21), 3545–3548 (1993)
79. L. Civale, L. Krusinbaum, J.R. Thompson, R. Wheeler, A.D. Marwick, M.A. Kirk, Y.R. Sun, F. Holtzberg, C. Feild, *Phys. Rev. B* **50**(6), 4102–4109 (1994)
80. L. Krusinbaum, J.R. Thompson, R. Wheeler, A.D. Marwick, C. Li, S. Patel, D.T. Shaw, *Appl. Phys. Lett.* **64**(24), 3331–3333 (1994)
81. J.J. Shi, J.Z. Wu, *Philos. Mag.* **92**(23), 2911–2922 (2012)
82. J.J. Shi, J.Z. Wu, *Philos. Mag.* **92**(34), 4205–4214 (2012)
83. J.J. Shi, J.Z. Wu, *J. Appl. Phys.* **118**(16) (2015)
84. J.Z. Wu, J.J. Shi, J.F. Baca, R. Emergo, T.J. Haugan, B. Maiorov, T. Holesinger, *Supercond. Sci. Technol.* **27**(4), 044010 (2014)

85. F.J. Baca, P.N. Barnes, R.L.S. Emergo, T.J. Haugan, J.N. Reichart, J.Z. Wu, *Appl. Phys. Lett.* **94**(10), 102512 (2009)
86. P. Mele, K. Matsumoto, A. Ichinose, M. Mukaida, Y. Yoshida, S. Horii, R. Kita, *Phys. C Superconduct. Appl.* **469**(15–20), 1380–1383 (2009)
87. V. Selvamanickam, M.H. Gharahcheshmeh, A. Xu, Y. Zhang, E. Galstyan, *Superconduct. Sci. Technol.* **28**(10), 072002 (2015)
88. V. Selvamanickam, M.H. Gharahcheshmeh, A. Xu, E. Galstyan, L. Delgado, C. Cantoni, *Appl. Phys. Lett.* **106**(3), 032601 (2015)
89. H. Tobita, K. Notoh, K. Higashikawa, M. Inoue, T. Kiss, T. Kato, T. Hirayama, M. Yoshizumi, T. Izumi, Y. Shiohara, *Supercond. Sci. Technol.* **25**(6), 062002 (2012)
90. T. Ozaki, Y. Yoshida, Y. Ichino, Y. Takai, A. Ichinose, K. Matsumoto, S. Horii, M. Mukaida, Y. Takano, *J. Appl. Phys.* **108**(9), 093905 (2010)
91. H. Yang, H. Wang, B. Maiorov, J. Lee, D. Talbayev, M.J. Hinton, D.M. Feldmann, J.L. MacManus-Driscoll, A.J. Taylor, L. Civale, T.R. Lemberger, Q.X. Jia, *J. Appl. Phys.* **106**(9) (2009)
92. J.Z. Wu, J.J. Shi, R. Emergo, F.J. Baca, T.J. Haugan, Preprint (2014)
93. T. Horide, F. Kametani, S. Yoshioka, T. Kitamura, K. Matsumoto, *ACS Nano* **11**(2), 1780–1788 (2017)
94. M.A.P. Sebastian, J.N. Reichart, M.M. Ratcliff, T.J. Bullard, J.L. Burke, C.R. Ebbing, G.Y. Panasyuk, C.-F. Tsai, W. Zhang, J. Huang, *IEEE Trans. Appl. Supercond.* **27**(4), 1–5 (2017)
95. J. Wu, G. Bibek, M.A. Sebastian, V. Ogunjimi, T. Haugan, J. Huang, S. Misra, F.J. Baca, J.C. Prestigiacomo, H. Wang, M. Osofsky, *IEEE Trans. Appl. Supercond.*, 1–1 (2019)
96. R. Emergo, F. Baca, J. Wu, T. Haugan, P. Barnes, *Supercond. Sci. Technol.* **23**(11), 115010 (2010)
97. J.F. Baca, T.J. Haugan, P.N. Barnes, T.G. Holesinger, B. Maiorov, R. Lu, X. Wang, J.N. Reichart, J.Z. Wu, *Adv. Funct. Mater.* **23**(38) (2013)
98. W.D. Si, H.C. Li, X.X. Xi, *Appl. Phys. Lett.* **74**(19), 2839–2841 (1999)
99. J.P. Locquet, J. Perret, J. Fompeyrine, E. Machler, J.W. Seo, G. Van Tendeloo, *Nature* **394**(6692), 453–456 (1998)
100. G. Chapelle, L.S. Peck, *Nature* **399**(6732), 114–115 (1999)
101. R.L.S. Emergo, F.J. Baca, J.Z. Wu, T.J. Haugan, P.N. Barnes, *Superconduct. Sci. Technol.* **23**(11), 5 (2010)
102. B. Gautam, M.A. Sebastian, S.H. Chen, J. Shi, T. Haugan, Y.B. Chen, Z.W. Xing, J. Prestigiacomo, M. Osofsky, J.Z. Wu, *IOP Conf. Ser.: Mater. Sci. Eng.* **279**, 012030 (2017)
103. B. Gautam, S.H. Chen, M.A. Sebastian, T. Haugan, Z.W. Xing, J. Wu, *IEEE Trans. Appl. Supercond.* **28**(4), 1–4 (2018)
104. M.A. Sebastian, G. Bibek, C.R. Ebbing, G. Panasyuk, M.A. Susner, J. Huang, W. Zhang, H. Wang, J. Wu, T. Haugan, *IEEE Trans. Appl. Supercond.* **29**, 1–1 (2019)

Chapter 3

Control of Vortex Pinning in YBCO Thin Films by Incorporating APCs Through Surface Modified Target Approach



Alok K. Jha and Kaname Matsumoto

3.1 YBa₂Cu₃O_{7- δ} : A Promising High Temperature Superconductor

YBa₂Cu₃O_{7- δ} (YBCO) was discovered as the first superconductor which exhibited superconducting transition above the liquid nitrogen temperature (77 K) [1]. The discovery of YBCO accelerated the search for higher transition temperature (T_c) materials leading subsequently to the discovery of other superconductors such as Bi₂Sr₂Ca₂Cu₃O_{10+ δ} [2] and HgBa₂Ca₂Cu₃O_{8+ δ} [3] which exhibited higher T_c than YBCO. YBCO, however, has couple of advantages over other cuprate superconductors which include easier synthesis methods and much larger critical current density (J_c) at 77 K. J_c is the most relevant parameter of a superconductor which decides the ability of a superconductor to be used in practical applications [4–6]. The electronic structure, critical temperature, and the mechanism of vortex pinning determine J_c in any superconductor. In addition, the irreversibility field (H_{irr}) for YBCO is also much larger than for any other cuprate superconductor at 77 K. H_{irr} is a very important parameter which determines the upper limit of J_c in a superconductor. The irreversibility line marks the separation between the solid-liquid phases of the vortex matter and much effort has been made to shift this line towards higher H - T regime by artificial pinning center technology [4, 6–8].

A. K. Jha (✉) · K. Matsumoto
Department of Materials Science and Engineering, Kyushu Institute of Technology, Kitakyushu,
Japan
e-mail: akjha@post.matsc.kyutech.ac.jp; matsu@post.matsc.kyutech.ac.jp

3.2 The Evolution of Critical Current Density of YBCO Superconductor over Time

Polycrystalline bulk samples of YBCO were observed to have very low J_c ($\sim 10^2$ A/cm²) despite exhibiting high T_c (~ 92 K), and relatively large $\mu_0 H_{irr}$ (~ 7 T at 77 K). The reason for low J_c in polycrystalline samples was ascribed to small coherence length of YBCO, which limits the percolation of electrical current across grain boundaries [9]. Additionally, the anisotropic character of its J_c (which is higher along the ab -plane than along the c -axis) is also partially responsible for low J_c in the polycrystalline samples. The alignment of the grains was improved by melt-texturing-growth (MTG) method [10, 11] which resulted in much higher J_c ($\sim 10^4$ A/cm²). However, still the value of J_c was too low for the possibility of any practical use of YBCO.

Thanks to the continuous efforts from researchers across the world, it became possible to make thin films of YBCO on single crystal substrates such as SrTiO₃, Al₂O₃, and MgO. [12]. Highly c -axis oriented thin films of YBCO on single crystal substrates exhibited $J_c > 10^6$ A/cm² (at 77 K) which was much higher than that for MTG YBCO samples. The fabrication and processing techniques developed over the years resulted in the current carrying capability of YBCO significantly enhanced. Through many deposition techniques such as pulsed laser deposition (PLD) [13], chemical solution deposition (CSD) [14], and metal organic chemical vapor deposition (MOCVD) [15], it became possible to prepare highly c -axis oriented YBCO thin films which exhibited high J_c of 1–5 MA/cm² at 77 K, self-field [16, 17].

3.3 Critical Current Density Under Applied Magnetic Field and Pinning of Vortices by APCs in YBCO Films

A type-II superconductor, when subjected to an applied magnetic field (H), remains in different states depending upon the strength of H [18]. It has two critical magnetic fields namely: (1) lower critical field (H_{c1}) and (2) upper critical field (H_{c2}). When $H < H_{c1}$, the superconductor exhibits perfect diamagnetism by expelling the magnetic field completely and is said to be in the Meissner state. When $H_{c1} < H < H_{c2}$, the magnetic field penetrates the superconductor in a form of small “tubes” (vortices), each with quantized flux $\Phi_0 = h/(2e)$. The number and thus density of the vortices continue to increase until the applied magnetic field reaches a value equal to H_{c2} . This state of a type-II superconductor is called mixed state or vortex state. When $H > H_{c2}$, the superconductor goes into the normal state.

When a type-II superconductor (such as YBCO) is in its mixed state and an electrical current is flown across it, the vortices experience a Lorentz force, whose density (F_L) is given by the vector product of the current density J and applied magnetic field $\mu_0 H$. This Lorentz force pushes the vortices in a direction

perpendicular to both the electrical current and the applied magnetic field. There are, however, some microscopic defects that are generated naturally during the growth of the superconducting samples which prevent the motion of the vortices under the influence of Lorentz force. The vortices are thus pinned by these defects and these defects, therefore, are termed as pinning centers. The force which resists the motion of vortices under the influence of the Lorentz force is called pinning force whose magnitude per unit volume is called pinning force density (F_p). The vortices remain stationary, as long as the pinning force is greater than the Lorentz force. When the Lorentz force on the vortices exceeds the pinning force, they start moving across the superconducting sample. If the vortices move with a velocity v , a finite electric field $E = \mu_0 H \times v$ would be generated. Since, current and the generated electric field have the same direction, a finite power would be dissipated in the system and the ability of the superconductor to sustain dissipation-free current flow would be lost. The vortices in YBCO thin films are pinned by some naturally occurring defects (which are formed during the growth of the film) such as dislocations, grain boundaries, twin boundaries, and oxygen vacancies. The strength of these naturally occurring defects, however, is not enough to counter thermal fluctuations and their densities are not sufficient to maintain large J_c at high magnetic fields [6, 19, 20].

It, therefore, became imperative to look for alternative ways which can be efficient for pinning the vortices even at high applied magnetic fields. This arose the need for artificial pinning centers (APCs) and their introduction turned out to be very effective for the immobilization of the vortices even at high applied magnetic fields leading to enhanced J_c of YBCO thin films for wide range of applied magnetic field. The introduction of APCs into YBCO films have been conducted through various methods which include heavy-ion irradiation [21], addition and/or substitution of rare-earth atoms [22, 23], or incorporation of secondary phase nanoinclusions into the YBCO film matrix [24–34]. Enhancement of vortex pinning properties of YBCO films through incorporation of secondary phase nanoinclusions has recently been extensively studied. The nanoinclusions of several materials such as Y_2BaCuO_5 [24, 25], Y_2O_3 [26], $BaZrO_3$ [27, 28], $BaSnO_3$ [29, 30], $BaIrO_3$ [31], YBa_2NbO_6 [32, 33], and YBa_2TaO_6 [34] have been successfully introduced into YBCO film matrix by using PLD technique, which led to the enhancement of J_c of YBCO thin films over a wide range of applied magnetic field.

3.4 Methods to Introduce APCs in YBCO Films Through PLD Technique

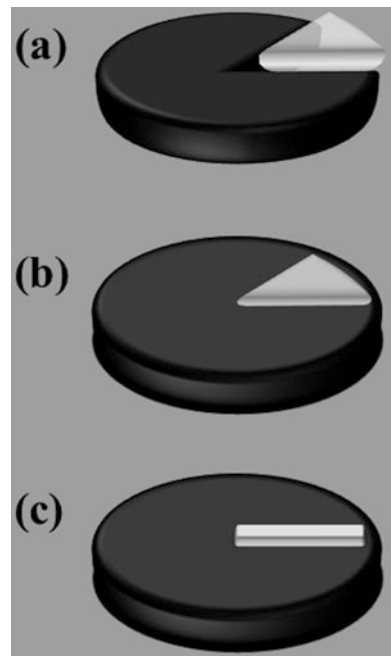
In PLD technique, a laser pulse is focused onto the surface of a target (the material whose thin film has to be prepared) inside a vacuum chamber. Above a certain threshold energy density, the target material is sputtered and the ejected species forms a luminous ablation plume. The sputtered material is directed towards a substrate where it condenses to form a film. In the case of YBCO films, the nanoinclusions of secondary phase materials are usually introduced by two methods:

(i) by mixing the secondary phase material with YBCO and making a premixed target and (ii) using two different targets of YBCO and secondary phase material and ablate them alternatively during the deposition process. The advantage of using premixed target is that it offers precise control over the volume percentage of the secondary phase into the YBCO film matrix. However, the secondary phase material needs to be non-reactive with YBCO in the sintering temperature range of 920–950 °C which is usually higher than the deposition temperature of the films (800–830 °C). The alternating target approach also provides precise control of the concentration of the secondary phase in YBCO films and also removes the possibility of any chemical reaction between YBCO and the secondary phase in the ablation target, but this process is time consuming.

3.5 The Surface Modified Target Method

In order to introduce nanoscale secondary phases into YBCO thin films using PLD technique, a novel method is adopted in which the surface of the ablation target is modified and that is why this method is named as surface modified target method. In this method, a thin sectored or rectangular shaped piece of secondary phase material is attached on the top of YBCO target using silver paste [35, 36]. The schematic diagram of this method is shown in Fig. 3.1. The main advantage of this approach is

Fig. 3.1 Schematic diagram of the ablation target used in surface modified target method. (a) Ideally, it is desired to cut a sectoral slot where a wedge-shaped secondary phase piece can be inserted. (b) Instead, a thin sectored slice of secondary phase materials is attached to the top surface of the YBCO target. (c) The secondary phase slice can also be made in rectangular form which can be attached to the top surface of YBCO target by means of silver paste



that the secondary phase material can be continuously introduced into YBCO film using a single target in which YBCO portion and secondary phase material portion are physically separate. Also, the concentration of the secondary phase can be varied just by changing the size of the sectored/rectangular shaped piece of secondary phase material while keeping the YBCO target the same. Mele et al. [37] have reported the observation of BaZrO_3 nanocolumns within YBCO film matrix for which YBCO+YSZ (yttria-stabilized zirconia) surface modified target was used.

It is quite interesting to compare surface modified target method with premixed target method from the point of view of growth mechanism of different phases in a thin film. In the mixed target method, the adatoms or molecules of both the species (YBCO and the secondary phase) are continuously supplied and the supersaturation of YBCO is higher than that of the secondary phase material (as the mixed target consists of YBCO phase in larger proportion than the secondary phase material). In the surface modified target method, however, the adatoms or molecules of different species are transported to the substrate surface in an alternative and periodic manner and for this reason the supersaturation of YBCO and the secondary phase may be considered as the same. In spite of the different scenario of supersaturation in these two methods, the microstructure of the final films reveals similar features: formation of nanocolumns or nanoparticles of secondary phases within YBCO matrix. The formation of yttria nanoparticles has been observed in an earlier report [26] in which alternating target method was employed and in that case, the formation of semi-coherent interfaces between the phases can be held responsible for such nanoparticle formation. Using surface modified target method, gold was introduced in the form of nanorods with widely varying diameters within $\text{GdBa}_2\text{Cu}_3\text{O}_{7.8}$ (GdBCO) film matrix [38]. According to this report, a gold sheet of 25 mm length and 2 mm width was attached to the top surface of the GdBCO target for supply of gold inside GdBCO film matrix. However, the driving force for the formation of gold nanorods within the GdBCO film matrix is not understood.

3.6 The Realization of Nanoscale Secondary Phase Inclusions with Different Geometries into YBCO Matrix

3.6.1 YBCO Films Consisting of Nanoparticles of Secondary Phases (3D APCs)

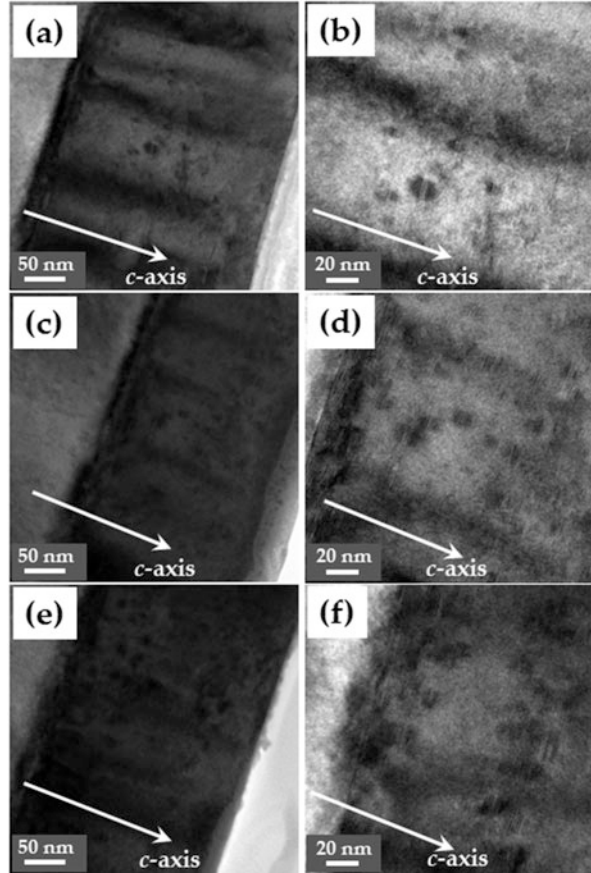
The layered structured of YBCO gives rise to an intrinsic anisotropy in its properties which is reflected in its J_c as well [39–41]. In general, at a given magnetic field; J_c for H parallel the ab -plane is higher than for H parallel the c -axis. In order to reduce this anisotropy (making J_c uniform for all the orientations of applied magnetic field), different kinds of APCs are studied which include spherical nanoparticles and columnar nanorods of different secondary phase materials.

In an ideal situation, the nanoparticles of secondary phase materials pin the vortices with the same strength irrespective of the applied magnetic field orientation. Although the vortex cross-section changes with the orientation of the applied magnetic field, the interacting volume of a vortex with a spherical nanoparticle does not change significantly and the pinning strength of such APCs does not change much with the orientation of applied magnetic field. For this reason, the nanoparticles of secondary phases are called 3D APCs. Nanocolumnar structures, on the other hand, are called 1D APCs which pin segments of the vortices depending upon the orientation of the applied magnetic field. As the applied field is tilted from the 1D APC orientation, the pinned segment of the vortex decreases and this leads to reduced pinning efficiency of 1D APCs. 3D APCs (nanoparticles), therefore, are preferred over 1D APCs (nanocolumns) for many applications where reduced anisotropy is desired.

The use of spherical nanoparticles or the so-called 3D APCs was reported by Haugan et al. [25] and Varanasi et al. [35] in which Y_2BaCuO_5 (Y211) nanoparticles were found to improve the in-field J_c of YBCO thin films. However, the angular dependent J_c study was not conducted in their reports. In these reports, however, the Y211 nanoparticles were introduced into YBCO thin film by alternating target method. Similarly, Y_2O_3 nanoparticles were also introduced as 3D APCs into YBCO thin films by alternating target method and they were effective in reducing the J_c anisotropy of YBCO thin films as observed in the angular dependent J_c study [42]. Later, both Y_2O_3 and Y211 nanoparticles were introduced into YBCO thin films independently by surface modified target method. Mele et al. [36] used the surface modified target method for the incorporation of Y_2O_3 nanoparticles into YBCO thin films. Although the microstructure clearly revealed the formation of Y_2O_3 nanoparticles within YBCO film matrix, the anisotropy in J_c could not be improved significantly. For higher concentration of Y_2O_3 into YBCO thin films, they were observed in the form of nanorods as well [43].

In a recent work, the incorporation of Y211 nanoparticles into YBCO films, through surface modified target method, has been reported [24]. The concentration of Y211 nanoparticles was varied systematically by changing the size of the Y211 surface modified piece on top of the YBCO target. Figure 3.2 shows the microstructure of the YBCO thin films with varying concentrations of Y211 nanoparticles. These Y211 nanoparticles not only enhanced the in-field J_c of YBCO thin films but also shifted the irreversibility line towards higher H - T regime. Angular dependent J_c studies for YBCO thin films with different concentrations of Y211 nanoparticles were conducted and it was found that these Y211 nanoparticles are very effective in reducing the J_c anisotropy of YBCO thin films. Figure 3.3 shows the angular dependent J_c curves for YBCO thin films, with varying concentrations of Y211 nanoparticles, measured at different magnetic fields at 65 K. These Y211 nanoparticles resulted in almost isotropic J_c of YBCO thin films barring only a narrow angular range near the ab -plane. This feature was further analyzed by existing theoretical models and it was suggested that in this narrow angular range of applied magnetic field, there is a cross-over from nanoparticle pinning to ab -plane pinning which results from the linear defects (planar defects such as stacking

Fig. 3.2 The cross-sectional TEM image of YBCO+Y211 nanocomposite films prepared using surface modified target method with varying concentrations of Y211 nanoparticles at two different magnifications. (a) and (b) represent least concentrations of Y211 nanoparticles, (c) and (d) represent medium concentration, and (e) and (f) represent maximum concentration. Reprinted from [24], with the permission of AIP Publishing



faults) aligned along the ab -plane. Figure 3.4 shows the schematic diagram of such a situation where pinning due to nanoparticles and pinning due to linear disorders along the ab -plane dominate for different angular range of applied magnetic field.

3.6.2 YBCO Films Consisting of Nanocolumns of Secondary Phases (1D APCs)

Columnar disorders along the c -axis of YBCO films are generated through heavy-ion irradiation or formation of self-assembled nanocolumns of some secondary phase materials such as BaZrO_3 (BZO), BaSnO_3 (BSO), BaHfO_3 (BHO), YBa_2NbO_6 (YBNO), and YBa_2TaO_6 (YBTO). The pinning efficiency of these columnar nanostructures (1D APCs) is very high which results in significantly enhanced in-field J_c of YBCO films. The efficiency of these 1D APCs, however,

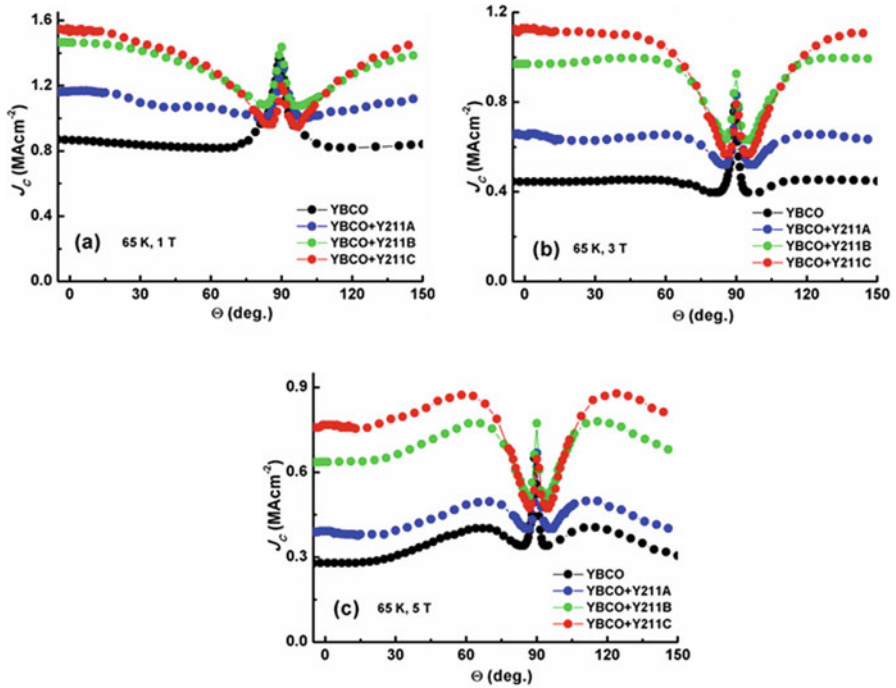


Fig. 3.3 Variation of J_c with the orientation of applied magnetic field for pristine YBCO and YBCO+Y211 films with varying concentrations of Y211 nanoparticles measured at 1, 3, and 5 T at 65 K. The isotropic enhancement in J_c of YBCO+Y211 films can be clearly observed at all the magnetic fields. Reprinted from [24], with the permission of AIP Publishing

is limited for a small angular range where the applied field is oriented along the c -axis or is slightly inclined with respect to the c -axis. For this reason, the angular dependent J_c of the YBCO thin films containing 1D APCs exhibits a peak when the applied field is along the c -axis.

The use of surface modified target to introduce 1D APCs into YBCO films started more than a decade ago when Varanasi et al. successfully introduced BSO nanostructures into YBCO thin films [44]. The incorporation of BSO nanostructures into YBCO thin films resulted in enhanced in-field J_c of YBCO thin films. However, the microstructure of the nanocomposite film was not studied in detail and it was assumed on the basis of planar view of the transmission electron microscope (TEM) image that the BSO nanostructures are organized in the form of nanoparticles inside YBCO film matrix. But, in subsequent studies [30, 45], the cross-sectional view of the YBCO+BSO nanocomposite film was observed which revealed columnar structures and self-assembly of BSO phase in the form of nanocolumns inside YBCO film matrix was confirmed. Figure 3.5 shows the cross-sectional TEM image of YBCO+BSO nanocomposite film deposited by surface modified target method in which columnar nanostructures can be clearly observed. The efficiency of these

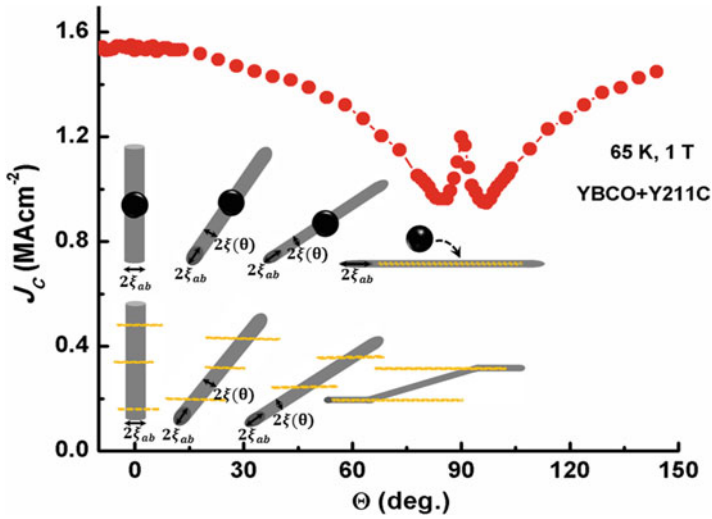


Fig. 3.4 Schematic diagram of dominating angular regime of pinning for Y211 nanoparticles and planar defects. As the vortices are inclined from the c -axis, the interaction volume with the spherical defects decreases and the pinning energy is decreased resulting in overall decrease in J_c . Planar defects along the ab -plane, can pin the vortices only for limited angular regime, and act as linear defects with small accommodation angle. Reprinted from [24], with the permission of AIP Publishing

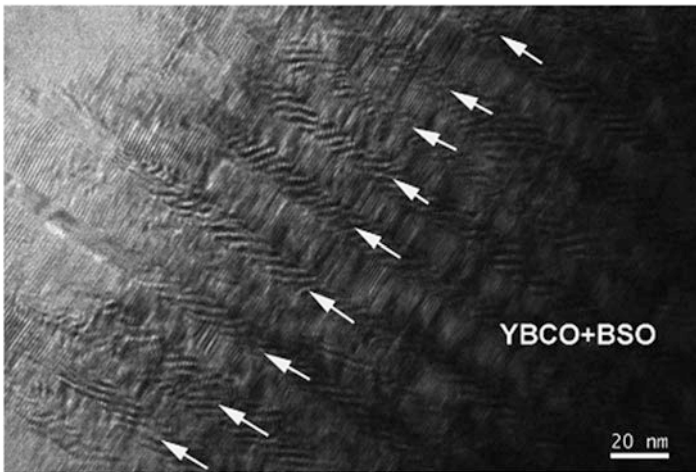


Fig. 3.5 Cross-sectional TEM image of YBCO film with BSO nanostructures deposited by surface modified target method using PLD technique. The image shows that BSO nanostructures are self-assembled in the form of nanocolumns aligned along the crystallographic c -direction. Reprinted from [30], with the permission of AIP Publishing

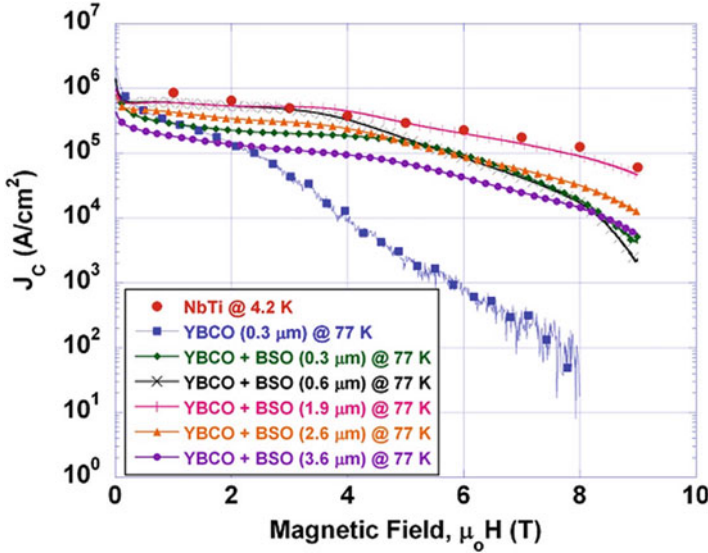


Fig. 3.6 Variation of J_c with applied magnetic field for pristine YBCO film and YBCO films with BSO nanoinclusions with varying thickness. The enhanced in-field J_c can be clearly observed in YBCO films incorporating BSO nanoinclusions. Reprinted from [30], with the permission of AIP Publishing

BSO nanocolumns can be seen in Fig. 3.6 in which significant enhancement in the in-field J_c of the nanocomposite films can be observed.

Apart from BSO, BZO and YBNO nanocolumns have also been successfully incorporated into YBCO film matrix by surface modified target method. Mele et al. used yttria-stabilized zirconia (YSZ) as a surface modified piece on top of YBCO target which led to the formation of BZO nanocolumns inside YBCO film matrix [46]. These columnar APCs resulted in enhanced in-field J_c of the YBCO+YSZ films. Figure 3.7 shows the cross-sectional TEM image of the YBCO+YSZ films in which the formation of 1D APCs can be clearly observed. Significant enhancement in the in-field J_c can be observed in Fig. 3.8 which is reflected in the much higher F_p values for the nanocomposite film (inset of Fig. 3.8). In another work, surface modified target method was used to incorporate YBNO nanocolumns into YBCO film matrix [47]. In this work, the concentration of the YBNO phase inside YBCO thin film was controlled by controlling the target rotation speed. Figure 3.9 shows the cross-sectional TEM image of YBCO+YBNO nanocomposite films in which not only formation of columnar YBNO nanostructures can be seen but also the variation in the density of YBNO nanocolumns can be observed. The incorporation of YBNO nanostructures inside YBCO films resulted in enhanced in-field J_c of the YBCO thin films which is shown in Fig. 3.10. Figure 3.10 (c) reveals the J_c peak for $H // c$ -axis for YBCO+YBNO nanocomposite thin films in the angular dependent J_c measurement.

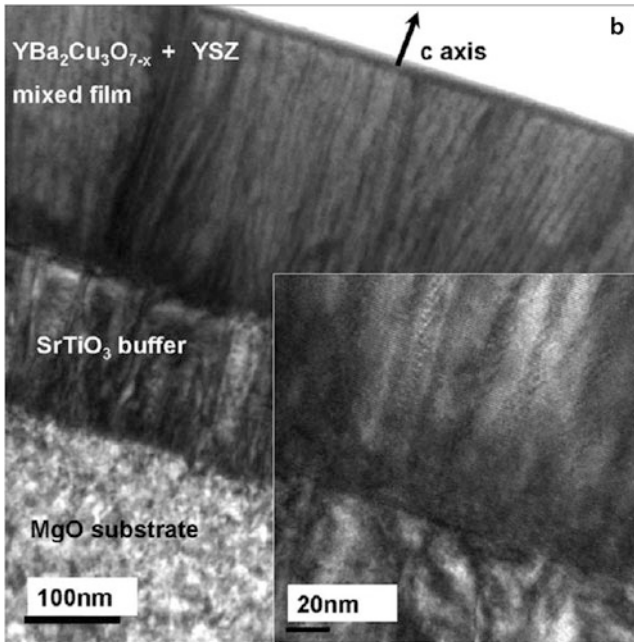


Fig. 3.7 Cross-sectional TEM image of YBCO+YSZ film deposited by surface modified target method using PLD technique. The formation of BZO nanorods can be seen clearly which were later confirmed by XRD measurement. Reprinted from [46], with the permission of Elsevier

3.6.3 *YBCO Films Consisting of both Nanoparticles and Nanocolumns of Secondary Phases (1D + 3D APCs)*

Both columnar nanostructures (1D APCs) and spherical nanoparticles (3D APCs) can be introduced into YBCO films and both can be effective in enhancing the in-field J_c . However, they have completely different effect on the J_c anisotropy. 1D APCs provide strong pinning but their efficiency is limited for a narrow angular range when applied magnetic field is parallel to the orientation of the columnar nanostructures. 3D nanoparticles, on the other hand, are less strong pinning centers but they provide isotropic pinning which is very much desired for many applications. In order to combine these different characteristics of both kinds of APCs, YBCO thin films with both kinds of APCs, called hybrid APCs, were studied. Surface modified target method has also been used to introduce hybrid APCs which turned out to be effective in enhancing the J_c as well as in reducing the J_c anisotropy.

The use of surface modified target for simultaneous incorporation of both 1D and 3D APCs into YBCO thin films was reported by Mele et al. who successfully introduced BZO nanocolumns and Y_2O_3 nanoparticles together into YBCO thin

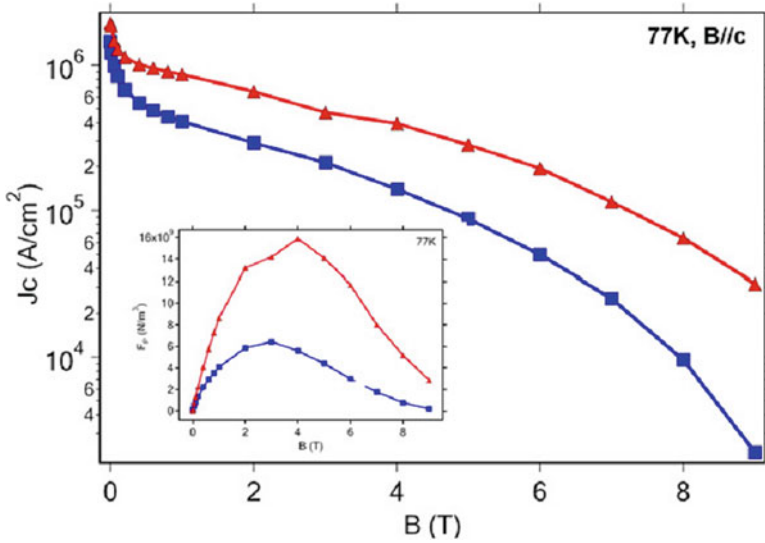
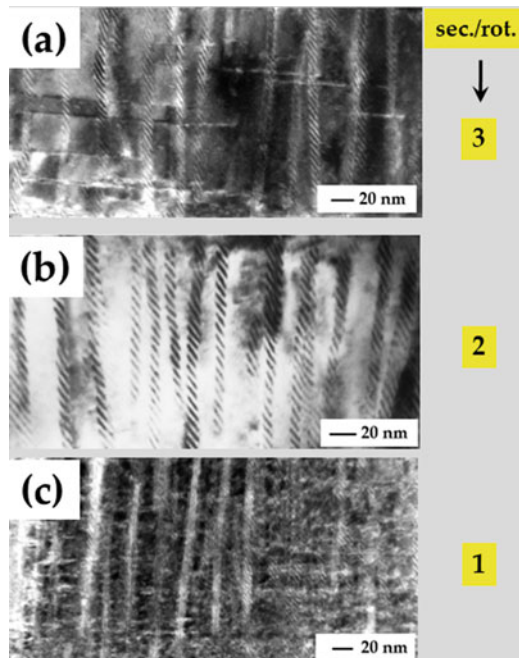


Fig. 3.8 Variation of J_c with respect to applied magnetic field for pristine YBCO (blue) and YBCO+YSZ (red) films prepared using surface modified target method. Inset shows the variation of F_p with applied magnetic field in which much higher F_{pmax} for the nanocomposite films can be observed. Reprinted from [46], with the permission of Elsevier

Fig. 3.9 Cross-sectional TEM image of YBCO film with YBNO nanocolumns prepared using surface modified target method. The density of the YBNO columns was varied by controlling the target rotation speed in the PLD system



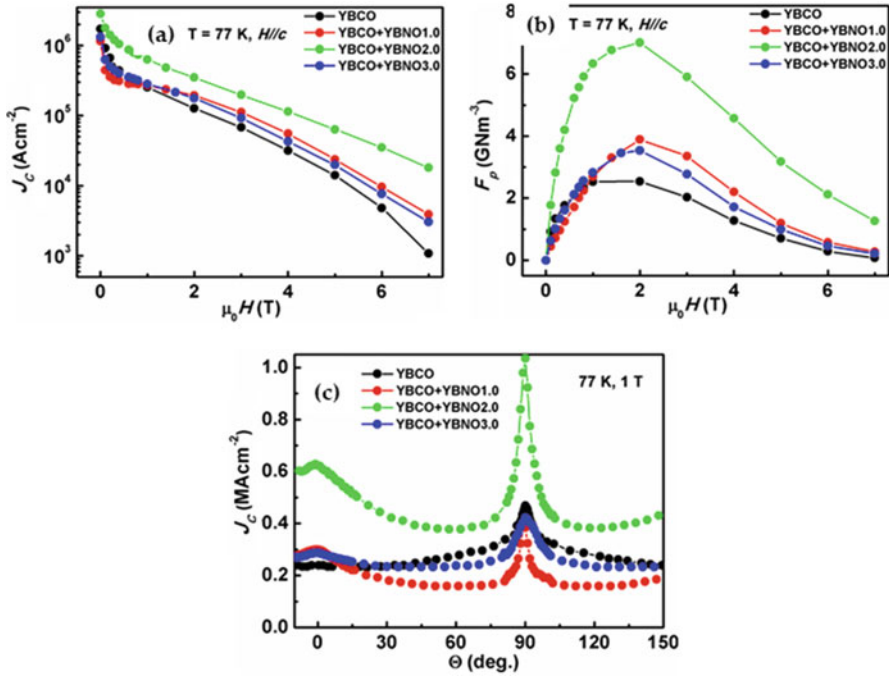
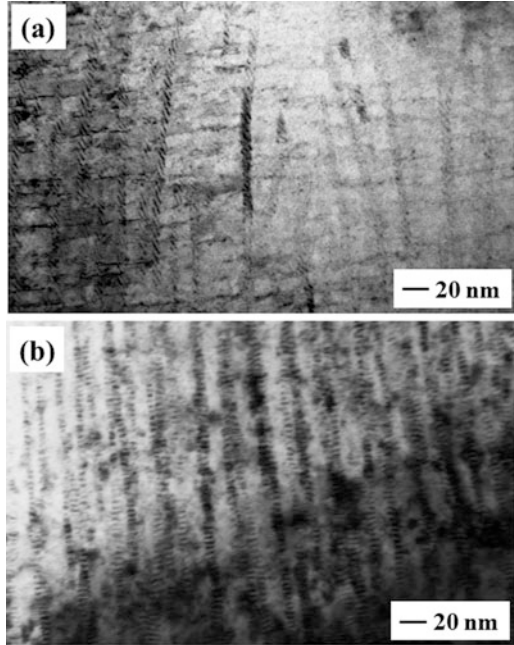


Fig. 3.10 Variation of (a) J_c and (b) F_p with respect to applied magnetic field for YBCO films with varying concentration of YBNO nanocolumns. YBCO+YBNO films exhibit superior in-field J_c as compared to pristine YBCO film. (c) Angular dependent J_c measurement shows that YBCO+YBNO films exhibit a J_c peak near 0 deg. ($H//c$ -axis)

films [48, 49]. This combination, however, could not improve the anisotropy of the YBCO film as compared to the YBCO thin film with single APCs (either BZO or Y_2O_3). This technique of using hybrid APCs was later attempted successfully to introduce BSO nanocolumns together with Y_2O_3 (YO) nanoparticles into YBCO thin films by means of surface modified target method [50, 51]. These hybrid APCs were very effective in improving the in-field J_c of YBCO films as well as reducing its angular anisotropy. Figure 3.11 shows the cross-sectional TEM image of YBCO+BSO3% and YBCO+BSO3% + Y_2O_3 nanocomposite thin films in which formation of only columnar structures in YBCO+BSO thin film and that of both nanocolumns and nanoparticles in YBCO+BSO + Y_2O_3 thin film can be clearly observed. Figure 3.12 shows the angular dependent J_c measurement conducted at 77 K, 1 T and 65 K, 3 T for pristine YBCO, YBCO+BSO, and YBCO+BSO + Y_2O_3 thin films. It can be clearly observed that the samples consisting of hybrid APCs exhibit superior in-field J_c not only along the c -axis but for entire angular range of applied magnetic field.

Fig. 3.11 Cross-sectional TEM image of YBCO films with (a) BSO nanocolumns and (b) BSO nanocolumns and Y_2O_3 nanoparticles deposited by surface modified target method. Reproduced from [50], with the permission from IEEE Publishing

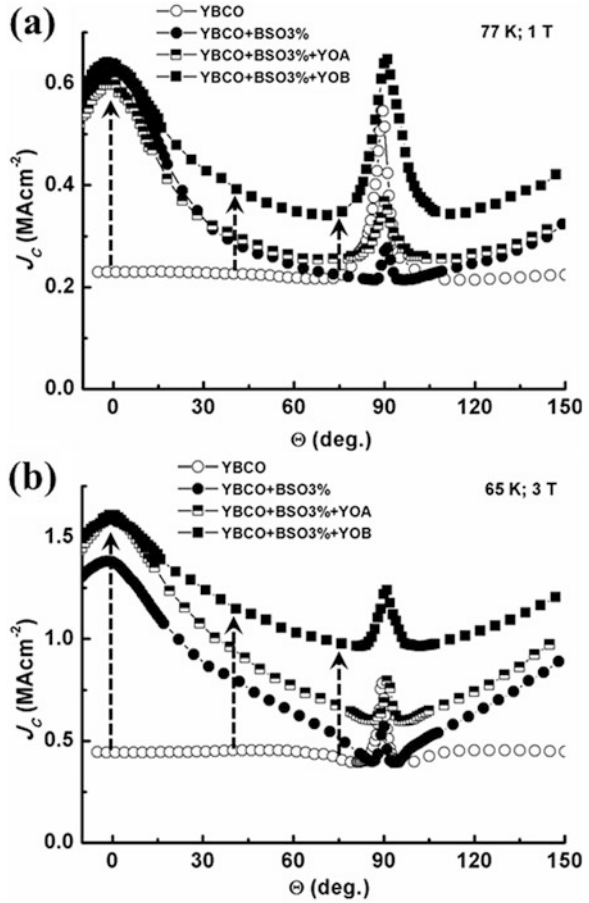


In another work, the successful incorporation of a different combination of nanocolumns and nanoparticles into YBCO thin films was reported in which BSO nanocolumns were combined with Y211 nanoparticles as hybrid APCs inside YBCO thin films by means of surface modified target method [52]. This new combination of hybrid APCs was also observed to be very effective in reducing the angular anisotropy of J_c of YBCO thin films. Figure 3.13 shows the cross-sectional micrograph of YBCO+Y211 and YBCO+BSO + Y211 thin films in which the formation of Y211 nanoparticles and that of BSO nanocolumns together with Y211 nanoparticles can be observed, respectively. The simultaneous incorporation of BSO nanocolumns and Y211 nanoparticles significantly improved the angular anisotropy of J_c in the hybrid APC sample which can be seen in Fig. 3.14. The thin film containing hybrid APCs exhibited the combined characteristics of nanoparticle pinning and nanocolumn pinning.

3.7 Factors Determining the Geometry/Morphology of Nanoscale Inclusions

Different secondary phase nanoinclusions inside YBCO film matrix exhibit different geometry and accordingly they are efficient for different range of applied magnetic field orientations. One of the fundamental parameters which decide the geometry

Fig. 3.12 Angular dependent J_c characteristics of pristine YBCO, YBCO+BSO, and YBCO+BSO + Y_2O_3 nanocomposite films measured at (a) 77 K, 1 T and (b) 65 K, 3 T. Two different sizes of sectored Y_2O_3 pieces, 2.2 area% and 3 area%, are referred as YOA and YOY, respectively. Reproduced from [50], with the permission from IEEE Publishing



of these nanoinclusions within YBCO film is the lattice misfit between the two phases. Another parameter which is important in determining the geometry of these nanoinclusions is the surface diffusion co-efficient of adatoms which is crucial in determining the interface between the two phases which may be coherent, semi-coherent, or non-coherent [53]. The surface energies of coherent and semi-coherent interfaces are much lower as compared to that of non-coherent interfaces. The high surface energies of non-coherent interfaces result in the coarsening of the grains in polycrystalline films [54], faceting of precipitates and grain boundaries [55]. In a recent work, it has been reported that the morphology of the secondary phase nanoinclusions is determined by the combined effect of the lattice mismatch and elastic properties of YBCO and secondary phase materials [56].

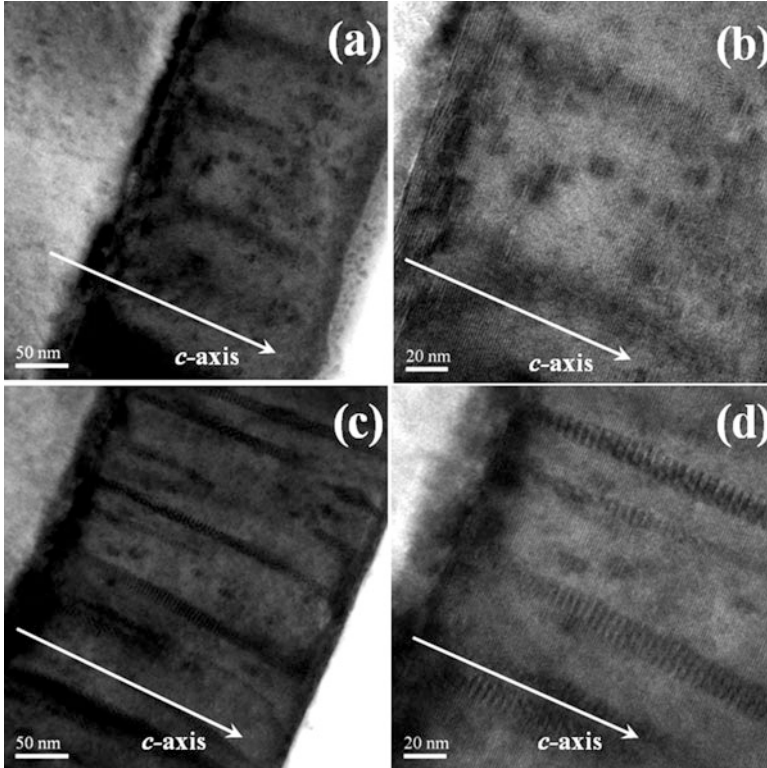
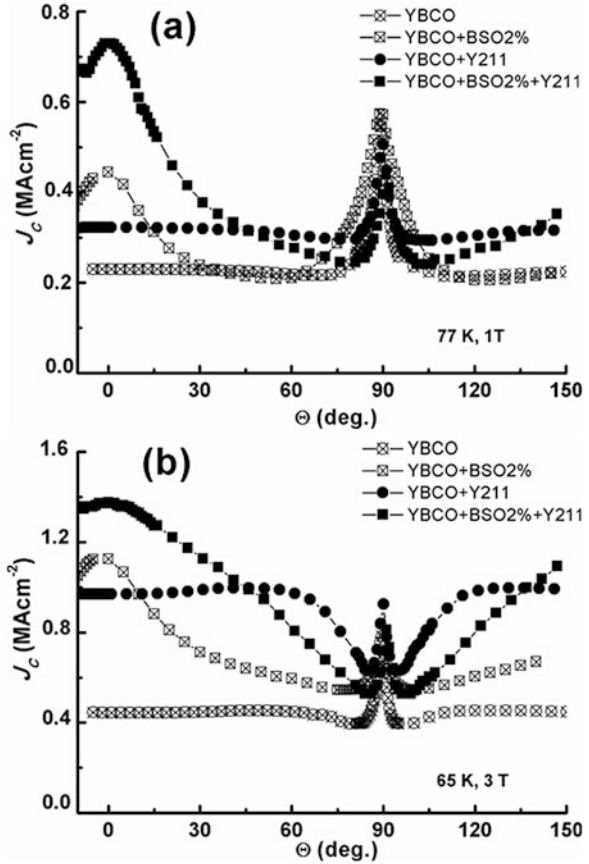


Fig. 3.13 Cross-sectional TEM image of YBCO thin films with Y211 nanoparticles (a, b) and BSO nanocolumns plus Y211 nanoparticles (c, d) deposited by surface modified target method. Reproduced from [52], with the permission from IEEE Publishing

3.8 Conclusions

In order to improve the in-field J_c of YBCO superconducting thin films, many methods have been tried and introduction of APCs is crucial for this purpose. In recent years, a variety of methods have been reported to intentionally introduce nanostructured secondary phases into the YBCO superconducting thin films and among them, surface modified target method in PLD technique has been found to be very useful. Different secondary phases are formed in different geometries when incorporated within YBCO matrix and all these geometries can be realized by surface modified target method. The geometry and concentration of the secondary phase can be varied just by changing the composition and/or size of the secondary phase acting as surface modified piece on the ablation target. This is not only an economical approach but also saves a lot of time in conducting such experiments where the variation in the geometry and density of secondary phase material inside YBCO matrix is desired.

Fig. 3.14 Angular dependent J_c characteristics of pristine YBCO, YBCO+BSO, YBCO+Y211 and YBCO+BSO + Y211 nanocomposite thin films measured at (a) 77 K, 1 T and (b) 65 K, 3 T. Reproduced from [52], with the permission from IEEE Publishing



The generation of nanoscale secondary phases with desired density, geometry, and orientation inside YBCO matrix is very much needed for control of vortex pinning in YBCO thin films deposited on single crystals and metallic tapes.

Acknowledgements We thank T. Horide, S. Saini, P. Mele, A. Ichinose, Y. Yoshida, and S. Awaji for cooperative research on vortex pinning studies in YBCO nanocomposite films.

References

1. M.K. Wu, J.R. Ashburn, C.J. Torng, P.H. Hor, R.L. Meng, L. Gao, Z.J. Huang, Y.Q. Wang, C.W. Chu, *Phys. Rev. Lett.* **58**, 908 (1987)
2. H. Maeda, Y. Tanaka, M. Fukutomi, T. Asano, *Jpn. J. Appl. Phys.* **27**, L209 (1988)
3. A. Schilling, M. Cantoni, J.D. Guo, H.R. Ott, *Nature* **363**, 56 (1993)
4. D. Larbalestier, A. Gurevich, D.M. Feldmann, A. Polyanskii, *Nature* **414**, 368 (2001)
5. A.P. Malozemoff, *Nat. Mater.* **6**, 617 (2007)

6. S.R. Foltyn, L. Civale, J.L. Macmanus-Driscoll, Q.X. Jia, B. Maiorov, H. Wang, M. Maley, *Nat. Mater.* **6**, 631 (2007)
7. K. Matsumoto, P. Mele, *Supercond. Sci. Technol.* **23**, 014001 (2010)
8. X. Obradors, T. Puig, *Supercond. Sci. Technol.* **27**, 044003 (2014)
9. D. Dimos, P. Chaudhari, J. Mannhart, *Phys. Rev. B* **41**, 4038 (1990)
10. S. Jin, T.H. Tiefel, R.C. Sherwood, R.B. van Dover, M.E. Davis, G.W. Kammlott, R.A. Fastnacht, *Phys. Rev. B* **37**, 7850 (1988)
11. M. Murakami (ed.), *Melt-Processed High-Temperature Superconductors* (World Scientific, Singapore, 1992)
12. D. Dijkkamp, T. Venkatesan, X.D. Wu, S.A. Shaheen, N. Jisrawi, Y.H. Min-Lee, W.L. McLean, M. Croft, *Appl. Phys. Lett.* **51**, 619 (1987)
13. B. Schey, Chapter 14 in *Pulsed Laser Deposition of Thin Films*, by R. Eason (Ed.), Wiley, New Jersey, pp. 313–331 (2007)
14. M. Miura, Chapter 5 in *Oxide Thin Films, Multilayers, and Nanocomposites*, by P. Mele, T. Endo, S. Arisawa, C. Li and T. Tsuchiya (Eds.), Springer, Cham, pp. 3–26 (2015)
15. A. Ignatiev, Chapter 15 in *Second-Generation HTS Conductors*, by A. Goyal (Ed.), Kluwer Academic Publishers, Dordrecht, pp. 245–259 (2005)
16. D. B. Chrisey, G. K. Hubler (eds.), *Pulsed Laser Deposition of Thin Films* (Wiley, New York, 1994)
17. R.K. Singh, D. Kumar, *Mat. Sci. Eng. R* **22**, 113 (1998)
18. T. Matsushita, *Flux Pinning in Superconductors* (Springer, Berlin, 2007)
19. B. Dam, J.M. Huijbregtse, F.C. Klaassen, R.C.F. Van der Geest, G. Doornbos, J.H. Rector, A.M. Testa, S. Freisem, J.C. Martinez, B. Stauble-Pumpin, R. Griessen, *Nature* **399**, 439 (1999)
20. J.M. Huijbregtse, F.C. Klaassen, A. Szepielow, J.H. Rector, B. Dam, R. Griessen, B.J. Kooi, J.T.M. de Hosson, *Supercond. Sci. Technol.* **15**, 395 (2002)
21. L. Civale, *Supercond. Sci. Technol.* **10**, A11 (1997)
22. S.H. Wee, A. Goyal, P.M. Martin, L. Heatherly, *Supercond. Sci. Technol.* **19**, 865 (2006)
23. C. Cai, B. Holzapfel, J. Hanishch, L. Fernandez, L. Schultz, *Phys. Rev. B* **69**, 104531 (2004)
24. A.K. Jha, K. Matsumoto, T. Horide, S. Saini, P. Mele, A. Ichinose, Y. Yoshida, S. Awaji, *J. Appl. Phys.* **122**, 093905 (2017)
25. T. Haugan, P.N. Barnes, R. Wheeler, F. Meisenkothen, M. Sumption, *Nature* **430**, 867 (2004)
26. A.A. Gapud, D. Kumar, S.K. Viswanathan, C. Cantoni, M. Varela, J. Abiade, S.J. Pennycook, D.K. Christen, *Supercond. Sci. Technol.* **18**, 1502 (2005)
27. J.L. MacManus Driscoll, S.R. Foltyn, Q.X. Jia, H. Wang, A. Serquis, L. Civale, B. Maiorov, M.E. Hawley, M.P. Maley, D.E. Peterson, *Nat. Mater.* **3**, 439 (2004)
28. A. Goyal, S. Kang, K.J. Leonard, P.M. Martin, A.A. Gapud, M. Varela, M. Paranthaman, A.O. Ijaduola, E.D. Specht, J.R. Thompson, D.K. Christen, S.J. Pennycook, F.A. List, *Supercond. Sci. Technol.* **18**, 1533 (2005)
29. P. Mele, K. Matsumoto, A. Ichinose, M. Mukaida, Y. Yoshida, S. Horii, R. Kita, *Supercond. Sci. Technol.* **21**, 125017 (2008)
30. C.V. Varanasi, J. Burke, H. Wang, J.H. Lee, P.N. Barnes, *Appl. Phys. Lett.* **93**, 092501 (2008)
31. J. Hanisch, C. Cai, R. Huhne, L. Schultz, B. Holzapfel, *Appl. Phys. Lett.* **86**, 122508 (2005)
32. D.M. Feldmann, T.G. Holesinger, B. Maiorov, S.R. Foltyn, J.Y. Coulter, I. Apodaca, *Supercond. Sci. Technol.* **23**, 095004 (2010)
33. S.H. Wee, A. Goyal, Y.L. Zuev, C. Cantoni, V. Selvamanickam, E.D. Specht, *Appl. Phys. Exp.* **3**, 023101 (2010)
34. S.H. Wee, A. Goyal, E.D. Specht, C. Cantoni, Y.L. Zuev, V. Selvamanickam, S. Cook, *Phys. Rev. B* **81**, 140503 (2010)
35. C. Varanasi, P.N. Barnes, J. Burke, J. Carpenter, T. Haugan, *Appl. Phys. Lett.* **87**, 262510 (2005)
36. P. Mele, K. Matsumoto, T. Horide, A. Ichinose, M. Mukaida, Y. Yoshida, S. Horii, *Supercond. Sci. Technol.* **20**, 616 (2007)

37. P. Mele, K. Matsumoto, T. Horide, A. Ichinose, M. Mukaida, Y. Yoshida, S. Horii, *Supercond. Sci. Technol.* **20**, 244 (2007)
38. T. Horide, K. Matsumoto, A. Ichinose, M. Mukaida, Y. Yoshida, S. Horii, *Supercond. Sci. Technol.* **20**, 303 (2007)
39. M. Tachiki, S. Takahashi, *Sol. St. Comm.* **70**, 291 (1989)
40. M. Tachiki, S. Takahashi, *Sol. St. Comm.* **72**, 1083 (1989)
41. L. Civale, B. Maiorov, A. Serquis, J.O. Willis, J.Y. Coulter, H. Wang, Q.X. Jia, P.N. Arendt, J.L. MacManus Driscoll, M.P. Maley, S.R. Foltyn, *Appl. Phys. Lett.* **84**, 2121 (2004)
42. S.K. Viswanathan, A.A. Gapud, M. Varela, J.T. Abiade, D.K. Christen, S.J. Pennycook, D. Kumar, *Thin Solid Films* **515**, 6452 (2007)
43. P. Mele, R. Guzman, J. Gazquez, T. Puig, X. Obradors, S. Saini, Y. Yoshida, M. Mukaida, A. Ichinose, K. Matsumoto, M.I. Adam, *Supercond. Sci. Technol.* **28**, 024002 (2015)
44. C.V. Varanasi, P.N. Barnes, J. Burke, L. Brunke, I. Maartense, T.J. Haugan, E.A. Stinzianni, K.A. Dunn, P. Haldar, *Supercond. Sci. Technol.* **19**, L37 (2006)
45. C.V. Varanasi, J. Burke, L. Brunke, H. Wang, M. Sumption, P.N. Barnes, *J. Appl. Phys.* **102**, 063909 (2007)
46. P. Mele, K. Matsumoto, T. Horide, A. Ichinose, M. Mukaida, Y. Yoshida, S. Horii, *Physica C* **463-465**, 653 (2007)
47. A.K. Jha, K. Matsumoto, T. Horide, S. Saini, P. Mele, Y. Yoshida, S. Awaji, *Supercond. Sci. Technol.* **27**, 025009 (2014)
48. P. Mele, K. Matsumoto, T. Horide, A. Ichinose, M. Mukaida, Y. Yoshida, S. Horii, R. Kita, *Physica C* **468**, 1631 (2008)
49. P. Mele, K. Matsumoto, T. Horide, A. Ichinose, M. Mukaida, Y. Yoshida, S. Horii, R. Kita, *Supercond. Sci. Technol.* **21**, 015019 (2008)
50. A.K. Jha, K. Matsumoto, T. Horide, S. Saini, P. Mele, Y. Yoshida, S. Awaji, *IEEE Trans. Appl. Supercond.* **25**, 8000505 (2015)
51. A.K. Jha, K. Matsumoto, T. Horide, S. Saini, P. Mele, A. Ichinose, Y. Yoshida, S. Awaji, *Supercond. Sci. Technol.* **28**, 114004 (2015)
52. A.K. Jha, K. Matsumoto, T. Horide, S. Saini, P. Mele, A. Ichinose, Y. Yoshida, S. Awaji, *IEEE Trans. Appl. Supercond.* **26**, 8000404 (2016)
53. J. Gutierrez, A. Llordes, J. Gazquez, M. Gibert, N. Roma, S. Ricart, A. Pomar, F. Sandiumenge, N. Mestres, T. Puig, X. Obradors, *Nat. Mater.* **6**, 367 (2007)
54. C.V. Thompson, *Annu. Rev. Mater. Sci.* **30**, 159–190 (2000)
55. A. Sutton, R. Balluffi, *Interfaces in Crystalline Materials* (Oxford Univ. Press, Oxford, 1996)
56. J. Wu, J. Shi, *Supercond. Sci. Technol.* **30**, 103002 (2017)

Chapter 4

Progress in Thick Film 2G-HTS Development



Goran Majkic

4.1 Introduction

The Second-Generation High-Temperature Superconductor (2G-HTS) technology has seen a tremendous progress over the last two decades. The brittle nature of YBCO ($\text{YBa}_2\text{Cu}_3\text{O}_{7-\delta}$) and its REBCO variants (RE = rare-earth), as well as other technical challenges have resulted in an impressive effort all over the world in an attempt to harvest the numerous advantages of this material in a functional form, resulting in what is probably the first technology to realize brittle ceramic materials deposited on flexible metallic substrates in kilometer lengths. The undeniable advantages of YBCO, including high critical temperature (T_c), high critical current (I_c), and critical current density (J_c), as well as very high irreversibility field (B_{irr}), have been a major driving force behind this impressive development.

The highly promising potential performance figures, however, have been faced with numerous practical obstacles. In particular, starting from the early experiments on thin film YBCO deposition on either single crystal substrates or flexible films, it has been realized that the dream of achieving arbitrarily high I_c by increasing film thickness is not a straightforward issue. Soon it was realized that critical current density, J_c , strongly decreases with film thickness. In the last two decades, significant effort has been devoted to scale-up of 2G-HTS conductors in practical film thicknesses of about $1\ \mu\text{m}$, as numerous researchers have encountered the same issue of degradation of J_c with thickness, irrespective of the deposition technique used. The practical limit of about $1\ \mu\text{m}$ has been spontaneously established, both in fundamental research and commercial 2G-HTS tapes. Starting from the early developments of 2G-HTS technology, researchers and manufacturers appear to have

G. Majkic (✉)

Department of Mechanical Engineering, Texas Center for Superconductivity, Advanced Manufacturing Institute, University of Houston, Houston, TX, USA
e-mail: gmajkic@uh.edu

taken one of the two approaches to increasing performance—either maximizing I_c within the ~ 1 micron film thickness or attempting to increase I_c by increasing film thickness and combating the J_c degradation issue. In parallel, many researchers have contributed to the understanding of the reasons behind deterioration of J_c with thickness. There have been various approaches to the issue, but the main dilemma has remained in the question—whether this issue is related to a physical limitation or simply stemming from a non-optimized deposition process. For example, several studies have reported that I_c saturates to a constant value above a certain thickness (approx. 1.5–2 μm), after which there is no increase in I_c with further increase in thickness, which will be elaborated on later in this chapter. This result implies that J_c drops to zero above a certain critical thickness. The material deposited beyond this critical thickness has also been termed “dead layer,” implying that it cannot carry any current. Without any further evidence, one can think of two immediate scenarios—either it is impossible to increase I_c with thickness due to some physical limitation, or the deposition process is faced by an unidentified issue that leads to this phenomenon. By reviewing the literature, one can see that both of these two ideas have been addressed in a number of studies, with varying degree of success in positively identifying the issue. For example, one view of the issue is centered on the fact that the self-field generated at progressively higher film thickness and therefore I_c increases, as will be discussed. Given the experimental evidence of a dead layer that has been reported in more than one study, a natural question arises on whether this dead layer is a natural limitation at high film thickness due to increase of the self-field generated by increasing current with thickness, eventually limiting the magnitude of current that can be carried in a film of a critical thickness where further increase of self-field limits the current to a maximum achievable value.

On the other hand, numerous studies have clearly demonstrated a microstructure phenomenon that occurs with an increase in film thickness, namely that of an increase in volume fraction of misoriented YBCO grains that grow in the orientation of a -axis perpendicular to film instead of the desired orientation where the c -axis is perpendicular to film. The grain boundaries between grains having c -axis and a -axis orientations block the super-current and naturally deteriorate the resulting I_c value. In addition, there are numerous reports on texture quality degradation with film thickness, even within the material having the desired c -axis orientation. Both of these experimental evidences point to another potential source of I_c degradation with thickness—which is microstructure degradation. This equally convincing argument leads to a different viewpoint on the issue—if microstructure deterioration is responsible for drop in J_c with thickness, then it would be necessary to understand the reason behind this instability in film growth. A full understanding of this issue would then provide the answer to the question on whether this microstructure deterioration can be addressed and avoided, resulting in breaking the barrier to further increase in I_c by increasing film thickness. Finally, a mixture of both of these scenarios is another possibility, and in this case, all of the above would apply. In addition, quantification of the relative contribution of each of the two possible mechanisms would be one important aspect to consider in order to assess their importance.

Regarding the thickness effect on I_c , it should be noted that the reported studies can be generally separated into two categories—degradation of J_c in the initial stages of film growth—from zero to several hundred nanometers, and the degradation of J_c in thick films beyond one micron. Significant amount of research has been done in both categories, often combined with combating other issues such as texture quality of YBCO films and the effect of buffer layer on this issue. Effects such as buffer/YBCO epitaxial mismatch and strain relaxation, misfit dislocations and similar have been studied and attempts have been made to correlate them to J_c degradation with thickness. On the other hand, attempts to grow films thicker than approx. 1 μm with minimized J_c degradation appear to be faced with different issues, such as the mentioned increase in fraction of a -axis oriented grains and texture deterioration. Given the amount of experimental evidence from both approaches, it is quite plausible that both effects play significant roles. However, understanding their relative importance at different thickness scales is critical to achieving further progress in pushing the I_c envelope up.

In addition to increasing the self-field I_c , tremendous progress has been realized in the last decade in increasing the in-field performance of 2G-HTS technology. The breakthrough in achieving dramatic increase in in-field critical current retention came with the discovery of the possibility to grow dual-phase HTS film consisting of YBCO matrix interspersed with a nano-columnar or “nanorod” secondary phase in the shape of c -axis aligned columnar or rod precipitates having diameter on the order of coherence length (several nm) and arbitrarily long lengths. These heterostructures containing such Artificial Pinning Centers (APC) have been demonstrated to exhibit a very strong increase in I_c retention in magnetic field, which has spurred intense research on understanding both the nanorod growth process and its effect on in-field performance of 2G-HTS tapes. Considering the main topic of this chapter, which is increasing I_c by increasing film thickness without degradation of performance, a question then arises regarding the possibility of growth of thick REBCO films with APCs and whether high pinning performance can be maintained in thick ($>1 \mu\text{m}$) films.

It should be pointed out that the issue is of critical importance for success and widespread utilization of the 2G-HTS technology. Namely, one of the most important issues that this technology has to overcome is the cost associated with realizing the 2G-HTS technology. If we take the cost/performance ratio as the main “effective” cost metric, say the $\$/\text{kA}\cdot\text{m}$ metric, which we can refer to as the effective “performance cost,” this value can be driven down either by reducing the raw cost associated with the manufacturing process, or by increasing the performance per meter of tape, which implies increasing the critical current, both for self-field and in-field applications. As the overhead cost of producing the 2G-HTS tape includes not only the cost of the HTS layer deposition but also the overhead of substrate tape processing, buffer stack deposition, silver and copper layer deposition, all of which are necessary, it appears that the most direct way of reducing the performance cost is by focusing on increasing the HTS layer performance. In other words, the raw cost of doubling the I_c by increasing HTS films thickness would constitute only a fractional increase in the total cost of tape (overhead + HTS film cost), while the

performance (kA-m) would double. This implies that this approach of, say, doubling the I_c would result in reduction of “performance cost” by a factor potentially close to 2. As such, one can see the tremendous value in the effort to increase I_c of 2G-HTS tapes directly by increasing film thickness.

In this chapter, we review the different viewpoints on the issue reported in the literature and look at the experimental and some theoretical results. We also review the very promising recent advances in producing thick 2G-HTS films with very high in-field performance that show strong evidence that significant increase in I_c can indeed be achieved by increasing film thickness. The author would also like to point out to a recently published excellent review paper on the same topic, which provides a compact overview on the subject [1].

4.2 Thickness Dependence of Self-Field J_c

Studies on thickness dependence of J_c have commenced practically immediately after the discovery of YBCO. As early as 1988, Luborsky, et al. have reported that the self-field critical current of films deposited by RF diode sputtering from a single target deteriorates with thickness [2]. In this study, single crystals of SrTiO₃ (STO) in 100 and 110 orientations, 9.5% yttria-stabilized zirconia (YSZ), and Si wafers with overlayers of ZrO₂ and HfO₂ were used, where the 100-oriented SrTiO₃ substrates resulted in highest quality YBCO films. The film thickness was varied from 0.09 to 2.4 μm. It is interesting to note that as early as 1988, the theme has been set—the critical temperature, T_c , has been found to be thickness-independent in this study, with average T_c of 85.6 K and transition width ΔT_c of 1.8 K, while J_c has been found to decrease from 8.1×10^5 A/cm² at 0.2 μm to about an order of magnitude lower values at film thickness of ~ 2 μm. The authors conclude that the decrease in J_c with the increase in film thickness is expected due to the gradual loss of crystal orientation with the increase in film thickness. It is worth to note that the authors have also conducted I_c measurements at 4.3 K utilizing magnetization measurements and reached the same conclusion. This result indicated very early that the phenomenon of J_c degradation with thickness is neither dependent on measurement technique nor magnitude of J_c , which was approx. two orders of magnitude higher at 4.3 K than at 77 K.

In 1993, Foltyn, et al. have reported a systematic study of deposition of YBCO by pulsed laser deposition (PLD) on yttria-stabilized zirconia (YSZ) substrates capped with CeO₂ [3]. In this study, a clear trend of monotonic decrease in J_c with thickness has been reported. Films ranging from 0.065 to 6.4 μm in thickness have been grown, resulting in critical current decrease from 5 MA/cm² to what seemed like an asymptotical decrease towards 1 MA/cm², as shown in Fig. 4.1.

As it can be seen, a very systematic trend has been observed, with high quality data that have little scatter around the trend. The authors have provided a fit (solid line) in the form of exponential decay with thickness plus the additional constant saturation term, in the form $J_c = Ae^{-\alpha t} + B$, with the fit values of $\alpha = 1.2 \mu\text{m}^{-1}$

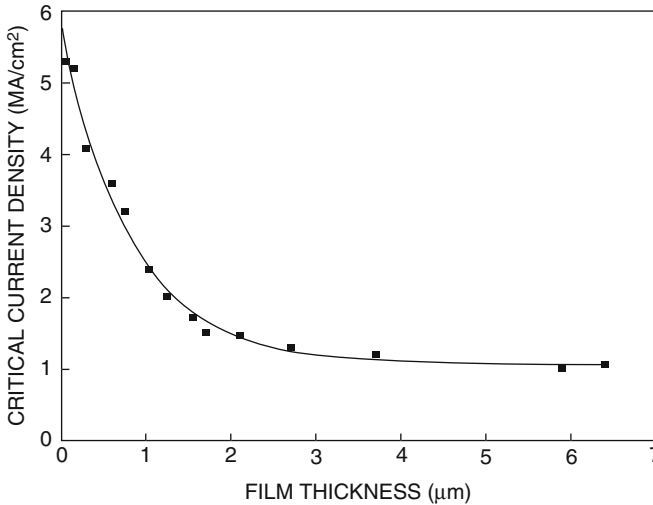


Fig. 4.1 Thickness dependence of J_c in YBCO films grown on single crystal YSZ substrates with CeO_2 cap layer. Reproduced with permission from [3]

and $B = 1.05 \text{ MA/cm}^2$ while the zero thickness constant $A + B$ has been estimated to 5.75 MA/cm^2 . The authors note that the exponential decay in J_c has been reported by others (3–5 in the original manuscript) and that it has been attributed to transition from c -axis to a -axis film growth. In contrast to these previous reports, Foltyn, et al., report that the decay rate of J_c in their study is much slower; where the previous studies reported decay of one or two orders of magnitude from ~ 0.4 to $2 \mu\text{m}$ with the asymptotic trend towards $J_c = 0$ at high thickness, their study has found much a slower decay and the asymptotic value of 1 MA/cm^2 in films with thickness of $>6 \mu\text{m}$. The importance of this result is that it has been shown that films can be produced with J_c not asymptotically converging to zero, but rather to a constant, non-negligible value (1 MA/cm^2). This is illustrated in Fig. 4.2, where the data from Fig. 4.1 have been used to calculate an equivalent critical current over 12 mm width, which is a typical 2G-HTS tape width commercially available today. The importance of these encouraging results lies in the fact that the films reported in this study do not exhibit a “dead-layer” behavior which occurs when J_c tends to be zero at high thickness; critical current is still increasing with thickness, despite the much lower rate of I_c increase. Later experiments have proven that replicating the results on metallic buffered substrates is not straightforward, and it took more than a decade of research to achieve performance close to single crystal substrates. Nevertheless, these early results on single crystal YSZ substrates have shown encouraging signs that, at minimum, dead layer can be avoided and thus I_c can be increased by increasing film thickness.

The authors examined several possibilities for the decay in J_c . The typical deterioration in texture, either in the form of progressive increase in a -axis oriented

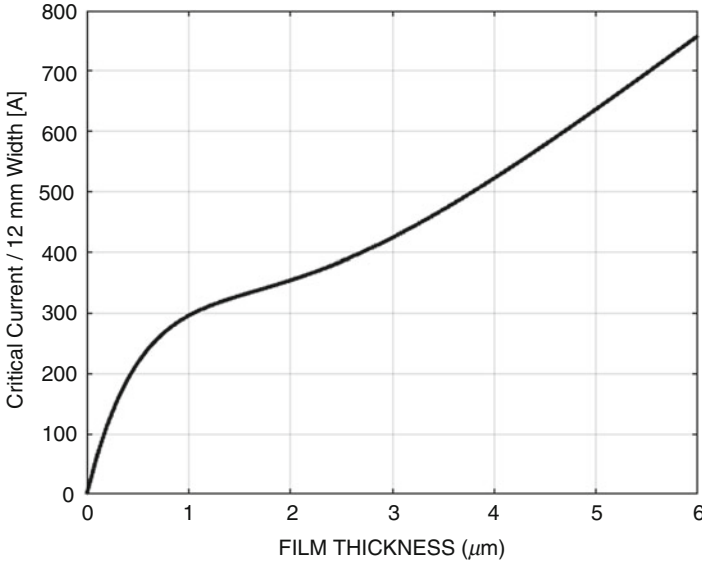


Fig. 4.2 Equivalent critical current for typical 12 mm 2G-HTS tape, calculated from data presented in Fig. 4.1 [3]

grains with thickness, or in-plane texture degradation, has been examined in a 2.2 μm film. While a -axis grains have been identified by X-Ray Diffraction (XRD), the peak ratio of c -axis to a -axis oriented grains was found to be over 100:1—which the authors interpret as a comparably small fraction relative to the large decrease in J_c . The in-plane texture analysis indicated that a small amount of YBCO was in-plane rotated 45° from the main texture orientation, but again with a peak ratio of 1:70, suggesting a negligible effect on J_c . The authors also provide information on Rutherford Backscattering Spectrometry (RBS), which indicated a χ_{min} value of 75%, in 2.2 μm on which the authors remark that this parameter is an indication of film disorder and that this value was far higher compared to that found in thin films. The authors hint at randomly oriented material (disordered microstructure) being responsible for this increase, but without further elaboration.

In 1999, a report by Foltyn, et al., on thickness dependence of I_c , both on single crystals and on the early developments of 2G-HTS technology (metallic substrates with textured buffer layers) was published [4]. The authors note several salient characteristics of both technologies that are true even today, 20 years after the publication. They remark that increasing I_c , even if it implies growth of thicker YBCO films, is one of the most direct or logical approaches to increasing engineering current density, J_e , which would, in turn, reduce the manufacturing cost relative to their performance (the metric that is termed “performance cost” in this review chapter). At the time, YBCO films on single crystal substrates with J_c over 5 MA/cm² have been commonly reported in literature, as noted by the authors; however, all attempts to grow films thicker than $\sim 1 \mu\text{m}$ resulted in J_c

quickly decreasing and saturating to a value of about 1 MA/cm^2 . At the time of the publication, plenty of experimental evidence from YBCO growth on single crystals already existed to show that this phenomenon is common to all YBCO deposition techniques, including pulsed laser deposition, liquid-phase epitaxy, chemical vapor deposition (CVD), BaF_2 , and metal organic CVD (MOCVD) deposition. The authors acknowledge that the cause of decrease in J_c with thickness remains unidentified. The work in question focuses on 2G-HTS technology, i.e., flexible metal tapes (Inconel 625) with YSZ layer deposited by Ion Beam Assisted Deposition (IBAD). The YSZ layer was then capped with a 20 nm thick Y_2O_3 layer before YBCO deposition.

In the manuscript [4], films with thicknesses ranging from 0.39 to $6.3 \mu\text{m}$ have been deposited using PLD and analyzed. Shown in Fig. 4.3 is a plot of J_c vs. thickness for IBAD-YSZ substrates on flexible Inconel tapes. The solid line represents a comparison with single crystal YSZ substrates from the mentioned previous study [3]. The authors note that the asymptotic J_c value for films on flexible substrates is less than one-fourth of the value for single crystal substrates.

Perhaps one of the most revealing plots that illustrate the nature of the problem is contained in Fig. 4.4, taken from [4]. In this plot, three samples of different thickness, ~ 0.68 , 3.0 , and $4.7 \mu\text{m}$, that have been incrementally Ar-ion beam etched at 300 eV. For the thinnest film, the I_c decreases with thickness as expected—nearly linearly. When the thickness was reduced to as low as 30 nm, the sample still carried current, reaching 4.1 MA/cm^2 , which is an indication of successful ion milling with

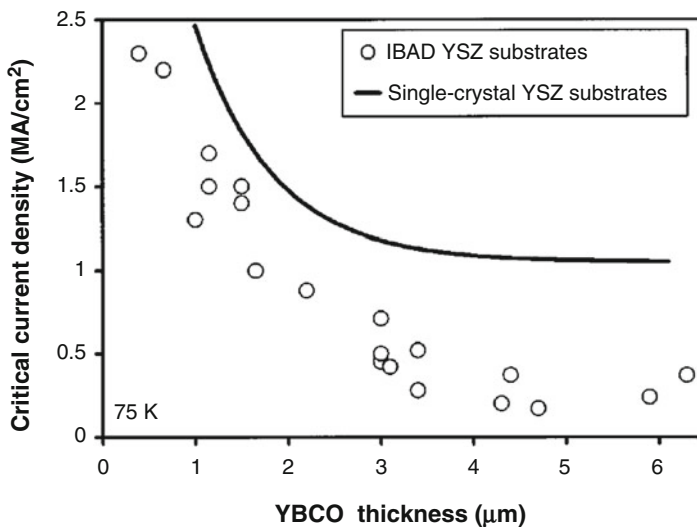


Fig. 4.3 Critical current density as a function of thickness for single crystal YSZ and IBAD-YSZ substrates on Inconel tapes. Compared to single crystal substrates, the asymptotic J_c value for IBAD-YSZ substrates drop to less than one-fourth of the single crystal substrates. Reproduced with permission from [4]

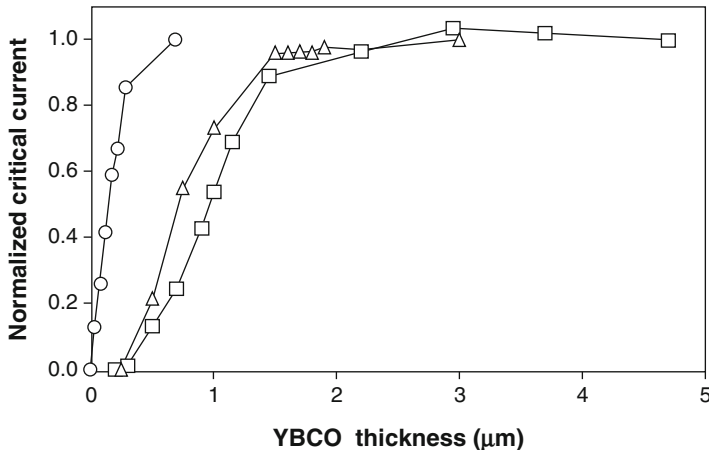


Fig. 4.4 Plot of critical current, normalized to the initial value, vs thickness of incrementally ion-milled samples. Reproduced with permission from [4]

no induced damage to the film. In contrast, the two thick films showed very different behavior. Critical current remained constant upon ion milling for both samples down to 1.5 μm of etched thickness. This initially discouraging result revealed the core of the problem—all material deposited above 1.5 μm thickness carried little or no current. In addition, another surprising result came at very low remaining thickness: both thick films showed zero I_c when the film thickness was reduced to about 250 nm. This result implies that due to an unknown mechanism, the critical current near the buffer/YBCO interface is degraded in thick films, but not in the thin 0.68 μm film. It should be noted that the manuscript also shows the extrapolated equivalent I_c values for 1 cm sample width based on the bridge measurements and compares them to the values obtained from single crystal substrates. Up to two micron thickness, both single crystal and tape samples showed comparable behavior, reaching ~ 200 A at 2 μm thickness. The largest difference occurred at thickness beyond 2 μm , where tape samples remained at constant critical current of ~ 200 A while single crystal samples continued to increase in I_c value with thickness at a lower rate, reaching near-500 A at ~ 4.5 μm thickness.

The authors attribute the degradation of I_c of thick samples near the buffer to impurity diffusion from the substrate. Indeed, the authors deposited a 0.46 μm film in 3 min and then left the sample at deposition temperature and pressure (775 $^\circ\text{C}$, 0.2 Torr O_2) for 1 h. The resulting J_c was an order of magnitude lower than a similar sample that was deposited without the subsequent 1-hr dwell. These and other later findings all pointed out to important issues related to 2G-HTS technology that have been later solved (e.g., in this case, the inter-diffusion problem that has been since solved by inserting a diffusion barrier layer).

In order to attempt to provide insight into the effect of decreasing J_c with thickness, the “dead layer” above ~ 1.5 μm was also investigated. The authors check

the hypothesis that in thick samples a large fraction of a -axis oriented grains exists, thus deteriorating the J_c . The authors report that their XRD χ scans of YBCO 102 peak revealed little or no a -axis orientation. The third assumption put forward by the authors, perhaps somewhat vague, is that film morphology becomes “rougher” with thickness increase, which could then be suspected as a potential reason for the dead layer. The authors show evidence of a 6 μm sample fractured in half and examined by Scanning Electron Microscopy (SEM), which suggests existence of a dense and smooth layer in the bottom 1–2 μm and a more “disordered with softer fracture features” layer on top. The authors speculate that the increase in surface roughness leads to micro-porosity which reduces J_c . The origin of the onset of porosity was not discussed.

The same group, very productive in attempts to combat the thickness dependence of J_c , reported a multilayer approach to minimizing or eliminating their reported micro-porosity at higher thickness in 2002 [5]. Their reported architecture consists of a sandwich sequence of YBCO/CeO₂, where the interlayer of CeO₂ was used with the idea of reducing the formation of defects such as voids, porosity, and a -grains. The authors report a private communication by Chen, who was reported to believe that such multilayered interfaces can control the dislocation density inside the film by terminating at each multilayered interface boundary. Without direct evidence, the authors report the opinion that in order to obtain constant J_c throughout the film, the dislocation density should be in the range of 10^{10} to 10^{12} /cm². However, the role of dislocations, in contrast to the well-evidenced porosity and roughness reported in [4], was much less clear and/or evidenced at the time. Nevertheless, the authors report on a sandwich multilayer structure grown by PLD, where each YBCO layer is 0.4 μm thick, and each intermediate CeO₂ layer is 50 nm thick. They directly compare the χ_{\min} values obtained by RBS from a trilayer YBCO with two CeO₂ intermediate layers to that of a single layer YBCO, both deposited on LaAlO₃ substrates and of the same total thickness of 1.2 μm . The multilayer film showed significantly lower χ_{\min} , 19 vs. 55%, which is an indication of the degree of disorder in the film. They then proceed with utilizing this approach to metallic substrates with YSZ buffer deposited by IBAD, then capped by CeO₂. The resulting XRD spectra revealed that single layer YBCO film of 1.1 μm thickness contained no appreciable a -axis oriented grains, while a single layer YBCO of 3.2 μm thickness revealed a significant fraction of a -grains. This is in contrast to their previous reported study on films with thickness up to 6 μm , where a -grains have been reported as a non-significant factor to reducing J_c . The multilayer structure consisting of three 1.1 μm thick YBCO films separated by CeO₂ interlayer revealed no presence of a -axis oriented grains, despite the same total thickness of ~ 3.2 μm . However, the authors note that this approach has practical problems with current transfer between adjacent YBCO layers, due to the presence of the CeO₂ interface. The authors report developing an electrical contact pattern to test the top and bottom YBCO layers in the multilayer structure independently. The reported J_c values for both top and bottom YBCO layers are 1.4–1.5 MA/cm², compared to the lower value of 0.88 MA/cm² in a single 2.2 μm thick YBCO layer at 75.2 K, resulting in a 60% increase of critical current density using this method. In short,

while the method is not practical for production, the reported study has shed light on the thickness issue, first by reporting an increasing fraction of a -grains in thick films and second by showing that a multilayer architecture can indeed preserve J_c among the layers. However, the actual mechanism of texture/microstructure degradation at this time was still unknown.

A significant advancement has been achieved in buffer development for 2G-HTS and understanding the role and importance of buffer texture quality. In a 2003 study, Foltyn, et al. have reported progress in MgO buffer development that has led to bridging the gap between single crystal and metallic substrate-based YBCO films [6]. The authors report on IBAD-MgO buffer which has been found to result in excellent texture quality in very thin layers (~ 10 nm), compared to about 100 times higher required film thickness for YSZ to achieve the same texture. Furthermore, electro-polished Hastelloy C276 substrate has been used in this study, which has remained the method of choice for several manufacturers to date. In this study, the IBAD-MgO film has been capped by a 50 nm thick SrRuO₃ layer for lattice matching to YBCO. A texture quality of 2.2° Full-Width-at-Half-Maximum (FWHM) in-plane and 1.2° out of plane (roughly coinciding to YBCO 00 L direction) was reported, which started to approach the values obtained on single crystals. The authors report that YBCO films deposited on IBAD-MgO were practically indistinguishable from YBCO films deposited either on single crystal MgO or YSZ, which constituted large improvement compared to previously reported discrepancy between single crystal and metallic substrate YSZ data. The authors duly note that this behavior was to be expected, as multiple studies, starting from the fundamental work by Dimos, et al. have shown the strong effect of grain boundary misalignment on critical current density [7]. While the thickness dependence was not the main subject of this study, the authors provide detailed data on up to ~ 4 μm thick films, again revealing exactly the same trend as previously reported YBCO films on single crystal YSZ, as shown in Fig. 4.5.

4.3 Local and Average Critical Current Density

It is evident from the studies reviewed so far that J_c has been found to monotonically decrease with thickness. This raises the question of local critical current density, which is different from the total integrated current density that one can directly measure as a function of thickness. In yet another study aimed at raising the critical current by means of increase in thickness, Foltyn, et al. have analyzed in more detail the available data at the time of writing (2005) [8]. A very simple yet important aspect is that the measured current density vs thickness is an integral or average J_c over the thickness in question. The authors separate the two concepts through a simple yet very representative model of typical I_c or J_c measurements as

$$J_c(t) = 1/t \int_0^t j_c(z) dz$$

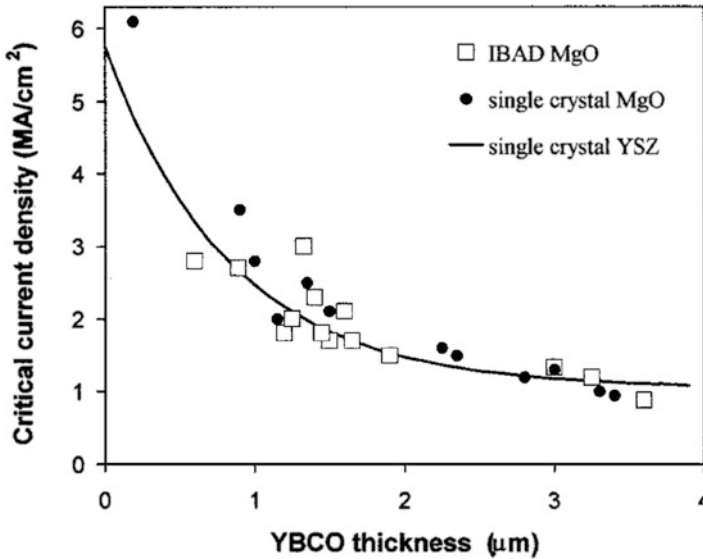


Fig. 4.5 Critical current density vs thickness for IBAD-MgO + SrRuO₃ on metallic substrates vs single crystal MgO and YSZ substrates, indicating a vanishing difference between single crystal and flexible substrates. However, the thickness dependence of critical current density has been still found to be a strongly decreasing function. Reproduced with permission from [6]

where $j_c(z)$ is the local or “true” current density at distance z from the buffer or substrate, while $J_c(t)$ is the total “integrated” current density for a film of thickness t , and as such represents an average J_c value for the thickness in question. The local J_c is also termed “incremental critical current density” in the original manuscript.

Equipped with two critical current density definitions—the practical measurable J_c and local or incremental j_c , one can analyze experimental data such as that presented in Fig. 4.5, for example, to obtain the local j_c from measured J_c . It should be noted that the same authors have used the relationship $J_c(t) = Ae^{-\alpha t} + B$ in the 1993 study [3] for the cumulative J_c fit vs thickness data. If the incremental J_c model is used, this exponential dependence translates to local current density of $j_c(t) = -A\alpha e^{-\alpha t}$. In contrast, the authors depart from this functional dependence in [8]. Instead, their new reasoning is as follows: there exist two characteristic j_c values, one in the limit of zero film thickness, which they refer to as the limiting value near the film-substrate interface, j_{ci} , and a lower bulk value, j_{cb} , which is the asymptotic local j_c limit at large film thickness. For simplicity, they assume a simple linear decrease from j_{ci} to j_{cb} with thickness. The thickness over which j_c drops from j_{ci} to j_{cb} is the only unknown parameter, which they refer to as z_r . From experimental data, an error minimization fit routine can be readily employed to extract the value for z_r . Using this approach, the authors provide data shown in Fig. 4.6.

Several features are particularly notable and outstanding in this result. First, the model fit to the data appears very well suited, as can be seen in Fig. 4.6a. However,

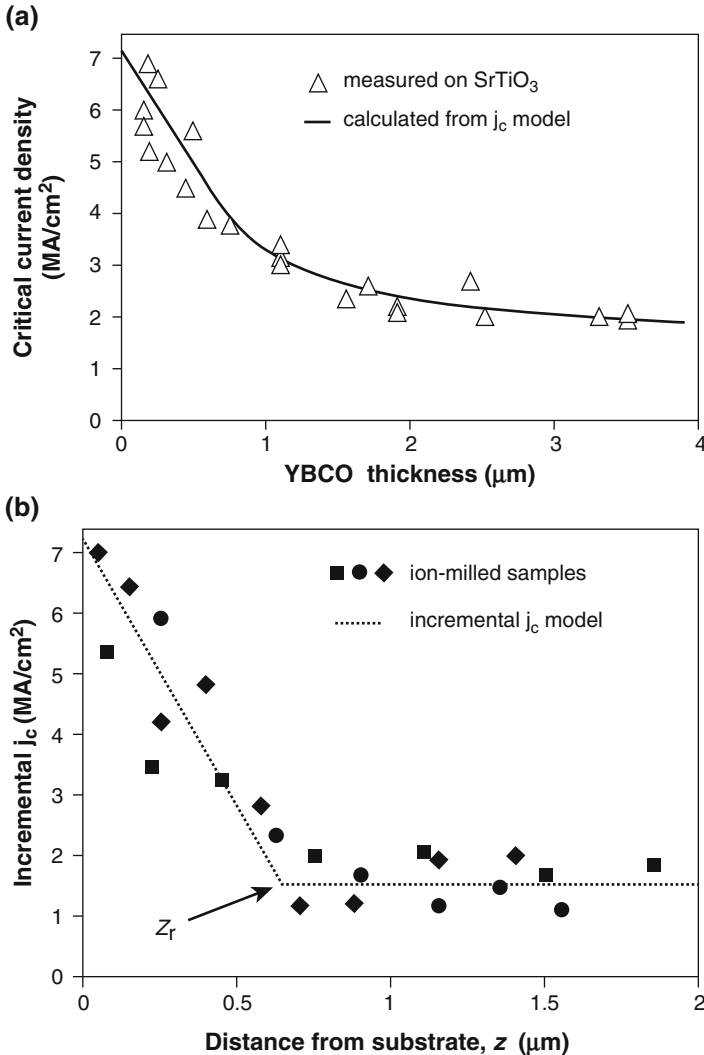


Fig. 4.6 (a) Average critical current density J_c , as a function of thickness for PLD deposited films on SrTiO₃ buffer. The solid line is the data fit to the linear incremental J_c model. (b) Incremental or local critical current density j_c obtained from incremental ion milling (solid symbols) and by replotting the fit from (a) on the incremental basis. Reproduced with permission from [8]

we have also witnessed a very good fit to the exponential model shown in Fig. 4.1. However, the results on incremental j_c , as shown in Fig. 4.6b are particularly interesting, given the fact that the incremental model fits independently very well to a separate experiment of incrementally ion-milling samples and determining J_c as a function of thickness. The observed j_{ci} limit reported in the article is 7.2

MA/cm², while the reported bulk limit is 1.4 MA/cm². The critical thickness, z_r , was determined from the fit to be 0.65 μm . It becomes obvious how much the coated conductors would benefit if the j_{ci} value of 7.2 MA/cm² could be maintained throughout the thickness, which has been a strong driving force behind this pursuit of understanding the J_c -thickness dependence mechanisms. Such a value, if attainable, would yield coated conductor tapes with ~ 860 , 1730, and 2600 A/12 mm width in 1, 2, and 3 μm thick films, respectively. All attempts to date have failed to reach such performance figures and the problem still appears elusive and not completely understood to date, despite the strong effort and progress achieved in raising the J_c in thick films.

The authors offer three alternative views on the reported thickness dependence of Fig. 4.6 [8]. The first is the microstructure point of view, and more specifically, linear defect density in form of dislocations that is argued to be higher at the film/buffer interface due to the inherent lattice mismatch and epitaxial growth. The authors put forward the idea that there is an inherent flux pinning structure in the bulk of the film that determines j_{cb} , while the buffer/film interface has a distinct pinning structure that results in enhancement of pinning near the interface, resulting in a bimodal j_c . The authors provide a cross-section a Transmission Electron Microscopy (TEM) micrograph of an example film in [8] that features a dark band near the buffer/film interface. The authors argue that this is exactly the feature that may contribute to such a scenario, which is in this case pertinent to SrTiO₃ buffer layer on MgO. The authors invoke arguments of localized formation of misfit dislocations near the buffer/film interface in epitaxial films. The second possible interpretation is in terms of flux vortices and their dynamics [9, 10]. The third scenario is related to the frequently observed deterioration of microstructure quality with an increase in film thickness. In this scenario, film quality and j_c is good up to j_{ci} , after which film texture quality deteriorates and contributes to decrease in j_c . The authors acknowledge that this effect can certainly contribute to a drop in j_c , where they point to their own earlier results on formation of porosity and reduced crystallinity in thicker samples. However, the authors mention that smoother substrates provided the ultimate solution to porosity. However, the question of other sources of texture degradation (a -grain formation, quantification of in-plane and out-of-plane texture) was not specifically addressed in this work. The authors also revisit the idea of YBCO/CeO₂ multilayers and provide evidence of one multilayer sample containing six 0.55 μm YBCO layers separated by 40 nm CeO₂ layers, resulting in a 3.5 μm film with J_c of 4.0 MA/cm². In contrast, a single layer YBCO film of 3.7 μm thickness resulted in J_c of only 1.3 MA/cm². In this work, authors provide several examples of ~ 3 μm thick multilayer films with I_c in the 1000–1400 A/cm range. However, many questions still remained open, ranging from the exact nature of the J_c enhancement in these films to the issue of the potential negative effect of the CeO₂ layers in current sharing between YBCO layers, as well as the practical feasibility of such a structure in large-scale production. Nevertheless, these results have provided very convincing and insightful results that provide strong evidence of the role of interfaces on J_c .

The incremental film thinning followed by J_c measurements has been reported by other groups as well. In 2003, in a study by Feldmann, et al. two samples, 2.0 and 2.9 μm in thickness, deposited on IBAD-YSZ substrates were investigated [11]. The YBCO film was grown by BaF_2 process. The two samples were reported to be deposited on substrates of similar yet slightly different texture, which was slightly better (5.9° vs. 6.9°) for the 2.9 μm film, based on (205) reflections in ϕ scans. Ar-ion milling at 500 eV and 45° inclination on samples cooled to 230 K was used. The authors have incrementally measured both I_c and resistivity at 300 K. The resulting J_c -thickness dependence is shown in Fig. 4.7, where, in addition to

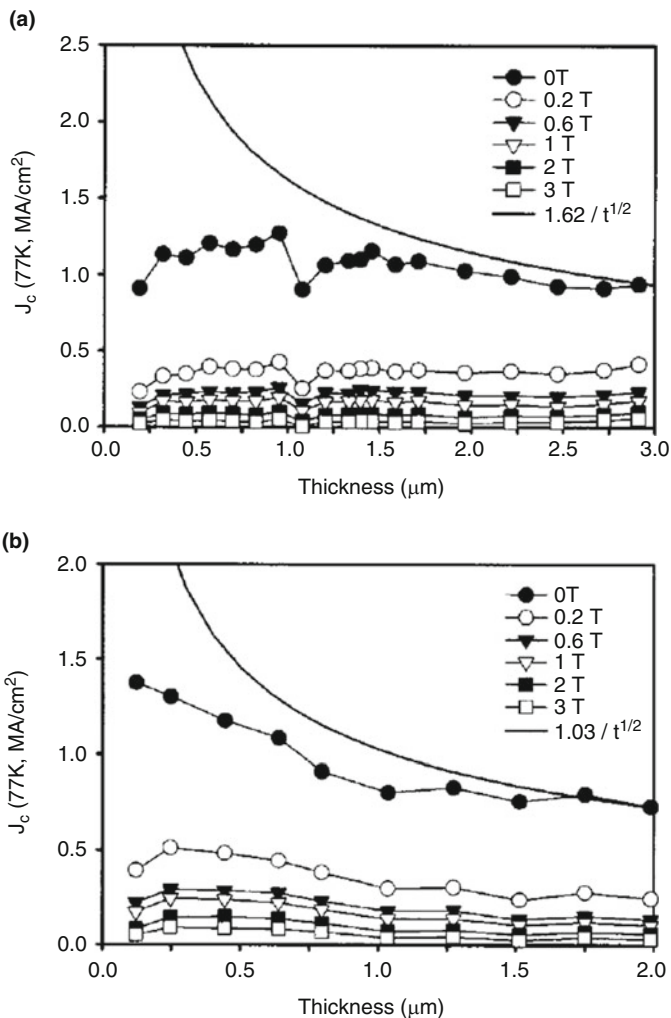


Fig. 4.7 J_c vs thickness of two incrementally ion-milled samples produced by BaF_2 process on IBAD-YSZ substrates. (a) 2.9 and (b) 2.0 μm initial thickness. Reproduced with permission from [11]

77 K, self-field data, in-field dependence of J_c on thickness is also provided for fields up to 3 T. The authors show a practically constant J_c of about 1 MA/cm² in the 2.9 μm film with slightly better texture, and a weakly increasing J_c in the 2.0 μm film, from ~0.73 MA/cm² at full thickness to nearly 1.5 MA/cm² near the buffer layer. The solid line is a $J_c \propto t^{-1/2}$ fit the authors provide based on what is referenced as unpublished data. The authors do, however, provide information that this fit was obtained from multiple films reacted from different precursor thickness, suggesting again a BaF₂ process. The main difference is that the fit is based on data from samples grown to different thickness, rather than incrementally milled. Based on this alone, the discrepancy may be possibly attributed to film degradation during ion milling, or, similarly to the observation of Foltyn [4], which the authors describe as possible time-dependent reaction that could have somehow degraded the bottom part of the ex situ YBCO. Another explanation is related to the ex situ BaF₂ process, where for thicker films both the required H₂O for conversion and the HF product must diffuse in and out of increasingly more material, so that thick films experience different growth conditions than their thin film counterparts. The authors also report that the 300 K resistivity measurement reveal a constant value of ~400 μΩ throughout the film, except for two data points closest to the substrate, where the resistivity increases up to ~700 μΩ, suggesting a reaction with the buffer layer. In summary, this study provides YBCO thickness dependence information from a very different growth process (BaF₂) compared to PLD. The common features are that the reported fit line obtained from samples grown to different thickness show qualitatively similar type of thickness dependence to that reported for PLD films: J_c decreases with film thickness. The reported $t^{-1/2}$ dependence diverges at zero thickness, unlike the dependences proposed by Foltyn [3, 8]; however, the exact functional form is secondary to the fact that the observed thickness- J_c trend is the same as that found in PLD. The flat J_c dependence reported for incrementally milled samples could potentially stem from the mentioned mechanism reported by the authors of increasing diffusion path with thickness, which is particular to the BaF₂ process. Another noteworthy feature is that the reported functional dependences of J_c on thickness are similar for both PLD and BaF₂, even though the J_c and the corresponding I_c values are very different. This is important from the viewpoint of the effect of self-field generated during transport I_c measurements and the corresponding attempts to view the thickness dependence issue in light of a self-limiting physical process related to the self-field.

In another study, PLD deposition on Rolling-Assisted Bi-axially Textured Substrates (RABiTS) was investigated [12]. Samples with thickness ranging from 1 to 6.4 μm were deposited on Ni-3 at% W/Y₂O₃/YSZ/CeO₂ substrates. The authors report significant improvement in texture due to use of Ni-3 at% W compared to Ni substrates, as well as due to the use of Y₂O₃ as the seed layer. The authors report no dead layer and only limited reaction between YBCO and CeO₂ layer. Good in-plane (YBCO (113)) texture quality of ~1° irrespective of thickness was reported, while the out-of-plane (YBCO(005)) texture was reported to gradually increase from 0.79 to 0.91° from 1 to 6.4 μm thickness. The *a*-axis grain fraction relative to *c*-axis orientation varied from 0 to 0.2. However, the reported values for J_c are ~1.18

MA/cm² for 1.0 μm and 0.65–0.81 MA/cm² for 4.3 μm films, which is again on the low side for a target of 1000 A/cm-width in reasonable thickness. Similar results were also reported in a related study [13].

A comprehensive review of the state of the art in 2G-HTS development was provided in a 2007 article [14]. Various aspects of development of the technology are covered in this document, including thickness dependence of J_c . The authors identify a target of 1000 A/cm for future development of 2G-HTS. The same figure has been established in a 2006 US DOE Office of Science Report [15]. In particular, the authors identify the issue as follows: “Simply expressed, the best-quality YBCO films available today exhibit a J_c that decreases with film thickness.” In the same report, the authors succinctly summarize the state of the art in this topic: “This qualitative behavior appears to be universal, for reasons that are poorly understood at best.” For this reason, the authors identify several thrust areas for a four-year period, including demonstration of 1000 A/cm over 1000 m at 77 K, self-field, and current proportional to HTS thickness. It can be seen that the problem remained largely elusive, as the 1000 A/cm over 1 km is still out of reach in 2018. Many other studies have been reported that confirm the prevailing thickness-dependent decrease in J_c [16–24]. Tremendous progress has been achieved towards commercialization and scale-up of 2G-HTS technology by developing several reel-to-reel substrate technologies (e.g., [25–28]), yet the issue of thickness dependence has still remained unsolved at the time.

4.4 The Effect of Dislocations on J_c -Thickness Dependence

In an alternative view on the subject, the thickness dependence of J_c has been analyzed predominantly in terms of the dislocation network structure that naturally forms in YBCO films on epitaxial substrates [29]. The authors note that the mechanism behind the J_c increase in the multilayer approach of Foltyn, et al., is still unclear. Certainly, if the exact physical mechanism behind this approach can be identified, it could potentially provide new approaches on harvesting the benefits of the mechanism without having to resort to the non-practical multilayer technique. The authors cite the work of Jia, et al. which shows that microstructure deterioration in YBCO films up to 4 μm thick deposited by PLD is perhaps more severe than previously reported, or alternatively, that the seemingly small increase in disorder has far more effect on J_c performance than one would intuitively expect [30]. The FWHM of the out-of-plane texture based on the 005 peak in this study increases from ~ 0.1 to close to 0.3° in this study as the film thickness is increased [30]. While both figures appear low, the J_c of YBCO material has been repeatedly proven to be very sensitive to texture quality. In addition, the authors report an increase in 45° in-plane rotated YBCO from near-zero to up to 10% as the thickness is increased towards 4 μm [30]. RBS channeling experiments also show a monotonic increase in χ_{min} from $<10\%$ up to $>60\%$ with thickness increase from submicron to 4 μm .

However, the authors reason that the deterioration of texture cannot alone account for the observed deterioration in J_c . The accuracy of this statement, however, is hard to clearly dismiss or accept, as the evidence provided is not exclusive to either claim. Nevertheless, the authors of the dislocation model [29] start from this assumption. Their study is experimentally based on High Resolution Transmission Electron Microscopy (HR-TEM) and Electron Back-Scattering Diffraction (EBSD) and is predominantly based on microstructure studies. Their analysis is centered around threading edge dislocations $a[001]$, which are aligned along the c -axis. Studies on the microstructure evolution at YBCO/substrate interface have commenced very early in the YBCO film development and evidence of threading dislocations and transition from island-like growth at the early stages to continuous film-like growth has been documented [31, 32]. The substrate/film lattice mismatch is the driving force behind their formation. Their later evolution with an increase in film thickness coincides with rotation of YBCO domains, effectively forming low angle grain boundaries. From energy balance between interface and elastic mismatch energy, the authors argue that this driving force creates a transition from the initial elastically strained state towards a relaxed state by such small rotations of neighboring domains. The resulting defect structure is one of a network of interface dislocations, consisting of edge and screw dislocations in the boundaries, as well as $a[001]$ threading edge dislocations in tilted low angle boundaries. Previous studies by TEM and EBSD showed evidence of significant change in the structure with thickness. At low thickness, a very high dislocation density is formed, as high as 10^{12} cm^{-2} , which can be termed “dislocation forest.” This same structure has also been reported in [8] as a dark band in TEM micrographs in the first 20 nm of a YBCO film deposited on YSZ. With an increase in thickness, the authors argue that the dislocations rearrange to form a more ordered structure, consisting of low angle boundaries or dislocation walls. The proposed mechanism is thermally activated polygonization by dislocation slide in (001) planes, which is facilitated with temperature. The authors provide TEM evidence of different appearance of low angle grain boundaries for samples grown at different temperatures, indicating much sharper in-plane orientation changes in a film grown at 780°C compared to a sample grown at 750°C . The authors report that this initially high and randomly distributed dislocation density is typically contained in ~ 100 nm thickness, consistent with reported maximum J_c in PLD films at ~ 100 – 200 nm thickness. After this, a remarkable change in microstructure occurs, where the dislocations rearrange to form near dislocation free domains separated by low angle grain boundaries formed by the regrouped dislocations. For more details, the reader is encouraged to access the original article. For the purpose of this book chapter, it is important to point out this line of thought of dislocations acting as a major source of pinning, especially in the view of the pioneering results by Foltyn, et al. on multilayers, which proved that J_c can be maintained in a stack of thin multilayers. In the simplest interpretation, the initially random dislocation forest near the interface can be prevented from ordering into domain walls if a new mismatched layer is inserted at a point where dislocations start forming domain walls. However, many questions still remain even in light of this approach. For example, the role of the degree of misorientation of the

underlying buffer layer, or the fact that in well-matched substrates such as LaMnO_3 , the dislocation forest at the interface is not typically observed or is of low density.

4.5 Misoriented Grain Formation

A frequently reported issue related to growth of YBCO films is the formation of *a*-axis oriented YBCO crystals during film growth, typically increasing in density and size with thickness. While some details on the mechanism of formation and the accompanying other secondary phases may vary, the most predominant feature in thick MOCVD films appears to be the growth of these *a*-axis oriented grains, as will be discussed, and similar features are frequently observed in PLD-grown films. On the other hand, the MOD process and its BaF_2 variants have their own characteristic microstructure imperfections that limit the J_c in thick films. In this section, we outline some of the important microstructure features of MOCVD and PLD-grown films.

Even if the dense dislocation network near substrate/film interface is responsible for local increase in J_c in ~ 100 nm thick films to up to 7 MA/cm^2 , the issue of *a*-grain formation has been shown to be very important, as films grown to thickness above $\sim 1 \mu\text{m}$ can result in predominantly *a*-grain oriented films at sufficiently high thickness, thereby effectively producing a dead layer. For example, the early studies have shown that an asymptotic J_c in the range of $1\text{--}2 \text{ MA/cm}^2$ can be obtained. For the case of asymptotic J_c of $\sim 1 \text{ MA/cm}^2$, Fig. 4.2 shows that I_c approaching 800 A could be produced, albeit in very thick films. In the example [8], an asymptotic cumulative J_c closer to 2 MA/cm^2 is reported. This implies I_c in the range of $800\text{--}1000 \text{ A}$ for $4\text{--}5 \mu\text{m}$ thick films, respectively, which approaches the 1000 A/cm -width target. However, if *a*-axis oriented grains are allowed to proliferate with thickness, the benefits of growing such thick films would be completely eliminated as J_c would drop to near-zero due to *a*-axis grain formation at higher thickness. While in these reported studies *a*-axis grain formation appears not to be of major concern, *a*-grain formation at higher thickness is known to be a major issue that prevents growth of high quality thick films. The typical microstructure well known to occur in MOCVD deposited films can be seen in the 1995 study by Dubordieu, et al. consisting of *c*-axis oriented matrix interspersed with *a*-grains [33], and many other examples have been since reported [12, 22, 24, 34–39]. Attempts to combat this problem have also been reported, e.g., [40, 41].

A very illustrative and representative example of the deterioration in microstructure is provided in [42]. In this 2009 study, MOCVD was used in an attempt to produce thick YBCO films with good texture and high J_c in a reel-to-reel fashion on IBAD-MgO flexible substrates capped with LaMnO_3 (LMO) substrate film. The authors resort to a multi-pass technique—YBCO is deposited in four passes of $0.7 \mu\text{m}$ each. The authors emphasize that multi-pass approach is critical for minimizing secondary phase formation. The resulting microstructure is shown in Fig. 4.8, showing microstructure evolution of YBCO films deposited using MOCVD

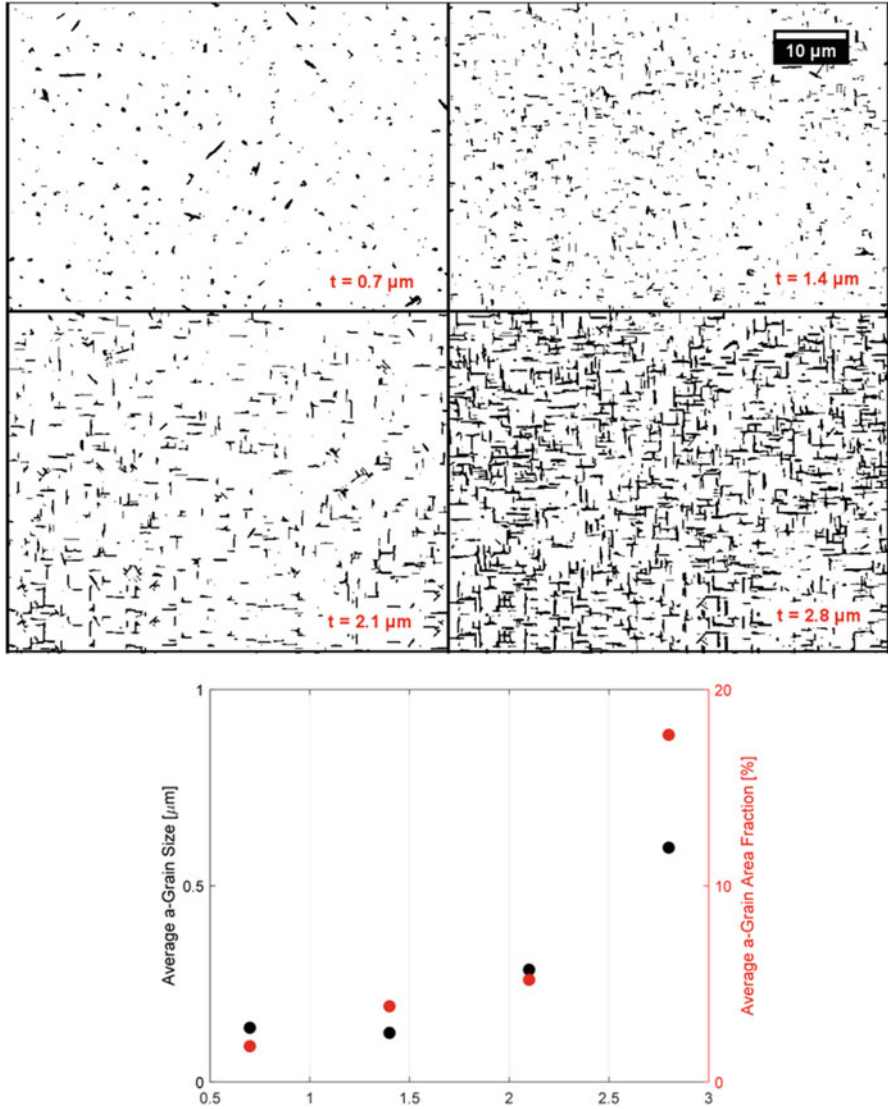


Fig. 4.8 Microstructure evolution of YBCO films deposited using MOCVD in four sequential passes, each having thickness of $0.7 \mu\text{m}$. The micrographs (a–d) correspond to film thickness of 0.7 , 1.4 , 2.1 , and $2.8 \mu\text{m}$, respectively. The dot-like features in (a) are predominantly CuO , while the progressively increasing density of elongated features in (a–d) correspond to a -axis oriented grains. The binary images and calculation of grain size and area fraction based on data reported in [42]

in four sequential passes, each having thickness of $0.7 \mu\text{m}$. The binary images were calculated from the corresponding micrographs and correspond to film thicknesses of 0.7 , 1.4 , 2.1 , and $2.8 \mu\text{m}$, respectively. The progressively increasing density of elongated features corresponds to a -axis oriented grains. It should be noted that the sides of the micrographs are aligned to the $\langle 100 \rangle$ directions in the film.

The authors use the term “Oriented Composite Defects” or OCD for all features other than CuO, in an attempt to emphasize that in cross-sectional view, these observable a -axis oriented grains on the film surface in Fig. 4.8 are typically accompanied by or “sandwiched” between other secondary phases. The authors identify those to be CuO (between closely spaced a -grains), RE_2O_3 (RE = rare-earth, in this case Y, Sm) which is coating the a -grains on the “outside,” as well as a composite particle cap, which the authors believe to be a $\text{RECuO}_2/\text{CuO}$ composite. In short, growth of a -axis grains can be accompanied by other secondary phases, but the main features (the elongated bright precipitates aligned along x and y axes) in Fig. 4.8 are practically a -grains. The problem of deterioration of microstructure in MOCVD is very well depicted in this series. It should be noted that this approach utilized a multi-pass technique, which minimized the proliferation of a -grains with thickness. In single-pass deposition, the surface is typically almost completely covered with a -grains at $2.8 \mu\text{m}$. Such features inevitably lead to a non-functional or dead layer at higher thickness. The multi-pass technique utilized here is certainly very illustrative in the sense that a decent degree of preferred crystallinity (c -axis growth) can be preserved up to nearly $3 \mu\text{m}$. However, for practical or scale-up purposes, such an approach would be prohibitively complex to implement. The films deposited in this study resulted in highest I_c of $720 \text{ A}/12 \text{ mm}$ or $600 \text{ A}/\text{cm}$ -width in a four layer sample with thickness of $2.8 \mu\text{m}$. The corresponding current density J_c was $2.1 \text{ MA}/\text{cm}^2$. While still far from the thin film limit of $\sim 7 \text{ MA}/\text{cm}^2$, the achieved I_c values and the reported microstructure deterioration have clearly pointed out that microstructure deterioration with thickness is indeed one of the major problems to be overcome. In parallel to this issue is the chase to reach the thin film $7 \text{ MA}/\text{cm}^2$ limit achieved in very thin films. However, if texture degradation with thickness is present as an additional problem, then any attempt to preserve the high J_c near the substrate would be marred by this effect, unless a radically different growth technique is utilized. As such, this issue appears to be of primary importance.

The authors also compare the microstructural features of PLD-grown YBCO to those found in MOCVD-grown films. They note that vapor deposition processes of PLD and MOCVD are very closely related, which as a consequence results in films with very similar properties and microstructures. This is in contrast with the MOD process where different microstructural features can arise due to its sequential deposition and crystallization nature. The authors note that the falloff in self-field J_c with thickness in optimized films is very similar between PLD and MOCVD-grown films [4, 43]. They note that degradation due to secondary phase formation still occurs in optimized films, but a minimized (optimized) rate. The authors conclude that there is still room for further control improvements to minimize the sources of degradation. This statement is put forward in 2009 and will be proven true based

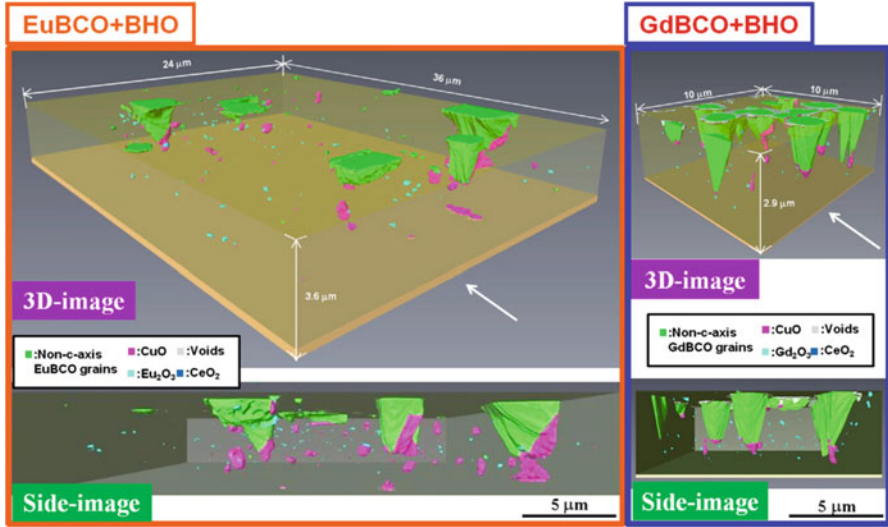


Fig. 4.9 Three-dimensional maps of secondary phase development in EuBCO and GdBCO films grown by PLD. Misoriented REBCO grains are shown in green. Copper oxide is found at the root of every misoriented REBCO grains. Misoriented grains grow in size with thickness, resulting in progressive deterioration of microstructure with thickness. Reproduced with permission from [44]

on recent advancement in 2G-HTS that show significant improvement in texture control and thus J_c vs thickness dependence, which will be discussed.

The issue of formation and growth of a -axis oriented grains has also been analyzed by sequential ion beam milling and SEM imaging to form three-dimensional maps of different phases formed in films grown by PLD [44]. This study provides an excellent summary of this problem illustrated in the 3D shown in Fig. 4.9. The maps are obtained on EuBCO and GdBCO films, revealing CuO precipitates at the root of each misoriented REBCO grain. Furthermore, the maps provide a clear illustration of the increase in size of misoriented grains with thickness, where the grains form a cone-like structure that occupies progressively more volume as the film thickness is increased. Identical behavior is found in MOCVD-grown films, resulting in rapid deterioration of J_c with an increase in film thickness.

For an excellent overview on some microstructure issues found in films processed by the MOD route at the time of writing (2008), the reader is directed to ref. [45]. While this process has distinct microstructure features that evolve during film growth, the common theme is the deterioration of J_c in thick films. One approach on a variant of the BaF₂ process in obtaining thick films at the time can be found in [46, 47]. The multi-coat approach has also been used in MOD to grow thick films [48–50]. Weak thickness dependence of J_c has also been reported by Kim, et al [51]., reporting a drop from ~ 4 to ~ 3 MA/cm² from near substrate to the thickness of ~ 1.1 μm in MOD films with high level of porosity ($\sim 30\%$), which was believed to contribute to strong three-dimensional pinning that results in the observed weak dependence of J_c on thickness.

Based on the published literature, it appears that in the late 2000s, as many high quality flexible substrate technologies have matured and became available (most notably IBAD and RABiTS), and as the various deposition techniques (most notably PLD, MOCVD, and MOD) have progressed, the focus has been shifted towards solving the microstructure degradation issues which became apparent in all of the YBCO deposition techniques in practice, regardless of the substrate used.

4.6 The Effect of Self-Field

The seemingly universal thickness dependence of J_c , regardless of the substrate or deposition technique used, raises the natural question—is there a natural physical limitation beyond microstructure that imposes the observed thickness dependence? In this light, it is important to review attempts to analyze the problem from this viewpoint. One such approach is based on the idea of the role of self-field generated as a function of current, and the idea that this self-field has an effect on J_c . Intuitively, without any in-depth analysis, the idea is plausible—thicker films potentially carry more current, thereby generating higher self-field. Accordingly, the J_c measured in zero external applied field is referred to as the self-field J_c value.

This approach has been studied by Rostila, et al. [52]. The authors state the problem in a succinct manner—to increase the critical current, either the J_c should be improved or the films made thicker. The observed result of the second approach is that J_c decreases with thickness, and the authors note that many attempts have been made to correlate this behavior to pinning or crystallographic imperfections. The authors point out that “it is often forgotten” that the self-field generated with higher current unavoidably reduces the J_c when the thickness and therefore total current is increased.

The authors state that the J_c variation with thickness cannot be explained exclusively on the basis of material quality, as the generated self-field effect reduces the critical current density with an increase in total current. This statement is very obvious and one cannot find flaws in this argument. It remains, however, to evaluate to what degree this effect is reflected on the measured J_c and whether it is marginal or not compared to experimentally observed deterioration in J_c with thickness, which this study has addressed [52]. The authors use a numerical scheme to obtain a current density distribution in the film that satisfies

$$J = J_c (B_{ext} + B_{self}(J))$$

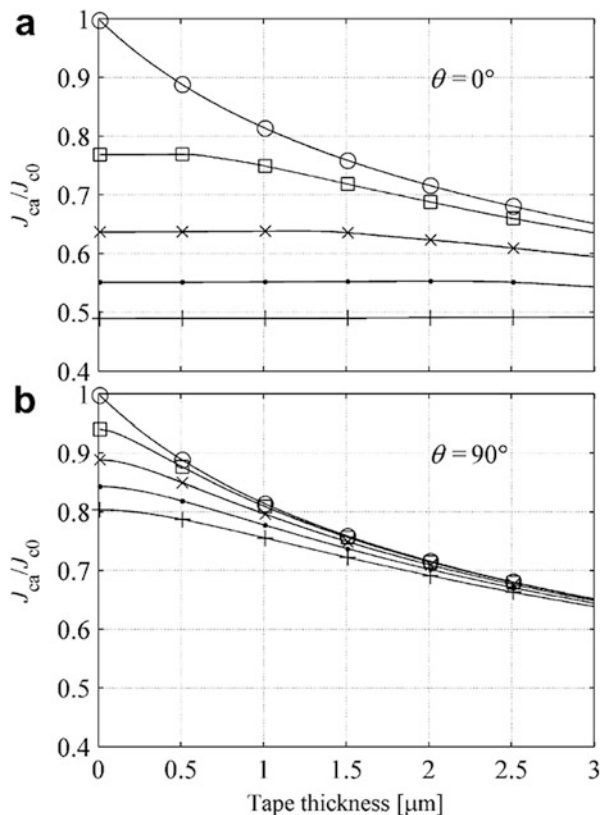
The authors use the $J_c(B)$ dependence according to the Kim model [53], modified to take into account material anisotropy [10]:

$$J_c(B) = J_{c0} \left(1 + \frac{\epsilon B}{B_0} \right)^{-\alpha}$$

$$\epsilon(\theta) = \sqrt{\cos^2(\theta_{loc}) + \gamma^{-2} \sin^2(\theta_{loc})}$$

where θ_{loc} is the local field angle between $B_{ext} + B_{self}$ and the c -axis. The problem then involves solving the Biot-Savart law for B_{self} consistent with the mentioned constraints. The problem is solved on a rectangular geometry using typical values for the listed parameters taken from literature, $J_{c0} = 3 \text{ MA/cm}^2$, $B_0 = 20 \text{ mT}$, $\alpha = 0.65$, and $\gamma = 5$. For all practical sample widths, J_c is essentially width-independent and depends only on thickness. The average magnetic field components B_x and B_y , along and perpendicular to tape width, respectively, were determined as a function of film thickness and width. The average field saturates to a constant value at sample widths $>1 \text{ mm}$ and increases, for example, for 1 to 3 μm thick films, from ~ 7 to $\sim 13 \text{ mT}$. The decrease in self-field J_c , as well as of J_c under small applied fields (10–40 mT), were calculated next. The results are shown in Fig. 4.10. Considering only the zero applied field case (circle symbols), the results suggest a non-negligible decrease in J_c with thickness. For example, at 1, 2, and 3 μm thickness, self-field J_c drops to ~ 80 , ~ 70 , and $\sim 65\%$ of the zero thickness limiting value. Comparing these values to the experimentally determined J_c shown

Fig. 4.10 J_c dependence on film thickness for constant intrinsic $J_{c0} = 3 \text{ MA/cm}^2$. The five datasets represent increasing applied magnetic field from 0 to 40 mT in 10 mT increments, where the plots with lower J_c correspond to increasing magnetic field. The plots shown in panels (a) and (b) correspond to applied field directions perpendicular ($\theta = 0^\circ$) and parallel to film ($\theta = 90^\circ$), respectively. Reproduced with permission from [52]



in Fig. 4.5, the values at 1 and 2 μm drop to about 44% and 26%, respectively, while the data from Fig. 4.6 exhibit the corresponding drop to 45% and 33%, respectively. Based on this comparison alone, one can conclude that the experimentally observed drop in J_c is stronger than the effect of self-field. This conclusion should be taken with caution, as the parameters listed above and used for the calculation may not be representative of the samples measured in the experimental studies to which the comparisons are made. However, the effect of self-field, according to this study, is by no means negligible. Taking a representative value of J_c drop at 1 and 2 μm as 80 and 70% for the calculated self-field effect and ~ 45 and 30% for the measured self-field decrease, one can conclude that approximately one-half of the experimentally observed decrease in J_c could potentially be accounted for by the calculated self-field J_c decrease, according to this study. Similar ideas on the effect of self-field on the effective J_c were considered in a number of publications [54–58].

4.7 Recent Progress

The progress within approximately last 8 years is summarized here. In summary, very high J_c approaching $\sim 7 \text{ MA/cm}^2$ has been demonstrated in YBCO on very thin films deposited on single crystal substrates, yet the task of achieving high enough J_c in thicker films to reach the 1000 A/cm-width target has remained elusive. However, great progress in understanding the origin of the limitation in J_c has been achieved by ~ 2010 , which has paved the way to further progress in pushing the A/cm-width envelope up. It should be noted that many other efforts have been ongoing simultaneously, greatly contributing not only to various aspects of 2G-HTS but to commercialization and production of long lengths of flexible tape. The burning issues were to obtain performance that is close to that of single crystals, even in thin films, on which significant effort was spent, resulting in impressive flexible substrate technologies unique to 2G-HTS. Issues such as flexibility, mechanical strength, prevention of poisoning of YBCO by diffusion of foreign elements from metallic substrates, tape smoothness, scalability and throughput, as well as many other aspects had to be perfected to produce the backbone of 2G-HTS—the flexible substrate. On top of that, the main effort was in improving the texture quality and lattice match of the cap layer for epitaxial growth of YBCO. The results of this effort are several substrate tape technologies scalable to km lengths with impressive levels of texture quality approaching that of single crystals. In parallel, film deposition techniques had to be developed to suit the peculiarities of YBCO material and be scalable, reproducible, and fast enough for commercial utilization. These issues were critical to 2G-HTS, which, perhaps, has demoted the issue of degradation of J_c with thickness to somewhat secondary priority; the fundamental issues with 2G-HTS on flexible tapes had to be solved first in order to even consider it a viable technology.

With 2G-HTS reaching a fair level of maturity by ~ 2010 , road was open to further progress. High quality flexible substrates became readily available; reel-to-

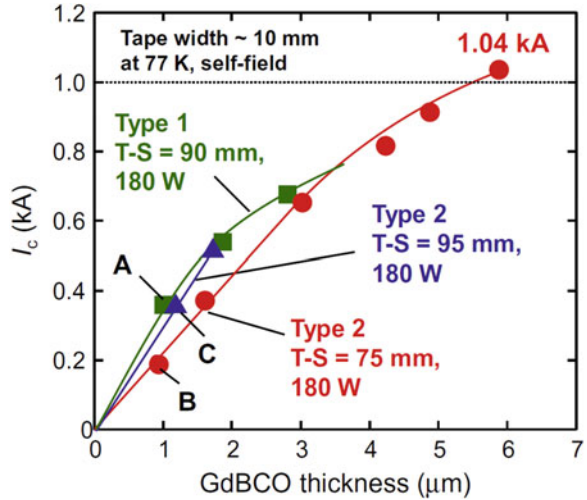
reel deposition techniques have been established and focus could be shifted to other issues, including the J_c vs thickness dependence. In this regard, we are witnessing remarkable progress in this area in recent years. Only the most recent results are highlighted here, as a summary of the current state-of-the-art in production as well as understanding of the I_c -thickness phenomenon.

In a summary of the findings established up to ~ 2010 , several key issues have been identified as potential blocks to achieving high I_c /cm-width. First, transition from single crystal to flexible substrates had to be matched with in-plane texture quality approaching that of single crystals in order to prevent or minimize occurrence of large inter-grain misorientation angles. In parallel, tapes had to be very smooth, again approaching single crystals. Inter-diffusion problems associated with metal substrates also had to be addressed. These issues have been largely solved by the time. Second, texture degradation with thickness has been meanwhile found to play a role much larger than perhaps the early studies have indicated, as illustrated in Fig. 4.8. It will soon become evident that this issue is the most likely obstacle to minimizing the reduction in J_c with thickness, as recent impressive reported results appear to confirm. Third, the idea of the effect of self-field on decrease in J_c with thickness has been put forward, which potentially could be addressed. If not, then this effect would put an upper envelope on the achievable J_c -thickness dependence. Finally, the thin film limit figure of 7 MA/cm² still appears out of reach, but this benchmark value, together with the early multilayer demonstration, gives hope that this performance may be captured in thick films in the future.

In 2010, a study on thick $\text{SmBa}_2\text{Cu}_3\text{O}_{7-x}$ (SmBCO) films deposited on LMO/IBAD-MgO substrates by reactive co-evaporation demonstrated 637 A/cm-w in a 3 μm thick film, corresponding to J_c of 2.12 MA/cm² [59]. In the same year, Igarashi, et al. have reported a study on high speed deposition of REBCO films using a hot-wall PLD system [60]. They report several achievements including a 170 m long tape with I_c over 600 A. However, perhaps the most notable feature related to this chapter is the reported attainment of I_c of about 1000 A/cm-w at a thickness of $\sim 6 \mu\text{m}$ in GdBCO. The authors attribute this result to the hot-wall reactor: they argue that the hot-wall heating system provides constant temperature of the film during growth, unlike contact heating techniques (usually—susceptor type heating). However, while the hot-wall reactor minimized a -axis grain formation up to $\sim 6 \mu\text{m}$ film thickness, resulting in 1.04 kA/cm-w, the authors note that at lower thickness, 1–2 μm , the contact heating resulted in higher J_c than the hot-wall reactor, even though at higher thickness the contact heating reached a saturation point (or “dead layer”). This trend is shown in Fig. 4.11. Other details, such as the effect of target-to-substrate distance, particular to PLD, are also presented. The common feature to both of these studies is the attribution of high I_c to the absence of a -axis grains. This will later be found in other studies as well, as will be shown.

In 2011, an interesting approach to increasing total tape I_c was reported—the idea of producing a double-sided 2G-HTS conductor. The authors report a study on regular single-sided tape but refer to the idea of growing a double-sided conductor. This idea has been in existence as a concept; however, it is explicitly referred to in this article. In view of recent progress and exceeding the

Fig. 4.11 Thickness dependence of GdBCO films grown in: A – hot-wall PLD reactor and B, C – PLD with contact heating of tape. T-S denotes different target-to-source distances used. Tapes processed by hot-wall reactor achieve over 1kA/cm-w at high thickness, unlike contact heating samples which experience saturation of I_c with thickness, despite higher I_c than hot-wall reactor at lower thickness. Reproduced with permission from [60]



1000A/cm-w, this approach could potentially double the current carrying capability of 2G-HTS, resulting in a prospective figure of over 2000 A/cm-w [35]. While the concept appears impractical for susceptor-based tape heating where one side of the tape is in contact with the susceptor, new approaches to heating during film growth open significant opportunities to pursue this route of further increasing engineering current density. In particular, the Advanced MOCVD (A-MOCVD) system developed by the author of this chapter and his coworkers utilizes direct ohmic tape heating of tape suspended in free space, without being in contact with any solid surface [61]. This feature is coupled with laminar cross-flow of MOCVD precursors. While A-MOCVD utilizes single-side deposition, it can be seen that the arrangement used can be readily extended to include double-sided deposition. One practical difficulty is that the carrier or buffer tape deposition also has to be developed to incorporate two-sided buffer, which requires time and effort, however, there are no physical obstacles to achieving this tape architecture. The hot-wall reactor utilized for PLD deposition could also be potentially employed for double-sided deposition [60, 62–66]. In addition, some processes involved in 2G-HTS like copper electroplating are inherently two-sided. Another issue to be addressed is the development of a feasibility study on utilization of such a tape for applications that would explore application aspects such as current sharing, thermal stability, mechanical integrity, and other aspects of this architecture.

In 2012, Durrschnabel, et al. report on a coated conductor exceeding 1000 A/cm [67]. The authors report use of $\text{DyBa}_2\text{Cu}_3\text{O}_{7.8}$ (DyBCO) on flexible Hastelloy substrates with MgO buffer layer grown by ISD (Inclined Substrate Deposition). The results are shown in Fig. 4.12. The highest achieved J_c was for the sample marked with the red star symbol, resulting in 1.7 MA/cm^2 for a $5.9 \mu\text{m}$ thick film. While the J_c value is below 2 MA/cm^2 , the result demonstrated the feasibility of growing films with critical current above 1000 A/cm. For this experiment,

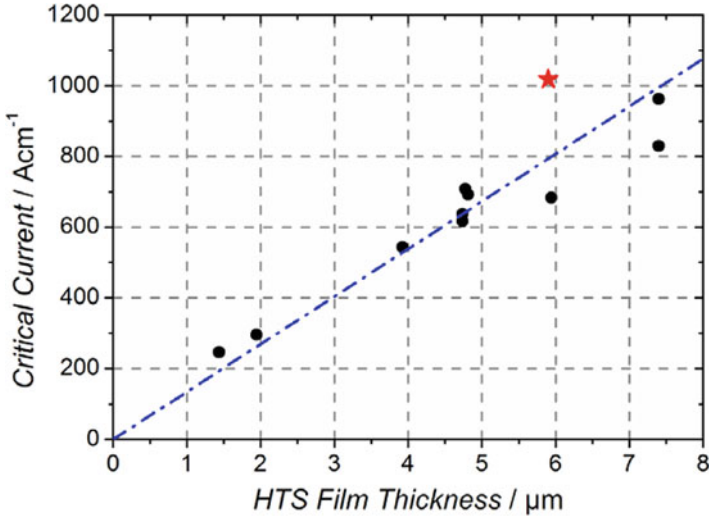


Fig. 4.12 Critical current, in A/cm, of DyBaCuO films grown on MgO buffer layers grown by ISD. Reproduced with permission from [67]

the authors report that in order to achieve this result, the tape was not moved, and the 400 nm of the DyBCO seed layer was grown on tilted substrate at 36° . This was followed by additional growth of DyBCO in a separate chamber for the total of $5.9 \mu\text{m}$ thickness. While potentially impractical, the approach has again demonstrated that this I_c level is achievable.

The authors report that this achievement is due to lack of formation of a -grains. The reason for the successful growth of a -axis free films is attributed to the ISD substrate. The authors reason that despite large lattice misfit between MgO and DyBCO, the 00 L direction of DyBCO was found to be always parallel to MgO 00 L direction, which they attribute to the inclined substrate that results in a non-zero component of the growth direction parallel to the ab -plane of DyBCO. The authors claim that this factor makes the c -axis growth very stable, resulting in suppression of a -axis grain formation. However, other than this verbal argument, the authors do not quantify or provide more specific details on the exact mechanism of suppression of a -axis grain formation.

In 2014, Kim, et al. have reported on very high performance HTS tapes utilizing $\text{SmBa}_2\text{Cu}_3\text{O}_{7.8}$ film of $5 \mu\text{m}$ thickness deposited as a single layer [68]. They report over 1000 A/cm-width for a 22 m long tape and over 1500 A/cm-w for a shorter 12 cm long tape. The authors report that no exponential deterioration of J_c with thickness was observed, exemplified by the figure of 3 MA/cm^2 that was achieved both in 1 and $5 \mu\text{m}$ tapes processed utilizing their method—specifically 3.08 MA/cm^2 for the $5 \mu\text{m}$ thick tape. The results are shown in Fig. 4.13. For the 22 m long tape, Hall probe measurements indicate I_c of over 1000 A/cm-w for most part of the tape. Some periodic fluctuations are evident in the figure, which

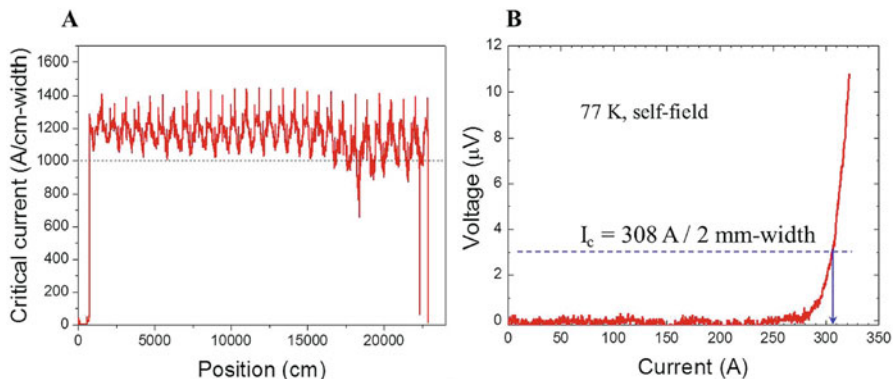


Fig. 4.13 (a) Critical current of a 22 m long SmBCO tape with film thickness of $\sim 5 \mu\text{m}$, measured using Hall sensors. (b) Transport I - V curve of a 12 cm long sample measured over a ~ 2 mm wide bridge, revealing I_c of 1540 A/cm-w and J_c of $\sim 3 \text{ MA/cm}^2$. Reproduced with permission from [68]

the authors ascribe to the deposition temperature variation along the circumference of the drum during the deposition. The short sample was measured by transport current on a 2 mm wide patterned bridge, resulting in I_c of 1540 A/cm-w and the corresponding J_c of $\sim 3 \text{ MA/cm}^2$. The authors utilize a batch-type reactive co-evaporation system utilizing a drum in a dual chamber. The drum is rotated, which causes the tape wound on it to alternate between two chambers, where one chamber is used for high vacuum deposition while diffusion/crystallization occurs in the other chamber. The authors report that tapes with high degree of uniformity can be deposited using this system which can be scaled up to kilometer long tape deposition. It is encouraging that thick films with high J_c are being demonstrated with more than one deposition technique, which gives a very optimistic perspective on the prediction that high performance tapes will become commercially available in long lengths in the near future. The authors state that the lack of any degradation in structural properties with thickness plays a critical role in maintaining high J_c in thick films. This statement is consistent with the findings established by other groups on films grown by different processes.

Similar results were also reported by the same group in 2015, but with an emphasis on non-destructive characterization of films in [69]. This work reinstates the need for microstructure control as the room temperature thermoelectric microscopy and low-temperature bolometric microscopy both revealed a spatial distribution of defects even in these films that were processed by the same drum in dual chamber process that has produced very high I_c in thick samples [68]. The authors do state that a -axis wedges (grains) in top part of the film and other misaligned grains are still a concern for applying the method for scale-up.

In 2015, Liu, et al. have reported on development of a fabrication line utilizing PLD deposition on a simplified tape architecture consisting of sputtered CeO_2 buffer layer directly on IBAD-MgO [70]. The authors report on achieving J_c of

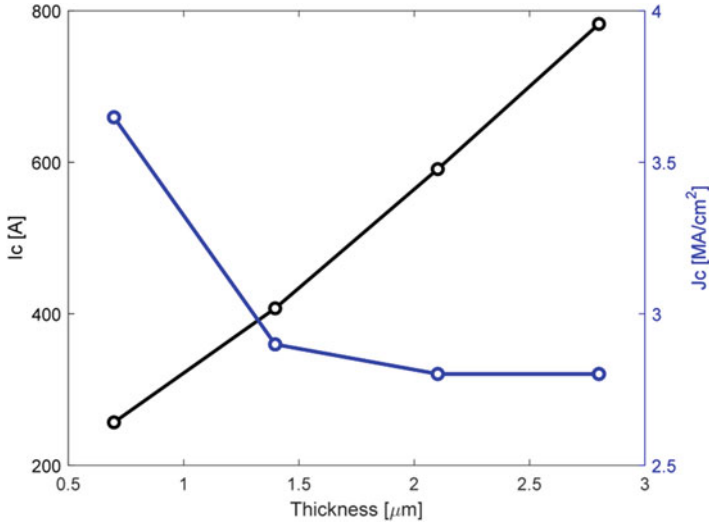


Fig. 4.14 I_c and J_c as a function of film thickness reported in [70], demonstrating reduced thickness dependence of J_c . The reported critical current is per cm-width. Replotted using data from [70]

over $3.0 \text{ MA}/\text{cm}^2$ in $1 \mu\text{m}$ thick REBCO films and over $2.5 \text{ MA}/\text{cm}^2$ in films with $2 \mu\text{m}$ thickness, as shown in Fig. 4.14. This result has been achieved on a scaled-up process capable of achieving up to 100 m/h deposition. They report on routine fabrication of 100 m long tapes with over $500 \text{ A}/\text{cm}^2$. Clearly, the J_c vs thickness values reported here have reached and/or exceeded the early benchmark values reported on single crystals discussed before, e.g., the performance shown in Figs. 4.1, 4.3, and 4.5.

The authors also report on the microstructure of 0.7 and $2.8 \mu\text{m}$ thick films [70]. The microstructure is in stark contrast with the deterioration in microstructure observed previously in both PLD and MOCVD, and illustrated in Fig. 4.8. This absence of microstructure degradation with thickness resulted in the reported thickness dependence of I_c and J_c shown in Fig. 4.14. It can be seen that an almost-flat, thickness-independent J_c of about $3 \text{ MA}/\text{cm}^2$ has been achieved up to $2.8 \mu\text{m}$ thickness, resulting in $780 \text{ A}/\text{cm}$ of critical current. A slight decrease in J_c is still present, with J_c decreasing from 3.64 to $2.78 \text{ MA}/\text{cm}^2$ from 0.7 to $2.8 \mu\text{m}$, but this decrease is marginal compared to the previously reported exponential type of dependence. The authors attribute this weakening of the thickness dependence to the decrease in density of a -axis oriented grains.

In the same year, the same group has reported more details on their fabrication of thick REBCO coated conductors [71]. In this study, they compare the thickness dependence of stoichiometric YBCO films to that of Y/Gd-doped films. For stoichiometric films, J_c was found to decrease near-linearly from $5 \text{ MA}/\text{cm}^2$ at $0.2 \mu\text{m}$ to $2.6 \text{ MA}/\text{cm}^2$ at $1.4 \mu\text{m}$ thickness. The authors provide the corresponding

values of the relative ratio of a -axis oriented grains and RMS roughness of these films. They report that the relative amount of a -axis oriented grains increased with thickness, first at a low rate up to ~ 1.2 μm thickness, after which the relative fraction of a -axis grains drastically increased from less than 0.1 in 1.2 μm film to over 0.8 in 2.0 μm thick films. The RMS roughness also increased from ~ 2 nm to ~ 5 nm as film thickness increased from 0.2 to 2.0 μm .

The authors then report results on films containing 1 mol% excess Y_2O_3 in a matrix of nominal composition of $\text{Y}_{0.5}\text{Gd}_{0.5}\text{Ba}_2\text{Cu}_3\text{O}_{7-\delta}$. The authors indicate that these films had preferential c -axis orientation and excellent crystallinity. The claim is that Gd substitution and Y_2O_3 doping can inhibit the growth of the a -axis grains. The resulting performance is that shown in Fig. 4.14.

Impressive recent results have been reported by Fujita, et al. in 2018 [65]. The recurring theme is the use of hot-wall PLD reactor which the group has pursued as a method for production of high quality films and has been under continuous development [62–64, 66]. Again, the authors emphasize the temperature control feature of hot-wall PLD – aptly described as “furnace-like stable substrate heating” in this work. They ascribe the homogeneous crystalline growth, implying absence of a -axis grain growth, to this feature. In this manuscript, they report on results achieved under two different deposition conditions, A – high J_c condition, with growth rate of 5–7 nm/s, and B – high growth rate condition, with growth rate of 20–30 nm/s. The reported values for various tapes with varying film thickness can be summarized by highlighting the highest J_c and the highest I_c samples. The highest J_c was achieved in the thinnest film, 0.9 μm , reaching 3.2 MA/cm² and 346 A/12 mm or 288 A/cm-w, while the maximum I_c was achieved in a 6.2 μm film, reaching 1.35 MA/cm² and 1006 A/12 mm or 838 A/cm-w. It should be noted that these films were BMO doped ($M = \text{Zr}$ or Hf), resulting in a dual-phase film consisting of the REBCO matrix and BMO nanorods. In-field enhancement at various fields and temperatures is also discussed. However, for the purpose of this chapter, it is remarkable to note that this level of self-field J_c is achieved even in BMO-doped films, which leads to the next section of this chapter.

4.8 Thickness Dependence of J_c in REBCO Films with Artificial Pinning Centers

The discovery of dual-phase REBCO/BMO systems with BMO self-assembled nanorods ($M = \text{Zr}$, Hf , Sn , etc.), has soon reinvigorated interest in thickness dependence of J_c through an apparent weakening of the thickness dependence, as observed experimentally in a number of studies, e.g., [72–76].

In a study on thickness dependence of critical current density in YBCO films with BaZrO_3 (BZO) and Y_2O_3 addition, Zhou, et al., have grown YBCO films with 5 mol% BZO and 5 mol% Y_2O_3 addition on single crystal STO substrates by PLD [72]. The authors report that the addition of the BZO nanorods and yttrium

oxide resulted in reduced thickness dependence of self-field J_c at 77 K compared to optimized non-doped YBCO films. The authors report that the “dead layer” did not appear up to thickness of 6.4 μm , and that significant enhancement of J_c was observed in the thick region above 2 μm . The J_c remained 2.3 MA/cm² in the thickest 6.4 μm film. Shown in Fig. 4.15 is the observed self-field J_c trend from this study, which is also compared to the optimized YBCO trend reported in [8]. The authors reason that the addition of BZO and Y₂O₃ not only provides secondary phase particles to act as pinning centers, but that they can also disrupt the YBCO matrix and create defects on the crystal level, which would then act as additional pinning sites.

A remarkable achievement of over 1000 A/cm-w has been reported in 2010, in films of only 2 μm thickness, with the corresponding J_c of 5.2 MA/cm² at 75.6 K, self-field. The authors utilize both BaZrO₃ and Y₂O₃ addition in PLD-grown YBCO samples, resulting in this impressively high current density and breaking the 1000 A/cm-w ceiling at only 2 μm thickness [77].

Wang, et al., have reported a study on YBCO/BZO films grown by PLD at two different temperatures, 790 and 810 °C, in order to control the density and length of aligned BZO nanorods, with a finding that higher growth temperature results in higher density and longer length of nanorods [73]. Most importantly, they report a surprising thickness dependence of these films. Films with thicknesses

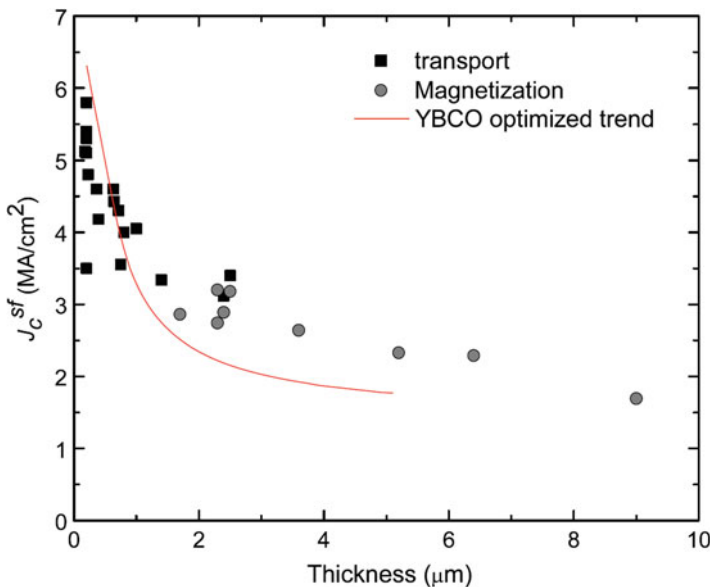
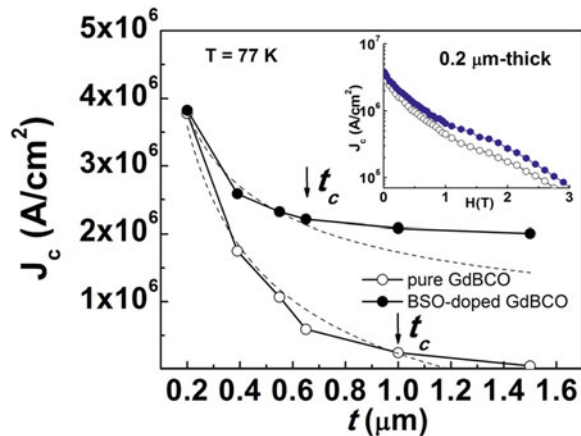


Fig. 4.15 Thickness dependence of 5 mol% BZO + 5 mol% Y₂O₃ added YBCO films (square and circle symbols), compared to the trend observed in pure YBCO films (red line). The thickness dependence is weakened in the presence of BZO and Y₂O₃. Reproduced with permission from [72]

between 0.1 and 0.6 μm have showed practically no dependence of 77 K, self-field J_c with thickness. The authors also examined the J_c behavior in lower fields in $B||c$ orientation up to 0.75 T and have found that films grown at higher temperature of 810 $^\circ\text{C}$ retained the thickness independence up to 0.5 T. At the highest field of 0.75 T, these films exhibited reverse thickness dependence, where the thicker film exhibited higher J_c than its thinner counterpart. For samples grown at lower temperature, a similar trend was observed, except that the reverse thickness dependence was even more pronounced. The overall self-field J_c values at 77 K were suppressed in this study, $\sim 1.4 \text{ MA/cm}^2$.

In a conceptually similar study, Tran, et al., have reported essentially the same trend of reduced thickness dependence of J_c in BaSnO_3 (BSO)-doped GdBCO films [75]. Both pure and 2 wt% Sn-doped films were grown by PLD in the thickness range from 0.2 to 1.5 μm . The results on thickness dependence are shown in Fig. 4.16. Very similar trend to that reported in [72] can be observed. In contrast to the study reported in [73], pure GdBCO and BSO-doped films grown in the same system under similar conditions are compared. A stark difference between the two sets of samples can be observed. Pure GdBCO films exhibit a dead-layer effect starting from 1 μm thickness, where J_c practically reduces to zero. In contrast, the BSO-doped films exhibit a decrease in J_c from ~ 4 to $>2 \text{ MA/cm}^2$ up to 1 μm thickness, after which it remains near-constant. The authors present TEM micrographs revealing nanorods of diameter $\sim 10 \text{ nm}$ and length of $\sim 150 \text{ nm}$. The authors reason that during the epitaxial growth of the BSO/GdBCO dual-phase system, misfit dislocations are likely to form at the interface between the two phases as a means of accommodation of elastic strain energy. The authors also report that the surface of the 1.5 μm thick BSO-containing films contained lower density of a -axis oriented grains compared to the pure GdBCO film of the same thickness. Other studies have since also reported a similar phenomenon where the thickness dependence is still present, but with a significantly weakened trend, resulting in absence of the dead layer at high thickness, e.g., [75, 76].

Fig. 4.16 Thickness- J_c dependence of 2 wt% BaSnO_3 -doped GdBCO films compared to pure GdBCO, at 77 K, self-field. In contrast to pure GdBCO that exhibits “dead-layer” effect starting from 1 μm , the BSO-doped film retains J_c over 2 MA/cm^2 up to 1.5 μm thickness. Reproduced with permission from [75]



Another study on thick REBCO films has been reported in 2018 [34]. Sieger, et al., also focus on incorporation of Artificial Pinning Centers (APC) in films with thicknesses up to 5 μm on buffered RABiTS, as well as substrate tapes made by ABAD deposition of ZrO_2 on stainless steel, with the REBCO film deposited using PLD [34]. The authors report that introduction of BaHfO_3 results in improved microstructure [78–80]. In the 2018 study, they report on 4.5 and 5 μm thick films. The resulting microstructures are shown in Fig. 4.17. For films of the reported thickness, the amount of a -axis oriented grains is remarkably low. Interestingly, the authors do not ascribe this achievement to any modifications in the deposition process, such as the one reported in the studies on hot-wall PLD reactor. Instead, the authors apparently ascribe this improvement solely to the presence of BHO nanorods. The authors report a relatively low J_c of 0.7 MA/cm² for the thickest films, with the corresponding critical currents of 300 and 340 A/cm-w for the films shown in Fig. 4.17 (a) and (b), respectively. Some of the hints for this relatively low J_c level despite the relatively low fraction of surface a -axis grains are provided in cross-sectional TEM micrographs, revealing other types of defects and large misoriented regions. Regardless of this, it is encouraging to witness another example where the issue of a -axis grain formation has been curbed.

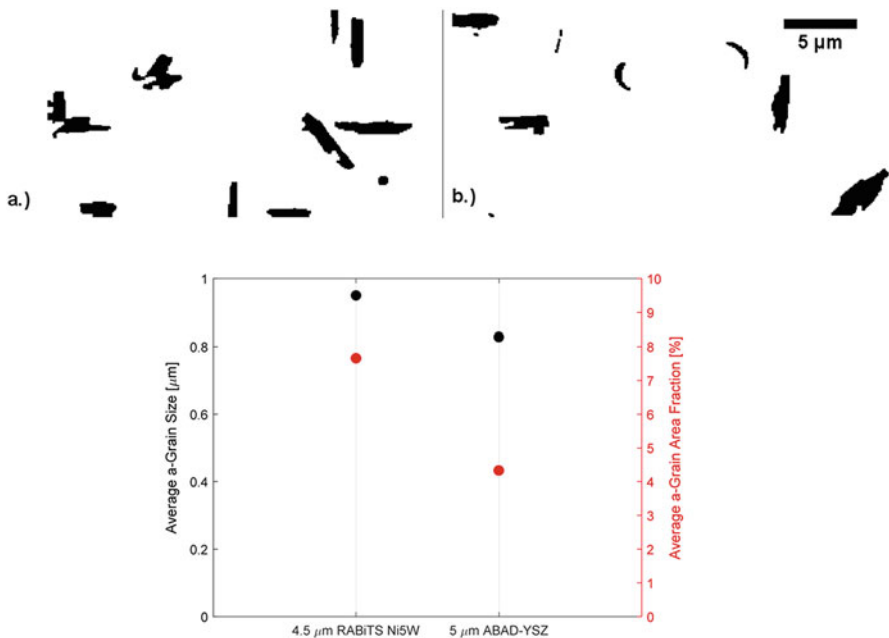


Fig. 4.17 Microstructure of BHO-doped REBCO films deposited by PLD: (a) 4.5 μm thick film deposited on RABiTS-Ni5W and (b) 5 μm thick film deposited on ABAD-YSZ [34]. Despite the high thickness, the microstructure has a relatively low fraction of a -axis oriented grains, as indicated by the measured average equivalent diameter and area fraction of the a -grains. The binary images were calculated from SEM micrographs reported in [34]

Considering the presented results on the effect of nanorods on the observed thickness dependence, the creation of defects in the REBCO matrix due to lattice mismatch with secondary phase particle has been pointed out as a possible reason for the weakening of the thickness dependence. In view of the results by Foltyn, et al., presented earlier in this chapter, and the observed dark band in TEM micrographs near the film/buffer interface, it was reasoned that the thin YBCO region near the buffer is rich in misfit dislocations that may be responsible for the very high observed J_c of near 7 MA/cm^2 in very thin films. In this scenario, it is plausible that the defects created by introduction of epitaxially grown nanorods as well as other particles such as Y_2O_3 contribute to the observed weakening of the thickness dependence of J_c . Many studies have since confirmed presence of high density of defects introduced around epitaxially grown secondary phase particles in YBCO as a mechanism of strain mismatch accommodation, e.g., [81–85]. In particular, high density of stacking faults has been observed at the nanorod/REBCO interfaces, as well as at interfaces with other epitaxially grown secondary phase particles. In addition, oxygen deficiency in the vicinity of nanorods has also been reported, providing evidence of yet another potential mechanism of defect formation due to the interface strain [86]. Most of these studies present TEM and/or STEM micrographs with a stunning level of disorder in the REBCO matrix due to lattice mismatch with secondary phases. Shown in Fig. 4.18 is an example of a bright field STEM image of a YBCO film with BZO addition, revealing a highly disordered YBCO matrix [83]. Many other examples, including high magnification aberration-corrected STEM micrographs revealing the structure of the disorder (consisting mostly of stacking faults) can be found in literature. A detailed study on correlation between nano-strain and pinning has been reported in [81].

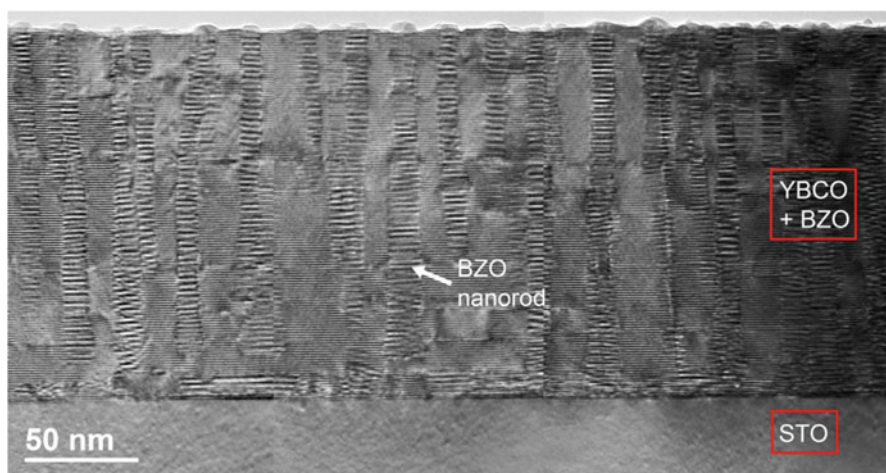


Fig. 4.18 Bright field STEM micrograph of a YBCO film containing BZO nanorods, revealing a high level of disorder in the YBCO matrix induced by mismatch strain between the two phases. Reproduced with permission from [83]

4.9 Growth of Thick Films by MOCVD

The most important findings on the issues associated the growth of thick films using MOCVD are presented in this section, due to the first-hand knowledge of the author. It will be seen that the issue of microstructure control, in particular a -grain formation with increasing thickness, has been found to be the critical factor that affects thick tape performance. MOCVD has been one of the leading deposition techniques for coated conductors, resulting in many demonstrations of successful scale-up to long lengths with high level of consistency in performance (e.g., [87–92]). The process has been subsequently tailored to the growth of dual-phase REBCO with incorporation of artificial pinning centers, consisting of 1D BaZrO₃ (BZO) nanorods and Y₂O₃ nanoparticles, aimed at in-field applications, which has been one of the major thrust areas of our group [39, 61, 92–114]. The peculiarities of MOCVD growth of REBCO films with artificial pinning centers will be outlined separately, while the general characteristics of MOCVD film growth, as well as the development of Advanced MOCVD for thick film growth will be outlined in this section.

A common theme in conventional MOCVD deposition is the severe degradation of texture and formation of a -axis oriented grains in films beyond 1 μm thickness. This issue is perhaps well summarized in the 2009 report on the attempts to grow thick films using MOCVD [90]. The authors report a steady progress in improving I_c by increasing film thickness in the period of 2006–2009. The important modification of the process in this study is the utilization of a multi-pass technique. Instead of growing thick films in a single pass, the tapes were processed in multiple MOCVD passes, where multiple layers of YBCO were deposited on top of each other in individual passes to build a thick film. Earlier studies utilized SmYBCO, resulting in ~ 600 A/cm-w in nearly 3 μm thick films. Further improvement was achieved by changing the composition to GdYBCO as well as doubling the number of passes for the same thickness, i.e., reducing the thickness of the film in each pass by half, resulting in near 800 A/cm-w at thicknesses above ~ 2 μm . The results are shown in Fig. 4.19. A notable feature is the appearance of the “dead layer” in the best performing tape from 2008; above ~ 2 μm , the critical current saturates to a constant value of ~ 800 A/cm-w. It should be emphasized that this level of performance is not achievable in single-pass MOCVD deposition utilizing a conventional MOCVD reactor. The multi-pass approach apparently results in slowing down the degradation of texture with thickness. However, multi-pass deposition results in increased complexity and time requirements compared to single-pass deposition. This is a likely reason why this route was not pursued in scale-up since this demonstration. In addition, while the reported values were measured over 1.2 m length, the authors mention the 2007 study where I_c of nearly 600 A/cm was achieved in 1 m length, and a minimum of nearly 200 A/cm in lengths of 500+ m. This large difference between maximum and minimum values succinctly describes the problem of scale-up and the difficulties associated with it, which has been a common theme to all REBCO deposition processes. Regardless, this study revealed impressive I_c values, from 6.6

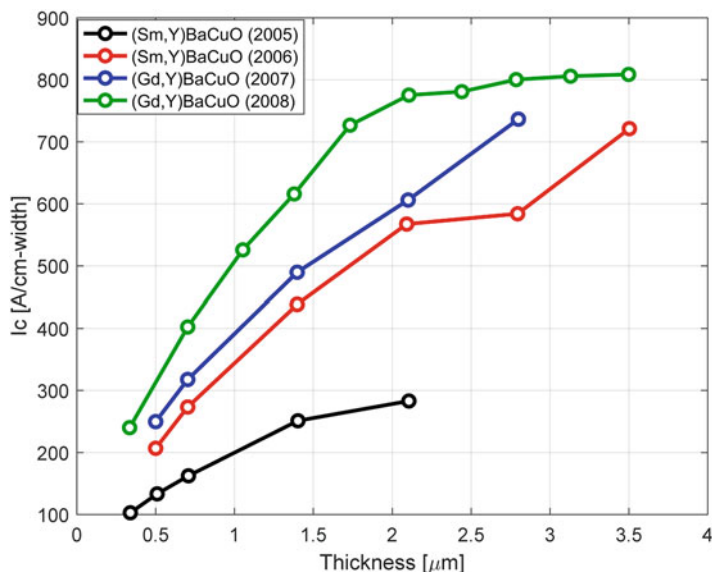


Fig. 4.19 Overview of progress in thick film deposition using multi-pass MOCVD, from 2005 to 2008. Data replotted from [90]

MA/cm² for the thinnest, 0.35 μm thick film, to 3.69 MA/cm² at 2.1 μm thickness. The same study also reports successful incorporation of BZO and significant in-field performance enhancement, which has since been transitioned to production.

In a 2010 study, focused on low temperature and high-field performance, three tapes produced by SuperPower Inc. were studied [115]. The three tapes were produced using conventional MOCVD and consisted of a “standard” tape, 2.13 μm thick, a BZO containing tape, 1.55 μm thick, and a “double layer” tape with thickness of 2.15 μm . The corresponding J_c values at 77 K, self-field for the three films were reported at 1.47 MA/cm², 1.40 MA/cm², and 1.85 MA/cm², respectively. The J_c values reported in this study are an illustration of achievable performance at the time when no extra measures of process modifications are employed. The values are significantly lower than that reported in multilayer tapes [90]. The double layer tape reported here showed $\sim 25\%$ improvement over the single layer tape of similar thickness.

In 2013, another study on tapes produced by conventional MOCVD with process modification was published, with reported J_c of 3.83 MA/cm² in 15 mol. % Zr-doped REBCO films of 1.1 μm thickness [39]. This value is remarkably high for such a high level of Zr doping; however, MOCVD process modification was again necessary.

In yet another study focused on in-field behavior between 30 and 77 K, three samples produced by MOCVD have been reported, all of them with heavy Zr doping, containing 25 mol. % Zr addition [116]. While the films were only 0.9 μm

thick, the reported 77 K, self-field J_c values ranged from 2.33 to 5.42 MA/cm², where the highest value is again significant for such a high level of Zr doping. While the focus of the study was again in-field performance, the study clearly confirms that very high level of doping and therefore high nanorod density can be achieved without deterioration in 77 K, self-field J_c . In fact, the reported value is within reach of the benchmark 7 MA/cm² established in early stages on single crystal substrates. The reason for the thickness limitation to 0.9 μm is again rooted in the peculiarities of the conventional MOCVD process. The remaining question was whether thicker films would result in deterioration of alignment of BZO nanorods or other potential issues.

The growth of well aligned BZO nanorods in thicker films has been demonstrated in 2015 using conventional MOCVD and the multi-pass technique [105]. The authors refer to reports that the alignment of BZO nano-columns degrades with film thickness, and the purpose of this study was to examine the possibility of growing thicker films with heavy Zr doping while maintaining BZO nanorod alignment throughout the film thickness. The main identified issue is that of changing the growth orientation and morphology of BZO from *c*-axis oriented nanorods to *ab*-plane aligned BZO platelets, which has been observed in films, as well as predicted using continuum elasticity [101, 117]. In this study, a 2.2 μm thick REBCO film with 20 mol% Zr addition was produced using multi-pass conventional MOCVD. The cross-section TEM micrographs reveal excellent alignment of BZO nanorods throughout the thickness, with no deterioration in alignment, demonstrating that high thickness is not an obstacle to producing REBCO films with artificial pinning centers. Many impressive results on in-field performance have been reported in this study. However, for the purpose of this section, the reported 77 K, self-field J_c is 2.94 MA/cm², which is a comparable figure to those achieved in thinner (~1 μm) films discussed above, and no microstructure degradation at this thickness was observed.

4.10 Advanced MOCVD

In earlier sections, progress in thick REBCO film development using several prominent deposition techniques has been discussed, resulting in notable improvements achieved with most deposition techniques. Film texture quality deterioration with thickness, including formation of *a*-axis oriented grains has been identified as the main issue, practically independent of the film growth process used. Impressive improvements have been achieved by addressing this issue through process modification, for example the use of a hot-wall reactor with PLD or batch processing using reactive co-evaporation in a dual chamber, as discussed earlier. The literature suggests that various groups utilizing different growth techniques have independently identified issues with their growth technique of choice that impeded successful growth of thick films. Interestingly, temperature control appears to be one of the main identified issues for most if not all growth techniques. What is common

among these very different processes is the material itself – YBCO and its rare-earth variants, which has a very narrow optimum temperature window for growth. In addition, many other variables, particular to the growth method used, affect the film quality, for example very different levels of ambient pressure between PLD and MOCVD. In this section, the details of the development of an Advanced MOCVD process are presented, together with the achieved results in terms of performance.

From the review of progress in MOCVD growth of thick films outlined above, it can be concluded that MOCVD has been demonstrated as a potentially very capable growth process if the deterioration of performance with thickness can be addressed. The issue has been suppressed by using a multi-pass technique which demonstrated impressive results. However, while this approach has provided great insight into the capabilities of MOCVD for thick film growth, it has remained impractical for scale-up. The problems associated with thick film growth using conventional MOCVD are best summarized in the study by Holesinger, et al., and illustrated in Fig. 4.8 [42].

The identified issues have prompted the author and coworkers to develop a new approach to MOCVD, which the authors term Advanced MOCVD, denoting the next step in advancement of this deposition process.

A detailed analysis of conventional MOCVD, including solid and gas phase heat transfer, precursor flow dynamics and other relevant details that influence the quality of the deposited film has been conducted with the aim of identifying the key issues that prevent growth of thick films with high quality. Based on these results, a new system was proposed and the development has commenced in 2012 as a part of ARPA-E Grid-Scale Rampable Intermittent Dispatchable Storage GRIDS program [61]. The result was the development of the Advanced MOCVD system. The first published results on the system can be found in [61]. The major issue with conventional MOCVD has been identified in temperature uniformity and control, due to the fact that the optimum temperature window for formation of *c*-axis oriented film is very narrow [93, 118–120]. In the case of conventional MOCVD, the microstructure development during deposition and the underlying issues are well documented in a detailed study reported by Aytug, et al., [93]. A detailed study by the author has revealed that the contact heating by a susceptor is an inefficient method to produce uniform tape temperature. This is exemplified in the fact that a large temperature gradient of over 200 °C exists between the susceptor body and the surface of the heated tape, which is due to very high thermal resistance at the susceptor/tape contact surface. In addition, the tape itself constitutes a very small thermal mass. The problem is exacerbated by the fact that not only the tape is coated with precursor material, but the susceptor as well. As the heating is largely achieved by tape/susceptor contact and the tape is in constant sliding motion over the susceptor, this makes the heat transfer very sensitive to any foreign particles that find their way between the tape and the susceptor, which originate from the stray material deposited on the substrate. The tape sliding over the susceptor is also a cause of friction and stick-slip motion that affects temperature stability. Finally, in conventional MOCVD there is a significant convective heat transfer from the tape to the gas phase in the form of the stream of precursor gas, carrier gas and evaporated

solvent. As MOCVD is a process operating at relatively high pressure compared to high vacuum techniques ($\sim 1\text{--}2$ Torr), this mode of heat transfer is non-negligible. Flow modeling of conventional MOCVD has revealed that the flow pattern and velocity is non-uniform, due to the top-down configuration of the showerhead and transition from vertical to horizontal flow as the gas travels from the showerhead towards the susceptor/tape and finally to the exhaust. In addition to the mentioned issues, the flow analysis has revealed that the precursor transfer to the tape is very inefficient due to the flow profile; most of the precursor never reaches the tape but instead flows directly to the exhaust. This results in a relatively poor efficiency or utilization of the precursor, which is typically on the order of 10%, i.e., about 90% of the precursor is wasted. As precursor cost alone is one of the major expenses associated with MOCVD of 2G-HTS, significant cost reduction can be achieved if the precursor-to-film conversion efficiency can be increased.

A simplified schematic of the Advanced MOCVD system is outlined in Fig. 4.20. In order to address the mentioned issues, a radical departure from conventional design was used. First, the susceptor is completely eliminated, and the tape is suspended in free space, in a recessed channel. The heating is accomplished by direct ohmic heating of the Hastelloy substrate – DC or AC current is applied along the tape, providing a very uniform source of heating. The method utilizes the fact that Hastelloy C-276 substrate has a favorable resistivity for this task, resulting in total resistance on the order of $1\ \Omega$. Tape temperature is directly monitored by using an optical probe or lightpipe, positioned under the tape. The precursor flow is introduced into a confined volume channel surrounding the tape, in a cross-flow configuration relative to tape axis. The flow is thus highly laminar and uniform, providing uniformity in both deposition and convective heat transfer. The volume confinement also serves as a means of increasing precursor conversion efficiency. Finally, the entire volume-confining channel is preheated to provide uniform background heat. The small thermal mass of the tape and the absence of tape contact with another solid results in rapid temperature response of the tape when subjected to change in input ohmic heating current, as illustrated in [61]. It can be seen that, while very different from other approaches, the common feature is

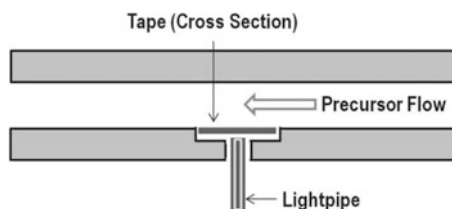


Fig. 4.20 Simplified schematic of the Advanced MOCVD system. HTS tape is suspended in free space and heating is accomplished by direct ohmic heating of the resistive Hastelloy substrate. Temperature is actively monitored and controlled by a lightpipe installed under the tape. Precursor flow is made highly laminar by using a confined volume flow channel that directs the precursor in a cross-flow pattern relative to tape axis. Reproduced with permission from [61]

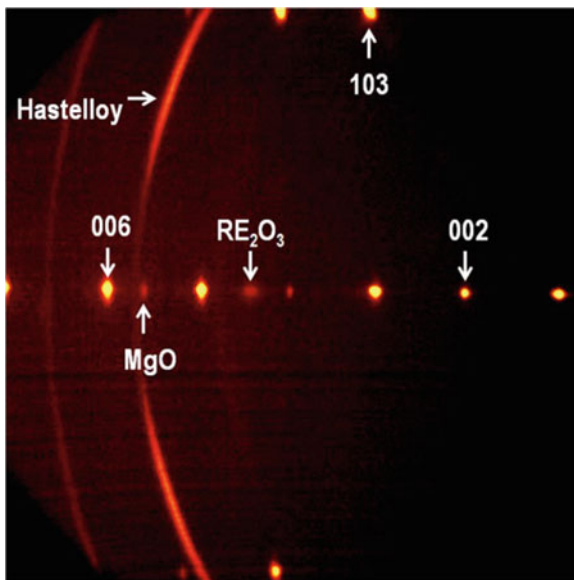
combating the tape temperature non-uniformity. For example, in the case of PLD, one successful approach is the use of a hot-wall reactor, as was discussed earlier. In the case of Advanced MOCVD, temperature uniformity was again addressed, together with other, MOCVD-specific issues.

The first results on tape quality of A-MOCVD processed 2G-HTS films have been reported in the same manuscript [61]. A 1.8 μm thick film was deposited in single pass, resulting in a film completely devoid of *a*-axis grains and featuring a mirror-like surface appearance. The 2D-XRD pattern of this film is shown in Fig. 4.21. The pattern reveals very sharp 00L REBCO peaks oriented in the direction perpendicular to tape, i.e., *c*-axis orientation. The sharpness of the peaks is indicative of excellent out-of-plane texture. In addition, the pattern does not reveal even smallest traces of *a*-axis oriented grains. More features, including surface appearance and FIB/SEM cross-section of the film can be found in [61].

The achieved critical current in this film was 916 A/12 mm width, which corresponds to J_c of 4.24 MA/cm². What is important in this demonstration is that this J_c is achieved in single-pass deposition, thus completely eliminating the need for the time consuming and complex multi-pass process. The achieved value is $\sim 15\%$ higher than that reported for a 2.1 μm film deposited using conventional MOCVD and the multi-pass approach.

The A-MOCVD system has been since demonstrated to be capable of depositing films in excess of 5 μm without any *a*-axis grain formation or deterioration in microstructure. The first mention of the achievable performance in very thick film can be found in a paper that focuses on achievements of multi-pass conventional MOCVD in 3.2 μm thick films at 4.2 K and 31.2 T [121]. Although A-MOCVD

Fig. 4.21 2D-XRD pattern of a 1.8 μm thick REBCO film deposited using Advanced MOCVD. The pattern reveals very sharp 00 L || tape normal pattern with excellent out-of-plane texture, as well as complete absence of *a*-axis oriented grains. Reproduced with permission from [61]



was not the main topic of this manuscript, the authors report on the limitations of conventional MOCVD and related challenges to produce high performance thick films, which can be overcome using A-MOCVD. The authors report the attainment of 77 K, self-field value of ~ 1500 A/12 mm width in films above $4 \mu\text{m}$ thickness, with the corresponding J_c of ~ 3.0 MA/cm 2 .

Recent progress in A-MOCVD has been submitted for publication in [122], with 77 K, self-field I_c and J_c data summarized in Fig. 4.22. Five tapes have been reported with thickness above $4 \mu\text{m}$ deposited in single pass. Consistency in I_c is shown in the fact that all tapes have critical current above 1400 A/12 mm. The highest value is over 1660 A/12 mm or near- 1400 A/cm-width, with the corresponding J_c of 3.28 MA/cm 2 . It should be noted that this critical current is very similar to the record self-field, 77 K value of ~ 1500 A/cm-width reported in [68] on $5 \mu\text{m}$ thick films grown by reactive co-evaporation, with the difference being that slightly lower thickness was used in the case of A-MOCVD in this study. However, the highest reported J_c value of 3.28 MA/cm 2 in A-MOCVD exceeds that reported in the $5 \mu\text{m}$ thick film grown by reactive co-evaporation (3 MA/cm 2). In summary, practically the same results have been achieved using two very different deposition techniques, demonstrating that this level of performance is achievable in 2G-HTS.

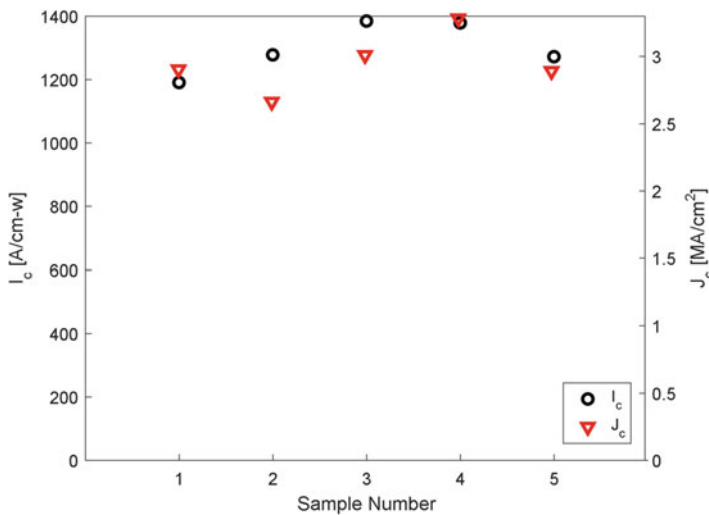


Fig. 4.22 Self-field I_c and J_c values of five tapes produced by Advanced MOCVD with film thickness above $4 \mu\text{m}$. Replotted using data from [122]

4.11 Growth of Thick REBCO Films with Artificial Pinning Centers Using MOCVD

Growth of REBCO films with APCs using MOCVD has been briefly reviewed in the section on growth of thick films by MOCVD, with a focus on the effect of APCs on self-field J_c performance at 77 K. Here, the topic of APCs and their growth in REBCO using MOCVD is examined in more detail and with respect to the resulting in-field performance at various temperatures.

There are many reports on advancements in growth of thick REBCO films with artificial pinning centers and their effect on in-field performance, utilizing different film growth techniques. In this section, findings from MOCVD-based studies of the authors' group will be outlined, again due to the authors' first-hand knowledge and due to space constraints. For other film growth processes, many excellent reports on growth of thick films with APCs and other techniques are available in the published literature. However, the quality and microstructural features of films with APCs are very similar between MOCVD and PLD, which makes these findings applicable to both techniques. For other growth techniques such as MOD, there are well-documented difficulties with growth of APCs by self-assembly, which stem from the nature of the MOD deposition process (sequential deposition and crystallization). For this case, different approaches to introducing high density of flux pinning centers have been developed (e.g., [123–125]).

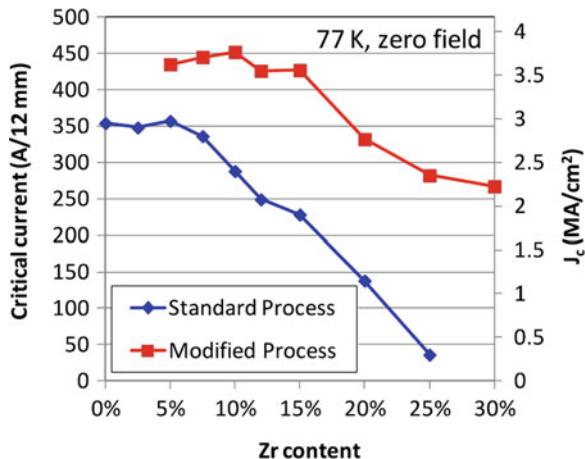
Ever since the first reports on hetero-epitaxial growth of BaZrO₃ and YBCO, as well as the demonstration of the nanorod growth along the YBCO c -axis (the “bamboo structure”) [126, 127], we have experienced continuous dramatic improvements in in-field performance of 2G-HTS over more than a decade of development, still with no apparent signs of saturation or exhaustion of the benefits of the methodology, as continuous improvements are being reported and new records are being set. Soon after the demonstration of the idea in PLD-grown films, growth of c -axis oriented BZO nanorods by self-assembly has also been confirmed in MOCVD-grown films [128]. Here, progress on understanding the control of nanorod morphology, size, and their effect on the properties and performance of the REBCO matrix in films grown by MOCVD by our group is succinctly summarized, as it pertains to the development of thick films with APCs.

After the successful demonstration of the growth of BZO nanorods in MOCVD-grown films [128], it has been realized that multiple parameters affect the alignment and size of nanorods. Good examples of these issues have been reported in [90, 128]. The splay in angles that BZO nanorods form relative to the c -axis of REBCO is evident in the published TEM micrographs of films grown by MOCVD. Also evident is the interplay between naturally occurring Y₂O₃ nanoparticles in films with Y-excess and the BZO nanorods. These studies provide evidence of a clearly visible splay in the angular range of the growth direction of nanorods around the crystallographic c -axis REBCO direction. The presence of Y₂O₃ has been attributed to enhancement of I_c in the field direction parallel to ab -planes, beyond the contribution of the intrinsic pinning. The films reported in these studies

had 6.5 mol% Zr addition and 30% Y, Gd excess. The authors report a number of factors that influence the performance and the morphology of the nanorods. Higher deposition rates were reported to result in films with little improvement in performance compared to films with no Zr addition. Decreasing the deposition rate from 0.5 to 0.13 $\mu\text{m}/\text{min}$ has been reported as a significant factor in improving the performance in Zr-added films. Excess rare-earth was also found to result in significant improvements, with the films having the nominal composition of Gd:Y:Ba:Cu = 0.65:0.65:2:3, and therefore significant rare-earth excess of 30%. Films with thicknesses of about 0.35 μm were grown, resulting in J_c values in excess of 5 MA/cm². Growth temperature was reported to have a strong effect on the angular J_c vs field angle performance, with an optimum temperature of 830 °C resulting in the most pronounced J_c peak at field orientations close to the REBCO c -axis, while higher and lower temperatures of 820 and 840 °C resulted in depression of the peak in J_c along the c -axis orientation. The multi-pass technique was used in order to increase the thickness, in 0.35 μm increments, up to over 3 μm of total thickness. Self-field I_c values started to saturate above ~ 1.5 μm thickness, converging to ~ 800 A/cm-w for the thickest sample. It is evident that even within one early study, a large number of parameters have been identified that significantly affect the resulting performance. Growth temperature was again found to be a very influencing factor, with temperature deviations of only 10 °C from the optimum resulting in very different properties. Growth rate, rare-earth content, amount of Zr, and other factors were all reported as affecting the performance. The large number of variables provides great latitude for optimization, but on the other hand, makes process control increasingly difficult.

A systematic study from 2009 on the feasibility of increasing the Zr dopant level in REBCO films is reported in [39], and the results again demonstrate strong potential for performance improvement by modification of the deposition process. At the time, the highest J_c values in low fields at 65–77 K have been found at 5 mol% Zr level in PLD and 7.5 mol% Zr in MOCVD [72, 95], and early attempts to increase the dopant level and thereby potentially the pinning performance have been marred by significant deterioration in J_c values at 77 K. In this study, Zr addition ranging from 0–15 mol% in 2.5 mol% and 20–30 in 5 mol% increments have been systematically studied in 1 μm thick films. The initial study has confirmed strong deterioration in J_c values with an increase in Zr content beyond 7.5 mol%, which was accompanied by a very similar trend in the decrease of T_c . This behavior was coincident with deterioration of out-of-plane texture and worsening of the microstructure, as evidenced by SEM micrographs that revealed an increase in density of needle-like secondary phases at Zr content above 10%. However, after process modification, a drastic increase in performance was observed. In addition to the expected significant improvement observed in the in-field performance, the effect of process modification is perhaps best illustrated by the trend in I_c at 77 K, self-field, shown in Fig. 4.23. The onset of degradation in I_c has been shifted from 7.5 to over 15 mol% Zr. At 25% Zr addition, the standard process resulted in near-zero I_c while the modified process resulted in a mild decrease of I_c from ~ 450 to ~ 300 A/12 mm. As expected, the improvements also reflected on 30 K in-field

Fig. 4.23 Self-field, 77 K I_c and J_c dependence on Zr content in MOCVD-grown REBCO films, using a standard and a modified/optimized process. A significant increase in BZO nanorod content and therefore in-field performance can be achieved with minimized degradation in J_c by process modification. Reproduced with permission from [39]



performance, where a J_c increase of 65% was reported at 30 K, 3 T in optimized 15 mol% Zr films compared to 7.5 mol% Zr films. The same approach has been used to produce films with significant improvement of in-field J_c performance at both 77 and 4.2 K and very high fields. In a 2014 publication, 0.9 μm thick films with 7.5 and 15 mol% Zr additions were characterized up to very high applied fields [103]. The increase in Zr content from 7.5 to 15 mol% has resulted in suppression of J_c at self-field, 77 K. However, the in-field behavior at 77 K, $B||c$, was significantly improved in 15 mol% Zr tape. The irreversibility field was extended from ~ 10 to ~ 15 T, and the pinning force behavior was comparable to that of optimized NbTi wire at 4.2 K. At 4.2 K, however, the increase in performance with Zr content was drastic, reaching $\sim 1.7 \text{ TN/m}^3$ in the 15 mol% Zr sample and remaining constant up to the maximum measured field of 31 T.

The next logical step was to reproduce the same level of in-field J_c performance in films with higher thickness. Using conventional MOCVD and the multi-pass deposition technique, 2.2 μm thick films with very high level of Zr doping of 20 mol% have been successfully grown [105]. The resulting J_c was above 15 MA/cm² at 30 K, 3 T, which was the target operating temperature and field for this study. This corresponds to I_c of 3963 A/12 mm or 3302 A/cm-w. Cross-section TEM micrographs revealed high level of alignment of BZO nanorods that were continuous throughout the film, despite the fact that the deposition was done in two passes, where the growth was stopped half-way through the deposition and then restarted. It should be noted that achieving continuous nanorods that permeate the whole thickness of the film was a challenging task early in the development of MOCVD-based BZO/REBCO films, with frequently observed short nanorod segments as well as *ab*-plane oriented BZO platelets, as was discussed earlier in this chapter. The microstructure presented in [105] over the entire 2.2 μm thickness and the corresponding in-field performance was therefore a significant step in demonstrating that a high degree of control of nanorod landscape is possible, and that REBCO

films with APCs have a tremendous potential for in-field applications at lower temperatures.

The same approach was later repeated with three-pass deposition to grow a 3.2 μm thick film, again with 20 mol% Zr addition, with focus on 4.2 K in-field performance [121]. The result was an engineering current density J_e over 1 kA/mm^2 at 31.2 T. The result is significant as this value exceeds the requirements of many high-field magnet applications at 4.2 K, opening significant opportunities for REBCO in the previously overlooked 4.2 K, high-field regime and the corresponding applications where other superconductor technologies have been traditionally used. It also emphasizes the advantage of very high irreversibility field of REBCO, this time harvested in the form of very high J_e value, which is the main figure to consider for high-field magnets and relevant applications at 4.2 K.

4.12 Control of Nanorod Size and Density

The reviewed studies on MOCVD-grown films with BZO nanorods have demonstrated that the level of Zr doping can be significantly increased beyond the initially found optimum at 5–10 mol% Zr addition, resulting in a significant increase in in-field performance by virtue of increasing the nanorod density without adversely affecting film texture and self-field critical current density. The amount of doping has been successfully increased up to 25 mol% Zr, with 20 mol% Zr samples achieving up to then record high J_c values at 30 K, 3 T, and 4.2 K at high fields [105, 121]. For a constant nanorod diameter, an increase in Zr levels would naturally increase the nanorod density and therefore matching field if the film integrity and nanorod continuity can be maintained, which was exactly the motivation behind pushing the limit of the Zr dopant level up.

The same issue of increasing the pinning site density can, however, also be looked at from a different perspective, which involves nanorod diameter as a major controlling parameter in determining the resulting nanorod density and therefore matching field. Namely, if d is nanorod diameter and a is the spacing between nanorods, then the nanorod density is proportional to $1/a^2$ and the volume fraction of nanorods is proportional to d^2/a^2 . Here, a square coordination of nanorods is assumed for simplicity, and nanorods are assumed to be continuous. Therefore, for a constant volume fraction of nanorods, reducing nanorod diameter in half would result in an increase in nanorod density by a factor of four. In other words, nanorod density would scale inversely with square of nanorod diameter. This implies that for typical 5–10 nm nanorod diameter reported in various studies, any non-marginal reduction in this value would result in a potentially large increase in density of pinning centers.

The mentioned approach is well illustrated in a study on films grown by Advanced MOCVD, where a drastic increase in nanorod density has been achieved in this manner [111]. Shown in Fig. 4.24 are plane view micrographs of two samples of 2 μm thickness, containing (a) 25 and (b) 11 mol% Zr addition. Despite the

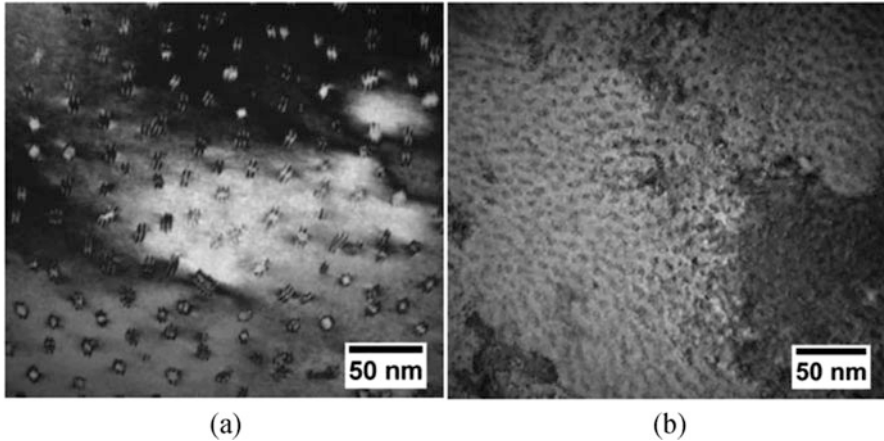


Fig. 4.24 Plane view micrographs of two BZO/REBCO samples processed by A-MOCVD. The sample shown in (a) contains 25 mol% Zr addition, while the sample (b) contains only 11 mol% Zr. Despite the 2.3-fold lower Zr content, the nanorod density as a factor of $\sim 6.7\times$ higher in the 11 mol% Zr sample, due to reduction in nanorod diameter. The corresponding matching fields are ~ 3 and ~ 20 T for samples shown in (a) and (b), respectively. Reproduced with permission from [111]

2.3-fold lower Zr content in sample (b), the achieved nanorod density is a factor of $\sim 6.7\times$ higher. This is achieved by reduction of nanorod diameter, as can be seen in the micrographs. The corresponding matching field has thus been increased from ~ 3 to ~ 20 T.

The possibility of control of nanorod size and therefore density has multiple consequences both on 77 K, self-field and in-field behavior. In a study on requirements to achieve high performance at 30 K, 3 T, several important trends have been reported [107]. The authors utilize lift factor, defined as the ratio of $J_c(T, B) / J_c(77 \text{ K}, 0 \text{ T})$, as a measure of performance. A compositional map of RE (Y + Gd), Ba + Zr and Cu content in the film and its effect on lift factor at 30 K, 2.5 T is presented, revealing that composition has a drastic effect on in-field performance at this particular field and temperature. Depending on composition, lift factor can vary over a very wide range, from ~ 1 to ~ 7 in this particular study. Another revealing trend is the correlation between J_c at 77 K, self-field and the lift factor at 30 K, 2.5 T. The authors report an inverse trend, i.e., the higher the J_c at 77 K, self-field, the lower the lift factor at 30 K, 2.5 T. However, this trend is an upper envelope on a dataset that shows very large scatter. In other words, having a low J_c at 77 K, self-field does not necessarily yield high lift factor. For example, two samples with the same J_c of 3.08 MA/cm^2 at 77 K, self-field exhibit very different lift factors of 4 and 7 at 30 K, 2.5 T. The reason for this trend has again been found in composition and the resulting nanorod diameter, density, and alignment. Shown in Fig. 4.25 are two TEM micrographs of the mentioned samples, where the micrographs (a) and (b) correspond to the samples with lift factors of 4 and 7, respectively. Both samples

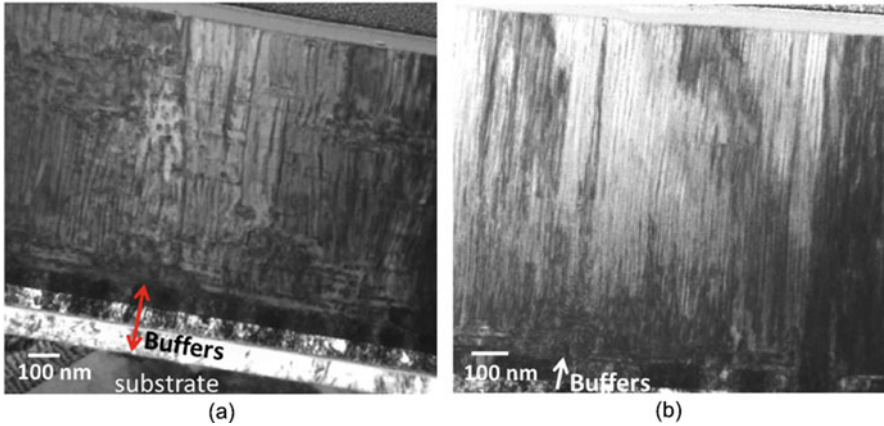


Fig. 4.25 TEM micrographs of two REBCO/BZO films grown with different (Ba + Zr)/Cu compositions of (a) 0.675 and (b) 0.737, respectively, revealing a strong effect of this parameter on the resulting BZO nanorod diameter, density, and alignment. Reproduced with permission from [107]

have the same 77 K, self-field J_c , yet very different in-field behavior at 30 K, 2.5 T. The sample (a) had a (Ba + Zr)/Cu composition of 0.675, while a value of 0.737 was reported for sample (b). The importance of the (Ba + Zr)/Cu parameter is well illustrated in the very good statistical correlation with lift factor at 30 K, 2.5 T reported in this study, revealing a practically linear trend. The authors note that a value of (Ba + Zr)/Cu above 0.71 is needed to achieve lift factor above 6 at 30 K, 2.5 T, and the microstructure observations indicate that this parameter has a strong influence on nanorod density and morphology.

Another important feature is reported in the same study, which is the correlation between the actual J_c values at 77 K, self-field and 30 K, 2.5 T, rather than the lift factor. The reported data indicate a bell-shaped curve in this dependence. The samples with highest J_c at 77 K, self-field of >4.5 MA/cm² resulted in worse in-field performance at 30 K, 2.5 T compared to the optimum samples at 30 K, 2.5 T with $J_c > 15$ MA/cm². All of the optimum 30 K, 2.5 T samples exhibited a suppressed J_c at 77 K, self-field. The best performing sample had $J_c(30$ K, 3 T) of over 20 MA/cm² while its $J_c(77$ K, self-field) value was only ~ 3 MA/cm². In contrast, samples with $J_c(77$ K, self-field) of over 5 MA/cm² had $J_c(30$ K, 2.5 T) of less than 10 MA/cm². The implication is that the data suggest that, at least in this approach to film growth and nanorod control, the 77 K, self-field performance is not indicative of the in-field behavior at lower temperatures.

More insight on the exact mechanism behind the effect of (Ba + Zr)/Cu parameter on nanorod size, density, and alignment observed in [107] has been published in an extended study focusing on the chemical composition of the REBCO/BZO films [112]. Shown in Fig. 4.26 is a plot of c -axis lattice parameter of (Gd,Y)BCO as a function of (Ba + Zr)/Cu. It is evident that this parameter has

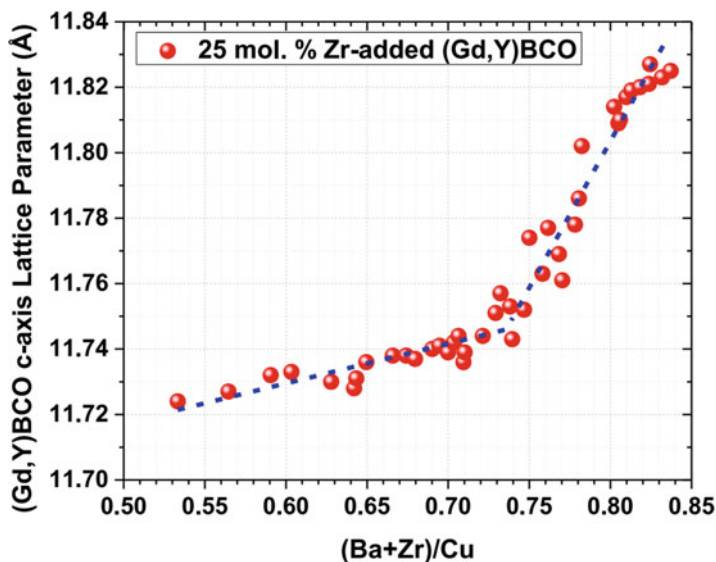


Fig. 4.26 The dependence of c -axis lattice parameter of (Gd,Y)BCO on (Ba+Zr)/Cu composition in films with 25 mol% Zr addition. Reproduced with permission from [112]

a strong effect on the c -axis lattice parameter of REBCO in the presence of Zr. An abrupt change in slope of the dependence is observed at $(\text{Ba} + \text{Zr})/\text{Cu} \sim 0.74$. This value approximately corresponds to stoichiometric Cu/Ba ratio 3:2. In Ba-rich region where $(\text{Ba} + \text{Zr})/\text{Cu} > 0.74$, a steep increase in c -axis lattice parameter is observed. This increase in c -axis lattice parameter of REBCO simultaneously results in a decrease of BZO lattice parameter parallel to c -axis of REBCO. The resulting REBCO/BZO lattice mismatch in REBCO c -axis direction thus decreases purely by composition control. This leads to a decrease in BZO nanorod diameter and an increase in BZO density while simultaneously promoting growth of continuous BZO nanorods that permeate the entire film thickness. While the best performing samples in terms of J_c at 77 K, self-field were found near the stoichiometric Cu/Ba ratio and c -axis lattice parameter of REBCO of 11.74 Å, the best J_c performance at 30 K, 3 T was found for samples with elongated c -axis lattice parameter of 11.76 Å in the Ba-rich region. This results in alignment and continuity of nanorods throughout the thickness, as well as an increase in nanorod density via reduction in their diameter. Further increase of Ba and lattice parameter to 11.78 Å decreases J_c at 30 K, 3 T, but results in peak J_c value at 9 T, indicating further increase in nanorod density and therefore matching field.

In conclusion, the reported studies reveal that the nanorod density and morphology can be controlled to a great degree with control of chemical composition of the REBCO/BZO system. Furthermore, these results indicate that the optimum composition for best J_c performance depends on the target operating field and temperature. These findings provide a tool for tuning of J_c performance for specific

applications. Growth of continuous and uniform nanorods is important for growth of thick films, and it has been shown that this condition can be achieved in films as thick as $3.2\ \mu\text{m}$ with excellent in-field performance. While all reported studies on this effect are based on MOCVD, it is expected that the results are be equally applicable to other in-situ growth techniques, most notably PLD, as the reported effects of composition are fundamentally related to the material properties of REBCO and BZO and as such should not strongly depend on the growth method.

4.13 Thick REBCO/BZO Films via Advanced MOCVD

We conclude this book chapter with two recent highlights where the advancements in growth of thick films using Advanced MOCVD and the understanding of control of nanorod morphology in MOCVD were combined to produce films over $4\ \mu\text{m}$ thick with record performance at intermediate fields and temperatures, as well as 4.2 K performance at high fields.

In a study on growth of thick films for applications requiring intermediate fields ($\sim 1\text{--}9\ \text{T}$) and temperatures (20–50 K), the Advanced MOCVD system was used to produce a (Y,Gd)BCO film with 15 mol% Zr addition and thickness of $4.8\ \mu\text{m}$ [114]. The films were optimized for in-field performance at 30 K, 3 T, in accordance to the findings from earlier MOCVD-based studies outlined earlier. The results are summarized in Fig. 4.27, showing in-field $I_c/12\ \text{mm}$ as a function of applied field along the c -axis at 30, 40, and 50 K, as well as the angular field dependence curves at 3 T for the three temperatures. The resulting film produced a J_c performance at 3 T, $B\parallel c$ of 15.1, 9.7, and $6.3\ \text{MA}/\text{cm}^2$ at temperatures of 30, 40, and 50 K, respectively. When multiplied by the film thickness of $4.8\ \mu\text{m}$, these J_c values translate to equivalent I_c values of 8705, 5586, and $3606\ \text{A}/12\ \text{mm}$ or 7254, 4655, and $3005\ \text{A}/\text{cm}$ -width, respectively. Considering the substrate thickness of $50\ \mu\text{m}$,

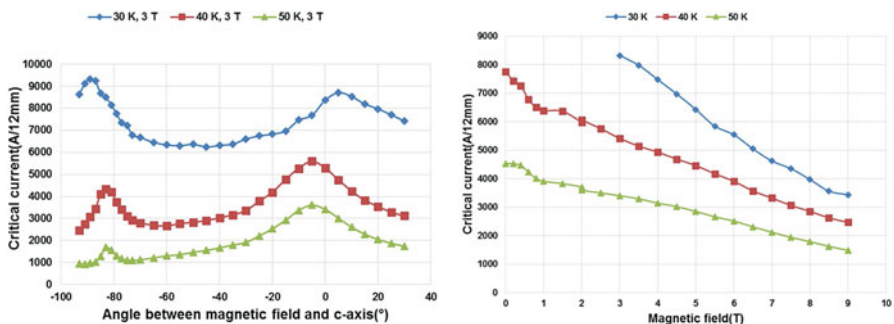


Fig. 4.27 In-field performance of $4.8\ \mu\text{m}$ thick (Y,Gd) BCO film with 15 mol% Zr addition grown by A-MOCVD, at 30, 40, and 50 K. Left—angular I_c dependence at 3 T. Right—In-field I_c dependence on magnetic field oriented parallel to the c -axis. Reproduced with permission from [114]

the buffer stack thickness and typical 40 μm thick copper stabilizer, this results in engineering current density J_e of 7.1, 4.5, and 2.9 kA/mm^2 .

The reported I_c of 8.7 $\text{kA}/12$ mm is a record high value, being over two times higher compared to the highest previously reported value of ~ 4 $\text{kA}/12$ mm that was obtained in 2.2 μm thick GdBCO films with 20 mol% Zr addition processed in two passes by conventional MOCVD [105]. The corresponding lift factor at 30 K, 3 T was nearly 11, which is again the highest value reported at this operating field and temperature.

Regarding the achieved critical current density of 15.1 MA/cm^2 , it is practically identical to the value reported for the mentioned 2.2 μm thick film with 20 mol% Zr addition processed by conventional MOCVD in two passes. It is interesting to note that the two values are essentially the same, despite the large difference in thickness between 4.8 and 2.2 μm , thereby clearly demonstrating that films with increased thickness of nearly 5 μm can be grown without deterioration in J_c . It should also be noted that at 3 T, the effect of self-field is expected to be negligible according to [52], perhaps partially explaining the almost identical J_c values obtained. Another notable feature is that the same performance was achieved with lower Zr content of 15 mol% in the 4.8 μm film compared to the 20 mol% addition in the 2.2 μm film. The reported microstructure shown in TEM micrographs reveals excellent alignment of nanorods over the entire film thickness. In addition, periodically occurring layers of dense arrays of Y_2O_3 precipitates arranged along ab -planes are reported. These arrays do not block the growth of BZO nanorods, which is known to be a potential issue in films grown under non-optimized conditions [96].

Another important metric to consider is the minimum I_c value in the angular field dependence. The minimum value of I_c at 30 K, 3 T, as shown in Fig. 4.27, is 6.3 $\text{KA}/12$ mm, which corresponds to a factor of 1.9 increase compared to the 2.2 μm reported previously [105]. In conclusion, the I_c values are about a factor of two higher over the entire angular range of field orientations.

The 2G-HTS technology offers a strong potential for high-field applications due to potentially very high engineering current density and irreversibility field at 4.2 K. The performance of YBCO with APCs can be tuned using the techniques described earlier to maximize in-field performance at the field of interest, and engineering current density can be significantly enhanced by growth of thick films. This approach has been used in a study aimed at 4.2 K performance, where two films of thicknesses of 4.3 and 4.6 μm have been grown using A-MOCVD [113]. The REBCO films again had 15 mol% Zr addition, but the composition of REBCO and the growth conditions were optimized for 4.2 K performance. Shown in Fig. 4.28 is a plot of engineering current density vs magnetic field oriented along c -axis of the two samples, together with the performance of other superconductor technologies in use at 4.2 K. The two samples, measured independently at two separate sites (National High Magnetic Field Laboratory—NHMFL and Lawrence Berkeley National Laboratory—LBNL), exhibited almost identical performance.

Both samples were found to have a high density of BZO nanorods of average diameter ~ 3.7 nm, as well as high density of RE_2O_3 precipitates interspersed between the nanorods. 2D-XRD scans revealed excellent out-of-plane texture of

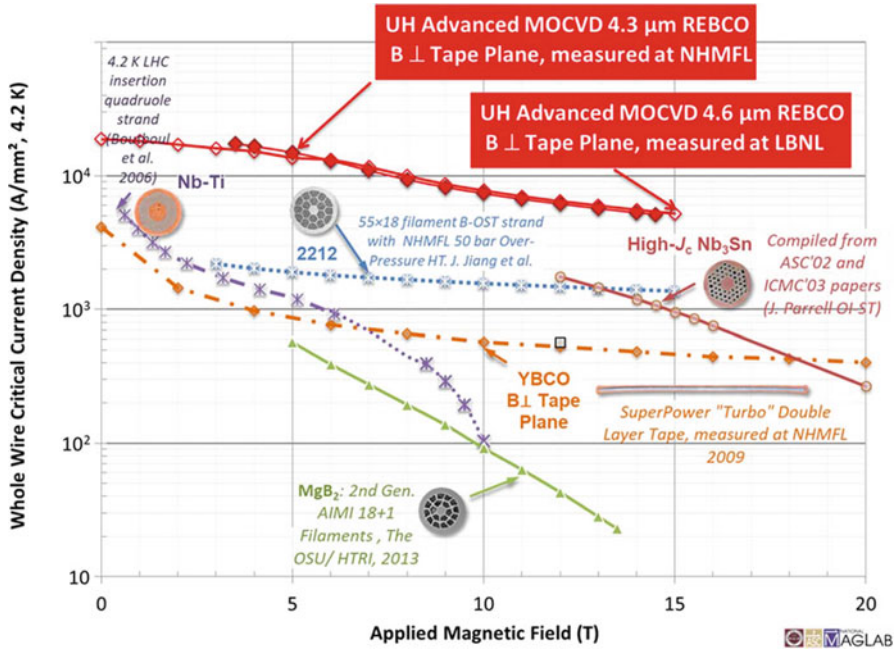


Fig. 4.28 Engineering current density vs field at 4.2 K of two >4 μm thick REBCO films with 15 mol% Zr addition grown using A-MOCVD, in comparison with in-field performance of other superconductor technologies. Reproduced with permission from [113]

the REBCO phase. The resulting I_c performance was 2247 and 2119 A/4 mm width at 4.2 K and magnetic field of 14 T in $B \parallel c$ orientation. This value is about a factor of two higher than the highest previously reported value at this field and temperature [121]. The corresponding critical current density and pinning force were over 12 MA/cm² and 1.7 TN/m³. The engineering current density, estimated using the tape thickness and assuming an additional 40 μm thick copper stabilizer, was over 5 kA/mm², which is over five times higher than Nb₃Sn and nearly four times higher than the highest reported value among all superconductor technologies other than 2G-HTS. This remarkable value demonstrates that 2G-HTS has a strong potential to be used for very high-field applications.

4.14 Summary

The 2G-HTS technology has witnessed tremendous progress in the course of last 30 years. The issue of degradation in critical current density with thickness has proven to be a very challenging task, despite very high critical current densities that were achieved in thin REBCO films. However, a large body of work over

the three decades has contributed to slow but steady progress in understanding the limitations and issues related to thick film growth, leading to continuous progress in increasing J_c in thick films. The developments can be succinctly summarized by several statements which capture the nature of the problem as well as the advancements achieved over the years.

1. The 77 K, self-field J_c benchmark of ~ 7 MA/cm² determined as a thin film limit from films grown on single crystal substrates has remained elusive in thick samples. However, values approaching this limit have been reported on flexible substrates. Values as high as 6.6 MA/cm² in 0.35 μ m thickness, as well as several reports of over 5 MA/cm² in films ranging in thickness from ~ 0.9 –2 μ m, have been achieved.
2. Multiple demonstrations of over 1000 A/cm-w have been reported, reaching or exceeding the target set in 2006 by US DOE Office of Science. The highest reported critical currents to date at 77 K, self-field are ~ 1500 and 1400 A/cm-w in ~ 5 and 4.2 μ m samples, corresponding to ~ 3 –3.3 MA/cm².
3. The main obstacle to reaching high J_c in thick films has been identified to be deterioration in film quality with thickness, mostly reported as progressive increase in fraction of misoriented or a -axis grains. The problem has been addressed and apparently largely solved for several film growth techniques, most notably PLD, MOCVD, and reactive co-evaporation. In essence, very tight control of process variables, most notably temperature, appears to be a necessary requirement for successful growth of thick films.
4. The increasing self-field generated at progressively higher thickness is a factor that inevitably causes reduction in J_c with thickness, albeit at a lower rate compared to many thickness dependence studies that contained both self-field and texture deterioration effects. The effect of self-field becomes negligible for in-field applications.
5. Multiple studies suggest that addition of artificial pinning centers significantly reduces the thickness dependence of J_c . Presence of high density of defects such as stacking faults as a means to accommodate lattice mismatch between REBCO and APCs is a likely reason for this effect, possibly similar to the high density of misfit dislocations observed at substrate/film interfaces, believed to be a reason behind very high J_c values observed in very thin films.
6. Growth of high density of nanorod precipitates, aligned and continuous along c -axis has been demonstrated in films up to ~ 5 μ m thickness, despite early reports that raised some doubt on whether this is achievable in very thick films. Significant progress has been achieved in understanding the effect of composition and film growth parameters on the resulting nanorod diameter, density, and morphology, opening ways for optimization of performance at target fields and temperatures.
7. Recent studies have demonstrated that the growth of thick films is particularly beneficial for in-field applications. Remarkably high critical currents have been achieved in >4 μ m thick films at intermediate fields and temperatures, exemplified by 3 T, $B||c$ performance of 7254, 4655, and 3005 A/cm-width at

30 T, 40 T, and 50 T, respectively. At 4.2 K, engineering current density of over 5 kA/mm^2 , which is five times higher than Nb_3Sn and nearly four times higher than the highest reported value among all superconductor technologies other than 2G-HTS.

The significant recent progress in thick film 2G-HTS development is likely to spur further research in this area, with the expected outcome of pushing the boundaries of achievable critical currents even further, in particular for in-field applications. The recently demonstrated remarkable results provide a glimpse of what is achievable with this technology and what can be achieved in applications if these results are transferred from laboratory scale to commercial offerings.

References

1. J.X. Lin, X.M. Liu, C.W. Cui, et al., A review of thickness-induced evolutions of microstructure and superconducting performance of $\text{REBa}_2\text{Cu}_3\text{O}_7$ -delta coated conductor. *Adv. Manuf.* **5**(2), 165–176 (2017)
2. F.E. Luborsky, R.F. Kwasnick, K. Borst, et al., Reproducible sputtering and properties of Y-Ba-Cu-O films of various thicknesses. *J. Appl. Phys.* **64**(11), 6388–6391 (1988)
3. S.R. Foltyn, P. Tiwari, R.C. Dye, et al., Pulsed-laser deposition of thick $\text{YBa}_2\text{Cu}_3\text{O}_7$ -delta films with JC-greater-THAN-1 ma/CM2. *Appl. Phys. Lett.* **63**(13), 1848–1850 (1993)
4. S.R. Foltyn, Q.X. Jia, P.N. Arendt, et al., Relationship between film thickness and the critical current of $\text{YBa}_2\text{Cu}_3\text{O}_7$ -delta-coated conductors. *Appl. Phys. Lett.* **75**(23), 3692–3694 (1999)
5. Q.X. Jia, S.R. Foltyn, P.N. Arendt, et al., High-temperature superconducting thick films with enhanced supercurrent carrying capability. *Appl. Phys. Lett.* **80**(9), 1601–1603 (2002)
6. S.R. Foltyn, P.N. Arendt, Q.X. Jia, et al., Strongly coupled critical current density values achieved in $\text{YBa}_2\text{Cu}_3\text{O}_7$ -delta coated conductors with near-single-crystal texture. *Appl. Phys. Lett.* **82**(25), 4519–4521 (2003)
7. D. Dimos, P. Chaudhari, J. Mannhart, et al., Orientation dependence of grain-boundary critical currents in $\text{YBa}_2\text{Cu}_3\text{O}_7$ -delta BICRYSTALS. *Phys. Rev. Lett.* **61**(2), 219–222 (1988)
8. S. Foltyn, H. Wang, L. Civale, et al., Overcoming the barrier to 1000 a/cm width superconducting coatings. *Appl. Phys. Lett.* **87**(16), 162505–162505-3 (2005)
9. A.I. Larkin, Y.N. Ovchinnikov, Pinning in type-II superconductors. *J. Low Temp. Phys.* **34**(3–4), 409–428 (1979)
10. G. Blatter, M.V. Feigelman, V.B. Geshkenbein, et al., Vortices in high-temperature superconductors. *Rev. Mod. Phys.* **66**(4), 1125–1388 (1994)
11. D.M. Feldmann, D.C. Larbalestier, R. Feenstra, et al., Through-thickness superconducting and normal-state transport properties revealed by thinning of thick film ex situ $\text{YBa}_2\text{Cu}_3\text{O}_7$ -x coated conductors. *Appl. Phys. Lett.* **83**(19), 3951–3953 (2003)
12. K.J. Leonard, S. Kang, A. Goyal, et al., Microstructural characterization of thick $\text{YBa}_2\text{Cu}_3\text{O}_7$ -delta films on improved rolling-assisted biaxially textured substrates. *J. Mater. Res.* **18**(7), 1723–1732 (2003)
13. S. Kang, A. Goyal, K.J. Leonard, et al., High critical current $\text{YBa}_2\text{Cu}_3\text{O}_7$ -delta thick films on improved rolling-assisted biaxially textured substrates (RABiTS (TM)). *J. Am. Ceram. Soc.* **88**(10), 2677–2680 (2005)
14. S.R. Foltyn, L. Civale, J.L. Macmanus-Driscoll, et al., Materials science challenges for high-temperature superconducting wire. *Nat. Mater.* **6**(9), 631–642 (2007)

15. J. Sarrao, W.-K. Kwok, I. Bozovic et al., *Basic Research Needs for Superconductivity*. Report of the Basic Energy Sciences Workshop on Superconductivity, May 8–11, 2006, DOE/SC (USDOE Office of Science (SC)), 2006
16. K. Himeki, M. Kiuchi, E.S. Otabe, et al., Dependence of superconducting layer thickness on critical current density of IBAD/CVD-processed YBCO coated conductors. *Physica C-Superconductivity and Its Applications* **469**(15-20), 1457–1461 (2009)
17. K. Kimura, M. Kiuchi, E.S. Otabe, et al., Dependence of superconducting layer thickness on critical current density of YBCO-coated conductors at high temperatures. *Phys. C Supercond. Appl.* **463**, 697–701 (2007)
18. T. Matsushita, K. Kimura, M. Kiuchi, et al., The dependence of pinning properties on superconducting layer thickness in IBAD/PLD YBCO-coated conductors. *Supercond. Sci. Technol.* **20**(9), S189–S196 (2007)
19. K. Ohki, K. Develos-Bagarinao, H. Yamasaki, et al., Origin of the thickness dependence of critical current densities in YBCO films prepared by pulsed laser deposition. *J. Phys. Conf. Ser.* **97** (2008)
20. H. Matsui, K. Tsukada, T. Tsuchiya, et al., Thickness dependence of the critical-current density and its relation to near-Interface crystal imperfections in fluorine-free-MOD YBCO films. *IEEE Trans. Appl. Supercond.* **21**(3), 2933–2936 (2011)
21. K. Kimura, M. Kiuchi, E.S. Otabe, et al., Film thickness dependence of critical current characteristics of YBCO-coated conductors. *Phys. C Supercond. Appl.* **445**, 141–145 (2006)
22. D.Q. Shi, R.K. Ko, K.J. Song, et al., Effects of deposition rate and thickness on the properties of YBCO films deposited by pulsed laser deposition. *Supercond. Sci. Technol.* **17**(2), S42–S45 (2004)
23. T. Matsushita, M. Kiuchi, K. Kimura, et al., Dependence of critical current properties on the thickness of the superconducting layer in YBCO coated tapes. *Supercond. Sci. Technol.* **18**(12), S227–S231 (2005)
24. K. Develos-Bagarinao, H. Yamasaki, J.C. Nie, et al., Thickness dependence of $J(c)$ for YBCO thin films prepared by large-area pulsed laser deposition on CeO₂-buffered sapphire substrates. *Supercond. Sci. Technol.* **18**(5), 667–674 (2005)
25. P.N. Arendt, S.R. Foltyn, Biaxially textured IBAD-MgO templates for YBCO-coated conductors. *MRS Bull.* **29**(8), 543–550 (2004)
26. F.A. List, A. Goyal, M. Paranthaman, et al., High $J(c)$ YBCO films on biaxially textured Ni with oxide buffer layers deposited using electron beam evaporation and sputtering. *Physica C* **302**(1), 87–92 (1998)
27. M.S. Bhuiyan, M. Paranthaman, S. Sathyamurthy, et al., MOD approach for the growth of epitaxial CeO₂ buffer layers on biaxially textured Ni-W substrates for YBCO coated conductors. *Supercond. Sci. Technol.* **16**(11), 1305–1309 (2003)
28. A. Goyal, M.P. Paranthaman, U. Schoop, The RABiTS approach: Using rolling-assisted biaxially textured substrates for high-performance YBCO superconductors. *MRS Bull.* **29**(8), 552–561 (2004)
29. Y.V. Cherpak, V.O. Moskaliuk, A.V. Semenov, et al., Thickness dependence mechanisms of the critical current density in high-T_c cuprate superconductor films. *Supercond. Sci. Technol.* **20**(12), 1159–1164 (2007)
30. Q.X. Jia, H. Wang, Y. Lin, et al., Microstructural evolution with the change in thickness of superconducting films. *IEEE Trans. Appl. Supercond.* **17**(2), 3243–3246 (2007)
31. S.K. Streiffer, B.M. Lairson, C.B. Eom, et al., Microstructure of ultrathin films of YBA₂CU₃O_{7- δ} on MGO. *Phys. Rev. B* **43**(16), 13007–13018 (1991)
32. S.J. Pennycook, M.F. Chisholm, D.E. Jesson, et al., Growth and relaxation mechanisms of YBA₂CU₃O_{7- δ} films. *Physica C* **202**(1–2), 1–11 (1992)
33. C. Dubourdieu, J.P. Senateur, O. Thomas, et al., High-quality YBA₂CU₃O_{7- δ} superconducting thin-films grown by MOCVD. *J. De Physique Iv* **5**(C5), 365–371 (1995)
34. M. Sieger, P. Pahlke, M. Lao, et al., Thick secondary phase pinning-enhanced YBCO films on technical templates. *IEEE Trans. Appl. Supercond.* **28**(4), 1 (2018)

35. B.W. Tao, N. Zhang, F. Zhang, et al., Thickness effect on the structural and electrical properties of sputtered YBCO coated conductors. *IEEE Trans. Appl. Supercond.* **21**(3), 2945–2948 (2011)
36. B.L. Low, S.Y. Xu, C.K. Ong, et al., Substrate temperature dependence of the texture quality in YBCO thin films fabricated by on-axis pulsed-laser ablation. *Superconductor Science & Technology* **10**(1), 41–46 (1997)
37. A. Ibi, H. Iwai, K. Takahashi, et al., Investigations of thick YBCO coated conductor with high critical current using IBAD-PLD method. *Phys. C: Supercond.* **426**, 910–914 (2005)
38. J.A. Smith, M.J. Cima, N. Sonnenberg, High critical current density thick MOD-derived YBCO films. *IEEE Trans. Appl. Supercond.* **9**(2), 1531–1534 (1999)
39. V. Selvamanickam, Y. Chen, T. Shi, et al., Enhanced critical currents in (Gd,Y)Ba₂Cu₃O_x superconducting tapes with high levels of Zr addition. *Supercond. Sci. Technol.* **26**(3), 9 (2013)
40. D.L. Zhu, J. Huang, H. Li, et al., A new method to preserve the c-axis growth of thick YBa₂Cu₃O₇-delta films grown by pulsed laser deposition. *Phys. C-Supercond. Appl.* **469**(22), 1977–1982 (2009)
41. F. Vassenden, G. Linker, J. Geerk, Growth direction control in YBCO thin-films. *Physica C* **175**(5–6), 566–572 (1991)
42. T.G. Holesinger, B. Maiorov, O. Ugurlu, et al., Microstructural and superconducting properties of high current metal-organic chemical vapor deposition YBa₂Cu₃O₇-delta coated conductor wires. *Supercond. Sci. Technol.* **22**(4), 045025 (2009)
43. T.G. Holesinger, S.R. Foltyn, P.N. Arendt, et al., The microstructure of continuously processed YBa₂Cu₃O_y coated conductors with underlying CeO₂ and ion-beam-assisted yttria-stabilized zirconia buffer layers. *J. Mater. Res.* **15**(5), 1110–1119 (2000)
44. T. Yoshida, A. Ibi, T. Takahashi, et al., Fabrication of Eu₁YBa₂Cu₃O₇-delta+BaHfO₃ coated conductors with 141 a/cm-w under 3 T at 77 K using the IBAD/PLD process. *Phys. C Supercond. Appl.* **504**, 42–46 (2014)
45. T.G. Holesinger, L. Civale, B. Maiorov, et al., Progress in nanoengineered microstructures for tunable high-current, high-temperature superconducting wires. *Adv. Mater.* **20**(3), 391–407 (2008)
46. V.F. Solovyov, H.J. Wiesmann, Q. Li, et al., Three- and four-mu m-thick YBa₂Cu₃O₇ layers with high critical-current densities on flexible metallic substrates by the BaF₂ process. *J. Appl. Phys.* **99**(1), 013902 (2006)
47. V.F. Solovyov, H.J. Wiesmann, M. Suenaga, Critical current densities and the structural quality of 3- and 4-mu m-thick superconducting YBa₂Cu₃O₇ layers synthesized using the ex situ process. *J. Appl. Phys.* **102**(5), 053902 (2007)
48. T. Izumi, H. Fuji, Y. Aoki, et al., R&D for long tapes with high I-c by advanced TFA-MOD process. *Phys. C Supercond. Appl.* **445**, 533–539 (2006)
49. Y. Aoki, R. Teranishi, K. Nakaoka, et al., Key factors for scale-up of YBCO coated conductors by the advanced TFA-MOD process. *Phys. C Supercond. Appl.* **445**, 540–544 (2006)
50. R. Teranishi, T. Izumi, Y. Shiohara, Highlights of coated conductor development in Japan. *Superconductor Science & Technology* **19**(3), S4–S12 (2006)
51. S.I. Kim, A. Gurevich, X. Song, et al., Mechanisms of weak thickness dependence of the critical current density in strong-pinning ex situ metal-organic-deposition-route YBa₂Cu₃O_{7-x} coated conductors. *Supercond. Sci. Technol.* **19**(9), 968–979 (2006)
52. L. Rostila, J. Lehtonen, R. Mikkonen, Self-field reduces critical current density in thick YBCO layers. *Phys. C Supercond. Appl.* **451**(1), 66–70 (2007)
53. Y.B. Kim, C.F. Hempstead, A.R. Strnad, Resistive states of hard superconductors. *Rev. Modern Phys.* **36**, 43 (1964)
54. A.A.B. Brojeny, J.R. Clem, Self-field effects upon the critical current density of flat superconducting strips. *Supercond. Sci. Technol.* **18**(6), 888–895 (2005)
55. A. Sanchez, C. Navau, N. Del-Valle, et al., Self-fields in thin superconducting tapes: Implications for the thickness effect in coated conductors. *Appl. Phys. Lett.* **96**(7), 072510 (2010)

56. F. Hengstberger, M. Eisterer, H.W. Weber, Thickness dependence of the critical current density in superconducting films: A geometrical approach. *Appl. Phys. Lett.* **96**(2), 022508 (2010)
57. C. Xue, Y.H. Zhou, The influence of geometry on critical current in thin high-T_c superconducting tape. *IEEE Trans. Appl. Supercond.* **24**(4) (2014)
58. C. Navau, N. Del-Valle, A. Sanchez, Macroscopic modeling of magnetization and levitation of hard type-II superconductors: The critical-state model. *IEEE Trans. Appl. Supercond.* **23**(1), 8201023 (2013)
59. H.S. Ha, J.H. Lee, R.K. Ko, et al., Thick SmBCO/IBAD-MgO coated conductor for high current carrying power applications. *IEEE Trans. Appl. Supercond.* **20**(3), 1545–1548 (2010)
60. M. Igarashi, K. Kakimoto, T. Hayashida, et al., High-speed deposition of RE123 film with large current capacity by hot-wall type PLD system. *Phys C Supercond. Appl.* **470**(20), 1230–1233 (2010)
61. G. Majkic, E. Galstyan, V. Selvamanickam, High performance 2G-HTS wire using a novel MOCVD system. *IEEE Trans. Appl. Supercond.* **25**(3), 1 (2015)
62. S. Fujita, M. Daibo, M. Igarashi, et al., In-field critical current property of IBAD/PLD coated conductors. *J. Phys. Conf. Ser.* **507** (2014)
63. S. Fujita, H. Satoh, M. Daibo, et al., Characteristics of REBCO coated conductors for 25 T cryogen-free superconducting magnet. *IEEE Trans. Appl. Supercond.* **25**(3), 1 (2015)
64. S. Fujita, S. Muto, T. Yoshida, et al., Strain characteristics of BMO doped REBCO coated conductors fabricated by hot-wall PLD. *J. Phys. Conf. Ser.* **871**, 012042 (2017)
65. S. Fujita, S. Muto, W. Hirata, et al., Development of long-length BMO-doped REBCO coated conductors by Hot-Wall PLD process. *IEEE Trans. Appl. Supercond.* **28**(4), 1 (2018)
66. Y. Iijima, K. Kakimoto, M. Igarashi, et al., BMO-doped REBCO-coated conductors for uniform in-field I_c by Hot-Wall PLD process using IBAD template. *IEEE Trans. Appl. Supercond.* **27**(4), 1 (2017)
67. M. Durrschnabel, Z. Aabdin, M. Bauer, et al., DyBa₂Cu₃O_{7-x} superconducting coated conductors with critical currents exceeding 1000 a cm⁽⁻¹⁾. *Supercond. Sci. Technol.* **25**(10), 105007 (2012)
68. H.S. Kim, S.S. Oh, H.S. Ha, et al., Ultra-high performance, high-temperature superconducting wires via cost-effective, scalable, co-evaporation process. *Sci. Rep.* **4**, 10 (2014)
69. G. Kim, H.J. Jin, W. Jo, et al., Ultra-large current transport in thick SmBa₂Cu₃O_{7-x} films grown by reactive co-evaporation. *Phys. C Supercond. Appl.* **513**, 29–34 (2015)
70. L. Liu, Y. Li, X. Wu, et al., Development of long REBCO coated conductors by PLD-REBCO/sputter-CeO₂/IBAD-MgO at SJTU and SSTC. *IEEE Trans. Appl. Supercond.* **25**(3), 1 (2015)
71. L.F. Liu, Y.Y. Li, G.N. Xiao, et al., Fabrication of thick REBCO-coated conductors with high performance on metal Tapes by pulsed laser deposition process. *J. Supercond. Nov. Magn.* **28**(2), 403–406 (2015)
72. H. Zhou, B. Maiorov, S.A. Baily, et al., Thickness dependence of critical current density in YBa₂Cu₃O_{7-delta} films with BaZrO₃ and Y₂O₃ addition. *Supercond. Sci. Technol.* **22**(8), 085013 (2009)
73. X. Wang, F.J. Baca, R.L.S. Emergo, et al., Eliminating thickness dependence of critical current density in YBa₂Cu₃O_{7-x} films with aligned BaZrO₃ nanorods. *J. Appl. Phys.* **108**(11), 113911 (2010)
74. D.H. Tran, W.B.K. Putri, C.H. Wie, et al., Thickness dependence of critical current density in GdBa₂Cu₃O_{7-delta} thin films with BaSnO₃ addition. *J. Appl. Phys.* **111**(7), 07D714 (2012)
75. D.H. Tran, W.B.K. Putri, B. Kang, et al., Reducing thickness dependence of critical current density in GdBa₂Cu₃O_{7-delta} thin films by addition of nanostructured defects. *J. Appl. Phys.* **113**(17), 17E134 (2013)
76. D.H. Tran, W.B.K. Putri, B. Kang, et al., A close correlation between nanostructure formations and the thickness dependence of the critical current density in pure and BaSnO₃-added GdBa₂Cu₃O_{7-delta} films. *J. Appl. Phys.* **115**(16), 163901 (2014)

77. D.M. Feldmann, T.G. Holesinger, B. Maiorov, et al., 1000 a cm(-1) in a 2 mu m thick YBa2Cu3O7-x film with BaZrO3 and Y2O3 additions. *Supercond. Sci. Technol.* **23**(11), 115016 (2010)
78. M. Sieger, J. Hanisch, P. Pahlke, et al., BaHfO3-doped thick YBa2Cu3O7-delta films on highly alloyed textured Ni-W Tapes. *IEEE Trans. Appl. Supercond.* **25**(3), 1 (2015)
79. P. Pahlke, M. Lao, M. Eisterer, et al., Reduced J(c) anisotropy and enhanced in-field performance of thick BaHfO3-doped YBa2Cu3O7-delta films on ABAD-YSZ templates. *IEEE Trans. Appl. Supercond.* **26**(3), 1 (2016)
80. M. Sieger, P. Pahlke, M. Lao, et al., Tailoring microstructure and superconducting properties in thick BaHfO3 and Ba2Y(Nb/ta)O-6 doped YBCO films on technical templates. *IEEE Trans. Appl. Supercond.* **27**(4), 1 (2017)
81. A. Llordes, A. Palau, J. Gazquez, et al., Nanoscale strain-induced pair suppression as a vortex-pinning mechanism in high-temperature superconductors. *Nat. Mater.* **11**(4), 329–336 (2012)
82. A. Palau, F. Valles, V. Rouco, et al., Disentangling vortex pinning landscape in chemical solution deposited superconducting YBa2Cu3O7-x films and nanocomposites. *Supercond. Sci. Technol.* **31**(3), 034004 (2018)
83. T. Horide, F. Kametani, S. Yoshioka, et al., Structural evolution induced by interfacial lattice mismatch in self-organized YBa2Cu3O7_(delta) nanocomposite film. *ACS Nano* **11**(2), 1780–1788 (2017)
84. M. Miura, B. Maiorov, M. Sato, et al., Tuning nanoparticle size for enhanced functionality in perovskite thin films deposited by metal organic deposition. *Npg Asia Materials* **9**, e447 (2017)
85. T. Maeda, K. Kaneko, K. Yamada, et al., Nanostructural characterization of artificial pinning centers in PLD-processed REBa2Cu3O7-delta films. *Ultramicroscopy* **176**, 151–160 (2017)
86. C. Cantoni, Y.F. Gao, S.H. Wee, et al., Strain-driven oxygen deficiency in self-assembled, nanostructured, composite oxide films. *ACS Nano* **5**(6), 4783–4789 (2011)
87. V. Selvamanickam, Y. Chen, X. Xiong, et al., Progress in scale-up of second-generation HTS conductor. *Phys. C Supercond. Appl.* **463**, 482–487 (2007)
88. V. Selvamanickam, Y. Chen, X. Xiong, et al., Recent progress in second-generation HTS conductor scale-up at SuperPower. *Appl. Supercond. IEEE Transactions on* **17**(2), 3231–3234 (2007)
89. V. Selvamanickam, Y. Chen, X. Xiong, et al., Progress in second-generation HTS wire development and manufacturing. *Phys. C: Supercond.* **468**(15), 1504–1509 (2008)
90. V. Selvamanickam, Y.M. Chen, X.M. Xiong, et al., High performance 2G wires: From R&D to pilot-scale manufacturing. *IEEE Trans. Appl. Supercond.* **19**(3), 3225–3230 (2009)
91. V. Selvamanickam, I. Kesgin, A. Guevara et al., *Progress in Research and Development of IBAD-MOCVD Based Superconducting Wires.*
92. V. Selvamanickam, Y. Chen, I. Kesgin, et al., Progress in performance improvement and new research areas for cost reduction of 2G HTS wires. *IEEE Trans. Appl. Supercond.* **21**(3), 3049–3054 (2011)
93. T. Aytug, M. Paranthaman, L. Heatherly, et al., Deposition studies and coordinated characterization of MOCVD YBCO films on IBAD-MgO templates. *Supercond. Sci. Technol.* **22**(1), 015008 (2009)
94. Y. Chen, V. Selvamanickam, Y. Zhang, et al., Enhanced flux pinning by BaZrO 3 and (Gd, Y) 2 O 3 nanostructures in metal organic chemical vapor deposited GdYBCO high temperature superconductor tapes. *Appl. Phys. Lett.* **94**(6), 062513–062513-3 (2009)
95. V. Selvamanickam, Y. Chen, J. Xie, et al., Influence of Zr and Ce doping on electromagnetic properties of (Gd,Y)-Ba-cu-O superconducting tapes fabricated by metal organic chemical vapor deposition. *Physica C-Superconductivity and Its Applications* **469**(23–24), 2037–2043 (2009)
96. V. Selvamanickam, Y. Chen, Y. Zhang, et al., Effect of rare-earth composition on microstructure and pinning properties of Zr-doped (Gd, Y)Ba2Cu3Ox superconducting tapes. *Supercond. Sci. Technol.* **25**(4), 6 (2012)

97. N.D. Khatri, G. Majkic, R.J. Wang, et al., Prefabricated metal Nanorods on Biaxially-textured templates on flexible substrates for REBCO superconductors. *IEEE Trans. Appl. Supercond.* **23**(3), 5 (2013)
98. N.D. Khatri, G. Majkic, T. Shi, et al., Pre-fabricated nanorods in RE-Ba-cu-O superconductors. *Supercond. Sci. Technol.* **26**(8), 7 (2013)
99. C.H. Lei, E. Galstyan, Y.M. Chen, et al., The structural evolution of (Gd, Y)Ba₂Cu₃O_x Tapes with Zr addition made by metal organic chemical vapor deposition. *IEEE Trans. Appl. Supercond.* **23**(3), 4 (2013)
100. Y. Liu, Y. Yao, Y. Chen, et al., Electromagnetic properties of (Gd, Y)Ba₂Cu₃O_x superconducting Tapes with high levels of Zr addition. *IEEE Trans. Appl. Supercond.* **23**(3), 4 (2013)
101. G. Majkic, Y. Yao, J.G. Liu, et al., Effect of High BZO Dopant Levels on Performance of 2G-HTS MOCVD Wire at Intermediate and Low Temperatures. *IEEE Trans. on Appl. Supercond.* **23**(3), 5 (2013)
102. V. Selvamanickam, A. Xu, Y. Liu, et al., Correlation between in-field critical currents in Zr-added (Gd, Y)Ba₂Cu₃O_x superconducting tapes at 30 and 77 K. *Supercond. Sci. Technol.* **27**(5), 7 (2014)
103. A. Xu, L. Delgado, N. Khatri, et al., Strongly enhanced vortex pinning from 4 to 77 K in magnetic fields up to 31 T in 15 mol.% Zr-added (Gd, Y)-Ba-Cu-O superconducting tapes. *Appl. Mater.* **2**(4), 8 (2014)
104. E. Galstyan, M.H. Gharahcheshmeh, L. Delgado, et al., Microstructure Characteristics of High Lift Factor MOCVD REBCO Coated Conductors With High Zr Content. *IEEE Trans. on Appl. Supercond.* **25**(3), 5 (2015)
105. V. Selvamanickam, M.H. Gharahcheshmeh, A. Xu, et al., Critical current density above 15MAcm⁻² at 30K, 3T in 2.2 μm thick heavily-doped (Gd,Y) Ba₂Cu₃O_x superconductor tapes. *Supercond. Sci. Technol.* **28**(7), 5 (2015)
106. V. Selvamanickam, M.H. Gharahcheshmeh, A. Xu, et al., High critical currents in heavily doped (Gd,Y)Ba₂Cu₃O_x superconductor tapes. *Appl. Phys. Lett.* **106**(3), 5 (2015)
107. V. Selvamanickam, M.H. Gharahcheshmeh, A. Xu, et al., Requirements to achieve high in-field critical current density at 30K in heavily-doped (Gd,Y)Ba₂Cu₃O_x superconductor tapes. *Superconductor Sci. Technol.* **28**(10), 5 (2015)
108. A.X. Xu, N. Khatri, Y.H. Liu, et al., Broad Temperature Pinning Study of 15 mol.% Zr-Added (Gd, Y)-Ba-Cu-O MOCVD Coated Conductors. *IEEE Trans. on Appl. Supercond.* **25**(3), 5 (2015)
109. A. Xu, L. Delgado, M.H. Gharahcheshmeh, et al., Strong correlation between J_c(T, H parallel to c) and J_c(77 K, 3 T parallel to c) in Zr-added (Gd, Y)BaCuO coated conductors at temperatures from 77 down to 20 K and fields up to 9 T. *Supercond. Sci. Technol.* **28**(8), 6 (2015)
110. M.H. Gharahcheshmeh, E. Galstyan, J. Kukunuru, et al., MOCVD of Heavily-Doped 25 mol.% Zr-Added (Gd, Y) Ba₂Cu₃O_{7-δ} Coated Conductors. *IEEE Trans. on Appl. Supercond.* **27**(4), 1 (2017)
111. G. Majkic, R. Pratap, E. Galstyan, et al., Engineering of Nanorods for Superior in Field Performance of 2G-HTS Conductor Utilizing Advanced MOCVD Reactor. *IEEE Trans. on Appl. Supercond.* **27**(4), 12 (2017)
112. M.H. Gharahcheshmeh, G. Majkic, E. Galstyan, et al., Control of in-field performance of 25 Mol.% Zr-added REBCO superconductor tapes. *Phys. C Supercond. Appl.* **553**, 26–32 (2018)
113. G. Majkic, R. Pratap, A.X. Xu, et al., Engineering current density over 5kAmm⁻² at 4.2K, 14T in thick film REBCO tapes. *Supercond. Sci. Technol.* **31**, 10 (2018)
114. G. Majkic, R. Pratap, A.X. Xu, et al., Over 15 MA/cm² of critical current density in 4.8 μm thick, Zr-doped (Gd,Y)Ba₂Cu₃O_x superconductor at 30 K, 3T. *Sci. Rep.* **8**, 12 (2018)
115. A. Xu, J. J. Jaroszynski, F. Kametani et al., Angular dependence of J_c for YBCO coated conductors at low temperature and very high magnetic fields. *Supercond. Sci. Technol.* **23**(1), 2010

116. A.X. Xu, Y. Zhang, M.H. Gharahcheshmeh, et al., Relevant Pinning for ab-Plane J(c) Enhancement of MOCVD REBCO Coated Conductors. *IEEE Trans. on Appl. Supercond.* **27**(4) (2017)
117. J.J. Shi, J.Z. Wu, Micromechanical model for self-organized secondary phase oxide nanorod arrays in epitaxial YBa₂Cu₃O_{7-δ} films. *Philos. Mag.* **92**(23), 2911–2922 (2012)
118. K. Takahashi, H. Kobayashi, Y. Yamada, et al., Investigation of thick PLD-GdBCO and ZrO₂ doped GdBCO coated conductors with high critical current on PLD-CeO₂ capped IBAD-GZO substrate tapes. *Superconductor Science and Technology* **19**(9), 924 (2006)
119. A. Ibi, H. Iwai, K. Takahashi, et al., Investigations of thick YBCO coated conductor with high critical current using IBAD-PLD method. *Physica C-Superconductivity and Its Applications* **426**, 910–914 (2005)
120. T. Kato, R. Yoshida, N. Chikumoto, et al., Microstructural characterization of GdBa₂Cu₃O_{7-δ} superconductive layer fabricated by in-plume pulsed laser deposition. *Physica C: Superconductivity* **471**(21), 1012–1016 (2011)
121. A. Xu, Y. Zhang, M.H. Gharahcheshmeh, et al., J(e)(4.2 K, 31.2 T) beyond 1 kA/mm² of a similar to 3.2 μm thick, 20 mol% Zr-added MOCVD REBCO coated conductor. *Scientific Rep.* **7**, 12 (2017)
122. R. Pratap, G. Majkic, E. Galstyan et al. Growth of High-Performance Thick Film REBCO Tapes Using Advanced MOCVD. *IEEE Trans. on Appl. Supercond.* Submitted, (2018)
123. Y. Jia, M. LeRoux, D.J. Miller, et al., Doubling the critical current density of high temperature superconducting coated conductors through proton irradiation. *Appl. Phys. Lett.* **103**, 12 (2013)
124. M. Leroux, K.J. Kihlstrom, S. Holleis, et al., Rapid doubling of the critical current of YBa₂Cu₃O_{7-δ} coated conductors for viable high-speed industrial processing. *Appl. Phys. Lett.* **107**(19), 10 (2015)
125. M.W. Rupich, S. Sathyamurthy, S. Fleshler, et al., Engineered Pinning Landscapes for Enhanced 2G Coil Wire. *IEEE Trans. on Appl. Supercond.* **26**(3), 31 (2016)
126. J.L. Macmanus-Driscoll, S.R. Foltyn, Q.X. Jia, et al., Strongly enhanced current densities in superconducting coated conductors of YBa₂Cu₃O_{7-x}+BaZrO₃. *Nat. Mater.* **3**(7), 439–443 (2004)
127. Y. Yamada, K. Takahashi, H. Kobayashi, et al., Epitaxial nanostructure and defects effective for pinning in Y(RE)Ba₂Cu₃O_{7-x} coated conductors. *Appl. Phys. Lett.* **87**(13), 27 (2005)
128. Y.M. Chen, V. Selvamanickam, Y.F. Zhang, et al., Enhanced flux pinning by BaZrO₃ and (Gd,Y)(₂)O-₃ nanostructures in metal organic chemical vapor deposited GdYBCO high temperature superconductor tapes. *Appl. Phys. Lett.* **94**(6), 15 (2009)

Chapter 5

Superconducting $\text{YBa}_2\text{Cu}_3\text{O}_{7-\delta}$ Nanocomposite Films Using Preformed ZrO_2 Nanocrystals via Chemical Solution Deposition



H. Rijckaert and I. Van Driessche

5.1 Introduction

People's concern about global warming and the rapid growth of the world population has prompted scientists to develop renewable electrical energy and to find new technologies with a minimum of carbon dioxide emissions. High-temperature superconducting technologies have the potential to transport electricity without resistance. In addition, their superior properties allow the development of generators with a higher power output than the conventional used designs [1, 2]. However, the implementation of these high-temperature superconductors in power applications is constrained due to the presence and movement of vortices in the presence of a medium-to-high magnetic field [2].

In this chapter, we focused on the improvement of the superconducting $\text{YBa}_2\text{Cu}_3\text{O}_{7-\delta}$ (YBCO) properties by immobilizing the vortices via the incorporation of preformed metal oxide nanocrystals as artificial pinning centers in the YBCO matrix [3]. However, the first experiments investigated in previously published scientific articles are based on YBCO nanocomposite films, growing via pulsed laser deposition (PLD) method. These nanocomposite films are commonly created with a non-superconducting perovskite-type BaMO_3 ($M = \text{Zr}, \text{Hf}, \text{and Sn}$) compound as nanocolumns into the YBCO films [4, 5]. This is done by modifying the film deposition process using the self-assembly process. These nanocolumns can generate good critical current densities (J_c) and its in-field performance is good, when the magnetic field is aligned parallel to them. However, it shows a limited J_c isotropy behavior which is an important restriction for power applications [2].

So, an enhancement of the J_c for the whole rotation in the magnetic field is necessary. This was possible through the introduction of non-correlated pinning

H. Rijckaert (✉) · I. Van Driessche
Department of Chemistry, Ghent University, Ghent, Belgium
e-mail: Hannes.Rijckaert@UGent.be; Isabel.VanDriessche@UGent.be

centers such as nanodots [6, 7]. Nevertheless, the PLD-based methods can deliver high-quality films and research has already led to deep insight into the control over the size, shape, and density of pinning centers [4, 8, 9]. However, this PLD-based method is considered to be too expensive due to the required high vacuum system during the deposition, hampering its applicability on industrial scale. For the commercial breakthrough of the implementation of high-temperature superconductors, an efficient and low-cost process becomes crucial. Over the last years, the chemical solution deposition (CSD) method has gained a lot of interest due to its low cost and easy scalability with high efficiency [10–12]. This method leads to significant advances towards economically scalable productions of high-quality superconducting films to implement the YBCO-coated conductors throughout the energy market.

5.2 Coated Conductor Architecture

After the discovery of high-temperature superconductors (HTS), lots of research was focused on the fabrication of long, strong, and flexible HTS tapes. As mentioned before, the two main disadvantages are the brittleness and the anisotropy of the material. Nowadays, there are several techniques to surmount these practical issues. The first approach was the first-generation (1G) HTS tape where $\text{Bi}_2\text{Sr}_2\text{Ca}_2\text{Cu}_3\text{O}_{10+x}$ (BSCCO-2223) wires were prepared using the *Oxide Powder in Tube* (OPiT) process. In this process, the malleable silver cladding tube are filled with the desired metal oxide powders and drawn into thin wires. These resulting small, individual wires are enclosed by a large silver tube and further drawn into a wire. This process results into fine parallel filaments of individual wires in a silver matrix, leading to the BSCCO-2223 superconductor (10^5 A cm^{-2}) with uniaxial crystal alignment with parallel aligned CuO planes after the multi-stage annealing and rolling processing [13]. Most prototypes and early stage commercial HTS systems are realized with 1G-HTS tapes. However, the use of 1G-HTS tape conductor for commercial equipment has already been greatly restricted by the high production price of the tape, due to the requirement of a large amount of silver (60% of total volume). So, it is desirable to reduce the production cost. Besides, BSCCO-2223 has a very high anisotropy (value of 30) and a low irreversible magnetic field (H_{irr}) which decreases the superconducting properties drastically when a small applied magnetic field is applied. This means that the operating conditions of these 1G-HTS tapes are limited to temperatures lower than 25 K [14, 15].

To offer the perspective for a more economical mass production and to overcome the low performances in high magnetic fields, second-generation (2G) HTS tapes or the so-called coated conductors (CCs) architecture was developed to fabricate flexible YBCO-HTS tapes. In contrast to 1G-HTS tapes, where the processing to thin filaments was preferred, 2G-HTS tapes are now based on thin film technology with multilayer architectures (e.g., protective layer/epitaxial YBCO layer/buffer layers) deposited onto metallic substrates. But this process is more complicated

compared to the OPiT process for the production of BSCCO due to the necessity of the epitaxial texture of YBCO. When the deposited YBCO is grown directly on the metallic substrate, it leads to a polycrystalline film with high-angle grain boundaries due to the high lattice mismatch, resulting in poor superconducting properties. In addition, the metallic substrates must also contribute to the stability and flexibility of the 2G-HTS tapes. Taking this into account, the substrates can be created according to three different strategies: *Ion Beam Assisted Deposition* (IBAD), *Inclined Substrate Deposition* (ISD), and *Rolling-Assisted Biaxial Texture Substrate* (RABiTS) [16]. The IBAD and ISD approach deliver high-quality CCs where the desired texture is induced via the growth of buffer layers on polycrystalline stainless steel or Hastelloy substrate. However, IBAD uses ion beam bombardment while ISD uses electron beam evaporation in high-vacuum conditions which is not interesting for industrial scalability due to the high investment costs [17]. The RABiTS approach was introduced to allow growing of textured buffer layers without using vacuum conditions. Here, an untextured face-centered cubic metallic substrate was multiple cold rolled and recrystallized to obtain a biaxial ($h00$) texture upon which epitaxial buffer layers can be deposited [18]. Thereby, the ceramic buffer layers are required to act as a texture template or texture transfer layer depending on the substrate approach. For this purpose, the lattice mismatch between buffer and superconducting layers should be as low as possible. These buffer layers can also act as a barrier in order to prevent the outdiffusion of metal ions from the substrates into the superconducting layer or the indiffusion of oxygen to avoid undesirable substrate oxidation during processing, which would cause problems in terms of mechanical stability [19]. In addition, the thermal expansion of the buffer layer needs to be similar to one of the superconducting layers in order to reduce the risk of cracking the architecture.

In general, CCs architecture is a delicate approach where buffer layers are commonly stacked on the substrate to meet all the requirements to make the growth of the biaxial textured YBCO thin film with excellent superconducting properties. Furthermore, state-of-the-art CCs are now being introduced by a variety of companies, including American Superconductor, SuperPower, Nexans, Deutsche Nanoschicht, SuNam Co., and Bruker. This path towards economic scalable productions of high-quality superconducting films allows us to implement the coated conductors throughout the energy market.

5.2.1 Chemical Solution Deposition

As CSD is a promising and low-cost technique, it makes very attractive for the fabrication of the coated conductors tape. The *ex situ* CSD deposition method offers control over the film composition on a molecular level through the control over the precursor solution chemistry and its stoichiometry. Typically, the YBCO precursor solution (Fig. 5.1, stage I), containing the required metal-organic salts and additives, is deposited on the substrate at ambient pressure. The as-deposited wet

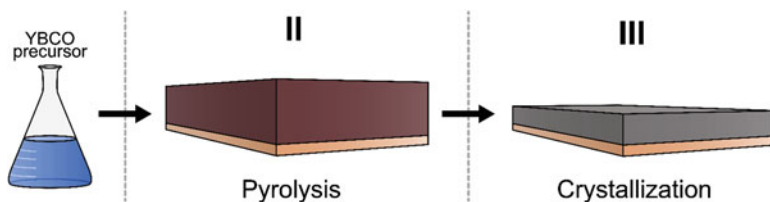


Fig. 5.1 Schematic illustration (not scaled) of the procedure for fabricating YBCO thin layer via CSD process. The process begins with (Stage I) the formulation of YBCO precursor solution. (Stage II) Deposition of YBCO precursor solution on desired substrate and its thermal decomposition. (Stage III) The pyrolyzed layer is thermally treated to crystallize epitaxial YBCO thin film

film is partially evaporated and decomposed (stage II) and subsequently crystallized into the desired crystalline YBCO thin film via an appropriate thermal processing procedure (stage III). The key to successful YBCO thin film starts with a precursor solution synthesis to obtain a stable and homogeneous precursor solution.

The most established CSD approach is based on the *ex situ* BaF_2 process and uses trifluoroacetate (TFA) salts typically dissolved in an organic solvent such as methanol. Several researchers [20, 21] have already demonstrated that this TFA route is a suitable metal-organic deposition (MOD) method to produce low-cost epitaxial YBCO thin films without the requirement of a high-vacuum system. The TFA-MOD process is based on the formation of BaF_2 as an intermediate phase, which is believed to be beneficial over the formation of BaCO_3 , as the latter can disrupt the YBCO formation due to its high decomposition temperature [22]. BaF_2 on the other hand is stable up to high temperatures, but can be decomposed at 650°C by the addition of a water vapor to the processing atmosphere [21]. This approach has expanded to one of the most successful growth methods of epitaxial YBCO films with a high J_c in self-field at 77 K on single crystal substrates.

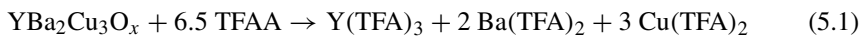
Nevertheless, some potential drawbacks can be identified in the YBCO solution preparation which could hamper the commercial implementation. Several authors have shown that the YBCO precursor can be converted into high-quality YBCO thin films by heat treatment under controlled conditions [23, 24]. Afterwards, critical current densities J_c of $>1 \text{ MA cm}^{-2}$ were obtained. Thus, a very important feature in TFA-based YBCO processing is controlling the growth of YBCO during the thermal treatment. However, the presence of possible impurities in YBCO precursor solutions can degrade the final microstructure and superconducting properties of the YBCO thin film due to the improper decomposition of the precursor [2, 3]. Araki et al. [25] have shown that the synthesis procedure for the preparation of TFA salts which starts from acetates and trifluoroacetic acid (TFAH), as described by Gupta et al. [21] exhibits an uncontrolled amount of water ($>3 \text{ wt}\%$) and other chemical impurities (i.e., acetic acid). Thus, they developed a purified YBCO precursor solution with a refining process and obtained a high J_c after a long pyrolysis step of $\sim 12 \text{ h}$ [25]. Therefore, several authors made large efforts towards the optimization of the TFA precursor synthesis procedure and the pyrolysis [26–

28]. The synthesis procedure of Roma et al. [26] starts from YBCO powder, which is dissolved in a mixture of excess trifluoroacetic acid anhydride (TFAA) and a small amount of TFAH (10 vol%) as catalyst resulting in the TFA metal-salts. This procedure typically generates an almost “anhydrous” TFA precursor with a water content of less than 1 wt%. However, this synthesis procedure still suffers from some disadvantages such as a long reaction time of 72 h and off-stoichiometry of TFAA. Additionally, the use of a conventional heat source (oil bath heating) results in an inefficient thermal energy transfer which may result in a temperature gradient in the reaction volume. The combination of these disadvantages may result in the formation of by-products other than the TFA metal-salts. The microwave processing method that we are introducing in this work can offer a solution to a number of problems stated above [29]. Microwave radiation provides rapid and uniform heating of the reagents and solvents by directly coupling to the molecules, hereby resulting in a more efficient energy transfer and an enhancement of the reaction rate [30, 31].

5.2.2 Preparation of YBCO Precursor Solution

In our research group, microwave heating was already introduced for nanocrystal synthesis which results in an obvious reduce of the synthesis time [32, 33]. By applying microwave radiation, we were able to dissolve commercial YBCO powder in a TFAA-acetone mixture, yielding extremely pure TFA salts. The TFA-YBCO precursor solution is prepared by dissolving desiccated commercial $\text{YBa}_2\text{Cu}_3\text{O}_x$ powder ($x \sim 6.7\text{--}9.5$) with a controlled stoichiometry of TFAA in acetone as solvent. First, the YBCO powder was dried in a vacuum oven at $150\text{ }^\circ\text{C}$ for 24 h to remove any adsorbed water. The 0.75 mmol dried YBCO powder was mixed with 6.5 equivalents TFAA and 3 mL dry acetone in a 10 mL microwave vial for the preparation of TFA-YBCO. This mixture was subjected to microwave heating under an inert atmosphere (Argon, to avoid the water absorption from the ambient) for 30 min at $100\text{ }^\circ\text{C}$ using a Discover SP CEM microwave operating at 2.45 GHz with a maximum power of 20 W. After the dissolution, a dark blue-green solution was obtained, which is centrifuged for 2 min at 3000 rpm or at a relative centrifugal force of $1620 \times g$. The supernatant was filtered with $5\text{ }\mu\text{m}$ filter and transferred to a 10 mL boiler flask and the solvent was evaporated under vacuum using a rotary evaporator. The desired mixture of TFA-YBCO became a viscous dark-green gel and is diluted with anhydrous methanol to obtain a total metal ion concentration of 1.5 mol L^{-1} . This solution is kept in sealed vials and can be stored for several months under an inert atmosphere without precipitation. This microwave-assisted method leads to a yield of about 98%, thus the YBCO powder almost completely dissolved in a stoichiometry of $\text{Y}:\text{Ba}:\text{Cu} = 1 \pm 0.01:2 \pm 0.01:3 \pm 0.01$ as confirmed by ICP-OES analysis. Compared to the conventional synthesis procedure as described by Roma et al. [26], we only used a stoichiometric amount of TFAA and removed the TFAH catalyst because microwaves themselves can be used to overcome high

activation energies for product formation by selectively coupling to intermediates in the transition states [31]. Due to this efficient energy transfer of microwave heating, the synthesis time can be facilitated [33, 34]. It results in a reduction of preparation time by a factor of 72 compared to conventional heating by oil bath as described by Roma et al. [26]. Instead, the chemical reaction of YBCO powder with TFAA via the microwave-assisted treatment is given in Eq. 5.1.



As TFAH is very hygroscopic [35] and is not introduced as catalyst in this microwave synthesis, it leads to the great advantage of the lack of water in this chemical reaction. Consequently, the water content depends now on the used solvents and starting precursors. Therefore, this microwave-assisted approach leads to a precursor solution with a very low H₂O content (<0.5 wt%, determined via the Karl Fischer method) when high purity starting products are used. Moreover, the microwave-assisted dissolution of YBCO powder always delivered highly stable TFA precursors with low water content, suitable for the deposition of YBCO films and potentially interesting for their industrial scalability.

The decomposition of the metal-organic precursor is one of the critical steps in CSD-based growth of high-quality ceramic films. TGA-DTA analysis can give detailed insights in the temperature dependency of the decomposition. Early works affirmed that TFA metal-salts start to decompose at the range between 200 and 250 °C [20]. From the TGA analysis (full black line), shown in Fig. 5.2, it can be seen that the weight loss starts at 100 °C and the precursor is fully decomposed at 340 °C with a total mass loss of around 70%. The mass loss as a function of the temperature can clearly be divided into three separate stages [3]. The first stage (from 50 to 100 °C) shows the dehydration and evaporation of organic solvents with a very small mass loss of around 2%, which is lower compared to the mass loss of 8% for non-purified TFA-YBCO precursor obtained via the conventional preparation method [25, 26], confirming the small water content. The second stage between 100 and 210 °C was previously attributed to the evaporation of coordinated solvents and results in a mass loss of approximately 10%. Starting at 210 °C, the thermo-oxidative decomposition of the TFA metal-salts takes place with a broad exothermic peak in the DTA signal which indicates the successful decomposition of the three TFA precursors, Y(TFA)₃, Cu(TFA)₂, and Ba(TFA)₂, leading to a large mass loss (~60%). As this can induce a large shrinkage during thin film processing, the third stage is considered to be the critical step in the decomposition of TFA precursors [26–28].

The TGA analysis of both microwave-assisted (full black line) and conventional (blue dotted line) heated TFA precursors starting from same TFA metal-salts shows a difference in the decay in the second stage (between 100 and 210 °C), as seen in Fig. 5.2. The broad exothermic peak of DTA signal (Fig. 5.2) of microwave-assisted TFA precursors also shows their successful decomposition. We hypothesized that the mass loss in the sample prepared by conventional heating is due to high boiling impurities, formed during the dissolution. To facilitate the analysis of the organic

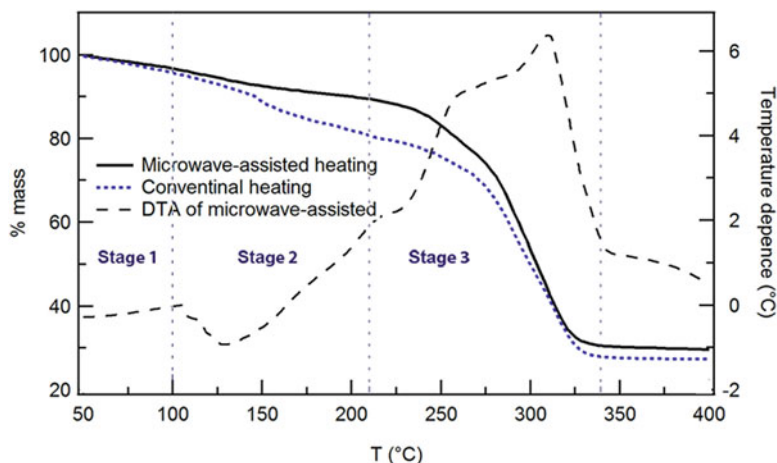


Fig. 5.2 TGA-DTA record of TFA precursor derived from microwave-assisted and conventional heating with heating ramp of 10 K min^{-1} and air atmosphere. Reprinted with permission from [29]. Copyright © 2017, John Wiley and Sons

content, both dissolution methods (microwave and conventional) were repeated in the absence of YBCO powder. After the microwave-assisted dissolution of the TFAA-acetone mixture, a yellow solution was obtained compared to a dark orange-brown solution after the conventional heating treatment, confirming the occurrence of by-products in the latter. The predominant compound 4-methylpent-3-en-2-one or mesityl oxide is recognized in the solution prepared via conventional heating without adding YBCO powder as confirmed via nuclear magnetic resonance and mass spectrometry analysis. Thus, the conventional heating mainly leads to the formation of mesityl oxide which originates from the aldol condensation of acetone acid catalyzed by TFAA [29–36]. When comparing our microwave-assisted acid dissolution with conventional oil bath heating, it becomes clear that the drastic shortening of the synthesis time by a factor of 72 and the high purity of the precursor solution led to significant advances towards more viable YBCO solution processing.

5.2.3 Generalization for the Preparation of the YBCO Precursor

Currently, CSD research is evolving towards the use of an YBCO precursor with a lower fluorine content to reduce the release of fluorinated compounds during the thermal process [27]. In general, complex additives or solvent mixtures are necessary during the preparation of low fluorine solutions to improve the stability of metal ions (mainly for copper) [37, 38]. Especially, the stabilization of the metal ions can lead to an improved growth mechanism, resulting in thin films

with high quality [39]. In this work, a low-fluorine (LF) YBCO precursor solution with a 66% reduction in fluorine content is synthesized via microwave heating. The precursor is prepared by mixing TFAA and propionic acid in acetone. This results in the formation of highly pure metal-salts with less impurities (or by-products) of the purified solution without the presence of YBCO powder. Thus, the aldol condensation is not catalyzed by the presence of propionic acid. This microwave-assisted method also results in stable YBCO precursor solution without the formation of precipitates and remains stable for several weeks without additives. It shows that the microwave-assisted method could result in YBCO precursor solutions with different contents of fluorine by adjusting the ratio between TFAA and propionate acid. However, the microwave-assisted method does not give the ability to tune YBCO stoichiometry. For this latter, we work in this chapter with LF-YBCO precursor solution prepared by dissolving Y-propionate, Ba-TFA, and Cu-propionate in a desired Y:Ba:Cu ratio plus additives in methanol. This reaction mixture is heated to 60 °C for 30 min on a hot plate and the total metal concentration of YBCO is subsequently adjusted to desired concentration (1.5 mol L^{-1}) by adding methanol.

5.2.4 Spin-Coating Technique

After obtaining a stable and reliable precursor solution, it has to be deposited on the appropriate substrate via different non-vacuum deposition techniques. These different techniques can be applied to obtain a homogeneous wet thin film which can be transformed to the crystalline thin film through thermal process. In this chapter, the spin-coating technique is commonly used because it is a rapid and useful technique for depositing thin films. However, spin-coating is a typical lab-scale technique and shows a limited scalability with regard to the processing. In contrast to spin-coating, other techniques such as dip-coating and ink-jet printing can further strengthen the industrial feasibility as these techniques can offer the opportunities for the deposition of large-scale production of coated conductors.

Spin-coating has three important aspects: wetting, thinning, and drying of the wet coating. In the first aspect, a quantity of the desired precursor solution is deposited onto an appropriate substrate via a pipette or syringe. It is important to ensure a good wetting of the precursor solution on the substrate as it results in a good coverage of the solution and thus a good coating quality. Next, the spin-coater is accelerated to a faster spinning speed (in the range of a couple of thousand rotations per minute, rpm) to spread out the precursor solution on the substrate and to remove the excess amount of precursor solution. The ramping rate and final spin speed have an impact on the final coating thickness (thinning) and may also have an influence on the uniformity of wet coating. Finally, this spin speed is kept constant for a period to dry of the wet coating via the solvent evaporation (often methanol). After spin-coating, the as-deposited substrates are subjected to further thermal processing. For Newtonian fluids, the final coating thickness (h_f) can be predicted in terms of the

key solution parameters according to:

$$h_f = c_0 \left(\frac{e}{2(1 - c_0) K} \right)^{1/3} \quad (5.2)$$

where e is the evaporation depending on the spin speed (ω) and $K = \rho\omega^2(3\eta)^{-1}$ depending on the metal concentration (c_0), density (ρ), and viscosity (η) of the precursor solution. Thus, the coatings have the best quality when the precursor solutions fulfill the fluid properties and when the solvent is not evaporating too quickly. In this work, the precursor solutions were deposited using a spin-coater model CHEMAT.

Experimental Spin-Coating of YBCO Precursor Solutions

In this work, we only show the ability to fabricate a TFA-YBCO thin film to confirm the introduction of microwave dissolution of YBCO powder and focus further on the use of LF-YBCO (66% fluorine reduction) precursor solutions as environmentally benign precursors. First, the TFA and LF-YBCO precursor solutions were deposited on (100)-LaAlO₃ single crystal substrates by means of spin-coating. Prior to coating, the substrates were first rinsed with isopropanol and afterwards heated to 400 °C on a hot plate in air to remove adsorbed organics and to improve wettability. The 1.5 M TFA-YBCO or 1.08 M LF-YBCO precursor solutions were spin-coated with the spin rate of 2000 rpm and a spin time of 1 min. The as-deposited layer was preheated at 65 °C for 3 min to evaporate the solvent.

Thermal Process of Fluorine-Based YBa₂Cu₃O_{7-δ} Layer

After the spin-coating, the coated gel films undergo a thermal process. The overall thermal process of fluorine-based YBCO film is already described in literature [29–40] and can be divided into three stages: (1) the thermal decomposition (pyrolysis), (2) crystallization (growth), and (3) the annealing process. The decomposition of the metal-organic precursor is one of the critical steps in CSD-based growth of fluorine-based YBCO films. The pyrolysis step (Fig. 5.3a) is implemented to remove organic constituents which have a detrimental effect on the final superconducting properties. The pyrolysis process consists of a heating rate (3–5 K min⁻¹) up to 190 °C under humid O₂ atmosphere. This wet atmosphere is introduced at 100 °C to avoid the early sublimation of Cu metal-salts. The inlet gas is humidified by passing it through a water bath maintained at room temperature. In the region between 190 and 220 °C, the densification [1] process starts which is an endothermic drying that can lead to a buckling effect. Therefore, a slow heating rate of 1 K min⁻¹ was introduced to avoid the buckling effect. Next, the metal-organic precursors [2] start to decompose between a temperature range of 220 and 400 °C (Vide infra) and it is

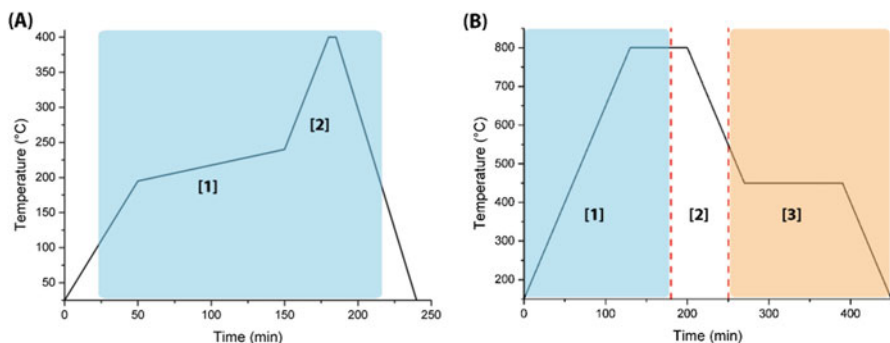
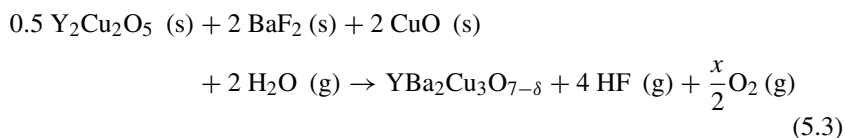


Fig. 5.3 Schematic representation of (a) the pyrolysis process and (b) the thermal process of fluorine-based YBCO layer. The regions marked in blue indicate that the flowing gas is humidified

an exothermic process, which can lead to a cracking effect [28]. After the pyrolysis step, the microstructure consists of CuO nanoparticles embedded in an amorphous matrix of $Ba_{1-x}Y_xF_{2-x}$.

To fabricate an YBCO layer (Fig. 5.3b), the pyrolyzed layers are heated [1] to a high temperature between 790 and 840 °C to crystallize the tetragonal phase of YBCO. A temperature of 840 °C cannot be exceeded because a decomposition of the YBCO phase will occur. During this heat treatment, a wet O_2 in N_2 atmosphere was introduced to decompose the BaF_2 phase (blue marked region in Fig. 5.3b) and is known as the ex situ BaF_2 process [20, 21]. However, the nucleation starts during the heating up to the crystallization temperature and takes place at the substrate interface. The YBCO growth rate depends on the water pressure, oxygen pressure, gas flow rate, and growth temperature. YBCO formation will not occur when the wet atmosphere is switched to a dry atmosphere and when cooling down [2].

The ex situ BaF_2 process is reported in literature where the $Y_2Cu_2O_5$, BaF_2 , and CuO are converted into YBCO by the release of HF by introducing H_2O at the growth interface. The overall reaction in the fluorine-based process is proposed as:



After the crystallization, the oxygenation [3] process follows, under a dry oxygen atmosphere, to convert finally the tetragonal $YBa_2Cu_3O_6$ phase into the superconducting orthorhombic YBCO phase. This process takes place between 350 and 600 °C. The dwell time is depending on the used oxygenation temperature. Theoretically, a lower temperature gives rise to better superconducting properties. However, a low temperature leads to a decrease in O_2 diffusion in the YBCO layer.

Structural Properties

The epitaxial quality of the YBCO thin film was analyzed by θ - 2θ diffraction patterns. The X-ray diffraction (XRD) spectrum of TFA-YBCO (Fig. 5.4) shows very strong (00ℓ) YBCO reflections— $2\theta = 22.8^\circ$ (003), 30.6° (004), 38.5° (005), and 46.6° (006)—without any sign of random YBCO or impurities. Next, the thin film should exhibit a smooth and homogeneous microstructure in order to achieve a J_c . Structural properties were characterized with an FEI Nova 600 Nanolab Dual Beam focused ion beam (FIB) scanning electron microscope (SEM) and a JEOL JEM 2200-FS transmission electron microscope (TEM). For the TEM measurements, a cross-sectional lamella was cut via the FIB in situ lift out procedure with an Omniprobe™ extraction needle and top cleaning. TEM has accelerating voltages of 60–300 kV which leads to an atomic resolution because the electrons exhibit a very small wavelength. It makes a very powerful technique for obtaining crystallographic information of the samples. In this chapter, the TEM analysis of YBCO film was investigated in-house with JEOL 2200FS TEM operating at 200 kV with a post-sample spherical aberration correction. Several TEM-modes were used throughout this work to obtain a specific amount of information. Crystallographic information can be obtained by high-resolution TEM in combination with selected area electron diffraction patterns. Bright field TEM was investigated to see the defects present in the matrix. Compositional information was observed via high-angle annular dark field (HAADF) STEM. This HAADF-STEM technique is highly sensitive to variations in the atomic number of atoms in the sample (Z-contrast images). Foreign phases in the YBCO matrix were determined via energy dispersive X-ray (EDX) spectroscopy in HAADF-STEM. SEM analysis shows that the thickness of the TFA-YBCO film is 200–250 nm determined from the cross-sectional view. More importantly, it is also clear from this cross-section and surface (Fig. 5.5a) that the film is homogeneous and crack-free without the presence of any a/b -oriented grains, which could decrease the superconducting properties.

In Fig. 5.5b, the $\text{LaAlO}_3/\text{TFA-YBCO}$ interface was studied by high-resolution (HR) TEM, which confirms that the YBCO layer grows fully (00ℓ) -oriented without the formation of secondary phases. The selected area electron diffraction (SAED) pattern is shown in the inset of Fig. 5.5b which further confirms the excellent biaxial alignment and the cube-on-cube orientation relationship between TFA-YBCO and LaAlO_3 . These excellent structural properties yielded TFA-YBCO films with J_c up to 3.5 MA cm^{-2} in self-field at 77 K (measured inductively with a voltage criterion of $50 \mu\text{V}$ in a Theva Cryoscan™ system), similar to the results obtained via the conventional TFA precursors by Roma et al. [26]. The LF-YBCO thin film, starting from 1.08 M LF-YBCO precursor solutions, shows the presence of a Y-rich secondary phases such as Y_2O_3 and $\text{Y}_2\text{Cu}_2\text{O}_5$ on the LF-YBCO surface as shown on SEM image (Fig. 5.5c). Nevertheless, compared to the standard TFA-YBCO thin film, the YBCO surface of the LF-YBCO film shows better homogenous and dense layers with a thickness of 250–270 nm (see inset Fig. 5.5c). The epitaxial growth was observed for the LF-YBCO precursor, giving rise to superconducting performances with J_c up to 4 MA cm^{-2} in self-field at 77 K compared to Palmer

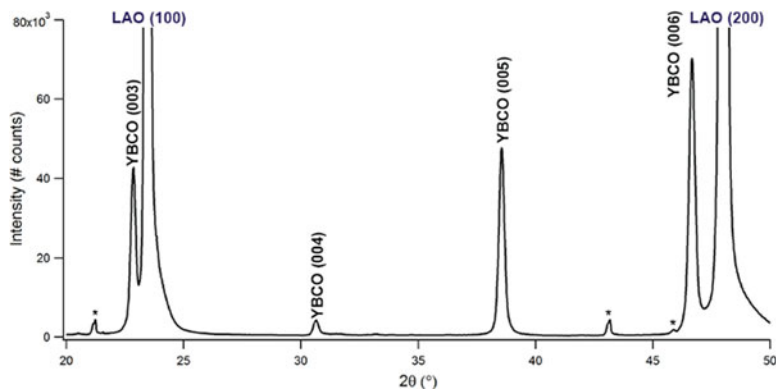


Fig. 5.4 The XRD diffraction θ - 2θ of a fully grown TFA-YBCO thin film on a LaAlO_3 substrate. (LAO and YBCO reflections by the secondary radiation of X-ray tube are marked with an asterisk.) Reprinted with permission from [29]. Copyright © 2017, John Wiley and Sons

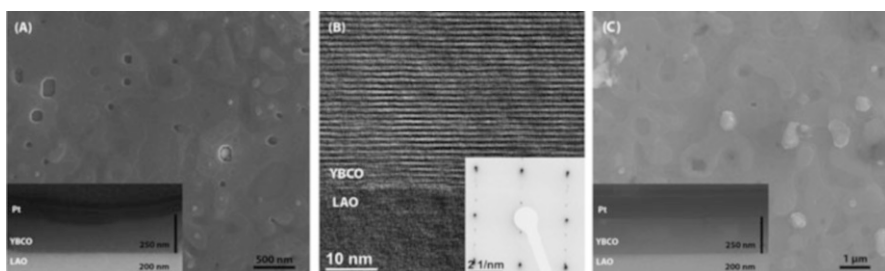


Fig. 5.5 TFA-YBCO thin film obtained after modifying the wetting behavior and the deposition parameters: (a) Topographical SEM image with cross-sectional view as inset and (b) HRTEM of LAO [100]/YBCO [001] interface (inset shows diffraction pattern). LF-YBCO thin film: (c) Topographical SEM image with cross-sectional view as inset. Reprinted with permission from [29]. Copyright © 2017, John Wiley and Sons

et al. [37]. As LF-YBCO processes are more environmentally benign, we focused on use of LF-YBCO precursors in this chapter which is suitable for industrial production.

5.2.5 Dip-Coating Technique

The dip-coating method is known as one of the simplest scalable deposition techniques and can be divided into three important stages, namely (1) immersion and dwell time, (2) drainage, and (3) evaporation of the solvent. The substrate is first immersed in the precursor solution reservoir with a constant speed followed by a certain dwell time for completing the wetting. The substrate is subsequently

withdrawn from the precursor solution with a constant speed. The thin wet film of precursor solution is entrained on the substrate and excess liquid will drain. The solvent will start to evaporate, forming the as-deposited thin film. This technique looks simple, however, the thickness of wet thin film is controlled by the Landau-Levich equation (Eq. 5.4) which describes the experimental thickness via the withdrawal speed (v , mm min⁻¹), gravitational forces (g , 9.81 m s⁻²), and the rheological parameters (e.g., the density ρ , the viscosity η , and the surface tension γ) of the solution precursor.

$$d = \frac{0.94(\eta v)^{2/3}}{\gamma^{1/6}(\rho g)^{1/2}} \quad (5.4)$$

In this coating process, there is an important link between the structure of the solution and the final thickness of the deposited film. The critical thickness may not be exceeded as it results in cracking or less uniformity of the wet thin film on the substrate. It is worth noting that this simple dip-coating is limited for this application due to fast evaporation of solvents (e.g., methanol) and contamination by the atmosphere due to open coating reservoir and long-term operation, resulting in the complete use of the precursor solution. In this work, we will use this dip-coating technique on industrial metallic substrates because it is very close to the slot-die coating technique which is often used in industry due to their similar uniformity of coating and solvent evaporation rate [41].

Experimental Dip-Coating of YBCO Precursor Solutions

The major issue for high superconducting performance is the orientated growth of the superconducting layer on a desired substrate. Therefore, a technical substrate—highly cube textured Ni-5 at %W (Ni5W) tapes—with chemical solution deposited La₂Zr₂O₇ (LZO) and a CeO₂ buffer layers were used (Fig. 5.6). However, the major drawback of the CeO₂ thin layer as a growth template for YBCO is the formation of barium cerate (BaCeO₃) as a secondary phase at the CeO₂/YBCO interface during the thermal process, resulting in barium deficiency into the YBCO film. It subsequently leads to poorer superconducting properties due to the presence of YBCO misorientation and the formation of undesired secondary phases. However, the fact is that CeO₂ layer is essential for the epitaxial growth of CSD-based YBCO layer. So, it is desirable to suppress the formation of BaCeO₃ phase by accurate control of the optimized process parameters of YBCO crystallization. When introducing a typical YBCO crystallization process at 800 °C with a slow heating rate (5 K min⁻¹) under 100 ppm O₂ in N₂ atmosphere on the pyrolyzed YBCO on Ni5W tapes, it results to more formation of the secondary phases—BaCeO₃ and Ba_xCu_yO_z phases—and less (00 ℓ) YBCO texture compared to YBCO on LaAlO₃ substrate (see Fig. 5.7). So, a strict optimization of the YBCO crystallization for YBCO layer on Ni5W tape is essential.

Fig. 5.6 Relative orientation of the layer-layer system of Ni5W-LZO-CeO₂-YBCO and its HAADF-STEM overview [19]

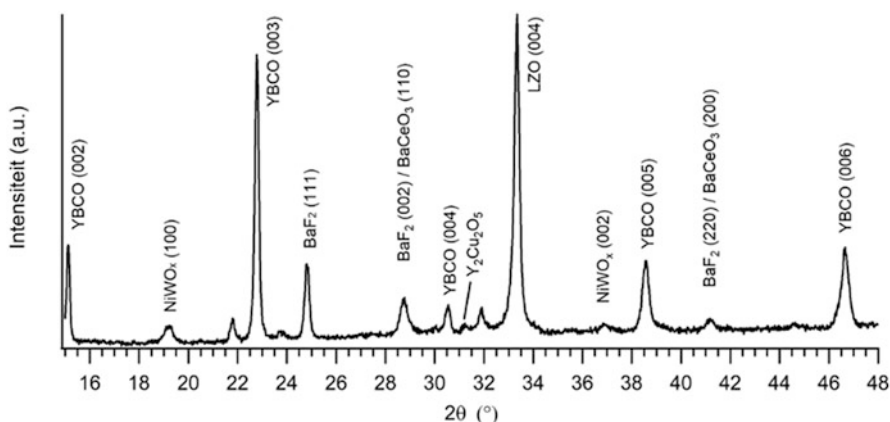
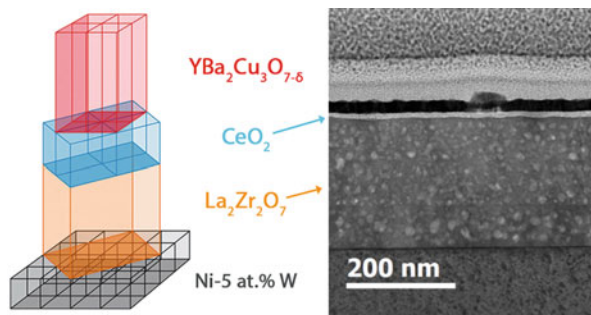


Fig. 5.7 The XRD diffraction θ - 2θ of YBCO layer on Ni5W tape after the same thermal processing of LaAlO₃ substrate. (Heating rate with 5 K min⁻¹ to 800 °C under wet 100 ppm O₂ in N₂ atmosphere with a dew point of 23 °C)

In this work, a highly textured Ni5W tape with triple LZO buffer layers and a CeO₂ cap layer was used, shown in Fig. 5.6. These buffer layers were coated in reel-to-reel processes on 10 nm wide rolling-assisted biaxially textured substrate. To build a thicker YBCO film via the dip-coating technique without any formation of cracks during the pyrolysis, Falter et al. [42] has shown four different methods: (1) Increasing the thickness using higher concentration of YBCO precursor solution, multiple deposition of YBCO precursor solution with (2) a pyrolysis step between each coating step or (3) without any pyrolysis step between, (4) withdrawing the substrate faster out the precursor solution.

In this work, we describe how to increase the YBCO film's thickness up to 450 nm via method (4). The low-fluorine (LF) YBCO precursor solution is prepared with dissolving Y-propionate, Ba-TFA, and Cu-propionate in methanol at 60 °C for 30 min on a hot plate in the ambient with YBCO concentration of 0.9 M, resulting in

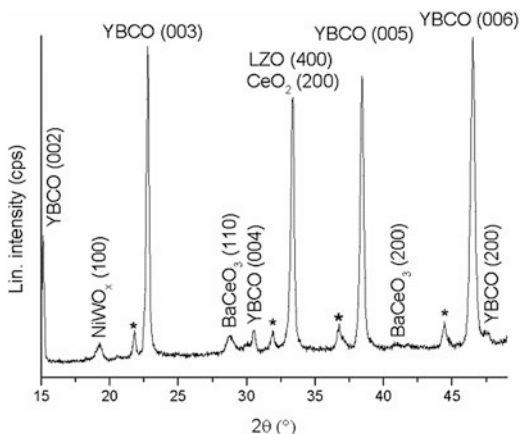
Table 5.1 The relationship between drawing speed of dip-coating and its thickness after pyrolysis and YBCO crystallization

Drawing speed mm min^{-1}	Film thickness (nm)	
	After pyrolysis	After crystallization
160	1200	660
130	800	455
100	500	315
70	400	245
40	300	200

a viscosity of 8.5 cP. This off-stoichiometric leads to Y-rich and Ba-poor films and results in high critical current density [43]. Priority to the dip-coating, the Ni5W substrates are cleaned by then washing with isopropanol and subsequently heat treated at 400 °C for 5 min to remove organic adsorbents. Afterwards, the substrates are dipped into the precursor solution and withdrawn out vertically with a speed in the range of 40–160 mm min^{-1} (Table 5.1). After the dip-coating procedure, the back-side of Ni5W substrate was cleaned with acetone to remove the excess wet film. Subsequently, the as-deposited Ni5W substrates undergo thermal process (pyrolysis, YBCO crystallization, and annealing). The thickness after pyrolysis and after YBCO crystallization was verified via FIB cross-sectional SEM images. The increase in thickness of YBCO layer is in line with the higher drawing speed while the pyrolyzed films are reduced with the factor after YBCO crystallization.

We dipped the cleaned Ni5W substrate into the YBCO precursor solution, left it there for 10 s and vertically drawn it out upwards with a drawing speed of 100 mm min^{-1} . After drying at 65 °C on a hot plate in the ambient to evaporate methanol for 5 min, the procedure is repeated with a drawing speed of 60 mm min^{-1} . This second procedure does not increase the film's thickness twice but makes the wet film more compact which leading to a better surface homogeneity after the thermal process. After full thermal process with a heating rate of 100 K min^{-1} , the thickness is 450 nm as verified via cross-sectional SEM image. The fast heating rate of 100 K min^{-1} was obtained via direct insertion of the decomposed films into a preheated tube furnace at 815 °C for 45 min in a flowing N_2 atmosphere containing 500 ppm O_2 . The inlet gas was humidified by passing it through a water bath maintained at 25 °C. After YBCO crystallization, the samples underwent an annealing procedure under pure O_2 atmosphere for 2 h. This fast heating rate and 500 ppm O_2 atmosphere during YBCO crystallization were introduced to accelerate the YBCO growth because the slow heating rate of 5 K min^{-1} results in more formation of large secondary phases such as $\text{Ba}_x\text{Cu}_y\text{O}_z$

Fig. 5.8 XRD θ - 2θ patterns of a fully processed YBCO film on Ni5W substrate, indicating good epitaxial quality. (Reflections by the secondary radiation of X-ray tube are marked with an asterisk)



and $Y_2Cu_2O_5$. These secondary phases can be ruled out by introducing the modified thermal process as shown on XRD θ - 2θ pattern (Fig. 5.8). There are also strong (00ℓ) YBCO reflections— $2\theta = 15.2^\circ$ (002), 22.8° (003), 30.6° (004), 38.5° (005), and 46.6° (006)—indicating good epitaxial quality of the YBCO film.

This excellent epitaxial growth leads to a T_c of 87.5 K and a critical current density of 0.2 MA cm^{-1} . These poor superconducting properties are due to the presence of large secondary phases (such as $Ba_xCu_yO_z$ and $Y_2Cu_2O_5$) in the YBCO matrix as observed in the HAADF-STEM image (Fig. 5.9). However, the YBCO layer shows the typical YBCO topographical structure (Fig. 5.10a and diffraction patterns on Fig. 5.9b), but with the presence of very large $Y_2Cu_2O_5$ phase (Fig. 5.10b in the YBCO matrix and Fig. 5.9c close to the YBCO/ CeO_2 interface) as confirmed via EDX analysis. This additional phase is probably formed due to a higher amount of Y in the YBCO precursor solution. It is remarkable that this phase does not induce the region of lots of stacking faults (SF) in YBCO matrix. However, some SF can be observed in YBCO matrix (See Fig. 5.10d).

Nevertheless, from the microstructural analysis, we can conclude that epitaxial YBCO with some secondary phases can be grown on the coated conductor architecture (Fig. 5.10b) with a CeO_2 top layer, three stacked LZO buffer layer (diffraction pattern in Fig. 5.9c shows pyrochlore structure) onto tungsten-doped nickel substrate (diffraction pattern in Fig. 5.9d shows cubic structure). However, some $BaCeO_3$ phases can be formed due to the reactivity of CeO_2 with Ba^{2+} without affecting the growth of YBCO. Based on these preliminary results, there is still room for further optimization such as adjusting the stoichiometric ratio of Y:Ba:Cu by means of a reduction in the excess of Y in the YBCO precursor solution.

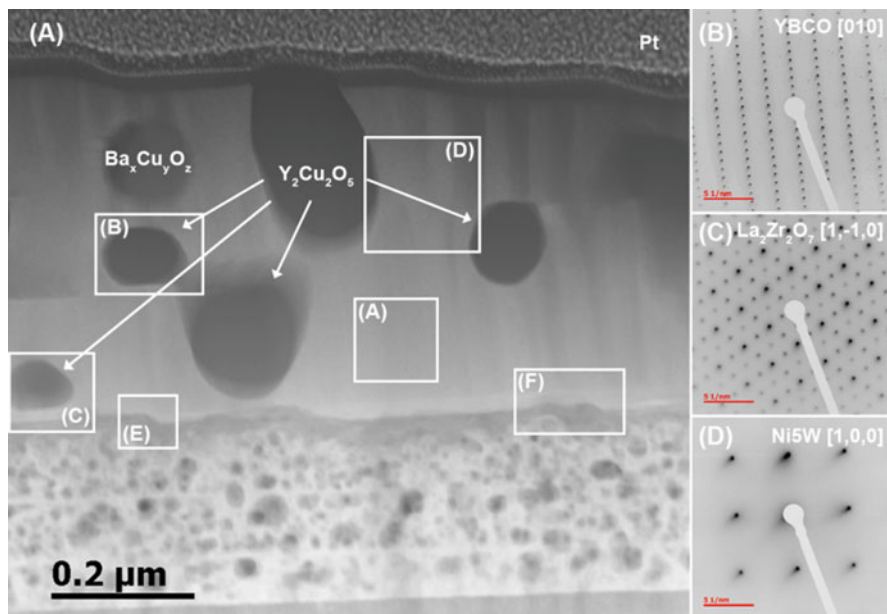


Fig. 5.9 (a) HAADF-STEM overview image of YBCO on Ni5W tape with its diffraction patterns of (b) YBCO film, (c) three stacked LZO buffer layer, and (d) nickel substrate. The marked regions in the HAADF image are enlarged in Fig. 5.10

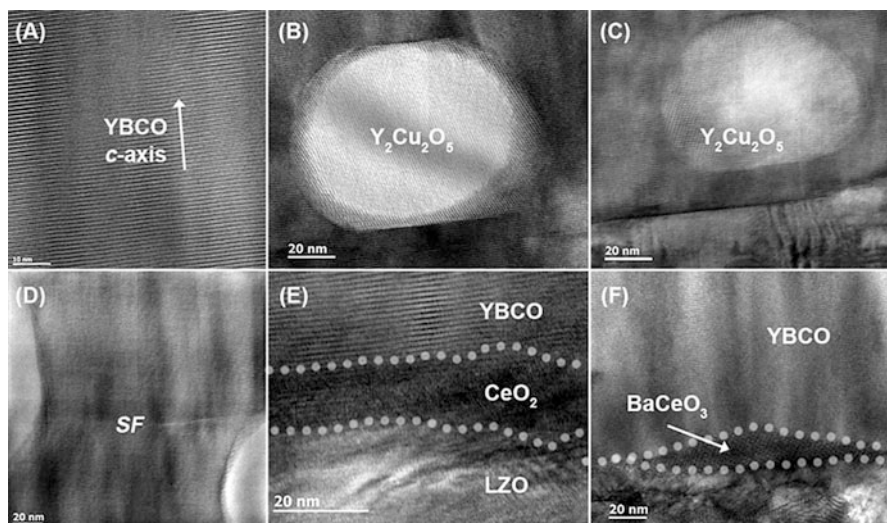


Fig. 5.10 High-resolution TEM images of YBCO film grown on Ni5W tape: (a) YBCO matrix, showing a good $(00l)$ -oriented, the presence of $\text{Y}_2\text{Cu}_2\text{O}_5$ phase in (b) YBCO matrix and (c) close to YBCO/ CeO_2 interface, (d) YBCO matrix showing a stacking fault (SF) between two secondary phases in the YBCO layer, (e) YBCO/Ni5W tape interface and (f) the formation of BaCeO_3 phase

5.3 $\text{YBa}_2\text{Cu}_3\text{O}_{7-\delta}$ Nanocomposite Architecture

The challenge is to achieve a cost-effective and high performance YBCO-coated conductor with strict requirements for power applications as generators, motors or magnets at high external magnetic fields. Unfortunately, the J_c performances start to drop in the mixed state of type II superconductor due to the vortex motion (Fig. 5.11). So, it becomes crucial to immobilize or to pin the vortices at a fixed position so *vortex pinning* has to enhance the performances of these devices. This means that the goal is to increase the pinning force and to displace the irreversibility field to a higher magnetic field. Vortex pinning is possible by the presence of pinning centers and can be divided into two categories: intrinsic defects in superconductor and artificial non-superconducting phases. As the vortex is depending on the Ginzburg-Landau parameters, namely the superconducting coherence length ξ (the core of vortex) and the London penetration depth λ , the size of the pinning center should be in the range of 2ξ (few nm) and homogeneously distributed in the superconducting matrix. The pinning centers can pin strongly or weakly according to the strength of the pinning force. Pinning is strong when the force is strong enough to deform the vortex. On the other hand, pinning centers smaller than 2ξ give a weak pinning. This means that many weak pinning centers (collective pinning) are needed to pin a vortex. So, the capability to pin vortex depends on the shape, size, and distribution of the pinning centers present in the superconducting matrix. The latter also has an influence on the superconducting matrix and its superconducting properties. Figure 5.11 (red curve) shows a simplified magnetic field dependence

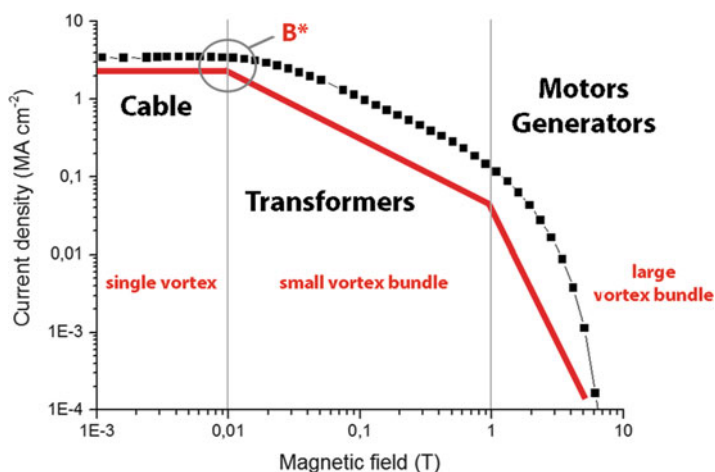


Fig. 5.11 Log-log plot showing the decay of critical current density in the presence of an external magnetic field. The requirements for devices clearly exceed the present performance at this temperature thus limiting the use of YBCO-coated conductors in high field power applications. Red curve shows a simplified magnetic field dependence of J_c to represent the pinning behavior in three different regions

of J_c to represent the pinning behavior in three different regions. The first region is a low magnetic field where the single vortex pinning is dominant, where each vortex is individually pinned to a defect and the J_c will remain constant. When the vortex–vortex interactions start above the accommodation field B_* (determined by the criterion $J_c(B^*) = 0.9J_c(0)$), the J_c will decrease according to the power-law α , but depends on the pinning center strength [44]. In this region, several vortices are pinned to each pinning center which is called as small vortex bundle pinning. When the magnetic field increases, large vortex bundle pinning makes the J_c decrease faster due to the irreversibility line [45].

5.3.1 Intrinsic Defects

Intrinsic or natural defects are the crystalline defects generated during the hetero-epitaxial thin film growth. These defects are typically oxygen vacancies, columnar defects, dislocations, twin boundaries, antiphase boundaries, stacking faults, intergrowths, etc. [46] and are created in an YBCO thin film. It is important to know that the defects are never superconducting and that they can act as vortex pinning. Noteworthy, it is not necessary that vortex pinning centers are non-superconducting but can just be worse superconducting if the order parameter is limited. The microstrained regions around the particles in the YBCO matrix are not the pinning center but they effectively increase the pinning size and thus the pinning force of the particles [47]. So, YBCO performances depend on the capabilities of the vortex pinning centers as well as on a good texture quality of the film. Because the introduction of a higher concentration of natural defects will result in a poorer texture and thus degrade the superconducting properties.

These defects can be classified on the basis of their dimensionality [48].

- 0D (punctual defects as atomic vacancies and cation disorder)
- 1D (dislocations and columnar defects)
- 2D (planar defects as grain boundaries, twin boundaries, and stacking faults)
- 3D (precipitates, secondary phases and voids)

The dimensionality and orientation of the defects must also be taken into account as an important criterion known as anisotropic pinning behavior. In this kind of pinning behavior, linear and planar defects are anisotropic pinning centers where the vortex pinning depends on the orientation of the magnetic field and is the strongest when it is in alignment with the defects. If the pinning centers are not depending on the relative orientation of the magnetic field, they are called isotropic pinning centers [49]. These pinning centers should be distributed throughout the superconducting material to pin a number of vortices as they are present with an average distance of 10–30 nm in between [12].

The effectiveness of these defects as pinning centers is also depending on the temperature and the magnetic field. The main conclusion is that the distribution, anisotropy, and dimension of the defects have an influence on the vortex pinning

properties and thus also on the performances of the YBCO. However, the intrinsic defects of superconducting materials are not strong enough to pin the vortices at high magnetic fields for the required applications. This leads to the next challenge to enhance the YBCO performances at high magnetic fields, by introducing artificial pinning centers in the superconducting materials without deterioration of the YBCO texture.

5.3.2 Introduction of YBCO Nanocomposite Layer

This benign CSD approach starting from microwave-based YBCO precursors led to good YBCO texture with good superconducting properties in self-field. Unfortunately, the J_c performances of this LF-YBCO thin film start to drop when the magnetic field is increased, due to the vortex motion. It becomes crucial to immobilize or to pin the vortices at a fixed position. So vortex pinning has to enhance the performances of electrodynamic devices. This means that the goal of this work is to increase the pinning force densities of the LF-YBCO thin film. At the moment, there are already scientific articles published concerning the introduction of non-superconducting secondary phases in the YBCO matrix via a spontaneous segregation during the fabrication of the TFA-YBCO thin film [50]. These secondary phases are introduced via the addition of extra metal-organic salts to the TFA-YBCO precursor solution to grow the desired secondary phases (e.g., Y_2O_3 , $BaZrO_3$, $BaHfO_3$, $BaCeO_3$, and Ba_2YTaO_6) [51–55]. This approach demonstrates enhanced in-field performances compared to undoped YBCO films. However, this approach offers limited control on the formation and size distribution of the nanostructures and faces issues with reproducibility. This in situ approach also requires a highly controlled heat treatment of the roll-to-roll processing equipment which makes it hard-to-reach.

To offer better control over the final microstructural properties of the YBCO nanocomposite films, colloiddally stable nanocrystals are introduced as artificial pinning centers. This preformed nanocrystal approach can provide more control over the final nanoparticles properties (e.g., size and distribution) in the YBCO matrix [2]. As this approach is very complicated, a new challenge has appeared for the researchers which have been thoroughly discussed in this work. Up to now, only a few attempts have been made at the synthesis of superconducting nanocomposite film using preformed nanocrystals (Au, CeO_2 , and ZrO_2) as artificial pinning centers in the TFA-based YBCO method [56–58]. The success has been limited because the nanocrystals are either pushed to the YBCO surface or accumulated at the substrate interface. The latter hampers the epitaxial growth of YBCO, leading to poor superconducting properties. However, it is important that the addition of preformed nanocrystals, as the so-called artificial pinning centers, can effectively decrease the magnetic field dependence of J_c . To confirm the success of this approach, the superconducting properties of ZrO_2 -doped YBCO layers on single crystal substrates were investigated via magnetic measurements. The reason is that it is easier to

study its pinning mechanism on LaAlO₃ substrates since extra parameters due to influences of the substrate are eliminated.

5.3.3 ZrO₂ Nanocrystals in YBCO Precursor Solutions

In this work, small 3–5 nm ZrO₂ nanocrystals (distorted tetragonal crystal structure [12]) were synthesized according to Joo et al. [59] and purified according to De Keukeleere et al. [60]. These nanocrystals appear to be capped with hydrophobic phosphorus-containing ligands after a heating-up synthesis with tri-*n*-octylphosphine oxide and can be redispersed in toluene, yielding a clear suspension with a solvodynamic diameter of 5.9 nm in Dynamic Light Scattering measurements (DLS, Table 5.2). However, a ligand exchange is necessary to stabilize these hydrophobic phosphorus-containing ligands capped ZrO₂ nanocrystals in the polar and highly ionic-based LF-YBCO precursor solution [29–61]. In this work, we are able to execute a ligand exchange and phase transfer ZrO₂ nanocrystals to methanol and in the LF-YBCO precursor solution with a solvodynamic diameter of 6.4 nm for the copolymer with phosphonate group, 8.1 nm for copolymer with bisphosphonate group, 5.9 nm for tartaric acid, and 5.8 nm for citric acid, confirmed by DLS analysis (Table 5.2) [62].

5.3.4 Nanocomposite Formation and the Influence of Ligands

After spin-coating of undoped and ZrO₂-doped YBCO precursors on LaAlO₃ substrates, the layers were pyrolyzed in a wet O₂ atmosphere (Fig. 5.1, stage II and Fig. 5.3a). Optically homogeneous layers were obtained without the formation of defects such as buckling or cracks, it means that the ligands do not disturb the decomposition of the LF-YBCO precursor itself. The microstructure of the pyrolyzed layers consists of CuO nanoparticles embedded in a matrix of Ba_{1-x}Y_xF_{2+x} [2]. After crystallization (Fig. 5.1, stage III and Fig. 5.3b), epitaxial YBCO was obtained for all pyrolyzed layers. The critical current density of the

Table 5.2 Overview of the LF-YBCO nanocomposite precursors with different ligands, their solvodynamic diameter in methanol, indicating the different critical current densities (self-field, inductively measured at 77 K, voltage criterion of 50 μ V)

Ligand	d_s nm	$J_{c,sf}$ (77 K) MA cm ⁻²
Phosphonate	6.4	3.1 \pm 0.1
Bisphosphonate	8.1	2.8 \pm 0.3
Citric acid	5.8	2.0 \pm 0.8
Tartaric acid	5.9	1.6 \pm 0.4

Adapted from [62]

citric acid, tartaric acid, and bisphosphonate-based nanocomposites are only in the range of 1.5–2.8 MA cm⁻² compared to 2.8 MA cm⁻² for undoped YBCO, while the phosphonate-based nanocomposite showed a critical current density of 3.1 MA cm⁻² (Table 5.2). Clearly, the nature of the ligands is crucial to the final superconducting performance of the nanocomposite. To study this effect in more detail, we analyzed samples that were thermally quenched as soon as they reached the growth temperature of 790 °C. The XRD analysis [62] features crystalline BaF₂ that is in the process of reacting towards epitaxial YBCO. The difference in BaF₂ intensities is due to the competing reaction with ZrO₂ nanocrystals (vide infra). Interestingly, the (005) reflection of YBCO is much lower for the short carboxylate-based nanocomposite, indicating a slower growth rate. We infer that the slow growth rate is symptomatic for poor epitaxial growth because of the changes in the nucleation process [3–63]. These changes can generate non-*c*-axis oriented grains, resulting in the lower critical current density.

5.3.5 Secondary Ion Mass Spectroscopy Analysis of Pyrolyzed Samples

As the growth of textured YBCO layers is a delicate process [3–29], the choice of stabilizing ligands need to be careful. Poorer YBCO growth due to the ligands is probably originated by the presence of possible impurities after the pyrolysis. Secondary ion mass spectroscopy (SIMS) has been used to analyze pyrolyzed undoped YBCO film (Fig. 5.12) and reveals the ratio of Ba/Y (red line) and Cu/Y (black line) in the amorphous matrix. This analysis indicates that more CuO

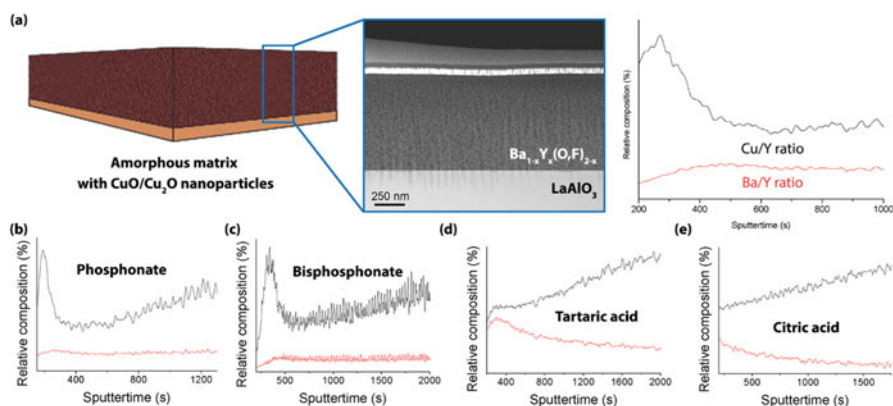


Fig. 5.12 The relative composition of Ba/Y and Cu/Y in pyrolyzed matrix of (a) undoped and (b–e) ZrO₂-doped YBCO films, determined via SIMS analysis. Reproduced from [62]

nanoparticles (probably coarsened or due to surface inhomogeneous) are on top of pyrolyzed matrix with a constant Ba/Y ratio throughout pyrolyzed sample.

Nevertheless, ZrO₂-doped pyrolyzed YBCO samples starting from different ligands show different metal distributions in the amorphous Ba_{1-x}Y_xF_{2+x} matrix. On the top surface, there is a Cu-rich zone by phosphonate and bisphosphonate-based ZrO₂-doped sample with constant Ba/Y ratio. This metal ion distribution into the matrix yields in excellent superconducting properties (e.g., high critical current density). However, short carboxylate-based ZrO₂-doped films show an inhomogeneous distribution of metal ions (i.e., irregular ratio of Ba/Y) into the matrix and result in lower superconductivity. It is possible that the quality of YBCO structure is sensitive to the inhomogeneity of metal content (especially Ba and Y) in the layer. To unravel this effect, all pyrolyzed samples underwent an YBCO crystallization process and were analyzed via XRD. Based on XRD data, short carboxylate-based nanocomposite films contain more secondary phases like as Ba₂Cu₂O₅ and Y₂Cu₂O₅ while steric dispersant-based films have minor secondary phases. It is probably due to the disturbed nucleation mechanism of the epitaxial YBCO film because the formation of the BaF₂ phase on the LAO interface is not beneficial. As SIMS indicates there are less Ba²⁺ present at the bottom layer of the pyrolyzed layer.

5.3.6 Magnetic Measurements

Good biaxial YBCO texture is an important matter but it is essential that the nanocrystals are incorporated into YBCO matrix to deliver good pinning properties. For this reason, the magnetic properties were measured with a Quantum Design Physical Property Measurement System (PPMS). The onset T_c values, defined with the AC Measurement System (ACMS) option of the PPMS from the onset temperature of the in-phase component of the AC-magnetization and calculated from the criterion of $\Delta T_c = T_c^{90\%} - T_c^{10\%}$, are listed in Table 5.3. The J_c 's of all samples are calculated using the Bean critical state model from the opening of the hysteresis loop up to 8 T, obtained by DC-magnetization [64]. The J_c was

Table 5.3 Collection of critical temperature T_c , critical current densities J_c at self-field and 1 T (magnetically measured at 77 K), accommodation field B_* , the power-law exponent α in undoped and ZrO₂-doped YBCO films on LaAlO₃ substrates

Ligand	T_c K	$J_{c,\text{mag}}$ (0 T) MA cm ⁻²	$J_{c,\text{mag}}$ (1 T) kA cm ⁻²	B_* mT	α
Undoped	90.0	2.37	41.54	7.62	0.68
Phosphonate	90.5	2.68	237.00	17.02	0.39
Bisphosphonate	91.5	2.14	79.05	9.85	0.58
Citric acid	90.5	1.65	120.32	15.52	0.40
Tartaric acid	89.0	0.74	72.76	20.06	0.40

Adapted from [62]

recorded with the electric field criterion of $215 \mu\text{V cm}^{-1}$. These magnetically measured transitions are very informative in order to get better understanding of overall film quality due to the current percolation throughout the YBCO film. The Bean critical state model is widely used because of the ease of use and its accuracy. However, the obtained J_c values must be carefully compared with the other J_c values obtained by different methods [65]. It can be concluded that the addition of nanocrystals slightly increase the magnetic transition by means of T_c and that there is probably some strain around the particles and structural defects in the YBCO matrix. However, the tartaric acid-based ZrO_2 -doped YBCO film shows a slight decrease and is probably explained due to lots of the secondary phases in the YBCO matrix. On the other hand, the magnetic field dependences of J_c 's were calculated at 77 K in maximum Lorentz force configuration in which the applied magnetic field direction is always perpendicular to the direction of the current flow and the fittings were made using a double logarithmic plot with $J_c(T, H) = A(T)B^{-\alpha}$ and are shown in Fig. 5.13. It is clear that the critical current densities are in the range of $1.5\text{--}3 \text{ MA cm}^{-2}$ except tartaric acid-based ZrO_2 -doped YBCO film, which only achieved a J_c of 0.74 MA cm^{-2} . This latter is due to a large amount of undesired secondary phases into YBCO matrix as confirmed via XRD analysis, which can degrade the superconducting film. To determine if the ZrO_2 nanocrystals in the YBCO matrix acts as the pinning centers, we studied the shape of the $J_c(B)$ curves. Copolymer, citric acid, and tartaric acid-based ZrO_2 -doped YBCO films show a smoother decay compared to undoped YBCO film. This is also confirmed by higher values of accommodation field B_* (determined by the criterion $J_c(B^*) = 0.9J_c(0)$ at

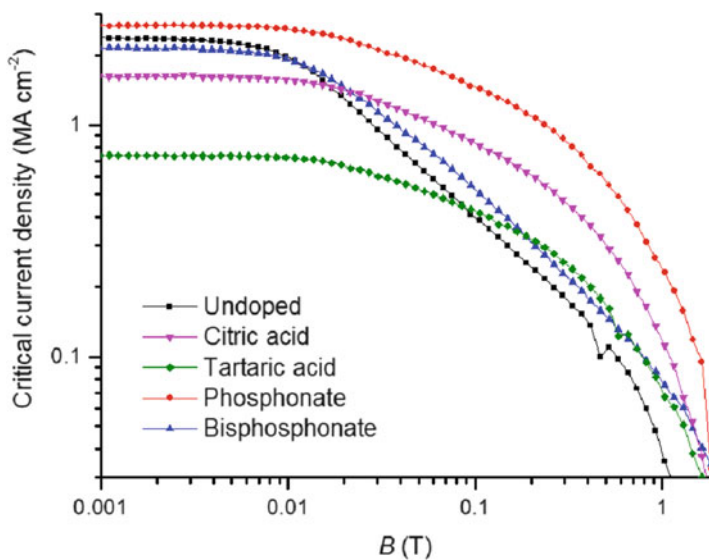


Fig. 5.13 Double logarithmic plots of critical current density vs. magnetic field B measured at 77 K for undoped and ZrO_2 -doped YBCO films on LaAlO_3 substrates. Reproduced from [62]

77 K) by lower values of the slope (power-law exponent α) in log-log plot (Table 5.3). The low field plateau below B_* is the single vortex pinning region where each vortex is pinned to a free pinning site [66]. At B_* collective pinning effects take place and a reduction of the slope of α is seen in log-log plot (Fig. 5.13).

The values of B_* and α are listed in Table 5.3. A clear difference between undoped and ZrO_2 -doped films (except bisphosphonate) can be seen. This means that the addition of preformed nanocrystals increase pinning mechanism (leading to higher B_* values) and results in slower decay (leading to lower α values) of critical current density in function of the magnetic field. However, the J_c value of tartaric acid-based ZrO_2 -doped YBCO nanocomposite is still lower than another ZrO_2 -doped films due to the presence of more secondary phases in the YBCO matrix. It is remarkable that the bisphosphonate-based ZrO_2 -doped nanocomposite did not show any improvement of pinning forces while the self-field J_c has an acceptable value (in the range of 2–2.5 MA cm⁻¹). This is explained in another work where it is clear that the ZrO_2 nanocrystals are coagulated during the YBCO growth to the size of approximately 200 nm. This particle is too large to act as a pinning center because it is not in the order of superconducting coherence length of 2–4 nm for YBCO at 77 K [62].

5.4 Epitaxial $\text{YBa}_2\text{Cu}_3\text{O}_7$ Nanocomposite Films, What Now?

Generators and other rotating devices used in energy conversion would be an ideal future application for the HTS Ni5W tapes. However, these parts of infrastructure operate at magnetic fields that would normally lower the performance of the superconductor significantly. To maintain the outstanding current transport properties of YBCO, the YBCO inks used to make the thin film need to be doped with preformed nanocrystals. In this work [12–62], it has been proven that the nanocrystal surface chemistry is a crucial step during the nanocomposite formation, yielding excellent structural properties. However, as the self-field critical currents of undoped and ZrO_2 -doped YBCO thin film show fairly low J_c values, it is an important matter to understand the mechanism and to improve it by strict optimization on the processing level. The nucleation and growth of fluorine-based YBCO systems can be found in literature [67–69] and is described as the ex situ BaF_2 process where the $\text{Ba}_{1-x}\text{Y}_x\text{F}_{2+x}$ phase transforms into $\text{Ba}(\text{O},\text{F})_2$ and Y_2O_3 composites while Y_2O_3 reacts with CuO nanoparticles to form $\text{Y}_2\text{Cu}_2\text{O}_5$ which is followed by the nucleation of the tetragonal $\text{YBa}_2\text{Cu}_3\text{O}_6$ (YBCO_6) phase at temperatures between 650 and 700 °C. However, the influence of nanocrystal addition on the nucleation and epitaxial growth process of LF-YBCO at the substrate surface is not completely understood. Understanding this process is particularly important for the fabrication of viable YBCO-coated conductors.

In previous work of the quench study [70], Ba^{2+} reacts with ZrO_2 nanocrystals to BaZrO_3 particles in the temperature range between 650 °C and 700 °C and the nucleation of YBCO occurs at ~650 °C. These results indicate that the formation

of the (002)-oriented BaF_2 superstructure is reduced between 650 and 700 °C compared to undoped YBCO. This can most likely be assigned to the reaction between the $\text{Ba}_{1-x}\text{Y}_x\text{F}_{2+x}$ phase and ZrO_2 nanocrystals, resulting in the formation of BaZrO_3 particles.

5.4.1 Introduction of an Intermediate Dwelling Step

In order to promote the nucleation of YBCO, we introduced an intermediate heat treatment step. Both undoped and 5 mol-% ZrO_2 (capped with copolymer with phosphonate group) doped YBCO precursor solutions with a total metal concentration of 1.08 M were spin-coated on LaAlO_3 substrates and pyrolyzed. The pyrolyzed YBCO films were subsequently treated to obtain the desired superconducting film with the high-temperature thermal treatment (Fig. 5.14) with a heating rate of 5 K min^{-1} to 650 °C [1] and dwelling for 60 min with 45 min in a humid 100 ppm O_2 in N_2 atmosphere and 15 min in a dry 100 ppm O_2 in N_2 atmosphere. After the additional dwelling step, fast heating to 800 °C (15 K min^{-1}) was introduced under dry conditions and switched back to humid conditions at 770 °C to avoid the formation of *alb* grains (between [1] and [2]). The inlet gas was

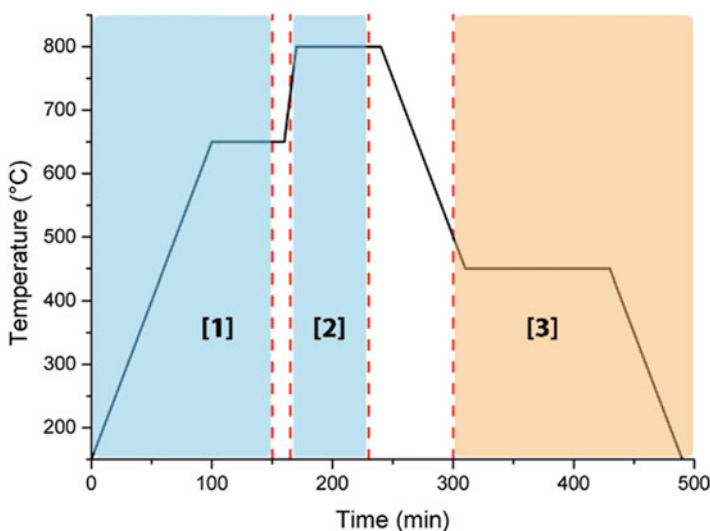


Fig. 5.14 Schematic representation of an YBCO thermal process with additional dwelling step: [1] Slow heating to the dwell temperature and dwelling under wet 100 ppm O_2 in N_2 atmosphere. After this dwelling, a fast heating to the crystallization temperature under dry 100 ppm O_2 in N_2 atmosphere was introduced to avoid the formation of *alb* grains [2]. The atmosphere was switched to a wet 100 ppm O_2 in N_2 atmosphere during the crystallization [3]. After this crystallization process, the oxygenation process under an O_2 atmosphere was introduced

bubbled through a water bath with a temperature of 23 °C. After this crystallization dwelling step of 60 min with 45 min wet, the flowing atmosphere was switched to dry atmosphere. O₂ atmosphere was introduced during the annealing step [3] at 450 °C for 2 h. This intermediate step at 650 °C clearly results in an improved J_c of 5–6 MA cm⁻² for both precursors [70]. So, ZrO₂ nanocrystals stabilized with copolymer with phosphonate group would lead to excellent superconducting properties in combination with the introduction of an intermediate dwelling step. This two-step process is used to improve the nucleation mechanism and therefore to control the microstructure.

To determine the extent of vortex pinning, transport current measurements of undoped YBCO and YBCO-5 mol-% ZrO₂ were measured and show a similar trend as the magnetic measurements. Transport critical current densities were measured in maximum Lorentz force configuration on laser-cut bridges ($l = 800 \mu\text{m}$, $w \sim 15\text{--}20 \mu\text{m}$, electrical field criterion $E_c = 1 \mu\text{V cm}^{-1}$) at magnetic fields up to 9 T in a Quantum Design PPMS. The magnetic field dependence of J_c in the maximum Lorentz force configuration was measured with logarithm steps of the increased magnetic field to see the effect of preformed nanocrystals more in details between 0 and 2 T. The $J_c(B||c)$ curves for temperatures at 77 K show clearly a higher performance (higher current) for the ZrO₂-doped nanocomposite compared to undoped YBCO (Fig. 5.15).

The pinning force curves $F_p(B)$ with $F_p = J_c \times B$ at 77 K show that the maximum pinning force density $F_{p,\text{max}}$ is more than tripled from 1.5 to 4.7 GN m⁻³ at 77 K (inset Fig. 5.15) by the introduction of 5 mol-% nanocrystal. This value is

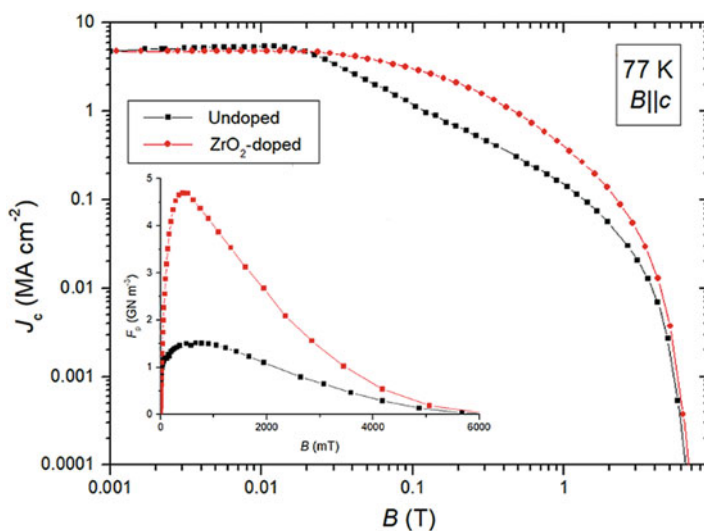


Fig. 5.15 $J_c(B)$ for undoped and 5 mol-% ZrO₂ nanocrystals doped YBCO films at 77 K and according pinning force curves at 77 K. Adapted with permission from [12]. Copyright 2017 American Chemical Society

slightly lower than the champion value ($10\text{--}22\text{ GN m}^{-3}$, 77 K) reported from the spontaneous segregation of BaZrO_3 particles in CSD-YBCO films [50]. The self-field J_c is still high for ZrO_2 -doped YBCO, so we believe that the $F_{P,\text{max}}$ can be increased by the addition of more ZrO_2 nanocrystals in the YBCO matrix provided they remain small in the order of superconducting coherence length (2–4 nm for YBCO structure at 77 K) and agglomeration-free (to reach a higher number density of defects in YBCO matrix) without affecting the YBCO microstructure [8].

The fully biaxial (00 ℓ) texture of the YBCO layer with cube-on-cube orientation between YBCO and LaAlO_3 is further corroborated by the HRTEM image of the $\text{LaAlO}_3/\text{YBCO}$ interface (Fig. 5.16a) with the SAED pattern as inset. There are no defect structures in the YBCO matrix around randomly oriented $\text{Ba}_x\text{Cu}_y\text{O}_z$ particles visible in the HRTEM image (Fig. 5.16b). Figure 5.16c shows a cross-sectional STEM image of undoped YBCO with $\text{Ba}_x\text{Cu}_y\text{O}_z$ and Y_2O_3 particles embedded in the YBCO layer. In the nanocomposite, BaZrO_3 particles are mainly homogeneously dispersed throughout the film although some are present at the interface (black dots in Fig. 5.16d). An isolated, randomly oriented BaZrO_3 particle is shown in Fig. 5.16e. The size distribution of BaZrO_3 particles shows a mean diameter of $13.0 \pm 5.5\text{ nm}$, which indicates that the initial ($3.5 \pm 0.4\text{ nm}$)

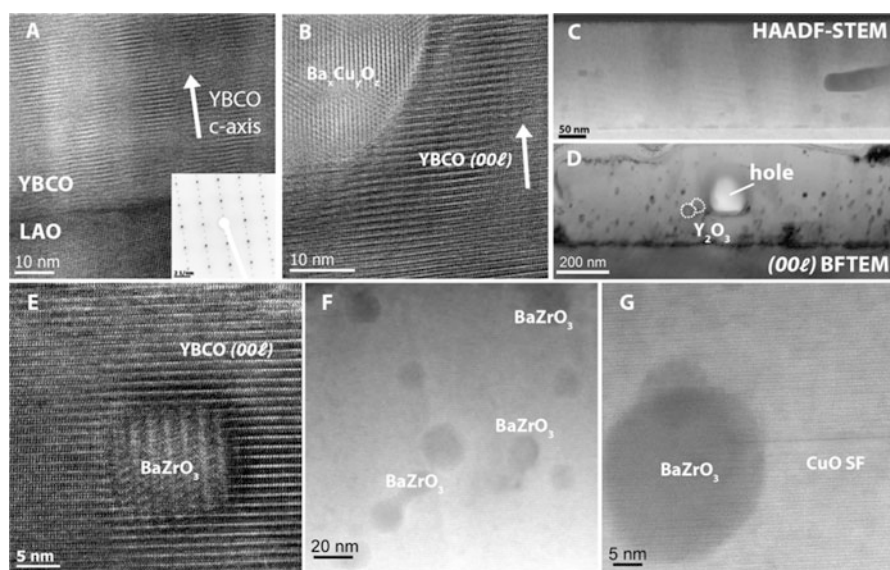


Fig. 5.16 Undoped YBCO film: (a) HRTEM images of the YBCO/ LaAlO_3 interface and its diffraction pattern (inset), (b) $\text{Ba}_x\text{Cu}_y\text{O}_z$ particles in the YBCO matrix and (c) High-angle annular dark field (HAADF)-STEM cross-sectional image. Nanocomposite film: (d) Cross-section bright field TEM image taken with a diffraction vector $\vec{g} = (003)$. (e) HRTEM image of randomly oriented BaZrO_3 particles embedded in the YBCO matrix. (f, g) HAADF-STEM Z-contrast image of YBCO-5 mol-% ZrO_2 nanocomposite. Black dots correspond to BaZrO_3 particles. Reprinted with permission from [12]. Copyright 2017 American Chemical Society

ZrO_2 nanocrystals have coarsened during the thermal process. The growth can be attributed to both their reactivity with Ba^{2+} and a slight degree of agglomeration in the film (Fig. 5.16f). The latter is driven by (1) aggregation in solution, (2) aggregation upon deposition and drying, and (3) aggregation during the thermal process. Regarding the final BaZrO_3 nanoparticle size, our results obtained with copolymer stabilized nanocrystals compare favorably with literature reports using zirconium salts in YBCO solution as nanocomposite precursors. In the latter case, the final BaZrO_3 particles were in the order of 30 nm in diameter [71], which is a 12-fold volume difference compared to the 13 nm particles described here.

The BaZrO_3 particles are mostly randomly oriented, while YBCO remains epitaxial, thus generating incoherent interfaces which can act as nucleation centers for Y124-type intergrowths. These short (<10 nm) Y124-type stacking faults are thought to be contributing for pinning [47] and seem to be absent in ZrO_2 -doped films as observed in the HRTEM images. However, we observed some local and long order Y124 regions (Fig. 5.16g) in the YBCO matrix which are possibly induced by the high amount of Y_2O_3 and non-stoichiometric amount of Ba^{2+} .

5.4.2 Influence of the Reactivity of Single Metal Oxide Nanocrystals with Ba^{2+}

As mentioned in literature [43], the off-stoichiometric of Y:Ba:Cu in YBCO precursor solution can lead to a higher self-field critical current density. Since the single metal oxide (e.g., ZrO_2) nanocrystals can react with Ba^{2+} during the YBCO growth into BaZrO_3 particles, there is also an off-stoichiometric during the YBCO formation due to the Ba^{2+} consumption. This deficiency has one advantage during the YBCO formation as Ba^{2+} deficiency results into less formation of undesired secondary phases like as $\text{Ba}_x\text{Cu}_x\text{O}_y$ in combination with more formation of in situ Y_2O_3 which can act as additional pinning centers if they remain small in the size of superconducting coherence length. To confirm that Ba^{2+} deficiency in YBCO growth would lead to higher self-field J_c , the undoped YBCO precursor solution with stoichiometric Y:Ba:Cu ratio of 1:1.8:3 (5 mol-% Ba^{2+} deficiency) was deposited on LaAlO_3 substrate and underwent a complete thermal process without an intermediate dwelling step. The superconducting properties and their magnetic dependency of this YBCO layer with Ba^{2+} deficiency were measured via MPMS system (Fig. 5.17). It is clear that the self-field J_c at 77 K is in the same order of undoped and 5 mol-% copolymer stabilized ZrO_2 -doped YBCO films. However, the behavior on increased magnetic field shows worse J_c decay compared to undoped YBCO film, which means that YBCO structure of Ba^{2+} deficiency is not improved.

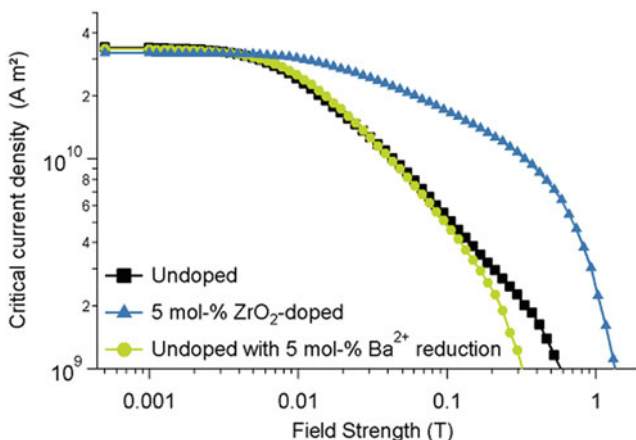


Fig. 5.17 Magnetic dependency of Y:Ba:Cu stoichiometric ratio of 1:2:3 based film without (black) or with (blue) 5 mol-% ZrO_2 nanocrystals and Y:Ba:Cu off-stoichiometric ratio of 1:1.8:3 based film without ZrO_2 nanocrystals

5.4.3 Transfer to Industrial Metallic Ni-W Substrates

This LF-YBCO CSD-based method with 5 mol-% ZrO_2 nanocrystals would be a success if these results could be transferred from LaAlO_3 substrates to industrial metallic Ni-W substrates. Despite the high J_c of undoped YBCO on LaAlO_3 substrates are not reproducible on metallic substrates, the CSD procedure via dip-coating technique is repeated with the addition of 5 mol-% ZrO_2 nanocrystals. As expected, the addition of ZrO_2 nanocrystals will delay the YBCO growth due to the Ba^{2+} -consumption but nevertheless, as shown in XRD patterns (Fig. 5.18), the YBCO layer shows a poor epitaxial texture. It is probably due to the combination of Ba^{2+} deficiency in the YBCO precursor solution, Ba^{2+} reactivity of the CeO_2 buffer layer leading to the formation of a BaCeO_3 phase and Ba^{2+} reactivity of ZrO_2 nanocrystals during YBCO growth (vide supra). To confirm this effect, the stoichiometric ratio of Y:Ba:Cu is changed with extra 5 mol-% Ba^{2+} into YBCO precursor solution which would react with ZrO_2 nanocrystals during the YBCO growth. This extra amount of Ba^{2+} results in good epitaxial texture but also in more formation of a/b -oriented YBCO as confirmed in XRD patterns (Fig. 5.18). These results are promising and will be studied in a follow-up project as YBCO film needs a perfect texture like single crystal for the high current density, which is a challenge for metallic substrates. It is due to another YBCO growth kinetic and the presence of grain boundaries. Both these can be affected by the incorporation of nanocrystals. So, an in-depth analysis is needed to understand the effect of nanocrystals on the YBCO texture by means of grain boundaries on metallic substrates to bring us a step closer to a commercial breakthrough.

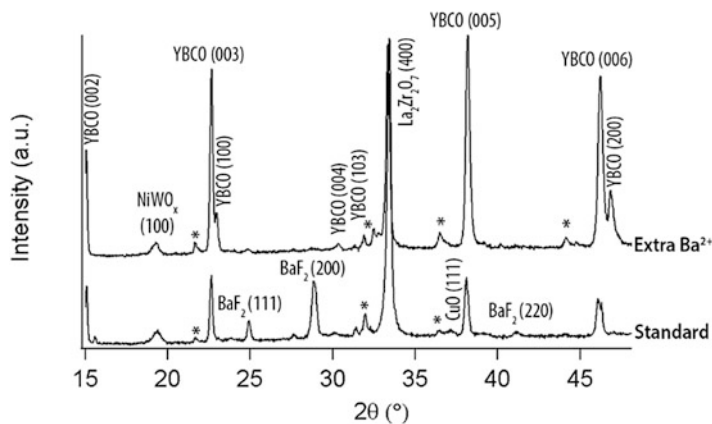


Fig. 5.18 XRD patterns of 5 mol-% ZrO_2 -doped YBCO film starting from YBCO precursor solution with and without extra 5 mol-% Ba^{2+} . (Reflections by the secondary radiation of X-ray tube are marked with an asterisk)

5.5 Conclusion

In this chapter, we have shown that the chemical solution deposition technique was suitable to fabricate a superconducting film on LaAlO_3 substrates for research purpose and on industrial metallic Ni5W substrates for the commercial market even though we have proven that it is possible to stabilize the preformed single metal oxide nanocrystals in a low-fluorine YBCO precursor solution.

The incorporation of single metal oxide nanocrystals lead to improved superconducting properties at low magnetic field. However, we believe that the introduction of the preformed double metal oxide nanocrystals can improve the final properties of YBCO nanocomposite film. Due to no reactivity of double metal oxide nanocrystals, the coarsening of these nanocrystals can be avoided if they remain agglomerate-free. This should lead to small pinning centers in the range of a few nm, enhancing the ability to pin vortices more efficiently. At the moment, the choice of stabilizing ligand is a very essential step and is the missing link between the nanocrystal synthesis and the nanocomposite formation.

The next step is to simplify the cumbersome transfer of YBCO nanocomposite film starting from preformed nanocrystals from single crystal substrate to metallic tape. On single crystal substrate, no orientation variations of YBCO are notable whereas orientation of YBCO on the metallic tape is attributed to the granularity of underlying template. This transfer is still in early stage and is still unclear what the effects of nanocrystals are on the granularity and the orientation distribution of YBCO structure. Here, additional research is required to fully understand the influence of the nanocrystal addition for optimizing both YBCO precursor solution and reel-to-reel process. This brings us one step closer to the implementation of economically efficient coated conductors in high and alternating magnetic field applications.

Acknowledgement The authors want to thank S. Van Oosterwijck (Ghent University) for dip-coating experiments and several institutes (University of Turku, IFW Dresden and Karlsruhe Institute of Technology) for their contributions.

References

1. D. Larbalestier, A. Gurevich, D.M. Feldmann, A. Polyanskii, High- T_c superconducting materials for electric power applications. *Nature* **414**(6861), 368–377 (2001)
2. X. Obradors, T. Puig, Coated conductors for power applications: materials challenges. *Supercond. Sci. Technol.* **27**(4), 044003 (2014)
3. X. Obradors, T. Puig, S. Ricart, M. Coll, J. Gazquez, A. Palau, et al., Growth, nanostructure and vortex pinning in superconducting $\text{YBa}_2\text{Cu}_3\text{O}_7$ thin films based on trifluoroacetate solutions. *Supercond. Sci. Technol.* **25**(12), 123001 (2012)
4. J. Hänisch, C. Cai, V. Stehr, R. Hühne, J. Lyubina, K. Nenkov, et al., Formation and pinning properties of growth-controlled nanoscale precipitates in $\text{YBa}_2\text{Cu}_3\text{O}_{7-\delta}$ /transition metal quasi-multilayers. *Supercond. Sci. Technol.* **19**(6), 534–540 (2006)
5. J. MacManus-Driscoll, S. Foltyn, Q. Jia, H. Wang, A. Serquis, L. Civale, et al., Strongly enhanced current densities in superconducting coated conductors of $\text{YBa}_2\text{Cu}_3\text{O}_{7-x} + \text{BaZrO}_3$. *Nat. Mater.* **3**(7), 439–443 (2004)
6. M. Malmivirta, H. Rijckaert, V. Paasonen, H. Huhtinen, T. Hynninen, R. Jha, et al., Enhanced flux pinning in YBCO multilayer films with BCO nanodots and segmented BZO nanorods. *Sci. Rep.* **7**(1), 14682 (2017)
7. J. Feighan, A. Kursumovic, J. MacManus-Driscoll, Materials design for artificial pinning centres in superconductor PLD coated conductors. *Supercond. Sci. Technol.* **30**(12), 123001 (2017)
8. T. Haugan, P. Barnes, R. Wheeler, F. Meisenkothen, M. Sumption, Addition of nanoparticle dispersions to enhance flux pinning of the $\text{YBa}_2\text{Cu}_3\text{O}_{7-x}$ superconductor. *Nature* **430**(7002), 867–870 (2004)
9. L. Opherden, M. Sieger, P. Pahlke, R. Hühne, L. Schultz, A. Meledin, et al., Large pinning forces and matching effects in $\text{YBa}_2\text{Cu}_3\text{O}_{7-\delta}$ thin films with $\text{Ba}_2\text{Y}(\text{Nb}/\text{Ta})\text{O}_6$ nano-precipitates. *Sci. Rep.* **6**, 21188 (2016)
10. G. Pollefeyt, S. Clerick, P. Vermeir, J. Feys, R. Hühne, P. Lommens, et al., Ink-jet printing of SrTiO_3 buffer layers from aqueous solutions. *Supercond. Sci. Technol.* **27**(9), 095007 (2014)
11. K. De Keukeleere, G. Pollefeyt, J. Feys, J. De Roo, H. Rijckaert, P. Lommens, et al., Chemical solution deposition of functional ceramic coatings using ink-jet printing. *Pure Appl. Chem.* **87**(3), 231–238 (2015)
12. H. Rijckaert, G. Pollefeyt, M. Sieger, J. Hänisch, J. Bennewitz, K. De Keukeleere, et al., Optimizing nanocomposites through nanocrystal surface chemistry: superconducting $\text{YBa}_2\text{Cu}_3\text{O}_7$ thin films via low-fluorine metal organic deposition and preformed metal oxide nanocrystals. *Chem. Mater.* **29**(14), 6104–6113 (2017)
13. M. Bäcker, Energy and superconductors—applications of high-temperature-superconductors. *Z. Kristallogr.* **226**(4), 343–351 (2011)
14. K.H. Sandhage, G.N. Riley, W.L. Carter, Critical issues in the OPIT processing of high- J_c BSCCO superconductors. *JOM* **43**(3), 21–25 (1991)
15. J. Maguire, J. Yuan, W. Romanosky, F. Schmidt, R. Soika, S. Bratt, et al., Progress and status of a 2G HTS power cable to be installed in the Long Island Power Authority (LIPA) grid. *IEEE Trans. Appl. Supercond.* **21**(3), 961–966 (2011)
16. M.P. Paranthaman, T. Izumi, High-performance YBCO-coated superconductor wires. *Mater. Res. Soc. Bull.* **29**(08), 533–541 (2004)
17. A. Malozemoff, S. Annavarapu, L. Fritzscheier, Q. Li, V. Prunier, M. Rupich, et al., Low-cost YBCO coated conductor technology. *Supercond. Sci. Technol.* **13**(5), 473 (2000)

18. A. Goyal, D. Norton, J. Budai, M. Paranthaman, E. Specht, D. Kroeger, et al., High critical current density superconducting tapes by epitaxial deposition of YBa₂Cu₃O_x thick films on biaxially textured metals. *Appl. Phys. Lett.* **69**(12), 1795–1797 (1996)
19. M. Bäcker, M. Falter, O. Brunkahl, B. Holzapfel, Superconducting films, in *Chemical Solution Deposition of Functional Oxide Thin Films*, ed. by T. Schneller, R. Waser, M. Kosec, D. Payne, (Springer, Wien, 2013), pp. 673–705
20. T. Araki, I. Hirabayashi, Review of a chemical approach to YBa₂Cu₃O_{7-x}-coated superconductors—metalorganic deposition using trifluoroacetates. *Supercond. Sci. Technol.* **16**(11), R71–R94 (2003)
21. A. Gupta, R. Jagannathan, E.I. Cooper, E. Giess, J. Landman, B. Hussey, Superconducting oxide films with high transition temperature prepared from metal trifluoroacetate precursors. *Appl. Phys. Lett.* **52**(24), 2077–2079 (1988)
22. P. Vermeir, I. Cardinael, J. Schaubroeck, K. Verbeken, M. Bäcker, P. Lommens, et al., Elucidation of the mechanism in fluorine-free prepared YBa₂Cu₃O_{7-δ} coatings. *Inorg. Chem.* **49**(10), 4471–4477 (2010)
23. P.C. McIntyre, M.J. Cima, M.F. Ng, Metalorganic deposition of high-*J_c* Ba₂YCu₃O_{7-x} thin films from trifluoroacetate precursors onto (100) SrTiO₃. *J. Appl. Phys.* **68**(8), 4183–4187 (1990)
24. J. Smith, M. Cima, N. Sonnenberg, High critical current density thick MOD-derived YBCO films. *IEEE Trans. Appl. Supercond.* **9**(2), 1531–1534 (1999)
25. T. Araki, H. Kurosaki, Y. Yamada, I. Hirabayashi, J. Shibata, T. Hirayama, Coating processes for YBa₂Cu₃O_{7-x} superconductor by metalorganic deposition method using trifluoroacetates. *Supercond. Sci. Technol.* **14**(9), 783 (2001)
26. N. Roma, S. Morlens, S. Ricart, K. Zalamova, J.M. Moreto, A. Pomar, et al., Acid anhydrides: a simple route to highly pure organometallic solutions for superconducting films. *Supercond. Sci. Technol.* **19**(6), 521–527 (2006)
27. A. Llordes, K. Zalamova, S. Ricart, A. Palau, A. Pomar, T. Puig, et al., Evolution of metal-trifluoroacetate precursors in the thermal decomposition toward high-performance YBa₂Cu₃O₇ superconducting films. *Chem. Mater.* **22**(5), 1686–1694 (2010)
28. K. Zalamova, N. Romà, A. Pomar, S. Morlens, T. Puig, J. Gázquez, et al., Smooth stress relief of trifluoroacetate metal-organic solutions for YBa₂Cu₃O₇ film growth. *Chem. Mater.* **18**(25), 5897–5906 (2006)
29. H. Rijckaert, J. De Roo, K. Roeleveld, G. Pollefeyt, J. Bennewitz, M. Bäcker, et al., Microwave-assisted YBa₂Cu₃O₇ precursors: a fast and reliable method towards chemical precursors for superconducting films. *J. Am. Ceram. Soc.* **100**(6), 2407–2418 (2017)
30. J.-S. Schanche, Microwave synthesis solutions from personal chemistry. *Mol. Divers.* **7**(2), 291–298 (2003)
31. J.A. Gerbec, D. Magana, A. Washington, G.F. Strouse, Microwave-enhanced reaction rates for nanoparticle synthesis. *J. Am. Chem. Soc.* **127**(45), 15791–15800 (2005)
32. J. De Roo, K. De Keukeleere, J. Feys, P. Lommens, Z. Hens, Van Driessche I. Fast, microwave-assisted synthesis of monodisperse HfO₂ nanoparticles. *J. Nanopart. Res.* **15**(7), 1778 (2013)
33. K. De Keukeleere, J. De Roo, P. Lommens, J.C. Martins, P. Van Der Voort, I. Van Driessche, Fast and tunable synthesis of ZrO₂ nanocrystals: mechanistic insights into precursor dependence. *Inorg. Chem.* **54**(7), 3469–3476 (2015)
34. J. Watté, P. Lommens, G. Pollefeyt, M. Meire, K. De Buysser, I. Van Driessche, Highly crystalline nanoparticle suspensions for low-temperature processing of TiO₂ thin films. *ACS Appl. Mater. Interfaces* **8**(20), 13027–13036 (2016)
35. P. Cayado, B. Mundet, H. Eloussifi, F. Valles, M.C. Bau, S. Ricart, et al., Epitaxial superconducting GdBa₂Cu₃O_{7-d}/Gd₂O₃ nanocomposite thin films from advanced Low-Fluorine solutions. *Supercond. Sci. Technol.* **30**, 125010 (2017). <https://doi.org/10.1088/1361-6668/aa8ffe>
36. A. Nikolopoulos, B.-L. Jang, J. Spivey, Acetone condensation and selective hydrogenation to MIBK on Pd and Pt hydrotalcite-derived Mg Al mixed oxide catalysts. *Appl. Catal. A Gen.* **296**(1), 128–136 (2005)

37. X. Palmer, C. Pop, H. Eloussifi, B. Villarejo, P. Roura, J. Farjas, et al., Solution design for low-fluorine trifluoroacetate route to $\text{YBa}_2\text{Cu}_3\text{O}_7$ films. *Supercond. Sci. Technol.* **29**(2), 024002 (2016)
38. L. Jin, C. Li, J. Feng, Z. Yu, Y. Wang, L. Lei, et al., Optimization of fluorine content in TFA-MOD precursor solutions for YBCO film growth. *Supercond. Sci. Technol.* **29**(1), 015001 (2015)
39. G. Pollefeyt, S. Clerick, P. Vermeir, P. Lommens, K. De Buysser, I. Van Driessche, Influence of aqueous precursor chemistry on the growth process of epitaxial SrTiO_3 buffer layers. *Inorg. Chem.* **53**(10), 4913–4921 (2014)
40. X. Obradors, T. Puig, A. Pomar, F. Sandiumenge, N. Mestres, M. Coll, et al., Progress towards all-chemical superconducting $\text{YBa}_2\text{Cu}_3\text{O}_{7-x}$ -coated conductors. *Supercond. Sci. Technol.* **19**(3), S13–S26 (2006)
41. S. Razza, S. Castro-Hermosa, A. Di Carlo, T.M. Brown, Research update: large-area deposition, coating, printing, and processing techniques for the upscaling of perovskite solar cell technology. *APL Mater.* **4**(9), 091508 (2016)
42. M. Falter, K. Demmler, W. Hassler, B. Schlobach, B. Holzapfel, L. Schultz, Chemical solution deposition (CSD) of $\text{YBa}_2\text{Cu}_3\text{O}_{7-x}$ films and oxide buffer layers by dip coating. *IEEE Trans. Appl. Supercond.* **13**(2), 2751–2754 (2003)
43. P. Paturi, H. Huhtinen, K. Laajalehto, R. Laiho, Reason for high critical current in thin YBCO films prepared by laser ablation from nanostructured target. *Supercond. Sci. Technol.* **13**(5), 622 (2000)
44. H. Huhtinen, K. Schlesier, P. Paturi, Growth and c-axis flux pinning of nanostructured YBCO/BZO multilayers. *Supercond. Sci. Technol.* **22**(7), 075019 (2009)
45. G. Blatter, M.V. Feigelman, V.B. Geshkenbein, A.I. Larkin, V.M. Vinokur, Vortices in high-temperature superconductors. *Rev. Mod. Phys.* **66**, 1125–1388 (1994)
46. S.R. Foltyn, L. Civale, J.L. MacManus-Driscoll, Q.X. Jia, B. Maiorov, H. Wang, et al., Materials science challenges for high-temperature superconducting wire. *Nat. Mater.* **6**(9), 631–642 (2007)
47. A. Llordés, A. Palau, J. Gázquez, M. Coll, R. Vlad, A. Pomar, et al., Nanoscale strain-induced pair suppression as a vortex-pinning mechanism in high-temperature superconductors. *Nat. Mater.* **11**(4), 329–336 (2012)
48. M. Kaname, M. Paolo, Artificial pinning center technology to enhance vortex pinning in YBCO coated conductors. *Supercond. Sci. Technol.* **23**(1), 014001 (2010)
49. T. Puig, J. Gutiérrez, A. Pomar, A. Llordés, J. Gázquez, S. Ricart, et al., Vortex pinning in chemical solution nanostructured YBCO films. *Supercond. Sci. Technol.* **21**(3), 034008 (2008)
50. J. Gutierrez, A. Llordés, J. Gázquez, M. Gibert, N. Roma, S. Ricart, et al., Strong isotropic flux pinning in solution-derived $\text{YBa}_2\text{Cu}_3\text{O}_{7-x}$ nanocomposite superconductor films. *Nat. Mater.* **6**(5), 367–373 (2007)
51. L. Lei, G. Zhao, H. Xu, N. Wu, Y. Chen, Influences of Y_2O_3 nanoparticle additions on the microstructure and superconductivity of YBCO films derived from low-fluorine solution. *Mater. Chem. Phys.* **127**(1), 91–94 (2011)
52. S. Ye, H. Suo, Z. Wu, M. Liu, Y. Xu, L. Ma, et al., Preparation of solution-based YBCO films with BaSnO_3 particles. *Phys. C* **471**(7), 265–269 (2011)
53. M. Erbe, J. Hänisch, R. Hühne, T. Freudenberg, A. Kirchner, L. Molina-Luna, et al., BaHfO_3 artificial pinning centres in TFA-MOD-derived YBCO and GdBCO thin films. *Supercond. Sci. Technol.* **28**(11), 114002 (2015)
54. F. Ding, H. Gu, T. Zhang, H. Wang, F. Qu, Q. Qiu, et al., Strong enhancement flux pinning in MOD- $\text{YBa}_2\text{Cu}_3\text{O}_{7-x}$ films with self-assembled BaTiO_3 nanocolumns. *Appl. Surf. Sci.* **314**, 622–627 (2014)

55. M. Coll, R. Guzman, P. Garcés, J. Gazquez, V. Rouco, A. Palau, et al., Size-controlled spontaneously segregated Ba₂YTaO₆ nanoparticles in YBa₂Cu₃O₇ nanocomposites obtained by chemical solution deposition. *Supercond. Sci. Technol.* **27**(4), 044008 (2014)
56. F. Martinez-Julian, S. Ricart, A. Pomar, M. Coll, P. Abellán, F. Sandiumenge, et al., Chemical solution approaches to YBa₂Cu₃O₇-Au nanocomposite superconducting thin films. *J. Nanosci. Nanotechnol.* **11**(4), 3245–3255 (2011)
57. P. Cayado, K. De Keukeleere, A. Garzón, L. Perez-Mirabet, A. Meledin, J. De Roo, et al., Epitaxial YBa₂Cu₃O_{7-x} nanocomposite thin films from colloidal solutions. *Supercond. Sci. Technol.* **28**(12), 124007 (2015)
58. K. De Keukeleere, P. Cayado, A. Meledin, F. Vallès, J. De Roo, H. Rijckaert, et al., Superconducting YBa₂Cu₃O_{7-δ} nanocomposites using preformed ZrO₂ nanocrystals: growth mechanisms and vortex pinning properties. *Adv. Electron. Mater.* **2**(10), 1600161 (2016)
59. J. Joo, T. Yu, Y.W. Kim, H.M. Park, F. Wu, J.Z. Zhang, et al., Multigram scale synthesis and characterization of monodisperse tetragonal zirconia nanocrystals. *J. Am. Chem. Soc.* **125**(21), 6553–6557 (2003)
60. K. De Keukeleere, S. Coucke, E. De Canck, P. Van Der Voort, F. Delpech, Y. Coppel, et al., Stabilization of colloidal Ti, Zr, and Hf oxide nanocrystals by protonated tri-n-octylphosphine oxide (TOPO) and its decomposition products. *Chem. Mater.* **29**(23), 10233–10242 (2017)
61. J. De Roo, S. Coucke, H. Rijckaert, K. De Keukeleere, D. Sinnaeve, Z. Hens, et al., Amino acid-based stabilization of oxide nanocrystals in polar media: from insight in ligand exchange to solution ¹H NMR probing of short-chained adsorbates. *Langmuir* **32**(8), 1962–1970 (2016)
62. H. Rijckaert, J. De Roo, M. Van Zele, S. Banerjee, H. Huhtinen, P. Paturi, et al., Pair distribution function analysis of ZrO₂ nanocrystals and insights in the formation of ZrO₂-YBa₂Cu₃O₇ nanocomposites. *Materials* **11**(7), 1066 (2018)
63. H. Chen, K. Zalamova, A. Pomar, X. Granados, T. Puig, X. Obradors, Growth rate control and solid-gas modeling of TFA-YBa₂Cu₃O₇ thin film processing. *Supercond. Sci. Technol.* **23**(3), 034005 (2010)
64. E. Gyorgy, R. Van Dover, K. Jackson, L. Schneemeyer, J. Waszczak, Anisotropic critical currents in Ba₂YCu₃O₇ analyzed using an extended Bean model. *Appl. Phys. Lett.* **55**(3), 283–285 (1989)
65. A.V. Pan, I. Golovchanskiy, S. Fedoseev, Critical current density: measurements vs. reality. *EPL* **103**(1), 17006 (2013)
66. P. Paturi, M. Malmivirta, H. Palonen, H. Huhtinen, Dopant diameter dependence of J(c)(B) in doped YBCO films. *IEEE Trans. Appl. Supercond.* **26**(3), 8000705 (2016)
67. K. Zalamova, A. Pomar, A. Palau, T. Puig, X. Obradors, Intermediate phase evolution in YBCO thin films grown by the TFA process. *Supercond. Sci. Technol.* **23**(1), 014012 (2009)
68. L.H. Jin, Y.F. Lu, J.Q. Feng, S.N. Zhang, Z.M. Yu, Y. Wang, et al., Evolution of low fluorine solution in decomposition and crystallization for YBa₂Cu₃O_y film growth. *J. Alloys Compd.* **568**, 36–41 (2013)
69. D. Wesolowski, M. Yoshizumi, M. Cima, Understanding the MOD process between decomposition and YBCO formation. *IEEE Trans. Appl. Supercond.* **17**(2), 3351–3354 (2007)
70. H. Rijckaert, J. Hänsch, G. Pollefeyt, M. Bäcker, I. Van Driessche, *J. Am. Ceram. Soc.* **102**(7), 3870–3878 (2019)
71. A. Llordes, A. Palau, J. Gazquez, M. Coll, R. Vlad, A. Pomar, et al., Nanoscale strain-induced pair suppression as a vortex-pinning mechanism in high-temperature superconductors. *Nat. Mater.* **11**(4), 329–336 (2012)

Chapter 6

High Vortex Activation Energies in the AC Magnetic Response of Superconductors Close to the DC Irreversibility Line



Lucica Miu, Ion Ivan, Alina M. Ionescu, Adrian Crisan, Dana Miu, Traian Petrisor, and Paolo Mele

6.1 Introduction

The analysis of the AC magnetic response registered at usual frequencies f (from ~ 1 Hz up to several kHz) and amplitudes h_{AC} (below approximately 15 Oe) became one of the most popular means of investigating vortex dynamics and the pinning of vortices in superconductors [1–15]. Moreover, in the framework of the strong pinning theory, a spectroscopy of the pinning landscape based on the linear AC magnetic signal has been recently proposed [16]. The phase-sensitive detection makes the AC techniques attractive, and supplemental information is obtained by varying f and h_{AC} , in addition to temperature T and the DC external magnetic field H .

As known, by applying an AC magnetic field $h(t) = h_{AC} \cos(2\pi ft)$ (where t is the time) to a superconductor, the flux variation through two identical, oppositely phased pickup coils (one of which is surrounding the specimen) leads to an overall voltage $u(t)$ proportional to the time derivative of the sample magnetic moment. This

L. Miu (✉) · I. Ivan · A. M. Ionescu · A. Crisan
Laboratory of Magnetism and Superconductivity, National Institute of Materials Physics, Magurele, Romania
e-mail: elmiu@infim.ro; ion.ivan@infim.ro; alina.ionescu@infim.ro; adrian.crisan@infim.ro

D. Miu
Laser Department, National Institute of Laser, Plasma, and Radiation Physics, Magurele, Romania
e-mail: dana.miu@infpr.ro

T. Petrisor
Center of Superconductivity, Spintronics, and Surface Science, Technical University of Cluj-Napoca, Cluj-Napoca, Romania
e-mail: traian.petrisor@phys.utcluj.ro

P. Mele
SIT Research Laboratories, Shibaura Inst. Tech. (Omiya campus), Tokyo, Japan
e-mail: pmele@shibaura-it.ac.jp

signal can be developed in a Fourier series,

$$u(t) = \sum_{n=1}^{\infty} [a_n \cos(2\pi nft) + b_n \sin(2\pi nft)], \quad (6.1)$$

with $a_n = 2f \int_0^{1/f} u(t) \cos(2\pi nft) dt$ and $b_n = 2f \int_0^{1/f} u(t) \sin(2\pi nft) dt$. The fundamental susceptibility χ_1 has the in-phase component $\chi_1' = b_1/C$, and the out-of-phase one $\chi_1'' = a_1/C$, where C is a factor depending of f and the experimental setup. The coefficients a_n and b_n in (6.1) can be analytically calculated [17], assuming, for example, that the AC field penetrates a cylindrical specimen according to the Bean model [18]. We refer below to the measured in-phase component of the AC magnetic moment, $m' = \chi_1' h_{AC}$, directly related to the presence of a screening current density J , and to the out-of-phase one, $m'' = \chi_1'' h_{AC}$. The $m''(T)$ variation exhibits a maximum, changing with f and h_{AC} , which was challenging for the interpretation of the AC magnetic response of superconductors.

In this context [19], the first type of models considers a T - and H -dependent relaxation time in the vortex system [20], with the $m''(T)$ peak appearing when the inverse of the relaxation time equals the frequency. The second type of models is based on the diffusive vortex motion and a linear resistivity, where the $m''(T)$ peak would correspond to the maximum of the ratio between the characteristic sample dimension and the penetration distance of the AC field, identified with the skin depth [21]. A third type of models deals with a nonlinear regime, where m'' is generated by the hysteretic vortex penetration [2]. In these conditions, m'' is a measure of dissipation, and the $m''(T)$ maximum at a peak temperature T_p (which decreases by lowering f) is related to the first full AC critical-state penetration starting from low temperatures. In the critical state-related models, the AC signal does depend on h_{AC} , and it is believed that it could vary with f if the critical current density itself is frequency dependent. Another alternative is to take into account the shortening of the relaxation time window with increasing f .

At relatively low h_{AC} values, a linear response [22, 23] is generated by reversible intravalley vortex oscillations. The AC perturbation (compression and tilt waves of vortices) decays within the specimen on a distance called the Campbell penetration depth. In this regime, the magnetic behavior of the vortex system is similar to a Meissner state [3].

There is no doubt that in the nonlinear regime analyzed below a thermally activated vortex-hopping process is present, as revealed by the linear variation of $\ln(f)$ with $1/T_p$ (at constant H and h_{AC}). The vortex activation energy U_{AC} in the AC magnetic response is unambiguously determined from such Arrhenius plots.

Recently, several characteristic aspects of the nonlinear AC magnetic signal of superconductors in the vortex state have been recalled [13, 24–26] in connection with the peculiar behavior of U_{AC} in the vicinity of the DC irreversibility line (IL).

The unexpectedly high U_{AC} values around and even above the IL are consistent with the dynamic critical current density as the relevant critical parameter for the AC magnetic response. The main point is a diminished effect of thermally induced vortex fluctuations on the pinning potential at short-time scales, which is of interest for the large-scale applications of high temperature superconductors.

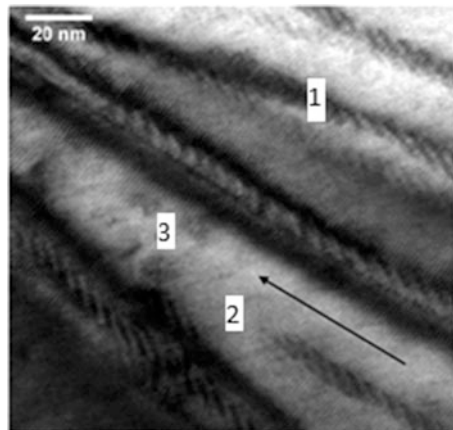
6.2 Samples and Experiments

The present analysis is based mainly on the AC and DC magnetic measurements performed for two $\text{YBa}_2\text{Cu}_3\text{O}_7$ (YBCO) films with strong pinning centers, and for almost decoupled $[\text{YBCO}]_n/[\text{PrBCO}]_4$ superlattices (Y_nPr_4), with $n = 4$ and 11 representing the thickness of the superconducting blocks in unit cells.

The first YBCO film (of dimensions $5 \text{ mm} \times 5 \text{ mm} \times 1100 \text{ nm}$) was prepared by pulsed laser deposition (PLD) from an YBCO target containing $\sim 4 \text{ vol.}\%$ BaZrO_3 (BZO) onto an Ag-nanodot decorated, (100) oriented SrTiO_3 (STO) substrate. The preparation conditions are presented in [27], and the thoroughly investigated film (denoted YBCONDBZO) has the critical temperature $T_c = 89.2 \text{ K}$ (taken at the onset of the DC diamagnetic signal in $H = 10 \text{ Oe}$). The film contains relatively long BZO nanorods, $\sim 10 \text{ nm}$ in diameter, with a separation of a few tens of nanometer (as revealed by the microstructure shown in Fig. 6.1). The observed significant nanorod splay leads to the inhibition of the detrimental double vortex-kink formation [28, 29] in DC conditions, as discussed in [30].

The second YBCO film ($\sim 2.2 \text{ mm} \times 2.2 \text{ mm} \times 400 \text{ nm}$) has embedded BZO nanorods ($\sim 4 \text{ vol.}\%$ relative to the composite volume), with a reduced splay, and Y_2O_3 (YO) nanoparticles ($\sim 1 \text{ vol.}\%$). Such films have been grown by PLD on STO-buffered MgO substrates, using an YBCO + BZO target with a thin YO sector stuck on the top. The preparation details and the microstructure can be found in

Fig. 6.1 TEM image of a cross section in YBCONDBZO [31], showing intertwined BZO nanorods (1) and YBCO nanocolumns (2) (striped and smooth regions, respectively), as well as some BZO nanoparticles (3) in YBCO. The arrow indicates the direction of the c axis of YBCO



[31], and the measured film (with $T_c = 88.6$ K) is denoted below as YBCOBZYO. The presence of nanoparticles inhibits the double vortex-kink formation as well [32, 33].

Y_nPr_4 superlattices have been obtained by sequential high-pressure DC sputtering on STO substrates, as presented in [34]. The overall thickness $d_0 = 200$ nm, and the measured specimens were disk-shaped, with the radius $R = 2$ mm. The critical temperature is 87 K for $Y_{11}Pr_4$ and 78.1 K in the case of Y_4Pr_4 . The presence of four unit-cell-thick non-superconducting PrBCO layers leads to almost decoupled superlattices [35], in the sense that the vortex correlation length is cut-off at the thickness of the YBCO blocks. These superlattices were considered here as model samples.

Some characteristic results for a slightly overdoped, plate-like $Bi_2Sr_2CaCu_2O_8$ single crystal (Bi2212, $T_c = 88$ K) in the (H, T) range of enhanced two-dimensional vortex fluctuations are also included.

The DC magnetic hysteresis curves have been registered with a commercial Quantum Design Magnetic Property Measurement System (MPMS), whereas the AC magnetic measurements have been performed with the same MPMS, or using a Physical Property Measurement System. The DC and AC fields were oriented along the c axis, as usual. The AC field amplitude was between 0.5 Oe and 6 Oe, and the frequency in the range 1 Hz–10 kHz. The demagnetization factor D was precisely determined from the initial slope of the DC magnetization curves, obtained by increasing H with a small step.

6.3 Vortex Activation Energy in the AC Magnetic Response of YBCO Films with Strong Pinning

We start our discussion with the nonlinear AC magnetic response of the relatively thick YBCO film with embedded BZO nanorods (YBCONDBZO). The temperature variation of the in-phase (screening) component m' of the AC magnetic moment and that of the dissipative (out-of-phase) one m'' for YBCONDBZO in $H = 10$ kOe are presented in Fig. 6.2. The AC signal was registered in increasing temperature (at a slow rate, of ~ 0.05 K/min), after the sample was cooled in H from above T_c down to $T = 80$ K, with $h_{AC} = 3$ Oe and f ranging between 21.5 Hz and 10 kHz. For the considered (H, T) domain, $m'(T)$ and $m''(T)$ do not depend on the field-temperature setting protocol.

As noted in Introduction, the main feature is a maximum in $m''(T)$ at the peak temperature T_p , corresponding to the first full AC critical-state penetration starting from low temperatures. An important point is that in the conditions of full AC critical-state penetration at T_p (where the magnetic relaxation at short-time scales has a significant role) the screening current density J_p is constant. While T_p decreases by lowering the frequency, $m'(T_p)$ does not change, as illustrated in Fig. 6.2 by a dashed line. For samples with the demagnetization factor D close to unity,

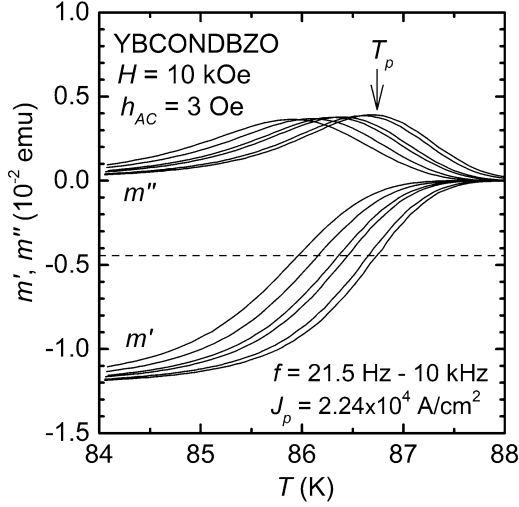


Fig. 6.2 Temperature T variation of the in-phase (m') and the out-of-phase (m'') components of the AC magnetic moment of the relatively thick film YBCONDBZO in an external magnetic field $H = 10$ kOe. The signal has been obtained with the AC field amplitude $h_{AC} = 3$ Oe, while the frequency f was between 21.5 Hz and 10 kHz, in increasing T at a slow rate (after the sample has been cooled in H from above T_c down to 80 K). The peak temperature T_p in $m''(T)$ shifts to lower values by decreasing f . The dashed line illustrates the constant $m' \sim -0.43 \times 10^{-2}$ emu at $T_p(f)$

$$J_p = 1.03h_{AC}/d, \quad (6.2)$$

where d is the film thickness [36]. In the case of YBCONDBZO, with $h_{AC} = 3$ Oe (6.2) leads to $J_p = 2.24 \times 10^4$ A/cm².

The Arrhenius plot [$\ln(f)$ versus $1/T_p$] obtained using the $T_p(f)$ data determined from Fig. 6.2 is shown in Fig. 6.3. The plot is accurately linear and supports strongly a thermally activated vortex-hopping process at $t = 1/f$ scales. The vortex activation energy U_{AC} is easily extracted with the Arrhenius law

$$f = f_0 \exp[-U_{AC}(T_p, J_p)/T_p]. \quad (6.3)$$

In (6.3), U_{AC} is in k_B units, and f_0 is a characteristic attempt frequency ($\sim 10^9$ – 10^{13} Hz [37]), which should be of the order of the phonon frequency in a vortex lattice [38]. As often noted, the fit of the $T_p(f)$ data with (6.3) is in agreement with the attempt frequency in the above domain if U_{AC} decreases linearly with increasing temperature,

$$U_{AC}(J_p, T) = U_0(J_p) \left(1 - \frac{T}{T_c}\right), \quad (6.4)$$

Fig. 6.3 The Arrhenius plot generated using the $T_p(f)$ data extracted from Fig. 6.2, where a linear fit (the continuous line) gives for YBCONDBZO in $H = 10$ kOe an apparent activation energy $U_0(J_p) \sim 5.8 \times 10^4$ K, and an attempt frequency $f_0 \sim 10^{12}$ Hz. The constant current density J_p is determined with (6.2)

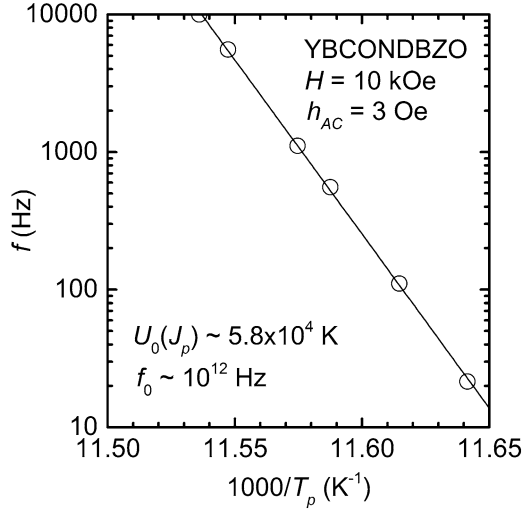
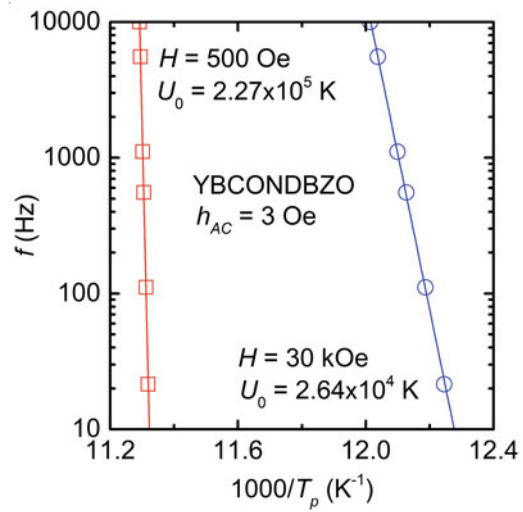


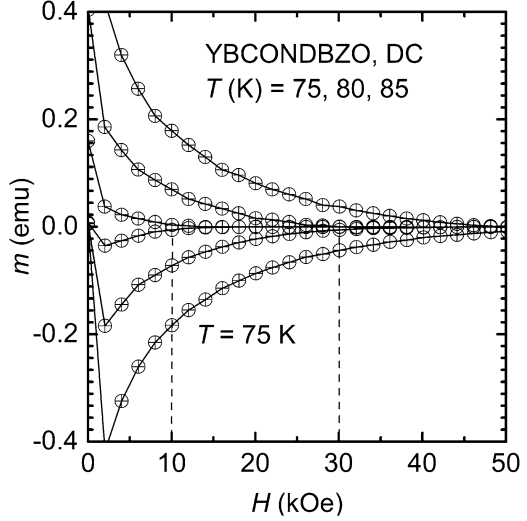
Fig. 6.4 Arrhenius plots for YBCONDBZO in $H = 500$ Oe and $H = 30$ kOe. The linear fit (represented by continuous lines) leads to $U_0(J_p) = 2.64 \times 10^4$ K at $H = 30$ kOe, while, by decreasing H to 500 Oe, $U_0(J_p) = 2.27 \times 10^5$ K



where U_0 is the apparent vortex activation energy at $T = 0$, and J_p is that from (6.2). For YBCONDBZO in $H = 10$ kOe, the linear fit in the Arrhenius plot from Fig. 6.3 supplies $U_0(J_p) = 5.8 \times 10^4$ K, and $f_0 \sim 10^{12}$ Hz. At $H = 30$ kOe, one obtains $U_0(J_p) = 2.64 \times 10^4$ K, while, by decreasing the DC field to $H = 500$ Oe, $U_0(J_p)$ overcomes 10^5 K, as shown in Fig. 6.4.

From the determined $U_0(J_p)$ values, it is of interest to extract $U_{AC}(T)$ around the IL, defined as the line in the (H, T) plane above which the irreversibility vanishes at the time scale of DC measurements. Figure 6.5 illustrates the DC magnetic hysteresis $m(H)$ curves of YBCONDBZO at several high temperatures, including

Fig. 6.5 DC magnetic hysteresis curves of YBCONDBZO at several high temperatures. The dashed lines indicate the field values $H = 10$ kOe and 30 kOe, for which the irreversibility appears, roughly, at $T = 85$ K and 80 K, respectively. However, the vortex activation energy in the AC magnetic response U_{AC} overcomes 10^3 K (see text)



$T = 80$ K (approximately, the irreversibility temperature for $H = 30$ kOe), and $T = 85$ K, where the IL is reached at $H \sim 10$ kOe.

Using (6.4), for YBCONDBZO in $H = 30$ kOe one has $U_{AC}(J_p, T = 80 \text{ K}) = 2.72 \times 10^3$ K, whereas $U_{AC}(J_p, T = 85 \text{ K}, H = 10 \text{ kOe}) = 2.73 \times 10^3$ K. Such high U_{AC} values close to the IL [11, 12] are intriguing, since on crossing the IL there is a continuous vortex system melting (thermal and disorder-induced), where the pinning energy and the thermal energy have the same order of magnitude. This means that the vortex activation energy in DC magnetic measurements $U_{DC} \sim T$. One notes that U_{AC} remains significant above the IL, whereas in the low H range U_{AC} is very high even in close proximity of T_c . For example, $U_{AC}(T = 85 \text{ K}, H = 30 \text{ kOe}) = 1.24 \times 10^3$ K, and $U_{AC}(T = 85 \text{ K}, H = 500 \text{ Oe}) = 1.07 \times 10^4$ K ($J = J_p$). Thus, the main aspect is that the pinning centers become effective at short-time ($1/f$) scales.

Written as $U_{AC} = T \ln(t/\tau_0)$, where $t = 1/f$ would be the relaxation time and $\tau_0 = 1/f_0$ is the microscopic attempt time, (6.3) suggests that the short-time relaxation in AC magnetic measurements should be different from the DC relaxation at long-time scales (flux creep). The latter is described by the general vortex-creep relation with logarithmic accuracy, $U_{DC} = T \ln(t/t_0)$ [39], in which $t_0(J, T, H)$ is a macroscopic time scale for creep [37], accounting for a thermally activated, diffusive vortex motion at relatively small mean vortex velocities.

6.4 Vortex Activation Energy in the AC Magnetic Response of Bi2212 Single Crystals and Superlattices

Unexpectedly large U_{AC} values around the IL have also been determined (with the same procedure) in the case of highly anisotropic superconductors. This is illustrated in Fig. 6.6 for Bi2212 (a) and Y_4Pr_4 (b) in $H = 5$ kOe.

At $H = 5$ kOe and the chosen temperatures ($T = 35$ K for Bi2212, and 55.5 K in the case of Y_4Pr_4), representing T_p for the highest used frequency in the Arrhenius plot (see the main panels in Fig. 6.6), the specimens are significantly above the IL. This is indicated by the DC magnetic hysteresis curves $m(H)$ plotted in the insets. (Bi2212 single crystals exhibit a second magnetization peak, representing a sudden enhancement of the effective pinning with increasing H [40]). This is usually associated with a pinning-induced disordering of the vortex system, leading to a better accommodation of vortices to the pinning landscape [41]. In layered superconductors, such as Bi2212, the disordering is triggered by the crossover field towards two-dimensional vortex fluctuations [37, 42], which, for the investigated specimen, is around 500 Oe). However, the ratio U_{AC}/T is still above 10 for a finite temperature interval in the vortex liquid phase, where, at first sight, vortex pinning should be irrelevant.

As known, on approaching the IL from below (starting from the vortex solid), a strong influence of vortex fluctuations on the pinning potential sets in. The thermal motion of vortices averages the pinning potential over an increasing area (given by the mean-squared value of the thermal vortex displacement, larger than the

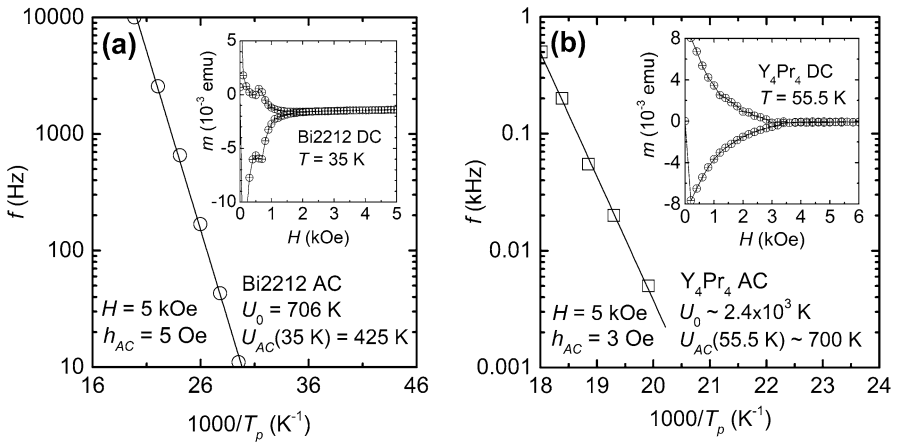


Fig. 6.6 Main panels: The Arrhenius plots obtained at $H = 5$ kOe with $h_{AC} = 5$ Oe for Bi2212 (a) and Y_4Pr_4 (b) lead to an apparent vortex activation energy in the AC magnetic response $U_0 = 706$ K (Bi2212), and $U_0 \sim 2.4 \times 10^3$ K (Y_4Pr_4), supplying $U_{AC}(T = 35$ K) = 425 K, and $U_{AC}(T = 55.5$ K) ~ 700 K, respectively. The corresponding DC $m(H)$ curves are plotted in the insets

vortex core size), and the effective pinning rapidly decreases [43]. This is certainly characteristic for the diffusive, thermally activated vortex motion at long-time scales (the DC case), where the pinning time t_p is much longer than the characteristic time t_{th} of the thermal fluctuations.

The pinning time can also be considered in connection with the existence of a “pinned” vortex liquid. This should be a viscous liquid, which is actually characterized by a “plastic time” $t_{pl} \gg t_{th}$, where t_{pl} represents the time scale of the plastic vortex deformations. If the new smoothing time $t_{pl} > t_p$, the thermal averaging over the pinning time is incomplete, and the vortex liquid can be pinned. A possible origin of such a long smoothing time t_{pl} in the vortex liquid was related to the presence of large barriers for the plastic vortex deformation ($\propto 1/\sqrt{H}$ [44]), associated with vortex cutting and reconnection in an entangled vortex system. However, it is not possible to explain the relatively high U_{AC} values around the IL in terms of such barriers. This is because vortex entanglement is excluded in our almost decoupled Y_nPr_4 superlattices (at least at low H , where the intervortex distance increases), and a detailed analysis of U_{AC} is needed.

6.5 Current Density Dependence of U_{AC}

As shown in Sect. 6.3, the Arrhenius plots (at constant H and h_{AC}) constructed with the $T_p(f)$ data are linear (see Figs. 6.3, 6.4, and 6.6, for example), reflecting the $U_{AC}(T)$ variation from (6.4), in the conditions of a constant current density $J_p(T_p)$. Using different J levels in the domain of full AC critical-state penetration and similar plots, one can determine the current density dependence of the apparent vortex activation energy $U_0(J)$, as shown below for the superlattice $Y_{11}Pr_4$.

Figure 6.7 illustrates the AC magnetic response of $Y_{11}Pr_4$ in $H = 5$ kOe, registered with $h_{AC} = 3$ Oe and f between 1 and 500 Hz. By considering horizontal lines $m' = \text{constant}$ in the full penetration range, as exemplified by the dashed line ($m' = -0.5 \times 10^{-4}$ emu), Arrhenius plots at different $J < J_p$ are constructed with the correspondent T and f values [13]. The m' data are rapidly converted to J , with J_p supplied by (6.2) and by taking into account that for full AC critical-state penetration one has $J \propto |m'|^{2/3}$ [36]. In the case of $Y_{11}Pr_4$, the thickness d in (6.2) is substituted by the effective superlattice thickness $(11/15)d_0$ (with $d_0 = 200$ nm), leading to a J_p value of 1.68×10^5 A/cm² (independent of H). The Arrhenius plots at $J < J_p$ obtained for the AC magnetic signal of $Y_{11}Pr_4$ from Fig. 6.7 are shown in the main panel of Fig. 6.8, and the determined $U_0(J)$ decreases linearly with $\ln(J)$ (see the inset of Fig. 6.8).

The logarithmic $U_{AC}(J)$ dependence has been proven by varying h_{AC} , as well. Such measurements were performed for the YBCO film with a complex pinning structure [25] (YBCOBZOYO, including BZO nanorods and YO nanoparticles) in $H = 2, 10, \text{ and } 30$ kOe. For a constant frequency between 11 and 5555 Hz, the AC signal has been registered at several h_{AC} values, as exemplified in Fig. 6.9 for

Fig. 6.7 Temperature dependence of the in-phase (m') and the out-of-phase (m'') components of the AC magnetic moment registered for the $Y_{11}Pr_4$ superlattice in $H = 5$ kOe ($h_{AC} = 3$ Oe, and f between 1 and 500 Hz), reproduced from the open access [13]. The dashed line represents a constant $m'(f)$ in the full AC critical-state domain, i.e., a constant current density

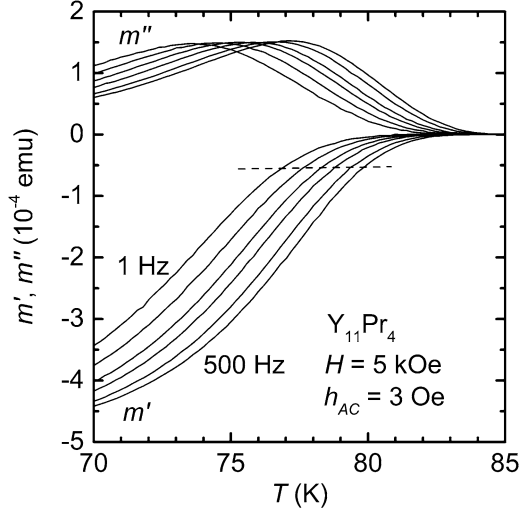
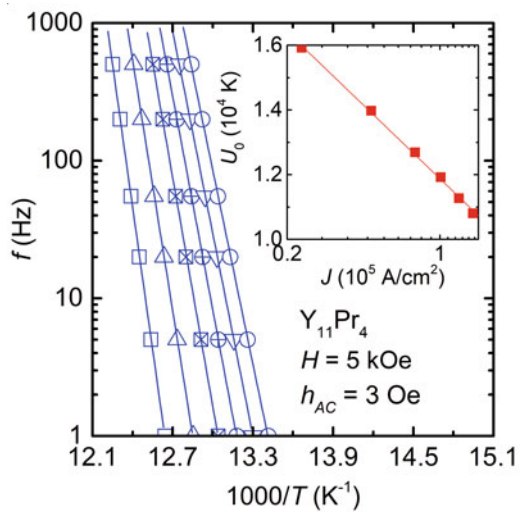


Fig. 6.8 Main panel: Arrhenius plots at various current density J levels below J_p obtained for $Y_{11}Pr_4$ using the AC magnetic response from Fig. 6.7, as reproduced from the open access [13]. A linear fit determines the apparent vortex activation energy in the low- T limit $U_0(J)$, which decreases linearly with $\ln(J)$, as illustrated in the inset. The continuous lines represent the linear fit



$f = 5555$ Hz ($H = 10$ kOe). When h_{AC} is larger, the dissipation peak increases, due to enhanced hysteretic AC losses.

The $U_0(J)$ values, where $J = J_p(h_{AC})$, have been extracted from the Arrhenius plots such as those included in the inset of Fig. 6.10 ($H = 2$ kOe). The semi-logarithmic plots from the main panel of Fig. 6.10 confirm the logarithmic $U_0(J)$ variation, and the current density dependence of U_{AC} can be expressed as $U_{AC}(J) = U_c \ln(J_{c0}/J)$, where U_c is the characteristic pinning energy in the AC magnetic response, whereas J_{c0} is the relaxation-free critical current density.

For constant H and T , (6.3) becomes $f = f_0 \exp[-U_{AC}(J)/T]$, indicating the meaning of J_{c0} . The vortex hopping barrier U_{AC} vanishes at the “depinning”

Fig. 6.9 The variation of the in-phase (m') and the out-of-phase (m'') components of the AC magnetic moment with temperature, registered for the film containing BZO nanorods and YO nanoparticles (YBCOBZOYO) in $H = 10$ kOe at different h_{AC} values between 0.5 Oe and 6 Oe, exemplified for a frequency $f = 5555$ Hz (reproduced from the open access [25]). With increasing h_{AC} , the (dissipation) $m''(T)$ maximum shifts to lower temperatures

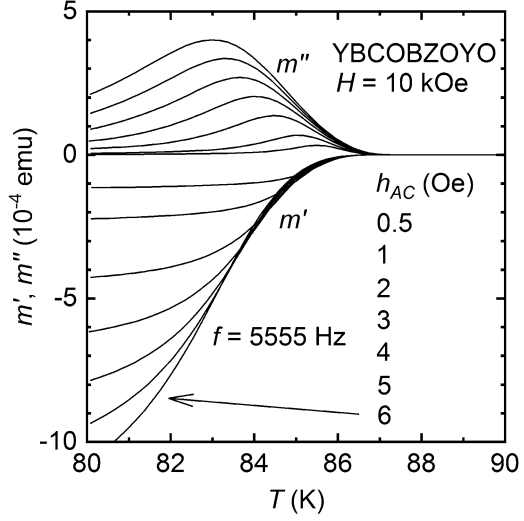
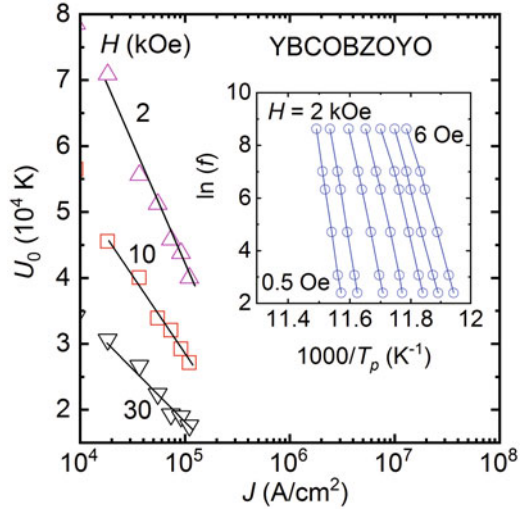


Fig. 6.10 Main panel: The apparent vortex activation energy in the low- T limit U_0 versus $\ln(J)$ at various H values, as reproduced from the open access [25] for YBCOBZOYO. The Arrhenius plots obtained at different h_{AC} (exemplified in the inset for $H = 2$ kOe) allow the determination of $U_0(J)$, where $J = J_p(h_{AC})$ is given by (6.2). The lines represent a linear fit



frequency f_0 , where, as shown in [45], for example, the dynamic critical current density J_d is reached. Above J_d , any influence of pinning becomes negligible, and one has a flow of pinning-free vortices, with the flux flow resistivity $\rho_{FF} = \rho_n H/H_{c2}$ [46], where ρ_n is the resistivity in the normal state and H_{c2} is the upper critical field. Thus, $U_{AC}(J)$ takes the form [47]

$$U_{AC}(J) = U_c \ln \left(\frac{J_d}{J} \right). \tag{6.5}$$

By considering the above expression and (6.3), it is obvious that $\ln(J)$ should be linear in $\ln(t = 1/f)$, and U_c is obtained from the $J(t)$ data as

$$U_c = -T \Delta \ln(t) / \Delta \ln(J). \quad (6.6)$$

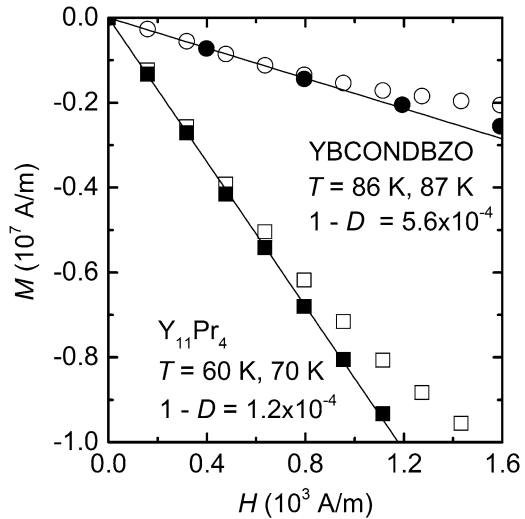
6.6 A Quantitative Analysis of U_{AC} at Low DC Fields

For an estimation of U_{AC} , we simplify the problem, by considering the isolated vortex limit (attained at relatively low H values), for samples where some parameters are known, such as the effective length of the hopping vortex segment (in the $Y_{11}Pr_4$ superlattice, for example), or the average distance between the pinning centers (YBCONDBZO, see Fig. 6.1).

In the used field orientation, the sample demagnetization factor D approaches unity, and the error in $1 - D$ becomes important. The demagnetization factor has been precisely determined from the initial slope of the DC magnetization curves $M(H)$ (where M is the volume magnetization) registered with a small step in H and at temperatures not far from the considered temperature interval for the AC magnetic measurements. As illustrated in Fig. 6.11, the procedure leads to $1 - D = 5.6 \times 10^{-4}$ for YBCONDBZO (close to the result obtained using the theoretical approach from [48]), and $1 - D = 1.2 \times 10^{-4}$ in the case of $Y_{11}Pr_4$.

The AC magnetic signal of $Y_{11}Pr_4$ in $H = 500$ Oe obtained with $h_{AC} = 3$ Oe and f between 11 and 500 Hz is illustrated in Fig. 6.12a, whereas the resulting Arrhenius plot is shown in Fig. 6.12b. The current density at the first full AC critical-state penetration starting from low temperatures in Fig. 6.12a [determined

Fig. 6.11 The demagnetization factor D has been determined from the initial slope of the DC magnetization curves $M(H)$ registered in zero-field cooling conditions with a small step in H , as shown here for YBCONDBZO ($T = 86$ K and 87 K), and $Y_{11}Pr_4$ (at $T = 60$ K and 70 K). The linear fit, represented by continuous lines, supplies $1 - D = 5.6 \times 10^{-4}$ for YBCONDBZO, and $1 - D = 1.2 \times 10^{-4}$ in the case of $Y_{11}Pr_4$



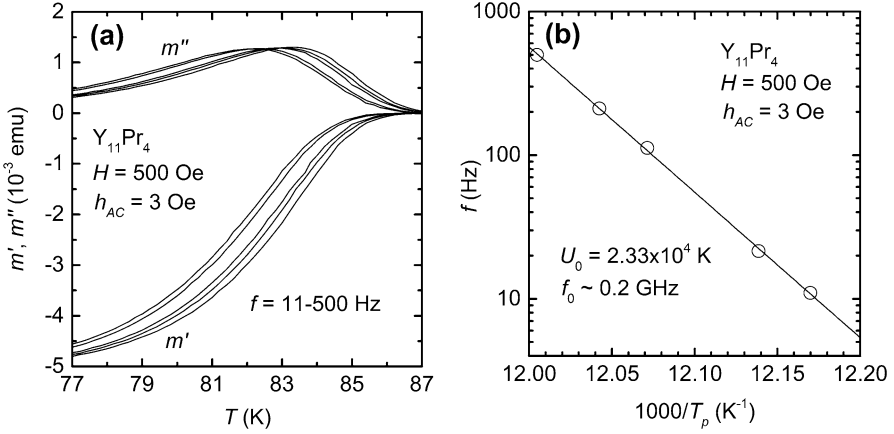


Fig. 6.12 (a) The AC magnetic response of the superlattice $Y_{11}Pr_4$ in $H = 500$ Oe ($h_{AC} = 3$ Oe and f between 11 and 500 Hz). The current density at the dissipation peak extracted with (6.2) is $J_p = 1.68 \times 10^5$ A/cm². (b) The linear fit in the constructed Arrhenius plot leads to an apparent activation energy in the low-temperature limit $U_0(J_p) = 2.33 \times 10^4$ K, and to a depinning frequency $f_0 = 0.2$ GHz

with (6.2)] is $J_p = 1.68 \times 10^5$ A/cm², the same as in Fig. 6.7 (independent of H , as noted above). The linear fit in the Arrhenius plot gives $U_0(J_p) = 2.33 \times 10^4$ K, and a depinning frequency $f_0 = 0.2$ GHz. The vortex activation energy at the peak temperature for the highest frequency in Fig. 6.12a, $T_p(500 \text{ Hz}) = 83.3$ K, takes the value $U_{AC}(J_p) = 1.02 \times 10^3$ K. The latter has been extracted from the apparent activation energy $U_0(J_p)$ with the linear $U_{AC}(T)$ variation from (6.4).

The ratio $U_{AC}(T)/T$ is above 10 around the IL, which may appear unphysical for superlattices (with point-like quenched disorder and enhanced two-dimensional vortex fluctuations). It is then instructive to compare this vortex activation energy with the pinning potential well created by an “ideal” pinning center.

Let us consider the pinning potential well in the isolated vortex limit created by a normal nanorod along the c axis of $Y_{11}Pr_4$ (neglecting the interface effects) with dimensions matching the core of the Abrikosov vortex in the YBCO block, i.e., with the length $L \sim 12$ nm (11 YBCO unit cells) and the radius c_0 equal to the coherence length ξ in the (a, b) plane. For the YBCO blocks, $\xi(T = 0) \sim 1.5$ nm, and the (a, b) plane London penetration depth $\lambda(T = 0) \sim 150$ nm [37]. When c_0 and ξ are comparable, the solution of the London and Ginzburg-Landau equations from [28] leads to a vortex pinning energy (unaffected by vortex fluctuations or a finite J) [49]

$$W = \left(\frac{L\varepsilon_0}{2} \right) \ln \left[1 + \frac{c_0^2}{2\xi^2} \right], \quad (6.7)$$

with the energy scale $\varepsilon_0 = (\Phi_0/4\pi\lambda)^2$, where Φ_0 is the magnetic flux quantum. In practical units, $\varepsilon_0[\text{K}/\text{nm}] = 1.964 \times 10^7 \times (\lambda[\text{nm}])^{-2}$ [37]. At $T = 83.3$ K, the temperature considered above for the determination of U_{AC} , with the standard $\lambda(T)$ variation and the $\xi(T)$ dependence used in [28], (6.7) leads to $W \sim 340$ K, significantly smaller than $U_{AC}(J_p) \sim 10^3$ K determined at this temperature ($H = 500$ Oe).

The order of magnitude of U_{AC} at low H is addressed below in terms of the linear approximation [50], with J_d as the relevant critical current density for the AC magnetic response, representing the induced current density at the depinning frequency f_0 , as argued in Sect. 6.5. In the present context, the linear approximation can still be used for the logarithmic $U_{AC}(J)$ from (6.5) if J and J_d are within the same order of magnitude.

For $Y_{11}\text{Pr}_4$ in $H = 500$ Oe, we measured m' as a function of f (between 11 and 500 Hz), with $h_{AC} = 3$ Oe, at $T = 83.3$ K, which is the peak temperature T_p for $f = 500$ Hz in Fig. 6.12a. This is plotted in the main panel of Fig. 6.13.

The $m'(f)$ variation from the main panel of Fig. 6.13 was converted to the relaxation data $J(t = 1/f)$ plotted in the inset, using J_p and the relation $J \propto |m'|^{2/3}$ in the domain of full AC critical-state penetration. As it can be seen, $\ln(J)$ versus $\ln(t = 1/f)$ is linear, and this relation has been proven in AC magnetic measurements for an extended f range, up to several MHz [4]. The extrapolation of the linear fit from the inset of Fig. 6.13 to $\ln(1/f_0)$, where $f_0 = 0.2$ GHz, as determined in Fig. 6.12b, leads to a critical current density $J_d = 8.4 \times 10^5$ A/cm².

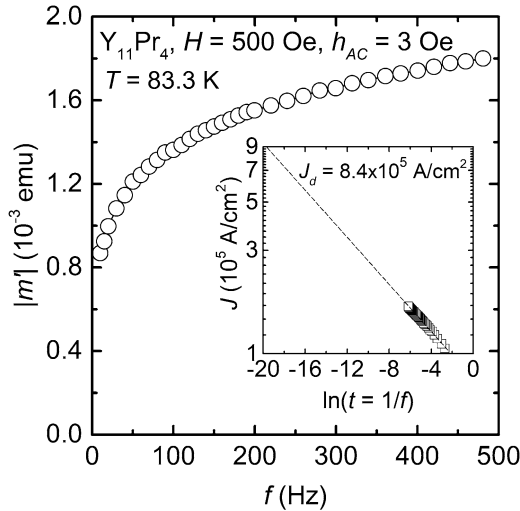


Fig. 6.13 Main panel: The $m'(f)$ variation for $Y_{11}\text{Pr}_4$ in $H = 500$ Oe in the domain of full AC critical-state penetration at $T = 83.3$ K ($h_{AC} = 3$ Oe). The chosen temperature corresponds to the T_p value at the highest used frequency in Fig. 6.12, which allows the rapid determination of the screening current density $J(f)$. Inset: $\ln(J)$ increases linearly by decreasing $\ln(f)$, the dashed line representing a linear fit. The extrapolation to $\ln(f_0)$ (where the depinning frequency $f_0 = 0.2$ GHz) gives the critical current density $J_d = 8.4 \times 10^5$ A/cm²

The same $m'(f)$ data allows the determination of the electric field E at the sample edge,

$$E = (R/2)(1 - D) dM'/dt, \tag{6.8}$$

where the magnetization M' is m' divided by the sample volume. The resulting $E(t)$ is plotted in Fig. 6.14a, whereas Fig. 6.14b illustrates the time dependence of the linear resistivity $\rho = E/J$ (with J from the inset of Fig. 6.13).

The origin of the high U_{AC} values is suggested by the linear Arrhenius plots reported for various superconductors, i.e., by (6.3), where $t = 1/f$ is directly related to the vortex hopping time t_h in a non-diffusive vortex motion process. During an AC cycle, vortices move towards the sample center and in the opposite direction, and $t_h = 1/2f$. With E at the sample edge, the average vortex velocity $v = E/\mu_0 H$, and the vortex hopping length $l_h = Et_h/\mu_0 H$. Figure 6.14a illustrates the $t = 1/f$ variation of v and l_h for $Y_{11}Pr_4$ in $H = 500$ Oe ($h_{AC} = 3$ Oe) at $T = 83.3$ K, with a time averaged $l_h = 163$ nm. Due to the inter-diffusion between YBCO and PrBCO, the superlattices have a dense point-like quenched disorder, and the above l_h is larger than the mean distance between the pinning centers.

As noted in Sect. 6.5, any influence of pinning becomes negligible for J above J_d only, i.e., at $f \geq f_0$, where the flow of pinning-free vortices is present, with a small viscous drag coefficient $\eta_0 = \mu_0 H_{c2} \Phi_0 / \rho_n$ [46] (10^{-7} – 10^{-6} Ns/m² in YBCO [45]). In the usually performed AC magnetic measurements (at f well below f_0 and, consequently, $J < J_d$), for a hopping length larger than the mean distance between the pinning centers, a pinning-enhanced viscous drag coefficient $\eta \sim \eta_0 \rho_{FF} / \rho$ [51] has

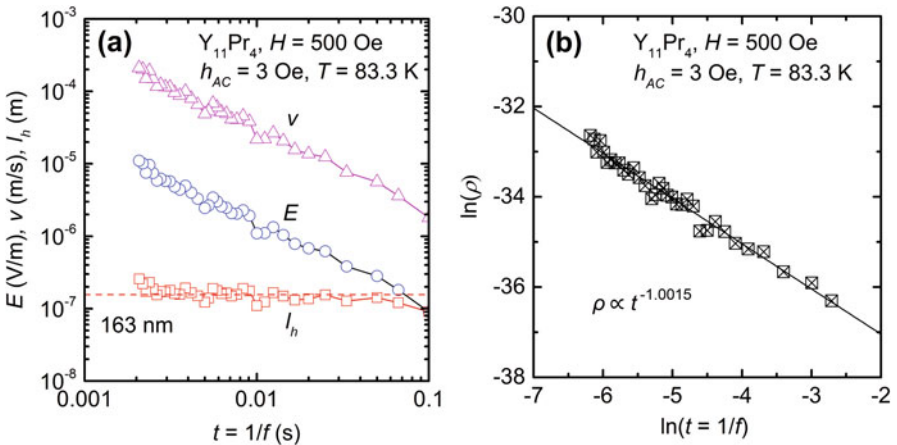


Fig. 6.14 (a) The electric field E , the vortex velocity v , and the averaged vortex hopping length l_h at the sample edge (~ 163 nm, the dashed line) versus $t = 1/f$ (in log-log scales), for $Y_{11}Pr_4$ in $H = 500$ Oe at $T = 83.3$ K ($h_{AC} = 3$ Oe). (b) With E from (a) and J from the inset of Fig. 6.13, the resistivity $\rho = E/J \propto 1/t$, as indicated by the linear fit (the continuous line)

to be taken into account. The viscosity increase is generated by successive pinning and depinning events [52] during the main vortex hopping over l_h . Owing to the short pinning times involved in such events, the smoothing of the pinning potential by thermally induced vortex fluctuations (see Sect. 6.4) is reduced, i.e., the pinning centers remain active.

The bare activation energy barrier U_{AC} at low H is obtained as the work for dragging a vortex segment of length L_{eff} over a distance l_h by setting $J = J_d$, in the conditions of a pinning-enhanced viscosity, which is $\eta\nu L_{\text{eff}}l_h = \Phi_0 L_{\text{eff}}l_h J_d$. With a finite J in the specimen, in the above approximation one has $U_{AC} = \Phi_0 L_{\text{eff}}l_h(J_d - J)$. Since U_{AC} was extracted using the peak temperature T_p (at which the AC critical state reaches the sample center, where E vanishes), one should consider an average vortex hopping length $\bar{l}_h \approx l_h/2$, i.e.,

$$U_{AC} = \Phi_0 L_{\text{eff}}\bar{l}_h (J_d - J). \quad (6.9)$$

Obviously, (6.9) is similar to that from the linear model [50], but with \bar{l}_h playing the role of the interaction length (instead of the pin radius, for example).

In the case of $Y_{11}P_4$ in $H = 500$ Oe and $h_{AC} = 3$ Oe, with U_0 from Fig. 6.12, we obtained at $T = 83.3$ K an activation energy $U_{AC}(J_p) = 1.02 \times 10^3$ K. At the same time, with $L_{\text{eff}} = 12$ nm (11 YBCO unit cells), $\bar{l}_h = 81.5$ nm (Fig. 6.14a), $J_d = 8.4 \times 10^5$ A/cm², and $J_p = 1.68 \times 10^5$ A/cm² (see Figs. 6.12a and 6.13, respectively), (6.9) gives $U_{AC}(J_p) = 986$ K, in agreement with the determined $U_{AC}(J_p)$.

The time $t = 1/f$ variation of the linear resistivity ρ from Fig. 6.14b is very close to $\rho(t) \propto 1/t$, which is an exact result for a self-organized AC critical state [53]. This supports the logarithmic $U_{AC}(J)$ [leading to power-law dependent $E(J)$ curves], since for an inductive process one has, roughly, $dJ/dt \propto \rho J \propto J/t$ [54], and the linear $\ln(J)$ versus $\ln(t)$ plot from the inset of Fig. 6.13 becomes evident.

For YBCONDZBO (the relatively thick YBCO film, with embedded BZO nanorods, grown on a nanodot-decorated STO substrate), the Arrhenius plot included in Fig. 6.4 ($H = 500$ Oe, $h_{AC} = 3$ Oe) leads to an apparent activation energy $U_0(J_p) = 2.27 \times 10^5$ K, where $J_p \sim 2.2 \times 10^4$ A/cm² was extracted with (6.2). At $T = 88.55$ K, representing the peak temperature T_p for the highest used frequency ($f = 10$ kHz in Fig. 6.4), with (6.4) one determines an activation energy $U_{AC}(J_p) = 1.65 \times 10^3$ K. This value is unexpectedly high, as well, since the considered temperature is very close to $T_c = 89.2$ K.

Figure 6.15a represents, in log-log scales, the time dependence of the induced current density J at $T = 88.55$ K ($H = 500$ Oe, $h_{AC} = 3$ Oe), obtained from the measured $m'(f)$ in the full AC critical-state penetration domain. A linear fit of the $J(t = 1/f)$ variation in the representation from Fig. 6.15a and (6.6) give a characteristic pinning energy $U_c = 1.58 \times 10^3$ K. With the determined $U_{AC}(J_p)$, U_c , and $J = J_p$ in (6.5), the dynamic critical current density $J_d = 6.3 \times 10^4$ A/cm² has been extracted.

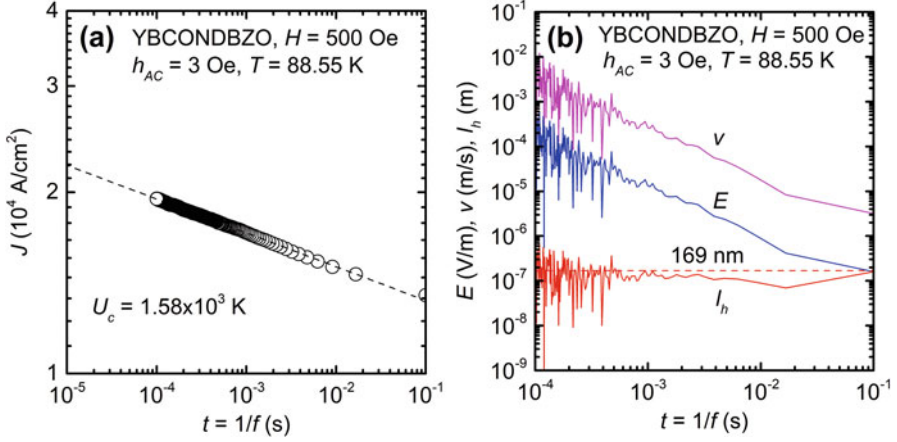


Fig. 6.15 (a) Time $t = 1/f$ dependence of the current density J (in log-log scales) for YBCONDBZO ($H = 500$ Oe and $h_{AC} = 3$ Oe) at $T = 88.55$ K $= T_p$ (10 kHz) (see Fig. 6.4). The characteristic pinning energy $U_c = 1.58 \times 10^3$ K was obtained with (6.6), the dashed line representing a linear fit. (b) The electric field E at the sample edge, the vortex velocity v , and the vortex hopping length l_h versus $t = 1/f$, in log-log scales, for YBCONDBZO in $H = 500$ Oe and $h_{AC} = 3$ Oe at $T = 88.55$ K. The linear fit (the dashed line) gives the time averaged $l_h \sim 169$ nm

The $m'(f)$ data registered for the square-shaped film YBCONDBZO in $H = 500$ Oe at $T = 88.55$ K ($h_{AC} = 3$ Oe) supplies the electric field at the sample edge,

$$E \sim (l/4) (1 - D) dM'/dt, \quad (6.10)$$

where the square side $l = 5$ mm.

Figure 6.15b shows the time variation of E , v , and l_h , with the electric field at the sample edge determined from (6.10).

The mean value of the vortex hopping length at the sample edge $l_h = 169$ nm overcomes the average distance between the pinning centers in YBCONDBZO (see Fig. 6.1), even if we disregard the existence of BZO nanoparticles and other types of quenched disorder usually present in YBCO films. In the above discussion about U_{AC} in superlattices, this aspect was only assumed.

It is worthy to note that the velocity of vortices in Fig. 6.14a, b (at usual frequencies) is several orders of magnitude below the “thermal” velocity [55].

According to (6.9), the higher vortex activation energy U_{AC} in YBCONDBZO relative to that obtained for $Y_{11}Pr_4$ can result from a larger length of the hopping vortex segment L_{eff} (which is limited to ~ 12 nm in the case of $Y_{11}Pr_4$). With the parameters determined above at $T = 88.55$ K ($H = 500$ Oe, $h_{AC} = 3$ Oe), i.e., $U_{AC}(J_p) = 1.65 \times 10^3$ K, $J_d = 6.3 \times 10^4$ A/cm², $J_p = 2.2 \times 10^4$ A/cm², and the averaged vortex hopping length $\bar{l}_h = 84.5$ nm, (6.9) gives $L_{eff} = 318$ nm. However, the considered temperature value is very close to T_c , and L_{eff} is certainly affected

Table 6.1 The apparent vortex activation energy (in the low- T limit) $U_0(J = J_p)$ for $Y_{11}P_4$ and YBCONDBZO at several H values

Sample, $J_p \backslash U_0(H)$	$U_0(500 \text{ Oe})$	$U_0(5 \text{ kOe})$	$U_0(10 \text{ kOe})$	$U_0(30 \text{ kOe})$
$Y_{11}P_4$ $J_p = 1.68 \times 10^5 \text{ A/cm}^2$	$2.33 \times 10^4 \text{ K}$	$9.7 \times 10^3 \text{ K}$	–	–
YBCONDBZO $J_p = 2.24 \times 10^4 \text{ A/cm}^2$	$2.27 \times 10^5 \text{ K}$	$8.24 \times 10^4 \text{ K}$	$5.8 \times 10^4 \text{ K}$	$2.64 \times 10^4 \text{ K}$

The current density J_p (independent of H) is given by (6.2), with the AC field amplitude $h_{AC} = 3 \text{ Oe}$

by the T_c distribution in thick YBCO films. A similar analysis of the AC magnetic measurements performed for YBCONDBZO in $H = 2 \text{ kOe}$ and $H = 10 \text{ kOe}$ (with $h_{AC} = 3 \text{ Oe}$) leads to $L_{\text{eff}}(T = 88 \text{ K}) \sim 500 \text{ nm}$, and $L_{\text{eff}}(T = 87 \text{ K}) \sim 700 \text{ nm}$, respectively, pointing towards a non-diffusive vortex motion during the AC cycle.

Finally, the values of the apparent vortex activation energy $U_0(J = J_p)$ determined for the thoroughly investigated specimens $Y_{11}P_4$ and YBCONDBZO at several external DC fields H are included in Table 6.1.

6.7 Conclusions

In summary, the vortex activation energy U_{AC} in the AC magnetic response of superconductors at usual frequencies and amplitudes takes surprisingly high values in the vicinity of the DC irreversibility line, especially at low DC magnetic fields. This is essentially different from the behavior of the vortex-creep activation energy in the vortex diffusion process at long relaxation time scales (the DC case), suggesting a change in the thermally activated vortex hopping at short-time scales. The large U_{AC} around and even above the DC irreversibility line (in the pinned vortex liquid domain) is consistent with the dynamic critical current density as the relevant critical parameter for the AC magnetic response and is generated by a non-diffusive, thermally activated vortex hopping during the AC cycle.

At least at low magnetic fields, the vortex hopping length is larger than the mean distance between the pinning centers, and the pinning-enhanced viscosity of the vortex system seems to be at the origin of the pinned vortex liquid. The viscosity increase is generated by successive pinning and depinning events accompanying the main vortex hopping during the half-period of the AC cycle. Owing to the short pinning time involved in such events, the smoothing of the pinning potential by thermally induced vortex fluctuations is reduced, and the pinning centers become active.

Acknowledgements Work supported by the Romanian Ministry of Research and Innovation through POC (European Regional Development Fund, Operational Fund Competitiveness), Project P-37_697, number 28/01.09.2016, and PED88/2016. The kind assistance of the Alexander von Humboldt Foundation is gratefully acknowledged.

References

1. J.I. Gittleman, B. Rosenblum, Phys. Rev. Lett. **17**, 734 (1966)
2. J.R. Clem, J. Appl. Phys. **50**, 3518 (1979)
3. E.H. Brandt, Phys. Rev. Lett. **67**, 2219 (1991)
4. L. Fàbrega, J. Foncuberta, L. Civale, S. Piñol, Phys. Rev. B **50**, 1199 (1994)
5. J. Giapintzakis, R.L. Neiman, D.M. Ginsberg, M.A. Kirk, Phys. Rev. B **50**, 16001 (1994)
6. F. Gömörý, Supercond. Sci. Technol. **10**, 523 (1997)
7. I. Joumard, T. Klein, J. Marcus, Phys. Rev. Lett. **87**, 167002 (2001)
8. M.G. Adesso, D. Uglietti, R. Flükiger, M. Polichetti, S. Pace, Phys. Rev. B **73**, 092513 (2006)
9. S. Monah, J. Sinha, S.S. Banerjee, Y. Myasoedov, Phys. Rev. Lett. **98**, 027003 (2007)
10. G. Pasquini, D.P. Daroca, C. Chliotte, G.S. Lozano, V. Bekeris, Phys. Rev. Lett. **100**, 247003 (2008)
11. E. Bartolomé, A. Palau, A. Llordés, T. Puig, X. Obradors, Phys. Rev. B **81**, 184530 (2010)
12. G. Prando, P. Carretta, R. De Renzi, S. Sanna, A. Palenzola, M. Putti, M. Tropeano, Phys. Rev. B **83**, 174514 (2011)
13. L. Miu, I. Ivan, A.M. Ionescu, D. Miu, AIP Adv. **6**, 065027 (2016)
14. M. Pissas, T. Tamegai, Supercond. Sci. Technol. **30**, 105011 (2017)
15. M.M. Bermúdez, E.R. Loudon, M.R. Eskildsen, C.D. Dewhurst, V. Bekeris, G. Pasquini, Phys. Rev. B **95**, 104505 (2017)
16. R. Villa, V.G. Geshkenbein, R. Prozorov, G. Blatter, Phys. Rev. Lett. **115**, 207001 (2015)
17. P. Fabbriatore, S. Farinon, G. Gemme, R. Musenich, R. Parodi, B. Zhang, Phys. Rev. B **50**, 3189 (1994)
18. C.P. Bean, Phys. Rev. Lett. **8**, 250 (1962)
19. X. Ling, J.I. Budnick, in *Magnetic Susceptibility of Superconductors and Other Spin Systems*, ed. by R. A. Hein, T. L. Francavilla, D. H. Liebenberg, (Springer Science + Business Media, New York, 1991), p. 377
20. M. Nikolo, R.B. Goldfarb, Phys. Rev. B **39**, 6615 (1988)
21. V.B. Geshkenbein, V.M. Vinokur, R. Fahrenbacher, Phys. Rev. B **43**, 3748 (1991)
22. A.M. Campbell, J. Phys. C **2**, 1492 (1969)
23. A.M. Campbell, J. Phys. C **4**, 3186 (1971)
24. L. Miu, P. Mele, I. Ivan, A.M. Ionescu, D. Miu, J. Supercond. Nov. Magn. **28**, 361 (2015)
25. I. Ivan, A.M. Ionescu, D. Miu, P. Mele, L. Miu, Supercond. Sci. Technol. **29**, 095013 (2016)
26. I. Ivan, A.M. Ionescu, V. Sandu, A. Crisan, L. Miu, Supercond. Sci. Technol. **31**, 105012 (2018)
27. P. Mikheenko, V.-S. Dang, M.M.A. Kechik, A. Sarkar, P. Paturi, H. Huhtinen, J.S. Abell, A. Crisan, IEEE Trans. Appl. Supercond. **21**, 3184 (2011)
28. D.R. Nelson, V.M. Vinokur, Phys. Rev. B **48**, 13060 (1993)
29. L. Miu, Phys. Rev. B **85**, 104519 (2012)
30. D. Miu, I. Ivan, A. Crisan, P. Mele, G. Jakob, L. Miu, Supercond. Sci. Technol. **26**, 045008 (2013)
31. P. Mele, K. Matsumoto, T. Horide, A. Ichinose, M. Mukaida, Y. Yoshida, R. Kita, Supercond. Sci. Technol. **21**, 015019 (2008)
32. T. Haugan, P.N. Barnes, R. Wheeler, F. Meisenkothen, M. Sumption, Nature **430**, 867 (2004)
33. L. Miu, P. Mele, A. Crisan, A. Ionescu, D. Miu, Physica C **500**, 40 (2014)
34. G. Jakob, P. Przyslupski, C. Stölzel, C. Tomé-Rosa, A. Walkenhorst, M. Schmitt, H. Adrian, Appl. Phys. Lett. **59**, 1626 (1991)
35. A. El Tahan, G. Jakob, H. Adrian, L. Miu, Physica C **470**, 1 (2010)
36. J.R. Clem, A. Sanchez, Phys. Rev. B **50**, 9355 (1994)
37. G. Blatter, M.V. Feigel'man, V.B. Geshkenbein, A.I. Larkin, V.M. Vinokur, Rev. Mod. Phys. **66**, 1125 (1994), and references therein
38. C.J. van der Beek, V.B. Geshkenbein, V.M. Vinokur, Phys. Rev. B **48**, 3393 (1993)
39. V.B. Geshkenbein, A.I. Larkin, Sov. Phys. JETP **60**, 369 (1989)

40. M. Däumling, J.M. Seuntjens, D.C. Larbalestier, *Nature (London)* **346**, 332 (1990)
41. D. Miu, T. Noji, T. Adachi, Y. Koike, L. Miu, *Supercond. Sci. Technol.* **25**, 115009 (2012)
42. L. Miu, P. Wagner, A. Hadish, F. Hillmer, H. Adrian, *Physica C* **234**, 249 (1994)
43. M.V. Feigel'man, V.M. Vinokur, *Phys. Rev. B* **41**, 8986 (1990)
44. V.M. Vinokur, M.V. Feigel'man, V.B. Geshkenbein, A.I. Larkin, *Phys. Rev. Lett.* **65**, 259 (1990)
45. M. Golosovsky, M. Tsindlenkht, H. Chayet, D. Davidov, *Phys. Rev. B* **50**, 470 (1994)
46. J. Bardeen, M.J. Stephen, *Phys. Rev. A* **140**, 1197 (1965)
47. E. Zeldov, N.M. Amer, G. Koren, A. Gupta, M.W. McElfresh, R.J. Gambino, *Appl. Phys. Lett.* **56**, 680 (1990)
48. E.H. Brandt, *Phys. Rev. B* **49**, 9024 (1994)
49. P. Mele, K. Matsumoto, T. Horide, A. Ichinose, M. Mukaida, Y. Yoshida, S. Horii, R. Kita, *Supercond. Sci. Technol.* **21**, 032002 (2008)
50. P.W. Anderson, Y.B. Kim, *Rev. Mod. Phys.* **36**, 39 (1964)
51. M. Vanević, Z. Radović, V.G. Kogan, *Phys. Rev. B* **87**, 144501 (2013)
52. A.M. Troyanovski, J. Aarts, P.H. Kes, *Nature (London)* **399**, 665 (1999)
53. V.B. Geshkenbein, M.V. Feigel'man, V.M. Vinokur, *Physica C* **185–189**, 2511 (1991)
54. M. Tinkham, *Introduction to Superconductivity* (McGraw-Hill, New York, 1966), p. 355
55. M. Buchacek, R. Villa, V.B. Geshkenbein, G. Blatter, *Phys. Rev. Lett.* **98**, 094510 (2018)

Chapter 7

An Atomic-Scale Perspective of the Challenging Microstructure of $\text{YBa}_2\text{Cu}_3\text{O}_{7-x}$ Thin Films



**Bernat Mundet, Roger Guzmán, Elena Bartolomé, Andrew R. Lupini,
Steven Hartman, Rohan Mishra, and Jaume Gázquez**

7.1 Introduction

The advent of high-temperature superconductivity has opened up a new frontier in advanced power systems and high-field magnets. However, in the early days, achieving high current densities in high-temperature superconductor (HTS) wires was a fundamental problem. This was attributed to grain boundaries that act as weak

B. Mundet · R. Guzmán · J. Gázquez (✉)

Department of Superconductivity, Institut de Ciència de Materials de Barcelona (ICMAB-CSIC),
Barcelona, Spain

e-mail: bmundet@icmab.es; rguzman@icmab.es; jgazqueza@gmail.com

E. Bartolomé

Escola Universitària Salesiana de Sarrià (EUSS), Barcelona, Spain

e-mail: ebartolome@euss.es

A. R. Lupini

Institute for Functional Imaging of Materials Oak Ridge National Laboratory, Oak Ridge, TN,
USA

Materials Sciences and Technology Division Oak Ridge National Laboratory, Oak Ridge, TN,
USA

e-mail: arl1000@ornl.gov

S. Hartman

Institute of Materials Science and Engineering, Washington University in St. Louis, St. Louis,
MO, USA

e-mail: steven.t.hartman@wustl.edu

R. Mishra

Institute of Materials Science and Engineering, Washington University in St. Louis, St. Louis,
MO, USA

Department of Mechanical Engineering and Materials Science, Washington University
in St. Louis, St. Louis, MO, USA

e-mail: rmishra@wustl.edu

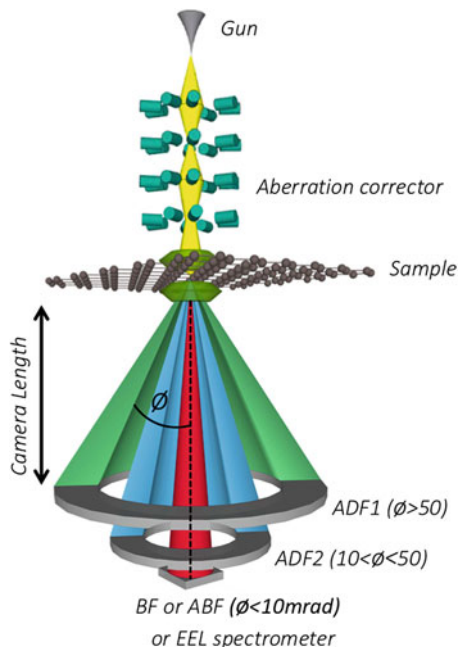
links in these materials by drastically limiting the current flow. The work of Dimos, Chaudhari, and Mannhart [1] provided a breakthrough to solve this grain boundary problem; by measuring the critical current of $\text{YBa}_2\text{Cu}_3\text{O}_{7-x}$ (YBCO) thin films deposited epitaxially on bicrystal substrates, which enabled control over the misorientation of grain boundaries in YBCO, they found that the critical-current density J_c across the grain boundary falls exponentially on increasing the misorientation angle of the grain boundaries. Their results suggested an alternative path to achieve long wires with high J_c : texturing the HTS material biaxially so as to limit the misorientation angle between adjacent grains to only a few degrees. This led to the second generation (2G) of HTS wires, also called coated conductors, with promise for bulk power transmission and magnet applications [2]. Nowadays, the epitaxial thin film structure of these materials allows generation of record critical-current densities observed so far in many high-temperature superconductors. Nevertheless, critical-current densities, and therefore power applications, can be tremendously boosted if nanostructured conductors with artificial pinning centers immobilizing quantized vortices at high-temperature and magnetic fields are produced. To date, all the proposed strategies for the preparation of nanostructured YBCO films involves the use of a secondary non-superconducting phase [3–8] either to use its normal-state volume or to generate defects within the matrix of YBCO that act as localization centers for vortices, which are quanta of magnetic flux [9–16].

The strategies to induce vortex pinning consist of creating non-superconducting regions—any defect that may break the crystallinity of the YBCO matrix—which will oppose the movement of vortices. If the Lorentz force, $\mathbf{J} \times \mathbf{B}$, on a vortex exceeds the pinning force induced by a defect, the magnetic flux lines move and generate resistive losses, thus limiting the critical current. Hence, achieving efficient vortex pinning is crucial for the application of superconductors as loss-free conductors in cables and in magnetic coils.

Furthermore, due to the very small coherence length ξ of YBCO ($\xi_{ab} \approx 2$ nm, $\xi_c \approx 0.4$ nm), the range of defects that can pin vortices is vast: point-defect clusters, dislocations, stacking faults, anti-phase boundaries, grain boundaries, voids, and secondary phases. However, the localization of the vortices' core at these insulating regions is not the only effective vortex-pinning mechanism. Recent results have pointed out the possibility that the formation of Cooper pairs might be quenched under tensile strain, thereby, enabling another strategy to pin vortices in high-temperature superconductors [17, 18].

Although YBCO has been long studied, the use of improved characterization techniques has shed light on the complex defect landscape of YBCO thin films and nanocomposites and unveiled the presence of previously disregarded defects embedded in YBCO with peculiar electronic and magnetic properties. All the defects shown herein may be found in any YBCO thin film, regardless of the deposition and growth method used to fabricate it. We will pay attention to the atomic structure of individual defects, the complexity of which can be shown in real space and with atomic resolution using aberration-corrected scanning transmission electron microscopy (STEM).

Fig. 7.1 Simplified schematic of an aberration-corrected STEM. The electrons are accelerated in the gun; condenser lenses are used to adjust the beam current and beam coherence and to couple to the aberration corrector. The objective lens focuses the probe, which is scanned across the sample by the scan coils. The Annular Dark Field detector 1 (ADF1) and 2 (ADF2) collect electrons scattered to high and low angles, respectively. The removable Bright Field or Annular Bright Field Detectors (ABF) are located at the center of the microscope column, as well as the electron energy loss spectrometer (EELS)



The implementation of spherical aberration correctors in modern electron microscopes has pushed their spatial resolution into the sub-Ångstrom regime and their sensitivity for imaging and spectroscopy of both light and heavy elements. In an aberration-corrected STEM, a schematic of which is shown in Fig. 7.1, an electron probe is focused to a spot size of ~ 1 Å and rastered over a very thin sample (5–100 nm thick). The scattered electrons are then collected to form the image as a function of the probe position over the sample. In addition, the use of post-specimen lenses and multiple detectors allows the simultaneous collection of electrons that are scattered to different angles, enabling the detection of complementary signals. Probably the main benefit of the STEM configuration is that it is possible to obtain the so-called Z-contrast image—with Z being the atomic number—which is formed by collecting the electrons scattered out to high angles by placing a high-angle annular dark field (HAADF) detector, ADF1 in Fig. 7.1. In this imaging mode, the brightness associated to each atomic column is approximately proportional to its Z^2 number [19–21]. This imaging mode has two main advantages, the first is that the resulting images are incoherent, which makes the simulation of the imaged structure unnecessary and therefore the interpretation of the image straightforward [22]. The second advantage is the possibility to form an image of point defects, as it is going to be shown in this chapter. The wider probe-forming aperture available after aberration correction gives a reduced depth of focus, making it possible to optically section through a sample in a way similar to confocal optical microscopy [23].

As mentioned above, all the transmitted electrons in an STEM can be gathered with different detectors, see Fig. 7.1, each one providing complementary information, either as an image, if another imaging detector is used, or as a spectra, with an electron energy loss spectrometer, which collects those electrons that have lost some energy as a result of inelastic scattering from the sample, which are typically deviated to low angles. Hence, we have combined High-Angle Annular Dark Field (HAADF), Low-Angle Annular Dark Field (LAADF), and Annular Bright Field (ABF) imaging modes with Electron Energy Loss Spectroscopy (EELS) in a STEM, and complemented with X-Ray absorption spectroscopy (XAS), X-Ray magnetic circular dichroism (XMCD), and density-functional-theory calculations (DFT) to probe the atomic structure, the chemistry, the magnetic and the electronic structure of the defects found in YBCO thin films.

7.2 The Structure of YBCO

To optimize superconductivity in cuprates, and YBCO in particular, several structural features are needed, resulting in a rather complex chemistry. First, copper oxide planes are essential. These have a stoichiometry of CuO_2 and form a corner-connected square-pyramidal plane (gray arrows in Fig. 7.2a). Hence, cuprates are described as *layered perovskites*. YBCO has two hole-doped CuO_2 planes separated by Y cations without allowing intercalation of O between Cu's in adjacent planes.

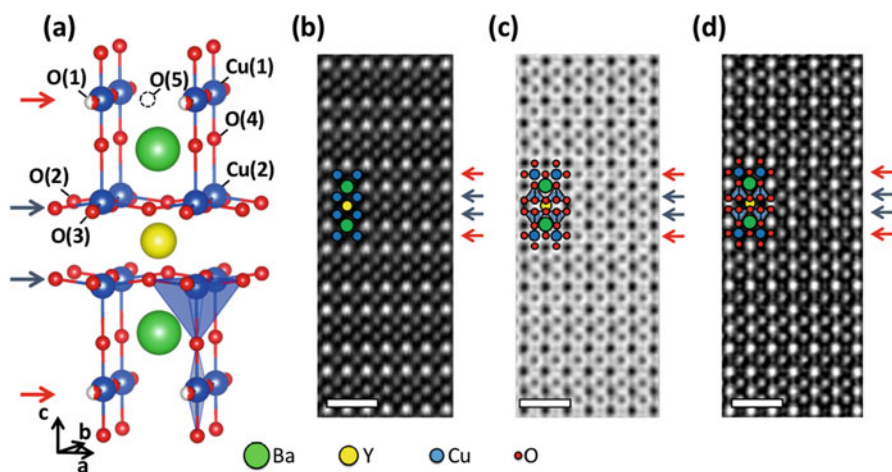


Fig. 7.2 (a) Sketch of the orthorhombic YBCO unit cell. (b) Z-contrast, (c) ABF, and (d) contrast-inverted ABF images, showing the YBCO crystal structure viewed along the [100] zone-axis direction. Scale bars: 1 nm. Ba, Y, Cu, and O are represented with green, yellow, blue, and red circles, respectively. The blue and red arrows signal two superconducting CuO_2 planes and two CuO chains, respectively. Data acquired at 300 kV on the aberration-corrected FEI Titan

A larger cation, Ba supports apical coordination of a further oxygen to copper, and provides connection to an additional CuO_x layer, also referred to as Cu-O chains. These CuO_x layers are termed as a “charge reservoir” as they compensate for the hole-doping of the CuO_2 planes. In the orthorhombic phase, the Cu-O chains align along the b axis and the oxygen occupies the so-called O(1) site, whereas the sites on the a axis [O(5)] are empty.

Figure 7.2b shows a high-resolution Z -contrast image where the YBCO structure is viewed along the [100] zone-axis orientation. As the brightness associated to each atomic column is roughly proportional to its Z^2 number, it allows distinguishing all the heavy atomic species in the structure, the Ba, Y, and Cu cations. In addition, one can simultaneously gather the electrons of the direct beam using an ABF detector, which discards the central part of the bright field disk. Such a detector enables us to visualize atomic columns composed of light atoms [24]. The ABF image displayed in Fig. 7.2c and its inverse-contrast image in Fig. 7.2d reveals the oxygen sub-lattice of YBCO. All O atoms belonging to the superconducting planes (blue arrows) are not confined at the same basal plane as the Cu atoms that they are bonded to. They are slightly shifted towards the Y cation, resulting in a rippling pattern with the Cu atoms when moving along the basal direction, see Fig. 7.2d.

From the electronic point of view, undoped YBCO (if one lowers the O content to 6) becomes insulating and contains Cu^{2+} (d^9 configuration) within the CuO_2 sheets. The uppermost $3d$ orbital is $3d_{x^2-y^2}$ and is singly occupied. This lone electron is localized on Cu due to strong Coulomb repulsion and aligned antiferromagnetically on the CuO_2 plane. In the remaining Cu chains, the Cu^{1+} ion has a closed-shell configuration (d^{10}) and is insulating. The addition of O in YBCO introduces trivalent Cu in the CuO_2 planes, being divalent in the Cu-O chains. The holes are transferred between them through the apical O(2) of the Ba-O plane [25]. Further hole-doping increases T_c , which reaches its maximum at a O content of about 6.92 [26].

Thanks to the particular geometry of the STEM, one can characterize the electronic structure of a compound with atomic resolution using EEL spectroscopy [19], which gives information about the energy that the transmitted electrons lose when they interact with the core electrons of the crystal, providing information of the electronic energy states that remain empty being above the Fermi energy. In perovskites, the O $2p$ - and transition metal $3d$ -states are strongly hybridized, as they have similar energies and lay close to the Fermi level, which helps to probe the metal-oxygen bond. In particular, the combination of STEM and EELS allows for measuring the O-K and Cu-L edges with sufficient spatial and energy resolution to distinguish the role of the superconducting planes and chains in real space, see Fig. 7.3a. Following the dipole-selection rules, the O-K near-edge structure arises from the excitations of the O $1s$ -electrons to the O $2p$ -states, whereas the Cu-L edge results from the excitation of the $2p$ -electrons into the empty $3d$ -states. Thus, any change in the electronic structure can be probed by studying the variations in the fine structure of both edges. For instance, the onset of the O-K edge pre-peak is observed to shift to higher energies when lowering the O content within the YBCO structure [27, 28].

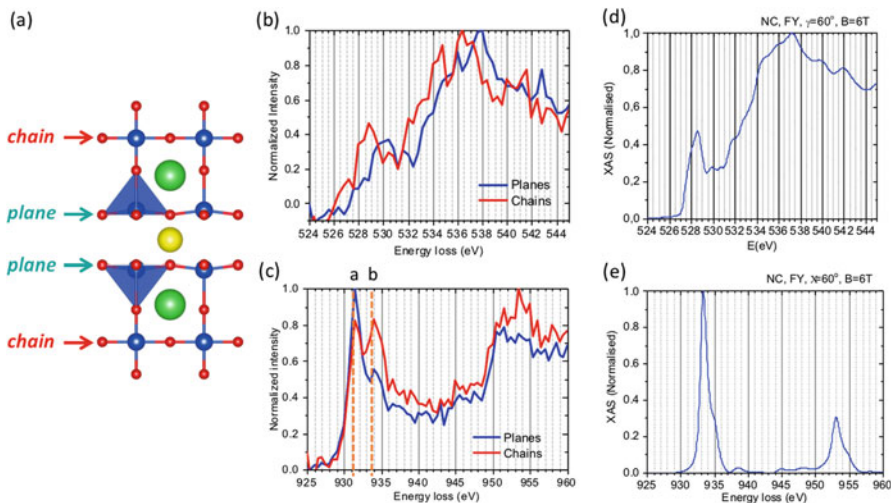


Fig. 7.3 (a) The crystal structure of the orthorhombic YBCO unit cell with arrows to show the Cu-O chain and the CuO₂ plane from which the EEL spectra in (b) and (c) were acquired. (b) Site-specific O-K edges associated to the chain (in red) and superconducting plane (in blue). (c) Site-specific Cu-L edges associated to the chain (in red) and superconducting plane (in blue). Data acquired at 100 kV on the aberration-corrected Nion UltraSTEM. (d, e) O-K and Cu-L XAS spectra. All spectra were obtained from a YBCO nanocomposite with Ba₂YTaO₆ nanoparticles

Figure 7.3b, c show the O-K and the Cu-L edges from the superconducting planes (in blue) and from the chains (in red), respectively. Both edges have been acquired from a YBCO nanocomposite thin film and are compared with the macroscopic and averaged X-ray absorption spectroscopy (XAS) data in Fig. 7.3d, e, respectively. One can clearly resolve significant differences between the O-K and Cu-L spectra in the chains and in the planes. Regarding the O-K edge, the most obvious is the difference in energy of the onset of the O-K pre-peak, which is found at 527 eV in the chains and at 528.5 eV in the planes, and their intensity, which is lower in the planes. In addition, the central peak, located in the 534–540 eV range, is also shifted to a higher energy in the planes.

The Cu-L edge fine structure also reveals differences between CuO₂ planes and Cu-O chains see Fig. 7.3c. At the chains, the L_3 peak splits into the *a* and *b* peaks, centered at 931.5 eV and 934 eV, respectively. A chemical shift towards higher energies is observed in the Cu-L edge when the Cu oxidation state is reduced [29, 30]. Peak *a* is associated to a Cu oxidation state of (+2) whereas peak *b* is associated to (+1). Therefore, the splitting of the L_3 peak suggests that a mixture of Cu+1/+2 cations is present within the single-chain layers. On the other hand, the L_3 peak associated to the superconducting Cu atoms is mainly composed by peak *a*, as it has an oxidation state of Cu⁺². The O-K and Cu-L edges spectra shown here for a nanocomposite film match extremely well with those obtained from a YBCO single crystal [28], and prove that aberration correction STEM is able to image the real-

space electronic structure in the planes and chains of YBCO thin films. This kind of characterization may help understanding the changes in the electronic structure with defects in YBCO with atomic resolution.

7.3 The Microstructure of YBCO Thin Films

Efficient and viable superconducting films require a fine balance between defects at both nanoscale and mesoscale levels. As stated above, both YBCO lattice defects and non-superconducting nanostructures can effectively pin the magnetic flux, thus enabling high J_c under external applied magnetic fields. Indeed, one of the most effective ways to enhance the physical properties of YBCO thin films is to introduce secondary phase nanoparticles within the YBCO film. Barium perovskite nanoinclusions BaMO_3 ($M = \text{Zr, Hf, Sn}$), double perovskites $\text{Ba}_2\text{RETaO}_6$ ($\text{RE} = \text{Y, Gd, Er}$) and binary rare earth oxides RE_2O_3 ($\text{RE} = \text{Y, Dy, Ho}$) have been successfully incorporated to YBCO epitaxial matrix by different deposition techniques leading to nanocomposite films with improved flux-pinning properties [6–8, 18, 31–39]. However, one must consider that the embedded nanostructures reduce the current-carrying cross section; therefore, the density, distribution, and separation among the pinning centers are also critical to establish a balance between flux-pinning and current-blocking. Understanding the influence of the nanoinclusions on the YBCO texture and microstructure is thus essential for correlating the structure with its superconducting properties.

The best way to visualize the complexity of a YBCO nanocomposite thin film microstructure is by using an aberration-corrected STEM. Figure 7.4a, b shows two low-magnification STEM images, acquired simultaneously, of a solution-based YBCO nanocomposite with Ba_2YTaO_6 (BYTO) nanoparticles embedded within the YBCO matrix [40]. The different contrast of these images is the result of using different acquisition modes. Figure 7.3a is a traditional HAADF image, in which the contrast ensues only from high-angle scattering of electrons. On the other hand, the image in Fig. 7.4b is the result of collecting electrons scattered to lower angles (LA). This LAADF imaging mode allows one to image contrast related to defects, i.e., deformations of the atomic columns that lead to a dechanneling of the incident electron beam [41, 42]. HAADF or Z-contrast STEM imaging is ideal for describing and identifying defects in such a highly distorted YBCO matrix, as resulting incoherent images provide almost direct interpretation; they do not suffer from contrast reversal due to the strong dependence on thickness and defocus in conventional phase-contrast TEM imaging [21]. At the same time, LAADF imaging allows for detecting the strain fields along defects and the distortions associated to them.

These images show that, apart from the secondary phases embedded within the superconductor matrix, the $\text{YBa}_2\text{Cu}_4\text{O}_7$ (Y124) intergrowth is the most common and most widespread structural defect in YBCO nanocomposite films, which shares, basically, the same structure as YBCO with the addition of a second CuO_x layer,

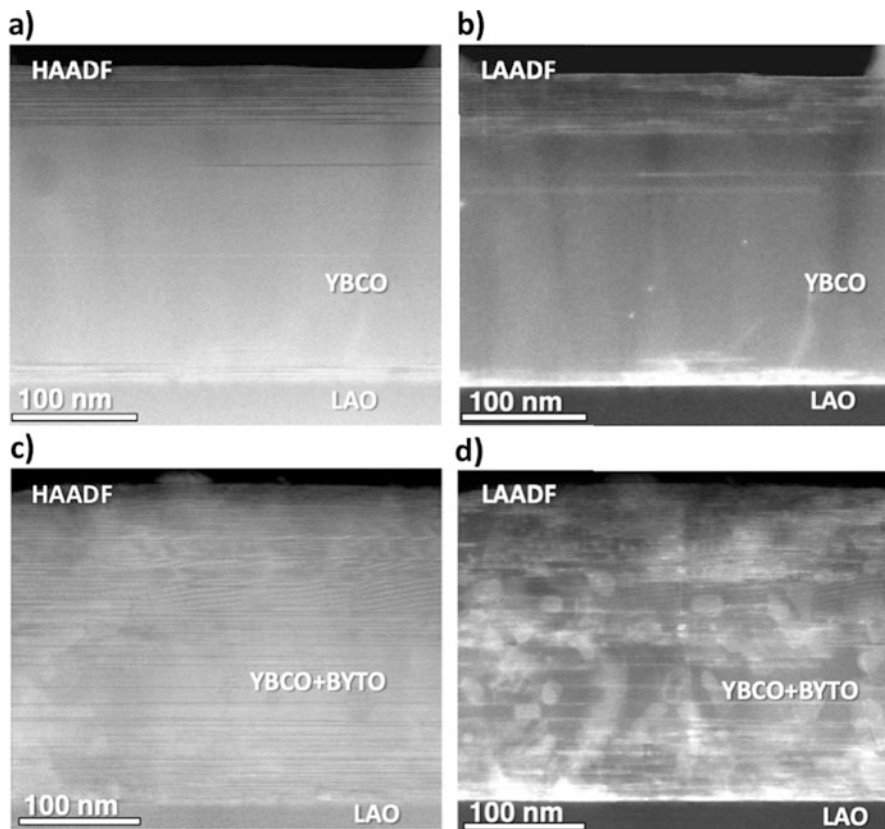


Fig. 7.4 Comparison between the microstructure of a pristine YBCO film and a YBCO-6% BYTO nanocomposite film. (a, b) and (c, d) are simultaneously acquired HAADF and LAADF low-magnification images, respectively. Data acquired at 300 kV on the aberration-corrected FEI Titan. Adapted from [13]

instead of one [43, 44], as shown in Fig. 7.5. Comparing the HAADF and LAADF images, one can realize that the introduction of secondary phase nanoparticles within the YBCO layer dramatically increases the number of these planar defects, which appear as dark stripes in the HAADF imaging mode and brighter in LAADF images. In addition, due to the presence of BYTO nanoparticles and the numerous intergrowths, the focus is lost in several parts of the image, revealing a highly distorted YBCO matrix, which accounts for strain-induced contrast as observed in the LAADF image in Fig. 7.4d.

The presence of an extra CuO chain in the YBCO lattice introduces a 1.9 Å increase along the c -axis and a non-conservative stacking fault with a displacement vector of $[0, b/2, c/6]$ [44], which shifts the two parts of the structure on either side of the fault laterally by $1/2 b$ when viewed along the $[100]$ direction, as shown in Fig. 7.5a, b. Accordingly, the Cu atoms in this double Cu-O chains have a triangle-

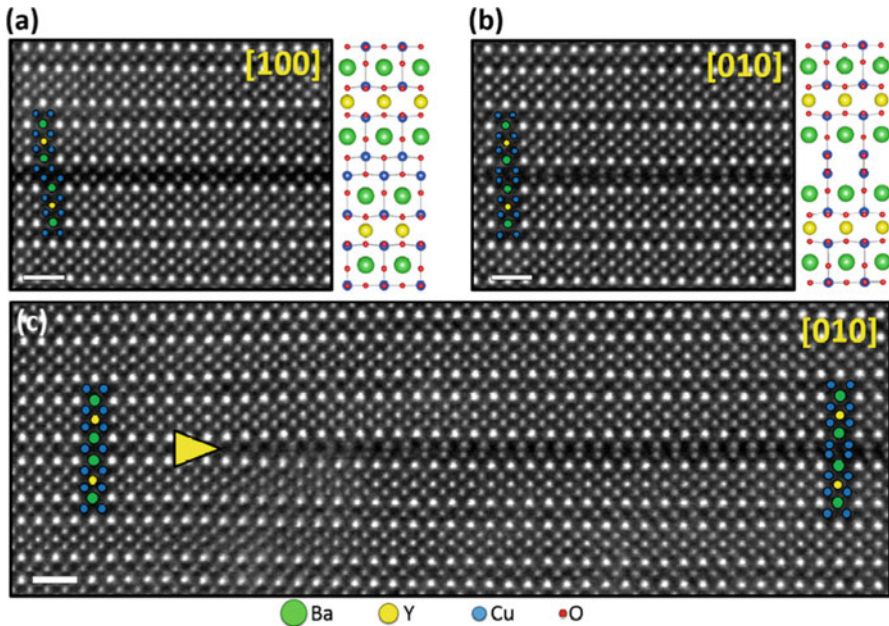


Fig. 7.5 High-resolution Z-contrast images of an isolated Y124 intergrowth embedded within the YBCO crystal structure, which are viewed along either the (a) [100] or, (b) and (c) [010] zone-axis directions. The edge of this planar defect, composed by a partial dislocation, is viewed in (c) (yellow arrow). The YBCO structure is sketched with green (Ba), yellow (Y), and blue (Cu) circles. Scale bars: 1 nm. Image acquired at 300 kV on the aberration-corrected FEI Titan

shaped atomic arrangement when viewed along the [100] zone axis, while they lay head-to-head when viewed along the [010] zone axis. When this double Cu-O chain occurs as a single layer with a finite lateral extent, it is structurally analogous to a Frank loop dislocation, i.e., an extrinsic stacking fault surrounded by a partial dislocation, see Fig. 7.5c.

The genesis of the Y124 intergrowths—which appear not only in YBCO nanocomposites but in all YBCO thin films, regardless of the growth method used—is expected to be linked to stress-related effects and stems from the fundamental crystal structure of YBCO superconductors, which have a marked two-dimensional behavior, which in turn determines their structural anisotropy and superconducting properties. Such anisotropy also affects the evolution of crystallographic defects, hindering the creation of correlated defects perpendicular to the superconducting CuO_2 planes. A common way to dissipate this strain energy is through the generation and growth of dislocations. However, dislocations in YBCO mostly belong to the glide systems $[100](001)$, $[010](001)$, and $\langle 110 \rangle (001)$, i.e., they are confined to the basal plane [45]. Given the large lattice parameter of YBCO along the c -axis ($c_{\text{YBCO}} = 11.68 \text{ \AA}$), such dislocations have a large energy associated with them—as the formation energy of a dislocation is proportional to the square of its

Burgers vector—essentially barring their formation. Alternatively, YBCO develops Y124 intergrowths as stacking faults parallel to the (001) plane by the insertion of an extra Cu-O atomic layer. As mentioned before, Y124's boundary may be considered as a partial dislocation with a Burgers vector $[0, 1/2, 1/6]$ [46], that is, a dislocation with both in- and out-of-plane components. Hence, as in other cubic and tetragonal perovskites [47], the appearance of Y124 intergrowths can be considered a mechanism by which the stress is relieved; an analogous situation to the nucleation of intergrowths at grain boundaries and Y_2BaCuO_5 -YBCO interfaces in melt-textured materials [48, 49].

In the particular case of metal-organic deposited YBCO films, Y124 planar defects are usually prevalent. In solution-derived nanocomposites, epitaxial YBCO nucleation and growth is delayed compared with nucleation and growth of the randomly distributed nanoparticles [9, 50]. Hence, stress is built up as YBCO encounters *obstacles*, such as randomly oriented nanoparticles [11, 13, 18, 51], during the growth process. On the other hand, in physical growth methods, such as pulsed laser deposition (PLD) and sputtering, both the YBCO and the secondary phases grow at the same time, and the interface between them is coherent or semicoherent. In this case, the elastic strain is mainly accommodated by the nanoparticles or the nanorods with misfit dislocations, interface distortions, and oxygen vacancies although limited to few unit cells [10, 15]. However, the appearance of Y124 intergrowths has also been reported when the mismatch or the concentration of secondary phases is high [8, 15, 16]. Therefore, by modifying the deposition technique one can ensure different microstructures, rendering dramatic changes in the flux-pinning mechanism: while films grown by PLD usually show directional effects in J_c , solution-derived composites exhibit a characteristic isotropic pinning behavior [9, 36, 52]. Regardless of the deposition technique, the presence of Y124 intergrowths within the YBCO films is highly desirable because they play an important role in vortex pinning, as their shape and size, as well as the strain generated around the associated partial dislocations at their boundaries, affect the flux-pinning and the critical current carried by the superconductor [9, 50, 53–56].

The larger amount of Y124 intergrowths and the presence of secondary phases within the nanocomposite films strongly affect another common defect in YBCO superconductors, twin boundaries (TB). Such defects appear to relieve the spontaneous strain that arises during the tetragonal-to-orthorhombic transition, which takes place during the last stage of the growth process, the oxygenation step [57]. In a defect-free environment, TBs can extend up to its critical twin-spacing, which is controlled by the film thickness and substrate constraints. In a 300 nm-thick YBCO film, the spacing between twins is around 100 nm [11, 58]. However, in the presence of Y124 defects the vertical TB coherence is broken. Figure 7.6a shows a Z-contrast image of a nanocomposite film, while Fig. 7.6b shows the ϵ_{xx} deformation tensor map ensuing from the {100} Bragg reflection. This deformation map has been generated using the Geometrical Phase Analysis (GPA) software, which is extremely useful for strain determination, as it is able to extract local displacements and rotations of atomic planes from the Fourier analysis of a high-resolution lattice image [59]. Here, [100] and [010] domains can be unambiguously distinguished

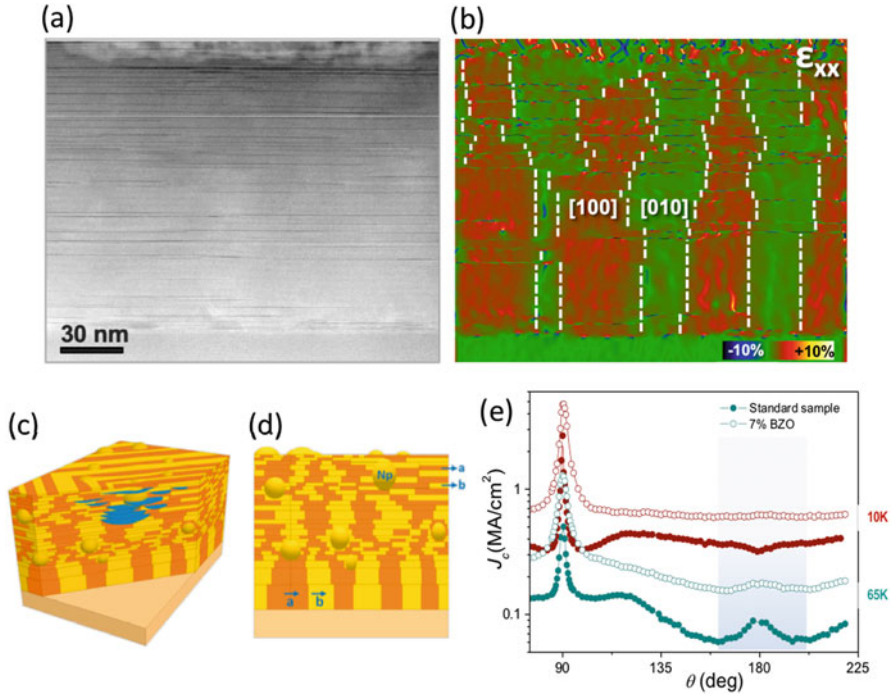


Fig. 7.6 (a) Low-magnification Z-contrast image of a YBCO-10% Y_2O_3 nanocomposite presenting a high density of Y124 defects, visible as dark stripes. Image acquired at 300 kV on the aberration-corrected FEI Titan. (b) ϵ_{xx} deformation map showing in colors (red and green) different deformation values, corresponding to the [100] and [010] twin domains. Notice that the twin coherence is broken along the film, thus denoting the strong structural interaction between both defects. (c, d) Sketches illustrating crystal twinning in highly faulted orthorhombic YBCO. Y124 intergrowths are shown in blue. (e) Angular dependence of J_c at 9 T for a standard YBCO film (closed symbols) and a nanocomposite (open symbols) at 10 K (red) and at 65 K (green). Adapted from [11]

by GPA due to the existing differences between a and b cell parameters in the orthorhombic phase of YBCO ($a = 0.382$ nm; $b = 0.388$ nm).

The higher density of defects produces a strong variation of the twin-spacing and a break in the twin boundary coherence; see the sketches in Fig. 7.6c, d. This scenario changes the understanding of TBs in nanocomposites, as they can act as pinning sites or as flux channels. The reduction of the TB vertical coherence has a relevant effect on precluding vortex channeling at low temperatures and thus avoiding a suppression of J_c for fields parallel to the c -axis ($\theta = 180^\circ$ in the image) [11, 58], see Fig. 7.6e.

The interaction between TBs and Y124 intergrowths is strain mediated, that is, the partial dislocation and its associated distortions constitute a barrier for propagation of the TB. This strain, as it changes the microstructure of the YBCO films, also transforms the pinning landscape of the nanocomposites. The localization

of the vortices' core at insulating regions (provided their dimension is in the range of the coherence length ξ) is not the only effective vortex-pinning mechanism; tensile strain can also quench the formation of Cooper pairs and constitute another effective pinning mechanism in high-temperature superconductors [17, 18, 60].

Although the combination of high-angle and low-angle ADF STEM images is an easy and straightforward method to visualize the nanoscale lattice deformations present in the YBCO matrix—that are associated to defects and nanoparticles—one needs to quantify the lattice deformation in order to infer the effectiveness of the partial dislocations associated to the Y124 intergrowths as a vortex-pinning site [17, 60], which can be done using GPA analysis. The Z-contrast image in Fig. 7.7a shows the presence of a Y124 intergrowth in an almost defect-free YBCO region, whereas Fig. 7.7c, d show the corresponding ε_{xx} and ε_{yy} deformation maps, respectively. The most evident lattice deformation is observed in the ε_{yy} map surrounding the partial dislocation core, which gradually vanishes away from the dislocation core, see Fig. 7.7d. On the other hand, the ε_{xx} map shows a $+1.4 \pm 1.1\%$ tensile deformation located right at the partial dislocation core, suggesting localized strain-induced pair suppression in YBCO, and thus constituting an effective vortex-pinning center [17]. The same occurs in Frank sessile dislocations, which are formed when a twin boundary crosses a Y124 intergrowth, as shown in Fig. 7.8a, b. The ε_{xx} GPA deformation map of the Z-contrast image shows two crystal domains, [010] domain in green and [100] domain in red, in addition to the compressive and tensile deformations around the dislocation core, signaled with an arrow. Since the Y124 structure involves the addition of an extra Cu-O chain and a structural shift of $1/2b_0$, a linear defect that separates the two crystal orientations must be present, this is a dislocation along the twin boundary plane, i.e., $\langle 100 \rangle_{\text{YBCO}}$ [13].

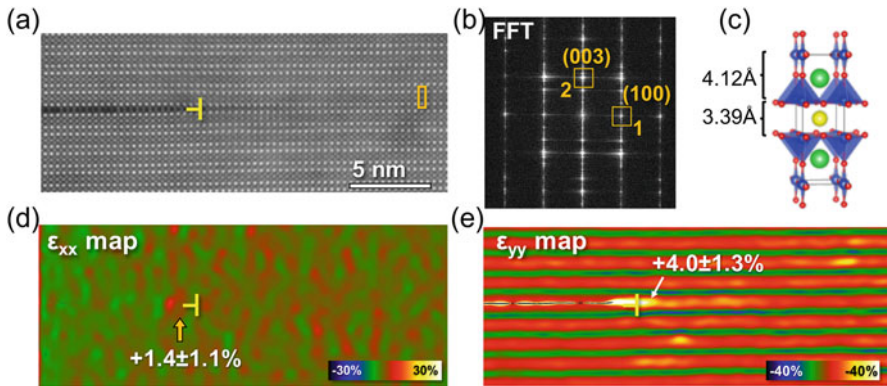


Fig. 7.7 (a) Z-contrast image of YBCO with a single isolated intergrowth. Image acquired at 300 kV on the aberration-corrected FEI Titan. (b) Fast Fourier Transform showing the Bragg reflections, {100} and {003}, used to generate the GPA deformation maps. (c, d) ε_{xx} and ε_{yy} deformation maps along $[100]_{\text{YBCO}}$ and $[001]_{\text{YBCO}}$ directions, respectively. The marked region in (a), the Z-contrast image is the reference lattice. (e) Sketch of the YBCO structure showing the two spacings that appear in the ε_{yy} deformation map. Adapted from [13]

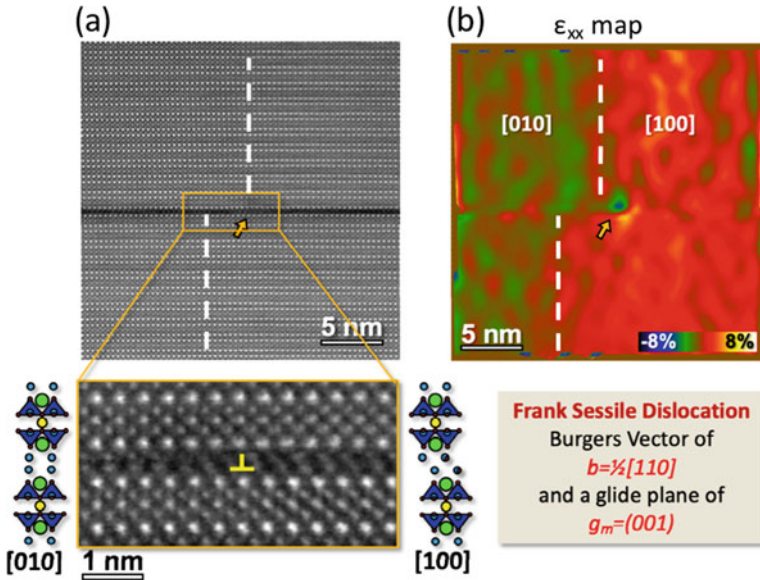


Fig. 7.8 (a, b) Show a Z-contrast image of an isolated Y124 intergrowth and its corresponding ε_{xx} GPA deformation map of the Z-contrast image. The two twin domains are shown in red and green colors. Image acquired at 300 kV on the aberration-corrected FEI Titan. The $\{100\}_{\text{YBCO}}$ Bragg reflections are used for computing the GPA map. Inset is a detailed image of the Frank sessile dislocation with a $1/2 [110]$ Burgers vector and a (001) glide plane located between the two CuO layers. The Y124 structure is illustrated in the image along $[100]$ and $[010]$ zone axes, where Green = Ba, Yellow = Y, Blue = Cu, and Red = O. The yellow symbol marks the position of the dislocation. Adapted from [13]

7.4 The Y124 Intergrowth: A Burst of Changes

As already mentioned, the presence of Y124 intergrowths is highly desirable because they play an important role in vortex pinning. However, it may be argued that the extra amount of Cu that would be needed for their formation would lead to a local Cu off-stoichiometry, as both the solution precursors and the targets (used in magnetron sputtering or pulsed laser deposition techniques) employed in YBCO synthesis have an exact 1:2:3 stoichiometry for Y, Ba, and Cu. The situation worsens in the case of YBCO nanocomposites, where the introduction of secondary phases within the layer may render a huge increase of Y124 intergrowths. For instance, this Cu off-stoichiometry could affect the critical temperature (T_c) of all the films that present a huge amount of these intergrowths, although, this detrimental effect has not been reported, being the $T_c \sim 90$ K in these defective films, which is similar to the pristine YBCO films. The reason, as it will be shown below, is that the system balances this deficiency of Cu by forming Cu and O vacancies buried within the very same intergrowth [12], thus preventing the stoichiometry catastrophe.

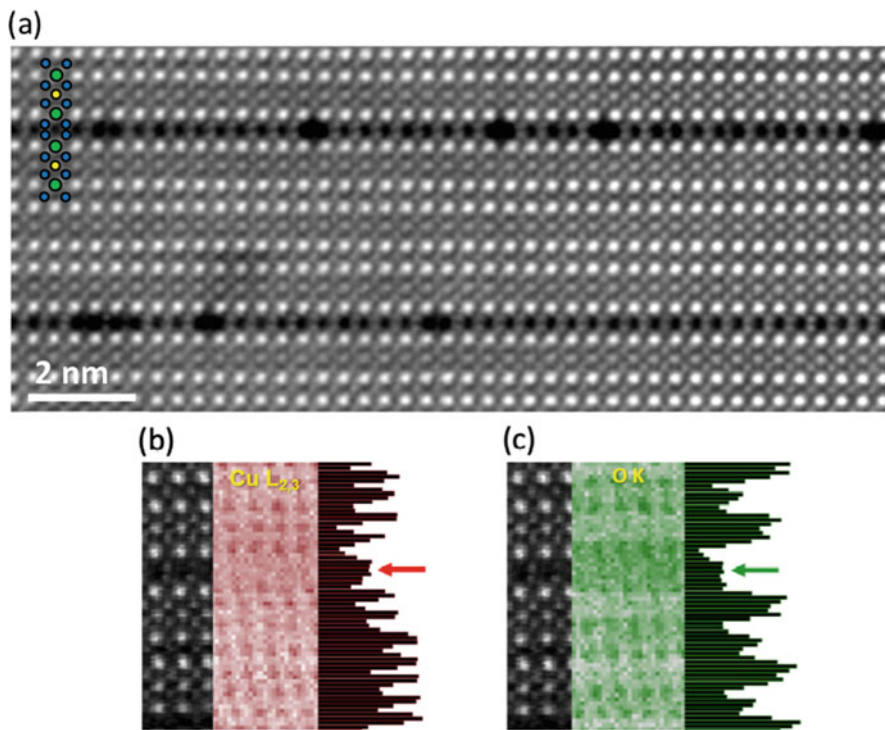


Fig. 7.9 (a) Z-contrast image of two Y124 intergrowths viewed along the [010] zone-axis direction. The Ba, Y, and Cu atomic columns are represented with green, yellow, and blue circles, respectively. Scale bar: 2 nm. Image acquired at 300 kV on the aberration-corrected FEI Titan. (b) Cu (red) and (c) O (green) EELS compositional maps. Each image displays, from left to right, the ADF simultaneous image, the EELS compositional map and the row-averaged EELS signal profile. The arrows point to the Y124 intergrowth position. Data acquired at 100 kV on the aberration-corrected Nion UltraSTEM. Adapted from [12]

Figure 7.9a shows a Z-contrast image of the YBCO phase with two Y124 intergrowth defects, each one viewed along the [010] zone-axis direction. The contrast within the double Cu-O chains randomly varies along the basal direction, with a lower brightness at some Cu columns. This lowering of intensity is ascribed to the presence of pairs of Cu vacancies (V_{Cu}) [12]. In Fig. 7.9b, c, the Cu and O EELS compositional maps are displayed as red and green color maps, respectively. The vertical profiles correspond to the relative atomic composition (Cu and O) depth-profiles, which are obtained by summing the intensities of each row in the map. In the double-chain (marked by red and green arrows), both the Cu and O signals are observed to be lower than in the single-chain positions, pointing towards the presence of complex Cu-O vacancies.

DFT calculations allowed for estimating the stability of different vacancy configurations by comparing their formation energies at 0 K. A supercell structure

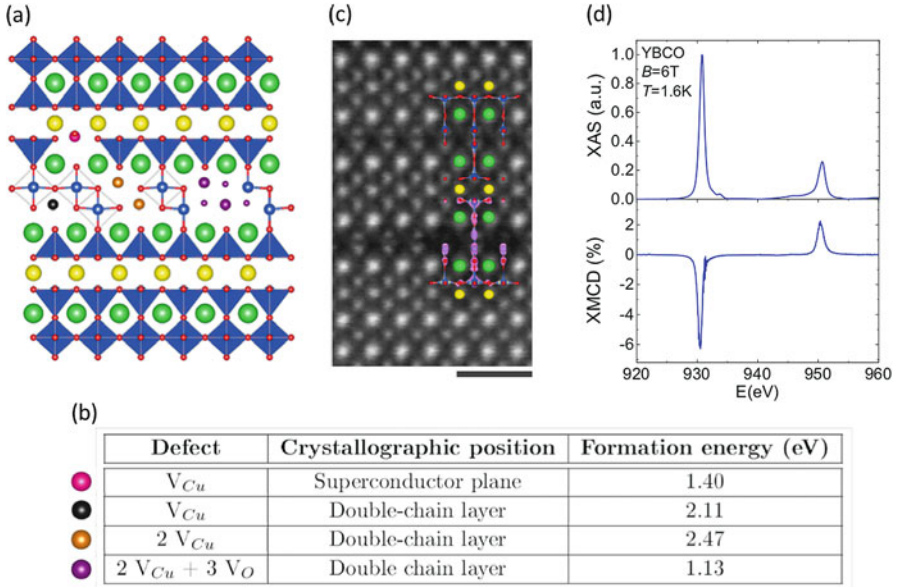


Fig. 7.10 (a) Illustration of the Y248 crystal structure. The pink, orange, black, and magenta circles indicate some of the crystallographic sites where single V_{Cu} and clusters of $V_{Cu} + V_O$ have been tested using DFT calculations. The Ba, Y, Cu, and O atomic columns are represented with green, yellow, blue, and red circles, respectively. (b) Formation energy associated with the specific vacancy configuration represented in (a) at 0 K. (c) Z-contrast image with the isosurface plot of the spin density showing the magnetic moment associated with a $2V_{Cu} + 3V_O$ defect in Y248. Image acquired at 200 kV on the aberration-corrected Nion UltraSTEM. (d) Cu $L_{2,3}$ edge (top) background-subtracted XAS and (bottom) XMCD spectra measured at 6 T, 1.6 K in normal incidence ($\theta = 0^\circ$) for the standard YBCO thin film in Total Electron Yield (TEY) mode. Scale bar: 1 nm. Adapted from [12]

composed by a $Y_2Ba_4Cu_8O_{16}$ (Y248) stoichiometry containing Cu-O double-chain layers instead of Cu-O single chains was used [12], which is represented in Fig. 7.10a. The formation energy of most relevant defects obtained from the DFT calculations is summarized in the table of Fig. 7.10b. The most favorable vacancy configuration—that also matches with the EELS experimental data—corresponds to the case where two Cu vacancies are accompanied with three oxygen vacancies ($2V_{Cu} + 3V_O$, purple in Fig. 7.8a), with one O vacancy located in the upper Cu-O chain and two in the lower one. DFT also allowed insights into the effect of these complex defects on the electronic and magnetic properties of the system in the metallic phase. The most striking effect is the fact that the O-decorated Cu vacancies give rise to a finite magnetic moment of $\approx 2.2 \mu_B$ per $2V_{Cu} + 3V_O$ defect cluster [12]. Figure 7.10c shows an isosurface plot of the spin density around one such defect cluster. Notice that the magnetization extends to the neighboring CuO_2 planes, which implies that the defect structure also provides an extra vortex-pinning contribution, since the magnetic vortices formed by flux lines should find

it favorable to go through this non-superconducting and magnetic defect with nanoscale dimensions.

X-ray magnetic circular dichroism (XMCD) at the Cu $L_{2,3}$ edge was used to experimentally prove the existence of the predicted magnetic moment associated with these complex defects. XMCD experiments were performed in Total Electron Yield (TEY) detection mode on two samples, a pristine YBCO film and a YBCO + BYTO nanocomposite thin film, both of which exhibited a high Y124 intergrowth concentration within the superficial TEY probing depth (~ 6 nm). XMCD is an element-sensitive technique which involves recording the difference between the X-ray absorption for left- and right-polarized photons. If the Cu-XMCD difference is non-zero, it suggests the presence of magnetic moments on the probed atoms, which in this case is Cu. This is demonstrated in Fig. 7.10d, which shows a dichroic signal obtained in a YBCO film measured at 6 T and at a temperature of 1.6 K. Both samples, the pristine YBCO film and the YBCO + BYTO nanocomposite, displayed qualitatively similar Cu $L_{2,3}$ edge fine structure and dichroic spectra. The XMCD as a function of the magnetic field dependence displayed a superparamagnetic behavior even below T_c , which was assigned to the presence of the complex $2V_{Cu} + 3V_O$ defects with an associated cluster ferromagnetic moment [12]. The same superparamagnetic signal has been detected in hybrid YBCO nanocomposites thin films, allowing to propose a model in which the magnetism of Cu atoms in superconducting YBCO films can be explained in terms of a superparamagnetic behavior of isolated ferromagnetic clusters, even below T_c [12, 61]. The fact that these defect clusters are found in large numbers in YBCO nanocomposites, which show at the same time an enormous enhancement of vortex-pinning efficiency, makes one wonder if this novel behavior plays a role in efficiently pinning vortices. Thus, they are an excellent playground to investigate the interaction between superconducting vortices and ferromagnetic clusters at low temperatures.

DFT calculations revealed that the $2V_{Cu} + 3V_O$ defect is more stable under low oxygen pressures, precisely the conditions under which the YBCO films are grown [12]. Therefore, one would expect that the single crystals, which are grown under higher oxygen pressures, did not present the most favorable conditions for the formation of the Cu divacancies. However, STEM analyses of a single crystal revealed the existence of both Cu and O vacancies within the Y124 intergrowths. The low-magnification image shown in Fig. 7.11a evidences that the presence of Y124 intergrowths is restricted to only a few nanometers below the surface of the single crystal, while the high magnification image shown in Fig. 7.11b demonstrates the existence of Cu divacancies within the intergrowths. Interestingly, the Cu-XMCD measurements in TEY (surface) mode from the very same sample presented a robust dichroic signal of about 5%. These results prove that whenever the Y124 intergrowths are present in YBCO there are Cu divacancies buried in them with an associated magnetic moment.

Furthermore, in order to attest the DFT-predicted structure of the $2V_{Cu} + 3V_O$ defects, one can use the ABF imaging mode, which is able to probe all the atomic sub-lattices. Figure 7.12a, b, respectively, show the Z-contrast and the ABF images

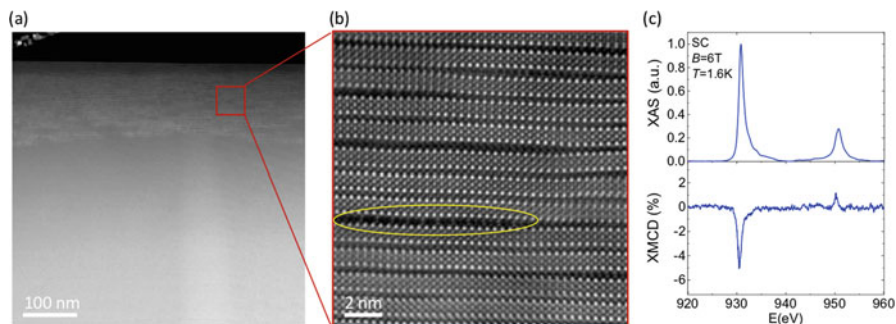


Fig. 7.11 (a) Z-contrast image of a YBCO single crystal. (b) Higher magnification Z-contrast image of the surface of the crystal showing a large concentration of Y124 intergrowths. A region with a visible concentration of Cu vacancies is marked with a yellow circle. Data acquired at 200 kV on the aberration-corrected Nion UltraSTEM. (c) Cu $L_{2,3}$ edge (top) background-subtracted XAS and (bottom) XMCD spectra measured at 6 T, 1.6 K in normal incidence ($\theta = 0^\circ$) for the YBCO single crystal obtained under TEY mode

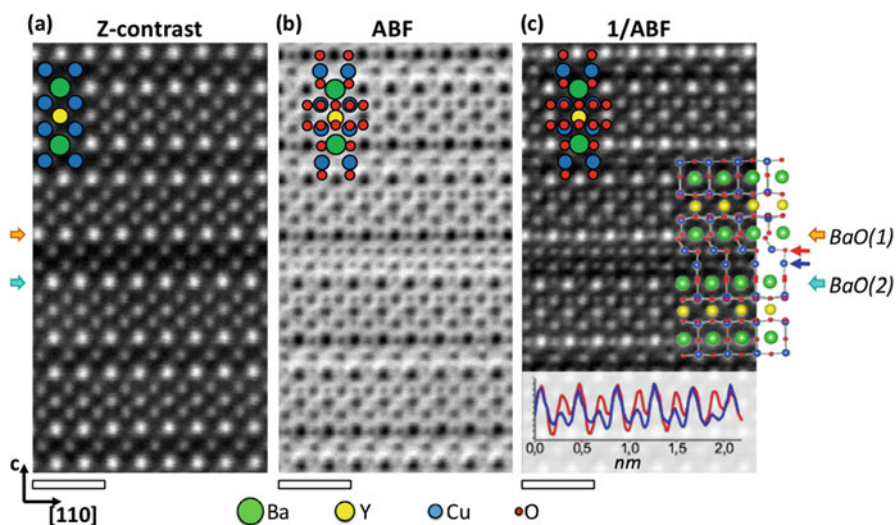


Fig. 7.12 (a) Z-contrast, (b) ABF, and (c) contrast-inverted ABF images of an isolated Y124 intergrowth viewed along the $[100]$ zone-axis direction. The DFT-simulated structure is superimposed in (c). The inset shows two horizontal intensity profiles measured along the upper (red) and lower (blue) Cu-O double-chains. Although not shown, the substrate is located downwards and defines what is called upper and lower Cu-O chains, with the lower chain being closer to the substrate. The Ba, Y, Cu, and O atomic columns are represented with green, yellow, blue, and red circles, respectively. Scale bars: 0.5 nm. Data acquired at 200 kV on the aberration-corrected Nion UltraSTEM

of the YBCO lattice with an isolated Y124 intergrowth along the $[100]$ zone axis. The inverted ABF image, Fig. 7.12c, unveils clearly the oxygen sub-lattice and shows a perfect match with the DFT-predicted structure. In particular, the experimental image shows that the relative O content of both Cu-O planes of the Y124 intergrowth is different. The lower Cu-O chain (blue arrow in Fig. 7.12c) contains more O vacancies, therefore, has a lower O atomic column intensity, as shown in the horizontal trace of the intensity profiles along the two Cu-O chains of the intergrowth, see inset of Fig. 7.12c. Remarkably, this uneven distribution of oxygen vacancies is general, as the lower Cu-O plane of the intergrowth (the one closer to the substrate, which is located at the bottom of the image, although not shown) always presents a lower content of oxygen. This suggests that the distribution of oxygen vacancies is dictated by kinetic effects, during the layer-by-layer bottom-to-top growth process. In addition, a careful inspection of the Ba-O plane right under the double Cu-O chain shows that some of the apical oxygens, those in the O(2) site, are slightly shifted upwards as well, resulting in a rod instead of a round atomic column in the contrast-inverted ABF image, which was also predicted by DFT calculations; see the sketched structure of the inset in Fig. 7.12c.

Yet, Y124 intergrowths hold in store more surprises, as subtle structural changes occur around them. Figure 7.13a–c show a high-resolution Z-contrast image of the YBCO matrix with two Y124 intergrowths, the out-of-plane spacings map between the heaviest cations (Y and Ba) and the averaged profile across the intergrowths, respectively. Notice that the profile distinguishes three different spacings: the Y–Ba, the Ba–Y, and the Ba–Ba spacings. These results show that close to the intergrowth the Ba–Y spacing is smaller than the Y–Ba spacing, as represented in Fig. 7.13d;

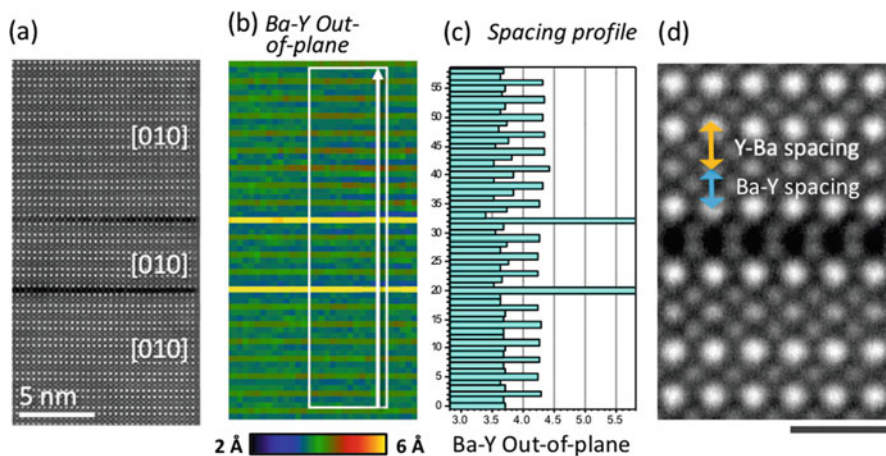


Fig. 7.13 (a) Atomic resolution image of YBCO lattice with two Y124 intergrowths imaged along the $[010]$ orientation. (b) Y–Ba, Ba–Y, and Ba–Ba out-of-plane spacings calculated from (a). (c) Y–Ba, Ba–Y, and Ba–Ba averaged spacing profile of (b). (d) higher resolution Z-contrast image of YBCO showing the Y–Ba and Ba–Y spacings. Scale bar: 1 nm. Data acquired at 300 kV on the aberration-corrected FEI Titan

whereas farther from the intergrowth (>5-unit cells) the spacings become equal and recover the expected value for defect-free YBCO.

What is the cause of such striking result? ABF imaging of the YBCO matrix in the presence of a Y124 intergrowth, as shown in Fig. 7.12, gives the answer to this question. In the inverted ABF image, see Fig. 7.12c, the O columns located within the BaO(1) plane that is present above the fault (orange arrow) appear brighter than those belonging to the lower BaO(2) plane (blue arrow). It should be noted that the difference in contrast between the BaO(1) and BaO(2) planes evidences that the latter contain oxygen vacancies, and also that of the two BaO planes that are present within the YBCO unit cell, the BaO(1) one is always closer to the film's surface. Although anticipated in previous results [62–65], this constitutes the first direct experimental observation of apical oxygen vacancies ($V_{\text{O}}^{\text{BaO}}$) in the BaO plane.

The presence of $V_{\text{O}}^{\text{BaO}}$ is linked to the Y124 intergrowths as these vacancies are absent farther from the intergrowths. Independent of the growth process used, and even for the YBCO single crystals, $V_{\text{O}}^{\text{BaO}}$ oxygen vacancies appear in every other Ba-O plane close to the intergrowths, which rules out the origin of these vacancies to the strain induced due to lattice mismatch of YBCO with a substrate. Instead, their existence seems to be related to the local strain generated when an extra Cu-O plane is added once a YBCO intergrowth is generated [to be published].

The stability of the $V_{\text{O}}^{\text{BaO}}$ has also been studied by DFT calculations. The plot in Fig. 7.14 shows the formation energy of apical or planar oxygen vacancies for varying concentrations, relative to the energies of the well-known $V_{\text{O}}^{\text{CuO}}$. $V_{\text{O}}^{\text{CuO}}$ is more favorable at high vacancy concentrations because multiple vacancies can order along the chains, which stabilizes them. However, in the optimal doping region,

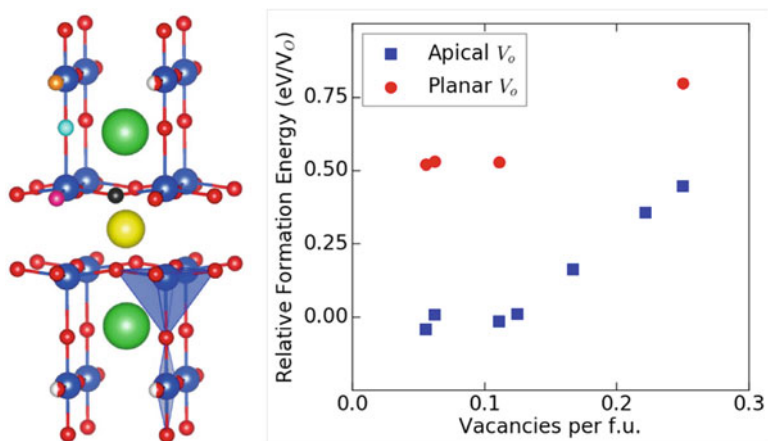


Fig. 7.14 Left panel, sketch of the YBCO unit cell with the position of the oxygen vacancies painted in different colors. Right panel, a plot of the formation energy of oxygen vacancies in different crystallographic sites as a function of vacancy concentration per formula unit (f.u.). The energies are calculated relative to the most stable ordering of $V_{\text{O}}^{\text{CuO}}$ at that concentration

V_{O}^{BaO} and V_{O}^{CuO} have nearly identical formation energies, indicating that they are equally likely to form. The formation energy increases when the V_O is placed in the superconducting planes, indicating that planar vacancies should not be present in large numbers. These theoretical calculations are in excellent agreement with the experimental observations.

Obviously, the presence of V_{O}^{BaO} will trigger structural distortions that can also be identified using the ABF imaging mode. Figure 7.15a shows a contrast-inverted ABF image of the YBCO lattice surrounding two Y124 intergrowths. A higher magnification contrast-inverted ABF image, shown in Fig. 7.15b, unveils, at first glance, the structural changes that take place in the oxygen sub-lattice. The oxygen atoms of the superconducting planes are shifted towards the Y cation in the undistorted structure, forming a rippling pattern with their neighboring Cu cations. This rippling is clearly identified in the superconducting plane that is farther away from the Ba-O plane containing oxygen vacancies. However, this rippling almost disappears in the upper superconducting plane. In addition, the apical oxygen atoms located in the Ba-O planes containing oxygen vacancies are shifted upwards, and as a result, the spacing between the Cu lying in the superconducting plane and its nearest apical oxygen (δ_{ap}) is greater than the lower one. These distortions modify the Cu-O bondings, in particular the in-plane and the apical oxygen height of the

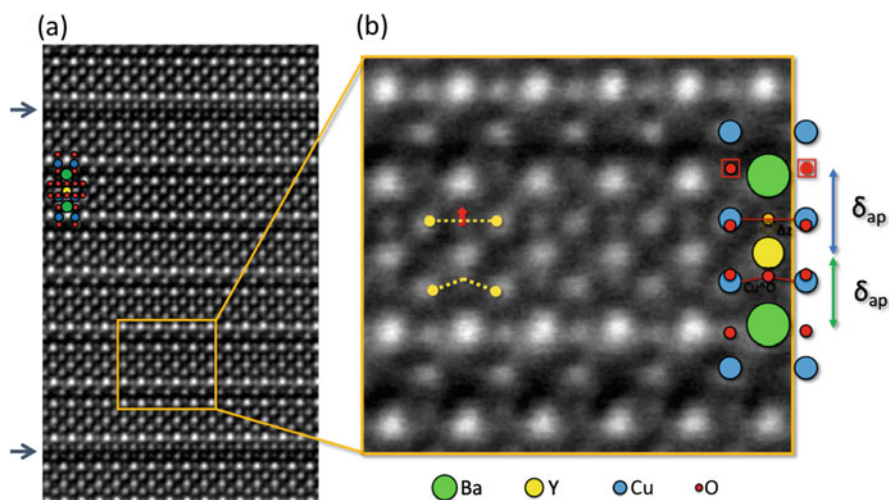


Fig. 7.15 (a) High-resolution contrast-inverted ABF image of a region in a YBCO thin film containing two Y124 intergrowths, signaled with blue arrows. Scale bar: 1 nm. The orange rectangular area is magnified in (b). The Ba, Y, Cu, and O atomic columns are represented with green, yellow, blue, and red circles, respectively. The change in the Cu–O–Cu angles is marked in yellow. The red arrow signals the upward shift of the apical oxygen. Data acquired at 200 kV on the aberration-corrected Nion UltraSTEM

superconducting planes, and will affect the electronic structure of the YBCO, and thus a detailed theoretical study of the electronic states locally around these defects is required.

7.5 Summary

Abraham Lincoln once said, “It has been my experience that folks who have no vices have very few virtues.” This bit of wisdom applies equally well to defects in materials. Defects are generally seen as detrimental to their functionality and applicability, however, in some complex oxides, they present an opportunity to enhance particular properties. A paradigmatic example is the high-temperature superconductor YBCO, in which defects play an essential role in pinning quantized magnetic vortices and preventing energy losses. As not all defects are effective, it is necessary to have a high degree of understanding of their structure, chemistry as well as of how defects behave and interact within the YBCO matrix. This is achieved by a combination of microscopic experiments and first-principles calculations.

In this chapter, it has been shown that by using a combination of aberration-corrected scanning transmission electron microscopy (STEM), electron energy loss spectroscopy (EELS), density-functional-theory (DFT) calculations and X-ray magnetic circular dichroism (XMCD), one can shed light on the complex defect landscape of YBCO thin films and nanocomposites and unveil the presence of previously disregarded defects embedded in YBCO, as well as measure their effect on the atomic spacings, hence quantifying strain at the unit-cell level, allowing the description of peculiar electronic and magnetic properties.

Acknowledgements Authors acknowledge the MICIN (NANOSELECT, DUARFS MAT2017-83468-R and MAT2014-51778-C2-1-R), Generalitat de Catalunya (2014SGR 753 and Xarmae), and the EU (EU-FP7 NMP-LA-2012-280432 EUROTAPES project). They also acknowledge financial support from the Spanish Ministry of Economy, Industry and Competitiveness, through the “Severo Ochoa” Programme for Centres of Excellence in R&D (SEV-2015-0496). STEM imaging and analysis at 200 kV was sponsored by the U.S. Department of Energy, Office of Science, Basic Energy Sciences, Materials Sciences and Engineering Division, and STEM imaging at 100 kV was conducted at the Center for Nanophase Materials Sciences, which is a DOE Office of Science User Facility. STEM imaging and analysis at 300 kV was conducted in the Laboratorio de Microscopías Avanzadas (LMA) at Instituto de Nanociencia de Aragón (INA) at the University of Zaragoza. J.G. also acknowledges the Ramón y Cajal program (RYC-2012-11709). The work at Washington University (S.T.H. and R.M.) was supported by the National Science Foundation (NSF) grant number DMR-1806147. This work used the computational resources of the Extreme Science and Engineering Discovery Environment (XSEDE), which is supported by National Science Foundation grants ACI-1053575 and ACI-1548562.

The authors are grateful to all the collaborators who made this work possible over the years, especially to Teresa Puig, Xavier Obradors, Mariona Coll, Anna Palau, Anna Llordes, Juan Salafranca, Maria Varela, Juan Carlos Idrobo, Cesar Magen, Pablo Cayado, S. Manuel Valvidares, Pierluigi Gargiani, Eric Pellegrin, Javier Herrero-Martin, Wolfgang Windl, Matt Chisholm, Sokrates T. Pantelides, and Stephen J. Pennycook.

References

1. D. Dimos, P. Chaudhari, J. Mannhart, *Phys. Rev. B* **41**, 4038 (1990)
2. M.P. Paranthaman, T. Izumi, *MRS Bull.* **29**, 533 (2004)
3. X. Song, Z. Chen, S.-I. Kim, D.M. Feldmann, D. Larbalestier, J. Reeves, Y. Xie, V. Selvamanickam, *Appl. Phys. Lett.* **88**, 212508 (2006)
4. Y. Yamada, K. Takahashi, H. Kobayashi, M. Konishi, T. Watanabe, A. Ibi, T. Muroga, S. Miyata, T. Kato, T. Hirayama, Y. Shiohara, *Appl. Phys. Lett.* **87**, 132502 (2005)
5. S. Kang, A. Goyal, J. Li, A.A. Gapud, P.M. Martin, L. Heatherly, J.R. Thompson, D.K. Christen, F.A. List, M. Paranthaman, D.F. Lee, *Science* **311**, 1911 (2006)
6. T. Haugan, P.N. Barnes, R. Wheeler, F. Meisenkothen, M. Sumption, *Nature* **430**, 867 (2004)
7. J.L. MacManus-Driscoll, S.R. Foltyn, Q.X. Jia, H. Wang, A. Serquis, L. Civale, B. Maiorov, M.E. Hawley, M.P. Maley, D.E. Peterson, *Nat. Mater.* **3**, 439 (2004)
8. P. Mele, R. Guzman, J. Gazquez, T. Puig, X. Obradors, S. Saini, Y. Yoshida, M. Mukaida, A. Ichinose, K. Matsumoto, M. Idries Adam, *Supercond. Sci. Technol.* **28**, 024002 (2015)
9. A. Llordés, A. Palau, J. Gázquez, M. Coll, *Nat. Mater.* **11**, 329 (2012)
10. C. Cantoni, Y. Gao, S.H. Wee, E.D. Specht, J. Gazquez, J. Meng, S.J. Pennycook, A. Goyal, *ACS Nano* **5**, 4783 (2011)
11. R. Guzman, J. Gazquez, V. Rouco, A. Palau, C. Magen, M. Varela, J. Arbiol, X. Obradors, T. Puig, *Appl. Phys. Lett.* **102**, 081906 (2013)
12. J. Gazquez, R. Guzman, R. Mishra, E. Bartolomé, J. Salafranca, C. Magén, M. Varela, M. Coll, A. Palau, S.M. Valvidares, P. Gargiani, E. Pellegrin, J. Herrero-Martin, S.J. Pennycook, S.T. Pantelides, T. Puig, X. Obradors, *Adv. Sci.* **3**, 1500295 (2016)
13. R. Guzman, J. Gazquez, B. Mundet, M. Coll, X. Obradors, T. Puig, *Phys. Rev. Mater.* **1**, 024801 (2017)
14. A.K. Jha, K. Matsumoto, T. Horide, S. Saini, P. Mele, A. Ichinose, Y. Yoshida, S. Awaji, *J. Appl. Phys.* **122**, 093905 (2017)
15. T. Horide, F. Kametani, S. Yoshioka, T. Kitamura, K. Matsumoto, *ACS Nano* **11**, 1780 (2017)
16. T. Maeda, K. Kaneko, K. Yamada, A. Roy, Y. Sato, R. Teranishi, T. Kato, T. Izumi, Y. Shiohara, *Ultramicroscopy* **176**, 151 (2017)
17. G. Deutscher, *Appl. Phys. Lett.* **96**, 1 (2010)
18. A. Llordés, A. Palau, J. Gázquez, M. Coll, R. Vlad, A. Pomar, J. Arbiol, R. Guzmán, S. Ye, V. Rouco, F. Sandiumenge, S. Ricart, T. Puig, M. Varela, D. Chateigner, J. Vanacken, J. Gutiérrez, V. Moshchalkov, G. Deutscher, C. Magen, X. Obradors, *Nat. Mater.* **11**, 329 (2012)
19. S.J. Pennycook, P.D. Nellist, *Scanning Transmission Electron Microscopy* (Springer, New York, 2011)
20. S.J. Pennycook, D.E. Jesson, *Ultramicroscopy* **37**, 14 (1991)
21. P.D. Nellist, S.J. Pennycook, *Ultramicroscopy* **78**, 111 (1999)
22. P.D. Nellist, S.J. Pennycook, *Science* **274**, 413 (1996)
23. A.Y. Borisevich, A.R. Lupini, S.J. Pennycook, *Proc. Natl. Acad. Sci. U. S. A.* **103**, 3044 (2006)
24. R. Ishikawa, E. Okunishi, H. Sawada, Y. Kondo, F. Hosokawa, E. Abe, *Nat. Mater.* **10**, 278 (2011)
25. W.M. Temmerman, H. Winter, Z. Szotek, A. Svane, *Phys. Rev. Lett.* **86**, 2435 (2001)
26. R. Liang, D.A. Bonn, W.N. Hardy, *Phys. Rev. B* **73**, 180505 (2006)
27. N.D. Browning, J. Yuan, L.M. Brown, *Phys. C Supercond.* **202**, 12 (1992)
28. N. Gauquelin, D.G. Hawthorn, G.A. Sawatzky, R.X. Liang, D.A. Bonn, W.N. Hardy, G.A. Botton, *Nat. Commun.* **5**, 4275 (2014)
29. D.G. Hawthorn, K.M. Shen, J. Geck, D.C. Peets, H. Wadati, J. Okamoto, S.-W. Huang, D.J. Huang, H.-J. Lin, J.D. Denlinger, R. Liang, D.A. Bonn, W.N. Hardy, G.A. Sawatzky, *Phys. Rev. B* **84**, 075125 (2011)
30. M. Griioni, J.F. van Acker, M.T. Czyżyk, J.C. Fuggle, *Phys. Rev. B* **45**, 3309 (1992)

31. P. Cayado, B. Mundet, H. Eloussifi, F. Vallés, M. Coll, S. Ricart, J. Gázquez, A. Palau, P. Roura, J. Farjas, T. Puig, X. Obradors, *Supercond. Sci. Technol.* **30**, 1361 (2017)
32. S.H. Wee, Y.L. Zuev, C. Cantoni, A. Goyal, *Sci. Rep.* **3**, 2310 (2013)
33. A.A. Gapud, D. Kumar, S.K. Viswanathan, C. Cantoni, M. Varela, J. Biade, S.J. Pennycook, D.K. Christen, *Supercond. Sci. Technol.* **18**, 1502 (2005)
34. J. Gutiérrez, A. Lordés, J. Gázquez, M. Gibert, N. Romà, S. Ricart, A. Pomar, F. Sandiumenge, N. Mestres, T. Puig, X. Obradors, *Nat. Mater.* **6**, 1893 (2007)
35. X. Obradors, T. Puig, S. Ricart, M. Coll, J. Gázquez, A. Palau, X. Granados, *Supercond. Sci. Technol.* **25**, 123001 (2012)
36. K. Matsumoto, P. Mele, *Supercond. Sci. Technol.* **23**, 14001 (2010)
37. P. Mele, K. Matsumoto, T. Horide, A. Ichinose, M. Mukaida, Y. Yoshida, S. Horii, R. Kita, *Supercond. Sci. Technol.* **21**, 015019 (2008)
38. T. Horide, N. Sakamoto, A. Ichinose, K. Otsubo, T. Kitamura, K. Matsumoto, *Supercond. Sci. Technol.* **29**, 105010 (2016)
39. D.M. Feldmann, T.G. Holesinger, B. Maiorov, S.R. Foltyn, J.Y. Coulter, I. Apodaca, *Supercond. Sci. Technol.* **23**, 095004 (2010)
40. M. Coll, S. Ye, V. Rouco, A. Palau, R. Guzman, J. Gázquez, J. Arbiol, H. Suo, T. Puig, X. Obradors, *Supercond. Sci. Technol.* **26**, 015001 (2013)
41. D.A. Muller, N. Nakagawa, A. Ohtomo, J.L. Grazul, H.Y. Hwang, **430**, 657 (2004)
42. P.J. Phillips, M. De Graef, L. Kovarik, A. Agrawal, W. Windl, M.J. Mills, *Ultramicroscopy* **116**, 47 (2012)
43. H.W. Zandbergen, R. Gronsky, G. Thomas, *Phys. Status Solidi* **105**, 207 (1988)
44. H.W. Zandbergen, R. Gronsky, K. Wang, G. Thomas, *Nature* **331**, 596 (1988)
45. J. Rabier, P.D. Tall, M.F. Denanot, *Philos. Mag. A* **67**, 1021 (1993)
46. J. Taftø, M. Suenaga, R.L. Sabatini, *Appl. Phys. Lett.* **52**, 667 (1988)
47. P. Hirel, P. Marton, M. Mrovec, C. Elsässer, *Acta Mater.* **58**, 6072 (2010)
48. F. Sandiumenge, T. Puig, J. Rabier, J. Plain, X. Obradors, *Adv. Mater.* **12**, 375 (2000)
49. F. Sandiumenge, J. Rabier, *Studies of High Temperature Superconductors* (Nova Science, Narliker, 1999)
50. T. Puig, J. Gutiérrez, A. Pomar, A. Lordés, J. Gázquez, S. Ricart, F. Sandiumenge, X. Obradors, *Supercond. Sci. Technol.* **21**, 34008 (2008)
51. J.A. Xia, N.J. Long, N.M. Strickland, P. Hoefakker, E.F. Talantsev, X. Li, W. Zhang, T. Kodenkandath, Y. Huang, M.W. Rupich, *Supercond. Sci. Technol.* **20**, 880 (2007)
52. A. Goyal, S. Kang, K.J. Leonard, P.M. Martin, A.A. Gapud, M. Varela, M. Paranthaman, A.O. Ijaluola, E.D. Specht, J.R. Thompson, D.K. Christen, S.J. Pennycook, F.A. List, *Supercond. Sci. Technol.* **18**, 1533 (2005)
53. T.G. Holesinger, L. Civale, B. Maiorov, D.M. Feldmann, J.Y. Coulter, D.J. Miller, V.A. Maroni, Z. Chen, D.C. Larbalestier, R. Feenstra, X. Li, Y. Huang, T. Kodenkandath, W. Zhang, M.W. Rupich, A.P. Malozemoff, *Adv. Mater.* **20**, 391 (2008)
54. H. Yamasaki, K. Ohki, I. Yamaguchi, M. Sohma, W. Kondo, H. Matsui, T. Manabe, T. Kumagai, *Supercond. Sci. Technol.* **23**, 105004 (2010)
55. E.D. Specht, A. Goyal, J. Li, P.M. Martin, X. Li, M.W. Rupich, *Appl. Phys. Lett.* **89**, 2006 (2006)
56. F. Vallés, A. Palau, V. Rouco, B. Mundet, X. Obradors, T. Puig, *Sci. Rep.* **8**, 5924 (2018)
57. C.J. Jou, J. Washburn, *J. Mater. Res.* **4**, 795 (1989)
58. V. Rouco, A. Palau, R. Guzman, J. Gázquez, M. Coll, X. Obradors, T. Puig, *Supercond. Sci. Technol.* **27**, 125009 (2014)
59. M.J.J. Hÿtch, E. Snoeck, R. Kilaas, *Ultramicroscopy* **74**, 131 (1998)
60. G. Deutscher, *J. Appl. Phys.* **111**, 112603 (2012)
61. E. Bartolomé, P. Cayado, E. Solano, C. Mocuta, S. Ricart, B. Mundet, M. Coll, J. Gázquez, A. Meledin, G. van Tendeloo, S.M. Valvidares, J. Herrero-Martín, P. Gargiani, E. Pellegrin, C. Magén, T. Puig, X. Obradors, *Adv. Electron. Mater.* **3**, 1700037 (2017)

62. J.C. Cheang Wong, C. Ortega, J. Siejka, I. Trimaille, A. Sacuto, L.M. Mercandalli, F. Mayca, *J. Alloys Compd.* **195**, 675 (1993)
63. A.P. Shapovalov, Y.M. Boguslavskij, A.I. Ruban, G.G. Gridneva, V.S. Melnikov, N.P. Pshentsova, *Supercond. Sci. Technol.* **5**, 283 (1992)
64. J.D. Jorgensen, M.A. Beno, D.G. Hinks, L. Soderholm, K.J. Volin, R.L. Hitterman, J.D. Grace, I.K. Schuller, C.U. Segre, K. Zhang, M.S. Kleefisch, *Phys. Rev. B* **36**, 3608 (1987)
65. J.D. Jorgensen, H. Shaked, D.G. Hinks, B. Dabrowski, B.W. Veal, A.P. Paulikas, L.J. Nowicki, G.W. Crabtree, W.K. Kwok, L.H. Nunez, H. Claus, *Phys. C Supercond.* **578**, 153–155 (1988)

Chapter 8

Growth, Properties, and Device Fabrication of Iron-Based Superconductor Thin-Films



Hidenori Hiramatsu and Hideo Hosono

8.1 Introduction

In 2006, the bulk superconductivity at a critical temperature (T_c) of ~ 4 K was reported in LaFePO [1] through a comprehensive study on electric and magnetic functionality in 3d transition metal-based quaternary oxypnictides ($RE T_M Pn O$, where RE = rare earth, T_M = 3d transition metal, and Pn = pnictogen) with the ZrCuSiAs-type layered crystal structure, which was inspired by an exhaustive research on wide band-gap p-type semiconductivity and room-temperature-stable exciton (i.e., electron–hole pair with large binding energy) in monovalent copper-based oxychalcogenides, $RE Cu Ch O$ (Ch = chalcogen) [2, 3] because novel and unique magnetic functionality originating from strong d–p orbitals interaction was expected in $RE T_M Pn O$ due to not only crystal structural but also electronic two-dimensional structures in this material family. Through the comprehensive study on $RE T_M Pn O$, the bulk superconductivity at ~ 3 K of LaNiPO was also found in 2007 [4]. However, both the T_c were as low as around 4 K.

Then, Kamihara et al. reported the bulk superconductivity at 26 K in fluorine-doped LaFeAsO in 2008 [5]. In this case, the parent (i.e., undoped) LaFeAsO is an antiferromagnetic metal, not a superconductor. Electron carrier doping by substitution of fluorine ions at oxygen sites suppresses and vanishes the long-range magnetic ordering in the parent, and then emerges its high- T_c superconductivity. This first report on an iron-based high- T_c superconductor gave a strong impact to the superconductivity research community because not only its high T_c and pairing mechanism were quite unique [6] but also iron metal (Fe) with a large

H. Hiramatsu (✉) · H. Hosono

Laboratory for Materials and Structures, Institute of Innovative Research, Tokyo Institute of Technology, Yokohama, Japan

Materials Research Center for Element Strategy, Tokyo Institute of Technology, Yokohama, Japan
e-mail: h-hirama@mces.titech.ac.jp; hosono@mces.titech.ac.jp

magnetic moment was believed to be harmful to inducing superconductivity due to the competition between the static ordering of electron spins and the formation of electron pairs (i.e., Cooper pairs). Through worldwide subsequent explorations of other iron-based and related materials [7], a lot of new superconductors have been discovered, and the maximum T_c of the iron-based family has reached 55 K of electron-doped SmFeAsO [8, 9] that is the second highest T_c at ambient pressure, next to high- T_c cuprates, among all superconductors. Replacement of La with Sm is thought to be “chemical pressure” effect because ionic radius of Sm is much smaller than that of La due to the lanthanide contraction.

In this chapter, we overview and introduce related materials and their superconducting properties, and the progress and current status of the growth and performance of thin films as well as the devices such as Josephson junctions and coated conductors. Corresponding perspectives are also discussed for practical application of this new class superconductor family.

8.2 Materials

Several tens of superconducting layered iron-based pnictides and chalcogenides have been reported. These materials contain a common local structure of a square lattice of Fe^{2+} with tetrahedral coordination with Pn or Ch . Figure 8.1 is a summary of the crystal structures of the parent materials. To date, six parent compounds are known, and each crystal structure can be derived from the insertion of metals and/or building blocks between the edge-sharing FePn_4 (or Ch_4) layers. Because the Fermi level of each parent compound is primarily governed by five Fe 3d orbitals, iron plays a critical role in their superconductivity. This observation is in sharp contrast to that in high- T_c cuprate superconductors, in which only one 3d orbital is associated with the Fermi level. In addition, iron-based superconductors have tetragonal symmetry in the superconducting phase, are Pauli paramagnetic metals in the normal state, and then undergo crystallographic/magnetic transition from the tetragonal to orthorhombic or monoclinic phase with antiferromagnetism at low temperatures. The exceptions are 11- and 111-type compounds exhibiting Pauli paramagnetism and 245-type compounds exhibiting antiferromagnetic insulating properties.

The superconducting properties are summarized in Table 8.1 for each parent material (see [6] for more detail). For comparison, those of representative metallic and cuprate superconductors are summarized in Table 8.2. The six parent phases mentioned above provide not only diverse relationships between superconductivity and magnetism, but also a large platform for research on superconducting thin films and devices. Superior superconducting properties such as a high $T_c = 20\text{--}55$ K and a large upper critical magnetic field (H_{c2}) > 50 T seem to be appropriate for wire, tape, and coated conductor applications for ultrahigh performance magnets, which has been practically used in magnetic resonance imaging systems. In addition, iron-based superconductors significantly differ from cuprates; the parent compounds of

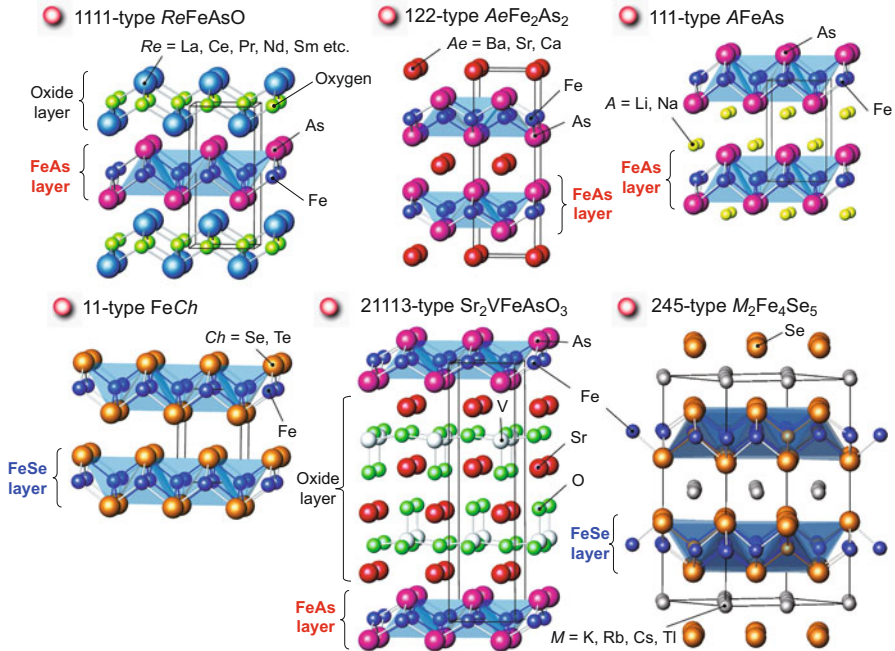
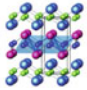
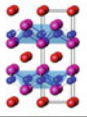
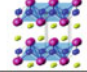
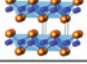
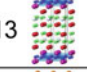
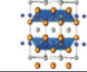


Fig. 8.1 Crystal structures of six parent materials of iron-based superconductors. For example, $LaFeAsO$ and $BaFe_2As_2$ are called 1111- (eleven eleven) and 122- (one two two) types according to the chemical composition ratios of constituent elements. Each material has a common local structure, which governs the superconductivity, of edge-sharing $FeAs_4$ or $FeCh_4$ tetrahedra layers (painted by light blue). The layers alternately stack along the c -axis

iron-based superconductors are “poor (bad)” metals in normal states and exhibit superconductivity in a tetragonal symmetry, whereas those of cuprates are Mott insulators and exhibit superconductivity in an orthorhombic symmetry. It should be noted that the iron-based superconductors have lower magnetic anisotropy factors (γ) in the superconducting properties than those of cuprates [the 122- and 11-type compounds have particularly low anisotropy (1–2)]. Moreover, the intrinsic nature of superconductivity in iron-based superconductors differs from that in cuprates; the former has a multi pocket structure on a Fermi surface and a higher symmetric order parameter (s -wave), but the latter has d -wave pairing although cuprates and iron-based superconductors have several features in common, including a layered crystal structure, superconductivity induced by carrier doping of parents, and the presence of competing antiferromagnetic orders.

Table 8.1 Superconducting properties of six parents of iron-based superconductors

Structure type	Parent composition	Dopant (site)	T_c (K)	$H_{c2}^{//ab}$ (T)	$H_{c2}^{//c}$ (T)	Anisotropy (γ)
1111 	SmFeAsO	F (O) or H (O) Co (Fe)	55	208	50	4
			17	99	19	5
122 	BaFe ₂ As ₂	K (Ba) Co (Fe) P (As)	38	80	75	1.1
			24	55	50	1.1
			31	104	59	1.8
111 	Li _{1-x} FeAs	–	18	24	15	1.6
11 	FeSe	Te (Se)	14	67	46	1.5
21113 	Sr ₂ VFeAsO ₃	Vacancy (O)	37	68.1		–
245 	K ₂ Fe ₄ Se ₅	Rb (K)	45	159	48	3.3

$H_{c2}^{//ab}$ and $H_{c2}^{//c}$ are upper critical magnetic fields along ab -plane and c -axis, respectively. Anisotropic factor γ is defined as $\gamma = (m_c/m_{ab})^{1/2} = \xi_{ab}/\xi_c = H_{c2}^{//ab}/H_{c2}^{//c}$, where m and ξ are effective mass and coherence length, respectively

Table 8.2 Summary of properties of conventional superconductors

Material	T_c (K)	$H_{c2}^{//ab}$ (T)	$H_{c2}^{//c}$ (T)	γ	Application
Nb	9.25	0.4		–	SQUID, sensor, SFQ circuits
Nb-Ti	9.08	15		–	Coils, magnets, etc.
Nb ₃ Sn (called A15)	18.3	29		–	Coated conductors, SQUID
MgB ₂	39.2	60	38	2	
YBCO	93	350	72	7	Electric power cables and wires
(Bi,Pb)-2223	110	850	60	50	

8.3 Thin Films

Similar to each bulk-sample synthesis procedure, the technical difficulties in thin-film growth strongly depend on the material system. Therefore, this section is divided into the following categories: 3-1. 1111-type oxypnictide films, 3-2. 122-type pnictide films, and 3-3. 11-type chalcogenide films. To date, there is no paper on film growth of 111-type and oxypnictides with thick oxide-block layers such as 2113-type due probably to technical difficulties, i.e., 111-type compounds have an alkali metal as the main element, and the film growth of the oxypnictides is difficult for the same reason as that of 1111-type films. Though insulating 245-type

parent films were fabricated, no superconductivity has been observed irrespective of electric-field induced high-density carrier doping [10].

8.3.1 1111-Type Oxypnictide Films

1111-type epitaxial films were first grown by pulsed laser deposition (PLD), in which the excitation light source of laser ablation was replaced from an usual ultraviolet excimer laser to the second harmonics ($\lambda = 532$ nm, i.e., visible light) of a Nd:YAG laser (see Fig. 8.2) to overcome the difficulty in achieving the as-grown phase formation by PLD [11]. However, no La1111 epitaxial films exhibited superconductivity down to 2 K mainly because of lack of fluorine dopant in the obtained epitaxial films. The origin of difficulty in the phase formation via PLD process still remains unclear. During the initial research on 1111 film growth, the formation of the 1111 phase and incorporation of the fluorine dopant in thin films were the most serious issues. Then, the fabrication of biaxially textured La1111 thin films via a two-step ex situ growth method, in which PLD at room temperature for film deposition was combined with post-deposition thermal annealing for crystallization. T_c^{onset} of the obtained La1111 film was 11 K [12]. Similar difficulty in fluorine incorporation in the 1111 films was also reported in the case of molecular beam epitaxy (MBE) [13]. However, the La1111 films, which exhibited clear superconducting transitions at $T_c^{\text{onset}} = 28$ K and $T_c^{\text{zero}} \approx 20$ K, were reported by reducing the oxygen partial pressure during post-deposition thermal annealing in the two-step ex situ process based on PLD [14]. In the case of MBE growth, it was reported that the growth time strongly affected the superconducting properties

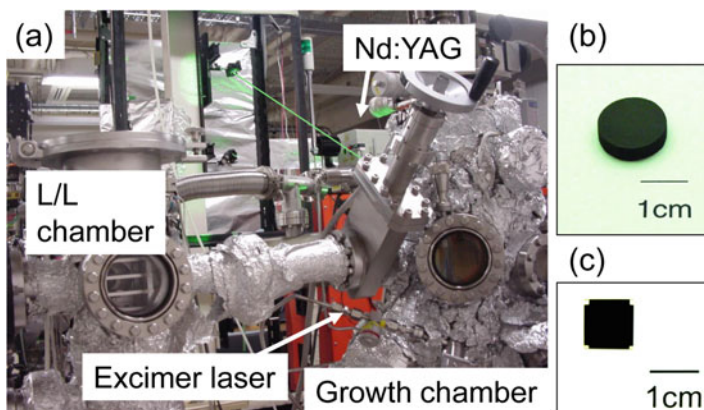


Fig. 8.2 Photographs of Nd:YAG PLD for 1111 epitaxial growth [11]. (a) A Nd:YAG laser and an ultraviolet excimer laser for ArF (193 nm) and KrF (248 nm) are set up to the same PLD growth chamber. (b) A high-purity polycrystalline La1111 bulk target for PLD. (c) Top view of a La1111 epitaxial film

of Nd1111 films [15]. Epitaxial fluorine-doped Nd1111 films were obtained by optimizing MBE growth time (longer time was better to obtain superconducting Nd1111 films). T_c of the Nd1111 films was $T_c^{\text{onset}} = 48$ K and $T_c^{\text{zero}} = 42$ K. This observation implies that the fluorine dopant can be effectively introduced/diffused in the Nd1111 films when longer MBE growth time was employed.

Then, several new fluorine-doping techniques for MBE film growth were developed; for example, gallium getter [16], diffusion from an overlayer of SmF_3 [17], co-evaporation of SmF_3 [18], or FeF_2 [19]. Maximum T_c reported for Sm1111 thin films grown by MBE now are comparable with that of bulk samples ($T_c \approx 56$ K). Therefore, MBE may be the most effective method for obtaining superconducting RE1111 films because each element source and flux rate can be controlled independently by tuning each cell temperature. Recently, also in the case of PLD, in situ fluorine-doping method has been reported [20]. In this case, F-diffusion in the Sm1111 films from CaF_2 substrates was effectively used during high-temperature growth by the Nd:YAG laser PLD. The reported maximum $T_c^{\text{onset}} = \sim 40$ K. Precise optimization of Nd:YAG PLD growth condition contributed to this successful in situ PLD growth of Sm1111 films [21].

As for critical current density (J_c), a J_c of ~ 0.1 MA/cm² at 4.2 K and scaling anisotropy was reported in [22] for the two-step grown La1111 films. The higher self-field J_c of >1 MA/cm² and in-field J_c of $>10^5$ A/cm² at 4.2 K under ultrahigh fields such as >20 T was demonstrated for MBE-grown Sm1111 [23] and Nd1111 films [24] (see Figs. 8.3 and 8.4).

Because of serious difficulty in film growth of 1111 phase, numbers of research papers and research groups that can successfully grow 1111-type films are still limited although 10 years have been passed since the first report on superconductivity of the 1111 phase. However, it is strongly expected that an effective vortex pinning center for 1111 films should further increase their critical current properties and should improve their anisotropic properties under magnetic fields for future application.

8.3.2 122-Type Pnictide Films

A unique doping method, which is the partial substitution of iron site with cobalt (i.e., “direct doping”) [25–27], was reported to induce superconductivity in 1111- and 122-type compounds in 2008. The effectiveness of the direct doping is the superior characteristic of iron-based superconductors because superconductivity is, in general, severely degraded by disturbances to substructures controlling the Fermi surface (i.e., iron square lattice). This finding was also contributed to the early realization of thin films and devices using 122-type iron-based superconductors because cobalt possesses a low vapor-pressure and is incorporated in thin films more easily than other dopants with high vapor-pressures such as fluorine for 1111-type and potassium for 122-type compounds. Especially, successful incorporation of alkali metals such as K in the 122-type films usually requires special techniques

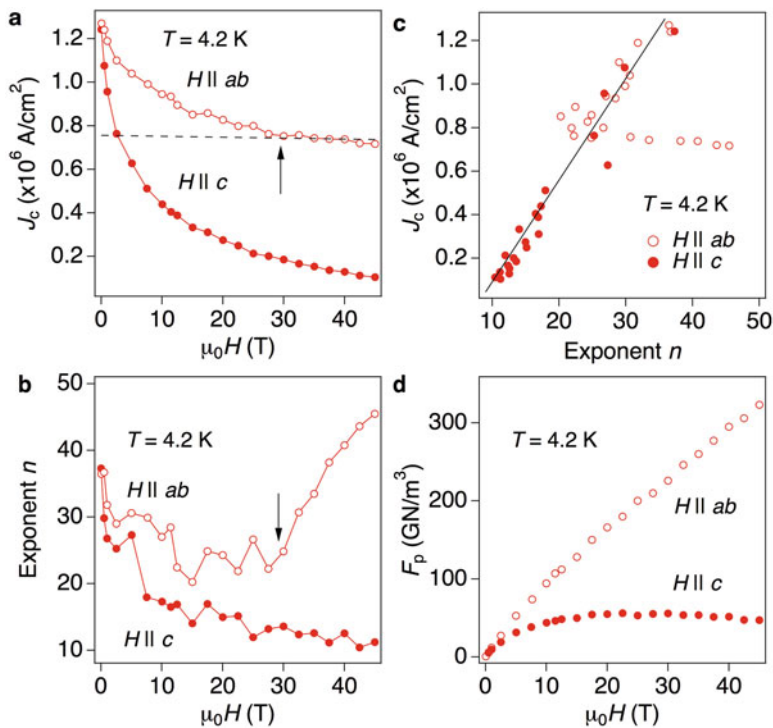


Fig. 8.3 In-field J_c performance of F-doped Sm1111 thin film grown by MBE. (a) Magnetic field dependence of J_c measured at 4.2 K up to 45 T and (b) the corresponding exponent n values. A crossover from extrinsic to intrinsic pinning is shown by the arrow. (c) Scaling behavior of the field dependent J_c . (d) The pinning force density F_p at 4.2 K as a function of external magnetic field [23]

such as post-deposition thermal annealing in tightly closed atmospheres due to its extremely high vapor-pressures [28–32], and K-doped 122-type thin-film samples are unstable in air. Therefore, K-doped 122-type films are not appropriate for thin films exhibiting high performance although K-doped Ba122 has the highest T_c among the 122-type family. Consequently, the direct cobalt-doping led to the rapid realization of high-quality and high- J_c thin films of cobalt-doped Ba122 especially at early stage for iron-based superconductor researches. (Recently, nickel-doped Ba122 films exhibiting comparable properties to Ba122:Co have started to being studied [33–35] because Ni is also an effectively low vapor-pressure dopant to 122 phase, like cobalt.)

Due to the above reasons, cobalt-doped Sr122 and Ba122 epitaxial films were first demonstrated in 2008 [36] and in 2009 [37], respectively. Sr122 phase seems to be more sensitive to air exposure than Ba122 [37, 38] and it led to a weak-link low J_c performance in Sr122:Co [39]. Additionally, Ca122 growth is difficult in the case of PLD [40] (whereas MBE growth of Ca122 films was reported in [41]). Therefore,

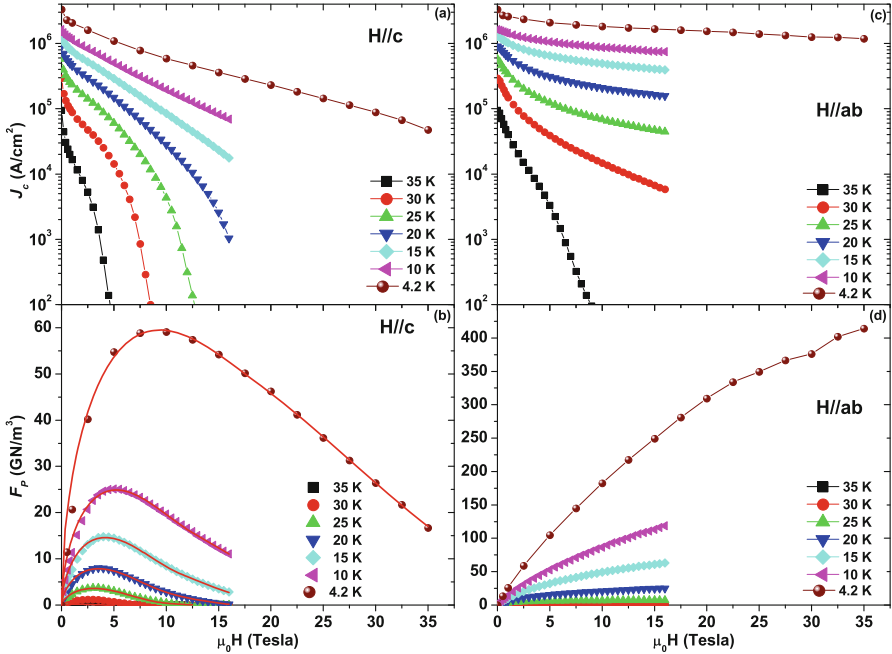


Fig. 8.4 Magnetic field dependence of J_c and pinning force density F_p of an F-doped Nd1111 thin film grown by MBE. The film was measured with field parallel to the c -axis (a, b) and the ab -plane (c, d) up to 16 T in the 35–10 K temperature range and in high-field up to 35 T at 4.2 K [24]

Ba122:Co has been studied most extensively among iron-based superconductor thin films. Then, strain effect in Ba122:Co epitaxial films was examined, leading to high $T_c \approx 25$ K on STO [42] and ≈ 25 –27 K on CaF₂ [43, 44], which are slightly higher than that of bulk Ba122:Co (~ 22 K). Water- or strain-induced superconductivity in undoped parent Sr122 and Ba122 films was also, respectively, reported in [38, 45]. To grow high-quality Ba122:Co epitaxial films, two kinds of effective buffer layers were proposed to solve in-plane lattice mismatch between Ba122:Co films and single-crystal substrates; one is perovskite oxides such as SrTiO₃ [46] and Fe metal layer [47, 48]. In both cases, ultraviolet KrF excimer laser was employed as an excitation laser for PLD process. However, in the case of Nd:YAG PLD [40, 49], no buffer layer is necessary to obtain high-performance Ba122:Co epitaxial films. Because such difference between KrF PLD and Nd:YAG PLD is interesting, four kinds of pulsed laser wavelengths (ArF (193 nm), KrF (248 nm), second harmonics (532 nm), and fundamental (1064 nm) of Nd:YAG) were used for Ba122:Co growth, and the effect of photon energy and critical factors for Ba122:Co epitaxial growth were examined [50] (see Fig. 8.1 for the experimental setup where an excimer and a Nd:YAG lasers are employed with a common PLD film-growth chamber). It was clarified that the optimal deposition rate, which could be tuned by pulse energy (i.e., laser fluence), was independent of laser wavelength. The high-quality Ba122:Co

film grown at the optimal pulse energy for each excitation laser (i.e., the optimum deposition rate) exhibited high- J_c over 1 MA/cm^2 irrespective of the excitation laser wavelength for PLD. The estimated optimum excitation energy density for KrF was $6.7\text{--}10 \text{ J/cm}^2$, which is quite higher than that of second harmonics ($2.2\text{--}3.2 \text{ J/cm}^2$) and fundamental ($1.3\text{--}1.6 \text{ J/cm}^2$) of Nd:YAG laser. Therefore, quite high excitation energy is necessary for high-quality Ba122:Co growth when KrF excimer laser is employed for PLD, as also observed in 122-type $\text{TlFe}_{1.6}\text{Se}_2$ growth [10]. This result would substantiate another advantage of Nd:YAG PLD, which is also effective for obtaining as-grown 1111-type films (see Sect. 8.3.1).

The main origin of their high- J_c of $>1 \text{ MA/cm}^2$ in the Ba122:Co films is c -axis oriented pinning centers [51–54]. Recently, in-field J_c performance under magnetic fields (i.e., isotropic and high- J_c under magnetic fields, e.g., 2.6 MA/cm^2 at 9 T) is much improved in Ba122:Co films [55]. Not only such naturally formed external pinning centers, some intentional approaches for realizing high pinning force along with isotropic properties were also examined, for example, proton irradiation [56], tuning oxygen impurity concentration [57], and undoped Ba122/Ba122:Co modulated superlattices [58, 59].

Utilizing Nd:YAG PLD, a metastable thin-film phase (i.e., not synthesized as 122-type bulk samples) of RE -doped Ba122 films (Ba122: RE , $RE = \text{La, Ce, Pr, and Nd}$) and Sr122:La films [60–63] was stabilized with the expectation that high T_c of $\sim 50 \text{ K}$ would be achieved in this indirectly doped 122-type thin films because it was reported that Ca122:La single crystals exhibit such high T_c [64, 65]. However, the maximum T_c achieved in the indirectly doped 122-type epitaxial films is the same as that of Ba122:Co [60, 61, 63].

Together with extensive researches on Ba122:Co epitaxial films, P-doped Ba122 (Ba122:P) epitaxial films were actively examined since 2012 [66–73] because its maximum T_c (31 K) is higher than that of Ba122:Co. Thus, higher J_c performance than that of Ba122:Co due mainly to its high T_c was expected. The Ba122:P epitaxial films have successfully been obtained by PLD and MBE. As expected, higher $T_c \approx 30 \text{ K}$ than Ba122:Co is reported. High self-field J_c (maximum $J_c^{\text{self}} > 10 \text{ MA/cm}^2$ [67]) is achieved in the Ba122:P films grown by MBE. In addition, an artificial pinning center, BaZrO₃ (BZO), is effective to enhance J_c performance of Ba122:P, like cuprates [69] (see Fig. 8.5). Contributing strong c -axis pinning, quite isotropic J_c is realized in Ba122:P grown by PLD [71] (see Fig. 8.6). High-performance in-field J_c exceeds 0.1 MA/cm^2 at 35 T for $H||ab$ and 18 T for $H||c$ at 4.2 K was demonstrated on Ba122:P films grown by MBE [73].

Figure 8.7 compares the in-field J_c performance of 122-type Ba122Co and Ba122:P films [55, 58, 59, 69, 71, 73–75]. In-field properties of Ba122:Co at early stage in 2010–2012 was not so superior. However, it should be noted that in-field J_c performance of Ba122:P is basically superior to the Ba122:Co due mainly to its high T_c and effective vortex pinning. Recently, a high- J_c and isotropic- J_c performance Ba122:Co film is demonstrated on CaF₂ substrates [55]. The highest J_c performance has reached $\gg 1 \text{ MA/cm}^2$ at 9 T.

Recently, additional interesting properties for future application of Ba122:P exhibiting high- J_c owing to addition of BZO was reported: that is very slow vortex

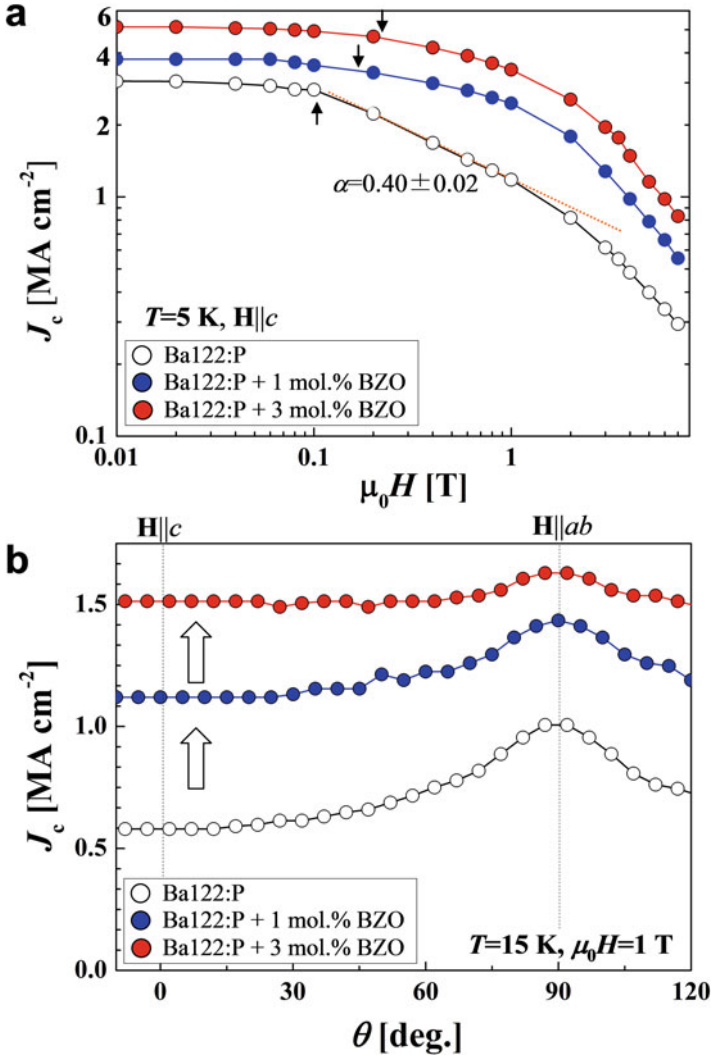


Fig. 8.5 Critical current density J_c of BZO-doped Ba122:P films as a function of magnetic field and angle. **(a)** J_c ($H||c$) at 5 K for Ba122:P + 1 mol.%BZO and Ba122:P + 3 mol.%BZO films compared with the Ba122:P film. The arrows indicate the positions of the crossover field. **(b)** Angular dependence of J_c at 15 K, 1 T for Ba122:P and Ba122:P films with BZO [69]. Copyright © 2013, Springer Nature

creep rate [76], which is a superior advantage to the “persistent mode operation” of high-field magnets such as Nb-Ti employed in magnetic resonance imaging systems. Figure 8.8 summarizes relationship between vortex creep ($S = |(d \ln J)/(d \ln t)|$) at reduced temperature of 1/4 and magnetic field of 1 T and squared Ginzburg number

Fig. 8.6 J_c as a function of angle of applied magnetic field θ_H for Ba122:P epitaxial films grown at three growth rates at 12 K and 3 T [71]. Copyright © 2014 AIP Publishing LLC

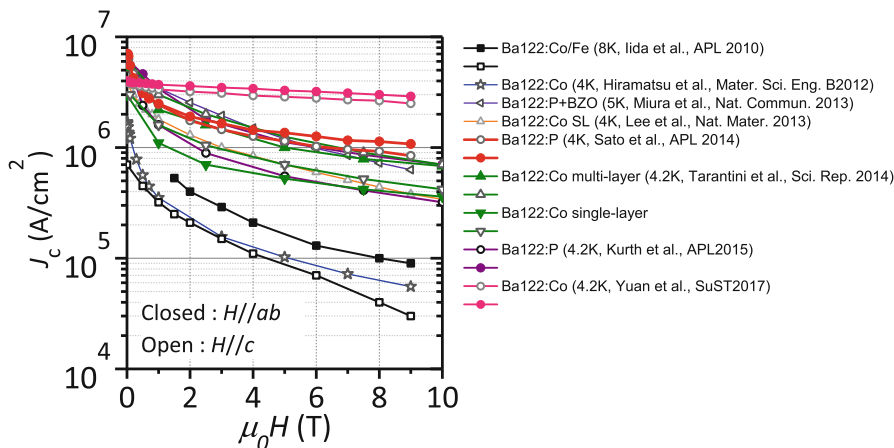
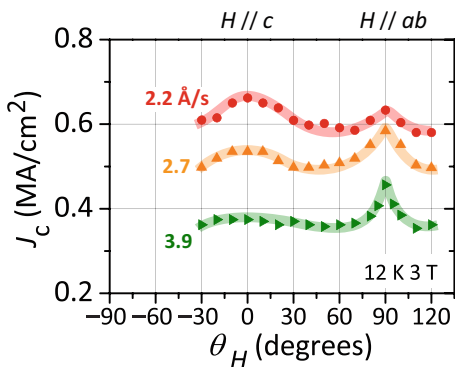


Fig. 8.7 In-field J_c performance for various 122-type epitaxial films at low temperature [55, 58, 59, 69, 71, 73–75]

($G_i^{1/2}$) for various superconductors. This result indicates that Ba122:P exhibits comparable S with those of MgB_2 and $Nb-Ti$.

8.3.3 11-Type Chalcogenide Films

Superconducting 11-type films of FeSe and Fe(Se,Te) started to be reported since 2009. However, particularly at the initial stage of this research, there were few reports of films with zero resistivity, implying the difficulty in fabrication of superconducting 11 thin films owing to the complicated phase diagram (i.e., precise control of chemical composition is necessary). Among a lot of works on 11 films [77–96], the highest T_c to date (except those of monolayer 11, which will be shown later) is $T_c^{onset} \approx 20$ K or slightly higher [80, 83–85], which is higher than that

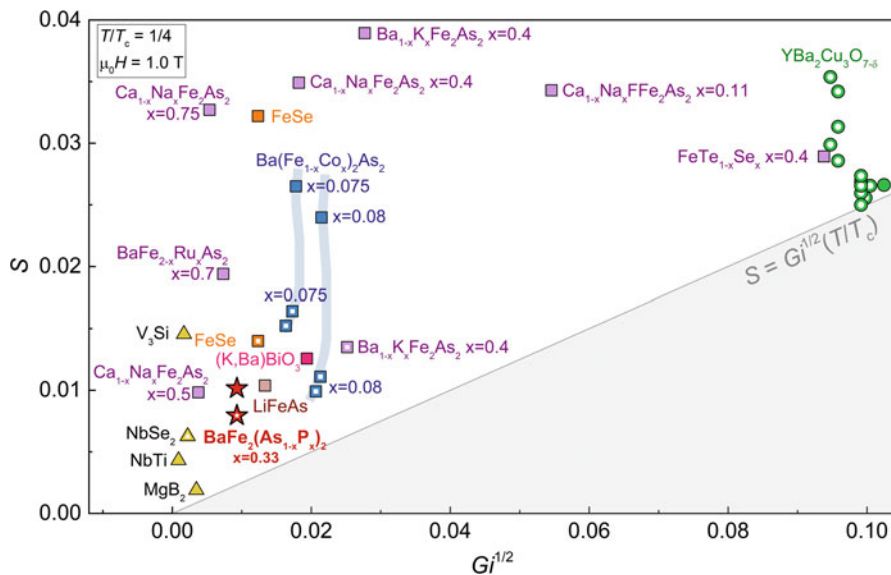


Fig. 8.8 The universal lower limit for vortex creep. Creep (S) at reduced temperature $T/T_c = 1/4$ and field of $\mu_0H = 1$ T for different superconductors plotted versus Ginzburg number $Gi^{1/2}$ [76]. © 2017 Macmillan Publishers Ltd., part of Springer Nature

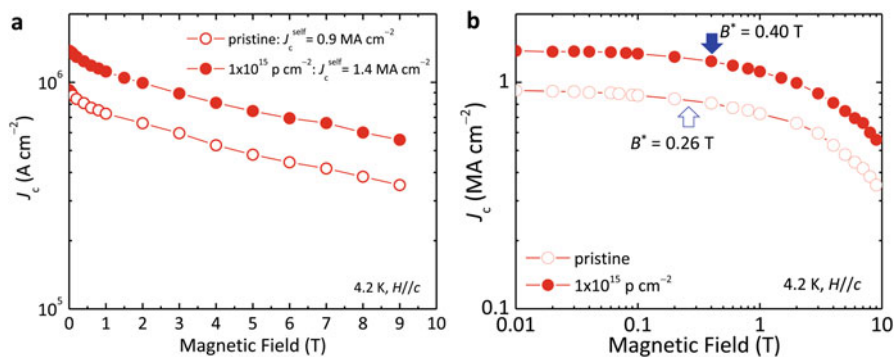


Fig. 8.9 J_c of 11-type Fe(Se, Te) films as a function of magnetic fields up to 9 T. (a) $J_c(H//c)$ at 4.2 K for the 11 film before and after 190 keV proton irradiation. (b) Same data plotted in log-log scale. The arrows indicate the field of the crossover field B^* [93]

of the bulk 11 phase at ambient pressure (~ 14 K) and is comparable to that of Sr/Ba122:Co thin films. Recently, in-field J_c performance of the 11 films is also improved rapidly. It has been comparable to that of Ba122:Co [92–96] (see Figs. 8.9 and 8.10 as examples).

In 2012, a high- T_c superconductivity at >50 K was reported in one unit-cell-thick FeSe monolayer [97]. Then extensive researches on the ultrathin FeSe monolayer have been rapidly performed [98–100]. The maximum T_c reaches 100 K (see

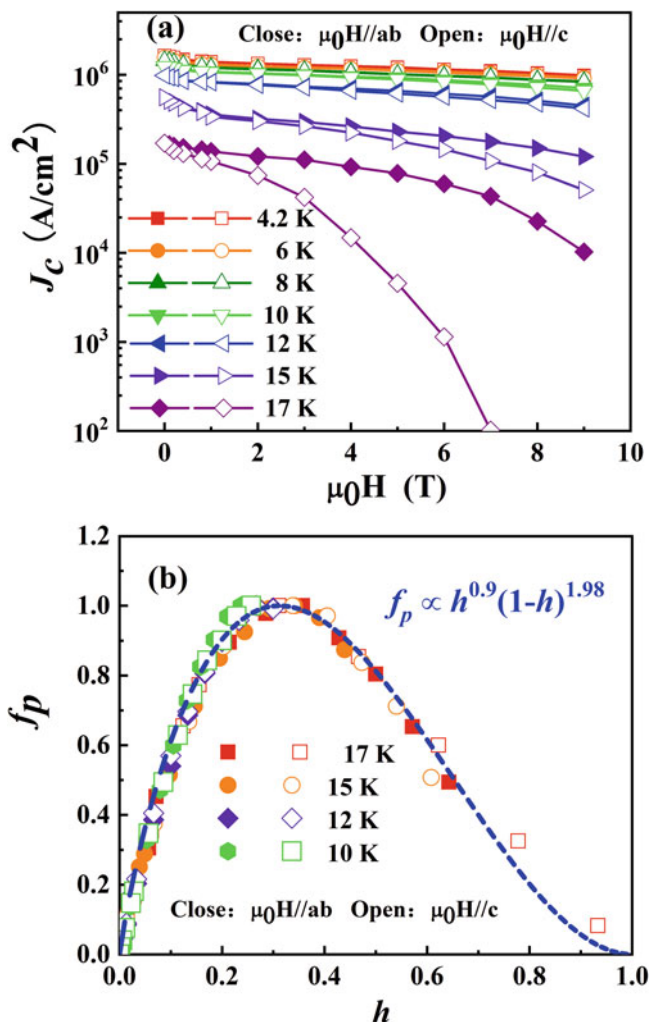


Fig. 8.10 (a) $J_c(H)$ of the 11-type Fe(Se, Te) films on a CaF₂ substrate at 4.2–17 K for $H//ab$ and $H//c$. (b) Kramer's scaling of pinning force density f_p versus reduced field h at 10–17 K [95]. © 2016 IOP Publishing Ltd.

Fig. 8.11 [99]. High T_c of >30 K have been reported also in electric double-layer transitions (EDLT) of FeSe [101–106] (see Fig. 8.12 for an example) after the report on phase transitions by the EDLT operation of 11-based superconductors such as 122-type TlFe_{1.6}Se₂ EDLT [10] and (Li,Fe)OHFeSe EDLT [107]. Because the surface of FeSe films is quite sensitive to air exposure [108], an FeSe EDLT device had to fabricate via an all in situ sample transfer system (see Fig. 8.13). These characteristic extremely high T_c are unique properties for the 11 phase among iron-based superconductors. Both of the atomically thin layer and EDLT structure seem

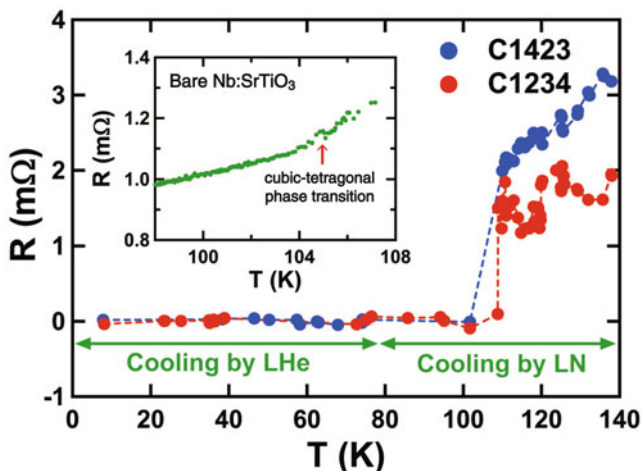


Fig. 8.11 Temperature dependence of the resistance of monolayer FeSe obtained from a linear fit to the I - V curves. Above 79 K the sample was cooled by liquid N_2 . The inset shows the temperature dependence of resistance taken on a bare STO surface [99]. © 2015 Macmillan Publishers Ltd.

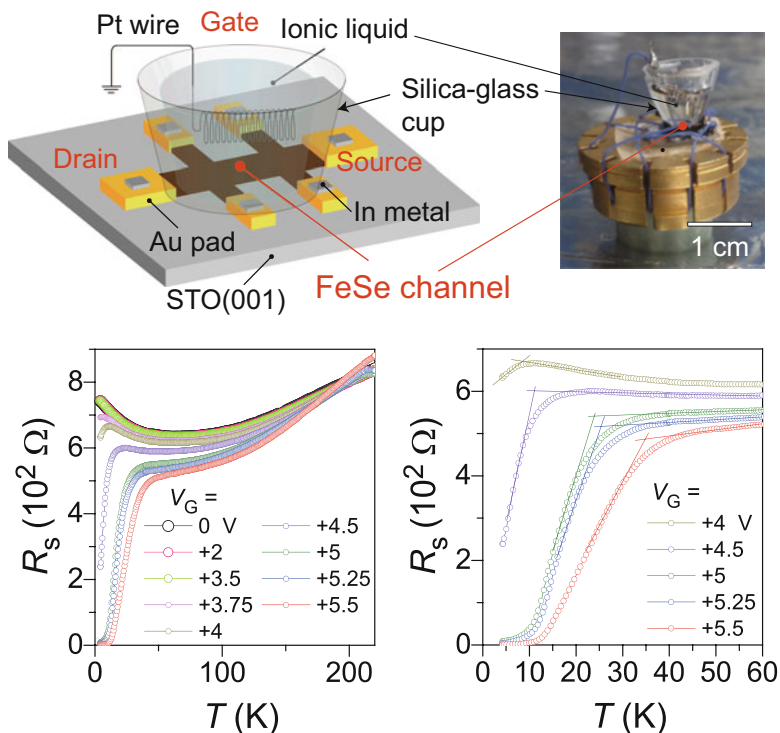


Fig. 8.12 Structure of the FeSe EDLT and its temperature dependence of sheet resistance under applying gate bias [103]. Copyright © 2019 National Academy of Sciences

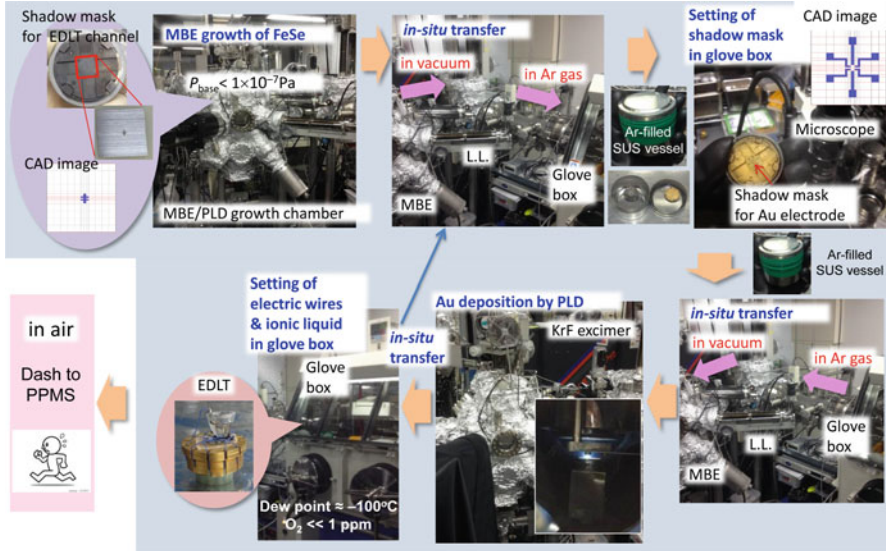


Fig. 8.13 All in situ process for fabrication of FeSe EDLT [103, 106]

not to be appropriate for application. However, clarification of the origin of such extremely high T_c should contribute to findings of new high- T_c materials exhibiting high performance.

8.4 Devices

8.4.1 Josephson Junction and SQUID

Thin-film Josephson junctions (JJ) using iron-based superconductors have been examined using Ba122 and 11 thin films mainly because of difficulty in phase formation of 1111 films. A weak-link behavior at grain boundary was first reported for Ba122:Co films on [001]-tilt SrTiO₃ bicrystal grain boundaries (BGB) in 2009 [109]. In 2010, thin-film JJ using Ba122:Co BGB were demonstrated using [001]-tilt (La,Sr)(Al,Ta)O₃ (LSAT) bicrystal substrates with a high misorientation angle (30°) [110] (see Fig. 8.14). For the BGB junctions, the shape of the I - V curve at $B = 0$ mT displays resistively shunted junction (RSJ) type behavior without hysteresis. The estimated normal-state resistance (R_N) and $R_N A$ (A is the cross-sectional area of the junction) of the BGB junctions are 0.012 Ω and 3.0×10^{-10} Ωcm^2 , respectively. On the other hand, I_c is clearly suppressed by a weak magnetic field of 0.9 mT. The large I_c modulation of 95% indicates that the Josephson current is responsible for most of the supercurrent through the BGB junction. Throughout the temperature range, J_c of the BGB junctions (i.e., intergrain J_c) is about 20 times smaller than

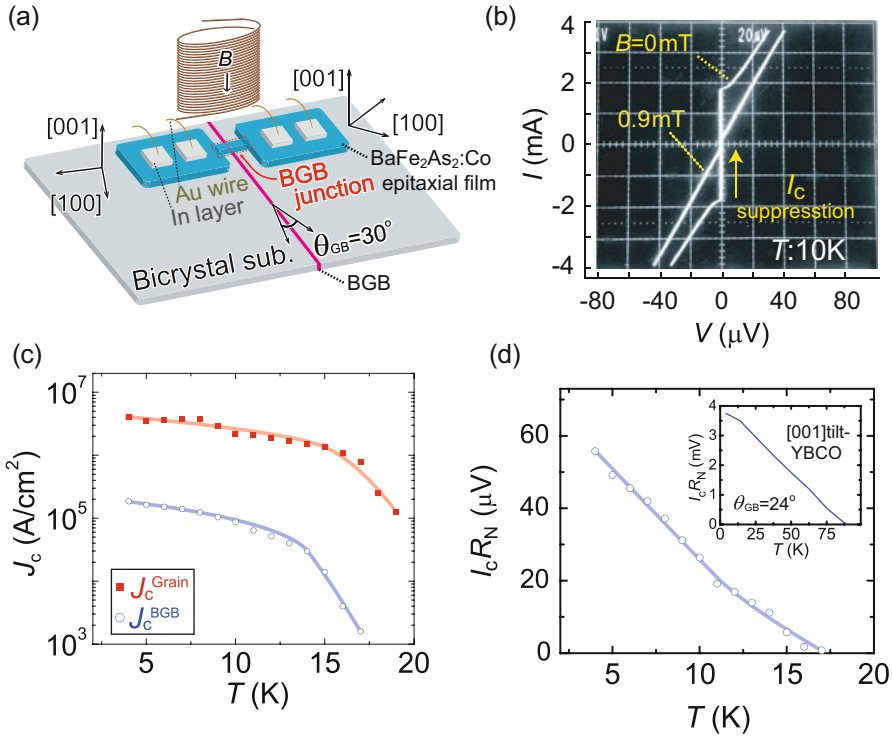


Fig. 8.14 Device structure of 10- μ m-wide Ba122:Co BGB junction fabricated on [001]-tilt LSAT bicrystal substrates with $\theta_{GB} = 30^\circ$ (a) I - V characteristic of Ba122:Co BGB junction with $\theta_{GB} = 30^\circ$ under external magnetic fields $B = 0$ and 0.9 mT at 10 K. (a) Temperature dependence of self-field J_c of grain (non-BGB, J_c^{Grain}) and BGB bridges (J_c^{BGB}) of Ba122:Co film on LSAT bicrystal substrate with $\theta_{GB} = 30^\circ$. (b) Temperature dependence of $I_c R_N$ of Ba122:Co BGB junction along with that of YBCO BGB junction with $\theta_{GB} = 24^\circ$ [110]. Copyright © 2010 AIP Publishing LLC

that of the non-BGB junctions (intra-grain J_c), indicating that BGBs work as weak-link GBs. The $I_c R_N$ product increases almost linearly with decreasing temperature, and the $I_c R_N$ product at 4 K is 55.8 μ V. The two orders of magnitude smaller $I_c R_N$ product compared with that of a YBCO BGB junction originates from the metallic nature of Ba122:Co BGB junctions.

A multi-layered (superconductor-normal metal-superconductor, SNS) JJ using a Ba122:Co film and PbIn counter electrodes with a 5-nm-thick Au barrier layer was also demonstrated [111]. Depending on the current bias direction, the I - V characteristic of the hybrid junction is slightly asymmetric, but the I - V curve has an RSJ-like nonlinear shape with hysteresis. The $I_c R_N$ product and J_c are 18.4 μ V and 39 A/cm² at 4.2 K, respectively. The I - V curves under microwave irradiation at frequencies of 10–18 GHz clearly display multiple Shapiro steps, confirming the Josephson Effect.

After that, an edge-type [112] and some improved BGB or hybrid-type Ba122:Co JJs were demonstrated [113–115]. All the $I_c R_N$ products, which are much smaller than YBCO BGBs, seem not to be drastically improved mainly because of intrinsic metallic nature of iron-based superconductors. Josephson Effect of nano-bridge fabricated in 11 films was reported in 2013 [116]. The $I_c R_N$ product of the bridge is as large as 6 mV although that of other 11 BGB junctions [117, 118] is comparable to that of Ba122:Co BGB junctions.

A dc superconducting quantum interference device (SQUID) composed of a superconducting loop with two BGB junctions in a Ba122:Co epitaxial film was fabricated on a bicrystal substrate [119] (Fig. 8.15). Periodic voltage modulation of $\Delta V = 1.4 \mu\text{V}$ was observed in the voltage-flux ($V-\Phi$) characteristics of the Ba122:Co dc-SQUID measured at 14 K. Furthermore, a flux-locked loop circuit was employed to evaluate the flux noise $S_\Phi^{1/2}$ spectrum of the dc-SQUID. The $S_\Phi^{1/2}$ level of the Ba122:Co dc-SQUID is more than ten times higher than YBCO dc-SQUIDs. The operation temperature of this Ba122:Co dc-SQUID must be close to its T_c because I_c rapidly increases with decreasing temperature. In addition, V_Φ is low due to the low R_N , which is attributed to the metallic nature of normal-

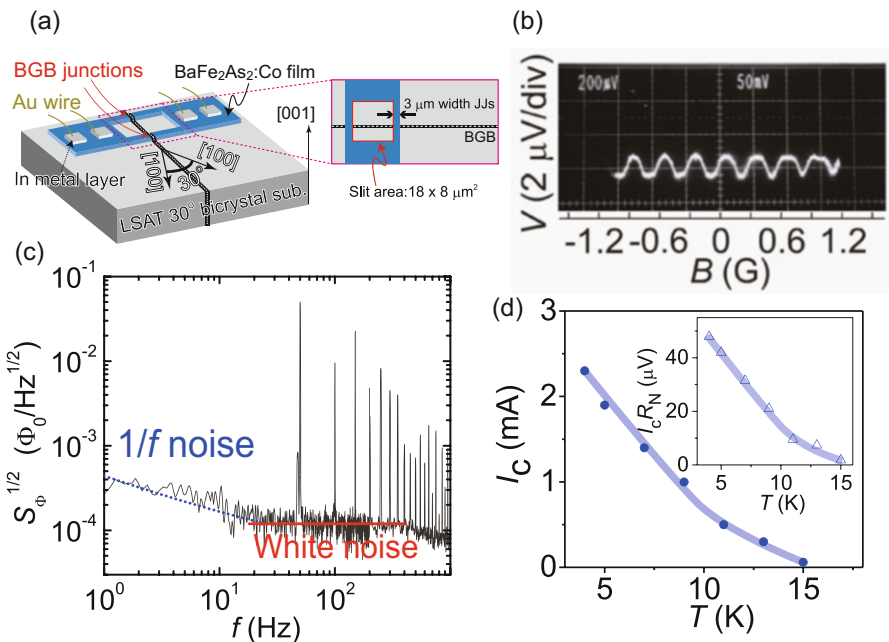


Fig. 8.15 dc-SQUID using Ba122:Co film. (a) Schematic illustration of dc-SQUID consisting of two 3-μm-wide Josephson junctions fabricated on [001]-tilt LSAT bicrystal substrate with $\theta_{GB} = 30^\circ$. A Ba122:Co superconducting loop with a slit area of $18 \times 8 \mu\text{m}^2$ was located across the BGB. (b) The voltage-flux ($V-\Phi$) characteristics at 14 K. (c) Flux noise ($S_\Phi^{1/2}$) as a function of frequency (f) at 14 K. (d) Temperature dependence of I_c . The inset shows $I_c R_N$ product as a function of temperature [119]. © 2010 IOP Publishing Ltd.

state Ba122:Co. Consequently, the high measurement temperature and low V_ϕ are responsible for the high noise level. Therefore, like JJs, artificial barriers with large junction resistances, such as superconductor-insulator-superconductor (SIS) junction structures, are necessary to realize high-performance SQUIDs with iron-based superconductors.

8.4.2 Coated Conductors on Practical Metal-Tapes

A critical issue in superconducting wires, tapes, and coated conductors of high- T_c cuprates is the grain boundary (GB) issue. The grains of high- T_c cuprates must be highly oriented to prevent the deterioration of J_c across misaligned GBs because J_c strongly depends on the misorientation angle of GBs (θ_{GB}). For example, a fundamental study on the intergrain J_c (J_c^{BGB}) for YBCO was conducted using several types of bicrystal substrates. Significantly misaligned adjacent grains cause J_c^{BGB} to decay exponentially as a function of θ_{GB} from 3 to 40°. Therefore, to produce YBCO coated conductors exhibiting a high- J_c , well-aligned buffer layers with a small in-plane misalignment of $\Delta\phi \ll 5^\circ$ on polycrystalline (i.e., non-oriented) metal substrates must be inserted using an ion beam-assisted deposition (IBAD) technique or rolling-assisted biaxially textured substrates (RABiTS). However, it is reported that an iron-based superconductor Ba122:Co has an advantageous GB nature against cuprates. That is J_c^{BGB} of Ba122:Co has a gentler θ_{GB} dependence than that of YBCO, as examined using high- J_c Ba122:Co epitaxial films on [001]-tilt LSAT and MgO bicrystal substrates with $\theta_{GB} = 3\text{--}45^\circ$. The deterioration of J_c^{BGB} due to the tilted GBs is negligible at θ_{GB} lower than $\theta_c = 9^\circ$ [120], which is twice as large as $\theta_c \approx 5^\circ$ for YBCO BGBs. Similar critical angle for J_c $\theta_c = 9^\circ$ was also reported on 11 films [118]. Therefore, the large θ_c allows a simpler and lower cost production process to be used to produce superconducting coated conductors of iron-based superconductors. The grain boundary of iron-based superconductors is reviewed in detail in another chapter of this book.

First coated conductors were demonstrated in Ba122:Co films [121–123] using IBAD-MgO technical metal-tape substrates mainly because high- J_c performance Ba122:Co films on single crystals were, at early stage, achieved rather than other iron-based superconductor films. The IBAD-MgO substrates consisted of a homoepitaxial MgO layer/IBAD-MgO layer/ Y_2O_3 buffer layer/Hastelloy C276 polycrystalline tape with $\Delta\phi_{MgO} = 5.5\text{--}7.3^\circ$. Values of self-field J_c of 1.2–3.6 MA/cm² at 2 K (J_c remained above 1 MA/cm² at 10 K) [122]. The in-field J_c of the Ba122:Co films on the IBAD substrates was substantially higher than that for the films on MgO single crystals, probably due to c -axis vortex pinning effects. These results imply that high- J_c coated conductors can be fabricated with Ba122:Co using less-well-textured templates and with large ϕ , which allows for a simple and low-cost process for high- J_c and high- H_c superconducting tapes.

Then, some 11-type coated conductors were demonstrated on IBAD-MgO [124, 125] and RABiTS [126]. In case of IBAD, self-field J_c (0.1 MA/cm² order) is

slightly lower than that of Ba122:Co conductors; while the in-field properties seem to be better than the Ba122:Co; ex. well over 0.1 MA/cm² at 9 T. Especially, in case of RABiTS [126], superior in-field J_c properties were reported by employing CeO₂ buffer layer; 0.1 MA/cm² at 30 T is achieved (see Fig. 8.16).

1111 conductors' [127] T_c (43 K) is the highest among the iron-based superconductor coated conductors. J_c^{self} is 0.07 MA/cm² at 5 K, and in-field properties are poorer than that of Ba122:Co. The authors suggest that grain boundaries in 1111 reduce J_c significantly compared to that in Ba122:Co and 11, and hence more biaxial texture is necessary for high- J_c .

Recently, Ba122:P conductors have been demonstrated as high-performance coated conductors [128–130]. The Ba122:P film exhibited higher J_c at 4 K when grown on the poorly aligned (8°) metal-tape substrate than on the well-aligned (4°) substrate even though the crystallinity was poorer (see Fig. 8.17). The observed strong pinning in the Ba122:P is attributed to the high-density grain boundaries with the misorientation angles smaller than the critical angle [128]. This result

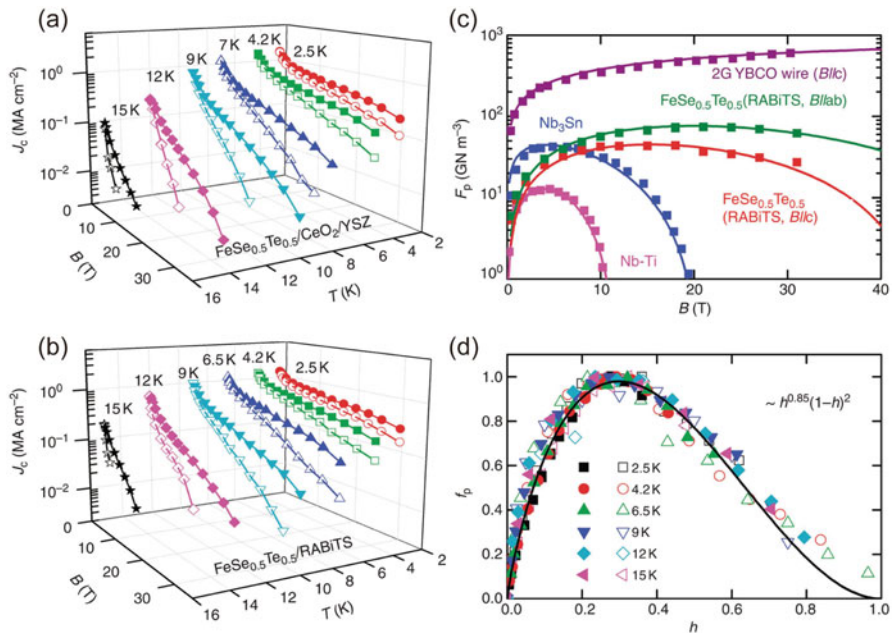


Fig. 8.16 Critical current densities (J_c) of 11 films. J_c of 11-type Fe(Se, Te) films on (a) a YSZ substrate with a CeO₂ buffer layer and (b) a RABiTS substrate at various temperatures with magnetic field parallel (solid symbols) and perpendicular (open symbols) to the ab -plane (tape surface). The self-field J_c of both films are above 1 MA/cm² at 4.2 K. Under 30 T of magnetic fields, both films still carry J_c around 0.1 MA/cm². (c, d) Pinning force analysis for a 11 film grown on RABiTS. (c) F_p at 4.2 K of a 11 film grown on a RABiTS substrate. (d) Scaling of pinning force density versus reduced field h for a 11 film grown on a RABiTS substrate at various temperatures with field perpendicular (solid symbols) and parallel (open symbols) to c -axis [126].

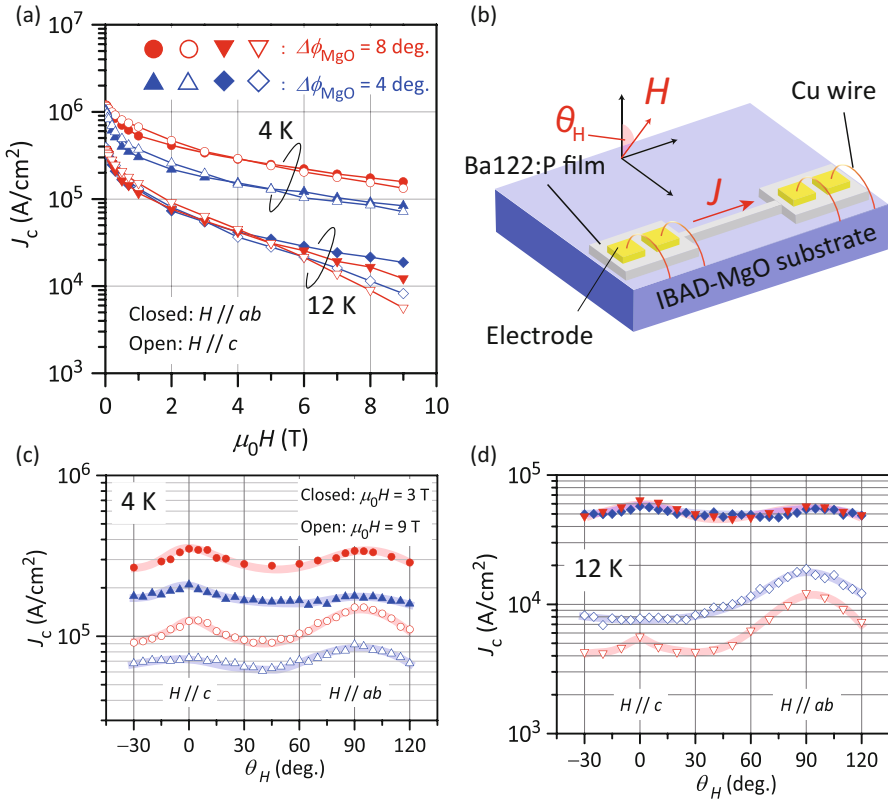


Fig. 8.17 J_c of Ba122:P coated conductors on two types of IBAD metal-tape substrate with $\Delta\phi_{\text{MgO}} = 8^\circ$ (poorly aligned, red symbols) and 4° (well aligned, blue symbols). (a) External magnetic field (H) dependence of J_c at 4 and 12 K. The closed and open symbols indicate the configurations of $H||ab$ plane and $H||c$ axis of the Ba122:P films, respectively. (b) Relationship between current (J) and H directions under J_c measurement. The external magnetic field angle (θ_H) was varied from -30 to 120° . (c, d) θ_H dependence of J_c at (c) 4 K and (d) 12 K. The closed and open symbols are the data under $\mu_0H = 3$ and 9 T, respectively [128]

reveals a distinct advantage over cuprate-coated conductors because well-aligned metal-tape substrates are not necessary for practical applications of the iron-based superconductors. Recently, in-field transport properties of the Ba122:P conductor on poorly aligned substrate were examined in detail [129]. The Ba122:P coated conductor exceeds a transport J_c of 0.1 MA/cm^2 at 15 T for main crystallographic directions of the applied field, which is favorable for practical applications and a superior in-field J_c over MgB_2 and NbTi , and a comparable level to Nb_3Sn above 20 T (see Fig. 8.18). Similar poorly aligned metal-tape substrates (7.7°) are also applicable to an 11-type coated conductor [125]. Therefore, this usefulness is the powerful advantage for 122- and 11-type coated conductors for future fabrication processes.

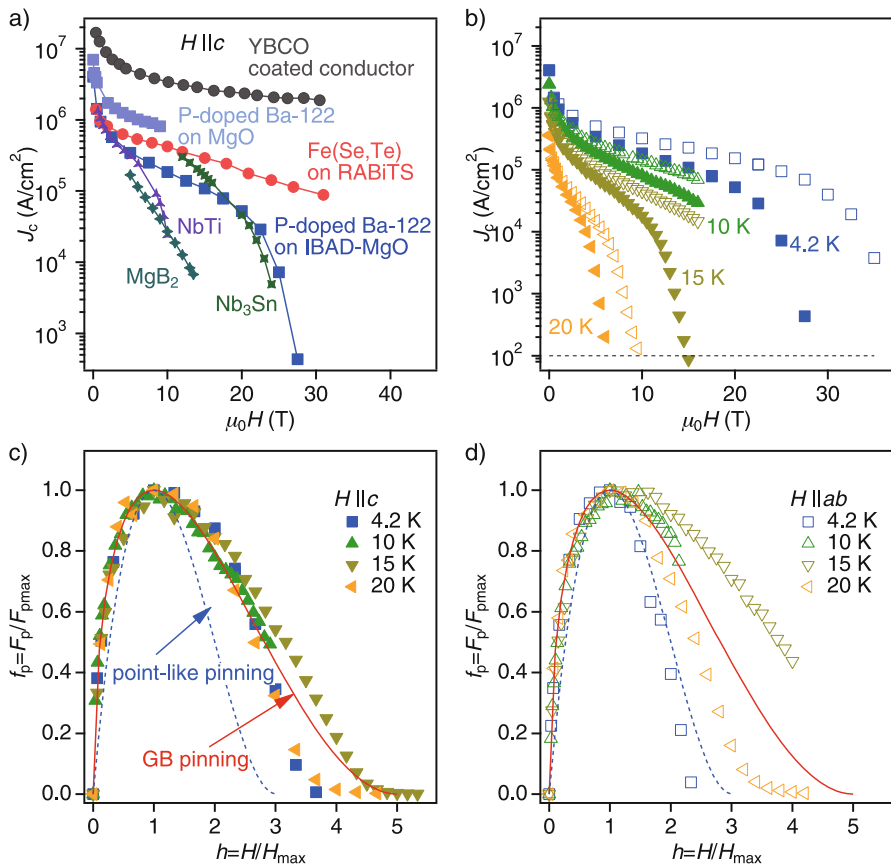


Fig. 8.18 Field dependence of J_c and analysis of the flux pinning density for a Ba122:P coated conductor on a poorly aligned ($\Delta\phi_{MgO} = 8^\circ$) IBAD-MgO tape substrate. (a) $J_c - H$ properties of the Ba122:P coated conductor sample at 4.2 K for $H \parallel c$. (b) $J_c - H$ properties of the Ba122:P coated conductor sample at various temperatures. (c, d) The normalized pinning force f_p as a function of reduced field [129]

The above coated conductors are all experimental sample scales in laboratories such as 1 cm-long, i.e., not practically large scales such as several tens or hundreds meters. To challenge longer scale, 15-cm-long Ba122:P coated conductors with critical current of 975 mA (estimated J_c is 0.2 MA/cm²) at 4.2 K were recently demonstrated by reel-to-reel PLD technique [7] (see Fig. 8.19).

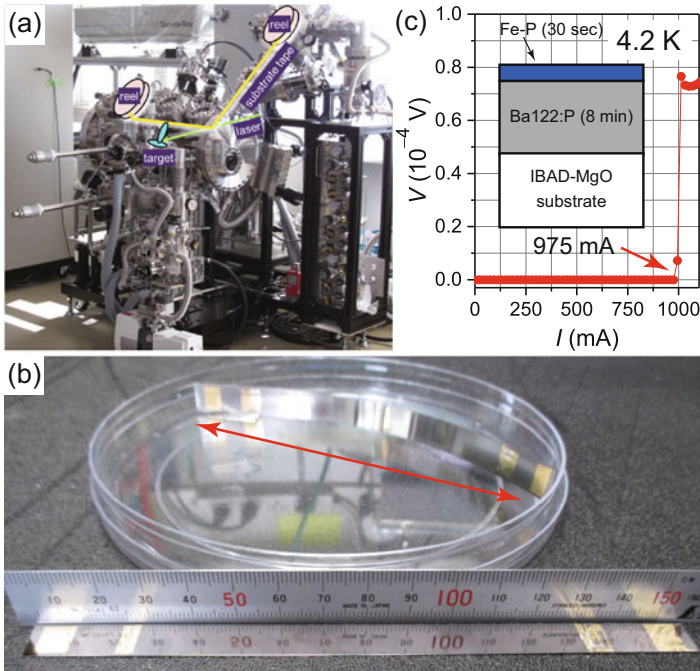


Fig. 8.19 Coated conductors fabricated by International Superconductivity Technology Center, Japan. (a) A photograph of reel-to-reel PLD system. (b) A photograph of a 15 cm-long coated conductor on IBAD-MgO metal-tape substrate. (c) Critical current at 4.2 K of the coated conductors. The inset shows the schematic stacking structure of the conductors [7]. © 2015 National Institute for Materials Science

8.5 Summary and Perspective

In this chapter, materials, thin-film growth, and devices of iron-based superconductors were reviewed to clarify the current status and issues that should be solved from the historical view point since the discovery of the first high- T_c iron-based superconductor fluorine-doped LaFeAsO in 2008 [5]. Here, we would like to introduce for readers that many informative review articles focusing on other insights have also been already published, for example, the ones on materials and fundamental physics [6, 131, 132], aspects for future application [133, 134], thin-film growth [135–141], electronics [142], and coated conductors [143].

Although the maximum T_c of iron-based superconductors is rather low compared with that of high- T_c cuprates, the iron-based superconductors have distinct advantages in terms of their grain boundary nature, low magnetic anisotropy, and high upper critical magnetic fields. Utilizing those advantages, coated conductors and wires for ultrahigh field magnets are the most promising candidates for future application targets, and some high-performance coated conductors using 122- and

11-type iron-based superconductors exhibiting practical level performance (e.g., $>0.1 \text{ MA/cm}^2$ at 9 T) have already been demonstrated in the laboratory sample-size scales. Additionally, those advantages arising low anisotropy and large critical grain boundary angle make it possible to apply the standard processing technique for alloy superconductors, the powder-in-tube method, to fabricate wires and tapes. Recent success in the fabrication of a $>100\text{-m}$ -long 122-type wire with a practical J_c represents a milestone [144, 145], casting a bright light for the future practical application. Different from high- T_c cuprates, liquid nitrogen cannot be applied as a cryogen for iron-based superconductors. However, liquid hydrogen (20 K) and refrigerator temperature (~ 10 K) are possible to operate the devices, i.e., high-cost liquid helium is not necessary.

The remaining issues on iron-based superconductor thin films especially for future application are summarized as follows:

1. Difficulty in growth of RE1111 epitaxial films is still a serious issue, especially for PLD. Now MBE completely overcomes this issue. Whereas only a few limited research groups achieve superconducting MBE-grown 1111 epitaxial films. Furthermore, to enhance its J_c performance, exploration of effective pinning center is necessary.
2. Application of iron-based superconductors to JJ seems not to be appropriate due to its intrinsically metallic nature. Artificial barriers with large junction resistances, such as SIS junction structures, are necessary to realize high-performance JJ and SQUID. But, this kind of devices would be powerful tools to examine superconducting mechanisms such as superconducting symmetry.
3. Although Ba122:P epitaxial films exhibit the best performance with respect to both T_c and J_c , and high- and isotropic- J_c performance coated conductors of Ba122:P and 11 has been demonstrated, effective artificial pinning centers (not only BZO for Ba122:P) should be explored to further enhance their J_c performance. Next target is the fabrication of the coated conductors on long length metal-tapes using reel-to-reel PLD process.
4. Very recently, heavy hydrogen-doping of Sm1111 epitaxial films, grown by Nd:YAG PLD, was demonstrated by topotactic chemical reaction using CaH_2 [146]. The maximum T_c reported is 48 K, which is slightly lower than those of H-doped polycrystalline bulks and F-doped epitaxial films. However, a large size ($1 \text{ cm} \times 1 \text{ cm}$) of epitaxial films with heavy hydrogen doping would contribute to direct observation of the electronic structure by angle-resolved photoemission spectroscopy because synthesis of large size of Re1111 single crystals is difficult [147]. This experiment should elucidate the still controversially debated mechanism of superconductivity in Fe-based superconductors.

Acknowledgments This work was supported by the Ministry of Education, Culture, Sports, Science, and Technology (MEXT) through the Element Strategy Initiative to Form Core Research Center. The authors would like to thank members of Tokyo Institute of Technology, Drs. Toshio Kamiya, Takayoshi Katase, Soshi Iimura, Hikaru Sato, and Kota Hanzawa, for valuable collaboration. H. Hiramatsu was also supported by the Japan Society for the Promotion of Science (JSPS) through Grants-in-Aid for Scientific Research (A) and (B) (Grant Nos. 17H01318 and 18H01700), and Support for Tokyotech Advanced Research (STAR).

References

1. Y. Kamihara, H. Hiramatsu, M. Hirano, R. Kawamura, H. Yanagi, T. Kamiya, H. Hosono, *J. Am. Chem. Soc.* **128**, 10012 (2006)
2. For a review, K. Ueda, H. Hiramatsu, M. Hirano, T. Kamiya, H. Hosono, *Thin Solid Films* **496**, 8 (2006)
3. For a review, H. Hiramatsu, H. Kamioka, K. Ueda, H. Ohta, T. Kamiya, M. Hirano, H. Hosono, *Phys. Status Solidi (a)* **203**, 2800 (2006)
4. T. Watanabe, H. Yanagi, T. Kamiya, Y. Kamihara, H. Hiramatsu, M. Hirano, H. Hosono, *Inorg. Chem.* **46**, 7719 (2007)
5. Y. Kamihara, T. Watanabe, M. Hirano, H. Hosono, *J. Am. Chem. Soc.* **130**, 3296 (2008)
6. For a review, H. Hosono, K. Kuroki, *Physica C* **514**, 399 (2015)
7. For a review, H. Hosono, K. Tanabe, E. Takayama-Muromachi, H. Kageyama, S. Yamanaka, H. Kumakura, M. Nohara, H. Hiramatsu, S. Fujitsu, *Sci. Technol. Adv. Mater.* **16**, 033503 (2015)
8. Z.-A. Ren, W. Lu, J. Yang, W. Yi, X.-L. Shen, Z.-C. Li, G.-C. Che, X.-L. Dong, L.-L. Sun, F. Zhou, Z.-X. Zhao, *Chin. Phys. Lett.* **25**, 2215 (2008)
9. T. Hanna, Y. Muraba, S. Matsuishi, N. Igawa, K. Kodama, S. Shamoto, H. Hosono, *Phys. Rev. B* **84**, 024521 (2011)
10. T. Katase, H. Hiramatsu, T. Kamiya, H. Hosono, *Proc. Natl. Acad. Sci. U. S. A.* **111**, 3979 (2014)
11. H. Hiramatsu, T. Katase, T. Kamiya, M. Hirano, H. Hosono, *Appl. Phys. Lett.* **93**, 162504 (2008)
12. E. Backen, S. Haindl, T. Niemeier, R. Hühne, T. Freudenberger, J. Werner, G. Behr, L. Schultz, B. Holzapfel, *Supercond. Sci. Technol.* **21**, 122001 (2008)
13. T. Kawaguchi, H. Uemura, T. Ohno, R. Watanabe, M. Tabuchi, T. Ujihara, K. Takenaka, Y. Takeda, H. Ikuta, *Appl. Phys. Express* **2**, 093002 (2009)
14. S. Haindl, M. Kidszun, A. Kauffmann, K. Nenkov, N. Kozlova, J. Freudenberger, T. Thersleff, J. Hänisch, J. Werner, E. Reich, L. Schultz, B. Holzapfel, *Phys. Rev. Lett.* **104**, 077001 (2010)
15. T. Kawaguchi, H. Uemura, T. Ohno, M. Tabuchi, T. Ujihara, K. Takenaka, Y. Takeda, H. Ikuta, *Appl. Phys. Lett.* **97**, 042509 (2010)
16. T. Kawaguchi, H. Uemura, T. Ohno, M. Tabuchi, T. Ujihara, Y. Takeda, H. Ikuta, *Appl. Phys. Express* **4**, 083102 (2011)
17. S. Ueda, S. Takeda, S. Takano, A. Yamamoto, M. Naito, *Appl. Phys. Lett.* **99**, 232505 (2011)
18. S. Ueda, S. Takeda, S. Takano, M. Naito, *Appl. Phys. Express* **5**, 053101 (2012)
19. H. Sugawara, T. Tsuneki, D. Watanabe, A. Yamamoto, M. Sakoda, M. Naito, *Supercond. Sci. Technol.* **28**, 015005 (2015)
20. S. Haindl, K. Hanzawa, H. Sato, H. Hiramatsu, H. Hosono, *Sci. Rep.* **6**, 35797 (2016)
21. S. Haindl, H. Kinjo, K. Hanzawa, H. Hiramatsu, H. Hosono, *Appl. Surf. Sci.* **437**, 418 (2018)
22. M. Kidszun, S. Haindl, T. Thersleff, J. Hänisch, A. Kauffmann, K. Iida, J. Freudenberger, L. Schultz, B. Holzapfel, *Phys. Rev. Lett.* **106**, 137001 (2011)
23. K. Iida, J. Hänisch, C. Tarantini, F. Kurth, J. Jaroszynski, S. Ueda, M. Naito, A. Ichinose, I. Tsukada, E. Reich, V. Grinenko, L. Schultz, B. Holzapfel, *Sci. Rep.* **3**, 2139 (2013)
24. C. Tarantini, K. Iida, J. Hänisch, F. Kurth, J. Jaroszynski, N. Sumiya, M. Chihara, T. Hatano, H. Ikuta, S. Schmidt, P. Seidel, B. Holzapfel, D.C. Larbalestier, *Sci. Rep.* **6**, 36047 (2016)
25. A.S. Sefat, A. Huq, M.A. McGuire, R. Jin, B.C. Sales, D. Mandrus, L.M.D. Cranswick, P.W. Stephens, K.H. Stone, *Phys. Rev. B* **78**, 104505 (2008)
26. A.S. Sefat, R. Jin, M.A. McGuire, B.C. Sales, D.J. Singh, D. Mandrus, *Phys. Rev. Lett.* **101**, 117004 (2008)
27. A. Leithe-Jasper, W. Schnelle, C. Geibel, H. Rosner, *Phys. Rev. Lett.* **101**, 207004 (2008)
28. N.H. Lee, S.-G. Jung, D.H. Kim, W.N. Kang, *Appl. Phys. Lett.* **96**, 202505 (2010)
29. S. Takeda, S. Ueda, T. Yamagishi, S. Agatsuma, S. Takano, A. Mitsuda, M. Naito, *Appl. Phys. Express* **3**, 093101 (2010)

30. T. Yamagishi, S. Ueda, S. Takeda, S. Takano, A. Mitsuda, M. Naito, *Physica C* **471**, 1177 (2011)
31. H. Hiramatsu, S. Matsuda, H. Sato, T. Kamiya, H. Hosono, *ACS Appl. Mater. Interfaces* **6**, 14293 (2014)
32. T. Hatakeyama, H. Sato, H. Hiramatsu, T. Kamiya, H. Hosono, *Appl. Phys. Express* **9**, 055505 (2016)
33. S. Yoon, Y.-S. Seo, S. Lee, J.D. Weiss, J. Jiang, M. Oh, J. Lee, S. Seo, Y.J. Jo, E.E. Hellstrom, J. Hwang, S. Lee, *Supercond. Sci. Technol.* **30**, 035001 (2017)
34. S. Richter, F. Kurth, K. Iida, K. Pervakov, A. Pukenas, C. Tarantini, J. Jaroszynski, J. Hänisch, V. Grinenko, W. Skrotzki, K. Nielsch, R. Hühne, *Appl. Phys. Lett.* **110**, 022601 (2017)
35. S. Richter, S. Aswartham, A. Pukenas, V. Grinenko, S. Wurmehl, W. Skrotzki, B. Büchner, K. Nielsch, R. Hühne, *IEEE Trans. Appl. Supercond.* **27**, 7300304 (2017)
36. H. Hiramatsu, T. Katase, T. Kamiya, M. Hirano, H. Hosono, *Appl. Phys. Express* **1**, 101702 (2008)
37. T. Katase, H. Hiramatsu, H. Yanagi, T. Kamiya, M. Hirano, H. Hosono, *Solid State Commun.* **149**, 2121 (2009)
38. H. Hiramatsu, T. Katase, T. Kamiya, M. Hirano, H. Hosono, *Phys. Rev. B* **80**, 052501 (2009)
39. B. Maiorov, S.A. Baily, Y. Kohama, H. Hiramatsu, L. Civale, M. Hirano, H. Hosono, *Supercond. Sci. Technol.* **22**, 125011 (2009)
40. T. Katase, H. Hiramatsu, T. Kamiya, H. Hosono, *Supercond. Sci. Technol.* **25**, 084015 (2012)
41. T. Hatano, T. Kawaguchi, R. Fujimoto, I. Nakamura, Y. Mori, S. Harada, T. Ujihara, H. Ikuta, *Supercond. Sci. Technol.* **29**, 015013 (2016)
42. K. Iida, J. Hänisch, R. Hühne, F. Kurth, M. Kidszun, S. Haindl, J. Werner, L. Schultz, B. Holzapfel, *Appl. Phys. Lett.* **95**, 192501 (2009)
43. Q.Y. Lei, M. Gollalikhani, D.Y. Yang, W.K. Withanage, A. Rafti, J. Qiu, M. Hambe, E.D. Bauer, F. Ronning, Q.X. Jia, J.D. Weiss, E.E. Hellstrom, X.F. Wang, X.H. Chen, F. Williams, Q. Yang, D. Temple, X.X. Xi, *Supercond. Sci. Technol.* **27**, 115010 (2014)
44. F. Kurth, E. Reich, J. Hänisch, A. Ichinose, I. Tsukada, R. Hühne, S. Trommler, J. Engelmann, L. Schultz, B. Holzapfel, K. Iida, *Appl. Phys. Lett.* **102**, 142601 (2013)
45. J. Engelmann, V. Grinenko, P. Chekhonin, W. Skrotzki, D.V. Efremov, S. Oswald, K. Iida, R. Hühne, J. Hänisch, M. Hoffmann, F. Kurth, L. Schultz, B. Holzapfel, *Nat. Commun.* **4**, 2877 (2013)
46. S. Lee, J. Jiang, Y. Zhang, C.W. Bark, J.D. Weiss, C. Tarantini, C.T. Nelson, H.W. Jang, C.M. Folkman, S.H. Baek, A. Polyanskii, D. Abrahimov, A. Yamamoto, J.W. Park, X.Q. Pan, E.E. Hellstrom, D.C. Larbalestier, C.B. Eom, *Nat. Mater.* **9**, 397 (2010)
47. T. Thersleff, K. Iida, S. Haindl, M. Kidszun, D. Pohl, A. Hartmann, F. Kurth, J. Hänisch, R. Hühne, B. Rellinghaus, L. Schultz, B. Holzapfel, *Appl. Phys. Lett.* **97**, 022506 (2010)
48. K. Iida, J. Hänisch, S. Trommler, S. Haindl, F. Kurth, R. Hühne, L. Schultz, B. Holzapfel, *Supercond. Sci. Technol.* **24**, 125009 (2011)
49. T. Katase, H. Hiramatsu, T. Kamiya, H. Hosono, *Appl. Phys. Express* **3**, 063101 (2010)
50. H. Hiramatsu, H. Sato, T. Katase, T. Kamiya, H. Hosono, *Appl. Phys. Lett.* **104**, 172602 (2014)
51. C. Tarantini, S. Lee, Y. Zhang, J. Jiang, C.W. Bark, J.D. Weiss, A. Polyanskii, C.T. Nelson, H.W. Jang, C.M. Folkman, S.H. Baek, X.Q. Pan, A. Gurevich, E.E. Hellstrom, C.B. Eom, D.C. Larbalestier, *Appl. Phys. Lett.* **96**, 142510 (2010)
52. Y. Zhang, C.T. Nelson, S. Lee, J. Jiang, C.W. Bark, J.D. Weiss, C. Tarantini, C.M. Folkman, S.-H. Baek, E.E. Hellstrom, D.C. Larbalestier, C.-B. Eom, X. Pan, *Appl. Phys. Lett.* **98**, 042509 (2011)
53. B. Maiorov, T. Katase, S.A. Baily, H. Hiramatsu, T.G. Holesinger, H. Hosono, L. Civale, *Supercond. Sci. Technol.* **24**, 055007 (2011)
54. H. Sato, T. Katase, W.N. Kang, H. Hiramatsu, T. Kamiya, H. Hosono, *Phys. Rev. B* **87**, 064504 (2013)
55. P. Yuan, Z. Xu, D. Wang, M. Zhang, J. Li, Y. Ma, *Supercond. Sci. Technol.* **30**, 025001 (2017)

56. B. Maiorov, T. Katase, I.O. Usov, M. Weigand, L. Civale, H. Hiramatsu, H. Hosono, *Phys. Rev. B* **86**, 094513 (2012)
57. C. Tarantini, S. Lee, F. Kametani, J. Jiang, J.D. Weiss, J. Jaroszynski, C.M. Folkman, E.E. Hellstrom, C.B. Eom, D.C. Larbalestier, *Phys. Rev. B* **86**, 214504 (2012)
58. S. Lee, C. Tarantini, P. Gao, J. Jiang, J.D. Weiss, F. Kametani, C.M. Folkman, Y. Zhang, X.Q. Pan, E.E. Hellstrom, D.C. Larbalestier, C.B. Eom, *Nat. Mater.* **12**, 392 (2013)
59. C. Tarantini, F. Kametani, S. Lee, J. Jiang, J.D. Weiss, J. Jaroszynski, E.E. Hellstrom, C.B. Eom, D.C. Larbalestier, *Sci. Rep.* **4**, 7305 (2014)
60. T. Katase, S. Iimura, H. Hiramatsu, T. Kamiya, H. Hosono, *Phys. Rev. B* **85**, 140516(R) (2012)
61. T. Katase, H. Hiramatsu, T. Kamiya, H. Hosono, *New J. Phys.* **15**, 073019 (2013)
62. T. Katase, H. Sato, H. Hiramatsu, T. Kamiya, H. Hosono, *Phys. Rev. B* **88**, 140503(R) (2013)
63. H. Hiramatsu, T. Katase, T. Kamiya, H. Hosono, *IEEE Trans. Appl. Supercond.* **23**, 7300405 (2013)
64. S.R. Saha, N.P. Butch, T. Drye, J. Magill, S. Ziemak, K. Kirshenbaum, P.Y. Zavalij, J.W. Lynn, J. Paglione, *Phys. Rev. B* **85**, 024525 (2012)
65. B. Lv, L. Deng, M. Gooch, F. Wei, Y. Sun, J.K. Meen, Y.-Y. Xue, B. Lorenz, C.-W. Chu, *Proc. Natl. Acad. Sci. U. S. A.* **108**, 15705 (2011)
66. S. Adachi, T. Shimode, M. Miura, N. Chikumoto, A. Takemori, K. Nakao, Y. Oshikubo, K. Tanabe, *Supercond. Sci. Technol.* **25**, 105015 (2012)
67. A. Sakagami, T. Kawaguchi, M. Tabuchi, T. Ujihara, Y. Takeda, H. Ikuta, *Physica C* **494**, 181 (2013)
68. M. Miura, S. Adachi, T. Shimode, K. Wada, A. Takemori, N. Chikumoto, K. Nakao, K. Tanabe, *Appl. Phys. Express* **6**, 093101 (2013)
69. M. Miura, B. Maiorov, T. Kato, T. Shimode, K. Wada, S. Adachi, K. Tanabe, *Nat. Commun.* **4**, 2499 (2013)
70. T. Kawaguchi, A. Sakagami, Y. Mori, M. Tabuchi, T. Ujihara, Y. Takeda, H. Ikuta, *Supercond. Sci. Technol.* **27**, 065005 (2014)
71. H. Sato, H. Hiramatsu, T. Kamiya, H. Hosono, *Appl. Phys. Lett.* **104**, 182603 (2014)
72. H. Sato, H. Hiramatsu, T. Kamiya, H. Hosono, *IEEE Trans. Appl. Supercond.* **25**, 7500305 (2015)
73. F. Kurth, C. Tarantini, V. Grinenko, J. Hänisch, J. Jaroszynski, E. Reich, Y. Mori, A. Sakagami, T. Kawaguchi, J. Engelmann, L. Schultz, B. Holzapfel, H. Ikuta, R. Hühne, K. Iida, *Appl. Phys. Lett.* **106**, 072602 (2015)
74. K. Iida, S. Haindl, T. Thersleff, J. Hänisch, F. Kurth, M. Kidszun, R. Hühne, I. Mönch, L. Schultz, B. Holzapfel, R. Heller, *Appl. Phys. Lett.* **97**, 172507 (2010)
75. H. Hiramatsu, T. Katase, Y. Ishimaru, A. Tsukamoto, T. Kamiya, K. Tanabe, H. Hosono, *Mater. Sci. Eng. B* **177**, 515 (2012)
76. S. Eley, M. Miura, B. Maiorov, L. Civale, *Nat. Mater.* **16**, 409 (2017)
77. M.J. Wang, J.Y. Luo, T.W. Huang, H.H. Chang, T.K. Chen, F.C. Hsu, C.T. Wu, P.M. Wu, A.M. Chang, M.K. Wu, *Phys. Rev. Lett.* **103**, 117002 (2009)
78. Y. Han, W.Y. Li, L.X. Cao, S. Zhang, B. Xu, B.R. Zhao, *J. Phys. Condens. Matter* **21**, 235702 (2009)
79. W. Si, Z.-W. Lin, Q. Jie, W.-G. Yin, J. Zhou, G. Gu, P.D. Johnson, Q. Li, *Appl. Phys. Lett.* **95**, 052504 (2009)
80. E. Bellingeri, I. Pallecchi, R. Buzio, A. Gerbi, D. Marrè, M.R. Cimberle, M. Tropeano, M. Putti, A. Palenzona, C. Ferdeghini, *Appl. Phys. Lett.* **96**, 102512 (2010)
81. Y. Imai, T. Akiike, M. Hanawa, I. Tsukada, A. Ichinose, A. Maeda, T. Hikage, T. Kawaguchi, H. Ikuta, *Appl. Phys. Express* **3**, 043102 (2010)
82. I. Tsukada, M. Hanawa, T. Akiike, F. Nabeshima, Y. Imai, A. Ichinose, S. Komiyama, T. Hikage, T. Kawaguchi, H. Ikuta, A. Maeda, *Appl. Phys. Express* **4**, 053101 (2011)
83. J.C. Zhuang, W.K. Yeoh, X.Y. Cui, J.H. Kim, D.Q. Shi, Z.X. Shi, S.P. Ringer, X.L. Wang, S.X. Dou, *Appl. Phys. Lett.* **104**, 262601 (2014)

84. P. Yuan, Z. Xu, H. Zhang, D. Wang, Y. Ma, M. Zhang, J. Li, *Supercond. Sci. Technol.* **28**, 065009 (2015)
85. Y. Imai, Y. Sawada, F. Nabeshima, A. Maeda, *Proc. Natl. Acad. Sci. U. S. A.* **112**, 1937 (2015)
86. M. Eisterer, R. Raunicher, H.W. Weber, E. Bellingeri, M.R. Cimberle, I. Pallecchi, M. Putti, C. Ferdeghini, *Supercond. Sci. Technol.* **24**, 065016 (2011)
87. K. Iida, J. Hänisch, M. Schulze, S. Aswartham, S. Wurmehl, B. Büchner, L. Schultz, B. Holzapfel, *Appl. Phys. Lett.* **99**, 202503 (2011)
88. K. Iida, J. Hänisch, E. Reich, F. Kurth, R. Hühne, L. Schultz, B. Holzapfel, A. Ichinose, M. Hanawa, I. Tsukada, M. Schulze, S. Aswartham, S. Wurmehl, B. Büchner, *Phys. Rev. B* **87**, 104510 (2013)
89. V. Braccini, S. Kawale, E. Reich, E. Bellingeri, L. Pellegrino, A. Sala, M. Putti, K. Higashikawa, T. Kiss, B. Holzapfel, C. Ferdeghini, *Appl. Phys. Lett.* **103**, 172601 (2013)
90. S. Molatta, S. Haindl, S. Trommler, M. Schulze, S. Wurmehl, R. Hühne, *Sci. Rep.* **5**, 16334 (2015)
91. F. Yuan, K. Iida, M. Langer, J. Hänisch, A. Ichinose, I. Tsukada, A. Sala, M. Putti, R. Hühne, L. Schultz, Z. Shi, *Supercond. Sci. Technol.* **28**, 065005 (2015)
92. Y. Sun, Y. Tsuchiya, S. Pyon, T. Tamegai, C. Zhang, T. Ozaki, Q. Li, *Supercond. Sci. Technol.* **28**, 015010 (2015)
93. T. Ozaki, L. Wu, C. Zhang, J. Jaroszynski, W. Si, J. Zhou, Y. Zhu, Q. Li, *Nat. Commun.* **7**, 13036 (2016)
94. C. Zhang, W. Si, Q. Li, *Appl. Phys. Lett.* **109**, 202601 (2016)
95. P. Yuan, Z. Xu, Y. Ma, Y. Sun, T. Tamegai, *Supercond. Sci. Technol.* **29**, 035013 (2016)
96. P. Yuan, Z. Xu, Y. Ma, Y. Sun, T. Tamegai, *IEEE Trans. Appl. Supercond.* **27**, 7500105 (2017)
97. Q.-Y. Wang, Z. Li, W.-H. Zhang, Z.-C. Zhang, J.-S. Zhang, W. Li, H. Ding, Y.-B. Ou, P. Deng, K. Chang, J. Wen, C.-L. Song, K. He, J.-F. Jia, S.-H. Ji, Y.-Y. Wang, L.-L. Wang, X. Chen, X.-C. Ma, Q.-K. Xue, *Chin. Phys. Lett.* **29**, 037402 (2012)
98. S. He, J. He, W. Zhang, L. Zhao, D. Liu, X. Liu, D. Mou, Y.-B. Ou, Q.-Y. Wang, Z. Li, L. Wang, Y. Peng, Y. Liu, C. Chen, L. Yu, G. Liu, X. Dong, J. Zhang, C. Chen, Z. Xu, X. Chen, X. Ma, Q. Xue, X.J. Zhou, *Nat. Mater.* **12**, 605 (2013)
99. J.-F. Ge, Z.-L. Liu, C. Liu, C.-L. Gao, D. Qian, Q.-K. Xue, Y. Liu, J.-F. Jia, *Nat. Mater.* **14**, 285 (2015)
100. For a review, Z. Wang, C. Liu, Y. Liu, J. Wang, *J. Phys. Condens. Matter* **29**, 153001 (2017)
101. J. Shioyai, Y. Ito, T. Mitsushashi, T. Nojima, A. Tsukazaki, *Nat. Phys.* **12**, 42 (2016)
102. B. Lei, J.H. Cui, Z.J. Xiang, C. Shang, N.Z. Wang, G.J. Ye, X.G. Luo, T. Wu, Z. Sun, X.H. Chen, *Phys. Rev. Lett.* **116**, 077002 (2016)
103. K. Hanzawa, H. Sato, H. Hiramatsu, T. Kamiya, H. Hosono, *Proc. Natl. Acad. Sci. U. S. A.* **113**, 3986 (2016)
104. W.-K. Wang, Y. Liu, J.-Y. Yang, H.-F. Du, W. Ning, L.-S. Ling, W. Tong, Z. Qu, Z.-R. Yang, M.-L. Tian, Y.-H. Zhang, *Chin. Phys. Lett.* **33**, 057401 (2016)
105. J. Shioyai, T. Miyakawa, Y. Ito, T. Nojima, A. Tsukazaki, *Phys. Rev. B* **95**, 115101 (2017)
106. K. Hanzawa, H. Sato, H. Hiramatsu, T. Kamiya, H. Hosono, *IEEE Trans. Appl. Supercond.* **27**, 7500405 (2017)
107. B. Lei, Z.J. Xiang, X.F. Lu, N.Z. Wang, J.R. Chang, C. Shang, A.M. Zhang, Q.M. Zhang, X.G. Luo, T. Wu, Z. Sun, X.H. Chen, *Phys. Rev. B* **93**, 060501(R) (2016)
108. H. Hiramatsu, K. Hanzawa, T. Kamiya, H. Hosono, Accepted for publication in *J. Supercond. Nov. Magn.* <https://doi.org/10.1007/s10948-019-5020-9>, arXiv:1901.08899
109. S. Lee, J. Jiang, J.D. Weiss, C.M. Folkman, C.W. Bark, C. Tarantini, A. Xu, D. Abrahimov, A. Polyanskii, C.T. Nelson, Y. Zhang, S.H. Baek, H.W. Jang, A. Yamamoto, F. Kametani, X.Q. Pan, E.E. Hellstrom, A. Gurevich, C.B. Eom, D.C. Larbalestier, *Appl. Phys. Lett.* **95**, 212505 (2009)
110. T. Katase, Y. Ishimaru, A. Tsukamoto, H. Hiramatsu, T. Kamiya, K. Tanabe, H. Hosono, *Appl. Phys. Lett.* **96**, 142507 (2010)

111. S. Schmidt, S. Döring, F. Schmidl, V. Grosse, P. Seidel, K. Iida, F. Kurth, S. Haindl, I. Mönch, B. Holzapfel, *Appl. Phys. Lett.* **97**, 172504 (2010)
112. S. Döring, S. Schmidt, F. Schmidl, V. Tympel, S. Haindl, F. Kurth, K. Iida, I. Mönch, B. Holzapfel, P. Seidel, *Supercond. Sci. Technol.* **25**, 084020 (2012)
113. S. Schmidt, S. Döring, F. Schmidl, V. Tympel, S. Haindl, K. Iida, F. Kurth, B. Holzapfel, P. Seidel, *IEEE Trans. Appl. Supercond.* **23**, 7300104 (2013)
114. S. Döring, M. Monecke, S. Schmidt, F. Schmidl, V. Tympel, J. Engelmann, F. Kurth, K. Iida, S. Haindl, I. Mönch, B. Holzapfel, P. Seidel, *J. Appl. Phys.* **115**, 083901 (2014)
115. C. Barone, F. Romeo, S. Pagano, M. Adamo, C. Nappi, E. Sarnelli, F. Kurth, K. Iida, *Sci. Rep.* **4**, 6163 (2014)
116. C.H. Wu, W.C. Chang, J.T. Jeng, M.J. Wang, Y.S. Li, H.H. Chang, M.K. Wu, *Appl. Phys. Lett.* **102**, 222602 (2013)
117. E. Sarnelli, M. Adamo, C. Nappi, V. Braccini, S. Kawale, E. Bellingeri, C. Ferdeghini, *Appl. Phys. Lett.* **104**, 162601 (2014)
118. W. Si, C. Zhang, X. Shi, T. Ozaki, J. Jaroszynski, Q. Li, *Appl. Phys. Lett.* **106**, 032602 (2015)
119. T. Katase, Y. Ishimaru, A. Tsukamoto, H. Hiramatsu, T. Kamiya, K. Tanabe, H. Hosono, *Supercond. Sci. Technol.* **23**, 082001 (2010)
120. T. Katase, Y. Ishimaru, A. Tsukamoto, H. Hiramatsu, T. Kamiya, K. Tanabe, H. Hosono, *Nat. Commun.* **2**, 409 (2011)
121. K. Iida, J. Hänisch, S. Trommler, V. Matias, S. Haindl, F. Kurth, I. Lucas del Pozo, R. Hühne, M. Kidszun, J. Engelmann, L. Schultz, B. Holzapfel, *Appl. Phys. Express* **4**, 013103 (2011)
122. T. Katase, H. Hiramatsu, V. Matias, C. Sheehan, Y. Ishimaru, T. Kamiya, K. Tanabe, H. Hosono, *Appl. Phys. Lett.* **98**, 242510 (2011)
123. S. Trommler, R. Hühne, J. Hänisch, E. Reich, K. Iida, S. Haindl, V. Matias, L. Schultz, B. Holzapfel, *Appl. Phys. Lett.* **100**, 122602 (2012)
124. W. Si, J. Zhou, Q. Jie, I. Dimitrov, V. Solovyov, P.D. Johnson, J. Jaroszynski, V. Matias, C. Sheehan, Q. Li, *Appl. Phys. Lett.* **98**, 262509 (2011)
125. Z. Xu, P. Yuan, Y. Ma, C. Cai, *Supercond. Sci. Technol.* **30**, 035003 (2017)
126. W. Si, S.J. Han, X. Shi, S.N. Ehrlich, J. Jaroszynski, A. Goyal, Q. Li, *Nat. Commun.* **4**, 1347 (2013)
127. K. Iida, F. Kurth, M. Chihara, N. Sumiya, V. Grinenko, A. Ichinose, I. Tsukada, J. Hänisch, V. Matias, T. Hatano, B. Holzapfel, H. Ikuta, *Appl. Phys. Lett.* **105**, 172602 (2014)
128. H. Sato, H. Hiramatsu, T. Kamiya, H. Hosono, *Sci. Rep.* **6**, 36828 (2016)
129. K. Iida, H. Sato, C. Tarantini, J. Hänisch, J. Jaroszynski, H. Hiramatsu, B. Holzapfel, H. Hosono, *Sci. Rep.* **7**, 39951 (2017)
130. H. Hiramatsu, H. Sato, T. Kamiya, H. Hosono, *Supercond. Sci. Technol.* **30**, 044003 (2017)
131. For a review, H. Hiramatsu, T. Kamiya, M. Hirano, H. Hosono, *Physica C* **469**, 657 (2009)
132. For a review on grain boundary, J.H. Durrell, C.-B. Eom, A. Gurevich, E.E. Hellstrom, C. Tarantini, A. Yamamoto, D.C. Larbalestier, *Rep. Prog. Phys.* **74**, 124511 (2011)
133. For a review, J. Shimoyama, *Supercond. Sci. Technol.* **27**, 044002 (2014)
134. For a review, H. Hosono, A. Yamamoto, H. Hiramatsu, Y. Ma, *Mater. Today* **21**, 278 (2018)
135. For a review, Q. Li, W. Si, I.K. Dimitrov, *Rep. Prog. Phys.* **74**, 124510 (2011)
136. For a review, H. Hiramatsu, T. Katase, T. Kamiya, H. Hosono, *J. Phys. Soc. Jpn.* **81**, 011011 (2012)
137. For a review, P. Mele, *Sci. Technol. Adv. Mater.* **13**, 054301 (2012)
138. For a review, S. Haindl, M. Kidszun, S. Oswald, C. Hess, B. Büchner, S. Kölling, L. Wilde, T. Thersleff, V.V. Yurchenko, M. Jourdan, H. Hiramatsu, H. Hosono, *Rep. Prog. Phys.* **77**, 046502 (2014)
139. For a review, Y. Imai, F. Nabeshima, A. Maeda, *Condens. Matter* **2**, 25 (2017)
140. For a review, M. Sakoda, K. Iida, M. Naito, *Supercond. Sci. Technol.* **31**, 093001 (2018)
141. For a review, J. Hänisch, K. Iida, R. Hühne, C. Tarantini, *Supercond. Sci. Technol.* in press (2019). <https://doi.org/10.1088/1361-6668/ab1c00>
142. For a review on Josephson junctions, P. Seidel, *Supercond. Sci. Technol.* **24**, 043001 (2011)

143. For a review on coated conductors, K. Iida, J. Hänisch, C. Tarantini, *Appl. Phys. Rev.* **5**, 031304 (2018)
144. X. Zhang, H. Oguro, C. Yao, C. Dong, Z. Xu, D. Wang, S. Awaji, K. Watanabe, Y. Ma, *IEEE Trans. Appl. Supercond.* **27**, 7300705 (2017)
145. For a review on wires, C. Yao, Y. Ma, *Supercond. Sci. Technol.* **32**, 023002 (2019)
146. J. Matsumoto, K. Hanzawa, M. Sasase, S. Haindl, T. Katase, H. Hiramatsu, H. Hosono, arXiv:1903.11819 (unpublished)
147. S. Iimura, T. Muramoto, S. Fujitsu, S. Matsuishi, H. Hosono, *J. Asian Ceram. Soc.* **5**, 357 (2017)

Chapter 9

Future Potential of New High T_c Iron-Based Superconductors



Shiv J. Singh and Paolo Mele

9.1 Introduction

In 1911, Heike Kamerlingh Onnes measured the electrical conductivity of numerous metals and discovered the abrupt disappearance of the resistance of a solid mercury wire in liquid Helium [1] as shown in Fig. 9.1. Subsequently, a wide range of superconductors have been found with increasing high transition temperatures (T_c), and it is hoped that a room temperature superconductor can ultimately be realized.

After the 100th years of its discovery, the challenges in superconducting materials still remain the same; the zero resistivity is observed at temperatures far below from the ambient temperature and suppression of superconductivity in the presence of desired magnetic field. From experimental point of view, new superconducting materials are being discovered frequently; however, there is no holistic understanding of the high temperature superconductivity. Before 2008, the research community generally supposed that the large magnetic moment element such as iron are harmful to the emergency of superconducting properties because, normally, the magnetic properties appear due to the static ordering of electron spins and compete with superconductivity where dynamic formation of electron pairs (Cooper pairs) is needed. In this regard, the discovery of iron-based superconductors (FeSCs) reported by Japanese group is a landmark result [2] and has invigorated the search for new superconducting systems with high transition temperature and field. Following the pioneer work, more than 100 compounds has been discovered in this category [3] and that can be categorized in several classes [4–7] such as oxypnictide

S. J. Singh (✉)

Clarendon Laboratory, Department of Physics, University of Oxford, Oxford, UK

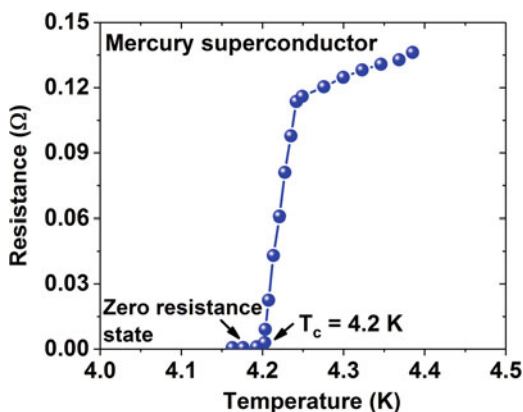
e-mail: shiv.singh@physics.ox.ac.uk

P. Mele

SIT Research Laboratories, Shibaura Inst. Tech. (Omiya campus), Tokyo, Japan

e-mail: pmele@shibaura-it.ac.jp

Fig. 9.1 First experiment of the temperature dependence of resistivity of mercury superconductor by Onnes [1]



Iron based superconductors

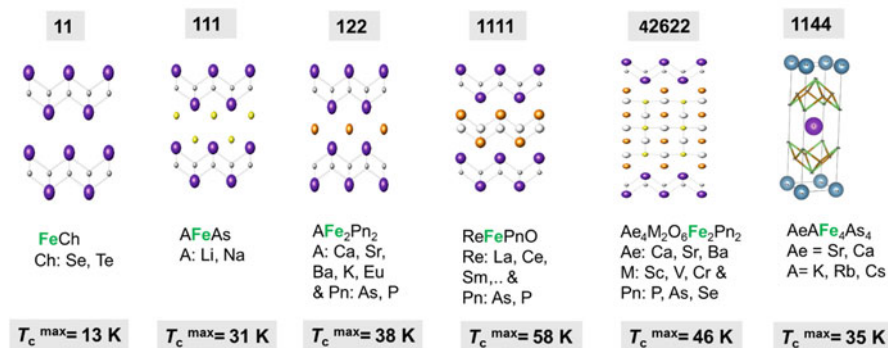


Fig. 9.2 Different categories of iron-based superconductors. They are named using an abbreviation of the ratio of the constituent atoms, for example, 11 is for FeCh

REOFeAs (1111), AFe₂As₂ (A = Ba, K, Ca) (122), FeSe_xTe_{1-x} (11), CaKFe₄As₄ (1144), and LiFeAs (111) as shown in Fig. 9.2. Pure arsenic (As) is highly toxic in case of inhalation or ingestion amongst the starting materials during the synthesis of iron-based superconductors. In order to avoid the complications, all the initial reactions are usually performed inside the glove box and all necessary precaution must be used during the reaction process. However, after completing the reactions, the final materials are safe and show low toxicity.

This new high T_c family has opened a new opportunity for a new pairing mechanism of high temperature superconductors with several disconnected Fermi surfaces, particularly in the presence of competing magnetic and superconducting correlations, and opportunities for high T_c superconductivity in multiband materials [3–7]. The maximum transition temperature (T_c) has reached up to 58 K [8] as shown in Figs. 9.2 and 9.3. Generally, the structure of the Fe-As tetrahedron in some families is playing the main role towards finding a high transition temperature

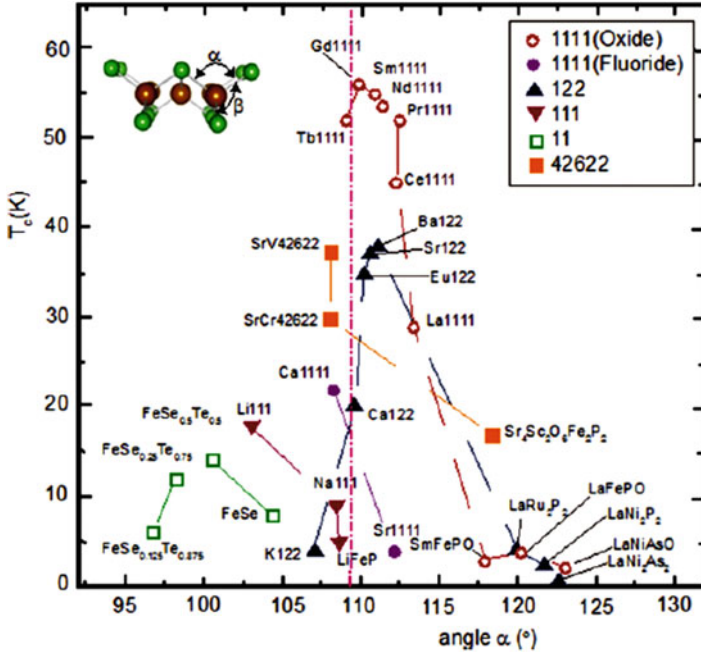


Fig. 9.3 The variation of transition temperature (T_c) with bond angle α of Pn(Ch)-Fe-Pn(Ch). Here, α is mainly considered at room temperature. T_c reached to maximum value for ideal bond angle (109°). The dash pink line is guide for eye for ideal bond angle. (Reproduced with permission from [3])

in oxypnictide superconductors. Actually, the Fe-Fe/Fe-As distances may not have a clear trend amongst different Fe-based superconductors [3–7], but it is observed that the system which has Fe-As-Fe bond angle equal to the ideal value of $109^\circ 47'$ for the perfect FeAs tetrahedron [4], shows the highest transition temperature (Fig. 9.3). Various studies concluded that the structure is more important than doping to find superconductivity in this new superconductor. So, the most efficient approach to increase the transition temperature (T_c) in FeSCs is to decrease the deviation of the Fe-As-Fe bond angle from the ideal value. In Fig. 9.3, the maximum T_c is lying near the bond angle $109^\circ 47'$. This suggests that there should be a correlation between the density of states near the Fermi energy and the geometry of the FeAs tetrahedron. Certainly, there is a correlation between the transition temperature (T_c) for various FeSCs with their structural properties, but a systematic trend between T_c and the Fe-As-Fe bond angles needs further insight. Superconductivity in this class of compounds has provided a novel opportunity for a deeper understanding of the mechanism of high temperature superconductivity. What is established now is that iron-pnictide superconductors are multiband materials with several disconnected Fermi surfaces [4]. Understanding the structure of the superconducting energy gap

and its influence on upper critical field (H_{c2}) and transition temperature (T_c) remain the key challenges in this rapidly evolving field.

There are many superconducting materials discovered over the last decades. The maximum transition temperature at atmospheric pressure is pegged at ~ 135 K in a mercury-based cuprate superconductor [9]. The superconductivity in this series of “high T_c ” compounds was discovered by Bednorz and Muller in late 1986 [10]. Before 2008, the cuprate-based materials have had monopoly as high temperature superconductors barring a brief intermediate phase of magnesium diboride (MgB_2) [11]. But one thing that was common in all those findings was that ferromagnetic materials destroy superconductivity. A breakthrough occurred in February 2008, when Kamihara and coworkers revealed iron containing superconductivity at $T_c = 26$ K in the fluorine-doped compound $LaOFeAs$ [2]. In some exceptional cases, iron has been considered to promote superconductivity and some superconducting compounds containing iron have been discovered recently but they all have very low T_c [12, 13]. Even pure iron of particular crystal structure generally shows superconductivity with $T_c = 1.8$ K under pressure [14].

The path to find higher transition temperature in FeSCs is similar to cuprate-based superconductors. High pressure experiments [15] first increased the transition temperature in Ba-doped La_2CuO_4 from 35 to 53 K. This was followed by chemical pressure effect by various doping where T_c was raised to 93 K [16] by replacing La with smaller Y. Similarly, Takahashi et al. reported the enhancement of T_c from 26 to 43 K by applying 4 GPa in F-doped $LaOFeAs$ [17]. This result again acted as a catalyst for researchers to use chemical pressure for these new superconductors by replacing La with other smaller rare earth. Soon, Chen et al. [18] reported the transition temperature at 43 K at ambient pressure by replacing La by Sm and then less than a month later the maximum $T_c = 55$ K was reported in the oxygen-deficient $SmFeAsO_{0.85}$ [19]. Currently, the highest T_c in this family is 58 K for F-doped $Sm1111$ [8].

9.2 General Properties of Iron-Based Superconductors

Iron-based superconductors have provided a great interest as a second-high T_c superconductor from a basic point of view as well as in the light of practical applications [6, 7]. This new family has layered structure and very rich substitution chemistry, so that many superconductors were found under this family, showing a very broad range of transition temperatures [3–5] (Figs. 9.2 and 9.3). Furthermore, this new high T_c superconductor has several advantages with respect to the cuprate-based high temperature superconductors, such as a metallic parent compound, a smaller anisotropy, and a more flexible doping and more doping sites. The superconducting order parameter is completely different from the cuprate superconductors, whereas grain boundaries behavior and impurities are not very much detrimental for its superconducting properties [3–7].

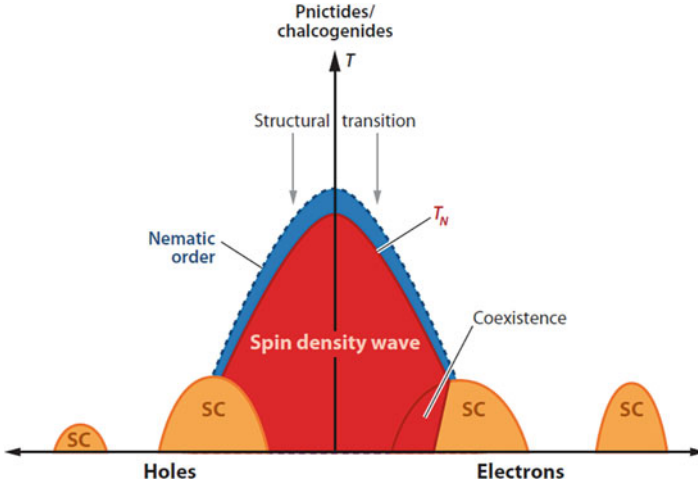


Fig. 9.4 General phase diagram for iron-based superconductors in the parameter space of temperature and doping (electrons/holes). Red region shows a spin density wave magnetic order (SDW) and the yellow region depicts the superconducting phase (SC). In the blue region above the SDW, the system develops the nematic order. At relatively small doping, SC, SDW, and nematic order co-exist. (Reproduced with permission from [20])

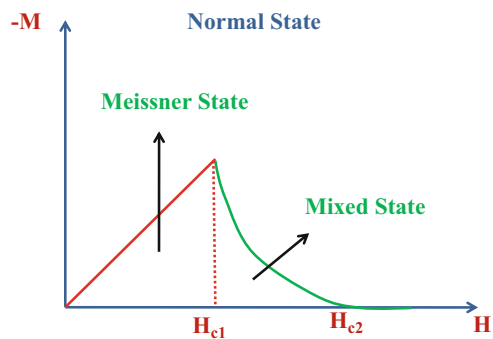
Figure 9.4 depicts the general phase diagram for different families of iron-based superconductors with distinct areas for the antiferromagnetically ordered spin density wave (SDW) and superconducting phase (SC) [20]. Most of the parent compounds normally show the antiferromagnetic transition and the structural transition from tetragonal to orthorhombic at temperatures close to the magnetic transition temperature [3–7]. Superconductivity arises by electron or hole doping or can be induced by external pressure or by isovalent doping. The iron-based superconductor has multiband nature similar to MgB_2 superconductors with the critical temperature $T_c = 40$ K [11, 21]. The superconducting properties of MgB_2 have been tuned and improved due to its multiband nature; however, doping at Mg or B sites has not been successful to enhance the transition temperature [21]. The iron-based superconductors have very rich substitution chemistry with various types of dopants at each elemental sites. Their layered structure allows designing new members of iron-based superconductor with new T_c , composite structures, or artificial multilayers [3–7]. For example, LaFeAsO belonging to 1111 family has shown superconductivity for various doping at each elemental sites: Sr at La sites, Co at Fe sites, Sb at As sites, and F at O sites. This versatility opens a new chapter to understand the properties with respect to different doping [3–7] in high T_c superconductors.

9.3 Magnetic Behavior of Superconductors

Bulk superconductivity is characterized by complete absence of electrical resistance and expulsion of an external magnetic field below a certain temperature (T_c) [22]. When a superconductor is placed in a small magnetic field, the field penetrates over a short penetration depth λ after which it decays rapidly to zero. This effect is called Meissner effect [22]. Broadly, superconductors are divided into two groups. In Type I superconductors, when the applied magnetic field increases above a certain value, superconductivity is completely destroyed. This value is called critical field H_c . In Type II superconductors, when the applied field is more than a critical value H_{c1} , a mixed state is achieved where the magnetic field penetrates the material in the form of quantized flux lines or vortices, but there remains no resistance to the flow of electrical current as long as the current is not too large. At much higher magnetic field, superconductivity is destroyed and this is called upper critical field H_{c2} . The region between H_{c1} and H_{c2} is called mixed state as shown in Fig. 9.5. The irreversibility field (H^*) denotes the onset of dissipation in the mixed state. The vortices are regions of normal core of radius equal to the coherence length (ξ) and a single vortex carries one quantum of magnetic flux Φ (2×10^{-7} G-cm²). They repel one another and try to form a hexagonal lattice, called Abrikosov lattice to minimize their energy. When an external current is applied to pass through a superconductor in the mixed state, these vortices experience Lorentz force. Due to this force, vortices start moving unless they are pinned at defect sites. Moving flux lines induce electric field in the direction of the current and this leads to resistance [23]. To achieve lossless transmission at higher current density, we, therefore, need to pin the vortices effectively via defect engineering.

When a magnetic field is applied from zero to high values for an ideal superconductor, it shows reversible magnetization. But, the real superconductor has much inhomogeneity such as lattice defects and impurities. These defects act as local energy minima for the vortex and therefore confine the motion of vortex due to flux pinning phenomenon. A defect with dimensions of the order of the coherence length ξ has the capability of pinning. High T_c superconductors have short coherence length (of the order of few Å). Due to this short coherence length,

Fig. 9.5 Magnetization (M) of Type II superconductor as a function of the external magnetic field (H)



a large number of defects, for example point defects, oxygen vacancies may act as effective pinning centers. In addition to this, both iron-based superconductors and cuprate high T_c ones have electromagnetic granular nature. The grains are coupled to each other and the intergrain region may also act as a pinning center. Due to the effects of pinning, a Type II superconductor shows irreversible magnetization. That is, when the magnetic field is increased beyond H_{c1} , vortex density increases, but on decreasing the field, some of the flux lines get trapped in the material through pinning centers, and therefore the magnetization exhibits hysteresis. The Bean model is appropriately used to determine the critical current density from the width (ΔM) of hysteresis M - H loops at different temperatures [22].

9.4 Multiband Superconductivity

The multiband superconductivity was predicted by Suhl et al. [24] over 50 years ago. The basic principle is that different bands like s or d bands in transition metal provide the different pairing interaction with different order parameters. But, at that time no material was known with such properties. The first candidate appears to be that of MgB_2 , reported as a superconductor in 2001, which was explained by a two-gap model [25, 26]. Meanwhile, different groups have taken a closer look at already known materials, such as Nb_3Sn [27], Nb_2Se , $LuNi_2B_2C$, YNi_2B_2C , and Chevrel phases [28–30], for which the multiband nature has been reported. The iron-based superconductors have many bands and several disconnected Fermi surfaces [31]. Basically, a Fermi surface is a closed equal-energy surface in momentum space that separates the empty and occupied electrons states. The electronic state near the FeAs Fermi levels are composed of mainly Fe $3d$ orbitals. All five $3d$ orbitals contribute to form separated electronic bands with various electrons and hole pockets. There is strong hybridization between the Fe $3d$ orbitals and As $4p$ orbitals, and the phase of the gap changes sign between the sheets that contain the Fermi surface [32, 33]. Thus, iron-based superconductors are multiband superconductors [34, 35].

The highest transition temperature is observed in 1111 type superconductor (Fig. 9.2). For this high T_c compound, Fermi surfaces are approximately disconnected cylinders [3–5]. In the case of multiple Fermi surfaces, the electron pairs can scatter from one Fermi surface to another. Suhl et al. [24] generalized the single band BCS theory with two Fermi surfaces and showed that superconductivity can occur if the intra- and inter-Fermi surface pair scattering are both of repulsive nature with dominant characteristic of inter pair scattering. In this condition, the order parameter will have an opposite sign on the two Fermi surfaces. The existence of multiple superconducting gaps creates complications for understanding various properties because there are both inter- and intra-band scattering processes [36].

The study of magnetic susceptibility [34, 37] has proved that FeSCs have a tendency to order antiferromagnetically and to be mediated by antiferromagnetic spin fluctuations. Cooper pairs in FeSCs have zero angular momentum because the total angular momentum must be antisymmetric with respect to exchange of

electrons. In this case, the orbital symmetry can be either “ s ” or “ d ”. Mazin et al. [34] have suggested that the antiferromagnetic spin fluctuation can induce the s_{\pm} pairing. Here, “ s ” represents the order parameter which remains the same by the symmetry operation of the crystal and “ \pm ” is related to the sign change of the order parameter between electron and hole pockets at Fermi surfaces. The F-doped LaFeAsO is the first example of multigap superconductor with a discontinuous sign change in the order parameter between the bands [34]. This property is different from the multiband s -wave superconductivity in MgB₂. This situation is based on the calculated Fermi surfaces for the undoped LaFeAsO, where superconductivity is induced by the nesting-related antiferromagnetic spin fluctuations near the wave vectors connecting the electron and hole pockets post appropriate doping [34].

9.5 Upper Critical Field (H_{c2})

Study of temperature-dependent upper critical field is one of the most important parameters which enable us to understand the mechanism of superconductivity. It provides crucial information about anisotropy (γ), coherence length (ξ), dimensionality of the superconductivity, and pair-breaking mechanism. It has been proposed that FeSCs possess multiband properties where strong inter-band pairing occurs due to spin excitation [38, 39]. This multiband nature is different from MgB₂ superconductor where these properties are due to the strong intra-band electron–phonon interaction and weak inter-band coupling [26]. However, the upper critical fields (H_{c2}) of bulk MgB₂ is relatively small, typically less than 20 T at 5 K. The addition of carbon to the system improves the H_{c2} [21, 40], but, it is still a low value in comparison with the FeSCs and cuprates. FeSCs are reported to have very high upper critical field ($H_{c2} \sim 100\text{--}200$ T) with high transition temperature and shorter coherence lengths ($\xi = \hbar v_F / 2\pi k_B T_c$) (1.8–2.3 nm for 1111, 1.5–2.4 nm for 122 and 1.2 nm for 11 family). Due to high transition temperature and low Fermi velocity, these iron-based superconductors are expected to sustain a stronger field ($H_{c2}(0) \approx \Phi_0 / 2\pi \xi^2$). At fields higher than upper critical field, the spacing between vortices $(H_{c2} / \Phi_0)^{1/2}$ becomes of the order of the diameter of non-superconducting vortex cores $\sim 2\xi$, and therefore the material turns normal.

The H_{c2} value at $T = 0$ K is estimated by extrapolating low-field H - T measurements by using WHH model [41] and provides the valuable information on fundamental superconducting properties. The BCS theory underlines that the conduction in superconductor is carried out by electron pairs (Cooper pairs) glued together by electron–phonon interaction [22]. Hence, the understanding of the mechanism of pair breaking is important to tune the superconductors. When magnetic field is applied, pair breaking occurs in two distinct ways, i.e., orbital and spin-paramagnetic effects as shown in Fig. 9.6. The orbital paramagnetic effect is related to superconducting currents around vortex cores and Lorentz force acting on the paired electrons with opposite momenta which then reduces the condensation energy of Cooper pairs. When the kinetic energy is greater than

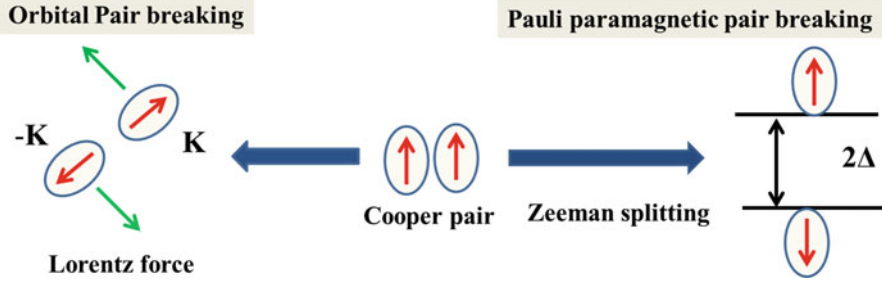


Fig. 9.6 Pair-breaking mechanism of singlet cooper pair in the presence of an external magnetic field. Where Δ is the superconducting gap

the condensation energy of cooper pairs, the superconductivity is destroyed. The orbital-limiting field is related to the critical field at which vortex cores start to overlap and is given as $H_{c2}^{\text{orbital}} = \Phi_0/2\pi\xi^2$. In the case of single band BCS superconductors, the calculated slope value dH_{c2}/dT of H - T phase diagram at T_c gives the $H_{c2}^{\text{orbital}}(0)$, given by $H_{c2}^{\text{orbital}}(0) = -0.693T_c(dH_{c2}/dT)_{T=T_c}$ for the dirty limit and $-0.73T_c(dH_{c2}/dT)_{T=T_c}$ for the clean limit (WHH approximations [41]).

On the other hand, the spin pair-breaking effect occurs due to the Zeeman splitting of spin singlet Cooper pairs, i.e., when the Pauli spin susceptibility energy exceeds the condensation energy, it leads to the partial alignment of the spins (breaking of singlet pair into unbound triplet). This is related to Pauli-limit field H_P where the splitting between the electronic levels induced by the field reaches the gap Δ . Assuming the Zeeman energy in the normal state compensates the superconducting condensation energy in the presence of magnetic fields, then Pauli-limiting field (H_P) is obtained by the expression $H_P(0) = g^{-1/2} \Delta/\mu_B$ [42, 43]; here g is the Lande g -factor, μ_B is the Bohr magnetron, and Δ is the superconducting gap. The H_P can be calculated using the BCS relation between Δ and T_c . According to the BCS theory, $2\Delta(0) = 3.52k_B T_c$, and $H_P(0)$ becomes $H_P^{\text{BCS}}(0) = 1.84T_c$.

For real systems, the upper critical field H_{c2} is generally affected by both orbital and spin-paramagnetic effects. The relative effect of both the orbital and spin-paramagnetic effects are explained in terms of the Maki parameter [44] $\alpha = 1.44H_{c2}^{\text{orbital}}(0)/H_P(0)$. It means that the flattening of $H_{c2}(T)$ at high field points to its limitation by the Pauli spin paramagnetism. This effect is measured in WHH model [41] by Maki parameter. Generally, the order of α is $\Delta(0)/E_F$ and $\ll 1$. However, the Fermi energy E_F becomes small for the materials which have a heavy electron mass or multiple small Fermi pockets. In this case, $\alpha \geq 1$. This case yields that the materials may be close to the Fulde-Ferrel-Larkin-Ovshnikov (FFLO) state for which Zeeman splitting causes a non-zero momentum of the Cooper pairs and a spatially modulated superconducting order parameter [45, 46].

MgB_2 is a two-gap superconductor and its upper critical field behavior shows either quite linear or even upward curvature closed to transition temperature (T_c)

and supports the multigap behavior [47]. In addition, the anisotropy of upper critical field also shows the strong temperature dependence, whereas single band superconductor has temperature-independent behavior of anisotropy. The iron-based superconductors have five d -orbitals which can contribute to the Fermi surfaces [34]. So, the multiband effects should also be considered in the orbital-limiting mechanism.

The iron-based superconductors have very high upper critical fields with a variety of very different temperature dependences. FeAs-based superconductors (1111) show the convex behavior in the H - T phase diagram for $H||c$ [48, 49] and support the behavior expected from orbital limited H_{c2} for multiband behaviors [36, 47]. On the other hand, the concave shape of $H_{c2}(T)$ curves has been observed for some members of 1111, Ba-122, LiFeAs, and FeSe-11 [48–52]. The concave shape of H_{c2} is the signature of strong Pauli-limiting behavior of upper critical field and, thus, these materials may be related to FFLO transition [44, 53–55]. The evidence of FFLO state has also been observed in heavy Fermions systems [56–58] and organic superconductors [59, 60] where an upturn in $H_{c2}(T)$ is found at low temperature, suggesting the existence of FFLO state. Various properties of iron-based superconductors support the FFLO states [36, 47]: first, for most of FBSs, the observed $H_{c2}(0)$ values exceed the BCS paramagnetic limit $H_p(T)$ where the pair-breaking Zeeman energy is greater than the binding energy of the Cooper pair. And second, many iron-based superconductors show steep increase in $H_{c2}(T)$ near the transition temperature followed by the flattening of $H_{c2}(T)$ at low temperature which may indicate that Pauli breaking is playing a dominate role over the orbital pair breaking. Non-magnetic impurities increase the upper critical field by enhancing the Zeeman (Pauli) pair breaking and suppress the FFLO instability [61], but the situation is complicated for d -wave superconductors such as cuprates. In the case of a multiband superconductor, the orbital pair breaking and the FFLO instability can be tuned by doping [62]. The remarkable flexibility of FeSCs towards high H_{c2} is improved by the interplay of orbital and paramagnetic pair breaking and also by the multiband $s\pm$ pairing [62].

In the case of newly discovered new family $\text{CaKFe}_4\text{As}_4$ (1144) of iron-based superconductors [63–65], the field and temperature dependence of the resistivity data inferred the anisotropic nature of H_{c2} and also revealed that:

1. The value of $H_{c2}(0)$ both parallel and perpendicular to c -axis extrapolate to the fields well above the single band BCS paramagnetic limit $H_p(T) = 1.84T_c = 64$ T. So, the Pauli pair breaking is essential, similar to the majority of other Fe-based superconductors.
2. As a result of different temperature dependencies of H_{c2} for c -axis and ab -plane, the anisotropy parameter decreases as T decreases, consistent with the interplay of orbital and Pauli pair breaking. The anisotropy of $\text{CaKFe}_4\text{As}_4$ is almost identical to that found for $\text{Ba}_{0.55}\text{K}_{0.45}\text{Fe}_2\text{As}_2$ (122) [63, 64]. Indeed, based on this and other similarities to near optimally doped 122, we can anticipate that the low temperature H_{c2} values will be relatively isotropic and of 60–80 T. More

quantitative analysis of our $H_{c2}(T)$ data shows that the dH_{c2}/dT values at T_c are -109 and -44 kOe/K for $H//ab$ and $H//c$, respectively [63, 64].

The largest H_{c2} slopes close to T_c are observed for iron-based superconductors in comparison with all the other high T_c superconductors. This feature makes them suitable for high field applications. Furthermore, the anisotropy of FeSCs is smaller than that of the cuprate $\text{YBa}_2\text{Cu}_3\text{O}_{7-\delta}$ (YBCO) family, where values from 4 to 14 have been reported [66–68] and it is much smaller than that of the $\text{Bi}_2\text{Sr}_2\text{CaCu}_2\text{O}_x$ (BSCCO) family [69, 70], where it is typically in the range 50–60. The anisotropy of a superconductor is a very important property. For example, the nearly two-dimensional nature and large anisotropy of high T_c cuprates are the main reasons for the weakness of the pinning and the significance of thermal fluctuations, which cause the broadening of the transition. By considering the coherence length ξ , the broadening behavior of the transition in a superconductor can be understood. The coherence length (ξ) along Fe planes (ab -planes) are 2.1, 2.9, 1.5, and 1.9 nm for 1111, 122, 11, and 1144 families, respectively [63, 64, 71]. These values must be compared with the distance (d) between the Fe-As planes, in order to understand the two-dimensional or three-dimensional character of a superconductor and consequently, the degree of dissipation in a magnetic field. The reported d values are around 0.86, 0.65, 0.6, and 0.24 nm in the 1111, 122, 11, and 1144, respectively. According to the largest ξ/d ratio amongst the FeSCs, 122 and 1144 families appear to be the most promising for applications. Thermal fluctuations can be the main reason for the broadening of the resistive transition in zero field, which can be parameterized by the Ginzburg number $\xi = (\pi\lambda_0^2 k_B T_c \mu_0 / 2\xi_c \varphi_0^2)^2$ where λ_0 is the London penetration depth at zero temperature, k_B the Boltzmann constant, and φ_0 the magnetic flux quantum. The values of ξ are 4×10^{-4} , 1.5×10^{-5} , 1×10^{-3} , 4×10^{-4} for the 1111, 122, 11, and 1144 [63, 64, 71], respectively. They should be compared to $\xi = 5 \times 10^{-4}$ for $\text{YBa}_2\text{Cu}_3\text{O}_{7-\delta}$ (YBCO) and 10^{-5} for MgB_2 . Furthermore, the 122 and 1144 are the most promising families of iron-based superconductors for applications since $T_c \sim 35$ K, $H_{c2} \sim 100$ T, $J_c \sim 10^7\text{--}10^8$ A/cm² and show a lower anisotropy with reduced thermal fluctuations [63].

9.6 Critical Current Density (J_c)

Another important property of a superconductor from a practical point of view is to carry the maximum electrical transport current with low dissipation below the transition temperature (T_c), i.e., the critical current density J_c . The J_c is strongly dependent on temperature and magnetic field, and it directly relates to the effectiveness of pinning. For high temperature superconductors, J_c in polycrystalline samples is strongly anisotropic and depends critically on the grain boundary and successful introduction of pinning centers [22]. Optimization of critical current J_c is the most demanding task in all bulk superconductors.

Strong pinning of vortices and high critical current densities $J_c(T, H)$ are reported for the iron-based superconductors since this family shows a short coherence length, similar to cuprates. The critical current density depends on the strength of the pinning force and the maximum pinning force occurs when the size of the non-superconducting defects is equal to the diameter of the vortex core $2\xi \sim 4\text{--}10\text{ nm}$ [72, 73]. Due to this reason, the natural crystalline defects such as grain boundaries, dislocations, and charge impurities in FeSCs may work as pinning centers. The critical current density J_c can also be enhanced by introducing the artificial pinning centers. For example, in the case of 122 (BaFe₂As₂), high critical current density $J_c \sim 4\text{ MA/cm}^2$ [74] has been reported by incorporating oxide nanopillars. It suggests that strong pinning in iron-based superconductors can be achieved. However, iron-based superconductors have also weak-link problem [75–80] similar to the cuprate superconductors. Weak-links are the kind of defects that limit dissipation-free transport current flow in a superconductor. Grain boundaries, nano- and micro-cracks, and planar precipitates of secondary phases are typical examples of weak-links regions in practical superconductors [81].

Measurements of the critical current density J_c in single crystal FeSCs have revealed a promising combination of high and nearly isotropic critical current densities along all crystal directions. Moreover, J_c is rather independent of the field at low temperatures, similar to YBa₂Cu₃O_{7- δ} [67, 82]. For the 1111 family, a high in-plane J_c of $2 \times 10^6\text{ A/cm}^2$ at 5 K in a SmFeAsO_{1-x}F_x crystal, almost field independent up to 7 T at 5 K, has been reported [83, 84]. Many single crystal results have been reported for the 122 system since larger crystals easily grow. Significant fishtail peak effects and large current carrying capability up to $5 \times 10^6\text{ A-cm}^{-2}$ at 4.2 K have been found in a K-doped Ba_{0.6}K_{0.4}Fe₂As₂ single crystal [85]. Fishtail effect and currents in the range 10^5 A-cm^{-2} at low temperature have also been reported for 122 in [86]. As for the 11 system, J_c of FeTe_{0.61}Se_{0.39} crystals with $T_c \sim 14\text{ K}$ exceeding 10^5 A-cm^{-2} at low temperatures has been reported [87]. Irradiation with Au ions [88] and neutrons [89] have emphasized that pinning can be further increased by introducing defects without affecting T_c .

In superconductors such as MgB₂ [90] and YBCO [91], the critical current measured in thin films is larger than that measured in polycrystals by orders of magnitude and it even achieves 20% of the ultimate intrinsic depairing limit. In iron-based superconductors, the critical current measured in thin films is promising [92, 93] and its investigation may yield important clues to enhance the performances of bulk samples, tapes, and wires. Comparative study of J_c values measured on FeSC single crystals and thin films concluded that the single crystal properties are excellent [5, 63]. Indeed, J_c is high and rather field independent as in the high T_c cuprates. The J_c anisotropy, defined as the ratio between the current flowing in-plane and out-of-plane, is less than 2 [63, 71, 94, 95] in the representative families of FeSCs (122, 11, 1144) which is much alike with the anisotropy in MgB₂ ($\gamma = 2\text{--}2.7$) and it is much lower than the values of up to 30–50 found in the cuprates [96]. This is a very significant result because it could imply that, contrary to the high T_c cuprates, the FeSCs do not require complex texturing processes for the fabrication of wires or tapes. Actually, the low J_c anisotropy is only a prerequisite for the current transport

in polycrystalline materials. Indeed, the second requirement is the transparency of the GBs to current flow. This issue is considered in the next section.

Critical current density and flux pinning behavior have been well studied in many iron-based superconductors. Many reports show high values of J_c value up to 10^6 – 10^7 A/cm² at 5 K for single crystal and this is almost field independent up to 10 T at 5 K [63, 71, 92, 97, 98]. All these results support that iron-pnictides can have high critical current value and show behavior at low temperature similar to cuprate-based YBCO. The high critical current density ($\sim 10^{10}$ A/m²) is also achieved by incorporating nanopillars in different iron-based superconductors [74] due to the enhancement of the pinning similar to cuprate such as YBCO ($\text{YBa}_2\text{Cu}_3\text{O}_{7-x}$). All these results show that Fe-based superconductors can be a potential candidate for next generation superconducting tapes or wires.

9.7 Effect of the Granular Nature

High current density and high critical field are not sufficient for a practical application of superconductors. The capability to carry currents over long lengths is one of the essential properties for the large application of superconductors. In a polycrystalline sample, the super currents flow across many grain boundaries (GB) regions [99]. In the case of the conventional superconductors with long coherence length, the cooper pairs generally show an outstanding ability to pass over the non-superconducting regions or areas with depressed order parameter. However, high T_c cuprate superconductors have high T_c , high H_{c2} , large anisotropy and, consequently, low coherence lengths (1–2 nm in the ab -plane and much lower along the c -axis). The grain boundaries between misoriented crystallites (Fig. 9.7a) impede current flow because the critical current density through a grain boundary drops exponentially as the misorientation angle increases. So, the spread of misorientation angle $\sim 40^\circ$ in polycrystals can reduce the critical current at grain boundaries by 2–3 orders of the magnitude [99]. A lot of effort has been made to grow textured superconducting tapes with small-angle GBs, but this approach is not yet fully exploited commercially. Recently, researchers have reported the theoretical understanding of grain boundaries in the cuprate superconductor and tried to understand why the currents are so sensitive to the GB mismatch [99, 101]. Hopefully, this study will help to make technologically viable superconducting wires.

In the case of MgB_2 , there is no any evidence of the grain boundaries problem [102]. A lot of applications of MgB_2 superconductor are currently developing, for example, bulk permanent magnet for commercial MRI systems. These premises highlight the importance of exploring the nature of GBs in novel superconducting materials. The iron-based superconductors have high H_{c2} value with small coherence lengths varying between 1 and 3 nm amongst the families. These values are reminiscent of those in the cuprates, but the reduced J_c anisotropy of iron-based

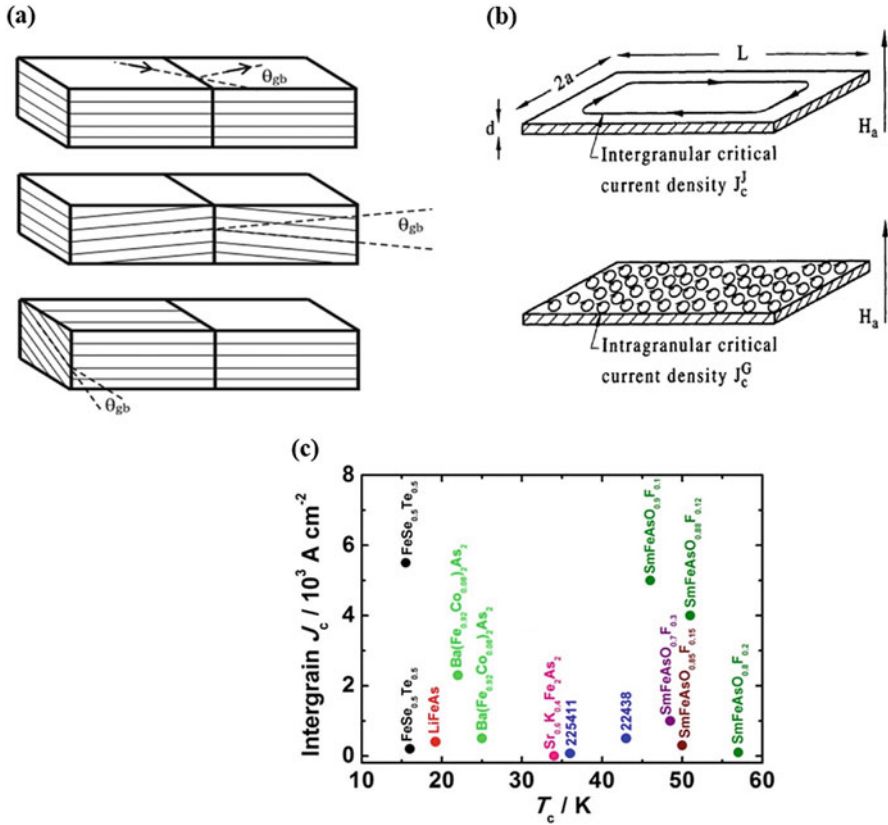


Fig. 9.7 (a) The grain boundaries curved planes in polycrystals are shown. The θ_{gb} indicates the grain boundaries misorientation (Reproduced with permission from [99]) contains from top to bottom a [0 0 1] tilt, a [1 0 0] tilt, and a [1 0 0] twist GB. In the top and bottom cases, the [0 0 1] direction (or the c -axis) is perpendicular to the top surface of the film. Although these planar, high-symmetry GBs are unusual in any sample in which independent nucleation occurs randomly (i.e., in most bulks and ex situ films), they are favored by in situ growth seeded by the substrate. (b) Comparison of inter- and intragranular current flow in a polycrystalline material (Reproduced with permission from [100]). (c) The reported intergrain J_c at 5 K for different families of iron-based superconductors. (Reproduced with permission from [78])

superconductors compared to the cuprates, allows current flow along the c -axis, thus making the requirement of texturing less stringent.

Early studies of the critical current density of 1111 polycrystals have emphasized the strong granularity of these compounds, which limits the global J_c flow across entire sample to very low values. In the polycrystalline bulk, there exist two kinds of critical currents: the large local critical current density (intra-grain currents J_c^{local}) flows inside the grains, while the small global critical current density (intergrain currents J_c^{global}) flows through the grains from the whole sample, as shown in Fig. 9.7b. This behavior is due to the significant granularity in polycrystalline bulk.

Wang et al. [100] reported a global current density of 1.1×10^8 A/m² at 5 K in self-field in contrast to intra-grain J_c of 10^{10} A/m² for F-doped SmO_{1-x}F_xFeAs. Two distinct scales of current flow have been found in polycrystalline Sm- and Nd-iron oxyprictides [77, 78, 98, 103] using magneto-optical imaging and studying the field dependence of the remanent magnetization. Low temperature laser scanning microscopy (LTLMS) and scanning electron microscopy (SEM) observations on polycrystalline Sm-1111 samples [76] emphasized cracks and wetting Fe-As phase at the GBs as the main mechanisms of current blocking in polycrystalline materials [78, 99]. The intergrain current dependence with temperature for studied iron-based superconductors is summarized in Fig. 9.7c [77, 78]. In fact, an intergrain J_c that is affected by weak-link behavior and strongly decreases upon applying a magnetic field is prevalent in bulk samples of FeSCs. The weak-links between grains are mainly related to the microstructure of the samples. Microstructure analysis has emphasized cracks, impurity phases at the grain boundaries and phase inhomogeneity as the main mechanism responsible for current blocking in polycrystalline material. Sample inhomogeneities manifesting as secondary phases may arise in a sample as given by the corresponding thermodynamic phase diagram. In particular, in chemically doped compounds, the addition of a dopant in the host lattice, where cobalt (Co) represents a typical dopant for pnictides, may complicate the situation and may also lead to additional inhomogeneities in a given sample [3–5].

Up to date, the difficulty to obtain fully dense single-phase polycrystalline materials of FeSCs seems to be one of the main reasons for the granular behavior of bulk materials. However, considering the strong similarities between cuprates and FeSCs, the existence of intrinsic mechanisms limiting the transmission of current in misaligned GB needs to be also carefully considered [81, 99].

9.8 Superconducting Wires and Tapes

From the view point of practical applications such as magnetic coils and cables, the development of superconducting wires/tapes processing techniques is highly desirable. FeSCs are mechanically hard and brittle and hence, it is difficult to form them into wires and tapes [5, 7, 105]. One of the most common approaches to develop superconducting wires for brittle superconductors is the powder in tube (PIT) method [106], as presented in Fig. 9.8. In this process, superconducting powder is sealed in a metal tube and then it is mechanically processed into a wire or tape form. Finally, it is reacted by heat treatment. Many groups reported the fabrication of superconducting wires/tapes with good J_c values which are constantly improving [5, 7, 105].

The PIT process has been widely used for the fabrication of electrical conductors from brittle superconducting materials such as Nb₃Sn, MgB₂, and ceramic Bi-cuprate superconductors (Bi-Sr-Ca-Cu-O). There are two types of PIT method: one

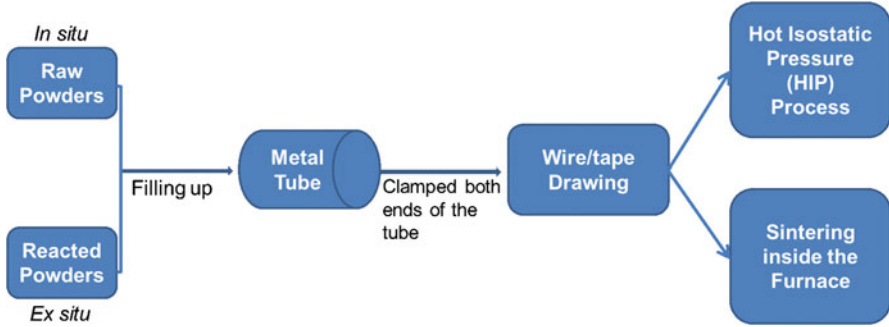


Fig. 9.8 The process for the powder in tube (PIT) method for the superconducting wires/tapes

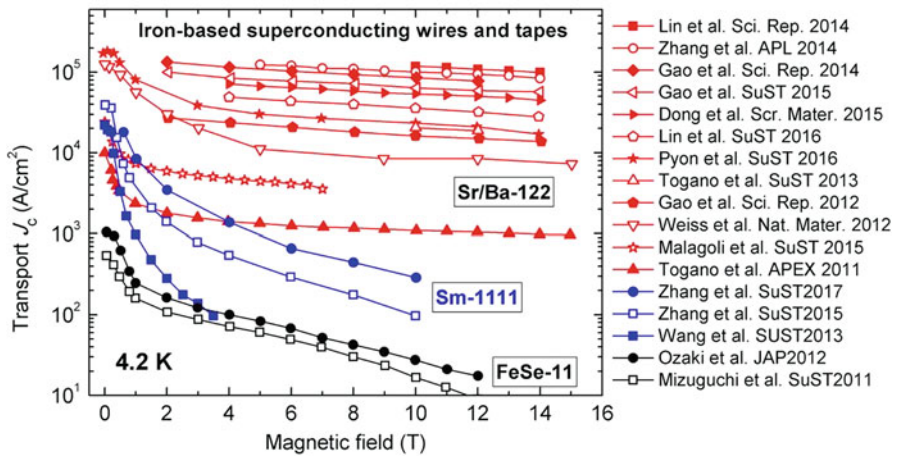


Fig. 9.9 At 4.2 K, Transport J_c as a function of applied magnetic field of different wires and tapes prepared through PIT method for different categories of iron-based superconductors. (Reproduced with permission from [5])

is in situ method in which a powder mixture of raw precursor is used as a starting material, and an ex situ method, in which powder of the reacted superconducting phase is used [5, 7, 105] (Fig. 9.8). In the early years of the pnictide wire development, the in situ PIT method was used, however, the transport J_c was very low, Fig. 9.9, due to the presence of a large amount of impurities, cracks, and voids within the superconducting cores. To solve this problem, Qi et al. [107] suggested the ex situ method with reacted superconducting powder. This process leads to fewer impurity phases and to high density of the superconducting core in the final wire. The ex situ method became the most successful approach for fabrication of high-performance iron-based superconducting wires. Remarkable, high J_c values have been obtained in ex situ iron-based superconducting wires and tapes: $J_c(4.2\text{ K}) \sim 10^4\text{--}10^5\text{ A/cm}^2$, as shown in Figs. 9.9 and 9.10.

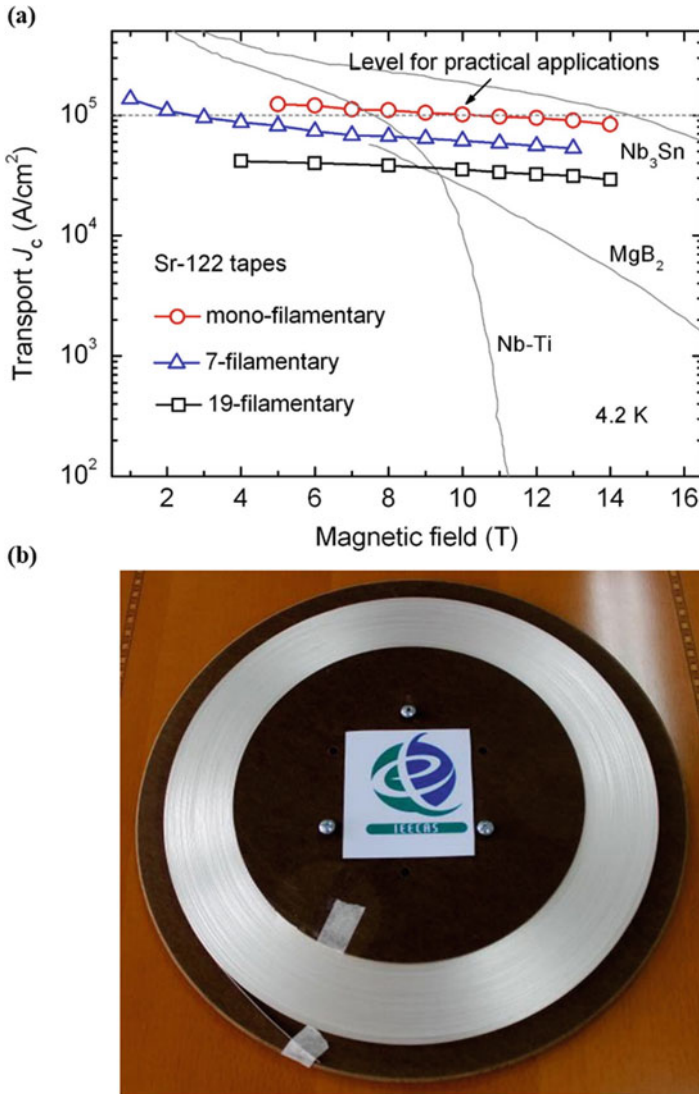


Fig. 9.10 (a) The applied field dependence of the transport J_c for hot-pressed mono- and multi-filamentary Sr-122 tapes (Reproduced with permission from [5]). For comparison point, the graph for MgB₂ and commercial NbTi and Nb₃Sn wires has also been included. (b) The first 100 m-class 122 type iron-based superconductor wire developed by the Chinese group. (Reproduced with permission from [5])

The selection of metal tube in PIT method is one of the important parameters. The metal sheath for the wire fabrication should not react with superconducting materials during the final heat treatment. In the case of FeSC, there are many sheath

materials such as Ag, Nb, Fe/Ti, Ta, and Cu [7, 105]. The sheath materials such as Nb, Ta, and Fe/Ti showed a markedly stronger reaction with pnictide due to the diffusion. Now, it has been established that Ag tube is the most appropriate sheath material for the wire and tape fabrication. Sometimes, Ag is also used in combination with an additional outer sheath made of Fe, Cu, or stainless steel to reduce the cost and to enhance the mechanical properties.

In the case of high T_c cuprates such as Bi-2212 and Bi-2223, only Ag can be used as a sheath material due to its inert behavior to the BSSCO and because its required permeable features to oxygen at the annealing temperature [108]. So, in the case of BSSCO wire, Ag represents about 60–70% of the BSSCO wire cost. Considering the price of the metal sheath, iron-based superconducting wires are expected to be much cheaper compared to that of the BSSCO wires.

Over the past years, the improvement of transport J_c of the FeSCs developed by using powder in tube (PIT) method has been the main topic for research and development. The J_c value is increased rapidly (Figs. 9.9 and 9.10). The highest critical current density is reported for 122-based materials and has exceeded 10^5 A/cm² at 4.2 K under 14 T. Such a large value enables high field application of iron-based superconductors. Figure 9.9 indicates that the transport J_c for 1111 and 11 families have 2–3 orders of magnitude lower in the high field region than those of 122 wires [7]. This might be because of large difficulties in wire/tape fabrication of 1111 and 11. For example, for 1111, fluorine doping provides the high transition temperature, but the control of fluorine is very difficult. The removal of excess iron for 11 wires is also a challenging task.

In iron-based superconductor suppression of the impurity phases formation, especially of non-superconducting phases which wet the grain boundaries is necessary. These non-superconducting phases located at grain boundaries produce a current blocking effect. There are many reports that showed that the impurities are partly responsible for the low critical current density [6, 7, 71, 75, 76, 78, 105]. Hence, the main issue to improve the critical current J_c is the decrease of the amount of impurity phases and of the porosity [105]. The global superconducting current of iron-based superconductors is limited by the intergrain current across grain boundaries (GB). Even with substantial blocking by GB phases, the intergranular current densities in FeSCs appear to be more than one order of magnitude larger at 4 K than in the early results on randomly oriented polycrystalline cuprates. Global currents flowing in the whole sample of the order of 4000 Acm⁻² have been evaluated at 4 K in self-field in the 1111 samples. Polycrystals of the 11 family synthesized at low temperature have also shown global current patterns in magneto-optical images with values of transport currents up to 700 Acm⁻².

In order to improve the grain connectivity, many experimental techniques such as metal additions, hot isostatic pressing (HIP), and texturing processes have been used [6, 7, 105]. It has been proved that addition of metals, such as Ag, Sn, In, Zn, or Pb, has significantly enhanced the J_c value without affecting the transition temperature (Figs. 9.9 and 9.10a). Interestingly, through co-doping with Ag, Sn, and Pb, the transport critical current density was significantly improved in the entire field region [7, 105, 109]. These additions can also effectively suppress the formation of

the glassy/amorphous phases and can fill in the pores and cracks, leading to better connections between grains, thus, enhancing J_c . The high J_c of 1.7×10^4 A/cm² at 10 T and 4.2 K for Sr122 tapes using Sn addition in combination with the rolling texture process (Fig. 9.10a) has been reported [7, 105, 109]. Reports on Sn-added 1111 family are also available and they also show improvement of J_c [109]. These studies indicate that the critical current density can be enhanced by using various technological routes and the potential application of iron-based superconductors can be expanded.

The possible existence of weak-links and electromagnetic granular behavior are the obstacles for application of FeSCs [77, 78, 98, 99, 109]. It is similar to the cuprates, although, as already noted, both impurities and grain boundaries are less detrimental to the superconducting properties of Fe-based high T_c superconductors compared to those of the cuprates. The intergrain coupling at grain boundaries plays an important role in transport applicability. Many experimental results, in particular studies of the remanent magnetization [77, 78, 98, 99, 109], have shown evidence of electromagnetic granular and weak-link behavior although its origin and underlying mechanisms are still under debate. Possible reasons for the weak-link behavior might be the presence of cracks, pores, and impurity phases along grain boundaries, short coherence length, and intrinsic anisotropy of superconducting properties. The weak-link problem has been well studied for different families of iron-based superconductors which show superconductivity only by carrier doping. A unique compound is LiFeAs belonging to the “111” family and showing superconductivity without doping at 18 K [78]. The MgB₂ also has superconductivity without doping at high T_c of 39 K, but it does not exhibit granular behavior or the weak-link problem at grain boundaries [11, 21].

Recently, it was demonstrated that the grain in 122 family becomes highly textured in Fe-sheath Sr-122 flat tapes by rolling with a large reduction ratio. This process can be used for the fabrication of 122 tapes on a large scale. In this process, addition with Sn results in significant enhancement of both core density and c -axis texturing of 122 phase. Due to the improvement of texture of 122 tapes, the current density was increased by more than an order of magnitude in magnetic field at 10 T to above 10^4 A/cm² at 4.2 K. Dong et al. [110] reported the enhancement of J_c for Ag clad Ba122 tapes using high quality precursor. At 4.2 K and 10 T, a higher transport J_c of 5.4×10^4 A/cm² and an engineering J_e of 1.5×10^4 A/cm² has been achieved for the iron-based superconductors [7]. The textured tapes have also small anisotropy, less than 1.5 as determined from measurements of J_c with applied magnetic field angle. It indicates that J_c is not highly sensitive with the angle between the tape surface and the direction of the magnetic field. In the case of cuprate superconductors, the highest J_c is obtained with magnetic field applied perpendicular to ab -plane. The low anisotropy behavior of 122 families is beneficial for the tapes practical applications. Densification is also needed for the improvement of J_c . Hot isostatic pressure (HIP) generally improves density and this is reflected on the enhancement of the current flow path [6, 7, 105]. The advantage of the HIP process is the ability to fabricate round wire, which is desirable for magnetic applications.

Apart from a high J_c , there are many other requirements for conductor applications. Superconducting conductors for large-scale applications must have a multifilament architecture, excellent mechanical properties, large engineering current density $J_e > 10^4$ A/cm² in magnetic fields, and small anisotropy of J_c with respect to field direction. Their cost should be low and they are scalable for large-scale production [6, 7, 105]. Sufficiently long length tapes and wires are required for winding the coils or for cabling. An easy and simple process is needed to balance the high performance with the production cost of the long wires.

Based on experience with the high-performance short samples and with subsequently developed multi-filamentary wires, research on fabrication of long FeSCs wires [105] started. In 2014, the first 11-m long $\text{Sr}_{1-x}\text{K}_x\text{Fe}_2\text{As}_2/\text{Ag}$ tape was produced by rolling. The process is scalable at industrial level and fabrication of a long wire in the 100 m class [111] was demonstrated. In August 2016, this rolling process was scaled up to produce the first 115-m-long with 7-filament $\text{Sr}_{1-x}\text{K}_x\text{Fe}_2\text{As}_2/\text{Ag}$ superconducting tape (Fig. 9.10b). The transport J_c at 4.2 K and 10 T was measured along the length of the 115-m Sr-122 tape [7]. A very uniform J_c distribution was observed throughout the tape, an average J_c of 1.3×10^4 A/cm² at 10 T was achieved. Fabrication of 100 m-class prototype wires is of great significance for promotion of practical applications of FeSCs. Assuming that the costs can be kept low, competition with NbTi and Nb₃Sn conductors appears probable, whereas competition with either BSCCO-based or YBCO-based HTS conductors will depend on future progress.

Granularity has so far limited the properties of pnictide wires. Yet, wires of the 11 family have been fabricated by powder in tube (PIT) method, exhibiting J_c values from 200 A/cm² [112] to 600 A/cm² [113]. Recently, values of 1000 A/cm² were reported in mono- and multi-filamentary Fe(Se, Te) wires prepared by ex situ method. As for wires of the 1111 family, values up to 4×10^3 A/cm² have been obtained. For the 122 family, the highest J_c values in wires fabricated by PIT are slightly above 10^4 A/cm². The 122 family appears to be the most promising, but the other families seem to catch up, particularly the 11 family. Most importantly, for all the three families, the maximum obtained J_c has been steadily increasing, suggesting that there is likely still a large edge of improvement.

Finally, it is worth mentioning that 122 and 11 films have been deposited on buffered metal-tape flexible substrates with outstanding results, namely J_c was 10^6 and 10^4 A/cm² [92], respectively. These encouraging results are likely due to the reduced J_c anisotropy of FeSCs, allowing the current flow along the *c*-axis. Once more it indicates that the requirement of texturing is less severe. The recently discovered stoichiometric 1144 has also huge potential for practical application and, hopefully, 1144 wires/tapes will show similar excellent properties as for 122 and 11 families.

Figures 9.11a, b depict the comparative temperature and field (*T-H*) phase diagram for different superconducting materials. The only representative members of FeSCs such as Fe(SeTe) (11), NdFeAsO_{0.7}F_{0.3} (Nd1111), and Ba_{0.55}K_{0.45}Fe₂As₂ (BaK122) single crystals are included in Fig. 9.11b. These FeSCs are compared with conventional superconductors NbTi, Nb₃Sn, with MgB₂, and with high T_c cuprates

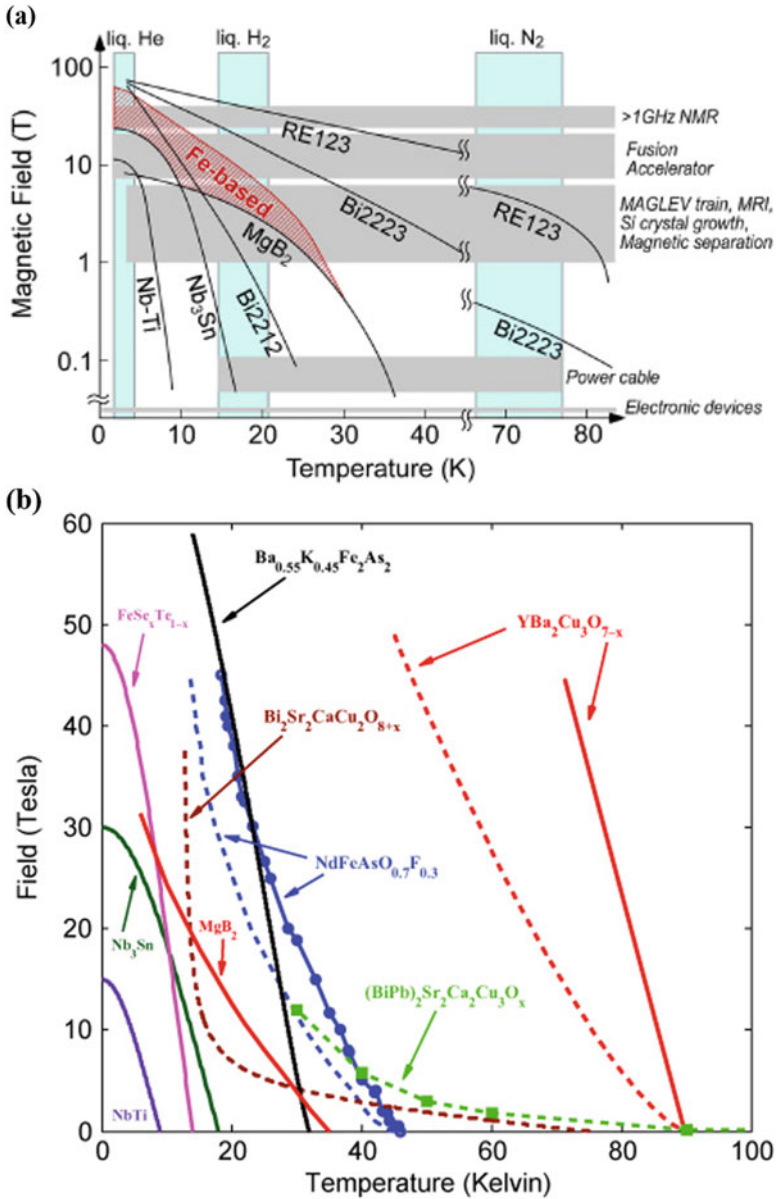


Fig. 9.11 (a) Magnetic field response of various superconductors with respect to temperature (Reproduced with permission from [6]). (b) The temperature dependence of the magnetic field for different superconducting materials are shown for $H//c$. The used solid line is for $H_{c2}(T)$ and dashed line is for irreversibility fields $H^*(T)$. (Reproduced with permission from [36])

($\text{Bi}_2\text{Sr}_2\text{CaCu}_2\text{O}_{8+x}$ single crystal, $(\text{BiPb})_2\text{Sr}_2\text{Ca}_2\text{Cu}_3\text{O}_x$ tapes, and $\text{YBa}_2\text{Cu}_3\text{O}_{7-x}$ single crystal). The FeSCs as BaK122 or Nd1111 have high irreversibility field H^* and H_{c2} up to 40–50 T at 20–30 K [6, 7]. The H_{c2} of BaK122 is much less anisotropic than for $\text{YBa}_2\text{Cu}_3\text{O}_{7-x}$ and Nd1111, indicating a useful feature for superconducting magnets. The extent to which poor grain connectivity in FeSCs polycrystals is intrinsic remains unclear, but grain boundaries for some FeSCs may be more transparent to current than for the others. As far as pinning is concerned, thin films and single crystals of FeSCs can carry high current densities $J_c = 10^6$ – 10^7 A cm⁻² at 4.2 K, making them competitive vs. conventional superconductors. The properties of FeSCs indicate good possibilities for magnet applications at 20–40 K. For instance, the arsenic-free Fe(SeTe) has a weakly anisotropic H_{c2} . The upper critical field is much higher than for Nb_3Sn and MgB_2 at 4.2 K, but very low carrier densities and shortage of chalcogenides can make them prone to poor grain connectivity. In turn, BaK122 may be a good magnet material due to its high H_{c2} ($H_{c2}(20\text{ K}) \sim 45\text{ T}$), moderately anisotropic, making it more useful than the more anisotropic Nd1111 with a higher T_c . Future experiments will tell if some of the FeSCs will eventually become high field magnet materials.

For application, the threshold J_c value of superconducting wires and tapes is generally recognized as being 10^4 – 10^5 A/cm² in the desired temperature and field regions. From the above discussion, it is clear that PIT processed tapes/wires have crossed the threshold value of practical transport J_c . Figure 9.11b summarizes the critical fields (upper) H_{c2} and (irreversibility) H^* as a function of temperature for various superconductors, while Fig. 9.11a presents their applicability domains. From the viewpoint of critical current properties, it seems that there is no market niche for the iron-based superconductors. However, the price of cuprate superconducting materials is still high, and they are not easy to use because of their highly anisotropic character. As described above, the production of long length conductors with improved J_c , and low cost are the key criteria to decide whether iron-based superconducting tapes and wires can be used in the future. We believe that the successful fabrication of long wires over 100 m with practical J_c opened a new chapter for the application of FeSCs in the near future. Studies on the magnetic field dependence of the J_c of wires and tapes have experimentally demonstrated their excellent robustness with respect to higher magnetic fields [7, 105]. By using the new high T_c materials, the refrigeration systems can operate at 20–30 K, i.e., without liquid He. We expect that FeSCs will become a real superconductor for practical applications.

9.9 Conclusions

The research progress in iron-based superconductors (FeSCs) is rapid. Before their discovery in 2008, it was beyond the imagination that iron can be one of the main component elements of high T_c superconductors. More than 5000 research papers have been published, studying the rich variety of superconducting materials and

enlightening the sophisticated mechanisms arising from the multiband nature of FeSCs. The transition temperature has reached 58 K and upper critical field is more than 100 T. The critical current density (J_c) is increased year by year and development of long wires and tapes have gradually enhanced the potential of these superconductors. At present, iron-based superconductors are considered to have huge potential to become a practical superconductor for high field applications, working in the temperature region 20–30 K.

References

1. H. K. Onnes, *Comm. Phys. Lab. Uni. Leiden* 120b, 122b, 124c (1911).
2. Y. Kamihara, T. Watanabe, M. Hirano, H. Hosono, *J. Am. Chem. Soc.* **130**, 3296 (2008)
3. H. Hosono et al., *Sci. Technol. Adv. Mater.* **16**, 033503 (2015)
4. D.C. Johnston, *Adv. Phys.* **59**, 803 (2010)
5. H. Hosono et al., *Mater. Today* **21**, 278 (2018)
6. J. Shimoyama, *Supercond. Sci. Technol.* **27**, 044002 (2014)
7. C. Yao, Y. Ma, *Supercond. Sci. Technol.* **32**, 023002 (2019)
8. S.J. Singh et al., *IEEE Trans. Appl. Supercond.* **23**, 7300605 (2013)
9. A. Schilling, M. Cantoni, J.D. Guo, H.R. Ott, *Nature* **363**, 56 (1993)
10. J.G. Bednorz, K.A. Muller, *Z. Phys.* **64**, 189 (1986)
11. J. Nagamatsu, N. Nakagawa, T. Muranaka, Y. Zenitani, J. Akimitsu, *Nature* **410**, 63–64 (2001)
12. H.F. Braun, *Phys. Lett.* **75A**, 386 (1980)
13. A.W. Graham, M. Kurmoo, P. Day, *J. Chem. Soc. Chem. Commun. Issue* **20**, 2061–2062 (1995)
14. K. Shimizu, T. Kimura, S. Furomoto, K. Takeda, K. Kontani, Y. Onuki, K. Amaya, *Nature* **412**, 316 (2001)
15. C.W. Chu, P.H. Hor, R.L. Meng, L. Gao, Z.J. Huang, *Science* **235**, 567 (1987)
16. M.K. Wu, J.R. Ashburn, C.J. Torng, P.H. Hor, R.L. Meng, L. Gao, Z.J. Huang, Y.Q. Wang, C.W. Chu, *Phys. Rev. Lett.* **58**, 908 (1987)
17. H. Takahashi, K. Igawa, K. Arii, Y. Kamihara, M. Hirano, H. Hosono, *Nature* **453**, 376 (2008)
18. X.H. Chen, T. Wu, G. Wu, R.H. Liu, H. Chen, D.F. Fang, *Nature* **453**, 761 (2008)
19. Z.A. Ren, G.-C. Che, X.L. Dong, J. Yang, W. Lu, W. Yi, X.-L. Shen, Z.-C. Li, L.L. Sun, F. Zhou, Z.X. Zhao, *Europhys Phys Lett* **83**, 17002 (2008)
20. D. N. Basov and Andrey V. Chubukov, *Nature Physics* **7**, 272–276 (2011)
21. C. Buzea, T. Yamashita, *Supercond. Sci. Technol.* **14**, R115 (2001)
22. M. Tinkham, *Introduction to Superconductivity*, 2nd edn. (McGraw-Hill, New York, 1996)
23. M. Campbell, J.E. Evetts, *Adv. Phys.* **21**, 199 (1972)
24. H. Suhl, B.T. Matthias, L.R. Walker, *Phys. Rev. Lett.* **3**, 552 (1959)
25. V. Guritani et al., *Phys. Rev. B* **70**, 184526 (2004)
26. A.Y. Liu, I.I. Mazin, J. Kortus, *Phys. Rev. Lett.* **87**, 087005 (2001)
27. S.V. Shulga et al., *Phys. Rev. Lett.* **80**, 1730–1733 (1998)
28. Y. Yokoya et al., *Science* **294**, 2518–2520 (2001)
29. E. Boaknin et al., *Phys. Rev. Lett.* **90**, 117003 (2003)
30. A.P. Petrović et al., *Phys. Rev. Lett.* **106**, 017003 (2011)
31. F. Wang, D.-H. Lee, *Science* **332**, 200 (2011)
32. D.J. Singh, M.-H. Du, *Phys. Rev. Lett.* **100**, 237003 (2008)
33. R.A. Jishi, H.M. Alyahyaei, *New J. Phys.* **11**, 083030 (2009)
34. I.I. Mazin, D.J. Singh, M.D. Johannes, M.H. Du, *Phys. Rev. Lett.* **101**, 057003 (2008)

35. H. Ding, P. Richard, K. Nakayama, K. Sugawara, T. Arakane, Y. Sekiba, A. Takayama, S. Souma, T. Sato, T. Takahashi, Z. Wang, X. Dai, Z. Fang, G.F. Chen, J.L. Luo, N.L. Wang, *Europhys. Lett.* **83**, 47001 (2008)
36. A. Gurevich, *Rep. Prog. Phys.* **74**, 124501 (2011)
37. K. Kuroki, S. Onari, R. Arita, H. Usui, Y. Tanaka, H. Kontani, H. Aoki, *Phys. Rev. Lett.* **101**, 087004 (2008)
38. I.I. Mazin, J. Schmalian, *Phys. C* **469**, 614 (2009)
39. W.Q. Chen, K.Y. Yang, Y. Zhou, F.C. Zhang, *Phys. Rev. Lett.* **102**, 047006 (2009)
40. A. V. Pogrebnyakov, X. X. Xi, J. M. Redwing, V. Vaithyanathan, D. G. Schlom, A. Soukiassian, S. B. Mi, C. L. Jia, J. E. Giencke, C. B. Eom, J. Chen, Y. F. Hu, Y. Cui, Qi Li, *Appl. Phys. Lett.* **85**, 2017 (2004)
41. N.R. Werthamer, E. Helfand, P.C. Hohenberg, *Phys. Rev.* **147**, 295 (1966)
42. A.M. Clogston, *Phys. Rev. Lett.* **9**, 266 (1962)
43. B.S. Chandrasekhar, *Appl. Phys. Lett.* **1**, 7 (1962)
44. K. Maki, *Phys. Rev. B* **148**, 362 (1962)
45. A. Fulde, R.A. Ferrel, *Phys. Rev.* **135**, A550 (1964)
46. L.W. Grunberg, L. Gunther, *Phys. Rev. Lett.* **16**, 996 (1966)
47. A. Gurevich, *Phys. Rev. B* **67**, 184515 (2003)
48. F. Hunte et al., *Nature* **453**, 903–905 (2008)
49. J. Jaroszynski et al., *Phys. Rev. B* **78**, 064511 (2008)
50. H. Yuan, Q et al. *Nature* **457**, 565–568 (2009)
51. K. Cho et al., *Phys. Rev. B* **82**, 060502(R) (2011)
52. T. Klein et al., *Phys. Rev. B* **82**, 184506 (2010)
53. P. Fulde, R.A. Ferrel, *Phys. Rev.* **135**, A550–A563 (1964)
54. A.I. Larkin, N. Ovchinnikov Yu, *Zh. Exp. Teor. Fiz* **47**, 1136–1146 (1964)
55. A.I. Larkin, N. Ovchinnikov Yu, *Sov. Phys. JETP* **20**, 762–769. (Engl. transl.) (1965)
56. A. Bianchi, R. Movshovich, C. Capan, P.G. Pagliuso, J.L. Sarrao, *Phys. Rev. Lett.* **91**, 187004 (2003)
57. M. Radovan et al., *Nature* **425**, 51–55 (2003)
58. M. Kenzelmann et al., *Science* **321**, 1652–1654 (2008)
59. S. Uji et al., *Phys. Rev. Lett.* **97**, 15701 (2006)
60. S. Yonezawa et al., *Phys. Soc. Jpn.* **77**, 054712 (2008)
61. L.N. Bulaevsii, A.A. Guseinov, *Sov. J. Low. Temp. Phys.* **2**, 140 (1976)
62. A. Gurevich, *Phys. Rev. B* **82**, 184504 (2010)
63. S.J. Singh et al., *Phys. Rev. Mater.* **2**, 074802 (2018)
64. W.R. Meier et al., *Phys. Rev. B* **94**, 064501 (2016)
65. A. Iyo et al., *J. Am. Chem. Soc.* **138**, 3410 (2016)
66. T.P. Orlando et al., *Phys. Rev. B* **36**, 2394 (1987)
67. P.P. Nguyen et al., *Phys Rev B* **48**, 1148 (1993)
68. J.S. Moodera et al., *Phys. Rev. B* **37**, 619 (1988)
69. T.T.M. Palstra et al., *Phys. Rev. B* **38**, 5102 (1988)
70. M.J. Naughton et al., *Phys. Rev. B* **38**, 9280 (1988)
71. M. Putti et al., *Supercond. Sci. Technol.* **23**, 034003 (2010)
72. G. Blatter, M.V. Feigelman, V.B. Geshkenbein, A.I. Larkin, V.M. Vinokur, *Rev. Mod. Phys.* **66**, 1125–1388 (1994)
73. E.H. Brandt, *Rep. Prog. Phys.* **58**, 1465–1594 (1995)
74. T. Katase, H. Hiramatsu, T. Kamiya, H. Hosono, *Appl. Phys. Exp.* **3**, 063101 (2010)
75. A. Yamamoto et al., *Supercond. Sci. Technol.* **21**, 095008 (2008)
76. F. Kametani et al., *Appl. Phys. Lett.* **95**, 142502 (2009)
77. S.J. Singh et al., *Supercond. Sci. Technol.* **26**, 065006 (2013)
78. S.J. Singh et al., *Supercond. Sci. Technol.* **28**, 025006 (2015)
79. S. Lee et al., *Appl. Phys. Lett.* **95**, 212505 (2009)
80. S. Heindl et al., *Phys. Rev. Lett.* **104**, 077001 (2010)
81. E.F. Talantsev, W.P. Crump, *Supercond. Sci. Technol.* **31**, 124001 (2018)

82. M.D. Lan et al., *Phys. Rev. B* **44**, 233 (1991)
83. N.D. Zhigadlo et al., *J. Phys. Condens. Matter* **20**, 342202 (2008)
84. P.J.W. Moll et al., *Nat. Mater.* **9**, 628 (2010)
85. H. Yang et al., *Appl. Phys. Lett.* **93**, 142506 (2008)
86. R. Prozorov et al., *Phys. Rev. B* **78**, 224506 (2008)
87. T. Taen et al., *Phys. Rev. B* **80**, 092502 (2009)
88. Y. Nakajima et al., *Phys. Rev. B* **80**, 012510 (2009)
89. M. Eisterer et al., *Supercond. Sci. Technol.* **22**, 095011 (2009)
90. X.X. Xi, *Supercond. Sci. Technol.* **22**, 043001 (2009)
91. B. Dam et al., *Nature* **399**, 439 (1999)
92. K. Iida et al., *Arxiv* 1812.10264 (2018).
93. I. Pallecchi et al., *Phys. C* **482**, 68 (2012)
94. M.A. Tanatar et al., *Phys. Rev. B* **79**, 094507 (2009)
95. C. Tarantini et al., *Appl. Phys. Lett.* **96**, 142510 (2010)
96. Santhanam et al., *Sci. News* **131**, 308 (1987)
97. N.D. Zhigadlo, S. Katrych, Z. Bukowski, S. Weyeneth, R. Puzniak, J. Karpinski, *J. Phys. Condens. Mater.* **20**, 342202 (2008)
98. A. Yamamoto, L. Balicas, J. Jaroszynski, C. Tarantini, J. Jiang, A. Gurevich, D.C. Larbalestier, R. Jin, A.S. Sefat, M.A. McGuire, B.C. Sales, D.K. Christen, D. Mandrus, *Appl. Phys. Lett.* **94**, 062511 (2009)
99. J.H. Durrell et al., *Rep. Prog. Phys.* **74**, 124511 (2011)
100. K.-H. Muller, C. Andrikidis, H. K. Liu and S. X. Dou, *Phys. Rev. B* **50** (1994) 10218
101. L. Wang, Z. Gao, Y. Qi, X. Zhang, D. Wang, Y. Ma, *Supercond. Sci. Technol.* **22**, 015019 (2009)
102. S. Graser et al., *Nat. Phys.* **6**, 609 (2010)
103. D.C. Larbalestier et al., *Nature* **410**, 186 (2001)
104. S.J. Singh et al., *Phys. C* **529**, 8–20 (2016)
105. Y. Ma, *Supercond. Sci. Technol.* **25**, 113001 (2012)
106. Y.C. Zhu et al., *Supercond. Sci. Technol.* **31**, 06LT02 (2018)
107. Y.P. Qi, X.P. Zhang, Z.S. Gao, Z.Y. Zhang, L. Wang, D.L. Wang, Y.W. Ma, *Phys. C* **469**, 717 (2009)
108. R.M. Scanlan et al., *Proc. IEEE* **92**(10), 1639 (2004)
109. S.J. Singh et al., *Supercond. Sci. Technol.* **27**, 085010 (2014)
110. C. Dong et al., *Scr. Mater.* **99**, 33 (2015)
111. X.P. Zhang et al., *IEEE Trans. Appl. Supercond.* **27**(4), 7300705 (2017)
112. T. Ozaki et al., *Supercond. Sci. Technol.* **24**, 105002 (2011)
113. Q.P. Ding et al., *Supercond. Sci. Technol.* **25**, 025003 (2012)

Chapter 10

Grain Boundaries in Fe-Based Superconductors



Jens Hänisch and Kazumasa Iida

10.1 Introduction

The discovery of Fe-based superconductors (FBS) [1, 2] had a huge impact on the condensed matter community, since understanding the mechanism of superconductivity of this class of materials shed light on exploring new high- T_c superconductors. Therefore, a lot of effort has been devoted to unveiling physics of these compounds, resulting in several important findings: (a) five orbitals of Fe $3d$ cross the Fermi level (i.e. multiband superconductors) [3], (b) the symmetry of the superconducting order parameter (OP) is identified as s_{\pm} wave (i.e. unconventional superconductor) both theoretically and experimentally (note: this may depend on the system and also doping level) [3–5], (c) the short coherence length results from the low Fermi velocity and small carrier concentration [6], and (d) the parent phase is an antiferromagnet. Although some of the features are similar to the cuprates, there are distinct differences between those two classes. For instance, (1) the symmetry of the OP for FBS is not a d -wave but an extended s -wave, (2) the parent compounds of FBS are not Mott insulators but semimetals [note: among the FBS only $A_{1-x}Fe_{2-y}As_2$ ($A=K, Cs, Rb, Tl$) is Mott insulator], (3) grain boundaries are of metallic nature, and (4) anisotropies of upper critical field (H_{c2}) and also critical current density (J_c) of FBS are smaller than those of the cuprates. Additionally, experiments on Co-doped $BaFe_2As_2$ (Ba122) bicrystal films revealed early on that exponential decay of J_c across the symmetric [001]-tilt grain boundary starts at a misorientation angle of 9° [7], which is almost twice as large as for the cuprates [8].

J. Hänisch (✉)

Institute for Technical Physics, Karlsruhe Institute of Technology, Eggenstein-Leopoldshafen, Germany

e-mail: jens.haenisch@kit.edu

K. Iida

Department of Materials Physics, Nagoya University, Chikusa, Nagoya, Japan

e-mail: iida@mp.pse.nagoya-u.ac.jp

Thanks to those features, J_c across grain boundaries in FBS is not severely reduced compared to the cuprates, which is favourable for wire as well as polycrystalline bulk applications.

To date, FBS wires and tapes have been fabricated by two methods: (1) the powder-in-tube (PIT) method for which precursor powders are put into metallic tube, swaged, drawn, and then heat-treated, and (2) the coated conductor method for which pseudo single crystalline films are deposited on technical metallic substrates. Hence, FBS wires and tapes contain grain boundaries.

Grain boundaries (GBs) as two-dimensional defects have huge influence on macroscopic properties of functional materials [9, 10] and are therefore of high interest in their development. They comprise the more or less planar structure between two adjacent crystallites of different crystallographic orientation. Grain boundaries are in general characterized by five parameters, i.e. the GB plane with respect to one of the crystallites (characterized by its normal vector \mathbf{n} (two parameters), the rotation axis \mathbf{u} (two parameters), and the GB angle θ_{GB} , for which the second crystallite is rotated around \mathbf{u} away from orientation of crystallite 1), Fig. 10.1. In polycrystalline bulk samples, in general different types of GBs co-exist. In well-defined experiments on single GBs, however, usually special types of GBs are used and investigated, such as twist-boundaries ($\mathbf{u} \parallel \mathbf{n}$), tilt-boundaries ($\mathbf{u} \perp \mathbf{n}$), symmetric boundaries (GB plane is mirroring the two crystallites), and low- Σ GBs (special GB angles for large coincidence lattices). A further classification may be done via the GB angle θ_{GB} [11]: Low-angle GBs (LAGBs) are comprised of an array of dislocations with distance $D = b / \{2 \sin(2\theta_{GB})\} \sim b / \theta_{GB}$ (Frank's formula) in the simplest and most symmetric case, where b is the magnitude of the dislocation's Burgers vector \mathbf{b} (usually a lattice constant) along the GB. At around 10–15°, depending on the material, the cores or distorted regions of adjacent dislocations start to get in contact to each other and it gets energetically favourable

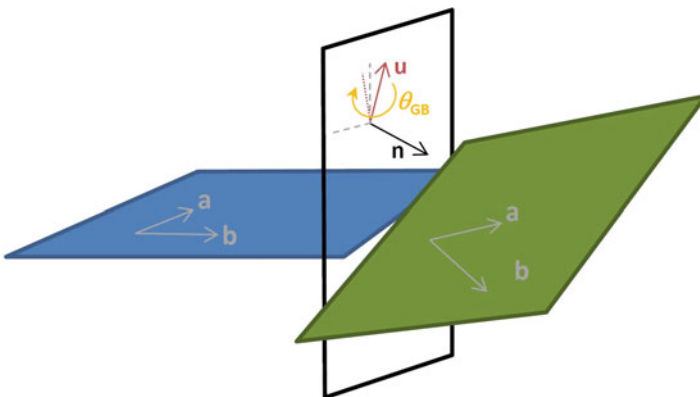


Fig. 10.1 Schematic of a grain boundary with grain boundary plane \mathbf{n} , rotation axis \mathbf{u} , and rotation angle θ_{GB} . The dashed lines represent the orthogonality of \mathbf{n} on the GB plane, the dotted line is the projection of \mathbf{u} on the GB plane

for the GB to reconstruct in bigger structural units. This is the angular regime of high-angle GBs (HAGBs).

In superconducting materials, GBs not only influence the structural and mechanical but also the electrical properties. In low- T_c superconductors, such as Nb_3Sn , GBs are known to be good flux pinning centres, so that an increase in GB density (or decrease in grain size) often leads to an increase of the critical current density J_c , e.g. [12]. In the high- T_c cuprates (HTS), however, GBs posed a huge obstacle for realizing high-current applications since high-angle GBs severely diminish the critical current densities J_c . In fact, above some critical angle θ_c , J_c falls exponentially with θ_{GB} , as has been measured for several cuprate compounds, such as $\text{YBa}_2\text{Cu}_3\text{O}_7$ (YBCO) [13] and $\text{Bi}_2\text{Sr}_2\text{Ca}_{n-1}\text{Cu}_n\text{O}_{2n+4}$ [14], see Fig. 10.2. For reviews on GBs in HTS bulks and films, see [8, 15]. There are several reasons for this strong $J_c(\theta_{\text{GB}})$ dependence: First of all, HTS are extreme type-II superconductors with very small coherence lengths ξ of only a few nm and very low charge carrier densities. This leads to depletion in Cooper pair density within the (high-angle) GB region which usually has a width comparable to or even larger than ξ , or around the dislocations of LAGBs due to e.g. stoichiometry deviations, band bending, charge inhomogeneities, and strain dependence of T_c . Therefore, HAGBs usually constitute weak links in HTS materials, and since the width of GBs approximately increases linearly with GB angle and tunnel currents fall exponentially with tunnel barrier width, an exponential decrease of J_c with GB angle θ_{GB} follows naturally. Depending on θ_{GB} and amount of faceting of the GB plane, J_c may be further diminished by possible destructive overlap of positive and negative regions of the wave function due to the d -wave symmetry in HTS [16]. Low-angle grain boundaries with sufficiently low θ_{GB} only minimally disturb the current flow, and their dislocations may even contribute to flux pinning [17].

In superconductors with low charge carrier concentrations, such as the HTS cuprates and to some part the Fe-based superconductors, there exists a further

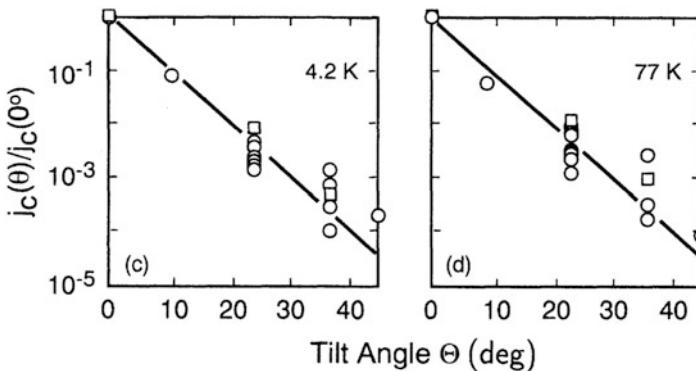


Fig. 10.2 Angle dependence of the reduced critical current density across [001]-tilt grain boundaries in YBCO (squares) and Bi2212 (circles) at 4.2 and 77 K. Reprinted figure with permission from [14]. Copyright (1995) by the American Physical Society

intermediate regime, where the electronically disturbed region around the dislocation cores is slightly larger than the structurally disturbed region. This has been discussed e.g. by a T_c reduction due to strain fields in cuprates. Therefore, in such GBs (with θ_{GB} slightly larger than the critical angle θ_c), the order parameter may be reduced along the entire GB plane and J_c would be reduced even though the GB is structurally still a LAGB. For GB angles slightly smaller than θ_c in contrast, the behaviour of the GB depends strongly on the applied magnetic field, since the magnetic field determines which kind of vortices are present within the GB plane—Abrikosov, Abrikosov-Josephson, or Josephson vortices.

In this chapter, GB issues of Fe-based superconductors will be discussed in more or less historical order on polycrystalline bulks and wires followed by bicrystal and polycrystalline thin films for the most-studied, application-relevant systems: $LnFeAs(O,F)$ (Ln lanthanoids), P-, Co-, and Ni-substituted $AeFe_2As_2$, (Ae : alkali earth) and Fe(Se,Te) in comparison to the cuprate high- T_c superconductors. Earlier reviews on GBs in FBS materials have been published by Deutscher [18] and Durrell et al. [19]. The topic of microelectronic junctions on bicrystal GBs in FBS has been reviewed, e.g. by Seidel [20], and is not covered here.

10.2 Grain Boundaries in Polycrystals and PIT Wires

Fe-based superconductors showed very high upper critical fields H_{c2} with low anisotropy despite anisotropic crystal structure. Hence, the community in applied superconductivity research has imagined this material class to have potential for conductor or bulk applications in high fields. And the question arose immediately which (critical) current can be circulated in polycrystalline bulk samples or transported in powder-in-tube (PIT) wires of Fe-based superconductors. To address this issue, many studies have been conducted on such polycrystalline samples. In this subsection, these studies on polycrystalline $LnFeAsO$, $LiFeAs$, $AeFe_2As_2$, and Fe chalcogenides will be introduced.

10.2.1 $LnFeAsO$ (Ln : Lanthanoids) Sintered Bulks

Sintered $SmFeAsO_{1-\delta}$ and $NdFeAs(O,F)$ bulk samples have been well characterized immediately after the discovery of FBS. Unlike $AeFe_2As_2$ ($Ae122$) and FeSe systems, sizable single crystals of $Ln1111$ were difficult to grow in the early stages of FBS research. Therefore, the electromagnetic properties of $Ln1111$ were characterized using polycrystalline samples. Figure 10.3 shows the microstructure of polycrystalline $SmFeAsO_{0.85}$ acquired by a scanning electron microscope [21]. Clearly, some of the plate-like $SmFeAsO_{0.85}$ grains were well connected (i.e. clean grain boundary without cracks). On the other hand, cracks between the $SmFeAsO_{0.85}$ grains as well as occasionally within grains (Fig. 10.4a) were

Fig. 10.3 SEM image of partially well-connected Sm1111 grains. Current transport is obstructed by FeAs, Sm_2O_3 and cracks at the grain boundaries. Republished with permission of IoP Publishing, from [21]; permission conveyed through Copyright Clearance Center, Inc.

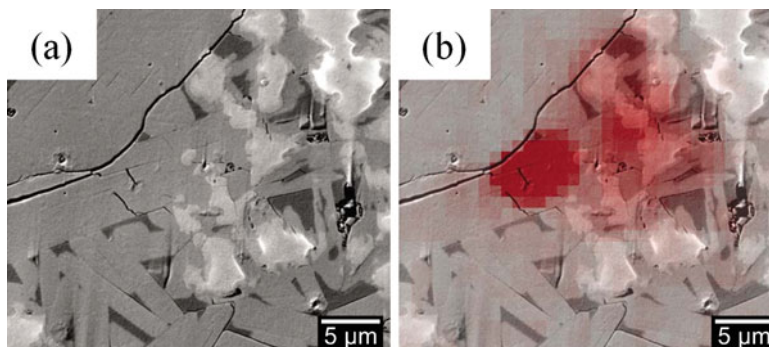
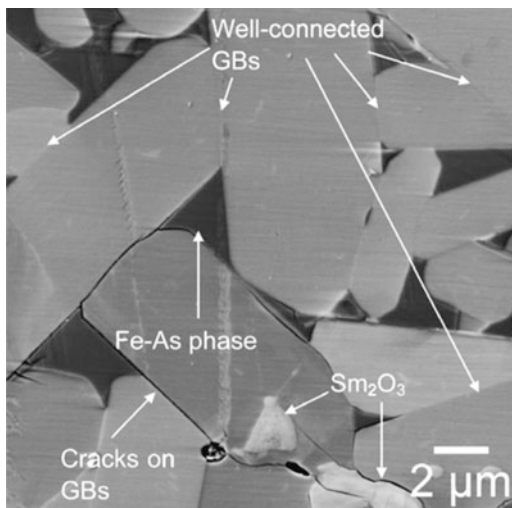
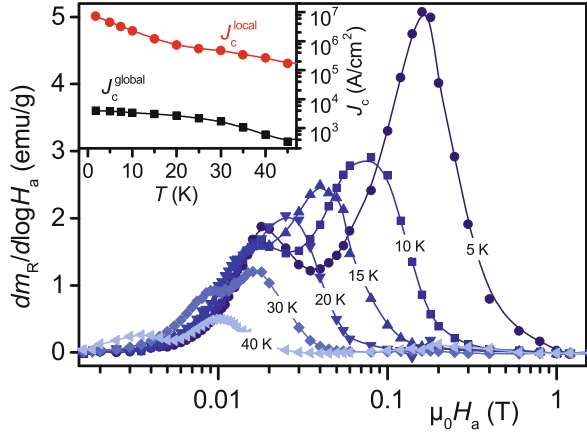


Fig. 10.4 Higher resolution SEM image (a) near a dissipation spot (red, b) in a $\text{SmFeAsO}_{0.85}$ polycrystal determined by low-temperature laser scanning microscopy (LTLSM). Current transport is obstructed by FeAs, Sm_2O_3 , and cracks. Reprinted from [22], with permission of AIP Publishing

frequently observed, which impedes the critical current flow within the grains. Also Sm_2O_3 as well as FeAs were observed around the $\text{SmFeAsO}_{0.85}$ grains, which act as global current blockers (i.e. the overall critical current flowing through a sample via adjacent grains is reduced). Indeed, strong dissipation spots were observed near such defects because the current is squeezed into narrow paths without current blockers (Fig. 10.4a, b) [22].

The derivatives of the field dependence of remnant magnetization (m_R) for the $\text{SmFeAsO}_{0.85}$ bulk sample revealed two distinct peaks (Fig. 10.5): the former reflects the global J_c (J_c^{global}) and the latter corresponds to the intra-grain one (J_c^{local} or J_c^{Grain}) [23]. The respective global and intra-grain J_c at 5 K were 3900 A/cm^2 and $4.5 \times 10^6 \text{ A/cm}^2$, indicating that SmFeAsO inherently possesses high J_c . Hence, eliminating such extrinsic defects like wetting FeAs and cracks would lead

Fig. 10.5 Derivatives of the remanent magnetization as a function of the maximum applied field for the SmFeAsO_{0.85} small bulk [23]. Data are normalized by sample mass. Inset shows the temperature dependences of the peak fields $\mu_0 H_{\text{peak}}$ for the first and second peaks. Data courtesy of A. Yamamoto



to high J_c^{global} . It is worth mentioning that J_c^{global} of SmFeAsO_{0.85} is much higher than that of sintered YBa₂Cu₃O₇ in early days (~ 100 A/cm² at 4 K) [24]. The temperature dependence of J_c^{global} at low-temperature regime is well described by $J_c^{\text{global}} \sim (T_c - T)^2$, which indicates that J_c^{global} is governed by an SNS (S: superconductor and N: normal metal) proximity coupled Josephson junction network [23]. Indeed, J_c^{global} is significantly reduced by a small magnetic field. In later SmFeAsO_{0.85} samples, a J_c^{global} of only ~ 250 A/cm² was measured despite much better phase purity and grain connectivity achieved by hot-isostatic pressing [25]. This was partially attributed to lower T_c values and a possibly different F content and distribution. Similar results of $J_c^{\text{global}} \sim 100\text{--}200$ A/cm² were measured by Eisterer et al. [26] and Otabe et al. [27] on SmFeAsO_{1-x}F_x bulk samples.

So far, we discussed only the effect of extrinsic factors on the inter-grain J_c . To understand the intrinsic effect, bicrystal experiments on well-defined, single grain boundaries should be necessary. Unlike Ae122 and FeSe systems, such experiments have not been reported until 2018. Very recently, misorientation angle dependence of the inter-grain J_c for NdFeAs(O,F) bicrystal films has been reported [28, 29], which will be discussed in Sect. 10.3.1.

Despite the absence of bicrystal experiments on Ln1111, several pieces of important information necessary to achieve high global J_c values were revealed by the studies mentioned above (i.e. reducing the amount of impurity phases like FeAs and Ln₂O₃, increasing the sample density and texturing to improve grain connectivity, and reducing the number of cracks within grains). Hence, a lot of activities for fabricating Ln1111 wires and tapes have kept going, resulting in the improvement of J_c performance step by step over time [30–33]. Here, the wire fabrication focuses on SmFeAs(O,F) because of the highest T_c among the FBS in the bulk form. One breakthrough for achieving high global J_c values in polycrystalline SmFeAs(O,F) wires was to add Sn to the precursor powders, which reduces the amount of FeAs wetting at grain boundaries due to the chemical reaction between FeAs and Sn producing FeSn₂ particles or discontinuous layers (Fig. 10.6) [30].

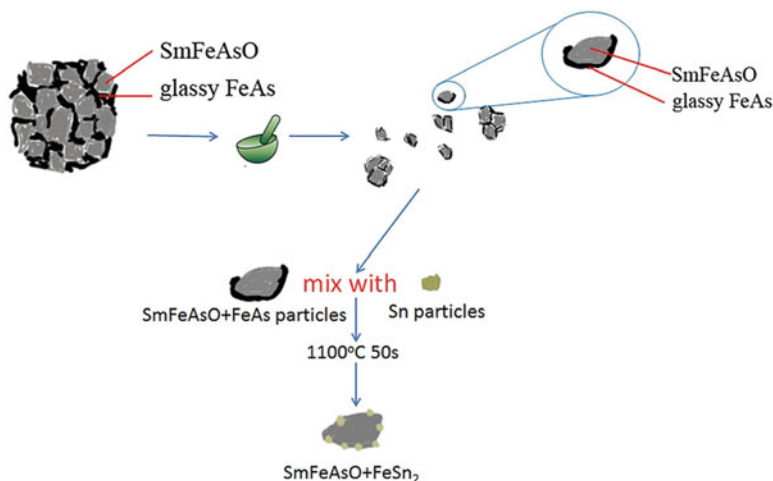


Fig. 10.6 Schematic diagram describing the Sn transformation which eliminates the detrimental FeAs wetting phase but also damages SmFeAsO_{1-x}F_x grains, i.e. reduces T_c . Reprinted from [30], with permission of AIP Publishing

Sn addition, however, leads to a slight decrease in T_c (T_{c0} decreased from 43.3 to 37 K). Another effect of Sn addition is filling voids and cracks, which improves the grain connectivity. Adding metallic elements such as Ag, Pb, and Sn have been reported in *Ae*122 for improving grain connectivity and hence, superconducting properties [34–36]. At present, the self-field J_c of SmFeAs(O,F) wires was achieved around 4×10^4 A/cm² at 5 K [37]. Although the significant improvement of wire performance of *Ln*1111 has been achieved since 2008, self-field as well as in-field J_c are still one or two order of magnitude lower than *Ae*122. One of the challenging issues for SmFeAs(O,F) wires is to control the F content. Employing low synthesis temperatures guarantees a high T_c of over 50 K, however, the presence of unreacted phase and low sample density still remain. Further optimization of the SmFeAs(O,F) wire fabrication is necessary.

10.2.2 *Ae*Fe₂As₂ (*Ae*: Alkali Earth Elements) Sintered Bulks

Although the maximum T_c of *Ae*122 is close to that of MgB₂ [between Fe(Se,Te) and SmFeAs(O,F)], the activity of wires and bulk fabrications using *Ae*122 is quite high thanks to the highest depairing current density among the FBS. For bulk and wire fabrications, high-energy ball-milling has been employed to synthesis *Ae*122 precursor powders [34–36, 38, 39]. During the ball-milling, partial Ba122 phase formation occurs. The resultant precursor powders are highly homogeneous and reactive. Hence, it is possible to reduce the heat treatment temperature, resulting in

the absence of GB wetting phases. The combination of fine precursor powders with highly phase-pure and high-pressure synthesis (i.e. cold and hot isostatic pressing) yields over 90% relative density in K-substituted Ba122 [38]. As a result, transport critical current densities of untextured bulks and round wires of K-doped Ba122 exceed 10^5 A/cm² in self-field at 4.2 K. Similarly, Co-doped Ba122 fabricated by the same method showed a self-field J_c of over 2×10^4 A/cm² at 4.2 K. These results highlight the application potential of FBS wires and bulk magnets.

The microstructures of a K-doped Ba122 sample prepared with high-energy ball-milling are shown in Fig. 10.7 [38]. As stated earlier, the grain boundaries are notably clean without FeAs wetting phase, which was frequently observed in *LnFeAs(O,F)*.

The detailed analyses by atom probe tomography (APT) revealed a trace of oxygen impurities along the GBs (see Fig. 10.8) [40], which is consistent with the results for K-doped Sr122 reported by Wang et al. [41]. It is still unclear whether the GB oxides are due to impurities of the precursor material or form during (bulk) sample preparation. A formation during APT sample preparation is less likely (the outer surfaces do not contain oxygen), however cannot be excluded completely. To understand whether this is an extrinsic effect, further experiments should be carried out.

Although K-doped Ba- and Sr122 bulks and wires contain high-angle GBs, their global J_c is in the order of $10^4 \sim 10^5$ A/cm² at 4.2 K with and without magnetic fields. Additionally, recent experiments on K-doped Ba122 bulk samples with 10 mm in diameter and 18 mm thickness (in total) revealed a large trapped magnetic field of over 1 T at 5 K [42]. Nevertheless, even though the microstructures are very similar, the J_c performance of Co-doped Ba122 is inferior to that of K-doped Ba122 by almost one order of magnitude [38]. This indicates that grain boundary properties depend on the kind of substituting elements (i.e., K, Co, and P) and perhaps *Ae* in *AeFe₂As₂* too, by extrinsic and/or intrinsic effects. To clarify this, bicrystal experiments on (Ba,K)Fe₂As₂ and (Sr,K)Fe₂As₂, which are still missing, are desirable.

It is reported that the inter-grain J_c of Co-doped Ba122 bicrystal films decays exponentially beyond a misorientation angle (θ_{GB}) of 9° [7]. However, the inter-grain J_c is almost constant $10^4 \sim 10^5$ A/cm² above $\theta_{GB} = 30^\circ$, which differs from the cuprates [8]. This level of J_c is consistent with the global J_c observed in polycrystalline K-doped Ba- and Sr122. Although bicrystal experiments on K-doped Ba- and Sr122 are absent, the same observations are highly likely. This similarity between bulk J_c^{global} and HAGBs in bicrystal films has two possible reasons: (1) Clean GBs may suffer from vortex channelling, which is larger in straight GBs such as in bicrystal films, (2) LAGBs in bulks may still contain oxides which let them appear as HAGBs by increasing the effective width. Hence, to further improve the global J_c for K-doped Ba- and Sr122, a texturing process might be useful. Indeed, textured 100 m long K-doped Sr122 tapes with an average large J_c of 10^4 A/cm² even at 10 T at 4.2 K have already been realized [43]. Besides texturing, clean oxide-free GBs in dense and crack-free materials are key for high J_c^{global} values.

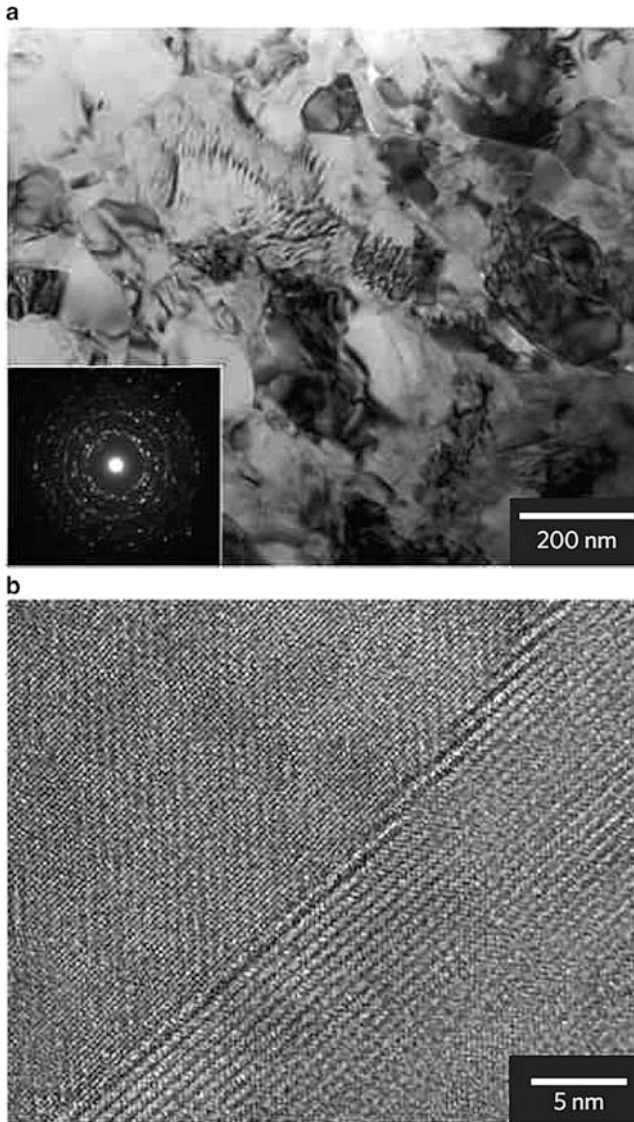


Fig. 10.7 Microstructure of K-doped Ba122 bulk investigated by TEM. **(a)** TEM image of polycrystalline K-doped Ba122 bulk material showing several equi-axed grains with average grain diameter of ~ 200 nm. Inset: A selected-area electron diffraction image of **(a)** indicating that the grains of the material are randomly oriented with many high-angle GBs. **(b)** HRTEM image of a typical K-doped Ba122 GB. The lattice fringes of upper and bottom grains meet at the GB without an amorphous contrast, indicating that the GB is clean without a wetting impurity phase. Reprinted by permission from: Springer Nature, Nature Materials [38], Copyright (2012)

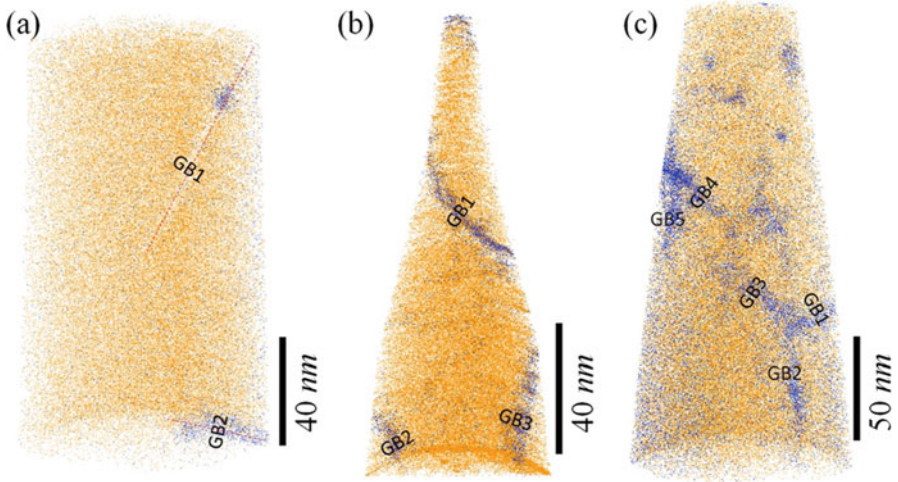


Fig. 10.8 A 3D atom probe tomographic reconstruction of: (a) $(\text{Ba}_{0.4}\text{K}_{0.6})\text{Fe}_2\text{As}_2$; (b) $(\text{Ba}_{0.4}\text{K}_{0.6})\text{Fe}_2\text{As}_2$; and (c) $\text{Ba}(\text{Fe}_{0.92}\text{Co}_{0.08})_2\text{As}_2$ superconductors. Oxygen atoms are in blue and Ba atoms are in orange, other elements are excluded for a clear display of grain boundary segregation. Each dot represents a single atom, but not to scale. Reprinted from [40], with permission of AIP Publishing

10.2.3 *FeSe and Fe(Se,Te) Sintered Bulks*

Most of the studies on *11* bulk samples focused on PIT-processed wires using FeSe and Fe(Se,Te) [45–48]. The strategy for achieving high transport J_c is the same as for other systems (i.e. eliminating extrinsic factors mentioned above together with texturing process). To realize the dense materials, Ding et al. reported a novel method to fabricate FeSe tapes [44]. In their method, an Fe sheet, $\sim 50 \times 5 \text{ mm}^2$ in size, and Se grains were sealed together in an evacuated quartz tube and thermally treated. During the heat treatment, Se vapour reacted with Fe, resulting in the formation of FeSe. The microstructure of the resultant FeSe contained many grains with $\sim 20 \mu\text{m}$ diameter (Fig. 10.9). Many cracks between grains were also observed. Although the self-field intra-grain J_c is as high as 10^4 A/cm^2 at 5 K, the inter-grain J_c at 4.2 K is 600 A/cm^2 .

One of the breakthroughs for improving the global J_c for Fe(Se,Te) is a novel process in which the precursor materials are melted, followed by annealing [49]. Figure 10.10 compares the microstructures of Fe(Se,Te) bulk samples after different preparations. As can be seen, a lot of pores were observed in the Fe(Se,Te) sintered sample with a grain size almost comparable to the pores. On the other hand, the melt-processed sample showed less porosity. Additionally, no secondary phases were observed at GBs. Annealing of that sample leads to stronger phase separation of regions with high and low Se-Te ratio as well as to formation of fine Fe-deficient precipitates (M+A). The resultant self-field J_c at 4.2 K is in the range of

Fig. 10.9 SEM image of an FeSe tape. Republished with permission of IoP Publishing, from [44]; permission conveyed through Copyright Clearance Center, Inc.

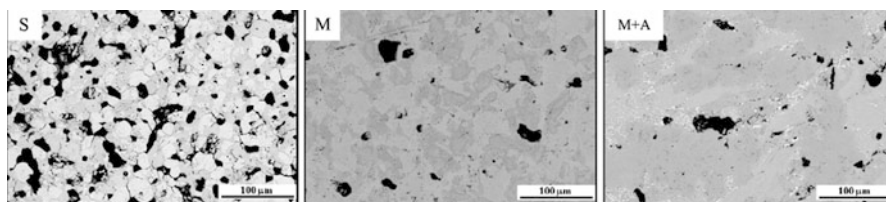
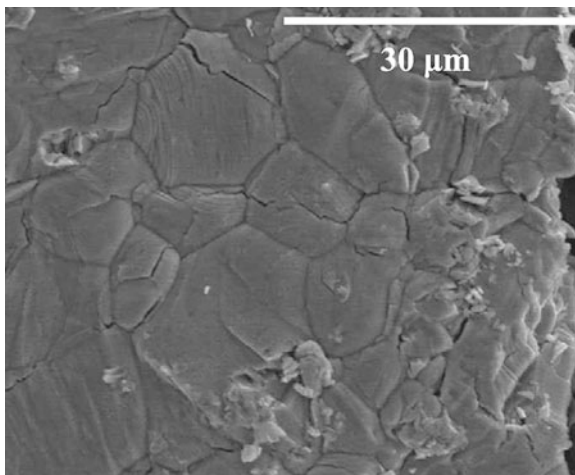


Fig. 10.10 Back-scattered SEM images of three polycrystalline Fe(Se,Te) samples. **S** sintered, **M** melted, **M+A** melted + annealed sample (at 550 °C, 17 days). Republished with permission of IoP Publishing, from [49]; permission conveyed through Copyright Clearance Center, Inc.

1000 A/cm², where the in-field J_c is almost constant up to 8 T. The level of J_c is two orders of magnitude lower than that of K-doped *Ae*122. The bicrystal experiments on Fe(Se,Te) showed the level of J_c at 4.2 K is between 10³ and 10⁴ A/cm² above $\theta_{GB} = 24^\circ$ [50], which is comparable to that of the melt-processed/annealed Fe(Se,Te) with dense microstructure and clean GBs. Hence it may be concluded, texturing is necessary for further improvement of J_c , which is similar to the *Ae*122 systems.

Mancusi et al. [51] used an FeSe_{0.5}Te_{0.5} polycrystalline bulk sample to study the effect of GB networks on the complex AC susceptibility response $\chi(T)$ near T_c . The transition shows clear two-step behaviour, especially for the imaginary part χ'' , for all AC fields and frequencies tested, which were fitted by taking into account the actual induced fields and relaxation times in the GB region and within the grains. Flux motion in both regions was found to be flux creep at low T and thermally activated flux flow (TAFF) at high T . T_c of the GB region with ~ 12 K was found to be considerably lower than the intra-grain value of ~ 14 K.

10.2.4 Sintered Bulks of LiFeAs and Other Compounds

The only GB study on *111* compounds has been conducted by Singh et al. [52] on LiFeAs polycrystalline bulk samples. This compound exhibits superconductivity ($T_c \sim 19$ K) without any doping. The samples were prepared by a solid-state reaction with a low-temperature of 600 °C. Although the precursor powder was uniaxially pressed into a pellet, followed by a low-temperature sintering, the sample had a relative density of 70%. Microstructural analysis revealed micro-cracks between the grains. Such micro-cracks may be formed due to the thermal stress. Another distinct feature is that the phase-pure LiFeAs sintered sample is chemically homogeneous. Therefore, micro-cracks are major current blockers, leading to a small inter-grain J_c of only ~ 440 A/cm² even at 5 K. As possible routes for future increase in inter-grain J_c , reducing the micro-crack density by process optimization, increasing the density by hot-isostatic pressing and texturing are suggested by Singh et al.

Also Fe-based superconductors with large blocking layers, (Fe₂As₂)(Ca₄(Mg_{0.25}, Ti_{0.75})₃O₈) (22438, $T_c = 43$ K) and (Fe₂As₂)(Ca₅(Sc_{0.5}Ti_{0.5})₄O₁₁) (225411, $T_c = 36$ K) have been investigated regarding their GBs [53]. Both compounds showed weak-link behaviour with the typical two-step transition in remanent magnetization vs. applied field, where 22438 shows slightly better grain connectivity due to cleaner GBs. The inter-grain J_c values around 0.5 and 0.07 MA/cm² are relatively low compared to other FBS bulks of similar T_c . Both samples show a double transition in the in-field temperature dependence of the resistivity which also has been attributed to electromagnetic granularity. However, since for the cuprates polycrystalline samples usually show a double transition also in self-field [54] and Bi₂Sr₂Ca_{*n*-1}Cu_{*n*}O_{2*n*+4} single crystals show similar in-field behaviour [55], this behaviour as well as the low J_c values might also be attributable to the extremely large electronic anisotropy in these compounds.

Recently, magnetization J_c values of a CaKFe₄As₄ (1144) single crystal have been compared to a pressed powder sample made from such a single crystal [56]. Whereas the single crystal shows exceptionally high J_c values (up to 200 MA/cm² for $B \perp c$ and 10 MA/cm² for $B \parallel c$ ¹), the powder exhibits much reduced J_c values (~ 40 kA/cm²) due to weak-link behaviour at the GBs. However, this is still larger than for other FBS bulks.

10.2.5 Summary

Also for FBS, high-angle GBs suppress the super-current flow due to the deterioration of the superconducting OP at GBs. Although the origins of the deterioration of the superconducting OP at GBs for the cuprates [46, 57] have been identified

¹Due to the complex microstructure of these samples with different kinds of stacking faults and intergrowths, the magnetically measured self-field J_c values differ for $B \parallel c$ and $B \perp c$.

[8], it is still ambiguous for FBS. Further investigations using bicrystal films are necessary to understand GB characteristics, which will help to tackle GB issues. What can be said, however, is that in bulk samples GBs are affected severely by extrinsic properties, such as compactness and cleanliness. As shown in Table 10.1, J_c^{global} is around three orders of magnitude lower than J_c^{local} , almost irrespective of the compound. This is a much larger reduction than observed for LAGB bicrystal junctions (typically 1–1.5 orders of magnitude), see below. Therefore, extrinsic effects must play a role in polycrystalline bulk samples.

Hecher et al. [60] pointed out that small grains might be one key to high-field applications of untextured polycrystalline FBS samples. The authors modelled the hysteresis of J_c for increasing and decreasing fields (which is due to the irreversible intra-grain currents) and found excellent agreement to detailed SQUID and scanning Hall probe microscopy (SHPM) measurements. As the authors concluded, the maximum magnetic field B_{max} at which a polycrystalline wire is still reasonably applicable for a certain application current density J_c^{app} is inversely proportional to the mode of the grain size distribution s_0 (i.e. the grain size s , where the probability density is maximum) and the thickness of the GB region d :

$$B_{\text{max}} \approx \frac{\phi_0}{2\pi^2} \frac{|J_0|}{J_c^{\text{app}}} \frac{1}{s_0 d}$$

where J_0 is the maximum Josephson current across a single GB.

Eisterer very recently proposed a mean-field percolation model for the J_c limitation in polycrystalline Fe-based superconductors [61]. Inputs of the model are the statistical abundance of GB angles for a given texture quality characterized by the in-plane and out-of-plane texture spreads ϕ_t and θ_t , and the GB angle dependence of J_c , which is assumed to be independent of the type of GB. Two

Table 10.1 Critical temperature T_c (transport or magnetization) as well as global ($\sim J_c^{\text{GB}}$) and local J_c ($\sim J_c^{\text{Grain}}$) for several Fe-based superconducting polycrystalline bulk samples at 5 K (except Fe(Se,Te) 4.2 K)

	Transp. T_c (K)	Magn. T_c (K)	Global J_c (kA/cm ²)	Local J_c (MA/cm ²)	References
Fe(Se,Te)	15.5		5.5	1.0	[49]
SmFeAsO _{0.85}	51		4.0	6.8	[23]
NdFeAsO _{0.94} F _{0.06}	44		2.0	4.2	[23]
LiFeAs	19.2		0.44	N.A.	[52]
Ba(Fe,Co) ₂ As ₂	25		6.0	N.A.	[39]
(Sr,K)Fe ₂ As ₂ w Ag		34	1.0	9.0	[58]
(Sr,K)Fe ₂ As ₂ w/o Ag		34	N.A.	40	[58]
(Ba,K)Fe ₂ As ₂		37.4	10	N.A.	[59]
CaKFe ₄ As ₄		35 K	40	10 (B c)	[56]
(Fe ₂ As ₂)(Ca ₄ (Mg _{0.25} Ti _{0.75}) ₃ O ₈)		43	0.5	N.A.	[53]
(Fe ₂ As ₂)(Ca ₅ (Sc _{0.5} Ti _{0.5}) ₄ O ₁₁)		36	0.07	N.A.	[53]

special cases are discussed: Equal texture spreads ($\phi_t = \theta_t$) which leads to roughly exponential decrease of J_c with θ_t similar to the single-GB dependence $J_c(\theta_{GB})$, and random in-plane orientation ($\phi_t = \infty$) which leads to a decrease in J_c to 9% for perfect fibre texture ($\theta_t = 0^\circ$) in the case of FBS and a slight decrease with θ_t . Considering the simple assumptions, the agreement to experimental data (shown for $\text{Bi}_2\text{Sr}_2\text{Ca}_{n-1}\text{Cu}_n\text{O}_{2n+4}$) is remarkable. Fully random textures cannot be modelled yet due to the lack of reliable information on HAGBs.

10.3 Single Grain Boundaries in Thin Films

There are in general two main reasons for investigating single GBs in superconducting films, mostly on bicrystal substrates having a single well-defined grain boundary: (1) to realize Josephson junctions with two superconducting electrodes for fundamental research and assessing their potential for electronics applications (usually on HAGBs), and (2) to check the J_c transparency of the GBs of several angles and hence determine $J_c(\theta_{GB})$, which is important information for wire applications (usually on rather LAGBs). The former has been reviewed in [20, 62] and is not covered here. To date, all bicrystal experiments on FBS have been conducted on symmetric [001]-tilt bicrystal substrates (SrTiO_3 , MgO , and $(\text{LaAlO}_3)_{0.3}(\text{Sr}_2\text{TaAlO}_6)_{0.7}$ [LSAT]). To obtain deeper knowledge of GB characteristics of FBS, grain boundary experiments using different types of bicrystals (i.e. valley or roof-top [010]-tilt, [100]-twist, and asymmetric grain boundaries) would be necessary, since in general, the inter-grain J_c depends on the GB type, as shown for $\text{YBa}_2\text{Cu}_3\text{O}_7$ deposited on various types of bicrystals [63]. Different results are expected in case of different order parameter symmetry (e.g. *s*-wave or *d*-wave) as well as strain sensitivity and charge carrier density. In the following, results on [001]-tilt GBs in FBS bicrystal films will be summarized and discussed. Furthermore, J_c is also influenced strongly by the local geometry of the GB since GBs often do not follow their macroscopic GB plane but may be faceted or meander. By faceting of GBs, usually observed in bicrystal films with 3D grain growth mode [64], the energy of the GB and its effective width can be reduced due to the formation of small segments of low- Σ GBs. Meandering of GBs occurs in films with lamellar growth mode such as $\text{YBa}_2\text{Cu}_3\text{O}_7$ grown by chemical solution deposition [65]. Both types of GB microstructures have a positive effect on J_c due to decreased flux channelling along the macroscopic grain boundary plane and therefore better flux pinning, as well as due to possibly decreased GB widths for faceted GBs. To date, no studies of these effects on FBS films have been reported though.

10.3.1 *LnFeAsO (Ln: Lanthanoids) Bicrystal Experiments*

To date, regarding the *1111* structure only NdFeAs(O,F) bicrystal films have been investigated. A first experiment [28] was conducted on films prepared by a two-step process [66]: The parent compound NdFeAsO was deposited at 800 °C, and subsequently a NdOF over-layer was deposited at the same temperature. During the NdOF over-layer deposition, F diffuses into NdFeAsO, resulting in the F doping. The inter-grain J_c of these films was reduced by 30% even at $\theta_{GB} = 6^\circ$, suggesting that the critical angle might be less than 6° . Microstructural analyses revealed that NdFeAs(O,F) and the MgO substrates were eroded by the fluorine, which diffuses preferentially along the GB. Hence, the obtained results were of extrinsic nature. To reveal the intrinsic GB characteristics of NdFeAs(O,F), excess F should be prevented. Later, the deposition temperature of NdOF was reduced to minimize this damage [29]. Figure 10.11 shows the misorientation dependence of the inter-grain J_c for these improved NdFeAs(O,F) films on [001]-tilt symmetric MgO bicrystal substrate. As a result, θ_c of NdFeAs(O,F) was found to be around 9° , which is almost the same angle as for Co-doped Ba122 and Fe(Se,Te). Although the deposition temperature of NdOF was reduced from 800 to 700 °C, the GB region for $\theta_{GB} = 24^\circ$ was damaged, resulting in zero inter-grain J_c . Even for

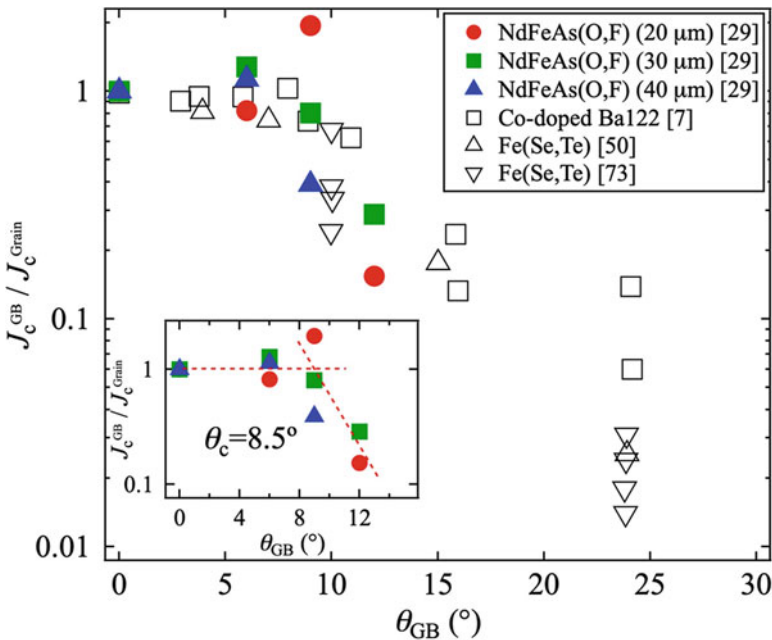


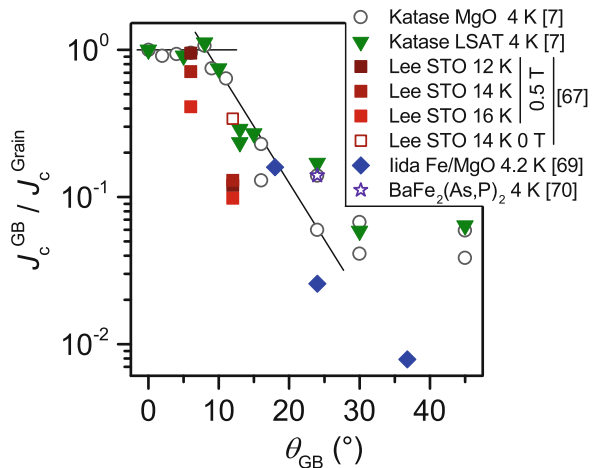
Fig. 10.11 Angle dependence of the reduced intra-grain critical current density (J_c^{GB}/J_c^{Grain}) for NdFeAs(O,F) bicrystal junctions (full symbols) measured using different bridge widths in comparison to Ba(Fe,Co)₂As₂ and Fe(Se,Te)

$\theta_{\text{GB}} = 6^\circ$ the GB region was partially compromised by F. It is not ruled out that the damage to GB region by F had influenced the obtained results. To address these issues and to further explore the intrinsic GB characteristics, F-free Ln1111 like $\text{Nd}(\text{Fe}_{1-x}\text{Co}_x)\text{AsO}$ would be interesting although T_c is around 25 K.

10.3.2 AeFe_2As_2 (Ae: Alkali Earths) Bicrystal Experiments

Already in 2009, Lee et al. reported on the weak-link behaviour of [001]-tilt GBs in Co-doped Ba122 [67]. They deposited 350 nm thick films on SrTiO_3 bicrystals with angles θ_{GB} of 3° , 6° , 9° , and 24° by pulsed laser deposition (PLD). In low-temperature laser scanning microscopy (LTLSM) and magneto-optical imaging (MOI) on these Co-doped Ba-122 bicrystal junctions, the weak-link behaviour was revealed even for low-angle GBs (6° and 9°). These results suggested a critical angle θ_c below 6° , which differs from the results reported 2 years later by Katase, Hiramatsu et al. [7, 68], who estimated the critical angle to be around 9° from their bicrystal experiments on Co-doped Ba122 on MgO ($T_c = 20.7$ K) and LSAT (21.6 K). We speculate that increased oxygen diffusion from the SrTiO_3 substrate in the GB region led to a slightly larger disturbed region compared to other substrates (MgO, LSAT) which may have limited the LAGB J_c of Lee's films. However, the higher magnetic field (0.5 T) and temperatures (12–16 K) used by Lee et al. have to be taken into account (*n.b.* data at 12 K/0.5 T and 14 K/0 T, respectively, i.e. at low T and B are comparable to data by Katase et al., Fig. 10.12). However, T_c was only minimally reduced across the 6° junction on SrTiO_3 (20.3 vs. 20.5 K) and the resistive transitions were sharp and clean. We investigated HAGBs in Co-doped Ba122 films on Fe/spinel/ SrTiO_3 -bicrystal templates [69]. The critical angle was estimated to 8° ; however, the normalized J_c of the HAGBs was one order of

Fig. 10.12 GB angle dependence of the reduced intra-grain critical current density for BaFe_2As_2 bicrystal junctions



magnitude lower than reported by Katase et al., which again might be attributable to defects within the GB due to the oxygen diffusion from the SrTiO₃ substrate.

For MBE-grown P-doped Ba122 on MgO bicrystal, an even higher inter-grain J_c of $>1 \text{ MA/cm}^2$ at 4 K for $\theta_{\text{GB}} = 24^\circ$ was reported by Sakagami et al. [70], which can be attributed to the higher T_c (29.5 K) and intra-grain J_c compared to Co-doped Ba122. Although the number of data points is insufficient for a definite conclusion, P-doped Ba122 most likely also has a higher critical angle than the cuprates.

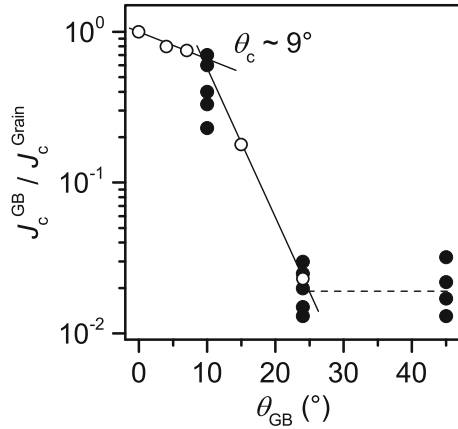
The GB angle dependence of J_c for GBs in BaFe₂As₂ is summarized in Fig. 10.12. Clearly, J_c remains equal to the intra-grain value up to $\theta_{\text{GB}} \sim 9^\circ$. Beyond this angle, the exponential decay of the inter-grain J_c sets in. Furthermore, J_c^{GB} is nearly constant for 30° and 45° .

In single HAGBs, pinning effects can be observed occasionally, even though overall J_c might not be increased compared to the intra-grain values. An example is the 24° GB junction of Ba(Fe,Co)₂As₂ on SrTiO₃ in [67]. Although J_c is decreased in all magnetic fields, it shows a peak effect around 5–6 T which is attributable to pinning of Abrikosov-Josephson vortices at defects in the GB and by Abrikosov vortices in the adjacent grains. On MgO bicrystals [7], this effect might be recognizable although not discussed by the authors. In contrast, for the 37° GB on Fe/MgO [69] with strongly reduced J_c it was not observed. HAGBs may also indirectly contribute to flux pinning. Nanometric Fe particles tend to grow in or near 45° GBs, as observed in [71], which is due to the increased diffusion rates in GBs and/or strain effects. Compared to a similar sample without 45° misorientations, J_c was overall increased at all fields and field directions θ at medium temperatures (due to the slightly higher T_c value) and $J_c(\theta)$ showed a pronounced c -axis peak which was attributed to both the GBs and the Fe particles which were slightly elongated in c -direction.

10.3.3 Fe(Se,Te) Bicrystal Experiments

The self-field inter-grain J_c at 4.2 K of Fe(Se,Te) across a 45° grain boundary was measured by Sarnelli et al. to be around 10^4 A/cm^2 , only one order of magnitude lower than the intra-grain J_c [73] (compared to four orders of magnitude for the cuprates). These results suggested that the J_c decrease with GB angle may not be as strong. Furthermore, J_c was more or less independent of bridge width and the Josephson current uniform across the junction width, which was explained by the s -wave symmetry in contrast to d -wave in cuprates. Later, these studies were completed by measuring the full $J_c(\theta_{\text{GB}})$ dependence by Si et al. [50] and Sarnelli et al. [72] where both groups came to similar and complementary results as shown in Fig. 10.13: Si et al. found that J_c^{GB} maintained $\sim 10^5 \text{ A/cm}^2$ at 4.2 K for 4° and 7° also in relatively large applied magnetic fields of $\sim 10 \text{ T}$, indicative of strong links. For $\theta_{\text{GB}} > 15^\circ$, J_c^{GB} was significantly suppressed already by a small magnetic field and showed a foot structure in the temperature dependence of the resistivity, $\rho(T)$, which has been attributed to an increased disturbed region. It would be worth

Fig. 10.13 Angle dependence of the reduced intra-grain critical current density for Fe(Se,Te) bicrystal junctions (open symbols Si et al. [50], full symbols Sarnelli et al. [72])



investigating whether or not intrinsic effects, such as thermally activated phase slippage [74], play a role in such behaviour. Based on the experimental results above, the authors concluded that the critical angle θ_c was around 9° . The level of J_c^{GB} is almost constant above 24° [72].

10.3.4 Summary and Discussion

As can be seen in Figs. 10.11, 10.12, and 10.13, for all FBS, the critical angle θ_c is around 9° , which indicates that in-plane misorientation alignments of FBS grains less than 9° usually do not impede the current flow. Therefore, grain boundary networks whose in-plane misorientation spread is less than 9° can be expected to work as flux pinning centres (see below) and the texture requirements for high current carrying capabilities is less severe for FBS than for YBCO. For the cuprates, critical angles between of 0° [14, 75] and $2\text{--}5^\circ$ [13, 76, 77], seldom 7° [78] were found, often a value around $4\text{--}5^\circ$ is taken as reasonable upper bound.

The exponential decay of J_c with GB angle above the critical angle is very similar for the cuprates and FBS [62], in contrast to early analyses which concluded a much slower decay. A distinct difference, however, between FBS and YBCO is recognized above 24° : whereas for the cuprates, J_c^{GB}/J_c^{Grain} continues to decrease exponentially with θ_{GB} , it remains constant for FBS. This can only partially be attributed to the different order parameter symmetry since only up to one third of the whole J_c decrease is explained by order parameter symmetry in cuprates [16]. What might also play a large role is that the grain boundaries in FBS are of metallic nature; band bending, strain effects, and charge carrier depletion though present might be

less severe. Furthermore, 24° and 45° [001]-tilt GBs in the tetragonal Ba122 and Fe(Se,Te) compounds are special, low- Σ GBs with a narrower structurally and electronically disturbed region than GBs with slightly different angles (this has been discussed for some high-current 45° GBs in YBCO as well, see [79]). It is plausible that the widths of 24° and 45° GBs as low- Σ GBs are similar and J_c is only affected by these structural parameters in FBS in contrast to the cuprates. To clarify this, 36° GBs (as another low- Σ GB) as well as intermediate angles should be investigated. The in-plane coherence length ξ_{ab} of cuprates [80] and Fe-based superconductors [6] are with $\sim 1.2 \dots 2.5$ nm quite comparable, which may explain the similar slope of $J_c(\theta_{GB})$ for θ_{GB} only slightly larger than θ_c [62].

Due to the exceptionally high J_c values in P-doped Ba122 films [70], this compound also showed a high inter-grain J_c of 1 MA/cm^2 at $\theta_{GB} = 24^\circ$, which is very promising for wire applications. Furthermore, J_c^{GB} for Ba122 is higher than for YBCO beyond 24° . Although P-doped Ba122 shows both higher intra- and inter-grain J_c than Co-doped Ba122, their normalized angle dependence of J_c^{GB} are similar, Fig. 10.12. The same holds for the Fe(Se,Te) films: even though the absolute values are below Ba122 most likely due to the lower T_c , the intra-grain-normalized J_c^{GB} is very similar.

For YBCO, the inter-grain J_c can be ameliorated by Ca-doping since it decreases the carrier density depletion at GBs [81], due to inhomogeneous and non-monotonic Ca segregation in the grain boundary with local channels of T_c enhancement [82] (here $\text{YbBa}_2\text{Cu}_3\text{O}_7$) and/or structural expansion of the dislocation cores [83]. On the contrary, Co-overdoped BaFe_2As_2 12° bicrystals did not show better performance than optimally doped films [19]. This might be explained by the lower influence of indirect, electronic reasons for the J_c decrease rather than direct, structural ones. However, detailed studies of the doping dependence of J_c^{GB} would be necessary to clarify this.

Talantsev and Crumb [84] very recently developed a model for estimating whether or not J_c of a quasi-two-dimensional superconducting film is limited by weak links. They combined their earlier model on self-field J_c depending solely on penetration depth and geometric factors [85] with the 2D fluctuation temperature of Emery and Kivelson [86] to obtain

$$J_{c,2D\text{fluct}} = \frac{\pi^3 \cdot \mu_0^{\frac{1}{2}} \cdot k_B^{\frac{3}{2}}}{\phi_0^2} \cdot \ln(\kappa + 0.5) + \left(\frac{T_c}{d}\right)^{\frac{3}{2}}$$

where μ_0 is the vacuum permeability, k_B the Boltzmann constant, ϕ_0 the flux quantum, κ the Ginzburg-Landau parameter, and d the interlayer spacing. If J_c is below this value, it is likely affected by weak links. It would be worth checking the effectiveness of this model also on polycrystalline and bicrystal FBS films.

10.4 Grain Boundary Networks in Fe-Based Superconducting Films

Grain boundary networks are mostly studied in films on polycrystalline, technical substrates, i.e. in proof-of-principle studies on coated conductor FBS samples. Such studies have been performed in all three crystal structure classes potentially relevant for applications—11, 122, and 1111, for a review see [62]. Nevertheless, also films on single crystals may contain GBs, either due to mere fibre texture for ex situ grown $\text{Ba}_{0.6}\text{K}_{0.4}\text{Fe}_2\text{As}_2$ [87] and PLD-grown FeSe film [88] on *c*-cut sapphire or due to anisotropic and highly 3D growth in sputtered FeSe films on (110)-cut SrTiO_3 [89].

Also the studies on GB networks suggest that clean GBs with angles below $\sim 9^\circ$ do not impede the current flow but occasionally even contribute to flux pinning. As summarized in Table 10.2, self-field J_c for a certain composition is influenced by the texture quality but also by T_c . J_c is in most cases rather isotropic with a ratio between $\mathbf{B}||\mathbf{ab}$ and $\mathbf{B}||\mathbf{c}$ of not more than 2 at 9 T, 4 K. In the following, these studies and data are discussed with respect to J_c limitation and flux pinning properties.

10.4.1 Polycrystalline Films on Single Crystals and Amorphous Templates

LaFeAs(O,F) The first weak-link studies on polycrystalline FBS films were conducted by Haindl et al. [91] on a PLD-grown and ex situ annealed LaFeAs(O,F) film on LaAlO_3 single crystal. The untextured film showed a rather broad transition ($T_{c90} = 28$ K, $T_{c0} = 20$ K), strong granularity effects in $R(T)$ in applied magnetic fields, and self-field J_c values as low as 2 kA/cm^2 at 2 K. This can be compared to a later epitaxial LaFeAs(O,F) film ($T_{c90} = 23$ K, $T_{c0} = 17$ K) grown by the same method which showed a self-field J_c of around 80 kA/cm^2 at 4 K [106].

$\text{Ba}_{0.6}\text{K}_{0.4}\text{Fe}_2\text{As}_2$ Hong et al. [87, 92] were recently able to prepare a 100 nm wide nanobridge across an individual, naturally formed GB in a ~ 400 nm thick polycrystalline $\text{Ba}_{0.6}\text{K}_{0.4}\text{Fe}_2\text{As}_2$ film on *c*-cut sapphire. The film had strong *c*-axis texture, which means the GBs are predominantly of [001]-tilt type. Even though the GB junction showed clear Josephson coupling with resistively shunted junction (RSJ) behaviour with multiple transitions, J_c^{GB} values for two of such bridges were estimated to $\sim 1.25 \text{ MA/cm}^2$ [92] and 0.2 MA/cm^2 [87] at 4.2 K, which is comparable to the intra-grain J_c or to bicrystal values at medium angles for P-doped Ba122, respectively. Although θ_{GB} of the investigated GBs are unknown, the results suggest that $J_c(\theta_{\text{GB}})$ is similar in magnitude for $\text{BaFe}_2(\text{As,P})_2$ and $(\text{Ba,K})\text{Fe}_2\text{As}_2$.

FeSe, Fe(Se,Te) The same method of nanobridge preparation was also applied on a (101)-oriented polycrystalline FeSe film on *c*-cut sapphire [88]. The $I(V)$ curves of the multigrain nanobridge showed flux flow and Josephson junction behaviour with strong thermal effects. Schneider et al. [89] recently prepared polycrystalline

Table 10.2 Summary of structural (in-plane, $\Delta\phi$, and out-of-plane, $\Delta\omega$, texture spread) and superconducting properties (critical temperature T_c for zero resistance and onset of transition as well as critical current density J_c at 4 K for self-field and 9 T for $\mathbf{B}||c$ and $\mathbf{B}||ab$) of FBS films with GB networks

Composition	Template	Method	$\Delta\phi$ (°)	$\Delta\omega$ (°)	$T_{c0}/T_{c\text{onset}}$ (K)	J_c^{sf} (MA/cm ²)	J_c (9T) $\mathbf{B} c/\mathbf{B} ab$ (MA/cm ²)	References
NdFeAs(O,F)	IBAD I	MBE	3.4	1.7	37/43	0.07	-	[90]
	LaAlO ₃	PLD*	poly	-	20/28	0.001	-	[91]
	c-Al ₂ O ₃	PLD*	-	-	27/37	1.25 ^s	-	[92]
Ba _{0.6} K _{0.4} Fe ₂ As ₂					31/37.5	0.2 ^s	-	[87]
	IBAD II	PLD	5.1	-	17.5/22	0.1 (8K)	0.003 (8 K)/-	[93]
Ba(Fe,Co) ₂ As ₂			1.7	-	22/23	2.0	0.13/0.20	[94]
	IBAD I		3.2	1.5	20/22	1.2	-	[95]
			3.3	-	20/22	1.6	0.09/0.20	[95]
			3.5	-	20/22	3.6	-	[95]
	IBAD III		5.6	2.4	19.0/20.2	1.14	0.86/0.96	[96]
Fe/LSAT	1.2 ⁽⁴⁵⁾			0.45			0.02/0.06 (12 K)	[71]
Fe/MgO	PLD		1-2 ^(45, 110)	-		0.006	0.0006	[97]

(continued)

Table 10.2 (continued)

Composition	Template	Method	$\Delta\phi$ (°)	$\Delta\omega$ (°)	$T_{c0}/T_c^{\text{onset}}$ (K)	J_c^{sf} (MA/cm ²)	$J_c(9T)$ $\mathbf{B} \mathbf{c} \mathbf{B} \mathbf{ab}$ (MA/cm ²)	References
BaFe ₂ (As,P) ₂	IBAD I	PLD	2.7	1.3	23/26	1.0	0.08/0.09	[98]
			8.0	1.3	19/23	1.1	0.13/0.15	[98]
			5.7	1.2	26/28.3	4.0	0.2/0.3	[99]
FeSe	IBAD I	PLD ^{rr}			24/26	0.175	–	[100]
	IBAD I				18/21	0.047	–	[100]
	c-Al ₂ O ₃	PLD	– ⁽¹⁰¹⁾		6.0/10.0	0.005 ⁿ	–	[88]
FeSe _{0.5} Te _{0.5}	(110)STO	sputtering	3.4/10.7 [#]	3.4	7.5/10.8	0.005/0.014 [#]	–	[89]
	Glass	PLD			8/10	0.014	–	[101]
	IBAD I	PLD	4.5	3.5	11/~14.5	0.2	0.1/0.15	[102]
FeSe _{0.1} Te _{0.9}	IBAD III	PLD	7.8	3.4	14.9/16	0.43	0.38/0.39	[103]
	RABiTS II	PLD	6.0		18.6/20	1.5	0.45/0.55	[104]
	RABiTS III	PLD	4.9	6.6	18.2/16.5	0.16	0.04/0.04	[105]
	Glass	PLD			10/12.3	0.021	–	[101]
	SS	PLD			5 / 10	0.013	–	[101]

[#]Two-step process, [§]single GB, ⁽⁴⁵⁾plus in-plane 45° rotated component, ⁽¹¹⁰⁾plus (110) component, ⁽¹⁰¹⁾predominantly (101) fibre texture, ^{rr}reel-to-reel, ⁿnanobridge, [#]for $j||[1-10]_{\text{STO}}$ and $j||[001]_{\text{STO}}$, IBAD I: MgO/Y₂O₃/Hastelloy, II: Fe/MgO/Y₂O₃/Hastelloy, III: SrTiO₃/LaMnO₃/MgO/Y₂O₃/Hastelloy, RABiTS I: Ni5%W, II: CeO₂/Y₂O₃/YSZ/CeO₂/Ni5%W, III: CeO₂/Ni5%W

FeSe films with anisotropic grain structure on (110)-oriented SrTiO₃ single crystals. The film is strongly biaxially (001)-oriented with small amounts of misoriented (<3%) and hexagonal α -FeSe (<8%) grains. The grains are elongated along the [001] direction of the substrate, and the in-plane texture spread in this direction is with $\Delta\phi = 3.4^\circ$ much smaller than in the transverse direction ($\Delta\phi = 10.7^\circ$). Since the latter is slightly larger than the critical angle θ_c , the resistivity shows a tail at low temperatures which is related to the granularity. For pinning properties of these films, see below. These films show significantly higher J_c values in all fields and temperatures as well as lower resistivities for currents applied parallel to the larger grain dimension (H) than perpendicular to it (V), Fig. 10.14. This effect can be explained by the higher GB density for currents perpendicular to the long axis and has been predicted [107] and shown [108] for cuprate coated conductors with elongated grains, where in contrast to the FeSe films the GBs acted as weak links. For both current directions, F_p could be well described with a parameter set of $(p, q) = (0.5, 2)$ which clearly indicated that surfaces, i.e. the grain boundaries dominated the pinning properties.

Huang et al. [101] prepared Fe(Se_{1-x}Te_x) films with $x = 0.5, 0.9$, and 1.0 on glass as well as with $x = 0.5$ on stainless steel (SS) tape covered with amorphous Al₂O₃ (a-Al₂O₃). All films showed strong (001) c -axis texture with local biaxial orientation, i.e. [001] tilt GB networks. T_c^{onset} values of these films were $\sim 12, 12.3, 10$, and 10 K, respectively, where the FeTe film on glass and the film on a-Al₂O₃/SS showed a higher transition width (4–5 K) due to the broader in-plane texture spread. Self-field J_c of the films with $x = 0.5$ and 0.9 on glass and the film on a-Al₂O₃/SS are

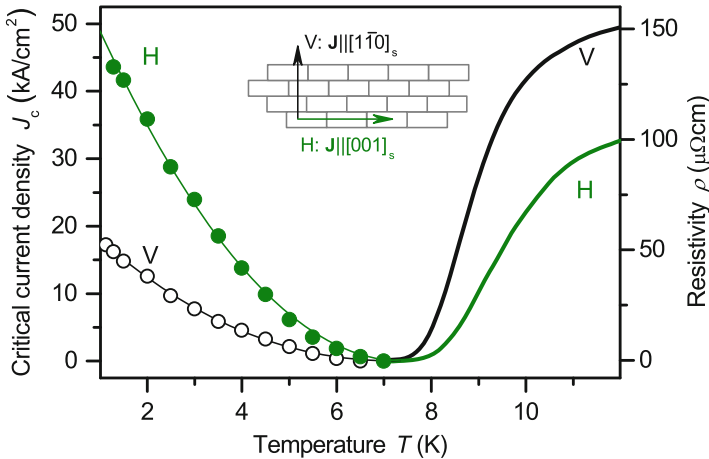


Fig. 10.14 Self-field J_c (left scale) and resistivity (right scale) vs. temperature for a bridge along the grains ($j \parallel [001]_{\text{STO}}$, H, red) and across the grains ($j \parallel [1-10]_{\text{STO}}$, V, blue) of a sputtered FeSe film on (110)-oriented SrTiO₃ [89]. Data courtesy of R. Schneider

with 21, 14, and 13 kA/cm² comparable to each other and one order of magnitude larger than bulk values.

10.4.2 Films on IBAD-MgO Templates

Most proof-of-principle studies of FBS coated conductors have been performed on IBAD-MgO templates supplied by iBeam Materials Inc., USA, or Shanghai Creative Supercond. Technol. Co Ltd., China.

NdFeAs(O,F) Only in 2014 have biaxially textured NdFeAs(O,F) films on technical substrates been fabricated by MBE at Nagoya University [90]. The film on IBAD-MgO template contained a small amount of 45° rotated grains and showed otherwise epitaxial growth. It had a self-field J_c of 70 kA/cm² at 5 K, only slightly larger than for a recent partially textured PIT-processed SmFeAs(O,F) tape [37] of around 40 kA/cm² at 4.2 K and 1.5 orders of magnitude lower than a film on MgO single crystal (3 MA/cm²) [109]. The reason for the low J_c values on IBAD templates is most likely the strong F diffusion in the GB regions and hence formation of current-blocking foreign phases, as revealed by bicrystal experiments [28], as discussed in Sect. 10.3.1.

Ba(Fe,Co)₂As₂ Already in 2011, we fabricated Co-doped Ba122 films on Fe-buffered IBAD-MgO templates by PLD [93]. Due to the relatively large in-plane mosaicity of the MgO of around 6°, the crystalline quality of Fe buffer and superconducting layer was poor (both ~5°). Although the biaxially textured Co-doped Ba122 film showed an onset T_c of 22 K ($T_{c0} = 17.5$ K), J_c at low temperatures (0.1 MA/cm² at 8 K 0 T) was almost one order of magnitude lower than on single crystalline MgO. Later, employing a high-quality MgO template (2.4° in-plane spread) avoided to strong granularity, Fig. 10.15, and improved J_c almost to the level of single crystalline substrates [94]. At the same time, Katase et al. reported on the fabrication of Co-doped Ba122 *directly* on IBAD-MgO [95]. Due to the self-epitaxy effect, a sharp texture (~3.2–3.5°) of the superconducting layer was obtained irrespective of the in-plane mosaicity of MgO templates.

GBs in FBS are, though J_c limiting in general, *advantageous* for two reasons: First, their larger critical angle θ_c compared to the cuprates allows using less-textured coated conductor architectures [7] or bulk samples and wires. Secondly, GBs can furthermore be advantageous for high current carrying capabilities since they may contribute to flux pinning [95]: Ba(Fe,Co)₂As₂ films grown on IBAD-MgO templates of different (in-plane) texture quality (5.5°, 6.1°, 7.3°) which led to Ba122 texture spreads of 3.1°, 3.2°, and 3.5° showed a strong positive correlation between texture spread and self-field J_c (1.2, 1.6, 3.6 MA/cm²). This can be explained by the GB angles being below θ_c (strong links) and an increasing dislocation density for larger misorientations. This is evidenced by the fact that the film on IBAD-MgO (6.1°) shows $J_c(B||c)$ values higher than for a comparable film

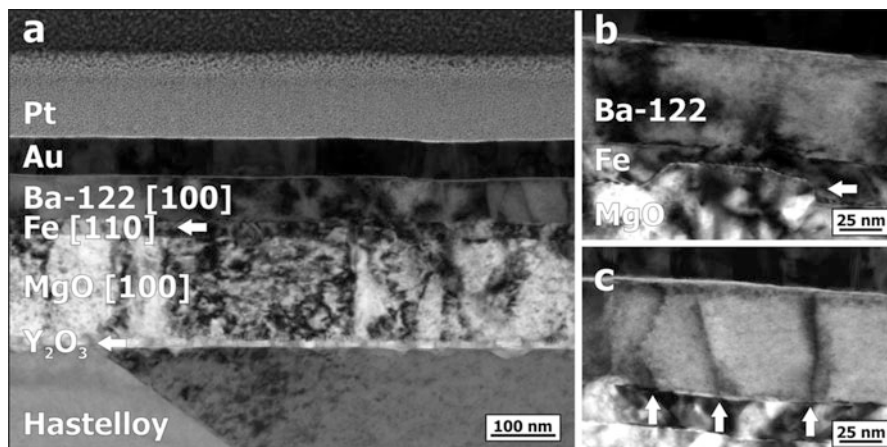


Fig. 10.15 Bright-field TEM images of a $\text{Ba}(\text{Fe},\text{Co})_2\text{As}_2$ film on Fe-buffered IBAD-MgO template, see also [94]. (a) Overview of the complete sample stack. (b) MgO step (white arrow) is overgrown by the Fe buffer layer, resulting in a sharp interface between Fe and Ba122. (c) Vertical defects (arrows) separated by $\sim 20\text{--}40$ nm penetrate the whole Ba122 film and may be identified as GBs. Image courtesy of E. Reich

on MgO single crystal for all fields at 4 and 12 K, and also higher than $J_c(B||ab)$ up to a temperature-dependent cross-over field.

Recently, Xu et al. fabricated Co-doped Ba122 on $\text{SrTiO}_3/\text{LaMnO}_3$ -buffered IBAD-MgO [96]. The film with $T_c = 20.2$ K ($T_{c0} = 19.0$ K) showed almost isotropic J_c at 4.2 K with 0.86 and 0.96 MA/cm^2 at 9 T and for $B||c$ and $B||ab$, respectively, and self-field J_c of 1.14 MA/cm^2 .

BaFe₂(As,P)₂ Also P-doped Ba122 films have been prepared on IBAD-MgO. Sato et al. deposited such films on templates with different in-plane spread, 4° and 8° [98]. As expected, the crystalline quality of the film on the 4° template was better; the 8° film showed several misorientations and a larger density of c -axis correlated defects besides the larger in-plane spread. Whereas T_c of the 8° film was 3 K lower which is caused by the strain effects [99], its self-field J_c at 4 K was comparable to the 4° sample (~ 1 MA/cm^2). For both samples, EDX scans in TEM cross sections revealed clean and homogeneous GB regions, and plane-view TEM revealed a grain size of ~ 100 nm and dislocation arrays in the GB regions, Fig. 10.16. Even though T_c of the 8° sample was reduced, it showed a stronger c -axis peak and J_c values overall higher by a factor of 1.5 than the well-textured sample. This can be explained by the much larger density of vertical defects in that sample which are related to the GB networks. At higher temperatures and fields (e.g. 12 K, 9 T), the well-textured sample takes over due to higher T_c and hence H_{irr} value; however, the less-textured sample continues to exhibit the stronger c -axis peak.

One of these samples on the 8° IBAD template with improved T_c was later investigated in high fields [99]. Analysis of the pinning force density curves, $F_p(B)$,

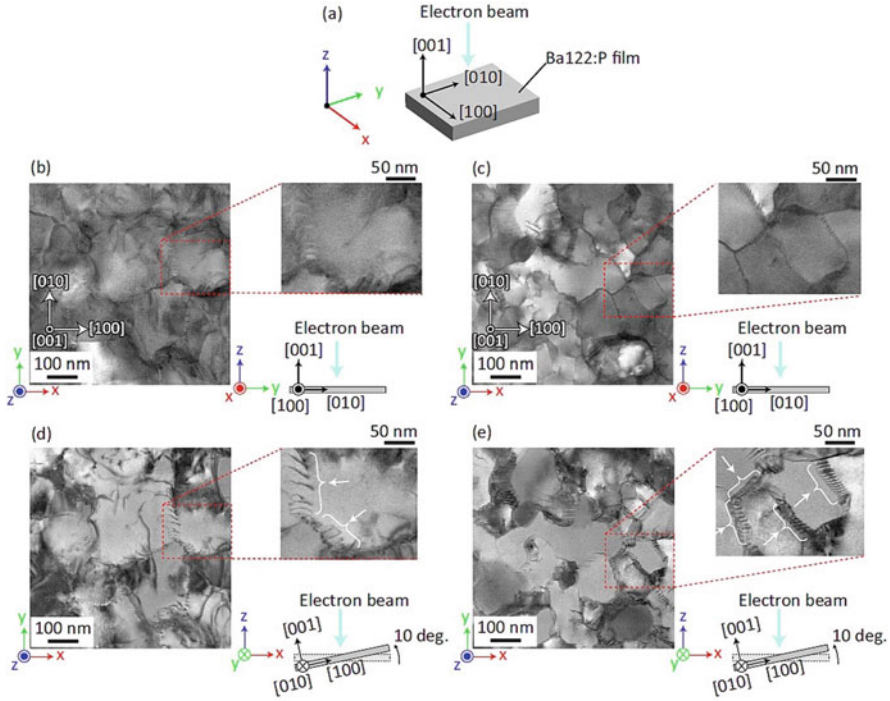


Fig. 10.16 Plane-view bright-field STEM images of $\text{BaFe}_2(\text{As,P})_2$ films on two IBAD templates with $\Delta\varphi_{\text{MgO}} = 4^\circ$ and 8° . (a) Relationship between film orientation, incident electron beam, and global axes (X , Y , and Z). (b, c) Typical plane-view images by normal electron beam incidence for $\Delta\varphi_{\text{MgO}} = 4^\circ$ (b) and 8° (c). (d, e) Slanted-angle images (tilting by 10°) for visualizing dislocations at same areas of (b, c), respectively. The arrows in the top right image of (d, e) show arrays of dislocations. Reprinted from [98] with permission by the authors under Creative Commons Attribution 4.0 International License

with modified Dew-Hughes functions, $F_p \sim b^p(1-b)^q$, $b = B/B_{\text{irr}}$, suggested in analogy to low-temperature superconductors that pinning is strongly dominated by surface pinning ($p, q = 0.5, 2$), i.e. on two-dimensional defects in the matrix, which was attributed to the GB and dislocation networks. The voltage-current characteristics showed a clear cross-over field between GB limitation [non-ohmic linear differential (NOLD) curves] at low fields and pinning limitation (power laws) at high fields. Similar NOLD characteristics have been measured for $\text{Ba}(\text{Fe,Co})_2\text{As}_2$ films with 45° and (110) misorientations [97] and polycrystalline $\text{SmFeAsO}_{0.85}$ [22].

A 10 cm long P-doped Ba122 tape has also been prepared by PLD with a reel-to-reel system [100], yet without fully optimized growth conditions. The film showed a slightly reduced T_{c0} compared to the static samples and a rather low I_c of 0.47 mA per cm-width at 4.2 K, corresponding to a J_c of 47 kA/cm². To improve the superconducting properties, $\text{Fe}_3\text{P/P}$ -doped Ba122 bilayers on IBAD-MgO were

tested. As a result, the superconducting properties were improved to $T_{c0} = 24$ K and $I_c = 975$ mA per cm-width ($J_c = 175$ kA/cm²) at 4.2 K.

Fe(Se,Te) Despite the large lattice mismatch between Fe(Se,Te) and MgO of 9.5%, Si et al. were able to grow epitaxial Fe(Se,Te) thin films on Hastelloy tapes with IBAD-MgO buffer architecture [102]. The respective in-plane and out-of-plane full width at half maximum of Fe(Se,Te) were $\Delta\phi = 4.5^\circ$ ($<\theta_c$) and $\Delta\omega = 3.5^\circ$. [010]-tilt GBs have probably a similar critical angle in FBS due to the small anisotropy and *s*-wave-type symmetry. Therefore, weak-link behaviour is not observed in these films. The lower $T_{c0} = 11$ K of that film compared to the film on LaAlO₃ substrate (~ 15 K) is most likely due to the lattice misfit and led to a low self-field J_c at 4 K of 0.2 MA/cm². Xu et al. also grew Fe(Se,Te) cube-textured thin films on IBAD-MgO with LaMnO₃ buffer layer [103]. T_c was 15.8 K, which is slightly larger than the bulk value due to compressive strain. Whereas the out-of-plane spread with $\Delta\omega = 3.4^\circ$ was similar to the film of Si et al., the in-plane spread of $\Delta\phi = 7.8^\circ$ was considerably larger and close to θ_c . Nevertheless, the self-field J_c was 0.43 MA/cm² at 4.2 K.

10.4.3 Films on RABiTS Substrates

To date, only Fe(Se_{1-x}Te_x) films ($x = 0, 0.5$) have been prepared on RABiTS templates, supplied by evico, ENEA, and ORNL.

Si et al. deposited Fe(Se,Te) thin films by PLD on CeO₂-buffered RABiTS [104]. The (110) lattice parameter of CeO₂ is around 3.82 Å, very close to Fe(Se,Te). Therefore, the film on RABiTS showed a high T_c of ~ 20 K with sharp transition. Despite the larger in-plane texture spread of 6° , which corresponds to the underlying template (7°), the film was capable of carrying large current densities (self-field $J_c = 1.5$ MA/cm² at 4.2 K). The authors concluded that CeO₂ as buffer has a larger impact on the superconducting properties of Fe(Se,Te) than the texture quality, i.e. LAGBs up to 7° do not hinder the critical current flow, in contrast to the cuprates. In an attempt to reduce the necessary number of buffer layers, Sylva et al. deposited Fe(Se,Te) by PLD on Ni5W with a single CeO₂ buffer layer in order to possibly reduce manufacturing costs of FSB coated conductors [105]. The film with a T_c of ~ 18 K showed a self-field J_c of ~ 0.16 MA/cm² as well as isotropic J_c above 20 kA/cm² in fields up to 18 T at 4.2 K. In contrast to Ba122, pinning is much more dominated by point-like disorder in Fe(Se,Te) films on IBAD [102] ($p, q = 1, 2$) and RABiTS [104] ($p, q = 0.85, 2$) which was attributed to Se-Te disorder.

Demura, Yamashita et al. proposed electrochemical deposition (ECD) as another, potentially economical method for producing FeSe films on RABiTS tapes [110, 111] and showed superconducting films with T_{c0} of 2.5 K. This process might be interesting with regard to low-cost production of FeSe coated conductors if further optimized.

10.5 Conclusion

We reviewed grain boundary characteristics of Fe-based superconductors in the form of polycrystalline bulks and thin films. A large difference in inter-grain J_c between polycrystalline bulk samples and bicrystal films indicates that the global currents in bulk samples are significantly affected by extrinsic factors. These extrinsic factors were identified by microstructural analysis as FeAs wetting of grains and cracks. The inter-grain J_c does not severely decrease at clean grain boundaries. Hence, eliminating extrinsic factors is a key to enhance the inter-grain J_c in polycrystalline samples.

Bicrystal experiments revealed the critical angle θ_c for FBS to be around 9° , which is around twice as large as for the cuprates. Similar to the cuprates, the critical angle may be governed by geometrical factors (i.e. the electronically disturbed region around dislocations is smaller in FBS due to their metallic nature) and by the symmetry of the order parameter: ($s\pm$ in FBS instead of d -wave in cuprates). Another distinct difference is that the inter-grain J_c for FBS is almost constant above $\theta_{GB} > 24^\circ$, whereas for the cuprates the inter-grain J_c is reduced exponentially with θ_{GB} above θ_c . Grain boundaries with misorientation angles less than θ_c act as pinning centres. Hence, increasing the density of such GBs improves the current carrying capability.

Although we learned all of the above already from experimental facts, the fundamental understanding of GBs in FBS is still insufficient. For instance, (1) the mechanism of exponential decay for inter-grain J_c above θ_c , (2) the large θ_c value of around 9° , (3) the reason for the constant inter-grain J_c for $\theta_{GB} > 24^\circ$, and (4) the transition of Abrikosov vortices via Abrikosov-Josephson vortices to pure Josephson vortices for $\theta_{GB} \sim \theta_c$ at certain fields and temperatures are not well understood. To address those issues, further investigations on grain boundaries are required.

Acknowledgments We sincerely thank Chiara Tarantini for her careful proof-reading and editing of our manuscript. We thank A. Yamamoto, R. Schneider, E. Reich, and H. Hiramatsu for information on and data for Figs. 10.5 and 10.14–10.16. We acknowledge Grant-in-Aid for Scientific Research (B) (Grant No. 16H04646) from the Japan Society for the Promotion of Science, JST CREST (Grant No. JPMJCR18J4), and the Helmholtz Association via the Recruitment Initiative of Prof. B. Holzapfel for financial support.

References

1. Y. Kamihara, H. Hiramatsu, M. Hirano, et al., Iron-based layered superconductor: LaOFep. J. Am. Chem. Soc. **128**(31), 10012–10013 (2006). <https://doi.org/10.1021/ja063355c>
2. Y. Kamihara, T. Watanabe, M. Hirano, et al., Iron-based layered superconductor La[O_{1-x}F_x]FeAs ($x = 0.05$ – 0.12) with $T_c = 26$ K. J. Am. Chem. Soc. **130**(11), 3296–3297 (2008). <https://doi.org/10.1021/ja800073m>

3. I.I. Mazin, D.J. Singh, M.D. Johannes, et al., Unconventional superconductivity with a sign reversal in the order parameter of $\text{LaFeAsO}_{1-x}\text{F}_x$. *Phys. Rev. Lett.* **101**(5), 057003 (2008). <https://doi.org/10.1103/PhysRevLett.101.057003>
4. K. Kuroki, S. Onari, R. Arita, et al., Unconventional pairing originating from the disconnected Fermi surfaces of superconducting $\text{LaFeAsO}_{1-x}\text{F}_x$. *Phys. Rev. Lett.* **101**(8), 087004 (2008). <https://doi.org/10.1103/PhysRevLett.101.087004>
5. T. Hanaguri, S. Niitaka, K. Kuroki, et al., Unconventional *s*-wave superconductivity in $\text{Fe}(\text{Se},\text{Te})$. *Science* **328**(5977), 474–476 (2010). <https://doi.org/10.1126/science.1187399>
6. M. Putti, I. Pallecchi, E. Bellingeri, et al., New Fe-based superconductors: properties relevant for applications. *Supercond. Sci. Technol.* **23**(3), 034003 (2010). <https://doi.org/10.1088/0953-2048/23/3/034003>
7. T. Katase, Y. Ishimaru, A. Tsukamoto, et al., Advantageous grain boundaries in iron pnictide superconductors. *Nat. Commun.* **2**(1), 409 (2011). <https://doi.org/10.1038/ncomms1419>
8. H. Hilgenkamp, J. Mannhart, Grain boundaries in high- T_c superconductors. *Rev. Mod. Phys.* **74**(2), 485–549 (2002). <https://doi.org/10.1103/RevModPhys.74.485>
9. L. Priester, *Grain Boundaries. Springer Series in Materials Science*, vol 172 (Springer, Dordrecht, 2013)
10. R.Z. Valiev, V.Y. Gertsman, O.A. Kaibyshev, Grain boundary structure and properties under external influences. *Phys. Stat. Sol.* **97**(1), 11–56 (1986). <https://doi.org/10.1002/pssa.2210970102>
11. P. Lejček, *Grain Boundary Segregation in Metals. Springer Series in Materials Science*, vol 136 (Springer, Berlin, 2010)
12. R.M. Scanlan, W.A. Fietz, E.F. Koch, Flux pinning centers in superconducting Nb_3Sn . *J. Appl. Phys.* **46**(5), 2244 (1975). <https://doi.org/10.1063/1.321816>
13. D.T. Verebelyi, D.K. Christen, R. Feenstra, et al., Low angle grain boundary transport in $\text{YBa}_2\text{Cu}_3\text{O}_{7-\delta}$ coated conductors. *Appl. Phys. Lett.* **76**(13), 1755–1757 (2000). <https://doi.org/10.1063/1.126157>
14. T. Amrein, L. Schultz, B. Kabius, et al., Orientation dependence of grain-boundary critical current densities in high- T_c bicrystals. *Phys. Rev. B* **51**(10), 6792–6795 (1995). <https://doi.org/10.1103/PhysRevB.51.6792>
15. J. Ayache, Grain boundaries in high temperature superconducting ceramics. *Philos. Mag.* **86**(15), 2193–2239 (2006). <https://doi.org/10.1080/14786430600640494>
16. H. Hilgenkamp, J. Mannhart, B. Mayer, Implications of $d_{x^2-y^2}$ symmetry and faceting for the transport properties of grain boundaries in high- T_c superconductors. *Phys. Rev. B* **53**(21), 14586 (1996). <https://doi.org/10.1103/PhysRevB.53.14586>
17. T. Horide, K. Matsumoto, Evaluation of vortex pinning across low angle grain boundary in $\text{YBa}_2\text{Cu}_3\text{O}_7$ film. *Appl. Phys. Lett.* **101**(11), 112604 (2012). <https://doi.org/10.1063/1.4752462>
18. G. Deutscher, Origin of weak-link behavior of grain boundaries in superconducting cuprates and pnictides. *Appl. Phys. Lett.* **96**(12), 122502 (2010). <https://doi.org/10.1063/1.3367723>
19. J.H. Durrell, C.-B. Eom, A. Gurevich, et al., The behavior of grain boundaries in the Fe-based superconductors. *Rep. Prog. Phys.* **74**(12), 124511 (2011). <https://doi.org/10.1088/0034-4885/74/12/124511>
20. P. Seidel, Josephson effects in iron based superconductors. *Supercond. Sci. Technol.* **24**(4), 043001 (2011). <https://doi.org/10.1088/0953-2048/24/4/043001>
21. F. Kametani, A.A. Polyanskii, A. Yamamoto, et al., Combined microstructural and magneto-optical study of current flow in polycrystalline forms of Nd and Sm Fe-oxypnictides. *Supercond. Sci. Technol.* **22**(1), 015010 (2009). <https://doi.org/10.1088/0953-2048/22/1/015010>
22. F. Kametani, P. Li, D. Abrahimov, et al., Intergrain current flow in a randomly oriented polycrystalline $\text{SmFeAsO}_{0.85}$ oxypnictide. *Appl. Phys. Lett.* **95**(14), 142502 (2009). <https://doi.org/10.1063/1.3224198>
23. A. Yamamoto, A.A. Polyanskii, J. Jiang, et al., Evidence for two distinct scales of current flow in polycrystalline Sm and Nd iron oxypnictides. *Supercond. Sci. Technol.* **21**(9), 095008 (2008). <https://doi.org/10.1088/0953-2048/21/9/095008>

24. D.C. Larbalestier, M. Daeumling, X. Cai, et al., Experiments concerning the connective nature of superconductivity in $\text{YBa}_2\text{Cu}_3\text{O}_7$. *J. Appl. Phys.* **62**(8), 3308–3313 (1987). <https://doi.org/10.1063/1.339339>
25. A. Yamamoto, J. Jiang, F. Kametani, et al., Evidence for electromagnetic granularity in polycrystalline Sm1111 iron-pnictides with enhanced phase purity. *Supercond. Sci. Technol.* **24**(4), 045010 (2011). <https://doi.org/10.1088/0953-2048/24/4/045010>
26. M. Eisterer, M. Zehetmayer, H.W. Weber, et al., Disorder effects and current percolation in FeAs-based superconductors. *Supercond. Sci. Technol.* **23**(5), 054006 (2010). <https://doi.org/10.1088/0953-2048/23/5/054006>
27. E.S. Otabe, M. Kiuchi, S. Kawai, et al., Global and local critical current density in superconducting $\text{SmFeAsO}_{1-x}\text{F}_x$ measured by two methods. *Phys. C Supercond. Appl.* **469**(21), 1940–1944 (2009). <https://doi.org/10.1016/j.physc.2009.06.013>
28. T. Omura, T. Matsumoto, T. Hatano, et al., Fabrication of grain boundary junctions using $\text{NdFeAs}(\text{O},\text{F})$ superconducting thin films. *J. Phys. Conf. Ser.* **1054**(1), 012024 (2018). <https://doi.org/10.1088/1742-6596/1054/1/012024>
29. K. Iida, T. Omura, T. Matsumoto, et al., Grain boundary characteristics of oxypnictide $\text{NdFeAs}(\text{O},\text{F})$ superconductors. *Supercond. Sci. Technol.* **32**(7), 074003 (2019). <https://doi.org/10.1088/1361-6668/ab1660>
30. Q. Zhang, C. Wang, C. Yao, et al., Combined effect of Sn addition and post-rolling sintering on the superconducting properties of $\text{SmFeAsO}_{1-x}\text{F}_x$ tapes fabricated by an ex-situ powder-in-tube process. *J. Appl. Phys.* **113**(12), 123902 (2013). <https://doi.org/10.1063/1.4795814>
31. L. Wang, Y. Qi, D. Wang, et al., Low-temperature synthesis of $\text{SmFeAsO}_{0.7}\text{F}_{0.3-8}$ wires with a high transport critical current density. *Supercond. Sci. Technol.* **23**(7), 075005 (2010). <https://doi.org/10.1088/0953-2048/23/7/075005>
32. C. Wang, C. Yao, H. Lin, et al., Large transport J_c in Sn-added $\text{SmFeAsO}_{1-x}\text{F}_x$ tapes prepared by an ex situ PIT method. *Supercond. Sci. Technol.* **26**(7), 075017 (2013). <https://doi.org/10.1088/0953-2048/26/7/075017>
33. Q. Zhang, C. Yao, H. Lin, et al., Enhancement of transport critical current density of $\text{SmFeAsO}_{1-x}\text{F}_x$ tapes fabricated by an ex-situ powder-in-tube method with a Sn-presintering process. *Appl. Phys. Lett.* **104**(17), 172601 (2014). <https://doi.org/10.1063/1.4874261>
34. L. Wang, Y. Qi, D. Wang, et al., Large transport critical currents of powder-in-tube $\text{Sr}_{0.6}\text{K}_{0.4}\text{Fe}_2\text{As}_2/\text{Ag}$ superconducting wires and tapes. *Phys. C Supercond. Appl.* **470**(2), 183–186 (2010). <https://doi.org/10.1016/j.physc.2009.12.030>
35. L. Wang, Y. Qi, Z. Zhang, et al., Influence of Pb addition on the superconducting properties of polycrystalline $\text{Sr}_{0.6}\text{K}_{0.4}\text{Fe}_2\text{As}_2$. *Supercond. Sci. Technol.* **23**(5), 054010 (2010). <https://doi.org/10.1088/0953-2048/23/5/054010>
36. Z. Gao, L. Wang, C. Yao, et al., High transport critical current densities in textured Fe-sheathed $\text{Sr}_{1-x}\text{K}_x\text{Fe}_2\text{As}_2+\text{Sn}$ superconducting tapes. *Appl. Phys. Lett.* **99**(24), 242506 (2011). <https://doi.org/10.1063/1.3671109>
37. Q. Zhang, X. Zhang, C. Yao, et al., Enhanced transport critical current density in Sn-added $\text{SmFeAsO}_{1-x}\text{F}_x$ tapes prepared by the PIT method. *Supercond. Sci. Technol.* **30**(6), 065004 (2017). <https://doi.org/10.1088/1361-6668/aa6850>
38. J.D. Weiss, C. Tarantini, J. Jiang, et al., High intergrain critical current density in fine-grain $(\text{Ba}_{0.6}\text{K}_{0.4})\text{Fe}_2\text{As}_2$ wires and bulks. *Nat. Mater.* **11**(8), 682–685 (2012). <https://doi.org/10.1038/nmat3333>
39. Y. Hayashi, A. Yamamoto, H. Ogino, et al., Influences of material processing on the microstructure and inter-granular current properties of polycrystalline bulk $\text{Ba}(\text{Fe},\text{Co})_2\text{As}_2$. *Phys. C Supercond. Appl.* **504**, 28–32 (2014). <https://doi.org/10.1016/j.physc.2014.01.010>
40. Y.-J. Kim, J.D. Weiss, E.E. Hellstrom, et al., Evidence for composition variations and impurity segregation at grain boundaries in high current-density polycrystalline K- and Co-doped BaFe_2As_2 superconductors. *Appl. Phys. Lett.* **105**(16), 162604 (2014). <https://doi.org/10.1063/1.4898191>

41. L. Wang, Y. Ma, Q. Wang, et al., Direct observation of nanometer-scale amorphous layers and oxide crystallites at grain boundaries in polycrystalline $\text{Sr}_{1-x}\text{K}_x\text{Fe}_2\text{As}_2$ superconductors. *Appl. Phys. Lett.* **98**(22), 222504 (2011). <https://doi.org/10.1063/1.3592580>
42. J.D. Weiss, A. Yamamoto, A.A. Polyanskii, et al., Demonstration of an iron-pnictide bulk superconducting magnet capable of trapping over 1 T. *Supercond. Sci. Technol.* **28**(11), 112001 (2015). <https://doi.org/10.1088/0953-2048/28/11/112001>
43. X. Zhang, H. Oguro, C. Yao, et al., Superconducting properties of 100-m Class $\text{Sr}_{0.6}\text{K}_{0.4}\text{Fe}_2\text{As}_2$ tape and pancake coils. *IEEE Trans. Appl. Supercond.* **27**(4), 7300705 (2017). <https://doi.org/10.1109/TASC.2017.2650408>
44. Q.-P. Ding, S. Mohan, Y. Tsuchiya, et al., Magneto-optical imaging and transport properties of FeSe superconducting tapes prepared by the diffusion method. *Supercond. Sci. Technol.* **25**(2), 025003 (2012). <https://doi.org/10.1088/0953-2048/25/2/025003>
45. Y. Mizuguchi, K. Deguchi, S. Tsuda, et al., Fabrication of the iron-based superconducting wire using Fe(Se,Te). *Appl. Phys. Express* **2**(8), 083004 (2009). <https://doi.org/10.1143/APEX.2.083004>
46. Q.-P. Ding, S. Mohan, Y. Tsuchiya, et al., Low-temperature synthesis of $\text{FeTe}_{0.5}\text{Se}_{0.5}$ polycrystals with a high transport critical current density. *Supercond. Sci. Technol.* **24**(7), 075025 (2011). <https://doi.org/10.1088/0953-2048/24/7/075025>
47. T. Ozaki, K. Deguchi, Y. Mizuguchi, et al., Transport properties and microstructure of mono- and seven-core wires of $\text{FeSe}_{1-x}\text{Te}_x$ superconductor produced by the Fe-diffusion powder-in-tube method. *Supercond. Sci. Technol.* **24**(10), 105002 (2011). <https://doi.org/10.1088/0953-2048/24/10/105002>
48. T. Ozaki, Y. Mizuguchi, S. Demura, et al., Enhancement of superconducting properties in FeSe wires using a quenching technique. *J. Appl. Phys.* **111**(1), 013912 (2012). <https://doi.org/10.1063/1.3673826>
49. A. Palenzona, A. Sala, C. Bernini, et al., A new approach for improving global critical current density in $\text{Fe}(\text{Se}_{0.5}\text{Te}_{0.5})$ polycrystalline materials. *Supercond. Sci. Technol.* **25**(11), 115018 (2012). <https://doi.org/10.1088/0953-2048/25/11/115018>
50. W. Si, C. Zhang, X. Shi, et al., Grain boundary junctions of $\text{FeSe}_{0.5}\text{Te}_{0.5}$ thin films on SrTiO_3 bi-crystal substrates. *Appl. Phys. Lett.* **106**(3), 32602 (2015). <https://doi.org/10.1063/1.4906429>
51. D. Mancusi, M. Polichetti, M.R. Cimberle, et al., Influence of the interaction between the inter- and intragranular magnetic responses in the analysis of the ac susceptibility of a granular $\text{FeSe}_{0.5}\text{Te}_{0.5}$ superconductor. *Supercond. Sci. Technol.* **28**(9), 095017 (2015). <https://doi.org/10.1088/0953-2048/28/9/095017>
52. S.J. Singh, R. Beck, S. Wurmehl, et al., Granular behavior observed in the polycrystalline superconducting LiFeAs . *Supercond. Sci. Technol.* **28**(2), 025006 (2015). <https://doi.org/10.1088/0953-2048/28/2/025006>
53. S.J. Singh, H. Ogino, J.-I. Shimoyama, et al., Weak-link behaviour observed in iron-based superconductors with thick perovskite-type blocking layers. *Supercond. Sci. Technol.* **26**(10), 105020 (2013). <https://doi.org/10.1088/0953-2048/26/10/105020>
54. R.M. Costa, A.R. Jurelo, P. Rodrigues, et al., Splitting of the bulk resistive transition in high- T_c superconductors: evidence for unconventional pairing. *Phys. C Supercond. Appl.* **251**(1), 175–182 (1995). [https://doi.org/10.1016/0921-4534\(95\)00399-1](https://doi.org/10.1016/0921-4534(95)00399-1)
55. T.T.M. Palstra, B. Batlogg, R.B. van Dover, et al., Dissipative flux motion in high-temperature superconductors. *Phys. Rev. B* **41**(10), 6621 (1990). <https://doi.org/10.1103/PhysRevB.41.6621>
56. S.J. Singh, M. Bristow, W.R. Meier, et al., Ultrahigh critical current densities, the vortex phase diagram, and the effect of granularity of the stoichiometric high- T_c superconductor $\text{CaKFe}_4\text{As}_4$. *Phys. Rev. Mater.* **2**(7), 074802 (2018). <https://doi.org/10.1103/PhysRevMaterials.2.074802>
57. C.C. Tsuei, J.R. Kirtley, Pairing symmetry in cuprate superconductors. *Rev. Mod. Phys.* **72**(4), 969–1016 (2000). <https://doi.org/10.1103/RevModPhys.72.969>

58. N. Yoshida, M. Kiuchi, E.S. Otake, et al., Critical current density properties in polycrystalline $\text{Sr}_{0.6}\text{K}_{0.4}\text{Fe}_2\text{As}_2$ superconductors. *Phys. C Supercond. Appl.* **470**, 1216 (2010)
59. M. Nikolo, J.D. Weiss, J. Singleton, et al., Critical properties of bulk-doped BaFe_2As_2 pnictides for magnet design. *IEEE Trans. Appl. Supercond.* **28**(3), 7300104 (2018). <https://doi.org/10.1109/TASC.2017.2775580>
60. J. Hecher, T. Baumgartner, J.D. Weiss, et al., Small grains: a key to high-field applications of granular Ba-122 superconductors? *Supercond. Sci. Technol.* **29**(2), 025004 (2016). <https://doi.org/10.1088/0953-2048/29/2/025004>
61. M. Eisterer, Predicting critical currents in grain-boundary limited superconductors. *Phys. Rev. B* **99**(9), 094501 (2019). <https://doi.org/10.1103/PhysRevB.99.094501>
62. K. Iida, J. Hänisch, C. Tarantini, Fe-based superconducting thin films on metallic substrates: growth, characteristics, and relevant properties. *Appl. Phys. Rev.* **5**(3), 031304 (2018). <https://doi.org/10.1063/1.5032258>
63. R. Held, C.W. Schneider, J. Mannhart, et al., Low-angle grain boundaries in $\text{YBa}_2\text{Cu}_3\text{O}_{7-\delta}$ with high critical current densities. *Phys. Rev. B* **79**(1), 014515 (2009). <https://doi.org/10.1103/PhysRevB.79.014515>
64. Q. Jin, S.-W. Chan, Grain boundary faceting in $\text{YBa}_2\text{Cu}_3\text{O}_{7-x}$ bicrystal thin films on SrTiO_3 substrates. *J. Mater. Res.* **17**(2), 323–335 (2002). <https://doi.org/10.1557/JMR.2002.0046>
65. D.M. Feldmann, T.G. Holesinger, R. Feenstra, et al., A review of the influence of grain boundary geometry on the electromagnetic properties of polycrystalline $\text{YBa}_2\text{Cu}_3\text{O}_{7-x}$ films. *J. Am. Ceram. Soc.* **91**(6), 1869–1882 (2008). <https://doi.org/10.1111/j.1551-2916.2008.02273.x>
66. T. Kawaguchi, H. Uemura, T. Ohno, et al., Molecular beam epitaxy growth of superconducting $\text{NdFeAs}(\text{O},\text{F})$ thin films using a F-Getter and a novel F-doping method. *Appl. Phys. Exp.* **4**(8), 083102 (2011). <https://doi.org/10.1143/APEX.4.083102>
67. S. Lee, J. Jiang, J.D. Weiss, et al., Weak-link behavior of grain boundaries in superconducting $\text{Ba}(\text{Fe}_{1-x}\text{Co}_x)_2\text{As}_2$ bicrystals. *Appl. Phys. Lett.* **95**(21), 212505 (2009). <https://doi.org/10.1063/1.3262953>
68. H. Hiramatsu, T. Katase, Y. Ishimaru, et al., Microstructure and transport properties of [001]-tilt bicrystal grain boundaries in iron pnictide superconductor, cobalt-doped BaFe_2As_2 . *Mater. Sci. Eng. B* **177**(7), 515–519 (2012). <https://doi.org/10.1016/j.mseb.2011.12.009>
69. K. Iida, S. Haindl, F. Kurth, et al., $\text{BaFe}_2\text{As}_2/\text{Fe}$ bilayers with [001]-tilt grain boundary on MgO and SrTiO_3 bicrystal substrates. *Phys. Proc.* **45**, 189–192 (2013). <https://doi.org/10.1016/j.phpro.2013.04.084>
70. A. Sakagami, T. Kawaguchi, M. Tabuchi, et al., Critical current density and grain boundary property of $\text{BaFe}_2(\text{As},\text{P})_2$ thin films. *Phys. C Supercond. Appl.* **494**, 181–184 (2013). <https://doi.org/10.1016/j.physc.2013.04.047>
71. J. Hänisch, K. Iida, F. Kurth, et al., The effect of 45° grain boundaries and associated Fe particles on J_c and resistivity in $\text{Ba}(\text{Fe}_{0.9}\text{Co}_{0.1})_2\text{As}_2$ thin films. *AIP Conf. Proc.* **1574**, 260–267 (2014). <https://doi.org/10.1063/1.4860633>
72. E. Sarnelli, C. Nappi, C. Camerlingo, et al., Properties of $\text{Fe}(\text{Se},\text{Te})$ bicrystal grain boundary junctions, SQUIDS, and nanostrips. *IEEE Trans. Appl. Supercond.* **27**(4), 7400104 (2017). <https://doi.org/10.1109/TASC.2016.2636248>
73. E. Sarnelli, M. Adamo, C. Nappi, et al., Properties of high-angle $\text{Fe}(\text{Se},\text{Te})$ bicrystal grain boundary junctions. *Appl. Phys. Lett.* **104**(16), 162601 (2014). <https://doi.org/10.1063/1.4871864>
74. R. Gross, P. Chaudhari, D. Dimos, et al., Thermally activated phase slippage in high- T_c grain-boundary Josephson junctions. *Phys. Rev. Lett.* **64**(2), 228–231 (1990). <https://doi.org/10.1103/PhysRevLett.64.228>
75. Z.G. Ivanov, P.Å. Nilsson, D. Winkler, et al., Weak links and dc SQUIDS on artificial nonsymmetric grain boundaries in $\text{YBa}_2\text{Cu}_3\text{O}_{7-\delta}$. *Appl. Phys. Lett.* **59**(23), 3030 (1991). <https://doi.org/10.1063/1.105783>
76. B. Holzapfel, D. Verebelyi, C. Cantoni, et al., Low angle grain boundary transport properties of undoped and doped Y123 thin film bicrystals. *Phys. C Supercond. Appl.* **341**(348), 1431–1434 (2000). [https://doi.org/10.1016/S0921-4534\(00\)00973-4](https://doi.org/10.1016/S0921-4534(00)00973-4)

77. D.T. Verebelyi, C. Cantoni, J.D. Budai, et al., Critical current density of $\text{YBa}_2\text{Cu}_3\text{O}_{7-\delta}$ low-angle grain boundaries in self-field. *Appl. Phys. Lett.* **78**(14), 2031 (2001). <https://doi.org/10.1063/1.1360230>
78. N.F. Heinig, R.D. Redwing, J.E. Nordman, et al., Strong to weak coupling transition in low misorientation angle thin film $\text{YBa}_2\text{Cu}_3\text{O}_{7-x}$ bicrystals. *Phys. Rev. B* **60**(2), 1409 (1999). <https://doi.org/10.1103/PhysRevB.60.1409>
79. S.-W. Chan, Nature of grain boundaries as related to critical currents in superconducting $\text{YBa}_2\text{Cu}_3\text{O}_{7-x}$. *J. Phys. Chem. Solids* **55**(12), 1415–1432 (1994). [https://doi.org/10.1016/0022-3697\(94\)90568-1](https://doi.org/10.1016/0022-3697(94)90568-1)
80. C.P. Poole, *Superconductivity*, 2nd edn. (Academic, Amsterdam, 2007)
81. G. Hammerl, A. Schmehl, R.R. Schulz, et al., Enhanced supercurrent density in polycrystalline $\text{YBa}_2\text{Cu}_3\text{O}_{7-d}$ at 77 K from calcium doping of grain boundaries. *Nature* **407**(6801), 162–164 (2000). <https://doi.org/10.1038/35025014>
82. P. Li, D. Abraimov, A. Polyanskii, et al., Study of grain boundary transparency in $(\text{Yb}_{1-x}\text{Ca}_x)\text{Ba}_2\text{Cu}_3\text{O}$ bicrystal thin films over a wide temperature, field, and field orientation range. *Phys. Rev. B* **91**(10), 104504 (2015). <https://doi.org/10.1103/PhysRevB.91.104504>
83. X. Song, G. Daniels, D.M. Feldmann, et al., Electromagnetic, atomic structure and chemistry changes induced by Ca-doping of low-angle $\text{YBa}_2\text{Cu}_3\text{O}_{7-d}$ grain boundaries. *Nat. Mater.* **4**(6), 470–475 (2005). <https://doi.org/10.1038/nmat1394>
84. E.F. Talantsev, W.P. Crump, Weak-links criterion for pnictide and cuprate superconductors. *Supercond. Sci. Technol.* **31**(12), 124001 (2018). <https://doi.org/10.1088/1361-6668/aae50a>
85. E.F. Talantsev, J.L. Tallon, Universal self-field critical current for thin-film superconductors. *Nat. Commun.* **6**, 7820 (2015). <https://doi.org/10.1038/ncomms8820>
86. V.J. Emery, S.A. Kivelson, Importance of phase fluctuations in superconductors with small superfluid density. *Nature* **374**(6521), 434 (1995). <https://doi.org/10.1038/374434a0>
87. S.-H. Hong, N.H. Lee, W.N. Kang, et al., Observation of weak coupling effects in $\text{Ba}_{0.6}\text{K}_{0.4}\text{Fe}_2\text{As}_2$ junctions patterned across a naturally formed grain boundary. *Supercond. Sci. Technol.* **27**(5), 055007 (2014). <https://doi.org/10.1088/0953-2048/27/5/055007>
88. S.-H. Hong, S.-G. Lee, S.-G. Jung, et al., Properties of FeSe nanobridges prepared by using a focused ion beam. *J. Korean Phys. Soc.* **61**(9), 1430–1434 (2012). <https://doi.org/10.3938/jkps.61.1430>
89. R. Schneider, A.G. Zaitsev, D. Fuchs, et al., Anisotropic grain-boundary effect on electronic transport in superconducting FeSe thin films. *Supercond. Sci. Technol.* **32**(2), 025001 (2019). <https://doi.org/10.1088/1361-6668/aaf077>
90. K. Iida, F. Kurth, M. Chihara, et al., Highly textured oxypnictide superconducting thin films on metal substrates. *Appl. Phys. Lett.* **105**(17), 172602 (2014). <https://doi.org/10.1063/1.4900931>
91. S. Haindl, M. Kitzun, A. Kauffmann, et al., High upper critical fields and evidence of weak-link behavior in superconducting $\text{LaFeAsO}_{1-x}\text{F}_x$ thin films. *Phys. Rev. Lett.* **104**(7), 077001 (2010). <https://doi.org/10.1103/PhysRevLett.104.077001>
92. S.-H. Hong, S.H. Lee, S.-G. Lee, et al., Fabrication of BaKFeAs intergrain nanobridges by using a focused ion beam. *J. Korean Phys. Soc.* **61**(9), 1449–1452 (2012). <https://doi.org/10.3938/jkps.61.1449>
93. K. Iida, J. Hänisch, S. Trommler, et al., Epitaxial growth of superconducting $\text{Ba}(\text{Fe}_{1-x}\text{Co}_x)_2\text{As}_2$ thin films on technical ion beam assisted deposition MgO substrates. *Appl. Phys. Exp.* **4**(1), 013103 (2011). <https://doi.org/10.1143/APEX.4.013103>
94. S. Trommler, J. Hänisch, V. Matias, et al., Architecture, microstructure and J_c anisotropy of highly oriented biaxially textured Co-doped BaFe_2As_2 on Fe/IBAD-MgO-buffered metal tapes. *Supercond. Sci. Technol.* **25**(8), 084019 (2012). <https://doi.org/10.1088/0953-2048/25/8/084019>
95. T. Katase, H. Hiramatsu, V. Matias, et al., Biaxially textured cobalt-doped BaFe_2As_2 films with high critical current density over 1 MA/cm^2 on MgO-buffered metal-tape flexible substrates. *Appl. Phys. Lett.* **98**(24), 242510 (2011). <https://doi.org/10.1063/1.3599844>

96. Z. Xu, P. Yuan, F. Fan, et al., Transport properties and pinning analysis for Co-doped BaFe_2As_2 thin films on metal tapes. *Supercond. Sci. Technol.* **31**(5), 055001 (2018). <https://doi.org/10.1088/1361-6668/aab261>
97. O. Rodríguez, A. Mariño, Voltage-current characteristics of epitaxial and misoriented $\text{Ba}(\text{Fe}_{1-x}\text{Co}_x)_2\text{As}_2$ thin films. *Phys. C Supercond. Appl.* **513**, 9–12 (2015). <https://doi.org/10.1016/j.physc.2015.03.008>
98. H. Sato, H. Hiramatsu, T. Kamiya, et al., Enhanced critical-current in P-doped BaFe_2As_2 thin films on metal substrates arising from poorly aligned grain boundaries. *Sci. Rep.* **6**, 36828 (2016). <https://doi.org/10.1038/srep36828>
99. K. Iida, H. Sato, C. Tarantini, et al., High-field transport properties of a P-doped BaFe_2As_2 film on technical substrate. *Sci. Rep.* **7**, 39951 (2017). <https://doi.org/10.1038/srep39951>
100. H. Hosono, K. Tanabe, E. Takayama-Muromachi, et al., Exploration of new superconductors and functional materials, and fabrication of superconducting tapes and wires of iron pnictides. *Sci. Technol. Adv. Mater.* **16**(3), 033503 (2015). <https://doi.org/10.1088/1468-6996/16/3/033503>
101. J. Huang, L. Chen, J. Jian, et al., A simplified superconducting coated conductor design with Fe-based superconductors on glass and flexible metallic substrates. *J. Alloys Compd.* **647**, 380–385 (2015). <https://doi.org/10.1016/j.jallcom.2015.06.109>
102. W. Si, J. Zhou, Q. Jie, et al., Iron-chalcogenide $\text{FeSe}_{0.5}\text{Te}_{0.5}$ coated superconducting tapes for high field applications. *Appl. Phys. Lett.* **98**(26), 262509 (2011). <https://doi.org/10.1063/1.3606557>
103. Z. Xu, P. Yuan, Y. Ma, et al., High-performance $\text{FeSe}_{0.5}\text{Te}_{0.5}$ thin films fabricated on less-well-textured flexible coated conductor templates. *Supercond. Sci. Technol.* **30**(3), 035003 (2017). <https://doi.org/10.1088/1361-6668/30/3/035003>
104. W. Si, S.J. Han, X. Shi, et al., High current superconductivity in $\text{FeSe}_{0.5}\text{Te}_{0.5}$ -coated conductors at 30 tesla. *Nat. Commun.* **4**, 1397 (2013). <https://doi.org/10.1038/ncomms2337>
105. G. Sylva, A. Augieri, A. Mancini, et al., $\text{Fe}(\text{Se},\text{Te})$ coated conductors deposited on simple RABiTS templates. *Supercond. Sci. Technol.* (2019) (accepted manuscript) <https://doi.org/10.1088/1361-6668/ab0e98>
106. M. Kidszun, S. Haindl, T. Thersleff, et al., Critical current scaling and anisotropy in oxypnictide superconductors. *Phys. Rev. Lett.* **106**(13), 137001 (2011). <https://doi.org/10.1103/PhysRevLett.106.137001>
107. G. Hammerl, A. Herrnberger, A. Schmehl, et al., Possible solution of the grain-boundary problem for applications of high- T_c superconductors. *Appl. Phys. Lett.* **81**(17), 3209–3211 (2002). <https://doi.org/10.1063/1.1516831>
108. J. Eickemeyer, D. Selbmann, R. Hühne, et al., Elongated grains in textured substrate tapes and their effect on transport currents in superconductor layers. *Appl. Phys. Lett.* **90**(1), 012510 (2007). <https://doi.org/10.1063/1.2429905>
109. C. Tarantini, K. Iida, J. Hänisch, et al., Intrinsic and extrinsic pinning in $\text{NdFeAs}(\text{O},\text{F})$: vortex trapping and lock-in by the layered structure. *Sci. Rep.* **6**, 36047 (2016). <https://doi.org/10.1038/srep36047>
110. S. Demura, M. Tanaka, A. Yamashita, et al., Electrochemical deposition of FeSe on RABiTS tapes. *J. Phys. Soc. Jpn.* **85**(1), 015001 (2016). <https://doi.org/10.7566/JPSJ.85.015001>
111. A. Yamashita, R. Matsumoto, M. Tanaka, et al., Observation of zero resistance in as-electrodeposited FeSe . *Solid State Commun.* **270**, 72–75 (2018). <https://doi.org/10.1016/j.ssc.2017.11.018>

Chapter 11

Control of the Critical Current Density Through Microstructural Design by Ho_2O_3 and Te Co-addition into MgB_2 Processed by Ex Situ Spark Plasma Sintering



P. Badica, G. Aldica, M. Burdusel, M. Grigoroscuta, A. M. Ionescu, V. Sandu, S. Popa, M. Enculescu, I. Pasuk, and A. Kuncser

11.1 Introduction

For superconducting applications of MgB_2 superconductor, enhancement and control of the superconducting properties such as critical current density J_c and the irreversibility field H_{irr} are of much interest. Many researchers have shown that these enhancements can be realized by doping with different materials. Additives can provide elements to substitute in the crystal lattice of MgB_2 (intrinsic effects) or they can generate new microstructures with modified grain boundaries, residual strain, nano-precipitates, and others (extrinsic effects). Microstructure, through connectivity, can strongly influence the superconducting transport properties. Specifics of the technology and of the raw materials should also be carefully considered and not rare are cases when, for a certain additive and composition, contradictory results were reported. Situation is complex and a careful comparative analysis is required.

In our work, we use Spark Plasma Sintering (SPS) and the ex situ route. In the ex situ route, MgB_2 compound is processed, as opposed to the in situ route where raw materials are Mg and B. Usually, in situ routes require heating temperatures up to 800–950 °C, while for ex situ temperatures are higher, up to 1200 °C. Nevertheless, Yang et al. [1] performed heating at high temperatures up to 1700 °C under 10 MPa of Ar for the in situ route. Depending on the route and processing conditions, the influence of the additives might be different.

P. Badica (✉) · G. Aldica · M. Burdusel · M. Grigoroscuta · A. M. Ionescu · V. Sandu · S. Popa · M. Enculescu · I. Pasuk · A. Kuncser
National Institute of Materials Physics, Magurele, Romania
e-mail: badica2003@yahoo.com; aldica2000@yahoo.com; mihai.burdusel@infim.ro;
alex_bebe07@yahoo.com; alina09i@yahoo.com; viorelsandu51@yahoo.com;
popastel@gmail.com; mdatcu@infim.ro; iuliana.pasuk@infim.ro; andrei.kuncser@infim.ro

Among the most popular doping elements is carbon. It substitutes boron and the consequences are the decrease of the a lattice parameter (c lattice parameter is approximately constant) and the enhancement of H_{irr} . At the same time, most reports show that carbon suppresses J_c at low fields and decreases the critical temperature T_c [2], thus limiting the application domain of MgB_2 . C-free additives deserve attention, and the literature on this topic is very rich, but, again, to compare different results obtained through different technologies and by using different raw materials may provide misleading conclusions. The criteria for selection of an effective additive to design the superconducting material with controlled properties are still poorly defined.

In our previous works, we explored the influence of different additives for ex situ SPS [3]. These additives were gathered into four categories. Type 1 are additives showing limited or no reaction with MgB_2 (h-BN, c-BN, graphene; h and c denote hexagonal and cubic crystal structure). Type 2 and 3 are reactive additives resulting in formation of secondary phases. Specifically, type 2 generates compounds with boron, M_uB_v (M = rare earth Ho, Eu, or La supplied from oxides), whereas type 3 generates compounds with magnesium, Mg_mM_n (M = Sb, Bi, Ge, Te, introduced as metals or oxides). Finally, type 4 contains additives or co-additions that provide carbon for boron substitution in MgB_2 (C_{60} , SiC, SiC+Te, $Ge_2H_{10}C_6O_7$, B_4C).

Structural data inferred that M elements from the type 2 and 3 additives have a very low solubility into MgB_2 . It was also found that for most additives (A), the optimal starting composition to maximize J_c is $((MgB_2)_{0.99}(A)_{0.01})$. Enhancement of J_c is in most cases at high fields, while suppression of J_{c0} is observed even for C-free additives, though it is not as strong as for C-doping. It is worthy to note that for our high density MgB_2 materials with additives and obtained by ex situ SPS, an enhancement of zero-field critical current density J_{c0} or of the maximum volume pinning force $F_{p, max}$ was not achieved.

Our results have also shown that the influence of the additives of type 1–3 is significant only at low substitutional carbon amounts, i.e., for $z \leq 0.018$ ($Mg(B_{1-z}C_z)_2$) [3]. Spreading of the pinning-force-related parameters [4, 5] is the highest for the type 2 additives and the reason is not clear. Since the carbon z -level is low and its variation is small, the extrinsic effects (composite microstructure) are expected to play an important role. In support of this statement, we observed for the additives of type 2 that the specific features (e.g., morphology, size, purity, others) of the raw (A)-powder strongly influences superconducting properties of the MgB_2 bulk [3, 6], but further investigations are needed.

In this work, co-addition of Ho_2O_3 and Te to MgB_2 (Alfa Aesar) is used for the optimal composition $((MgB_2)_{0.99}(Te_x(HoO_{1.5})_y)_{0.01})$. Results of co-addition show the possibility of control and improvement of superconducting properties through the systematic microstructural changes of the bi-composite material (composed of relatively “clean” and “dirty” MgB_2 regions) induced by wise and careful selection of the additives. To the best of the authors’ knowledge, this is the first report on co-additions where one additive is reacting with B (type 2) and another one with Mg (type 3). The Ho_2O_3 additive of type 2 is supplied by Sigma-Aldrich and our experiments have shown that this powder diminishes the suppression of J_{c0} (powder

B in [6]) and H_{irr} is constant. The Te addition (type 3), used in this work, has been shown to enhance H_{irr} without a significant decrease of J_{c0} [3, 7]. Therefore, both powders show a positive influence on superconducting parameters and expectations are that their co-addition will control and further enhance them. Indeed, we found that by changing the ratio x/y between Te and Ho_2O_3 , both J_{c0} and $F_{p, \text{max}}$ are enhanced and the maximum values are found for $x/y = 0.4/0.6 = 0.67$. We discuss this effect in connection with microstructural changes. At the same time, the critical temperature at midpoint $T_{c, \text{midpoint}}$ and H_{irr} show a small variation ($T_{c, \text{midpoint}}$ decreases up to 0.7 K and H_{irr} increases up to 10% at 5 K). For the optimum sample with $x/y = 0.4/0.6 = 0.67$, $F_{p, \text{max}}$ is 9.2 GN/m^3 at 5 K and 4.4 GN/m^3 at 20 K. These values are the highest we have obtained when compared with pristine and added samples fabricated by ex situ SPS [3].

From a practical viewpoint, our result enables MgB_2 design with controlled J_{c0} , which was not previously achieved, as already addressed.

Remarkable is also that for high Ho_2O_3 amounts (i.e., when x/y decreases and it takes values below 0.67) a shoulder occurs around $F_{p, \text{max}}$ which becomes more noticeable with the decrease of x/y . Changes in the shape of the pinning force curve $F_p(\mu_0 H)$ may contribute the large scattering of the pinning-force-related parameters for type 2 additions that was mentioned in the beginning of *Introduction*.

11.2 Experimental

Powders of MgB_2 (Alfa Aesar, 99.5% metal basis), Ho_2O_3 (Sigma-Aldrich, 99.9%), and Te-metal (99.99%) were manually mixed. Starting compositions are $((\text{MgB}_2)_{0.99}(\text{Te}_x(\text{HoO}_{1.5})_y)_{0.01})$, where $x/y = 0/0, 0.73/0.27, 0.57/0.43, 0.4/0.6, 0.31/0.69, 0.27/0.75$ (Table 11.1). Powder mixtures were loaded into graphite dies and processed by SPS (FCT Systeme GmbH – HP D5, Germany) at $1150 \text{ }^\circ\text{C}$ for a dwell time of 3 min. The heating rate was $110 \text{ }^\circ\text{C/min}$ and the maximum pressure applied on the graphite punches with a diameter of 20 mm attained 95 MPa. Details of processing are presented in [9].

Apparent densities ρ_a^{SPS} (Table 11.1) of the SPSed pellets were measured by Archimedes method in toluene. Theoretical densities ρ_t^{SPS} of the composites were determined according to [10] considering that samples contain MgB_2 (2.63 g/cm^3), MgO (3.58 g/cm^3), MgB_4 (2.49 g/cm^3), MgTe (3.822 g/cm^3), and HoB_4 (8.892 g/cm^3). The weight fraction of the phases (Table 11.1 and Fig. 11.2) used in the calculations was extracted by Rietveld analysis (MAUD 2.31) of the X-ray diffraction (XRD) patterns measured with a Bruker AXS D8 Advance diffractometer ($\text{CuK}_{\alpha 1}$ radiation). From Rietveld simulations, lattice parameters a and c of MgB_2 and the crystallite size for different phases were also determined (Table 11.1). The relative densities R^{SPS} (%) were calculated as $\left(R^{\text{SPS}} (\%) = \frac{\rho_a^{\text{SPS}}}{\rho_t^{\text{SPS}}} \times 100\right)$ and they are presented in Table 11.1. The displacement values of the punches were registered during processing by the SPS equipment. They were used as input data

Table 11.1 Samples and their initial composition ($(\text{MgB}_2)_{0.99}(\text{Te}_x(\text{HoO}_{1.5})_{0.01})_z$), apparent density, lattice parameters a and c of MgB_2 , z -carbon ($\text{Mg}(\text{B}_{1-z}\text{C}_z)_2$) where z is determined as a function of a (nm) [8]: $z = -21.9 a + 6.76$, and temperature of the beginning of the densification T_d during SPS

Sample	Composition and ratio x/y	Apparent density, ρ_a^{SPS} (g/cm^3)/Relative density, R^{SPS} (%)	Lattice parameters of MgB_2		Amount of carbon	Phase content (wt.%)	Crystallite size (nm) of					T_d ($^\circ\text{C}$)	
			a (\AA)	c (\AA)			z_{Carbon}	MgB_2	MgO	MgB_4	MgTe		HoB_4
	Raw powder	- / -	3.087	3.522	0.002(3)	87.5	-	-	-	-	-	130	-
"a"	0/0	2.55/95.7	3.083	3.529	0.008	83	95	73	-	-	-	140	818
"b"	0.73/0.27 = 2.7	2.6/98	3.084	3.528	0.006	79	104	87	79	80	153	146	821
"c"	0.57/0.43 = 1.32	2.6/97.1	3.084	3.528	0.006	77.1	109	93	84	71	146	146	846
"d"	0.4/0.6 = 0.67	2.59/95.7	3.083	3.528	0.008	75.5	103	89	81	53	134	134	927
"e"	0.31/0.69 = 0.45	2.66/97.0	3.083	3.529	0.008	69.1	113	86	72	52	140	140	932
"f"	0.25/0.75 = 0.33	2.62/94.4	3.083	3.527	0.008	71.6	92	85	82	43	119	119	957

to estimate and plot the curves of the R^{SPS} evolution by following the procedure described in [9]. The temperature of densification T_d is defined as the temperature where the relative density curve vs. time deviates 1% from the horizontal “green” level.

Microstructure of the samples was investigated by scanning electron microscopy, SEM, (Zeiss EVO 50 equipped with an EDS detector) on fresh fractured surfaces and by transmission electron microscopy, TEM (JEOL JEM2100) on ground samples.

Temperature dependence of the magnetization was investigated with a MPMS (Quantum Design) equipment. The critical temperature $T_{c, \text{midpoint}}$ is the temperature for which magnetization is half of the diamagnetic moment. The magnetic hysteresis loops $m(H)$ at different temperatures were registered with a Vibrating Sample Magnetometer (VSM-9 T, Cryogenic). Samples were parallelepipeds ($t \times L \times l = 0.05 \times 0.15 \times 0.15 \text{ cm}^3$, $t = \text{thickness}$, $L = \text{length}$, $l = \text{width}$) cut from the center of the pellet. The critical current density J_c was determined with Bean formula for a plate-like geometry of surface $L \times l$, $L > l$, perpendicular to the applied magnetic field H [11]:

$$J_c = 20 |m \uparrow - m \downarrow| / (V l (1 - (l / (3 L)))) \quad (11.1)$$

where m is magnetic moment in emu for ascending and descending magnetic field and $V = t \times L \times l$ is the volume of the sample in cm^3 . The pinning force was calculated and plotted as a function of H . Next, these curves were the subject of the pinning force scaling procedure [4, 5]. Self-field J_{c0} (in A/cm^2) was estimated for a modified Bean relation, considering the descending branch of the hysteresis loop [12]:

$$J_c = 60 |m \downarrow| / (V l) \quad (11.2)$$

This approach is useful to avoid the complications with macro flux jumps that occur at low temperatures and with estimation of $|m \uparrow - m \downarrow|$ in the classic Bean model. The irreversibility field H_{irr} was established for a criterion of $100 \text{ A}/\text{cm}^2$.

11.3 Results and Discussion

11.3.1 Sample Consolidation, Structural and Microstructural Details, Critical Temperature

Samples prepared by SPS have high relative densities, above 94% (Table 11.1). Consolidation process is influenced by the additives; therefore, the relative density R^{SPS} is similar or higher for the added samples than for the pristine sample “a” (an exception is sample “f” with $x/y = 0.25/0.75 = 0.33$). At lower x/y values, i.e.,

for a higher Ho_2O_3 amount (samples “b” to “f”), the temperature of the beginning of the densification T_d increases (Table 11.1). The reason is possibly related to the much higher melting temperature of Ho_2O_3 (2415 °C) than for Te (449 °C). Nevertheless, during SPS heating, added MgB_2 undergoes chemical reactions that will influence consolidation behavior. XRD data (Fig. 11.1) evidenced the presence of the following secondary phases in the SPSed samples: MgO , MgB_4 , HoB_4 , and MgTe . Some low intensity lines in XRD patterns might be ascribed to traces of TeO_2 . The amount of residual Te (ICDD – 04-555) is small (< 0.2 wt. %). Therefore,

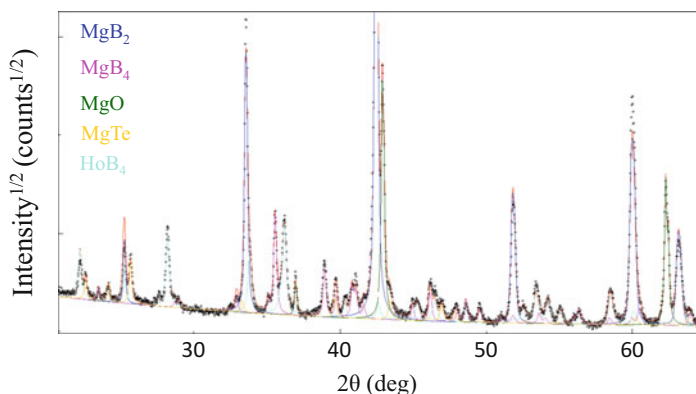
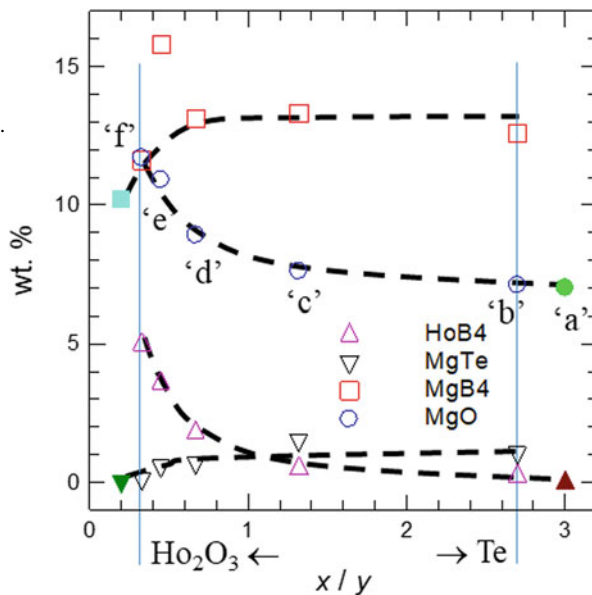
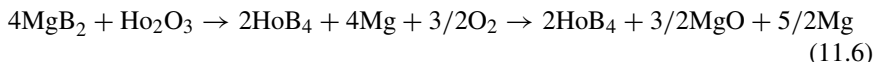
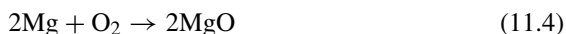


Fig. 11.1 X-ray diffraction pattern for sample “d” and Rietveld whole powder pattern fitting. MgB_2 , MgO , MgB_4 , HoB_4 , and MgTe were identified and simulated according to ICDD 38–1369, ICDD 35–0821, ICDD 15–0299, ICDD 025–0377, and ICDD 065–3416, respectively

Fig. 11.2 Phase concentration as a function of the x/y ratio (0.33–2.7) in the starting mixture $((\text{MgB}_2)_{0.99}(\text{Te}_x(\text{HoO}_{1.5})_y)_{0.01})$. Full symbols arbitrary located at $x/y = 0.2$ or 3 are for pristine sample “a”. Dashed lines are guides for eyes



both Te and TeO₂ were not considered in Table 11.1 and Figs. 11.1 and 11.2. Variation of the weight fraction for different secondary phases with the ratio x/y is presented in Fig. 11.2. We included in this graph also data for the pristine sample “a” by taking arbitrary values for x/y of 0.2 or 3. Although the weight fraction for both secondary phases HoB₄ and MgTe in the pristine sample is zero, these points are useful as a reference for the weight fraction variation as a function of x/y . The difference to 100% of the total weight fraction of the secondary phases is the weight fraction of MgB₂ (Table 11.1). When the ratio x/y decreases, the amounts of MgB₂, MgB₄, MgTe (an exception is for sample “e”) decrease, while those of MgO and HoB₄ increase. Reactions established for ex situ SPSed pristine or individually added samples were reported in refs. [6, 7] and they are:



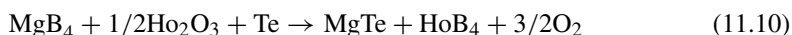
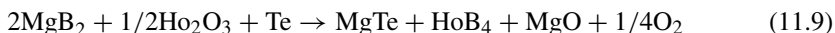
Oxygen released in reaction (11.6) is promoting reaction (11.4) with formation of MgO. We mention that oxygen is also available in the SPS furnace (pressure in the chamber is 30 Pa) and is also absorbed on the surface of the powder particles. The presence of TeO₂ in our co-added samples suggests that oxygen can also react with Te:



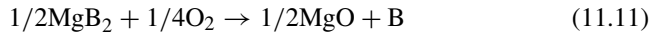
However, we have reported in [7] that TeO₂ reacts with MgB₂ with formation of MgTe:



Reaction (11.7) is not favored and this explains that the amount of TeO₂ in the co-added samples is low. Reactions (11.3)–(11.6) can be considered as the main ones for the co-added samples although they were written for individual additives. Reactions (11.5) and (11.6) are independent. This status would be preserved in the co-added sample if, e.g., reaction (11.5) occurs before (11.6). We can assume that during heating, (11.6) takes place at a lower temperature than (11.4) and this is somehow justified by low and high melting points of Te and Ho₂O₃, as mentioned before. For co-added samples, it is necessary to view simultaneous contribution of both additives and the following reactions can be written:



Both reactions provide oxygen. If we assume that this oxygen mainly reacts to form MgO (i.e., reaction (11.5) is not active and oxygen gas is not released from the sample), to accommodate this situation, MgB₂ or MgB₄ should decompose with formation of B-rich phases. For example, if taking as a reference Eq. (11.9), the decomposition reaction will be:



Similar tendency will be obtained by following reaction (11.10). In practice, free-B is not observed in MgB₂ samples, but higher Mg-borides and phases in the Mg-B-O system are revealed by microscopy. Being usually at nano scale, they are not detected by XRD in most cases. Boron-rich phases can be observed for our samples in Fig. 11.3.

SEM and XRD information indicate that our samples are composites. Microstructure (Fig. 11.4) observed in backscattering mode is composed of relatively “clean” and “dirty” regions of MgB₂ containing secondary phases. Lighter areas are associated with the presence of heavy elements. The atomic weight of Ho is 164.93 and of Te is 127.6. Thus, white and gray regions contain Ho and Te, respectively. White and gray regions are easily distinguished at high magnification (Fig. 11.4). The clean and dirty regions show a non-uniform gray-distribution. This indicates that both Ho and Te are present inside them. Size and distribution of the “clean” and “dirty” regions are influenced by x/y ratio. Clean regions can be identified with colonies of MgB₂ as reported in [13]. When x/y is high, colonies are not well defined and they are in direct contact with each other, forming the matrix that surrounds dirty regions. The decrease of x/y is accompanied by the colonies separation. They are fully separated for $x/y \leq 0.67$ and “dirty” regions form the new matrix that includes the colonies. For lower x/y values, the size of the colonies is decreasing. This controlled modification of the composite microstructure influences $J_c(H)$ curves. Details are addressed in Sect. 11.3.2.

Other observations of interest are:

1. The average crystallite size of MgB₂ and of the secondary phases does not change much among the samples (Table 11.1). Apparently, there is a trend of a decreasing crystallite size of HoB₄ when x/y decreases, but errors are high and a firm conclusion cannot be reached. The decrease of the HoB₄ crystallite size suggests that the presence of Te supports coarsening of HoB₄, but other explanations might also be possible and the result is open to further discussions. A higher number of boundaries and smaller precipitates, with size comparable with the coherence length of MgB₂ (10–30 nm [14]), can play the role of effective pinning centers. The average crystallite size of the secondary phases is between 43 and 109 nm, and this is more than 1.4 times larger than the coherence length of MgB₂. Therefore, the secondary phases would not contribute directly as pinning centers. This observation needs careful assessment since a small fraction of the secondary phases can be in the required nano range size. A second aspect is that crystallites in our estimations are considered spherical

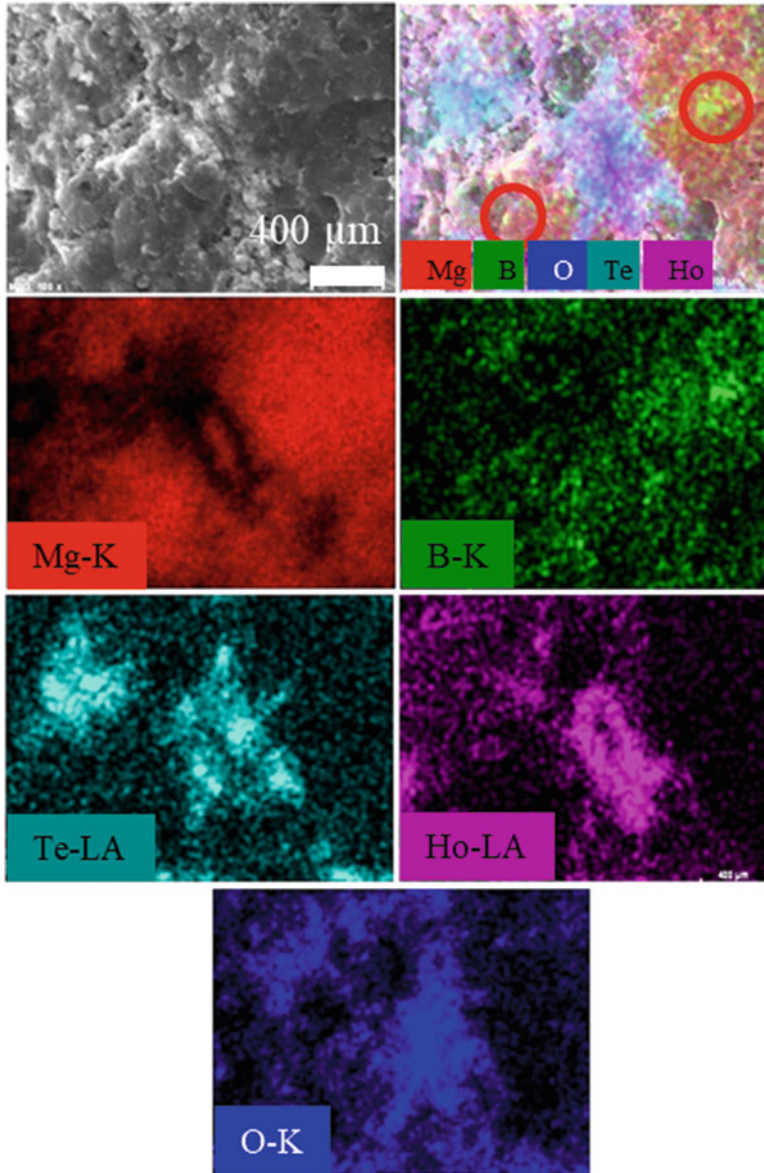


Fig. 11.3 SEM image and EDS maps of Mg, B, Te, Ho, and O and the red-blue-green RBG image of the overlapped maps for sample “F”. Circles indicate boron-rich grains

(3D) although TEM data suggests also the presence of 1 or 2D morphologies. Secondary phases are located at MgB_2 - MgB_2 grain boundaries. TEM/EDS data show grains containing Ho, Te, and O (Fig. 11.5). The average size is comparable

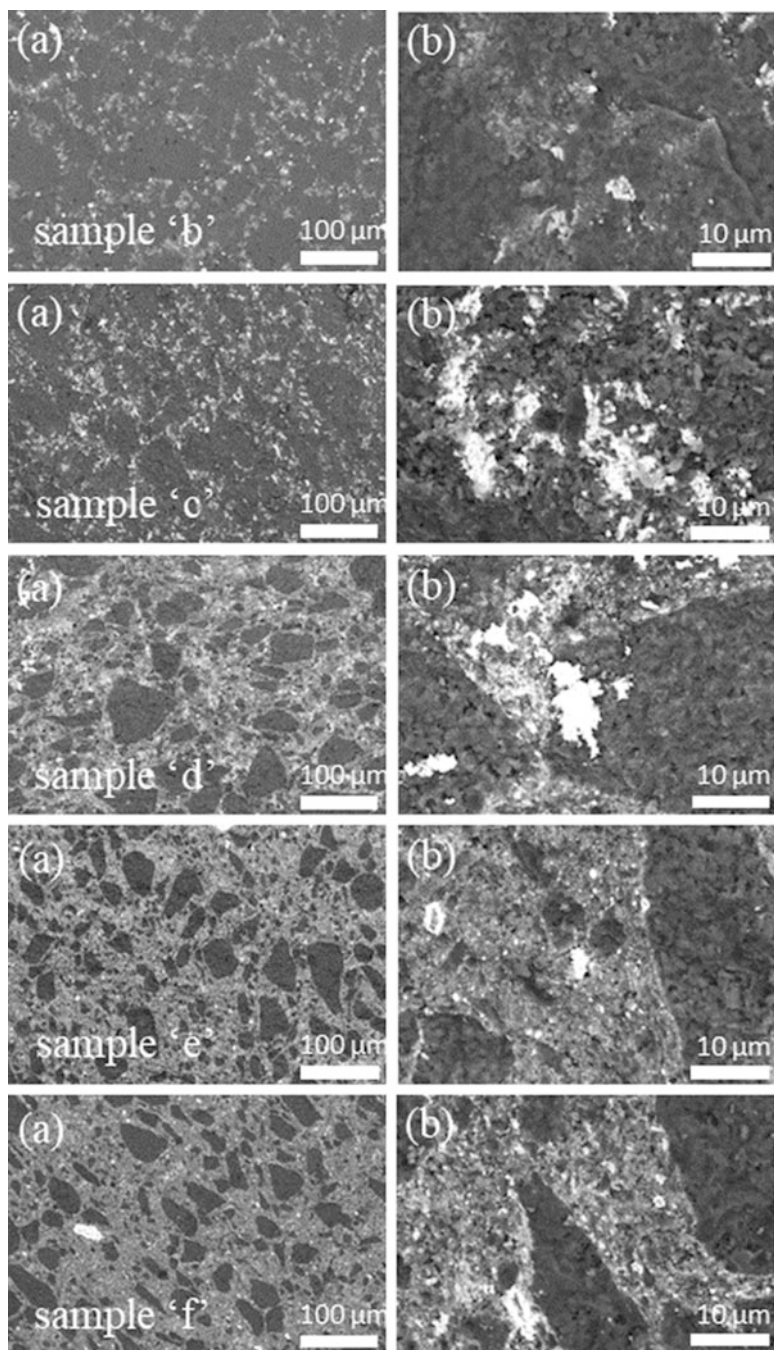


Fig. 11.4 Backscattering SEM images of samples “b”-“f” (sample notation is as in Table 11.1) taken for magnifications: (a) $\times 500$ and (b) $\times 5000$

with that for crystallites determined by XRD for phases HoB_4 , MgO , and MgTe . For the phases with Ho and Te, grains morphology is mostly of 3D type and the grain size spreads from 5 to 300 nm. 2D layer-like grains also form and they are often found to contain Te (Fig. 11.5e, g, l, n). Their thickness is in the nano range (5–40 nm), while the other dimensions are about one order of magnitude larger. 3D grains containing Ho are surrounded by MgO grains or are in direct contact with Mg-B grains (Fig. 11.5h–n). This can be associated with a core-shell structure. The Mg-B grains are ascribed to MgB_2 phase and for some of them EDS measurements indicate a B-deficient stoichiometry ($\text{MgB}_{2-\lambda}$, $\lambda < 0.7$). Information is qualitative since detection by EDS of light elements like boron is subject to high errors. 3D grains containing Te also promote a kind of core-shell structure as for Ho, but in this case grains are surrounded by B-rich phases in the Mg-B(O) system (Fig. 11.5o).

2. Lattice parameters of MgB_2 for SPSed pristine “a” and co-added “b”-“f” samples are approximately the same (Table 11.1). When Ho and Te were added individually, no chemical substitution effects were revealed [6, 7]. This result can be considered applicable for the co-added samples from this work. If so, carbon substitution effects can be observed. When carbon substitutes for boron in the crystal lattice of SPSed MgB_2 [6, 7], a lattice parameter changes, while c is constant. This is the case if raw powder is compared with SPSed samples “a”-“f”. The amount of carbon z (Table 11.1) for SPSed samples (0.006–0.008) is higher than in the raw MgB_2 powder (0.002) due to carbon intake from the graphite die used in the SPS processing. Among the SPSed samples, z values can be considered constant within the errors (± 0.001). On the other hand, for our samples, $T_{c,\text{midpoint}}$ systematically decreases (Fig. 11.6a) and suggests that distortion of the MgB_2 lattice occurs. Enhancement of the carbon content z promotes lattice distortion and usually correlates with the decrease of $T_{c,\text{midpoint}}$, but in our case z is almost constant. Therefore, the origin of $T_{c,\text{midpoint}}$ decrease is related to the presence of additives.

Samples with a lower x/y have a lower $T_{c,\text{midpoint}}$ so that distortion is mainly contributed by the introduction of the Ho_2O_3 addition. Since chemical substitution effects of Ho were ruled out, distortion can be induced by the local strain and/or by non-stoichiometry of MgB_2 at its interface with Ho-based secondary phases. A lattice mismatch relationship between MgB_2 and HoB_4 can be considered (two ac -planes of MgB_2 fit one ac plane of HoB_4). On one direction, the lattice mismatch is low ($(a_{\text{HoB}_4} - 2c_{\text{MgB}_2})/a_{\text{HoB}_4} = 0.41\%$), but on the other is too high ($(c_{\text{HoB}_4} - a_{\text{MgB}_2})/c_{\text{HoB}_4} = 23\%$) and decreases the probability that epitaxial lattice matching between MgB_2 and HoB_4 can play an important role. The residual strain of MgB_2 has a small variation between 0.13 and 0.14%, but the dependence with x/y could not be observed. We have also pointed out that reactions in the co-added samples promote formation of boron-rich phases and, in turn, this can favor boron nonstoichiometry in MgB_2 . The idea is supported, as already presented, by TEM data, and by the decrease of $T_{c,\text{midpoint}}$. In [1] addition of Dy_2O_3 that forms DyB_4 slightly decreased $T_{c,\text{midpoint}}$ [1], similar to our case, but the difference is that samples were

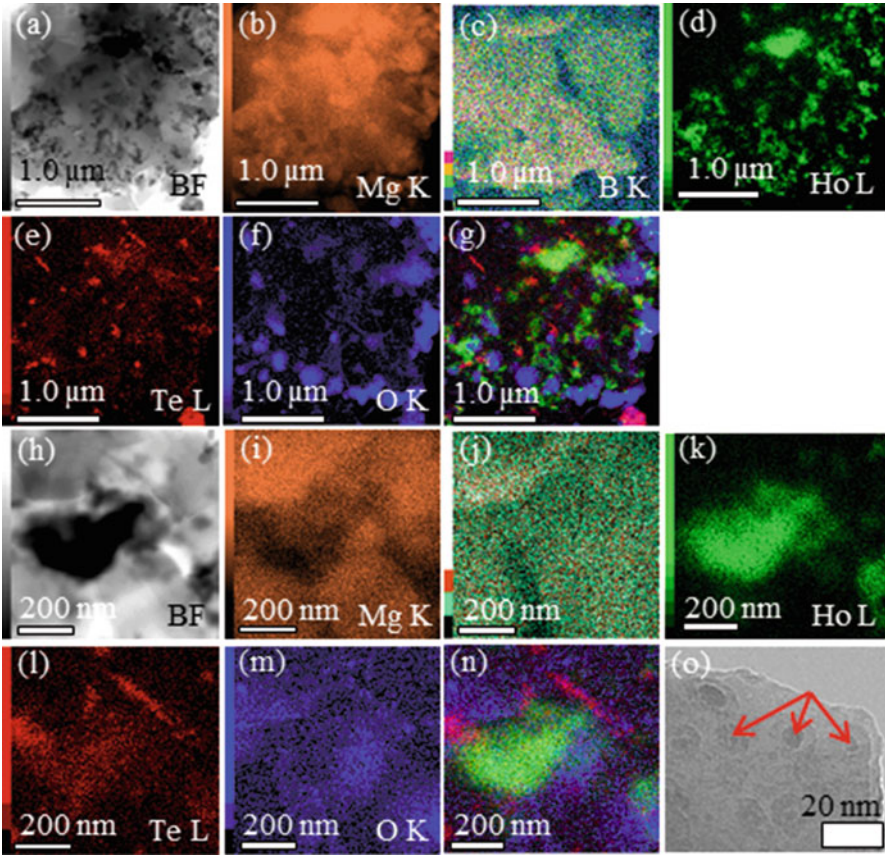
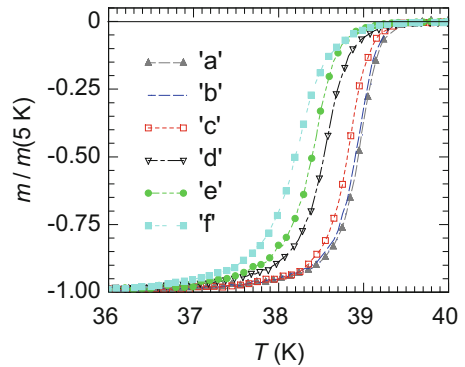


Fig. 11.5 Sample "d" ($x/y = 0.67$): TEM images, EDS maps, and red-green-blue images obtained by overlapping individual EDS maps for Ho, Te, and O. Images (a–g) and (h–o) are for low and high magnifications, respectively. In (o) core nano grains containing Te from the core-shell structures are indicated with arrows

Fig. 11.6 Reduced magnetization curves vs. temperature



prepared by an in situ infiltration process. In [15] the boron nonstoichiometry of MgB_2 is considered the microscopic origin of the J_c enhancement at high magnetic fields. In agreement with this observation, all our co-added samples show a slightly higher H_{irr} than for the pristine sample (see Sect. 11.3.2). However, the inferred boron nonstoichiometry of MgB_2 phase in our samples needs further studies.

11.3.2 Critical Current Density, Irreversibility Field, Pinning Force

Critical current density, irreversibility field, and pinning force parameters are presented in Figs. 11.7, 11.8, and 11.9.

All co-added samples show marginally higher J_c at high magnetic fields, and this is reflected in somehow enhanced H_{irr} comparative to the pristine samples (Fig. 11.7). The most interesting feature of our samples is that J_{c0} has a maximum as a function of x/y . This behavior is accompanied by a similar tendency for the $F_{p, \text{max}}$. Due to high values of J_{c0} and small variation of H_{irr} , the product $\mu_0 H_{\text{irr}} J_{c0}$ (Fig. 11.8d) has a similar behavior with x/y . The product is used to compare samples and provides information on the balance between low and high field properties [3]. The maximum values of J_{c0} , $F_{p, \text{max}}$, and $\mu_0 H_{\text{irr}} J_{c0}$ are for $x/y = 0.67$. Improvement of J_{c0} and $F_{p, \text{max}}$, in the ex situ SPS samples, was not detected in our previous research summarized in [3]. Specifically, the added samples showed in general lower or, at least, similar values to those for the pristine sample. The maximum values of $F_{p, \text{max}}$ at all investigated temperatures are superior for the optimally co-added sample “d” ($x/y = 0.67$) than for any other SPSed samples we have produced. The value of $F_{p, \text{max}}$ is as high as 6.4 GN/m^3 at 15 K. For the same temperature, Susner [16] reported a value of about 2 GN/m^3 for an undoped MgB_2 wire. Maximization of J_{c0} and $F_{p, \text{max}}$ at $x/y = 0.67$ coincides with separation of the MgB_2 colonies in the microstructure of the co-added samples (see Sect. 11.3.1).

Birajdar and Eibl [13] defined few microstructural parameters that influence $J_c(H)$: (a) the grain size of MgB_2 (determined from TEM observations) influences the amount of grain boundary pinning, (b) the volume fraction and the size of the secondary phases control the area of superconducting-normal interfaces which can also affect pinning, (c) the size of the MgB_2 colonies and the volume fraction of MgB_2 which promote a higher connectivity when they are larger. They made their analysis considering transport measurements of pristine and SiC-added MgB_2 samples fabricated by in situ and ex situ methods. They found that the irreversibility field is higher for a smaller MgB_2 grain size and for a certain optimal volume fraction of the secondary phases, while J_{c0} is higher for larger MgB_2 colonies and a higher volume fraction of MgB_2 . To compare their results with ours, we use the crystallite size as extracted from XRD data and the weight fraction of different phases (Fig. 11.2). We observed in [17] that the crystallite size from structural measurements is similar with the grain size from the TEM measurements.

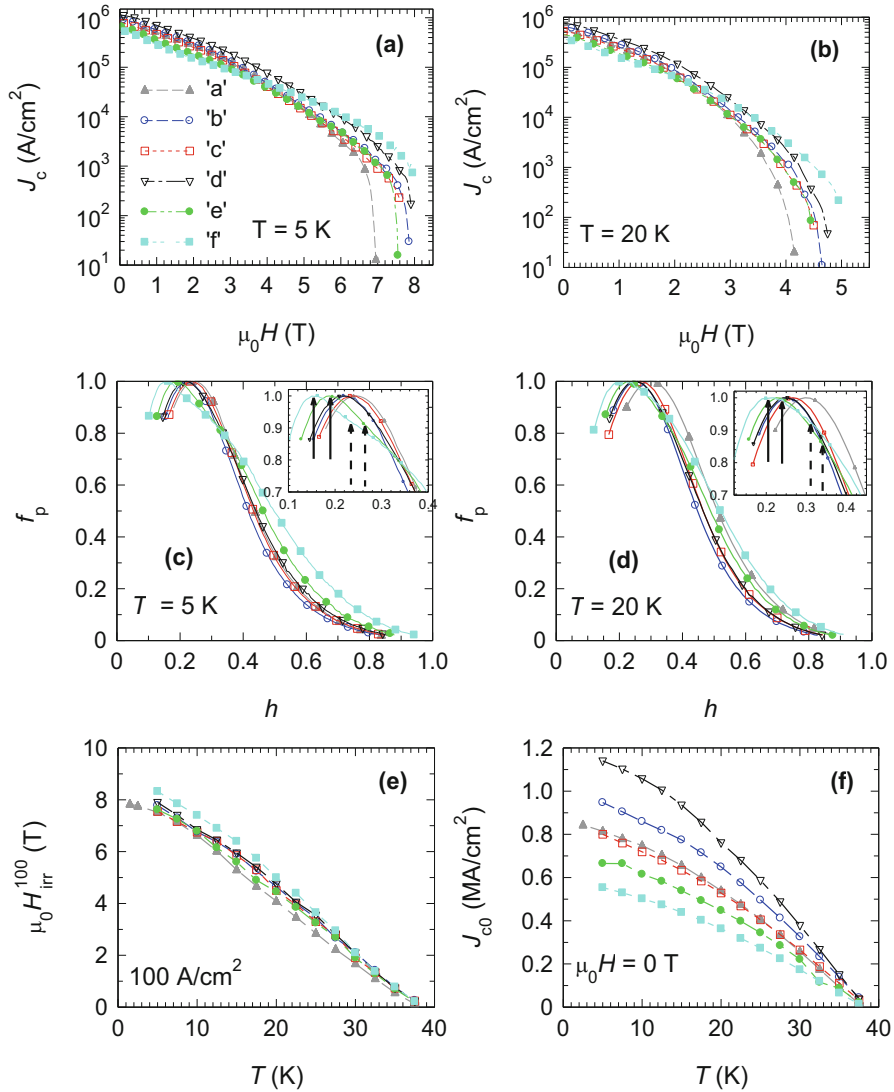


Fig. 11.7 Field dependence of the critical current density J_c at (a) -5 K and (b) -20 K , reduced pinning force f_p as a function of reduced magnetic field h at (c) -5 and (d) -20 K , (e) the irreversibility field H_{irr} , and (f) zero-field critical current density J_{c0} vs. temperature. In insets to (c) and (d) one observes occurrence of the second peak (dashed arrows) in the curves of pinning force $f_p(h)$ (location of the $f_{p,\max}$ is indicated with full arrows) for samples “e” and “f”

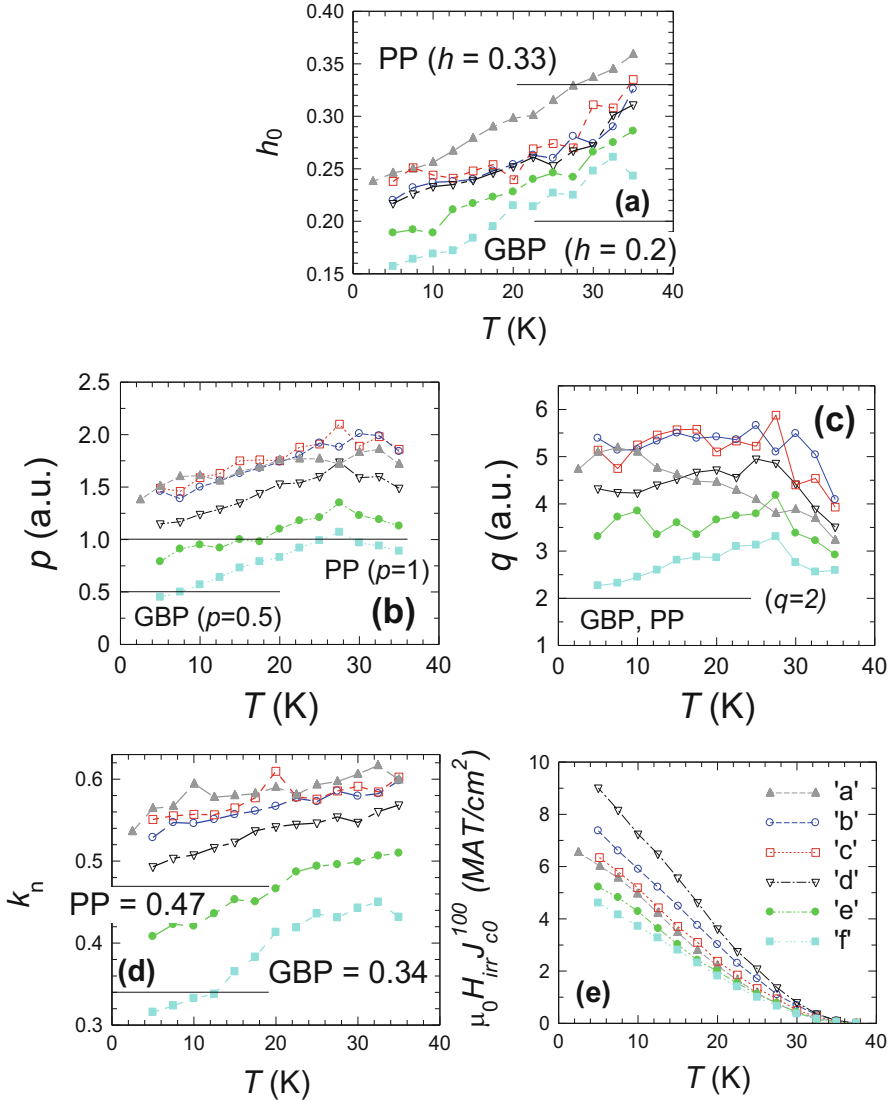


Fig. 11.8 Temperature dependence of the pinning force parameters (a) $-h_0$, (b) $-p$, (c) $-q$, (d) $-k_n$, and (e) the product $\mu_0 H_{irr} J_{c0}$. Theoretical values of the parameters for PP and GBP [5, 18] are indicated

The crystallite size of MgB₂ is almost constant (or slightly decreases for sample “F”, Table 11.1), while H_{irr} has a small variation (Fig. 11.7e) showing similar or slightly higher values than for the pristine one. This result is in agreement with Ref [13], but clarifications are needed as follows:

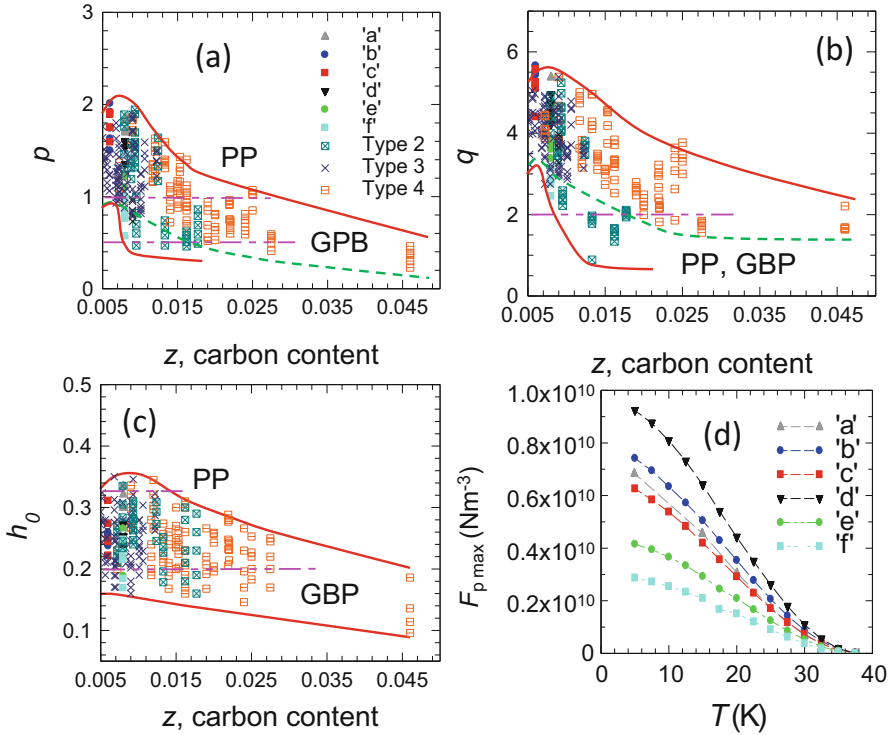


Fig. 11.9 Pinning force parameters (a) $-p$, (b) $-q$ and (c) $-h_0$ as a function of z -carbon content, and (d) the maximum pinning force as a function of temperature. Experimental points type 2, 3, and 4 [3] are for different additives (see text). Lines are guides for the eyes and theoretical values of the parameters for PP and GBP [5] (horizontal dashed lines) are also indicated. Thick green dashed lines in (a) and (b) show the lower limit of the domain in which p and q take values for samples of type 3 and 4 from [3]

For a lower x/y , the amount of MgB₂-MgB₂ boundaries decreases because the weight fraction of MgB₂ is lower for approximately constant MgB₂ crystallite size. Since grain boundaries act as pinning centers in MgB₂, one can expect a lower level of pinning and a decrease of high field properties. On the other hand, secondary phases are located at MgB₂-MgB₂ boundaries and their presence introduces superconductor-normal interfaces. The number of interfaces increases for a lower x/y because the total weight fraction of the secondary phases estimated from XRD increases (Table 11.1) and, as presented in Sect. 11.3.1, microstructural changes (Fig. 11.4) reveal an increase of the “dirty” MgB₂ regions at the expense of the “clean” ones. More interfaces are also obtained if the crystallite size of the secondary phases is decreasing, as for HoB₄ when x/y is smaller. A higher number of interfaces are expected to promote a stronger pinning and this pinning is of surface type. In our samples, surface pinning (denoted grain boundary pinning, GBP) will be contributed by MgB₂-MgB₂ boundaries and superconductor-normal interfaces, but

their effects on pinning are opposite. Small variation of high field properties, such as H_{irr} and small decrease in $T_{\text{c, midpoint}}$, is due to some disorder (see Sect. 11.3.1). As a measure of the disorder level, the residual strain is observed. We have seen that for our samples, residual strain variation is very small and this situation may suggest that the effects of the boundaries and of the interfaces cancel each other. Our analysis promotes the idea that GBP in our samples would be constant. By applying the universal pinning force scaling law [4, 5].

$$f_p = Ah^p(1-h)^q, \quad (11.12)$$

the pinning-force-related parameters p , q , and h_0 were extracted ($f_p = F_p / F_{p, \text{max}}$, $h = H/H_{\text{irr}}$, $h_0 = h(F_{p, \text{max}})$), where the volume pinning force is given by $F_p = \mu_0 H J_c$. Contrary to proposed image, it is remarkable that when x/y decreases, temperature-dependent curves of pinning-force-related parameters h_0 , q , and k_n (Fig. 11.8a,c,d) shift to lower values, where the GBP is the major mechanism. Exponent p also shows this tendency (except for pristine sample at $T > 10$ K). Theoretical values for GBP are $h_0 = 0.2$, $p = 0.5$, $q = 2$, $k_n = 0.34$ and for point pinning (PP) they are $h_0 = 0.33$, $p = 1$, $q = 2$, $k_n = 0.47$ [5]. Parameter k_n is defined as $k_n = h_0/h(F_{p, \text{max}}/2)$ [18]. To accommodate results and to solve the encountered contradiction related to GBP behavior, one has to consider that PP decreases for a lower x/y . The problem is that variation of the pinning force-related parameters is unusually high (Figs. 11.8 and 11.9) with the decreasing x/y and, thus, suppression of PP appears to be atypical. On the other hand, large variation of the pinning parameters for more Ho_2O_3 (x/y decreases) in the samples confirms that type 2 reactive additives with formation of borides promote the largest scattering of the pinning force parameters (when $z < 0.018$): in Fig. 11.9 a, b samples “e” and “f” with the highest amount of Ho_2O_3 and samples with type 2 additives from [3] show the lowest values of p and q located in between the lower full red and dashed green arbitrary lines. The green dashed line defines the lower limit of the values determined for samples with additives of type 3 and 4. The carbon content in our samples is almost constant; hence, carbon is not at the origin of this effect. A closer look shows that for high $x/y > 0.67$, where the “clean” regions are the matrix and they are expected to control the percolative current path, the pinning force parameters show a relatively small decrease if compared with the much stronger decrease when $x/y < 0.67$ and the matrix is formed by the “dirty” region that surrounds the islands (colonies) of “clean” MgB_2 . Therefore, our MgB_2 material acts in a complex manner and can be considered as a composite within a composite. The two composites, “dirty” and “clean,” change their microstructure with x/y . The interplay between composite regions has to be considered. Nevertheless, J_{c0} , $F_{p, \text{max}}$, and the decrease of the pinning force parameters indicate that contribution of the “clean” composite is strong for $x/y > 0.67$ and of the “dirty” one for $x/y < 0.67$, while sample “d” with intermediate $x/y = 0.67$ is the optimum one. We noted in [3] that J_{c0} , $F_{p, \text{max}}$ and the pinning force parameters strongly reflect the behavior of the added MgB_2 samples at low and intermediate fields. According to Birajdar and Eibl [13], larger MgB_2 colonies promote connectivity, thus, leading to higher J_{c0} values. This result

seems applicable for decreasing $x/y \leq 0.67$, but it does not reflect the situation for $x/y > 0.67$ because the highest values of J_{c0} and $F_{p, \max}$ are obtained for sample “d” ($x/y = 0.67$) and not for pristine sample “a”. For our samples, connectivity and pinning have to be understood in a larger context, i.e., for each composite component and, ultimately, for their bi-composite overall structure. Systematic evolution of the microstructure and of the properties for our samples suggest the possibility of MgB₂ materials design with controlled functional characteristics required for applications.

Another interesting aspect is occurrence and separation of a shoulder in the $f_p(h)$ curves around $F_{p, \max}$ for the decreasing $x/y \leq 0.67$ (Fig. 11.7 c, d insets). Details are addressed in Sect. 11.3.3.

11.3.3 Aspects of the Pinning Force Separation

Pinning force curves $f_p(h)$ with unusual shapes around $F_{p, \max}$ are reported in literature [1, 19–26], but an analysis is not provided. For our SPSed samples with different additives, a clear and controlled change around $F_{p, \max}$ towards separation of two peaks in $f_p(h)$ was not revealed before [3]. The effect is found in samples with $x/y < 0.67$. To investigate this effect, we try to analyze $f_p(h)$ curves by applying the scaling law at low and high fields (Fig. 11.10). This exercise is also meaningful for samples with $x/y \geq 0.67$ for which visually there is only one typical maximum in $f_p(h)$. Examples are presented in Fig. 11.10 a, b inset for samples “d” ($x/y = 0.67$) and “f” ($x/y = 0.33$). If Eq. (11.1) is valid for low and high field domains, the plot of $\frac{d \ln(f_p)}{d \ln(h)}$ vs. $x = h/(1-h)$ for each region must be linear. Line intercept is equal to p and its slope to q . Both regimes obey Eq. (11.1), but with different exponents p and q denoted p_1, q_1 and p_2, q_2 for low and high fields, respectively. A crossover between the two regimes (Fig. 11.10a) occurs at a certain $x_c =$ (e.g., 0.83 in sample “d”) which corresponds to a crossover scaled field $h_c = \frac{x_c}{1+x_c}$ (0.45 in sample “d”). For sample “d” ($x/y = 0.67$), $p_1 = 1.5, q_1 = 4.9, p_2 = -0.6,$ and $q_2 = 2.3$ and for sample “f” ($x/y = 0.33$) $p_1 = 1.57, q_1 = 8.36, p_2 = 0.61,$ and $q_2 = 2.52$. We note that for sample “d”, p_2 is negative and the physical meaning is not clear. For the samples with lower x/y , this situation does not occur. It is possible that other functional dependences are present so that their contribution is revealed by the dependence of the logarithmic derivative and it affects results for sample “d”. We also observe that the absolute values are far from the theoretically predicted p and q values [5] and for q_1 they are even higher than those determined by scaling with Eq. (11.1) in the entire field domain (Fig. 11.9). Although the physical meaning of p and q taking abnormal values remains an unsolved problem for our samples and in general for MgB₂, our analysis shows the following details:

1. For samples “e” ($x/y = 0.45$) and “f” ($x/y = 0.33$), the crossover from low to high fields is within a reduced field range (e.g., for sample “f” $0.18 < h < 0.27$ at $T = 5$ K, Fig. 11.10b). Transformation of the crossover point x_c (Fig. 11.10a)

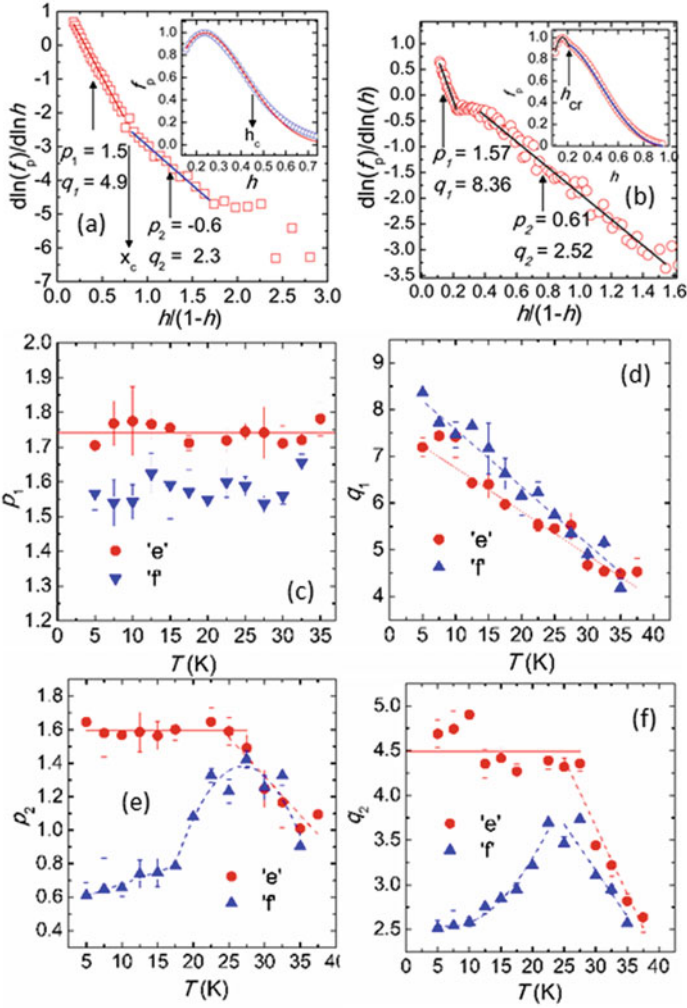


Fig. 11.10 Plot of the logarithmic derivative of the normalized pinning force f_p vs. $h/(1-h)$ and parameters p_1 , q_1 for low field and p_2 , q_2 for high field (see text) for: (a) sample “d” at 10 K and (b) sample “f” at 5 K. Insets to (a) and (b) show experimental points and the fit with Eq. (11.12) of the pinning force $f_p(h)$. Panels (c–f) present the temperature dependence of p_1 , p_2 , q_1 , and q_2 . Dashed lines are the least-square fits with linear or polynomial functions

into a crossover region mirrors the major shape change noticed in the f_p vs. h plots around the $F_{p, \max}$ in the samples with $x/y < 0.67$.

- Variation of the pinning parameters p_1 , p_2 and q_1 , q_2 with temperature for samples “e” and “f” are presented in Fig. 11.10c–f. The exponent p_1 , which depicts the behavior at low fields, by the least-square fit with a linear function

gives almost constant values, with the average values $p_1 = 1.74$ (dispersion $\sigma_1 = 0.042$) and $p_1 = 1.58$ ($\sigma_1 = 0.036$) for the samples “e” and “f”, respectively (Fig. 11.10c). The parameter q_1 decreases with temperature in approximately linear manner (Fig. 11.10d). Values of q_1 are higher for sample “f” and the drop vs. temperature is faster. We conclude that both samples “e” and “f” follow similar tendencies with temperature at low field. At high field, situation is significantly different.

For sample “e”, up to about 25 K, p_2 and q_2 are approximately constant and at higher temperature they decrease, while for sample “f” both $p_2(T)$ and $q_2(T)$ curves show a maximum located around 25 K. A decrease in p and q at $T > 25$ K is also visible in Fig. 11.8b when scaling is performed in the entire field domain. The result suggests that this decrease, which was also observed for other series of SPSed MgB₂ (pristine [8] or added [3]) samples is related to high field pinning properties at high temperatures.

Our analysis performed for low and high fields brings strong arguments for a complex behavior in our samples as anticipated in Sect. 11.3.2.

11.4 Conclusion

Co-addition of Ho₂O₃ and Te into MgB₂ samples obtained by ex situ spark plasma sintering were tested. By changing the ratio between additives, microstructure shows a controlled change that is reflected on the systematic variation of J_{c0} and $F_{p, \max}$. They reach a maximum for $x/y = 0.67$. The maximum $F_{p, \max}$ takes values higher than for reported MgB₂ samples obtained by SPS.

When x/y decreases for values $x/y < 0.67$, in the $F_{p, \max}(H)$ curve, around the maximum, the shape changes, namely, a shoulder occurs and gets more conspicuous. Analysis of this behavior indicates on a complex contribution of different pinning mechanisms.

Two distinctive regimes of pinning behavior are for temperatures below and above 25 K. Pinning force-related parameters show a small variation for $x/y > 0.67$ and a large one for $x/y < 0.67$. Overall, a decreasing x/y and for lower temperatures produces a stronger grain boundary pinning contribution.

The x/y variation does not deteriorate significantly $T_{c, \text{midpoint}}$ and co-added samples show a similar or slightly higher H_{irr} than for pristine sample.

In conclusion, the influence of the microstructural change with x/y is important for the pinning-force control and the results of this work indicate on the possibility of the composite design with desired properties. The proposed approach demonstrates new possibilities for further improvements of the MgB₂ superconductor.

Acknowledgements Authors gratefully acknowledge financial support from MCI-UEFISCDI Romania through Core Program 2017/2018 and project POC 37_697 no. 28/01.09.2016 REBMAT.

References

1. Y. Yang, M.D. Sumption, E.W. Collings, Influence of metal diboride and Dy₂O₃ additions on microstructure and properties of MgB₂ fabricated at high temperatures and under pressure. *Sci. Rep.* **6**, 29306 (2016)
2. S.X. Dou, W.K. Yeoh, J. Horvat, M. Ionescu, Effect of carbon nanotube doping on critical current density of MgB₂ superconductor. *Appl. Phys. Lett.* **83**, 4996 (2003)
3. P. Badica, G. Aldica, A.M. Ionescu, M. Burdusel, and D. Batalu, The Influence of Different Additives on MgB₂ Superconductor Obtained by Ex Situ Spark Plasma Sintering: Pinning Force Aspects, *Correlated Functional Oxides Ch. 4* (2017) 75 ISBN 978-3-319-43777-4
4. W.A. Fietz, W.W. Webb, Hysteresis in superconducting alloys—Temperature and field dependence of dislocation pinning in niobium alloys. *Phys. Rev. B* **178**, 657 (1969)
5. D. Dew-Hughes, Flux pinning mechanisms in type II superconductors. *The Philos. Mag.: J. Theor. Exp. Appl. Phys.* **3**, 293 (1974)
6. G. Aldica, S. Popa, M. Enculescu, D. Batalu, L. Miu, M. Ferbinteanu, P. Badica, Addition of Ho₂O₃ of different types to MgB₂ in the ex-situ spark plasma sintering: Simultaneous control of the critical current density at low and high magnetic fields. *Mater. Chem. Phys.* **146**, 313 (2014)
7. G. Aldica, S. Popa, M. Enculescu, P. Badica, Enhancement of critical current density and irreversibility field by Te or TeO₂ addition to MgB₂ bulk processed by spark plasma sintering. *Scripta Mater.* **66**, 570 (2012)
8. G. Aldica, S. Popa, M. Enculescu, I. Pasuk, A.M. Ionescu, P. Badica, Dwell time influence on spark plasma-sintered MgB₂. *J. Supercond. Nov. Mag.* **31**, 317 (2018)
9. G. Aldica, D. Batalu, S. Popa, I. Ivan, P. Nita, Y. Sakka, O. Vasylykiv, L. Miu, I. Pasuk, P. Badica, Spark plasma sintering of MgB₂ in the two-temperature route. *Physica C* **477**, 43 (2012)
10. G.W. Marks, L.A. Monson, Effect of certain group IV oxides on dielectric constant and dissipation factor of barium titanate. *Ind. Eng. Chem.* **47**, 1611 (1955)
11. C.P. Bean, Magnetization of hard superconductors. *Phys. Rev. Lett.* **8**, 250 (1962)
12. L. Miu, G. Aldica, P. Badica, I. Ivan, D. Miu, G. Jakob, Improvement of the critical current density of spark plasma sintered MgB₂ by C₆₀ addition. *Supercond. Sci. Technol.* **23**, 095002 (2010)
13. B. Birajdar, O. Eibl, Microstructure critical current density model for MgB₂ wires and tapes. *J. Appl. Phys.* **105**, 033903 (2009)
14. J.C. Loudon, S. Yazdi, T. Kasama, N.D. Zhigadlo, J. Karpinski, Measurement of the penetration depth and coherence length of MgB₂ in all directions using transmission electron microscopy. *Phys. Rev. B* **5**, 91054505 (2015)
15. J.H. Kim, S. Oh, Y.-U. Heo, S. Hata, H. Kumakura, A. Matsumoto, M. Mitsuhashi, S. Choi, Y. Shimada, M. Maeda, J.L. MacManus-Driscoll, S.X. Dou, Microscopic role of carbon on MgB₂ wire for critical current density comparable to NbTi. *NPG Asia Mater.* **4**, e3 (2012)
16. M.A. Susner, S.D. Bohnenstiehl, S.A. Dregia, M.D. Sumption, Y. Yang, J.J. Donovan, E.W. Collings, Homogeneous carbon doping of magnesium diboride by high-temperature high-pressure synthesis. *Appl. Phys. Lett.* **104**, 162603 (2014)
17. M. Burdusel, G. Aldica, S. Popa, M. Enculescu, P. Badica, MgB₂ with addition of Sb₂O₃ obtained by spark plasma sintering technique. *J. Mater. Sci.* **47**, 3828 (2012)
18. M. Eisterer, Magnetic properties and critical currents of MgB₂. *Supercond. Sci. Technol.* **20**, R47 (2007)
19. D. Wang, H. Zhang, X. Zhang, S. Tang, Y. Ma, H. Oguro, S. Awaji, K. Watanabe, Effects of three different homemade nanocarbons doping on the superconducting properties of MgB₂ tapes. *Physica C* **508**, 49 (2015)
20. Z. Ma, Y. Liu, W. Hu, Z. Gao, L. Yu, Z. Dong, The enhancement of J_c in nano SiC-doped MgB₂ superconductors rapidly synthesized by activated sintering at low-temperature. *Scripta Mater.* **61**, 836 (2009)

21. L.B.S. Da Silva, D. Rodrigues Jr., G.D. Serrano, V.C.V. Metzner, M.T. Malachevsky, and A. Serquis, MgB₂ Superconductors With Addition of Other Diborides and SiC, *IEEE Trans. Appl. Supercond.* **21**, 2639 (2011)
22. E. Martínez, P. Mikheenko, M. Martínez-López, A. Millán, A. Bevan, J.S. Abell, Flux pinning force in bulk MgB₂ with variable grain size. *Phys. Rev. B* **75**, 134515 (2007)
23. K.A. Ziq, P.C. Canfield, J.E. Ostenson, D.K. Finnemore, Scaling of flux pinning with the thermodynamic critical field. *Phys. Rev. B* **60**, 3603 (1999)
24. A.F. Salem, K.A. Ziq, A.A. Bahgat, Scaling behavior in aluminum doped MgB₂ superconductor. *J. Supercond. Nov. Magn.* **26**, 1517 (2013)
25. Q. Cai, Y. Liu, Z. Ma, H. Li, L. Yu, Variation of pinning mechanism and enhancement of critical current density in MgB₂ bulk containing self-generated coherent MgB₄ impurity. *Appl. Phys. Lett.* **103**, 132601 (2013)
26. Q. Cai, Y. Liu, Z. Ma, L. Yu, Significant enhancement of critical current density in Gly-doped MgB₂ bulk by tailoring the formation of MgO. *Scripta Mater.* **67**, 92 (2012)

Chapter 12

Superconductivity in the Two-Dimensional Electron Gas at Transition Metal Oxide Interfaces



J. C. Nie

12.1 Introduction

In recent years, the development of the silicon-based semiconductor industry has encountered bottlenecks. Scientists have begun to search for new materials and devices that have more advantages in speed, functionality, energy consumption, and portability. Due to the coupling of multiple degrees of freedom such as charge, spin, and lattice in transition metal oxides, together with the further regulation of these degrees of freedom by the boundary, the transition metal oxide heterojunction shows rich properties and functions that are unmatched by traditional semiconductors. Among them, the high carrier mobility in the two-dimensional electron gas (2DEG) of $\text{LaAlO}_3/\text{SrTiO}_3$ (LAO/STO) heterojunctions has attracted much attention. This system shows many novel physical properties, including tunability, superconductivity, ferromagnetism, coexistence of superconductivity and ferromagnetism, Rashba spin-orbit coupling, etc. It has broad prospects for new devices such as superconductivity, spintronics, and topologically related applications. On the other hand, some basic issues have not been solved, yet. We mention the origin of 2DEG at the interface, the superconducting pairing mechanism, the origin of ferromagnetism, the coexistence of superconductivity and ferromagnetism, and so on. Therefore, the study of LAO/STO and other transition metal oxide heterojunction is full of opportunities and challenges. This chapter tries to make a brief presentation of the state of the art in the field based on literature and contributions from our group at Beijing Normal University (BNU).

J. C. Nie (✉)

Department of Physics, Beijing Normal University, Beijing, People's Republic of China
e-mail: jcnie@bnu.edu.cn

12.2 Different Aspects of 2DEG

12.2.1 Discovery and Formation of 2DEG at LAO/STO Interface

In 2002, A. Ohtomo et al. successfully prepared the heterojunction of Mott insulator LaTiO_3 (LTO) and band insulator SrTiO_3 (STO) [1]. Unexpectedly, they discovered that the LTO/STO double-layer structure is conductive, and its conductivity stems from charge transfer: the electrons in the LTO are transferred to the STO [2]. Two years later, they used pulsed laser deposition (PLD) to prepare two different types of LAO heterojunctions [3] on (001) oriented STO substrates. This crystalline perovskite structure ABO_3 can be seen as a stack of two layers of AO and BO_2 . Therefore, for the LAO/STO(001) interface, there are two different ways of stacking, as shown in Fig. 12.1. In the left figure, LAO is deposited on the TiO_2 -terminated STO, and the right figure on the SrO-terminated STO. In this way, stacking structures of $(\text{LaO})^+ / (\text{TiO}_2)^0$ and $(\text{AlO}_2)^+ / (\text{SrO})^0$ are formed at the interface. It was found that the interface formed for the first stacking mode $(\text{LaO})^+ / (\text{TiO}_2)^0$ is highly conductive, while the interface formed by the second stacking mode $(\text{AlO}_2)^+ / (\text{SrO})^0$ is insulating. As it is well known, both LAO and STO belong to band insulators, and intrinsically they are not conductive. However, their interfaces have good conductivity, and the conductivity depends on the stacking mode of the two structures. That is, if an atomic layer of SrO is artificially inserted at the beginning of the sample preparation process, it will cause a huge difference in interface conductivity.

In Fig. 12.2 are shown the results of the electrical transport measurement on the $(\text{LaO})^+ / (\text{TiO}_2)^0$ interface prepared at different oxygen pressures. It can be seen that this type of interface has good conductivity. The oxygen pressure during film

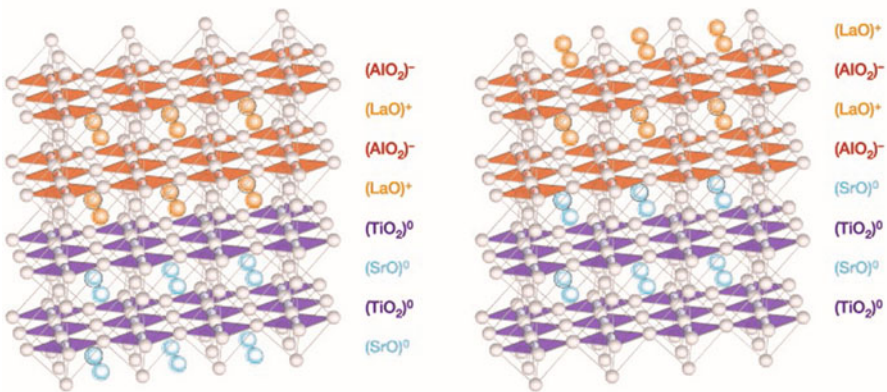


Fig. 12.1 Two different LAO/STO stacking structures reproduced with permission from [3]

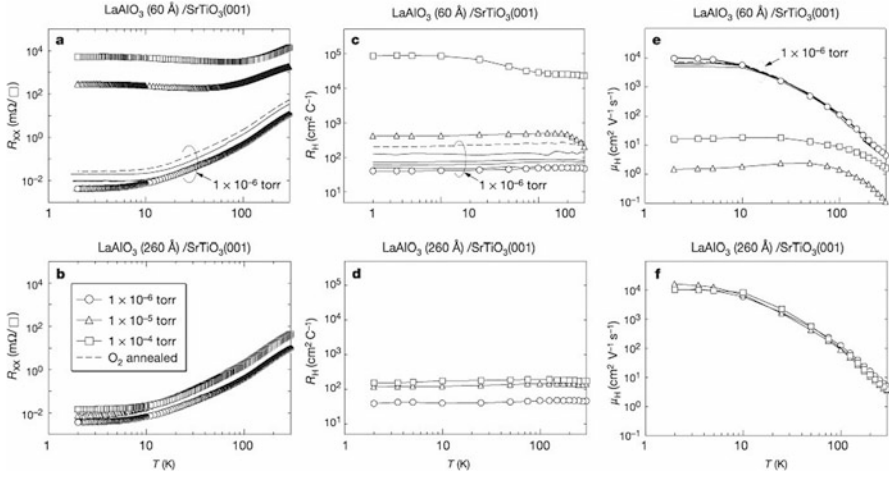


Fig. 12.2 Transport properties of $(\text{LaO})^+ / (\text{TiO}_2)^0$ interface prepared at different oxygen pressures reproduced with permission from [3]

growth has a weak influence on the conductivity of the thicker LAO heterojunction interfaces and has a strong influence on the conductivity of the thin LAO heterojunction interfaces. For the heterojunction with a thin LAO layer, the carrier mobility in the interface at low temperature is as high as $10,000 \text{ cm}^2 \text{ V}^{-1} \text{ s}^{-1}$. There is also a significant oscillation of the magnetoresistance at low temperatures [4].

12.2.2 The Origin of 2DEG

Observations from the previous section lead to the following key questions: what is the reason for the conductivity of the LAO/STO(001) interface and what is the mechanism? In a first instance, we note the difference between the LAO and STO materials, the two different stacking types constructing this interface, and the valence states of the elements (Sr^{2+} , Ti^{4+} , La^{3+} , Al^{3+} , O^{2-}). For STO, its stacking layer is electrically neutral ($(\text{SrO})^0, (\text{TiO}_2)^0$) and nonpolar. The LAO stacking layer has a charge ($(\text{AlO}_2)^-, (\text{LaO})^+$) and is polarized. In this way, the interface formed by the nonpolar STO and the polar LAO will produce a built-in electrical field E , which will lead to a potential that changes with the thickness of the LAO. The interface is polar-discontinuous, and the discontinuity is named “polar catastrophe” [5–7]. For the n-type interface (Fig. 12.3a), to offset the “polar catastrophe,” half an electron is transferred from LAO layer to the interfacial TiO_2 layer. Thus, the distribution of potential along the LAO thickness is limited. For the p-type (see Fig. 12.3b), the process is similar to the n-type, except that half of the electron is transferred from the SrO layer to the LAO layer. This electronic reconstruction results in a net

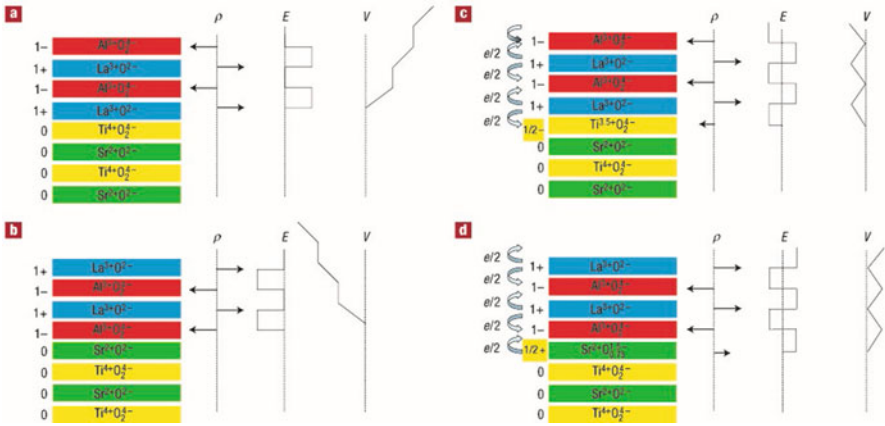


Fig. 12.3 The polar catastrophe illustrated for atomically abrupt (001) interfaces between LAO and STO reproduced with permission from [5]

transfer of half an electron and in the n-type interface it allows good conductivity as expected and as it is determined experimentally. One of the important evidences supporting this viewpoint is the critical thickness of LAO [8]: only when LAO's thickness $d \geq 3$ u.c., the interface will have conductivity.

Although the above simple model explains well the metallic behavior of the LAO/STO interface, according to this model, the p-interface should also be conductive, but it is actually insulating [3, 9, 10]. The conductivity of the interface measured experimentally depends closely on the oxygen pressure during film growth and post-annealing, suggesting that the oxygen vacancy in the STO can be used as an electronic donor to provide carriers (Fig. 12.4a) [11]. Furthermore, charge exchange (cation intermixing) between different valence cations at different interfaces cannot be ignored (Fig. 12.4b) [12, 13]. The experimental results of transmission electron microscopy and X-ray diffraction indicates that the interface of the heterojunction at atomic level is not always clear [5, 14, 15].

Despite having been extensively studied for more than 10 years, the origin of the 2DEG at (001) LAO/STO interfaces is still under debate [5, 14–21]. Three main mechanism were proposed:

1. The most popular mechanism is the polar catastrophe model [3, 5], already mentioned in the above paragraphs. In order to avoid divergence of the electrostatic potential induced by polar discontinuity at the $(\text{LaO})^+ / (\text{TiO}_2)^0$ interface, at a critical thickness (t_c) of four monolayers (ML) of LAO [8, 17, 22–24], half an electron is transferred from LAO to the interface to form the 2DEG, so that Ti^{3+} occurs and the accumulated electric field in LAO is eliminated. However, within t_c , the predicted electric field was not found [23, 25, 26], and unexpected Ti^{3+} signals appeared instead [25, 27, 28]. Beyond t_c , a built-in field across LAO still exists [19]. Moreover, recent experiments indicate that even at (110)

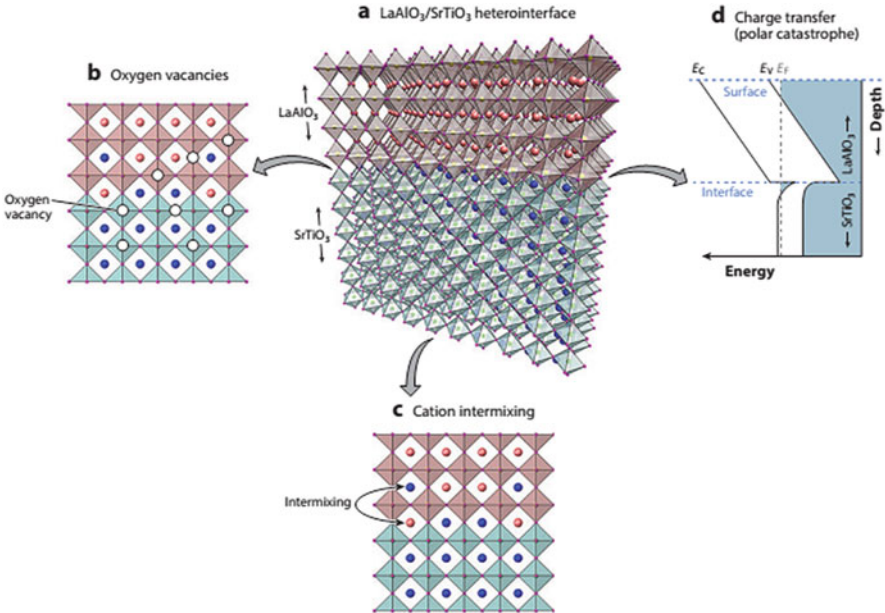


Fig. 12.4 (a) Conductivity mechanism of LAO/STO interface reproduced with permission from [16]; (b) oxygen vacancies, (c) cation intermixing, and (d) polar catastrophe

LAO/STO interfaces, where both LAO and STO stacking have the sequence $(\text{ABO})^{4+}/(\text{O}_2)^{4-}$ avoiding any polar discontinuity in the ionic limit [29, 30], unexpectedly high-mobility metallic conductivity was found [30, 31]. Recently, 2D superconductivity at (110) LAO/STO interfaces was also reported [32, 33]. These observations place some doubt on the most popular mechanism.

2. “ $\text{La}_{1-x}\text{Sr}_x\text{TiO}_3$ intermixing layers” were observed at the (001) LAO/STO interfaces in many studies [14, 34–37], and they were used to explain the conductivity based only on the fact that the $\text{La}_{1-x}\text{Sr}_x\text{TiO}_3$ bulk is metallic between $x = 0.05$ and 0.95 [38, 39]. But the microscopic physical nature of the $\text{La}_{1-x}\text{Sr}_x\text{TiO}_3$ intermixing layer is still unclear and little attention has been paid to this mechanism until now.
3. “Oxygen vacancies in STO” contribute extra carriers [12, 18, 21, 40]. This cannot be the underlying origin because the conductivity is preserved in the post-annealed samples [21]. In addition, the p-type [(001) LAO/SrO-STO] interfaces would be conductive if the “oxygen vacancies” mechanism would be valid [3].

To sum up, the biggest controversies mainly focus on the (i) and (ii) mechanisms, which have been considered to be independent or even mutually exclusive ones. The two mechanisms are debated for more than 10 years without a conclusion. The question on what exactly is the key ingredient for the formation of the 2DEG at LAO/STO interfaces remains open for discussions. In the next paragraph, despite

its limitations, we shall return to the polar catastrophe mechanism and discuss some details reconsidering also the other models.

As mentioned above, if the most widely accepted “polar catastrophe” mechanism works, the (110) LAO/STO interfaces should not be conductive, but actually it is just the opposite situation. In fact, for conventional semiconductor heterojunctions, the 2DEG is generated at a potential well created by band bending due to the presence of an electrostatic field at the interfaces. Han et al. at BNU [41] reported that this mechanism still works in a multivalent oxide heterojunction: for (110)LAO/STO heterojunctions, the coexistence of La and Ti in the unit cell of the ABO₃ perovskite at the interface reduces the valence of Ti, generating a local field leading to band bending in the interfacial STO layers (Fig. 12.5). The extra free electrons are trapped in this bent conduction band forming a 2DEG. The proposed electrostatic model unifies two independent mechanisms for 2DEG at LAO/STO interfaces, namely the “polar catastrophe” and the “La_{1-x}Sr_xTiO₃ layers” models. It also opens new possibilities for atomic-scale band engineering to control the behavior of complex oxide heterojunctions.

The 2DEG at transition metal oxide interface is of two main types:

- One is the *c*-2DEG: it forms at a crystalline/crystalline interface (*c*-interface), such as crystalline *c*-LAO/STO [3].
- The other type is *a*-2DEG: it forms at an amorphous/crystalline interface (*a*-interface), such as *a*-LAO/STO [30].

They have similar physical properties in terms of superconductivity [42, 43], potential-well depth [44], and so on. The *a*-2DEG presents also many notable

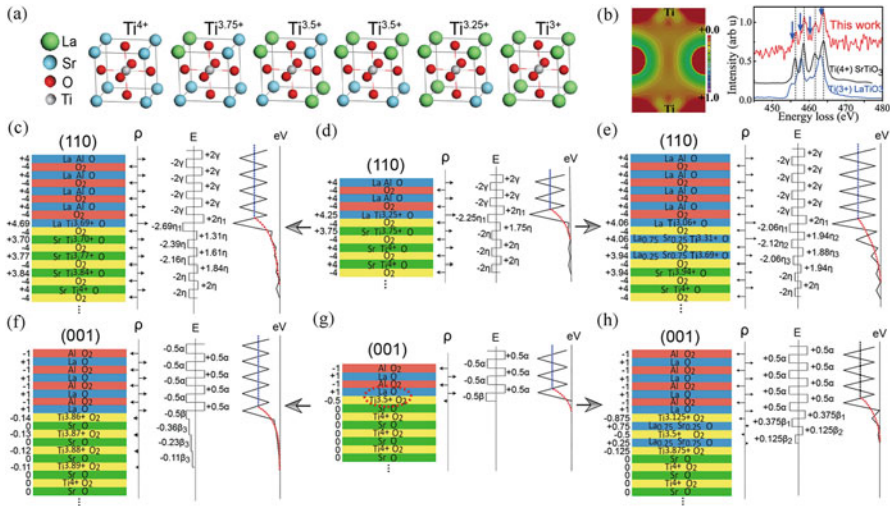


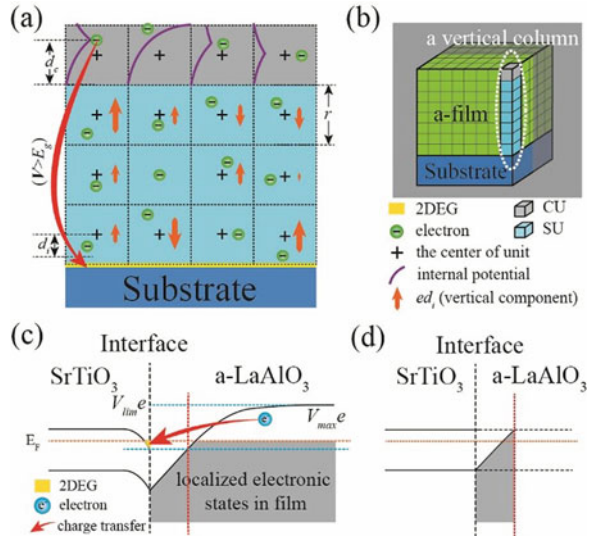
Fig. 12.5 Electrostatic models of band bending in STO of both (001) and (110) LAO/STO interfaces reproduced with permission from [41]

differences compared with *c*-2DEG, such as less lattice strain at the interface, a higher interface carrier density (n_s), and considerably fewer requirements for growth. For example, a high growth temperature and TiO₂-terminated substrates are not needed for STO-based *a*-2DEG [21, 45, 46]. Unlike *c*-2DEG, t_c of *a*-2DEG formation and the electronic transport properties depend highly on the growth conditions, especially on the oxygen pressure [21, 45]. These differences make the *a*-2DEG a powerful, controllable, and easy to manufacture 2DEG system. Research on the *a*-2DEG is relatively scarce, and its origin requires in-depth future exploration. Noteworthy are also other differences between *a*- and *c*-interfaces related to their nature. As addressed before, the properties of the films and the polar discontinuity at the interfaces are considered the key factors in the *c*-interface systems [20, 47, 48]. Properties of the amorphous films are quite different from those of the crystalline films and there is no polar discontinuity at *a*-interfaces. The amorphous films grow at significantly lower temperature than their crystalline counterparts. The dependence on oxygen pressure of the amorphous and crystalline films will be different meaning that the influence of the oxygen vacancies in the two systems is not comparable [21, 45]. Therefore, the experimental and theoretical findings for *c*-interfaces cannot be directly applied to *a*-interfaces. The current supposition is that the *a*-2DEG originates from oxygen vacancies that form in the substrate near the interface (oxygen vacancy theory) [49–51]. In this theory, oxygen ions diffuse from the STO substrate to the film, causing formation of a high-concentration of oxygen vacancies at the STO side near the interface, thus generating the *a*-2DEG. This theory is important and innovative. Oxygen vacancies are a critical factor, but other fundamental mechanisms may also be involved in the formation of the *a*-2DEG. Li et al. at BNU [52] found that the percentage of low valence cations, the ionization energy of cations in film, and the band gap of substrates should be considered decisive for the formation of 2DEG at the interface of amorphous/crystalline oxide (*a*-2DEG). Following these findings, Li et al. inferred that the charge transfer from the film to the interface should be the main mechanism of the *a*-2DEG formation. The charge transfer is induced by oxygen defects in the film and can be eliminated by the electron-absorbing process of cations in the film (Fig. 12.6). Based on this, they proposed a simple dipole model that successfully explains the origin of the *a*-2DEG.

12.2.3 Dimensionality of the Interface Conductivity

In the conductive LAO/STO interface, one of the most interesting questions is whether conductivity occurs in a 3D STO or at the 2D interface. Herranz et al. reported that the high-mobility conduction has three-dimensional characteristics [40], and Basletic et al. indicated that the STO substrate is conducting [53]. Hence, the electron gas may be distributed near the interface with a specific distribution. The approaches to study the thickness of the electron gas at LAO/STO interfaces are divided into two main categories:

Fig. 12.6 (a) Schematic diagram of “dipole model” model. (a) is a cutaway view of (b), the gray plane in (b) is the cut plane. (c, d) The schematic diagram of the band alignment of a-LAO/STO interface when the film is thicker (c) or thinner (d) than the critical thickness of charge transfer (the red vertical dashed lines) reproduced with permission from [52]



- One method is to achieve this by directly probing the cross section of LAO/STO samples. Conducting-tip atomic force microscopy (CT-AFM), which can map out the local resistance with a resolution of nanometers, can reveal the spatial distribution of the electrons. Figure 12.7a shows the mapping diagram of resistance between needle tip and sample by the cross-sectional CT-AFM scans of the annealed LAO/STO(001) heterojunction. The area of the small resistance is very narrow, with a width of about 7 nm [54]. The cross-sectional scanning tunneling microscope (STM) can also directly measure the size of the conductive area of the interface. Figure 12.7b shows the cross-sectional distribution of differential conductivity for the annealed LAO/STO (001) heterojunction [55]. The metallic region is very narrow, of about 0.8 nm. These experimental results [54, 55] show that in the LAO/STO (001) interface, conductivity is 2D at room temperature. However, an irrecoverable damage occurs in LAO/STO samples when CT-AFM and STM are used to scan the cross sections.
- The other method uses electrical transport measurements, including Shubnikov–de Haas (SdH) oscillations [40] and the orbital effect [56]. The frequency of the SdH oscillations and orbit-dependent magnetoresistance (MR) observed along the in-plane and out-of-plane directions are the key observations.

None of the above reports on the electron gas thickness address its temperature dependence and the critical factors that contribute to it. Xue H. X. et al. at BNU [57] studied the temperature dependence of the conductive layer thickness at the LAO/STO heterointerface. By comparing the in-plane and out-of-plane orbit-dependent magnetoresistance under a magnetic field of 9 T, the conductive layer thickness of the LAO/STO interface is determined for temperatures between 45 and 300 K. Since the influence of spin-orbit coupling cannot be ignored when

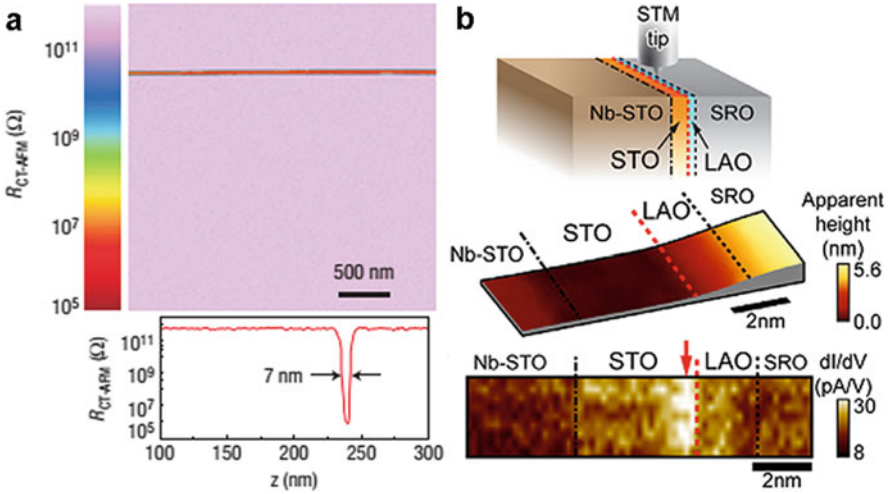


Fig. 12.7 (a) The mapping diagram of resistance by the cross-sectional c-AFM scans [53]. (b) The cross-sectional distribution of differential conductivity reproduced with permission from [55]

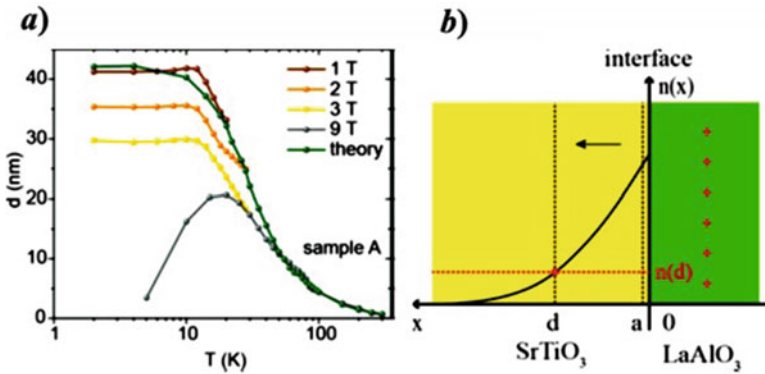


Fig. 12.8 (a) Comparison between experimental results for the conductive layer thickness d and theoretical predictions as a function of temperature between 2 and 300 K. (b) Schematic diagram of the electron gas distribution on the STO side reproduced with permission from [57]

considering the conductive layer thickness dependence at temperatures below 45 K, a lower magnetic field is employed. The results show that the thickness increases gradually and then remains constant as the temperature decreases (Fig. 12.8). Such a tendency is well reproduced theoretically by considering the equilibrium between drift and diffusion of electrons near the interface. The thickness mainly depends on the relative permittivity of the SrTiO₃ and the electron mobility, and it is independent of the sheet carrier density. These investigations show that the dimensionality of the confined zone for electrons can be controlled and can be used as a reference for other interfacial systems.

12.3 Interface Superconductivity

As early as the 1960s, physicists proposed the concept of interface superconductivity [58–62]. Does 2D superconductivity exist? What are the characteristics of 2D superconductivity? How does the reduced dimensionality affect the transition temperature of superconductors? And so on . . . These questions have always been of great concern to researchers. Subsequently, the discovery of high-temperature superconductors (HTSs) consisting of 2D superconducting layers (see Fig. 12.9) made it possible to pay more and more attention to the superconductivity of low-dimensional systems, and the development of technology allowed growth of flat 2D structures at atomic level [63]. The study of superconductivity at interfaces can bring a new understanding of the physics of high-temperature superconductivity. The effects of disorder, fluctuation, and correlation in low-dimensional systems can also be studied in the interface superconducting systems with new opportunities and challenges in materials physics.

12.3.1 2D Superconductivity at the LAO/STO Interface

Superconductivity has been found at various interfaces, such as insulator/insulator interface, semiconductor/semiconductor interface, and metal/insulator interface. The most representative superconducting system is the LAO/STO interface. LAO and STO are band insulators. Superconductivity and insulation features are independent behaviors. One of the prerequisites for superconducting condensation is the presence of carriers on the Fermi level. As early as 1980, it has been reported that Nb:SrTiO₃ has multiband superconductivity [64–66].

In 2007, Reyren et al. discovered superconductivity [42] at LAO/STO (001) interface. As shown in Fig. 12.10, near 200 mK, the resistance of 2DEG begins to drop sharply, and zero resistance is attained at lower temperatures. The zero resistance state is completely suppressed under a magnetic field of 180 mT perpendicular to the interface. The coherence length in the plane is about 70 nm. The legitimate question

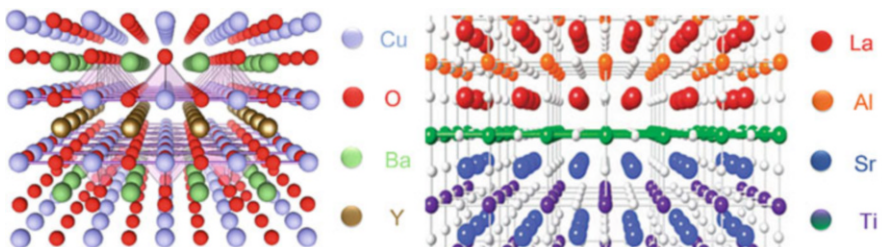


Fig. 12.9 Comparison of atomic structures of copper oxide HTS YBaCuO_{7-x} and LAO/STO(001) heterojunction

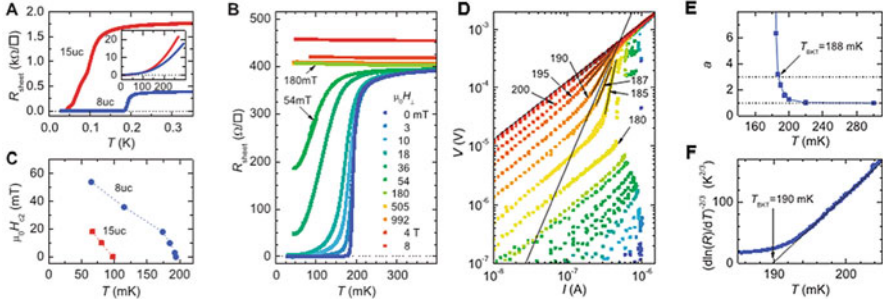


Fig. 12.10 2D superconductivity of LAO/STO(001) interface reproduced with permission from [42]

is: Does superconductivity at the interface, belong to a 3D type as for bulk SrTiO₃ or to 2D and it is specific for the interface? To provide a reply, the I-V characteristics of the superconducting interface were measured and analyzed. Results are in good agreement with Berezinskii-Kosterlitz-Thouless (BKT) transition [67–71]. For BKT transition, at its characteristic transition temperature T_{BKT} , the vortex-antivortex pair of the system will be broken and the superconducting state will be transformed into a non-superconducting state [72]. During BKT transition, the current-induced Lorentz force causes dislocation-antidislocation pairs to unbind, resulting in a $V \propto I^\alpha$ behavior, with $\alpha(T_{\text{BKT}}) = 3$ [73, 74]. In addition, the $R(T)$ characteristics are consistent with a BKT transition, for which, close to T_{BKT} , a $R = R_0 \exp(-bt^{-1/2})$ dependence is expected [75]. Here, R_0 and b are material parameters and $t = T/T_{\text{BKT}} - 1$. The experimental results are in good agreement with the two relationships and $T_{\text{BKT}} \sim 190\text{mK}$. The superconducting transition of the samples is therefore consistent with that of a 2D superconducting film. Subsequently, Reyren et al. [76] reported that the critical magnetic field at the LAO/STO(001) interface has anisotropy $\epsilon = H_{c2}^{\parallel}/H_{c2}^{\perp} \approx 25$. (Fig. 12.11). The thickness of the superconducting layer at the LAO/STO(001) interface is about 10 nm, which further verifies the 2D nature of the superconductivity at the interface.

In addition to LAO/STO(001) interface superconductivity, 2D superconductivity at other oxide interfaces has been found successively, such as LaTiO₃/SrTiO₃(001) [77, 78], amorphous Al₂O₃/SrTiO₃(001) [79], and also LAO/STO(110) by Han et al. at BNU [32].

12.3.2 Unconventional Superconductivity at LAO/STO Interface

Because both STO and LAO have high dielectric constants, the properties of the 2DEG can be controlled by applying an external electrical field. Being at the core of the field effect transistor device, the electrostatic control method has been widely

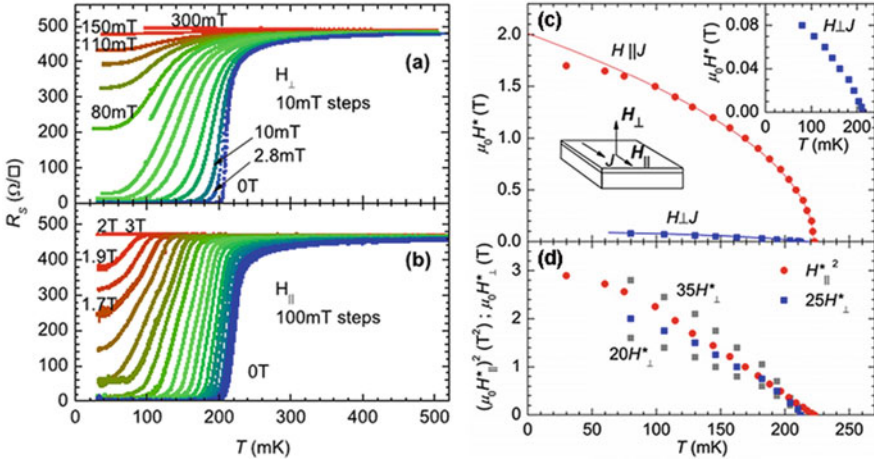


Fig. 12.11 Anisotropic critical magnetic field at LAO/STO interface. Reproduced from [76]

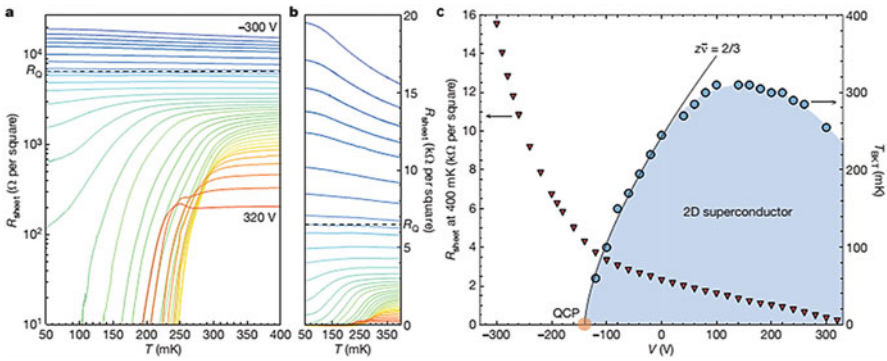


Fig. 12.12 Field-effect modulation of the transport properties of the LAO/STO interface reproduced with permission from [81]

used to study many materials. By changing the carrier concentration of the system, the properties of materials can be greatly changed [80]. In 2008, A. D. Caviglia et al. tuned the superconductivity of LAO/STO (001) interface by applying an electrical field on the back of STO, and the back-gate-voltage (V_G) induced the quantum phase transition from superconductor to insulator [81]. In Fig. 12.12a, the transition from superconducting to insulating ground state occurs at a critical sheet resistance of $R_c \approx 4.5 \text{ k}\Omega$ per square, close to the quantum of resistance for bosons with charge $2e$, $R_Q = h/4e^2 \approx 6.45 \text{ k}\Omega$. A further increase in the electron density produces first a rise of the critical temperature (T_c) to a maximum of $\sim 310 \text{ mK}$. For larger voltages, T_c decreases again, forming a dome-like superconducting region similar to that of HTSs, with “underdoped” and “overdoped” regions. The appearance of the dome-shaped superconducting region similar to copper oxide HTSs suggests that the superconducting pairing mechanism of LAO/STO interface may be unconventional.

In 2013, Richter et al. directly measured the superconducting energy gap of superconductivity at LAO/STO(001) interface using a Au/LAO/STO(001) planar junction [82]. Using this metal-insulator-superconductor tunnel junction, the electron state density near the Fermi surface in the superconductor can be measured. As mentioned in the previous paragraph, the back-gate-voltage can greatly tune the superconductivity of the interface. By changing the back-gate-voltage, the tunnel spectrum at different V_G can be measured. A typical superconducting spectrum is in Fig. 12.13: the energy gap is very small, only a few tens of μeV . Surprisingly, for all V_G , there is always an energy gap and it increases as V_G decreases. On the other hand, with the change of V_G , the T_c of the system has a dome-shaped dependence. In general, the change in the superconducting energy gap should be consistent with T_c , and this experimental result shows that the energy gap has always existed, even in non-superconducting regions. For copper oxide HTS, there is the so-called “pseudogap” in its phase diagram, and its superconducting region is also dome-shaped. The pseudogap has always existed above the superconducting region, and it increases with the decrease of hole concentration. Similar phenomena were also observed by other groups [83–86]. For superconductivity at LAO/STO interface, the

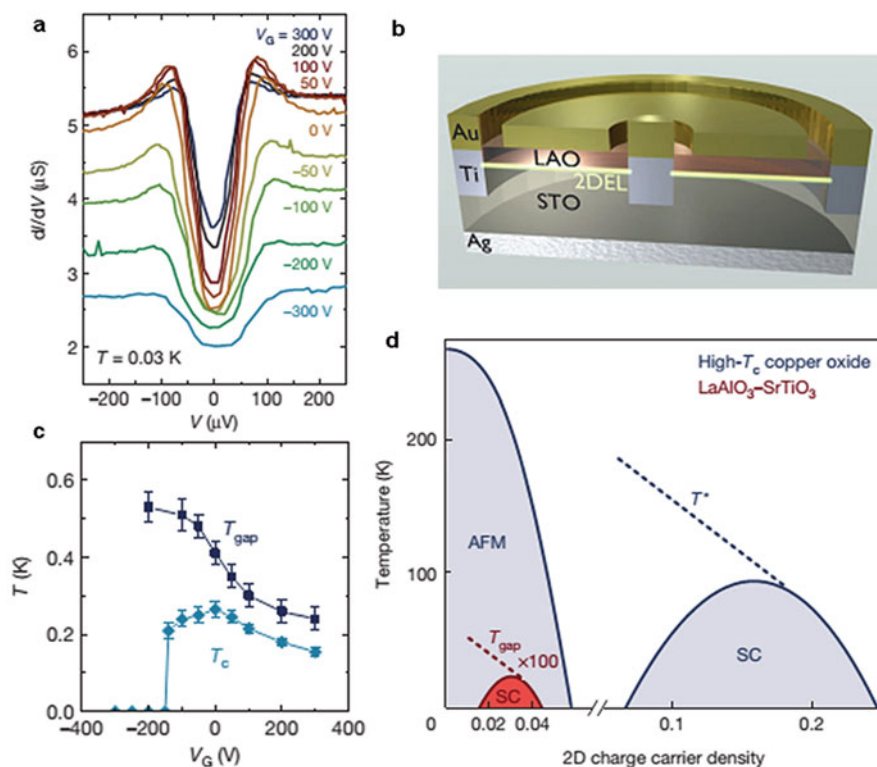


Fig. 12.13 Pseudogap-like behavior in LAO/STO(001) interface reproduced with permission from [82]

existence of the analogous phase diagram to that of HTS, point on an unconventional superconducting pairing mechanism claimed for HTS systems.

12.3.3 Coexistence of Superconductivity and Ferromagnetism

In the LAO/STO(001) interface, apart from the superconducting state, the ground state may also have ferromagnetism [87–91]. There is even coexistence of superconductivity and ferromagnetism [92–97] (Fig. 12.14). In 2007, Brinkman et al. reported that the LAO/STO(001) interface growing under high oxygen pressure is

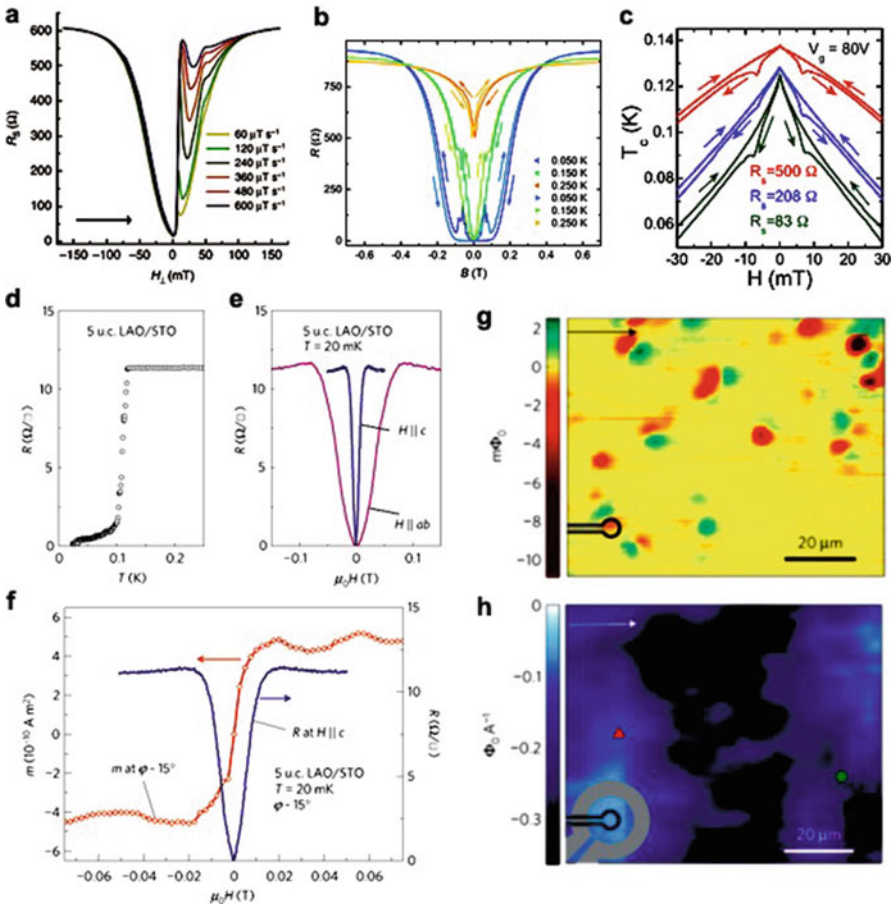


Fig. 12.14 Coexistence of superconductivity and ferromagnetism at LAO/STO interface reproduced with permissions from [102] (panel (a)); [97] (panel (b)); [92] (panel (c)); [94] (panels (d), (e), (f)); [95] (panels (g), (h))

magnetic [87]. Shortly after, Dikin et al. found the coexistence of superconductivity and ferromagnetism at the LAO/STO(001) interface [92]. Recently, Shen et al. at BNU reported [97] similar hysteretic magnetoresistance at the superconducting LAO/STO(110) interfaces as the transport evidence for coexistence of superconductivity and ferromagnetism. These experimental results indicate that the LAO/STO(001) interface may have unconventional superconductivity. A series of theoretical studies also support unconventional superconductivity. For example, Michaeli et al. [98] introduced a theoretical model to explain the phenomenon of the coexistence of superconductivity and ferromagnetism at the interface. A half-charge per unit cell is transferred to the interface layer and forms a lattice of local moments due to Coulomb repulsion. The local moments order ferromagnetically via exchange with lower density bands of mobile electrons residing in Ti layers near the interface. The large ferromagnetic exchange would usually kill superconductivity in these mobile bands. However, the presence of a large spin-orbit coupling enables the formation of a Fulde-Ferrell-Larkin-Ovchinnikov (FFLO) state [99, 100], which can coexist with strong magnetism. In the FFLO state, Cooper pairs form with finite pair momentum perpendicular to the direction of magnetic ordering. Scheurer and Schmalian established a model to study the symmetry of superconducting order parameter and concluded that electron pairing is non-traditional and is directly related to nontrivial topological invariants. Topology and unconventional superconductivity exist at the LAO/STO interface [101].

Some researchers believe that the superconductivity of the LAO/STO interface is a traditional Bardeen-Cooper-Schrieffer (BCS) pairing mechanism. Bert J. A. et al. measured the local magnetization associated with superfluid density in the LAO/STO(001) interface by a scanning superconducting quantum interface device (Scanning-SQUID) [103]. It was found that the temperature dependence of the superfluid density at different gate voltages collapses to a single curve that is characteristic of a full superconducting gap. Benfatto et al. [104] and Caprara et al. [105–107] explained the superconducting phase diagram of LAO/STO(001) interface analogous to that of HTSs, as being the consequence of finite-size effects, mesoscopic inhomogeneities of T_c and of the electron density, which may cause the percolation transition. To explain the coexistence of superconductivity and ferromagnetism, some studies suggested that it may be due to the phase separation of the ferromagnetic region and the superconducting region [95], or ferromagnetism and superconductivity come from different orbital states [108].

Section 3.3 indicates that the origin of the ferromagnetism and the coexistence of superconductivity and ferromagnetism are unsolved problems for the LAO/STO interface systems, and they deserve more attention.

12.3.4 Unconventional Superconducting Pairing Mechanism

In the microscopic mechanism of superconductivity, the most important thing is the formation of Cooper pairs. The reason why the BCS theory requires two

electron pairs with opposite spins is to satisfy Pauli's principle of incompatibility: the two electrons of Cooper pair, as Fermions, satisfy the condition that the total wave function is antisymmetric after the position exchange. Since BCS theory first studied the most basic two electrons in the same orbit, the requirement is that spin is opposite (spin singlet). After BCS theory was proposed, the possible pairing mechanisms of superconductivity, spin singlet and triplet pairing, were identified and studied. S-wave is the conventional pairing of spin singlet, d-wave is the unconventional pairing of spin singlet, and p-wave is the unconventional pairing of spin triplet. In conventional superconductors and high-temperature copper oxide superconductors, Cooper's space wave functions are described as "s-wave" and "d-wave", respectively. Their total orbital quantum numbers L are 0 and 2, and the total spin quantum numbers S are 0 meaning that pairs are singlet. Sr_2RuO_4 is considered to be a "p-wave" superconductor of spin-triplet pairing [109–112], and the orbital quantum number L is 1 and the spin quantum number S is equal to 1. This is very similar to the situation of the He3 condensed state, but more powerful experiments are needed to finally determine the p-wave structure of its electron pair.

In the 2DEG at the LAO/STO interface, the combination of 2D superconductivity and Rashba spin-orbit coupling (SOC) is expected to give rise to an unconventional superconducting ground state [101, 113], including a mix of spin-singlet and spin-triplet components [114, 115]. Recently, Stornaiuolo D. et al. [116] studied the superconducting state of the 2DEG at the LAO/STO interface using Josephson junctions as spectroscopic probes. The transport properties of these devices reveal the presence of two superconducting gap-structures and of an unconventional superconducting π channel. These features provide evidence of an unconventional superconducting ground state, possibly related to the interplay between superconductivity and the large Rashba spin-orbit coupling in the 2DEG. For the triplet pairing of p-wave superconductors, spins of Cooper pair are not required to be opposite. Therefore, there can be residual spins to generate magnetism, which is an important direction to study the coexistence of superconductivity and ferromagnetism.

To determine the pairing of the electrons, the phase sensitivity experiments are essential [117–124]: pairing is detected by the quantum interference effect of the Josephson junction. These experiments are only related to the phase of the superconducting energy gap function, not being sensitive to the absolute value of the energy gap. The experimental results completely depend on the macroscopic quantum coherence of the Josephson junction, so that many details of the individual materials are not important. In addition, a sensitive probe of unconventional order is its response to a symmetry-breaking field. For example, in order to probe the proposed $p_x \pm ip_y$ topological superconducting state of Sr_2RuO_4 , Hicks C.W. et al. [125] constructed an apparatus capable of applying both compressive and tensile strains of up to 0.23%. Strains applied along $\langle 100 \rangle$ crystallographic directions yield a strong, strain-symmetric increase in the superconducting transition temperature T_c . $\langle 110 \rangle$ strains give a much weaker, mostly antisymmetric response. This is also an effective method for the assessment of the p-wave superconductors.

Exploration of the pairing mechanism in interface systems should continue and more experiments are necessary.

12.4 Superconductor Insulator/Metal Transition

In physics, there is a phase transition that occurs at absolute zero temperature. This phase transition is called quantum phase transition. It belongs to continuous phase transitions [126–128]. By changing one of the non-thermal parameters of the system, such as magnetic field [129–132], disorder [133, 134], doping [135, 136], and electrostatic regulation [137], the system undergoes a phase transition between different ground states. Since the absolute zero temperature cannot be achieved, we usually study quantum phase transitions by measuring the physical properties affected by quantum fluctuations at finite temperatures. One of the most important examples in quantum phase transitions is the superconductor-insulator phase transition [138–140]. The superconductor-insulator phase transition has been widely studied. In many different types of materials, phase transitions can be observed by changing different parameters. Studies of new materials at lower temperatures or higher fields and new technologies promote discovery of new phenomena and a better understanding of the known ones. In this section, few outstanding issues such as the interaction of disorder and superconductivity in the phase transitions and the properties of insulating states will be addressed.

At present, there are four different scenarios for the disappearance of superconductivity at the 2D limit caused by disorder or magnetic field:

- The first is the so-called Fermion picture [141–143]. This is based on the microscopic perturbation description of a uniform system and considers the interaction between attraction forces and repulsion forces under disorder. In this microscopic description, due to the existence of disorder, long-range Coulomb's repulsion and the suppression of critical temperature follow the renormalization of electronic interactions in the Cooper channel. Disorder causes the inhibition of superconducting order parameters, Cooper pairs split into fermions, and these fermions are localized in the 2D condition.
- The second is the Boson model [144–146]. It holds that in the critical region, the phase fluctuation of Cooper pairs cannot be ignored, Cooper pairs move in a diffusion manner, and these Cooper pairs can be approximately regarded as bosons. In ultrathin films, the superconductor-insulator phase transition can be seen at the zero temperature limit [130, 147]. If it is assumed that Cooper pairs and vortices have complete duality, the critical resistance is the quantum resistance $h/4e^2$.
- The third type is the dissipation model of the resistance shunt Josephson junction array based on granular superconductors [148].
- The fourth type involves percolation effects, especially for the inhomogeneous samples [149].

As introduced before, the 2DEG of LAO/STO interface shows a rich phase diagram, which has different ground states (ferromagnetism, superconductivity), so this system can also be used to study quantum transitions that occur between different ground states. In general, when the parameters cross a certain critical value, the system undergoes a phase transition. The critical behavior of this physical quantity is universal. It is mainly related to the basic properties of systems such as dimensionality and symmetry and has nothing to do with microscopic details. For the magnetic field-induced superconductor-insulator phase transition, it has two significant signs. One is the platform where the resistance does not change with temperature, and the other is that the magnetic resistance at different temperatures intersects at one point. Recently, J. Biscaras et al. reported a magnetic field-induced phase transition from superconducting 2DEG to weakly localized metal in $\text{LaTiO}_3/\text{SrTiO}_3$ (LTO/STO) interface [150]. They found that the magnetoresistance curves at different temperatures intersect at two points. As shown in Fig. 12.15, the magnetic resistance of the high-temperature region (0.1~0.2 K) intersects at one point, and the magnetic resistance of the low temperature region (0.04~0.07 K) intersects at another point. After finite scale analysis, the system has two different critical coefficients. They attributed this to inhomogeneity. The system consists of superconducting islands and non-superconducting metal regions. The system has two characteristic lengths, the de-phase length L_ϕ and the size of the superconducting region L_d . At high temperatures, $L_\phi < L_d$. Therefore, two kinds of critical behaviors are observed.

Shen S. C. et al. at BNU [97] reported the superconductor-metal transition driven by a perpendicular magnetic field in superconducting 2DEG formed at the LAO/STO(110) interface, which offers an appealing platform to study the quantum phase transition from a superconductor to a weakly localized metal. Interestingly, when approaching the quantum critical point, the dynamic critical exponent is not a constant but a diverging value (Fig. 12.16), which is a direct evidence of a quantum Griffiths singularity arising from quenched disorder at ultralow temperatures. The diverging dynamic critical exponent in the 2DEG provides a new way to verify the quantum Griffiths singularity which was also observed in the Ga thin film [151]. This may be considered a hint that different superconducting systems can be possibly treated within a uniform theoretical framework.

In 2014, Shi X. et al. also observed two types of critical behaviors in the poorly doped $\text{La}_{2-x}\text{Sr}_x\text{CuO}_4$ copper oxide superconducting thin films, and the magnetic resistance of the high-temperature zone and of the low temperature zone intersects at two points, respectively [152]. With the increase of the magnetic field, the vortex lattice changes to the vortex glass state, and this transition corresponds to a critical field. With further increase of the magnetic field, the system becomes insulating. This transition also corresponds to a critical field (Fig. 12.16).

Presented experimental results show that for understanding of the superconductor-insulator/metal phase transition further investigations are required (Fig. 12.17).

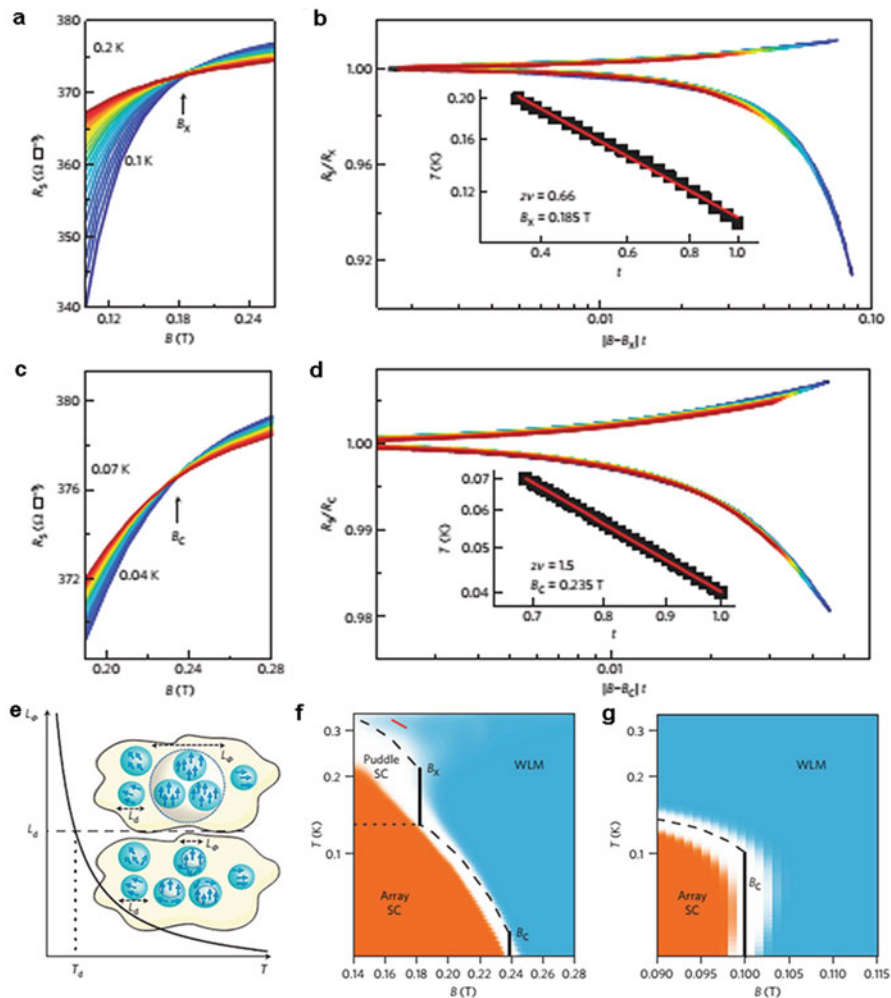


Fig. 12.15 Superconductor-insulator phase transition induced by magnetic field at the LTO/STO(001) interface reproduced with permission from [150]

12.5 Concluding Remarks

Let us briefly recapitulate our main themes.

LAO/STO interface has a high mobility of 2DEG, in which specific physical phenomena such as superconductivity, ferromagnetism, and the coexistence of superconductivity and ferromagnetism are observed. Other transition metal oxide interface systems also show high mobility and similar novel quantum phenomena. Superconducting 2DEG at the LAO/STO interface offers an appealing platform to

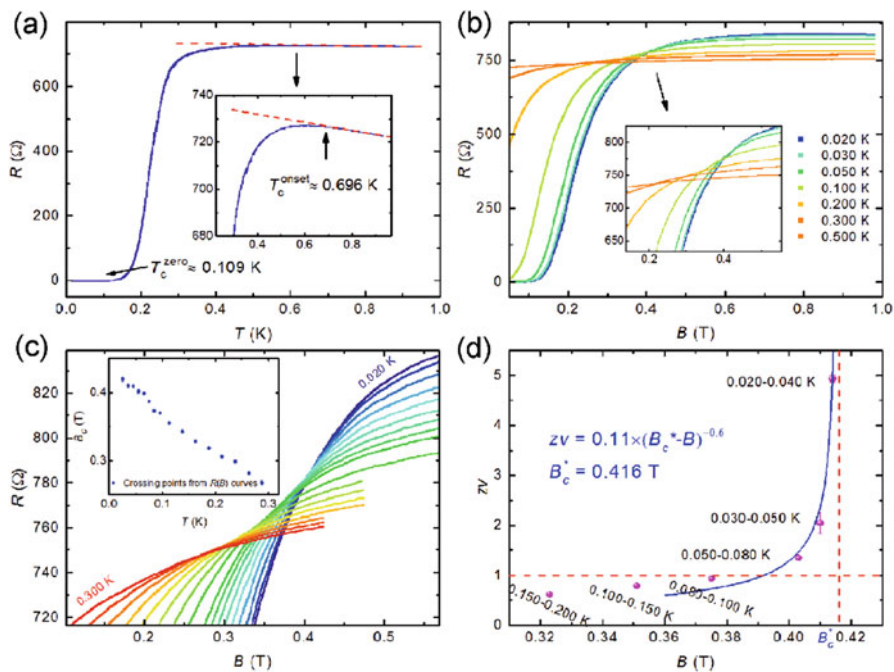


Fig. 12.16 The quantum Griffiths singularity at the LAO/STO(110) interface reproduced with permission from [97]

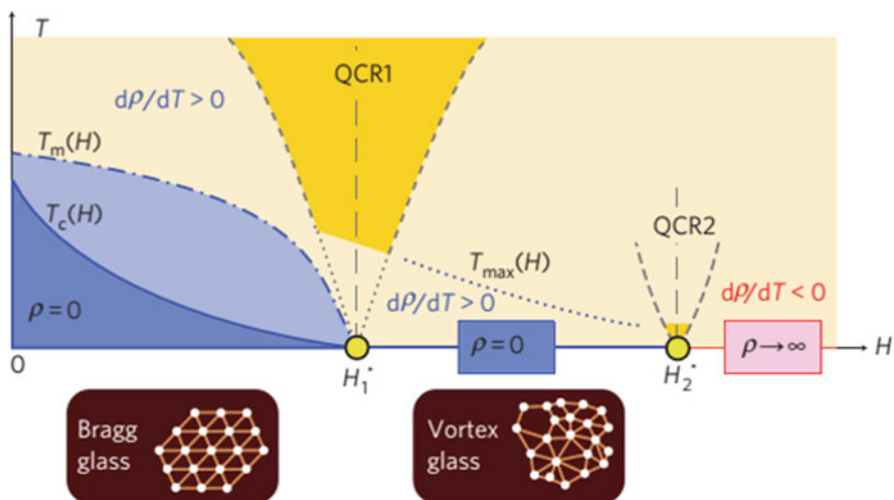


Fig. 12.17 H - T phase diagram of $\text{La}_{2-x}\text{Sr}_x\text{CuO}_4$ copper oxide superconducting thin film reproduced with permission from [152]

study the quantum phase transition from a superconductor to a weakly localized metal.

A general observation is that, although the research on the transition metal oxide interfaces is extensive, there are many outstanding unsolved details and questions, such as the origin of 2DEG, the superconducting pairing mechanism of 2DEG, the origin of ferromagnetism and the coexistence of superconductivity and ferromagnetism, etc. More research is needed.

Study of 2DEG is rewarding and can promote a better understanding of quantum phenomena, in particular of superconductivity and especially of HTS. Once this is accomplished expectations are also to provide new practical ideas.

Acknowledgments This work is supported by the National Natural Science Foundation of China (Grants No. 11674031 and No. 11474022) and the National Basic Research Program of China (Grants No. 2014CB920903 and No. 2013CB921701) for the financial support.

References

1. A. Ohtomo, D.A. Muller, J.L. Grazul, H.Y. Hwang, Artificial charge-modulation in atomic-scale perovskite titanate superlattices. *Nature* **419**(6905), 378–380 (2002)
2. S. Okamoto, A.J. Millis, Electronic reconstruction at an interface between a Mott insulator and a band insulator. *Nature* **428**(6983), 630–633 (2004)
3. A. Ohtomo, H.Y. Hwang, A high-mobility electron gas at the $\text{LaAlO}_3/\text{SrTiO}_3$ heterointerface. *Nature* **427**(6973), 423–426 (2004)
4. A.D. Caviglia, S. Gariglio, C. Cancellieri, B. Sacepe, A. Fete, N. Reyren, M. Gabay, A.F. Morpurgo, J.-M. Triscone, Two-dimensional quantum oscillations of the conductance at $\text{LaAlO}_3/\text{SrTiO}_3$ interfaces. *Phys. Rev. Lett.* **105**, 236802 (2010)
5. N. Nakagawa, H.Y. Hwang, D.A. Muller, Why some interfaces cannot be sharp. *Nat. Mater.* **5**(3), 204–209 (2006)
6. G. Baraff, J.A. Appelbaum, D.R. Hamann, Self-consistent calculation of electronic-structure at an abrupt GaAs-Ge interface. *Phys. Rev. Lett.* **38**(5), 237 (1977)
7. W.A. Harrison, E.A. Kraut, J.R. Waldrop, R.W. Grant, Polar heterojunction interfaces. *Phys. Rev. B* **18**(8), 4402 (1978)
8. S. Thiel, G. Hammerl, A. Schmehl, C.W. Schneider, J. Mannhart, Tunable quasi-two-dimensional electron gases in oxide heterostructures. *Science* **313**(5795), 1942–1945 (2006)
9. A. Ohtomo, H.Y. Hwang, A high-mobility electron gas at the $\text{LaAlO}_3/\text{SrTiO}_3$ heterointerface. *Nature* **441**(7089), 120–120 (2006)
10. J. Nishimura, A. Ohtomo, A. Ohkubo, Y. Murakami, M. Kawasaki, Controlled carrier generation at a polarity-discontinued perovskite heterointerface. *Jpn. J. Appl. Phys. Part 2-Lett. & Express Lett.* **43**(8A), L1032 (2004)
11. Kwok, H. L., *Charge transfer and re-distribution in the $\text{TiO}_2\text{-SrTiO}_3$ heterostructure*[C], IOP Conference Series-Materials Science and Engineering, IOP Publishing, 2010, 8: 012031
12. W. Siemons, G. Koster, H. Yamamoto, W. Harrison, G. Lucovsky, T. Geballe, D.H.A. Blank, M.R. Beasley, Origin of charge density at LaAlO_3 on SrTiO_3 heterointerfaces: Possibility of intrinsic doping. *Phys. Rev. Lett.* **98**(19), 196802 (2007)
13. L. Qiao, T.C. Droubay, T.C. Kaspar, P.V. Sushko, S.A. Chambers, Cation mixing, band offsets and electric fields at $\text{LaAlO}_3/\text{SrTiO}_3$ (001) heterojunctions with variable La:Al atom ratio. *Surf. Sci.* **605**(15), 1381–1387 (2011)

14. P.R. Willmott, S.A. Pauli, R. Herger, C.M. Schlepuezt, D. Martocchia, B.D. Patterson, B. Delle, R. Clarke, D. Kumah, C. Cionca, Y. Yacoby, Structural basis for the conducting interface between LaAlO_3 and SrTiO_3 . *Phys. Rev. Lett.* **99**(15), 155502 (2007)
15. J. Mannhart, D.H.A. Blank, H.Y. Hwang, A.J. Millis, J.-M. Triscone, Two-dimensional Electron gases at oxide interfaces. *MRS Bull.* **33**(11), 1027–1034 (2008)
16. J.A. Sulpizio, S. Ilani, P. Irvin, J. Levy, Nanoscale Phenomena in Oxide Heterostructures. *Ann. Rev. Mater. Res.* **44**(1), 117–149 (2014)
17. M.L. Reinle-Schmitt, C. Cancellieri, D. Li, D. Fontaine, M. Medarde, E. Pomjakushina, C.W. Schneider, S. Gariglio, P. Ghosez, J.-M. Triscone, P.R. Willmott, Tunable conductivity threshold at polar oxide interfaces. *Nat. Commun.* **3**, 932 (2012)
18. J.N. Eckstein, Oxide interfaces - watch out for the lack of oxygen. *Nat. Mater.* **6**(7), 473 (2007)
19. G. Singh-Bhalla, C. Bell, J. Ravichandran, W. Siemons, Y. Hikita, S. Salahuddin, A. Hebard, H.Y. Hwang, R. Ramesh, Built-in and induced polarization across $\text{LaAlO}_3/\text{SrTiO}_3$ heterojunctions. *Nat. Phys.* **7**, 80 (2011)
20. E. Breckenfeld, N. Bronn, J. Karthik, A.R. Damodaran, S. Lee, N. Mason, L.W. Martin, Effect of growth induced (non) stoichiometry on interfacial conductance in $\text{LaAlO}_3/\text{SrTiO}_3$. *Phys. Rev. Lett.* **110**, 196804 (2013)
21. Z.Q. Liu, C.J. Li, W.M. Lu, X.H. Huang, Z. Huang, S.W. Zeng, X.P. Qiu, L.S. Huang, A. Annadi, J.S. Chen, J.M.D. Coey, T. Venkatesan, Ariando, Origin of the Two-Dimensional Electron Gas at $\text{LaAlO}_3/\text{SrTiO}_3$ Interfaces: The Role of Oxygen Vacancies and Electronic Reconstruction. *Phys. Rev. X* **3**, 021010 (2013)
22. J. Lee, A.A. Demkov, Charge origin and localization at the n-type $\text{SrTiO}_3/\text{LaAlO}_3$ interface. *Phys. Rev. B* **78**, 193104 (2008)
23. Y. Segal, J.H. Ngai, J.W. Reiner, F.J. Walker, C.H. Ahn, X-ray photoemission studies of the metal-insulator transition in $\text{LaAlO}_3/\text{SrTiO}_3$ structures grown by molecular beam epitaxy. *Phys. Rev. B* **80**, 241107 (2009)
24. R. Pentcheva, W.E. Pickett, Electronic phenomena at complex oxide interfaces: Insights from first principles. *J. Phys. Condens. Matter* **22**, 043001 (2010)
25. M. Takizawa, S. Tsuda, T. Susaki, H.Y. Hwang, A. Fujimori, Electronic charges and electric potential at $\text{LaAlO}_3/\text{SrTiO}_3$ interfaces studied by core-level photoemission spectroscopy. *Phys. Rev. B* **84**, 245124 (2011)
26. G. Berner, A. Mueller, F. Pfaff, J. Walde, C. Richter, J. Mannhart, S. Thiess, A. Gloskovskii, W. Drube, M. Sing, R. Claessen, Band alignment in $\text{LaAlO}_3/\text{SrTiO}_3$ oxide heterostructures inferred from hard x-ray photoelectron spectroscopy. *Phys. Rev. B* **88**, 115111 (2013)
27. M. Sing, G. Berner, K. Goss, A. Mueller, A. Ruff, A. Wetscherek, S. Thiel, J. Mannhart, S.A. Pauli, C.W. Schneider, P.R. Willmott, M. Gorgoi, F. Schaefer, R. Claessen, Profiling the Interface Electron gas of $\text{LaAlO}_3/\text{SrTiO}_3$ Heterostructures with hard X-ray photoelectron spectroscopy. *Phys. Rev. Lett.* **102**, 176805 (2009)
28. A. Savoia, D. Paparo, P. Perna, Z. Ristic, M. Salluzzo, F.M. Granozio, U.S. di Uccio, C. Richter, S. Thiel, J. Mannhart, L. Marrucci, Polar catastrophe and electronic reconstructions at the $\text{LaAlO}_3/\text{SrTiO}_3$ interface: Evidence from optical second harmonic generation. *Phys. Rev. B* **80**, 075110 (2009)
29. Y. Mukunoki, N. Nakagawa, T. Susaki, H.Y. Hwang, Atomically flat (110) SrTiO_3 and heteroepitaxy. *Appl. Phys. Lett.* **86**, 171908 (2005)
30. G. Herranz, F. Sanchez, N. Dix, M. Scigaj, J. Fontcuberta, High mobility conduction at (110) and (111) $\text{LaAlO}_3/\text{SrTiO}_3$ interfaces. *Sci. Rep.* **2**, 758 (2012)
31. A. Annadi, Q. Zhang, X.R. Wang, N. Tuzla, K. Gopinadhan, W.M. Lu, A.R. Barman, Z.Q. Liu, A. Srivastava, S. Saha, Y.L. Zhao, S.W. Zeng, S. Dhar, E. Olsson, B. Gu, S. Yunoki, S. Maekawa, H. Hilgenkamp, T. Venkatesan, Ariando, Anisotropic two-dimensional electron gas at the $\text{LaAlO}_3/\text{SrTiO}_3$ (110) interface. *Nat. Commun.* **4**, 1838 (2013)
32. Y.L. Han, S.C. Shen, J. You, H.O. Li, Z.Z. Luo, C.J. Li, G.L. Qu, C.M. Xiong, R.F. Dou, L. He, D. Naugle, G.P. Guo, J.C. Nie, Two-dimensional superconductivity at (110) $\text{LaAlO}_3/\text{SrTiO}_3$ interfaces. *Appl. Phys. Lett.* **105**, 192603 (2014)

33. G. Herranz, G. Singh, N. Bergeal, A. Jouan, J. Lesueur, J. Gazquez, M. Varela, M. Scigaj, N. Dix, F. Sanchez, J. Fontcuberta, Engineering two-dimensional superconductivity and Rashba spin-orbit coupling in LaAlO₃/SrTiO₃ quantum wells by selective orbital occupancy. *Nat. Commun.* **6**, 6028 (2015)
34. A.S. Kalabukhov, Y.A. Boikov, I.T. Serenkov, V.I. Sakharov, V.N. Popok, R. Gunnarsson, J. Borjesson, N. Ljustina, E. Olsson, D. Winkler, T. Claeson, Cationic disorder and phase segregation in LaAlO₃/SrTiO₃ Heterointerfaces evidenced by medium-energy ion spectroscopy. *Phys. Rev. Lett.* **103**, 146101 (2009)
35. S.A. Chambers, M.H. Engelhard, V. Shutthanandan, Z. Zhu, T.C. Droubay, L. Qiao, P.V. Sushko, T. Feng, H.D. Lee, T. Gustafsson, E. Garfunkel, A.B. Shah, J.M. Zuo, Q.M. Ramasse, Instability, intermixing and electronic structure at the epitaxial LaAlO₃/SrTiO₃(001) heterojunction. *Surf. Sci. Rep.* **65**, 317 (2010)
36. L. Qiao, T.C. Droubay, T. Varga, M.E. Bowden, V. Shutthanandan, Z. Zhu, T.C. Kaspar, S.A. Chambers, Epitaxial growth, structure, and intermixing at the LaAlO₃/SrTiO₃ interface as the film stoichiometry is varied. *Phys. Rev. B* **83**, 085408 (2011)
37. R. Yamamoto, C. Bell, Y. Hikita, H.Y. Hwang, H. Nakamura, T. Kimura, Y. Wakabayashi, Structural comparison of n-type and p-type LaAlO₃/SrTiO₃ interfaces. *Phys. Rev. Lett.* **107**, 036104 (2011)
38. Y. Fujishima, Y. Tokura, T. Arima, S. Uchida, Optical-conductivity spectra of Sr_{1-x}La_xTiO₃-filling-dependent effect of the electron correlation. *Phys. Rev. B* **46**, 11167 (1992)
39. M. Takizawa, H. Watati, K. Tanaka, M. Hashimoto, T. Yoshida, A. Fujimori, A. Chikamatsu, H. Kumigashira, M. Oshima, K. Shibuya, T. Mihara, T. Ohnishi, M. Lippmaa, M. Kawasaki, H. Koinuma, S. Okamoto, A.J. Millis, Photoemission from buried interfaces in SrTiO₃/LaTiO₃ superlattices. *Phys. Rev. Lett.* **97**, 057601 (2006)
40. G. Herranz, M. Basletic, M. Bibes, C. Carretero, E. Tafrá, E. Jacquet, K. Bouzehouane, C. Deranlot, A. Hamzic, J.-M. Broto, A. Barthelemy, A. Fert, High mobility in LaAlO₃/SrTiO₃ heterostructures: Origin, dimensionality, and perspectives. *Phys. Rev. Lett.* **98**, 216803 (2007)
41. Y.L. Han, Y.W. Fang, Z.Z. Yang, C.J. Li, L. He, S.C. Shen, Z.Z. Luo, G.L. Qu, C.M. Xiong, R.F. Dou, X. Wei, L. Gu, C.G. Duan, J.C. Nie, Reconstruction of electrostatic field at the interface leads to formation of two-dimensional electron gas at multivalent (110) LaAlO₃/SrTiO₃ interfaces. *Phys. Rev. B* **92**, 115304 (2015)
42. N. Reyren, S. Thiel, A.D. Caviglia, L.F. Kourkoutis, G. Hammerl, C. Richter, C.W. Schneider, T. Kopp, A.-S. Ruetschi, D. Jaccard, M. Gabay, D.A. Muller, J.-M. Triscone, J. Mannhart, Superconducting interfaces between insulating oxides. *Science* **317**(5842), 1196–1199 (2007)
43. G.E.D.K. Prawiroatmodjo, F. Trier, D.V. Christensen, Y. Chen, N. Pryds, T.S. Jespersen, Evidence of weak superconductivity at the room-temperature grown LaAlO₃/SrTiO₃ interface. *Phys. Rev. B* **93**, 184504 (2016)
44. G. De Luca, A. Rubano, E. di Gennaro, A. Khare, F.M. Granozio, U.S. di Uccio, L. Marrucci, D. Paparo, Potential-well depth at amorphous-LaAlO₃/crystalline-SrTiO₃ interfaces measured by optical second harmonic generation. *Appl. Phys. Lett.* **104**, 261603 (2014)
45. Y.Z. Chen, D.V. Christensen, F. Trier, N. Pryds, A. Smith, S. Linderoth, On the origin of metallic conductivity at the interface of LaAlO₃/SrTiO₃. *Appl. Surf. Sci.* **258**, 9242–9245 (2012)
46. E. Beyreuther, D. Paparo, A. Thiessen, S. Grafstroem, L.M. Eng, Conducting and insulating LaAlO₃/SrTiO₃ interfaces: A comparative surface photovoltage investigation. *J. Appl. Phys.* **114**, 243709 (2013)
47. P. Xu, Y. Ayino, C. Cheng, V.S. Pribyl, R.B. Comes, P.V. Sushko, S.A. Chambers, B. Jalan, Predictive control over charge density in the two-dimensional Electron gas at the Polar-Nonpolar NdTiO₃/SrTiO₃ Interface. *Phys. Rev. Lett.* **117**, 106803 (2016)
48. M.P. Warusawithana, C. Richter, J.A. Mundy, P. Roy, J. Ludwig, S. Paetel, T. Heeg, A.A. Pawlicki, L.F. Kourkoutis, M. Zheng, M. Lee, B. Mulcahy, W. Zander, Y. Zhu, J. Schubert, J.N. Eckstein, D.A. Muller, C.S. Hellberg, J. Mannhart, D.G. Schlom, LaAlO₃ stoichiometry is key to electron liquid formation at LaAlO₃/SrTiO₃ interfaces. *Nat. Commun.* **4**, 2351 (2013)

49. F. Gunkel, S. Hoffmann-Eifert, R.A. Heinen, D.V. Christensen, Y.Z. Chen, N. Pryds, R. Waser, R. Dittmann, Thermodynamic ground states of complex oxide Heterointerfaces. *ACS Appl. Mater. Interfaces* **9**, 1086–1092 (2017)
50. Y.Z. Chen, N. Pryds, J.E. Kleibeuker, G. Koster, J.R. Sun, E. Stamate, B.G. Shen, G. Rijnders, S. Linderoth, Metallic and insulating interfaces of amorphous SrTiO₃-based oxide Heterostructures. *Nano Lett.* **11**, 3774–3778 (2011)
51. S.W. Lee, Y.Q. Liu, J. Heo, R.G. Gordon, Creation and control of two-dimensional Electron gas using Al-based amorphous oxides/SrTiO₃ Heterostructures grown by atomic layer deposition. *Nano Lett.* **12**, 4775–4783 (2012)
52. C.J. Li, Y.P. Hong, H.X. Xue, X.X. Wang, Y.C. Li, K.J. Liu, W.M. Jiang, M.R. Liu, L. He, R.F. Dou, C.M. Xiong, J.C. Nie, Formation of two-dimensional Electron gas at Amorphous/crystalline oxide interfaces. *Sci. Rep.* **8**, 404 (2018)
53. M. Basletic, J.-L. Maurice, C. Carretero, G. Herranz, O. Copie, M. Bibes, E. Jacquet, K. Bouzehouane, S. Fusil, A. Barthelemy, Mapping the spatial distribution of charge carriers in LaAlO₃/SrTiO₃ heterostructures. *Nat. Mater.* **7**(8), 621–625 (2008)
54. O. Copie, V. Garcia, C. Boedefeld, C. Carretero, M. Bibes, G. Herranz, E. Jacquet, J.-L. Maurice, B. Vinter, S. Fusil, K. Bouzehouane, H. Jaffres, A. Barthelemy, Towards two-dimensional metallic behavior at LaAlO₃/SrTiO₃ interfaces. *Phys. Rev. Lett.* **102**, 216804 (2009)
55. B.C. Huang, Y.-P. Chiu, P.C. Huang, W.C. Wang, V.T. Tra, J.C. Yang, Q. He, J.Y. Lin, C.S. Chang, Y.H. Chu, Mapping band alignment across complex oxide Heterointerfaces. *Phys. Rev. Lett.* **109**(24), 246807 (2012)
56. M. Ben Shalom, C.W. Tai, Y. Lereah, M. Sachs, E. Levy, D. Rakhmilevitch, A. Palevski, Y. Dagan, Anisotropic magnetotransport at the SrTiO₃/LaAlO₃ interface. *Phys. Rev. B* **80**, 140403 (2009)
57. H.X. Xue, C.J. Li, Y.P. Hong, X.X. Wang, Y.C. Li, K.J. Liu, W.M. Jiang, M.R. Liu, L. He, R.F. Dou, C.M. Xiong, J.C. Nie, Temperature dependence of the conductive layer thickness at the LaAlO₃/SrTiO₃ heterointerface. *Phys. Rev. B* **96**, 235310 (2017)
58. D. Saint-James, P.G. Gennes, Onset of superconductivity in decreasing fields. *Phys. Lett.* **7**, 306 (1963)
59. M. Strongin, O.F. Kammerer, D.G. Schweitzer, P.P. Craig, A. Paskin, Surface superconductivity in type 1+type 2 superconductors. *Phys. Rev. Lett.* **12**, 442 (1964)
60. V.L. Ginzburg, On surface superconductivity. *Phys. Lett.* **13**, 101 (1964)
61. M. Strongin, O.F. Kammerer, J.E. Crow, R.D. Parks, D.H. Douglass, M.A. Jensen, Enhanced superconductivity in layered metallic films. *Phys. Rev. Lett.* **21**, 1320 (1968)
62. S. Gariglio, M. Gabay, J. Mannhart, J.-M. Triscone, Interface superconductivity. *Physica C* **514**, 189–198 (2015)
63. G. Logvenov, A. Gozar, I. Bozovic, High-temperature superconductivity in a single copper-oxygen plane. *Science* **326**, 699 (2009)
64. G. Binnig, A. Baratoff, H.E. Hoenig, J.G. Bednorz, 2-band superconductivity in Nb doped SrTiO₃. *Phys. Rev. Lett.* **45**(16), 1352 (1980)
65. V. Koerting, Q.S. Yuan, P.J. Hirschfeld, T. Kopp, J. Mannhart, Interface-mediated pairing in field effect devices. *Phys. Rev. B* **71**(10), 104510 (2005)
66. N. Pavlenko, T. Kopp, Electrostatic interface tuning in correlated superconducting heterostructures. *Phys. Rev. B* **72**(17), 174516 (2005)
67. V. Berezinskii, Destruction of long-range order in one-dimensional and 2-dimensional systems having a continuous symmetry group 1-classical systems. *Sov. Phys. JETP* **32**, 493–500 (1971)
68. V. Berezinskii, Destruction of long-range order in one-dimensional and 2-dimensional systems possessing a continuous symmetry group.2. Quantum systems. *Sov. Phys. JETP* **34**, 610 (1972)
69. J.M. Kosterlitz, D.J. Thouless, Long-range order and metastability in 2-dimensional solids and superfluids. *J. Phys. C* **5**(11), L124 (1972)

70. J.M. Kosterlitz, D.J. Thouless, Ordering, metastability and phase-transitions in 2 dimensional systems. *J. Phys. C* **6**(7), 1181 (1973)
71. J.V. José, *40 Years of Berezinskii-Kosterlitz-Thouless Theory[M]*. (World Scientific, Singapore, 2013)
72. M. Beasley, J.E. Mooij, T.P. Orlando, Possibility of vortex-antivortex pair dissociation in 2-dimensional superconductors. *Phys. Rev. Lett.* **42**(17), 1165 (1979)
73. M. Gabay, A. Kapitulnik, Vortex-antivortex crystallization in thin superconducting and superfluid films. *Phys. Rev. Lett.* **71**(13), 2138 (1993)
74. K. Medvedyeva, B.J. Kim, P. Minnhagen, Analysis of current-voltage characteristics of two-dimensional superconductors: Finite-size scaling behavior in the vicinity of the Kosterlitz-Thouless transition. *Phys. Rev. B* **62**(21), 14531 (2000)
75. B.I. Halperin, D.R. Nelson, Resistive transition in superconducting films. *J. Low Temp. Phys.* **36**(5–6), 599–616 (1979)
76. N. Reyren, S. Gariglio, A.D. Caviglia, D. Jaccard, T. Schneider, J.–M. Triscone, Anisotropy of the superconducting transport properties of the $\text{LaAlO}_3/\text{SrTiO}_3$ interface. *Appl. Phys. Lett.* **94**(11), 112506 (2009)
77. J. Biscaras, N. Bergeal, A. Kushwaha, T. Wolf, A. Rastogi, R.C. Budhani, J. Lesueur, Two-dimensional superconductivity at a Mott insulator/band insulator interface $\text{LaTiO}_3/\text{SrTiO}_3$. *Nat. Commun.* **1**, 89 (2010)
78. J. Biscaras, N. Bergeal, S. Hurand, C. Grossetete, A. Rastogi, R.C. Budhani, D. LeBoeuf, C. Proust, J. Lesueur, Two-dimensional superconducting phase in $\text{LaTiO}_3/\text{SrTiO}_3$ Heterostructures induced by high-mobility carrier doping. *Phys. Rev. Lett.* **108**(24), 247004 (2012)
79. D. Fuchs, R. Schaefer, A. Sleem, R. Schneider, R. Thelen, H. von Loehneysen, Two-dimensional superconductivity between SrTiO_3 and amorphous Al_2O_3 . *Appl. Phys. Lett.* **105**(9), 092602 (2014)
80. C.H. Ahn, A. Bhattacharya, M. Di Ventra, J.N. Eckstein, C.D. Frisbie, M.E. Gershenson, A.M. Goldman, I.H. Inoue, J. Mannhart, A.J. Millis, A.F. Morpurgo, D. Natelson, J.M. Triscone, Electrostatic modification of novel materials. *Rev. Mod. Phys.* **78**(4), 1185 (2006)
81. A.D. Caviglia, S. Gariglio, N. Reyren, D. Jaccard, T. Schneider, M. Gabay, S. Thiel, G. Hammerl, J. Mannhart, J.-M. Triscone, Electric field control of the $\text{LaAlO}_3/\text{SrTiO}_3$ interface ground state. *Nature* **456**(7222), 624–627 (2008)
82. C. Richter, H. Boschker, W. Dietsche, E. Fillis-Tsirakis, R. Jany, F. Loder, L.F. Kourkoutis, D.A. Muller, J.R. Kirtley, C.W. Schneider, J. Mannhart, Interface superconductor with gap behaviour like a high-temperature superconductor. *Nature* **502**(7472), 528–531 (2013)
83. S.C. Shen, B.B. Chen, H.X. Xue, G. Cao, C.J. Li, X.X. Wang, Y.P. Hong, G.P. Guo, R.F. Dou, C.M. Xiong, L. He, J.C. Nie, Gate dependence of upper critical field in superconducting (110) $\text{LaAlO}_3/\text{SrTiO}_3$ interface. *Sci. Rep.* **6**, 28379 (2016)
84. G.E.D.K. Prawiroatmodjo, M. Leijnse, F. Trier, Y.Z. Chen, D.V. Christensen, M. von Soosten, N. Pryds, T.S. Jespersen, Transport and excitations in a negative-U quantum dot at the $\text{LaAlO}_3/\text{SrTiO}_3$ interface. *Nat. Commun.* **8**, 395 (2017)
85. G. Singh, A. Jouan, L. Benfatto, F. Couedo, P. Kumar, A. Dogra, R.C. Budhani, S. Caprara, M. Grilli, E. Lesne, A. Barthelemy, M. Bibes, C. Feuillet-Palma, J. Lesueur, N. Bergeal, Competition between electron pairing and phase coherence in superconducting interfaces. *Nat. Commun.* **9**, 407 (2018)
86. Z.Y. Chen, A.G. Swartz, H. Yoon, H. Inoue, T. Merz, D. Lu, Y.W. Xie, H.T. Yuan, Y. Hikita, S. Raghu, H.Y. Hwang, Carrier density and disorder tuned superconductor-metal transition in a two-dimensional electron system. *Nat. Commun.* **9**, 4008 (2018)
87. A. Brinkman, M. Huijben, M. Van Zalk, J. Huijben, U. Zeitler, J.C. Maan, W.G. Van der Wiel, G. Rijnders, D.H.A. Blank, H. Hilgenkamp, Magnetic effects at the interface between non-magnetic oxides. *Nat. Mater.* **6**(7), 493–496 (2007)
88. Z. Salman, O. Ofer, M. Radovic, H. Hao, M. Ben Shalom, K.H. Chow, Y. Dagan, M.D. Hossain, C.D.P. Levy, W.A. MacFarlane, G.M. Morris, L. Patthey, M.R. Pearson, H. Saadaoui, T. Schmitt, D. Wang, R.F. Kiefl, Nature of weak magnetism in $\text{SrTiO}_3/\text{LaAlO}_3$ multilayers. *Phys. Rev. Lett.* **109**(25), 257207 (2012)

89. B. Kalisky, J.A. Bert, B.B. Klopfer, C. Bell, H. Sato, M. Hosoda, Y. Hikita, H.Y. Hwang, K.A. Moler, Critical thickness for ferromagnetism in $\text{LaAlO}_3/\text{SrTiO}_3$ heterostructures. *Nat. Commun.* **3**, 922 (2012)
90. J.-S. Lee, Y.W. Xie, H.K. Sato, C. Bell, Y. Hikita, H.Y. Hwang, C.-C. Kao, Titanium d(xy) ferromagnetism at the $\text{LaAlO}_3/\text{SrTiO}_3$ interface. *Nat. Mater.* **12**(8), 703–706 (2013)
91. F. Bi, M.C. Huang, S. Ryu, H. Lee, C.W. Bark, C.B. Eom, P. Irvin, J. Levy, Room-temperature electronically-controlled ferromagnetism at the $\text{LaAlO}_3/\text{SrTiO}_3$ interface. *Nat. Commun.* **5**, 5019 (2014)
92. D. Dikin, M. Mehta, C.W. Bark, C.M. Folkman, C.B. Eom, V. Chandrasekhar, Coexistence of superconductivity and ferromagnetism in two dimensions. *Phys. Rev. Lett.* **107**(5), 056802 (2011)
93. Ariando, X. Wang, G. Baskaran, Z.Q. Liu, J. Huijben, J.B. Yi, A. Annadi, A.R. Barman, A. Rusydi, S. Dhar, Y.P. Feng, J. Ding, H. Hilgenkamp, T. Venkatesan, Electronic phase separation at the $\text{LaAlO}_3/\text{SrTiO}_3$ interface. *Nat. Commun.* **2**, 188 (2011)
94. L. Li, C. Richter, J. Mannhart, R.C. Ashoori, Coexistence of magnetic order and two-dimensional superconductivity at $\text{LaAlO}_3/\text{SrTiO}_3$ interfaces. *Nat. Phys.* **7**(10), 762–766 (2011)
95. J.A. Bert, B. Kalisky, C. Bell, M. Kim, Y. Hikita, H.Y. Hwang, K.A. Moler, Direct imaging of the coexistence of ferromagnetism and superconductivity at the $\text{LaAlO}_3/\text{SrTiO}_3$ interface. *Nat. Phys.* **7**(10), 767–771 (2011)
96. N. Pavlenko, T. Kopp, E.Y. Tsymbal, G.A. Sawatzky, J. Mannhart, Magnetic and superconducting phases at the $\text{LaAlO}_3/\text{SrTiO}_3$ interface: The role of interfacial Ti 3d electrons. *Phys. Rev. B* **85**(2), 020407 (2012)
97. Shen S. C., Xing Y., Wang P. J., Liu H. W., Fu H. L., Zhang Y. W., He L., Xie X. C., Lin X., Nie J. C., and Wang J., Observation of quantum Griffiths singularity and ferromagnetism at superconducting $\text{LaAlO}_3/\text{SrTiO}_3(110)$ Interface, *Phys. Rev. B*, 2016, 94: 144517
98. K. Michaeli, A.C. Potter, P.A. Lee, Superconducting and ferromagnetic phases in $\text{SrTiO}_3/\text{LaAlO}_3$ oxide interface structures: Possibility of finite momentum pairing. *Phys. Rev. Lett.* **108**, 117003 (2012)
99. P. Fulde, R.A. Ferrell, Superconductivity in strong spin-exchange field. *Phys. Rev.* **135**(3A), A550 (1964)
100. A.I. Larkin, Y.N. Ovchinnikov, Inhomogeneous state of superconductors. *Sov. Phys. JETP* **20**, 762–769 (1965)
101. M.S. Scheurer, J. Schmalian, Topological superconductivity and unconventional pairing in oxide interfaces. *Nat. Commun.* **6**, 6005 (2015)
102. M.M. Mehta, D.A. Dikin, C.W. Bark, S. Ryu, C.M. Folkman, C.B. Eom, V. Chandrasekhar, Evidence for charge-vortex duality at the $\text{LaAlO}_3/\text{SrTiO}_3$ interface. *Nat. Commun.* **3**, 955 (2012)
103. J.A. Bert, K.C. Nowack, B. Kalisky, H. Noad, J.R. Kirtley, C. Bell, H. Sato, M. Hosoda, Y. Hikita, H.Y. Hwang, K.A. Moler, Gate-tuned superfluid density at the superconducting $\text{LaAlO}_3/\text{SrTiO}_3$ interface. *Phys. Rev. B* **86**(6), 060503 (2012)
104. L. Benfatto, C. Castellani, T. Giamarchi, Broadening of the Berezinskii-Kosterlitz-Thouless superconducting transition by inhomogeneity and finite-size effects. *Phys. Rev. B* **80**(21), 214506 (2009)
105. S. Caprara, M. Grilli, L. Benfatto, C. Castellani, Effective medium theory for superconducting layers: A systematic analysis including space correlation effects. *Phys. Rev. B* **84**(1), 014514 (2011)
106. S. Caprara, F. Peronaci, M. Grilli, Intrinsic instability of electronic interfaces with strong Rashba coupling. *Phys. Rev. Lett.* **109**(19), 196401 (2012)
107. S. Caprara, J. Biscaras, N. Bergeal, D. Bucheli, S. Hurand, C. Feuillet-Palma, A. Rastogi, R.C. Budhani, J. Lesueur, M. Grilli, Multiband superconductivity and nanoscale inhomogeneity at oxide interfaces. *Phys. Rev. B* **88**(2), 020504 (2013)
108. S. Banerjee, O. Erten, M. Randeria, Ferromagnetic exchange, spin-orbit coupling and spiral magnetism at the $\text{LaAlO}_3/\text{SrTiO}_3$ interface. *Nat. Phys.* **9**(10), 626–630 (2013)

109. Y. Maeno, H. Hashimoto, K. Yoshida, S. Nishizaki, T. Fujita, J.G. Bednorz, F. Lichtenberg, Superconductivity in a layered perovskite without copper. *Nature* **372**, 532 (1994)
110. Y. Maeno, S. Nishizaki, K. Yoshida, S. Ikeda, T. Fujita, Normal-state and superconducting properties of Sr_2RuO_4 . *J. Low Temp. Phys.* **105**, 1577 (1996)
111. K. Ishida, Y. Kitaoka, K. Asayama, S. Ikeda, S. Nishizaki, Y. Maeno, K. Yoshida, T. Fujita, Anisotropic pairing in superconducting Sr_2RuO_4 : Ru NMR and NQR studies. *Phys. Rev. B* **56**, R505 (1997)
112. A.P. Mackenzie, R.K.W. Haselwimmer, A.W. Tyler, G.G. Lonzarich, Y. Mori, S. Nishizaki, Y. Maeno, Extremely strong dependence of superconductivity on disorder in Sr_2RuO_4 . *Phys. Rev. Lett.* **80**, 161 (1998)
113. K. Yada, S. Onari, Y. Tanaka, J. Inoue, Electrically controlled superconducting states at the heterointerface $\text{SrTiO}_3/\text{LaAlO}_3$. *Phys. Rev. B* **80**, 140509 (2009)
114. V. Kozii, L. Fu, Odd-parity superconductivity in the vicinity of inversion symmetry breaking in spin-orbit-coupled systems. *Phys. Rev. Lett.* **115**, 207002 (2015)
115. S. Nakosai, Y. Tanaka, N. Nagaosa, Topological superconductivity in bilayer Rashba system. *Phys. Rev. Lett.* **108**, 147003 (2012)
116. D. Stornaiuolo, D. Massarotti, R. Di Capua, P. Lucignano, G.P. Pepe, M. Salluzzo, F. Tafuri, Signatures of unconventional superconductivity in the $\text{LaAlO}_3/\text{SrTiO}_3$ two-dimensional system. *Phys. Rev. B* **95**, 140502R (2017)
117. D.A. Wollman, D.J. Vanharlingen, J. Giapintzakis, D.M. Ginsberg, Evidence for $d(x^2-y^2)$ pairing from the magnetic-field modulation of $\text{YBa}_2\text{Cu}_3\text{O}_{7-\delta}$ Josephson-junctions. *Phys. Rev. Lett.* **74**, 797 (1995)
118. R. Jin, Y. Zadorozhny, Y. Liu, D.G. Schlom, Y. Mori, Y. Maeno, *Phys. Rev. B* **59**, 4433 (1999)
119. C.C. Tsuei, J.R. Kirtley, Pairing symmetry in cuprate superconductors. *Rev. Mod. Phys.* **72**, 969 (2000)
120. R. Jin, Y. Liu, Z.Q. Mao, Y. Maeno, Experimental observation of the selection rule in Josephson coupling between in and Sr_2RuO_4 . *Europhys. Lett.* **51**, 341 (2000)
121. I. Bonalde, B.D. Yanoff, M.B. Salamon, D.J. Van Harlingen, E.M.E. Chia, Z.Q. Mao, Y. Maeno, Temperature dependence of the penetration depth in Sr_2RuO_4 : Evidence for nodes in the gap function. *Phys. Rev. Lett.* **85**, 4775 (2000)
122. A. Sumiyama, T. Endo, Y. Oda, Y. Yoshida, A. Mukai, A. Ono, Y. Onuki, The Josephson effect in contacts between the spin-triplet superconductor Sr_2RuO_4 and conventional superconductors. *Physica C* **367**, 129 (2002)
123. S.K. Yip, O.F.D. Bonfim, P. Kumar, Supercurrent tunneling between conventional and unconventional superconductors—a Ginzburg-Landau approach. *Phys. Rev. B* **41**, 11214 (1990)
124. Y. Liu, K.D. Nelson, Z.Q. Mao, R. Jin, Y. Maeno, Tunneling and phase-sensitive studies of the pairing symmetry in Sr_2RuO_4 . *J. Low Temp. Phys.* **131**, 1059 (2003)
125. C.W. Hicks, D.O. Brodsky, E.A. Yelland, A.S. Gibbs, J.A.N. Bruin, M.E. Barber, S.D. Edkins, K. Nishimura, S. Yonezawa, Y. Maeno, A.P. Mackenzie, Strong increase of T-c of Sr_2RuO_4 under both tensile and compressive strain. *Science* **344**, 283 (2014)
126. S. Sachdev, *Quantum phase transitions[M]* (Cambridge University Press, Cambridge, 2011)
127. S.L. Sondhi, S.M. Girvin, J.P. Carini, D. Shahar, Continuous quantum phase transitions. *Rev. Mod. Phys.* **69**(1), 315 (1997)
128. L. Carr, *Understanding Quantum Phase Transitions[M]*. City (CRC, 2010)
129. J.S. Parker, D.E. Read, A. Kumar, P. Xiong, Superconducting quantum phase transitions tuned by magnetic impurity and magnetic field in ultrathin a-Pb films. *Europhys. Lett.* **75**(6), 950 (2006)
130. A.F. Hebard, M.A. Paalanen, Magnetic-field-tuned superconductor-insulator transition in 2-dimensional films. *Phys. Rev. Lett.* **65**(7), 927 (1990)
131. G. Sambandamurthy, L.W. Engel, A. Johansson, D. Shahar, Superconductivity-related insulating behavior. *Phys. Rev. Lett.* **92**(10), 107005 (2004)

132. T.I. Baturina, J. Bentner, C. Strunk, M.R. Baklanov, A. Satta, From quantum corrections to magnetic-field-tuned superconductor-insulator quantum phase transition in TIN films. *Physica B* **359**, 500–502 (2005)
133. M. Strongin, R.S. Thompson, O.F. Kammerer, J.E. Crow, Destruction of superconductivity in disordered near-monolayer films. *Phys. Rev. B* **1**(3), 1078 (1970)
134. R.C. Dynes, J.P. Garno, J.M. Rowell, 2-dimensional electrical-conductivity in quench-condensed metal-films. *Phys. Rev. Lett.* **40**(7), 479 (1978)
135. S. Oh, T.A. Crane, D.J. Van Harlingen, J.N. Eckstein, Doping controlled superconductor-insulator transition in $\text{Bi}_2\text{Sr}_{2-x}\text{La}_x\text{CaCu}_2\text{O}_{8+\delta}$. *Phys. Rev. Lett.* **96**(10), 107003 (2006)
136. K. Semba, A. Matsuda, Superconductor-to-insulator transition and transport properties of underdoped $\text{YBa}_2\text{Cu}_3\text{O}_y$ crystals. *Phys. Rev. Lett.* **86**(3), 496 (2001)
137. K.A. Parendo, K.H. Sarwa, B. Tan, A. Bhattacharya, M. Eblen-Zayas, N.E. Staley, A.M. Goldman, Electrostatic tuning of the superconductor-insulator transition in two dimensions. *Phys. Rev. Lett.* **94**(19), 197004 (2005)
138. A. Goldman, Superconductor-insulator transitions. *Int. J. Mod. Phys. B* **24**(20–21), 4081–4101 (2010)
139. V.F. Gantmakher, V.T. Dolgoplov, Superconductor-insulator quantum phase transition. *Physics-Uspokhi* **53**(1), 1–49 (2010)
140. Y.-H. Lin, J. Nelson, A.M. Goldman, Superconductivity of very thin films: The superconductor-insulator transition. *Physica C* **514**, 130–141 (2015)
141. S. Maekawa, H. Fukuyama, Localization effects in two-dimensional superconductors. *J. Phys. Soc. Jpn.* **51**(5), 1380–1385 (1982)
142. H. Ebisawa, H. Fukuyama, S. Maekawa, Superconducting transition-temperature of dirty thin films in weakly localized regime. *J. Phys. Soc. Jpn.* **54**(6), 2257–2268 (1985)
143. A.M. Finkelshtein, Superconducting transition-temperature in amorphous films. *JETP Lett.* **45**(1), 46–49 (1987)
144. M.P.A. Fisher, Quantum phase-transitions in disordered 2-dimensional superconductors. *Phys. Rev. Lett.* **65**(7), 923 (1990)
145. M.P.A. Fisher, G. Grinstein, S.M. Girvin, Presence of quantum diffusion in two dimensions: Universal resistance at the superconductor-insulator transition. *Phys. Rev. Lett.* **64**(5), 587 (1990)
146. M.-C. Cha, M.P.A. Fisher, S.M. Girvin, M. Wallin, A.P. Young, Universal conductivity of 2-dimensional films at the superconductor-insulator transition. *Phys. Rev. B* **44**(13), 6883 (1991)
147. D.B. Haviland, Y. Liu, A.M. Goldman, Onset of superconductivity in the two-dimensional limit. *Phys. Rev. Lett.* **62**(18), 2180 (1989)
148. A. Larkin, Superconductor-insulator transitions in films and bulk materials. *Ann. Phys.* **8**(7–9), 785–794 (1999)
149. Y.M. Strel'niker, A. Frydman, S. Havlin, Percolation model for the superconductor-insulator transition in granular films. *Phys. Rev. B* **76**(22), 224528 (2007)
150. J. Biscaras, N. Bergeal, S. Hurand, C. Feuillet-Palma, A. Rastogi, R.C. Budhani, M. Grilli, S. Caprara, J. Lesueur, Multiple quantum criticality in a two-dimensional superconductor. *Nat. Mater.* **12**(6), 542–548 (2013)
151. Y. Xing, H.M. Zhang, H.L. Fu, H.W. Liu, Y. Sun, J.P. Peng, F. Wang, X. Lin, X.C. Ma, Q.K. Xue, J. Wang, X.C. Xie, Quantum Griffiths singularity of superconductor - metal transition in Ga thin films. *Science* **350**, 542 (2015)
152. X.Y. Shi, P.V. Lin, T. Sasagawa, V. Dobrosavljević, D. Popović, Two-stage magnetic-field-tuned superconductor-insulator transition in underdoped $\text{La}_{2-x}\text{Sr}_x\text{CuO}_4$. *Nat. Phys.* **10**(6), 437–443 (2014)

Chapter 13

Prospects of Superconducting Magnet Technology in the Medical Field: A New Paradigm on the Horizon?



Santosh Miryala

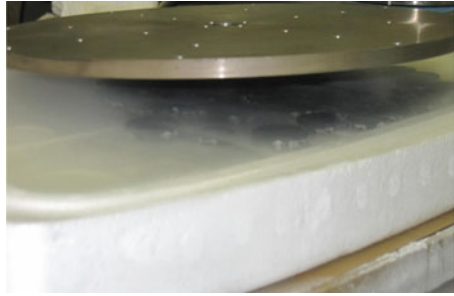
13.1 Introduction

The discovery of magnetism dates back to 600 BC where a Greek shepherd, Magnes, had first observed it when ferrule of his stick was attracted to a magnetic rock [1]. In 1600, a notable Englishman called Dr. William Gilbert had successfully examined the properties of magnetism through scientific method and was able to publish his experimental results in *De Magnete* [2]. During 1911, prominent Dutch physicist Heike Kamerlingh Onnes had first noted superconductivity in mercury at Leiden University and had initially suggested the construction of electromagnets along with superconducting wire [3]. Further, G.B. Yntema had attained the development of very first superconducting magnet by utilizing niobium wire which had produced a magnetic field of 0.7 T at 4.2 K [4]. In 1987, high temperature superconductivity was discovered by prominent IBM researchers—Georg Bednorz and K. Alex Muller—that had opened a door for numerous families of new materials ranging from BSCCO to YBCO [5, 6]. This new class of materials obtains the potential of exhibiting its superconducting properties at temperatures above liquid nitrogen's boiling point (77.3 K) and showcases its potential of trapping high magnetic fields within an order of magnitude 100 times higher compared to hardest ferromagnetic materials. As a result, melt-processed YBCO single-grain superconducting disks are capable of exhibiting levitation principle that could be applied for human levitation platform (see Fig. 13.1). Further, it is intriguing to note that all of these materials have a common feature of being different forms of copper oxide. During 2007, a magnet with YBCO windings had attained a world record magnetic field of 26.8 tesla. Finally, National High Magnetic Laboratory was able to produce an YBCO magnet in 2017 with strength of 32 tesla [7].

S. Miryala (✉)

Faculty of Arts and Science, University of Toronto, Toronto, ON, Canada
e-mail: santoshjuly6@gmail.com

Fig. 13.1 Levitation of heavy disk utilizing a repulsive force between melt-processed $\text{YBa}_2\text{Cu}_3\text{O}_y$ pellets and Fe-Nd-B magnets



13.2 Classification of Magnets

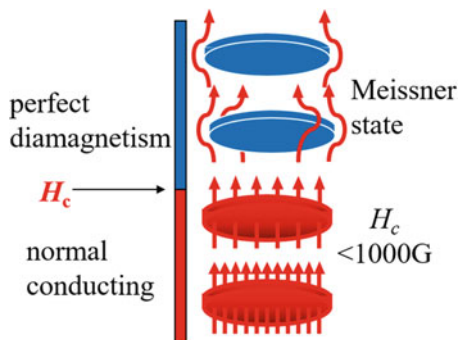
In theory, magnets are classified as materials that exert a certain magnetic field. It is general to note that magnets are normally classified in two areas: electromagnets and permanent magnets. Electromagnet is a type of magnet where magnetic field is extensively generated from an electric current; whereas, permanent magnet is a type of material that is capable of producing its own persistent magnetic field [8]. On the other hand, superconducting magnets are normally wrapped around by superconducting wires since a minimal to zero power dissipation is observed due to its zero resistivity. Furthermore, superconducting magnets are able to produce strong magnetic fields but are somewhat limited in practical applications by the significant parameters of superconducting sample. Due to the aforementioned reason, researchers from worldwide are investing great efforts to enhance the superconducting magnetic performance to further produce high critical current density.

13.3 Fundamental Properties of Super-Conducting Materials

13.3.1 *Meissner Effect*

The Meissner effect is a phenomenon that enables expulsion of magnetic field within a superconductor where transition is observed from normal state to superconducting state (see in Fig. 13.2): this property prevents the penetration of external magnetic field [9]. In 1933, two notable German researchers, Robert Ochsenfeld and Walther Meissner, had discovered this effect as they both observed the field distribution of magnetic properties outside of superconducting lead and tin samples [10]. It is intriguing to note that this property was detected in an indirect manner as exterior field had increased with a proportional decrease within interior field. Furthermore, this early experiment suggested that superconductors obtained the

Fig. 13.2 Diagram of Meissner effect. Magnetic field lines (represented as arrows) are excluded from a superconductor when it is below its critical temperature



ability of expulsion effect due to their unique nature of equilibrium that was established due to the neutralization processes within unit cell of superconducting magnetic materials. However, more recently researchers remarked the implications of Meissner effect in regard to the fabrication of small, powerful superconducting magnets for Nuclear Magnetic Resonance (NMR) applications.

13.3.2 Type I and Type II Superconductors

Type I superconductors are commonly indicated as soft superconductors due to their nature of easily losing their superconducting properties and for perfectly obeying Meissner effect. In theory, type I superconductors are distinguished materials that lose its superconductivity abruptly within its presence in an external magnetic field (see Fig. 13.3, left); therefore, they will keep out the total magnetic field as the critical applied field H_c had been attained. Hence, type I superconductor would not be considered as a conventional superconductor above a certain field. On the other hand, Shubnikov and Rjabinin had experimentally discovered type II superconductors that are characterized by their unique establishment of magnetic vortices with an applied magnetic field (see Fig. 13.3, right); furthermore, this key phenomenon is observed when the superconducting material reaches above a critical field strength H_{c1} [11]. Moreover, type II superconductors enables a wider range of technological applications due to flow of current throughout the material and their ability to not exhibiting a perfect Meissner Effect. All high temperature superconductors are categorized as type II and present an intermediate Mixed State, allowing the magnetic flux to penetrate the material in a quantized fashion. This property allows superconducting super-magnets attractive for several industrial applications.

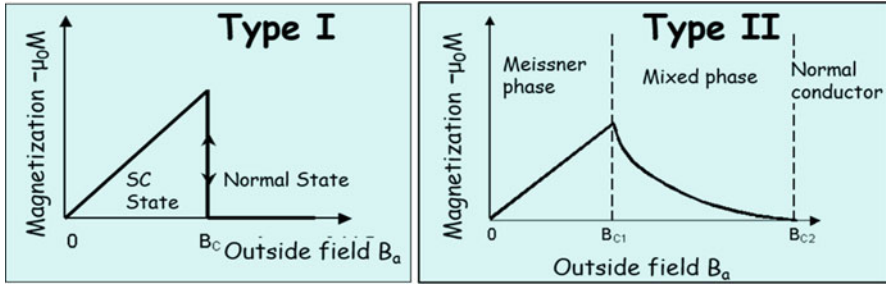


Fig. 13.3 Phase diagram for a type I (left) and type II (right) superconductor

13.4 Applications of Superconducting Magnetic Technology in Medicine

13.4.1 Magnetic Resonance Imaging (MRI)

Magnetic resonance imaging (MRI) is a medical imaging technique used in radiology to generate pictures of the anatomy and the physiological processes of the body in both health and disease situations. MRI scanners use strong magnetic fields, magnetic field gradients, utilizing the superconducting super-magnets. Among all medical facilities, magnetic resonance imaging proved to dominate the current commercial market by utilizing superconductors as it had established a \$3.5 billion outcome so far [12]. MRI was first discovered by Paul Lauterbur in 1973 and had proved to be a rich tool for medical research. Its uses include magnetic resonance spectroscopy, magnetic resonance elastography, magnetic transfer contrast, functional magnetic resonance imaging, and MRI angiography [13]. It should be noted that functional magnetic resonance imaging is utilized to investigate and analyze brain functional system in animals and humans. Additionally, functional magnetic resonance imaging is operated in a manner where it will detect paramagnetic deoxy-hemoglobin's magnetic field which will affect MRI signal; thus, it effectively helps to indicate the location of neural activity within MRI scan [14]. The methodology of locating brain activity is indicated as blood oxygen level dependence fMRI (BOLD) and is currently going through an extensive research enhancement towards the development of medical applications that identifies brain pathologies.

In terms of development of superconducting magnets in MRI, Thierry Schild and Denis Le Bihan had indicated that 11.7 T under 500 MHz resonance frequencies proves to be the world's strongest MRI magnet [15]. The magnetic scanner is able to generate images within the scale of 100 μm , establishing innovative biomarkers towards neurological disorders. Furthermore, Rory Warner from Tesla Engineering showed that utilization of 70 UHF whole body superconducting magnets allows a great reduction in weight along with no cryogen costs for its associated operation [13].

Numerous researchers around the world postulate that high temperature superconductors will play a valuable role in future prospects of MRI. In recent days, most of the commercial MRI devices were employed with low temperature superconductors as they utilize NbTi wires to function. Thus, high temperature superconductors were only utilized in MRI for construction of experimental RF receiver coils. Also, it is intriguing to note that HTS requires fabrication of cost-effective cryogenic systems; however, HTS wires at present status are extremely expensive and NbTi wires are 100 times cheaper [16]. Further, HTS materials comes with additional disadvantages such as limited manipulability compared to NbTi wires due to their defined geometry and length. In addition, HTS materials possess a sub-optimal pinning within a range of 77 K. Due to the reasons addressed above research institutions worldwide are investing great efforts to successfully produce a MRI where HTS will substitute NbTi wires.

13.4.2 Magnetic Drug Delivery System (MDDS)

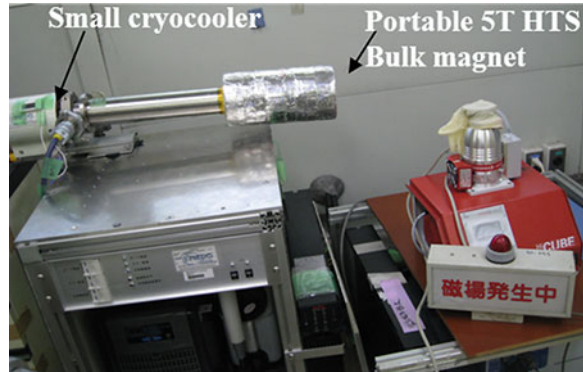
A small sized 20 mm melt-processed Y-123 superconductor bulk pellet is demonstrated to trap large magnetic fields with an extremely high field gradient. This allowed scientists to implement a magnetic drug delivery system.

When a drug is consumed in a conventional manner to treat a medical condition, it is widely noted that just a small percentage of drug will reach and tackle the targeted site. Thus, conventional methodologies of consuming a drug might result as a waste and in the most severe cases drugs might even harm the human body. The main essence of Magnetic Drug Delivery System (MDDS) is that it will effectively transport and operate drug delivery to the targeted region with the highest accuracy. In terms of historical aspect, the research and development of MDDS had begun in 1970s. At that time, medical researchers and physicians did not have powerful magnets to produce a magnetic force strong enough to systematically guide magnetically seeded drug (containing ferromagnetic fine particles) to locally cure certain lesions. More recently, MDDS becomes a fundamental therapy technology employing a superconducting magnetic force, which allows to deliver high concentration drug targeting a diseased organ. This will lead to eradication and reduction of high toxicity levels within a normal tissue and will also show a promising role in the future of DDS. In the recent days, Hitachi had developed DDS that successfully utilizes single-grain Gd-123 material (see in Fig. 13.4).

13.4.3 Medical Accelerators in Cancer Therapy

In the current generation, cancer is regarded as a second leading cause of death for both males and females. According to National Institute of Health, during a period of 1990–2006, cancer mortality rate in the United States had tremendously

Fig. 13.4 Next generation of magnetic drug delivery system (MDDS) apparatus developed under the NEDO support at Tokyo Women Medical University utilizing the high temperature bulk Gd-123 superconducting super-magnets



decreased from 215 to 175 per 100,000 people in a population as novel treatment methodologies had been developed [17]. Moreover, radiotherapy serves as a significant treatment technique towards cancer as radiation is capable of killing cancerous cells while sparing healthy tissues of a body. In the recent days, more than 90% of radiation therapy utilizes powerful energy of Bremsstrahlung radiation supplied from electron linear accelerators.

The recent technology enabled superconducting magnets to play a powerful role in cyclotron accelerators within hadron therapy. Pursuing this topic further, this is a particular form of radiation treatment that effectively utilizes ionized particle beams in the place of X-ray to operate on pediatric cancer tumors [18]. The implementation of high field superconducting cyclotrons had captured the attention of numerous physicists worldwide as it was an option of compact accelerators that decreased high operating costs along with inconvenient infrastructure. On the other hand, one can note that basic magnetic design and configuration of superconducting cyclotrons are somewhat exactly the same as resistive magnetbased cyclotrons originally proposed by Lawrence.

More recently, an innovative, conceptual design of compact superconducting synchrocyclotron, without iron in its core design, had been developed. It is essential to note that light weight concentric field shaping coils would replace heavy iron pole tips as it displayed the potential of generating powerful beams through high acceleration [19]. As a whole, iron-free design could further expand clinical treatment and studies as a single facility can operate on numerous ion species ranging from carbon to ion. Also, this newly developed innovation would enable radiation oncologist to utilize best type of treatment for each type of cancer associated with the patient.

13.4.4 Nuclear Magnetic Resonance (NMR)

More recently, Nuclear Magnetic Resonance (NMR) had become a widely utilized medical imaging technique in which conventional superconducting magnetic materials are widely used. It is evident that NMR imaging possess a wide range of advantages as it may replace several medical diagnostic techniques which include positron emission tomography scan, CT scanning, myelograms, digital subtraction radiography, angiogram, and so on [20]. NMR imaging plays a promising role to measure blood flow to detect future strokes, examine soft-tissues within kidney, brain, and liver, and conduct high magnetic field chemical biopsy [21]. However, the successful implementation of superconducting magnet NMR imaging within hospitals will be dependent on economic, political, and technical factors.

NMR scanning functioned as a fundamental tool for drug discovery along with protein structure determination. The protein structure is an essential property to comprehend its biochemical function along with its biological properties [22]. Thus, superconducting magnets within core of NMR spectrometer enabled scientists to analyze protein structure with high precision, resolution, and homogeneity. Continuous support from research and development of superconducting magnets for NMR facilities is essential to envision the future advancement of NMR imaging [23].

13.4.5 Magnetoencephalography (MEG)

Magnetoencephalography (MEG) is a crucial technique within clinical and basic neuroscience research as it enables scientists to closely study the brain activity by recording high magnetic field generated by neural currents [24]. In terms of mechanical structure, MEG is operated by high- T_c superconducting quantum interference devices (SQUID), using liquid nitrogen rather than liquid helium as a coolant. Moreover, high- T_c MEG had demonstrated its capability of examining new rhythms which is an essential quality to act as a marker for cognitive degeneration like Alzheimer's disease [25]. Finally, it can be noted that MEG gives distinct advantages as compared to EEG and fMRI as it allows researchers to obtain temporal characteristics of brain activation with millisecond precision.

13.5 Conclusions

Superconducting magnetic technology had widely expanded in the field of medical applications, ranging from MRI to MEG. It is widely noted around the globe that medical applications count for 24% of total estimated market for superconducting

technology with significant funding opportunities. As a whole scale scenario, superconducting technology had vastly opened up innovative medical application market; however, strong leadership along with governmental support is further needed to expand the contribution of superconducting materials in medical research.

Acknowledgments I would like to thank Dr. Collin Nguyen (Director of TLS) for his kind support and encouragement in regard to my medical career aspirations. Furthermore, I am grateful for the earthwarming encouragement and love received by my family members in regards to my career developmental goals.

References

1. J. Nagamatsu, N. Nakagawa, T. Muranaka, Y. Zenitani, J. Akimitsu, *Nature* **410**, 63 (2001)
2. A.Y. Ganin, Y. Takabayashi, Y.Z. Khimiyak, S. Margadonna, A. Tamai, M.J. Rosseinsky, K. Prassides, *Nature Mat.* **7**, 367 (2008)
3. D. Drung, *Supercond. Sci. Technol.* **16**(12), 1320–1336 (2003)
4. A.I. Ahonen, M.S. Hamaliainen, M.J. Kajola, J.E.T. Knuutila, O.V. Lounasmaa, J.T. Simola, C.D. Tesche, V.A. Vilkmán, *IEEE Trans. Magn.* **27**, 2793 (1991)
5. J.G. Bednorz, K.A.Z. Müller, *Phys. B* **64**, 189–193 (1986)
6. E.H. Brandt, *Appl. Phys. Lett.* **53**, 1554–1556 (1988)
7. N. Del-Valle, A. Sanchez, D.X. Navau Chen, *IEEE Trans. Appl. Supercond.* **19**, 2070–2074 (2009)
8. M. Santosh, *Acta Phys. Pol. A* **126**, 808 (2014)
9. M. Santosh, M.R. Koblichka, *Europ. J. Phys. Educ.* **5**, 1 (2014)
10. M. Santosh, *Oxide Thin Films, in Multilayers, and Nanocomposites*, ed. by P. Mele, T. Endo, S. Arisawa, C. Li, T. Tsuchiya, (Springer, New York, 2015), p. 97
11. Weinstein, R., Chen, I. G., Liu, J., Xu, J., Obot, V., & Foster, C., *73*(10), 6533–6535 (1993)
12. D. Le Bihan, T. Schild, *Supercond. Sci. Technol.* **30**, 033003 (2017)
13. M. Parizh, Y. Lvovsky, M. Sumption, *Supercond. Sci. Technol.* **30**, 014007 (2017)
14. C. Poole, T. Baig, R. Deissler, M. Martens, *IEEE Trans. Appl. Supercond.* **27**, 4700605 (2017)
15. N. Amemiya, K. Akachi, *Supercond. Sci. Technol.* **21**, 095001 (2008)
16. J. Ling, J. Voccio, S. Hahn, T. Qu, J. Bascuñán, Y. Iwasa, *Supercond. Sci. Technol.* **30**, 024011 (2017)
17. D. Krischel et al., *IEEE Trans. Appl. Supercond.* **17**(2), 2307–2310 (2007)
18. E. O. Lawrence, U.S. Patent 1 948 384, 20, (1934)
19. K.M. Subotic, Multipurpose air-core superconducting cyclotrons. *Proc. X Int. Conf. IEEE Cyclotrons Their Appl.*, 469–471 (1984)
20. M. Muralidhar, K. Suzuki, A. Ishihara, M. Jirsa, Y. Fukumoto, M. Tomita, *Supercond. Sci. Technol.* **23**, 124003 (2010)
21. M. Scippers et al., presented at the European Cyclotron Progress Meeting (ECPM), PSI, Villigen, (2012)
22. C. Bert, M. Durante, Motion in radiotherapy: Particle therapy. *Phys. Med. Biol.* **56**, R113–R144 (2011)
23. R. Strangis et al., *Proceedings of Cyclotrons and their applications* (2007), pp. 251–253
24. G. Kraft, *Prog. Part. Nucl. Phys.* **45**, S473S544 (2000)
25. E. Pedroni et al., The PSI gantry 2: A second generation proton scanning gantry. *Z. Med. Phys.* **14**, 25–34 (2004)

Editorial Note

Dear Readers,

I am pleased to deliver the Special Book “Superconductivity: From Materials Science to Practical Applications,” inspired from the Symposium A-3 “Superconducting Materials and Applications” during conference IUMRS-ICAM 2017 in Kyoto University.

The authors of this book are distinguished colleagues and friends, most of them are participants and contributors to Symposium A-3 in IUMRS-ICAM 2017. After almost 2 years, this book was finally edited and delivered today.

I would like to warmly thank my colleagues for their wonderful contributions, and everyone who strongly helped during the revision and editing of this book, with a special deserved mention to Dr. Alok K. Jha, Dr. Anna Palau, Prof. Petre Badica, and Dr. Chiara Tarantini.

Tokyo, Japan
May 9, 2019

Paolo Mele (Shibaura Institute of Technology)

Index

A

- AC magnetic response of superconductors
 - analysis, 169
 - Bi2212 single crystals, 176–177
 - superlattices, 176–177
 - YBCO films, 172–175
- Advanced MOCVD (A-MOCVD), 98, 109–113, 118, 121–123
- $AeFe_2As_2$, 272, 275–278, 284–285
- Angular regimes
 - angle dependence, 15, 16
 - HAGBs, 271
 - in-plane field angle variation, 17–21
 - wire asymmetry, 16–17
 - wire utilisation, 15
- Anisotropy
 - angular, 16, 65
 - field dependences, 3
 - H -dependent approach, 46
 - numerical models, 15
 - scaling, 218
 - structural, 197
 - superconducting properties, 261
- APCs of mixed morphologies, 31, 32, 46
- Artificial pinning centres (APCs)
 - angular behaviour, 16
 - APC/RE-123
 - matching field B_* , 40–41
 - nanocomposites, 33–35
 - pinning efficiency, 1D APCs, 36–40
 - B_{max} and matching field B_* correlation, 41–42
 - FeSCs, 254
 - heterostructures, 75

- in HTS nanocomposites, 29, 31–32
- magnetic field orientation-independent J_c , 45–48
- nanocrystals, 152
- nanoscale, 30
- REBCO films, 102–106
- strain field, 42–45
- strain-mediated in situ self-organization, 33–35
- thickness dependence (*see* Thickness dependence)
- YBCO thin films (*see* Yttrium barium copper oxide (YBCO))

B

- Bicrystal
 - BGB, 227
 - device structure, 228
 - FBS (*see* Fe-based superconductors (FBS))
 - Fe(Se,Te), 285–286
 - K-doped $Ae122$, 279
 - $LnFeAsO$, 283–284
 - LSAT and MgO, 230
 - polycrystalline bulks, 272
 - substrates, 190
- Bulks
 - FeSCs, 257
 - flux pinning structure, 85
 - metastable thin-film phase, 221
 - polycrystalline, 54
 - sintered, 272–275, 278–280
 - superconductivity (*see* Superconductivity)
 - Y-123 superconductor, 357

C

Chemical solution deposition (CSD), 135–137, 139, 141, 152, 160, 162

Co-addition of H_2O_3 and Te, 304, 305, 308, 309, 313, 319, 322

Coated conductors (CCs)

architecture

CSD, 135–137

dip-coating (*see* Dip-coating technique)

spin-coating (*see* Spin-coating technique)

YBCO precursor solution, 137–140

fabrication, 157

field dependence, 233

grain boundary network, 11

HTSc, 30

International Superconductivity

Technology Center, 234

large-scale production, 140

practical metal-tapes, 230–234

REBCO, 101

Coexistence of superconductivity and

ferromagnetism, 325, 338–340, 345

Coherent and semi-coherent interface, 67

Complex pinning structures, 5, 85

Critical current

angle dependence, 16, 18, 271

densities, 231, 253–255

density and fundamental limiting factors, 29–30

field dependence, 9, 10

local and average density, 82–88

log-log plot, 150

magnetic field, 54–55

measurement system, 21

plot, 80

relaxation-free, 178

SmBCO tape, 100

thickness dependence, 102

Critical current density (J_c)

angle dependence, 283

applied magnetic field, 54–55

doping elements, 304

electrical transport current, 253

flux pinning behavior, 255

and fundamental limiting factors, 29–30

global, 256, 273, 274, 276, 278, 281

intra-grain, 228, 257, 285, 288

iron-based superconductors, 261

J_c^{GB}/J_c , 283, 286

local, 83, 281

log-log plot, 150

measurements, 254

pinning of vortices, 54–55, 254

self-field, 117

substitutional carbon amounts, 304

YBCO (*see* Yttrium barium copper oxide (YBCO))

D

DC irreversibility line, 170, 186

Defects

α -2DEG formation, 331

categories, 150

intergrowth, 202

intrinsic, 151–152

pinning, 5

REBCO matrix, 106

semi-coherent BZO 1D APC/YBCO

interface, 37

YBCO films, 31

Y211 nanoparticles, 61

Delamination strength, 24

Density-functional-theory (DFT) calculations,

192, 202–207, 209

Devices

construction and testing, 1

Josephson junctions (JJ), 227–230

LAO/STO, 325

in situ sample transfer system, 225, 227

SQUID, 227–230

superconducting, 6

vortex pinning, 150

Dip-coating technique

and ink-jet printing, 140

YBCO precursor solutions, 145–149

E

Electrical characterisation, 3

Energy loss spectrometer (EELS), 191–193,

202, 203, 209

Epitaxy, 30, 79, 217, 292

HTS (*see* High-temperature superconductivity (HTS))

nanocomposite films

industrial metallic Ni-W substrates, 162, 163

intermediate dwelling step, 158–161

single metal oxide nanocrystals, 161, 162

1111-type, 217–218

YBCO thin films, 136

Ex-situ processing

BaF₂ process, 142

CSD deposition method, 135

fibre texture, 288

- SPS samples, 315
 - superconducting powder, 258
 - temperatures, 303
 - YBCO, 87
- F**
- Fe-based superconductors (FBS)
 - BCS paramagnetic limit, 252
 - current density, 275
 - IBAD-MgO templates, 292–295
 - polycrystalline films, 288–292
 - RABiTS substrates, 295
 - Ferromagnetism
 - coexistence, 338–339
 - superconductivity, 325, 340
 - FeSe
 - Fe(Se,Te) sintered bulks, 278–279
 - GBs, 291
 - monolayer, 224
 - structure, 226
 - temperature dependence, 226
 - Fe(Se,Te)
 - bicrystal experiments, 285–286
 - lattice mismatch, 295
 - mono- and multi-filamentary, 262
 - sintered bulks, 278–279
 - 111-type films of FeSe, 223
 - wires and bulk fabrications, 275
 - Field regimes
 - BSCCO, 8
 - dependence, 9
 - in-plane field asymmetry, 11–14
 - out-of-plane hysteresis, 9–11
 - REBCO, 8
 - Flux pinning
 - buffer/film interface, 85
 - complexity, 4
 - field dependence, 233
 - GB widths, 282
 - in-plane misorientation, 286
 - ion irradiation, 5
 - low-temperature, 5
 - nanocomposite films, 195
 - superconductor, 198
 - Fulde-Ferrell-Larkin-Ovshnikov (FFLO)
 - superconductor, 251, 252, 339
- G**
- Grain boundaries (GBs)
 - angle dependence, 271
 - charge carrier concentrations, 271
 - FBS, 269, 270
 - Fermi velocity, 269
 - network (*see* Fe-based superconductors (FBS))
 - polycrystal (*see* Polycrystal)
 - superconducting materials, 271
 - in thin films (*see* Thin films)
 - two-dimensional defects, 270
 - Granular nature, 249, 255–257
- H**
- High-temperature superconductivity (HTS)
 - bulks (*see* Bulks)
 - copper oxide, 334
 - HTScc, 30
 - materials, 30
 - MRI, 357
 - nanocomposites, 31–32
 - 2G-HTS technology (*see* Second-generation high-temperature superconductor (2G-HTS) technology)
 - wire database (*see* HTS wire database)
 - HTS wire database
 - characterisation systems, 2–3
 - large-scale applications, 1–2
 - mechanical strength, 24
 - n*-value, 21–24
 - targeted selection, 25
 - Hybrid coils, 17
- I**
- Interface superconductivity
 - coexistence, 338–339
 - LAO/STO interface, 334–335
 - pairing mechanism, 339–341
 - unconventional, 335–338
 - Ion beam assisted deposition (IBAD)
 - Ba122:P coated conductors, 232
 - and ISD approach, 135
 - MgO templates, 292–295
 - superconducting properties, 289–290
 - texturing, 17
 - YSZ buffer, 81, 86
 - YSZ layer, 79
 - Ion irradiation, 5, 10, 33, 55, 59
 - Iron-based superconductors (FeSCs)
 - categorized, 243–244
 - general properties, 246–247
 - superconducting materials, 246
 - T_c family, 244
 - temperature dependence, 244
 - transition temperature, 245

- Iron-based superconductors (FeSCs) (*cont.*)
 upper critical field, 250–253
 zero resistivity, 243
- Irreversibility field, 9, 53, 73, 116, 117, 263, 264, 307, 315–320
- L**
- LaAlO₃/SrTiO₃ (LAO/STO) heterojunction
 conductivity mechanism, 329
 discovery and formation, 326–327
 interface, 332
 phase diagram, 339
 superconductivity and ferromagnetism, 338
 2D superconductivity, 334–335
 2DEG, 325, 342
 unconventional superconductivity, 335–338
- Ln*FeAsO, 272–275, 283–284
- M**
- Magnetic drug delivery system (MDDS), 357, 358
- Magnetic field
 critical current density, 54–56
 double logarithmic plots, 156
 economical mass production, 134
 HTS devices, 32
 log-log plot, 150
 nanocolumns, 133
 orientation-independent J_c , 45–48
 out-of-plane sample rotation, 2
 temperature, 5
 YBCO films, 54–55
- Magnetic resonance imaging (MRI), 15, 19–21, 356–357, 359
- Magnetism
 Cu atoms, 204
 scientific method, 353
 superconducting thin films, 214
- Magnetoencephalography (MEG), 359
- Medical accelerators, 357–358
- Metal organic chemical vapor deposition (MOCVD)
 A-MOCVD, 98, 109–113
 BZO/REBCO films, 121–123
 microstructure features, 90
 REBCO films, 114–117
 thick films growth, 107–109
 YBCO films, 91
- MgB₂
 critical current density, 315–320
 critical temperature, 307–315
 experiment, 305–307
 irreversibility field, 315–320
 pinning force, 315–320
 sample consolidation, 307–315
 separation, pinning force, 320–322
 SPS, 303
 structural and microstructural details, 307–315
 superconducting properties, 303
- Microstructure
 aberration-corrected STEM, 191
 co-added samples, 315
 extrinsic effects, 304
 HTS, 189–190
 SEM and XRD, 310
 spherical aberration correctors, 191
 STEM, 192
 vortex pinning, 190
 YBCO thin films, 190, 195–201
 Y124 intergrowth, 201–209
- Misorientation angle, 97, 190, 230, 231, 255, 269, 274, 296
- MOD, 90, 92–94, 114, 136
- Multiband nature, 247, 249, 250, 265
- N**
- Nanocomposites
 APC/RE-123 (*see* Artificial pinning centres (APCs))
 BHO DD, 46
 double-doped, 39
 epitaxy (*see* Epitaxy)
 HTS, 32–33
 YBa₂Cu₃O_{7- δ}
 formation and influence of ligands, 153–154
 intrinsic defects, 151–152
 magnetic measurements, 155–157
 secondary ion mass spectroscopy analysis, 154–155
 YBCO layer, 152–153
 ZrO₂ nanocrystals, 153
 YBCO, 47
- Nanoparticles
 BYTO, 196
 CuO, 142
 1D + 3D APCs, 63–67
 3D APCs, 45
 YBCO films, 57–59
- Nanorods
 BZO, 103, 106, 107, 109, 114, 172, 179

GdBCO film matrix, 57
 nano-columnar, 75
 size and density, 117–121
 vortex-kink formation, 171
 Nanoscale inclusions, 66–68
 Nonlinear regime, 170
 Nuclear magnetic resonance (NMR), 355, 359
 Nucleation and growth, 157, 198
 n -value, 2, 21–24

O

One-dimensional (1D) APCs
 BZO and BHO, 48
 c -axis aligned, 32
 magnetic vortices, 31
 matching field B_* , 40–41
 pinning efficiency, 36–40
 self-organization, 34
 Operating current margin, 14, 20
 Oxygen vacancies, 55, 151, 206–208, 249,
 328, 329, 331

P

Pinned vortex liquid, 177, 186
 Pinning efficiency
 APCs, 31–32
 challenges and critical issues, 32–33
 critical current density, 29–30
 fundamental limiting factors, 29–30
 Pinning force
 analysis, 293–294
 1D APCs, 31
 density, 41, 55
 irreversibility, 150
 LF-YBCO thin film, 152
 magnetic field dependence, 220
 parameters, 304
 Pinning time, 177, 184, 186
 Polycrystal
 $AeFe_2As_2$, 275–278
 FeSe, 278–279
 Fe(Se,Te) sintered bulks, 278–279
 $LnFeAsO$, 272–275
 mean-field percolation model, 281
 SHPM, 281
 sintered bulks, 280
 Powder in tube (PIT), 257–260, 262, 264,
 272–282, 292
 Pulsed laser deposition (PLD), 33, 54, 76, 79,
 133, 201, 217, 326
 fabrication, 100
 films

BHO-doped REBCO, 105
 EuBCO and GdBCO, 93
 grown phase formation, 217
 RABiTS, 87
 superconducting properties, 289–290
 YBCO films, 55–56
 YBCO+YSZ film, 63
 p-wave superconductor, 340

R

REBCO films, 75, 97, 101–106, 114–117, 122,
 123
 Relationship between microstructure and
 pinning force
 B_{max} and matching field B_* correlation,
 41–42
 1D APC/RE-123 interface, 36–40
 magnetic field orientation, 45–48
 matching field B_* , 40–41
 strain field, 42–45
 strain-mediated in situ self-organization,
 33–35
 Rolling-assisted bi-axially textured substrates
 (RABiTS), 12, 17, 87, 105, 135,
 230, 231, 295

S

Scanning transmission electron microscopy
 (STEM)
 aberration-corrected, 191, 195
 HAADF, 143, 148, 160
 micrographs, 106
 plane-view bright-field, 294
 Secondary ion mass spectroscopy (SIMS), 154,
 155
 Second-generation high-temperature
 superconductor (2G-HTS)
 technology
 APC, 75
 categories, 75
 critical current density, 82–88
 microstructure deterioration, 74
 misoriented grain formation, 90–94
 non-optimized deposition process, 74
 recent progress, 96–102
 self-field effects, 94–96
 utilization, 75
 YBCO deposition, 73
 Single crystal
 Bi2212, 176–177
 in-plane texture quality, 97
 SrTiO₃, 76

- Single crystal (*cont.*)
 and tape samples, 80
 YBCO, 54
 YSZ substrates, 77, 79
 ZrO₂-doped YBCO layers, 152
- Spark plasma sinterin (SPS), 303–309, 313, 315, 322
- Spin-coating technique
 CHEMAT, 141
 important aspects, 140
 structural properties, 143–144
 thermal process, 140–142
 YBCO precursor solutions, 141
- Spin triplet pairing, 340
- SuperCurrent I_c measurement system, 3
- Superconducting paring mechanism, 213
- Superconducting wires and tapes, 8, 255, 257–263
- Superconductivity
 coupling, 325
 discovery and formation, 326–327
 Fe-As-Fe bond angles, 245
 Fermi level, 214
 inhomogeneous distribution, 155
 interface conductivity, 331–333
 iron-based superconductors, 215
 LAO/STO, 325
 Meissner effect, 354–355
 multiband, 249–250
 origin of 2DEG, 327–331
 type I and type II superconductors, 355–356
 water-/strain-induced, 220
- Superconductor insulator/metal transition, 341–343
- Superconductors
 antiferromagnetic metal, 213
 APCs (*see* Artificial pinning centres (APCs))
 and dielectric buffer layers, 12
 FeSCs (*see* Iron-based superconductors (FeSCs))
 general properties, 246–247
 in-plane angle dependence, 19
 insulator/metal transition, 341–343
 magnetic behavior, 248–249
 magnetic fields, 6
 materials, 214–216
 MgB₂ (*see* MgB₂)
 multiband, 249–250
 YBa₂Cu₃O_{7- δ} (*see* YBa₂Cu₃O_{7- δ})
- Superlattices, 171, 172, 176–178, 180, 181, 185, 221
- Super-magnets
 classification of magnets, 354
 levitation, 354
 properties of magnetism, 353
- Surface modified target, 56–66, 68
- ## T
- Texture
 buffer layers, 135
 deterioration, 77
 microstructure degradation, 82
 quality degradation, 74, 94
 RABiTS, 17
- Thermal vortex fluctuations, 176
- Thick film
 MOCVD (*see* Metal organic chemical vapor deposition (MOCVD))
 2G-HTS technology (*see* Second-generation high-temperature superconductor (2G-HTS) technology)
 SrTiO₃ bicrystals, 284
- Thickness dependence
 dislocation effects, 88–90
 REBCO films, 102–106
 self-field J_c, 76–82
- Thin films
 AeFe₂As₂, 284–285
 discussion, 286–287
 Fe(Se,Te) bicrystal experiments, 285–286
 film disorder, 78
 LnFeAsO, 283–284
 microstructure, 195–201
 ID APCs, 60
 pyrolyzed layer, 136
 single crystal substrates, 54
 TEM image, 68
 11-type chalcogenide, 223–227
 1111-type oxypnictide, 217–218
 122-type pnictide, 218–223
 XRD diffraction, 144
 YBCO (*see* Yttrium barium copper oxide (YBCO))
- Traction transformer, 5–8
- Transition metal oxide interface
 2DEG, 330
 superconductivity (*see* Superconductivity)
- Transition temperature, 32, 53, 243–247, 250–253, 340
- Transmission electron microscope (TEM), 35, 40, 43, 60–66, 104–106, 143, 149, 195, 297, 307, 311, 315
- Two-dimensional electron gas (2DEG)
 discovery and formation, 326–327
 interface conductivity, 331–333

LAO/STO, 325, 340, 343
 origin, 327–331

U

Unconventional superconductivity, 335–339
 Upper critical field, 54, 179, 246, 248,
 250–253, 265, 269, 272

V

Vortex activation energy
 AC magnetic response, 172–177
 characteristic sample dimension, 170
 current density dependence, 177–180
 fluctuations, 171
 in-phase component, 170
 linear response, 170
 pinning theory, 169
 quantitative analysis, 180–186
 samples and experiments, 171–172
 Vortex hopping length, 183–186
 Vortex pinning, 55, 150–152, 159, 176, 190,
 198, 200, 201, 221, 230
 Vortex velocity, 183, 185

W

Wind power generator, 13–14
 Wire characterisation systems
 different regimes
 angular (*see* Angular regimes)
 field (*see* Field regimes)
 temperature, 4–8

measurement system, 2
 The Robinson Research Institute, 3

X

X-Ray magnetic circular dichroism (XMCD),
 192, 203, 205, 209

Y

$\text{YBa}_2\text{Cu}_3\text{O}_{7-\delta}$
 CCs architecture (*see* Coated conductors
 (CCs))
 nanocomposite architecture (*see*
 Nanocomposites)
 PLD, 133
 superconductor (*see* Superconductors)
See also Yttrium barium copper oxide
 (YBCO)
 Yttrium barium copper oxide (YBCO)
 critical current density (*see* Critical current
 density (J_c))
 high temperature superconductor, 53
 microstructure, 195–201
 PLD technique, 55–56
 secondary phases
 both nanoparticles and nanocolumns,
 1D+3D APCs, 63–66
 nanocolumns, 1D APCs, 59–63
 nanoparticles, 3D APCs, 57–59
 structure, 192–195
 surface modified target method, 56–57
 Y124 intergrowth, 201–209